RPSEA

FINAL REPORT

DE-AC26-07NT42677

Petrophysics and Tight Rock Characterization for the Application of Improved Stimulation and Production Technology in Shale

Contract 11162-23

June 26, 2016

Principal Investigators:

OSU: Jim Puckette, Jack Pashin, Peter Clark, Sayeed Mohamed, and Jeff White
GSA: David Kopaska-Merkel, Guohai Jin, Jamekia Dawson, and Denise Hills
UAB: Peter Walsh and Michael Hannon

LEGAL NOTICE

This report was prepared by the Oklahoma State University, the Geological Survey of Alabama and the University of Alabama at Birmingham as an account of work sponsored by the Research Partnership to Secure Energy for America, RPSEA. Neither RPSEA, members of RPSEA, the National Energy Technology Laboratory, the U.S. Department of Energy, nor any person acting on behalf of any of the entities:

a. MAKES ANY WARRANTY OR REPRESENTATION, EXPRESS OR IMPLIED, WITH RESPECT TO ACCURACY, COMPLETENESS, OR USEFULNESS OF THE INFORMATION CONTAINED IN THIS DOCUMENT, OR THAT THE USE OF ANY INFORMATION, APPARATUS, METHOD, OR PROCESS DISCLOSED IN THIS DOCUMENT MAY NOT INFRINGE PRIVATELY OWNED RIGHTS, OR

b. ASSUMES ANY LIABILITY WITH RESPECT TO THE USE OF, OR FOR ANY AND ALL DAMAGES RESULTING FROM THE USE OF, ANY INFORMATION, APPARATUS, METHOD, OR PROCESS DISCLOSED IN THIS DOCUMENT.

THIS IS AN INTERIM REPORT. THEREFORE, ANY DATA, CALCULATIONS, OR CONCLUSIONS REPORTED HEREIN SHOULD BE TREATED AS PRELIMINARY. REFERENCE TO TRADE NAMES OR SPECIFIC COMMERCIAL PRODUCTS, COMMODITIES, OR SERVICES IN THIS REPORT DOES NOT REPRESENT OR CONSTITUTE AN ENDORSEMENT, RECOMMENDATION, OR FAVORING BY RPSEA OR ITS CONTRACTORS OF THE SPECIFIC COMMERCIAL PRODUCT, COMMODITY, OR SERVICE.

OKLAHOMA STATE UNIVERSITY (OSU)
GEOLOGICAL SURVEY OF ALABAMA (GSA)
UNIVERSITY OF ALABAMA AT BIRMINGHAM (UAB)

Petrophysics and Tight Rock Characterization for the Application of Improved Stimulation and Production Technology in Shale

FINAL REPORT

Reporting Period: June 27, 2013- June 26, 2016

by

OSU: Jim Puckette, Jack Pashin, Peter Clark, Sayeed Mohamed, and Jeff White
GSA: David Kopaska-Merkel, Guohai Jin, Jamekia Dawson, and Denise Hills
UAB: Peter Walsh and Michael Hannon

Prepared for the Research Partnership to Secure Energy for America (RPSEA) under Contract 11122-63

Stillwater, Oklahoma
2016

EXECUTIVE SUMMARY

The rapid expansion of shale-gas development in Paleozoic rocks prompted a need to develop a systematic methodology for geologically characterizing reservoirs and identifying ways to minimize formation damage caused by fracturing fluids. To address this issue, which is encountered in both established and potential shale-gas plays, a research team consisting of Oklahoma State University, the Geological Survey of Alabama and the University of Alabama at Birmingham investigated shale-gas reservoirs representing diverse basins and ages. A multidisciplinary workflow was employed that began with geologic and petrologic characterization of cores, augmented by selected outcrops. A range of petrologic and petrophysical techniques were employed to establish the composition, fabric and pore structure and improve our understanding of how fluids move through and interact with these ultra-fine grained rocks. Petrologic techniques employed include core description, thin-section microscopy and scanning electron microscopy/energy dispersive spectroscopy (SEM/EDS), augmented by x-ray computed tomography (CT) and focused ion beam (FIB) microscopy, and discrete fracture network (DFN) modeling. Fluid (gas) flow through fractured and unfractured shale was examined under brine saturated and unsaturated conditions. Permeability of shale to gas was measured using steady flow at reservoir conditions. A new procedure called Full Immersion Pressure-Pulse Decay (FIPPD) was tested that provides permeability perpendicular and parallel to bedding. The resource potential of gas shale was evaluated using adsorption tests and modeled. Interaction of gas shale with drilling and treatment fluids was examined using immersion tests that evaluated the effects additives such as polymers and stabilizing salts on clay minerals. Maturity of gas shales was evaluated during petrologic and petrophysical characterization and tested using

nuclear magnetic resonance (NMR). These topics all address the overall objective of improved efficiency of hydraulic fracturing by understanding shale composition, thermal history, resource potential, reservoir properties and reactivity to drilling and completion fluids.

This research program examined how stimulation fluids and additives interact with shale matrix. Achieving this goal required a fundamental understanding of petrology, petrophysics, and fluid-rock interactions. The results include specific recommendation to minimize formation damage caused by fracturing fluids, improving the effectiveness of hydraulic fracturing, and decreasing the need for refracturing. Included is a manual that identifies best practices for evaluating petrology, petrophysics and fluid sensitivity in shale gas reservoirs. Our goal was to benefit operations in active shale gas plays by lowering risk and uncertainty and help bring emerging and marginal plays to market, which will be required for the natural gas industry to continue to meet market demand.

TABLE OF CONTENTS

OKLAHOMA STATE UNIVERSITY

Petrophysics and Tight Rock Characterization for the Application of Improved Stimulation and Production Technology in Shale

FINAL REPORT

Reporting Period: June 27, 2013- June 26, 2016

by

Jim Puckette, Jack Pashin, Peter Clark, Sayeed Mohamed, and Jeff White

Prepared for the Research Partnership to Secure Energy for America (RPSEA) under Contract 11122-63

Stillwater, Oklahoma
2016

TABLE OF CONTENTS

FIGURES

TABLES

OVERVIEW

Oklahoma State University (OSU), in partnership with the Geological Survey of Alabama (GSA), the University of Alabama (UA), and the University of Alabama at Birmingham (UAB), conducted a two-year study that focused on petrophysics and tight-rock characterization of shale formations. The goals of this research were to (1) improve petrophysical characterization methods, identify best practices, and propose standards for shale analysis; (2) improve understanding of fluid-rock interaction in shale; and (3) use knowledge of petrophysics and fluid-rock interactions to optimize well completions. These goals were achieved primarily through laboratory testing of core samples from Paleozoic formations in the eastern and south-central U.S. (fig. 1). Twenty eight cores representing 11 formations were selected and used in this study. Cores of the Woodford Shale in Oklahoma were augmented by outcrop sections in Missouri and Oklahoma as part of the effort to analyze the context of the Woodford Shale and stratal equivalents Chattanooga Shale and Arkansas Novaculite in a tectonic and depositional framework. A range of petrologic, petrophysical, and tight-rock analytical techniques were employed and a systematic workflow (fig. 2) was developed to serve as a model for the petrologic and petrophysical evaluation of fluid-rock interactions in shale formations.

This report follows the basic workflow to address the five major topics is shown in Figure 2. It begins with the selection of cores and geological characterization, followed by petrologic characterization, petrophysical characterization, fluid-rock interactions, and fluid evaluation and optimization. The research methods and approach to addressing each of these topics are addressed in detail in their respective sections in the report.

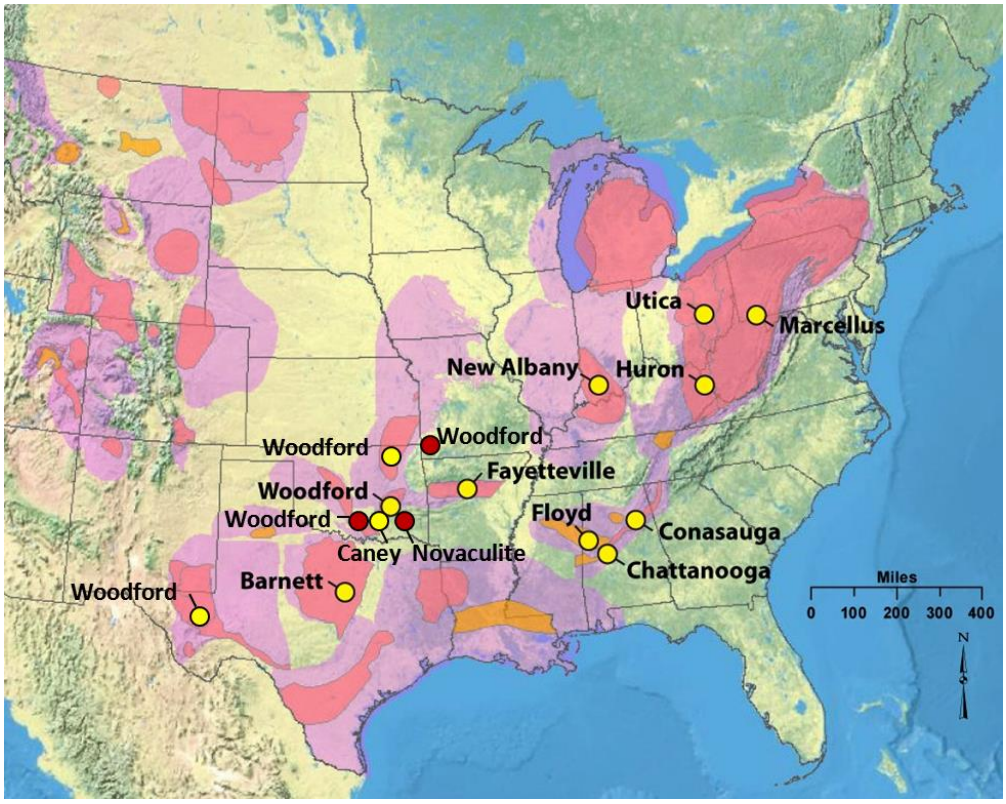

Figure 1.—Map of major Paleozoic shale plays in the eastern and south-central United States. Yellow circles highlight formations that were targeted for analysis during the proposed study. Red circles highlight outcrops. Formations studied in depth in core and/or outcrop were the Barnett Shale, Woodford Shale (Texas), Woodford Shale (Oklahoma and Missouri), Caney Shale (Oklahoma) and Arkansas Novaculite (Oklahoma), Floyd Shale (Alabama), Chattanooga Shale (Alabama) and Conasauga Shale (Alabama) (map source: Energy Information Administration).

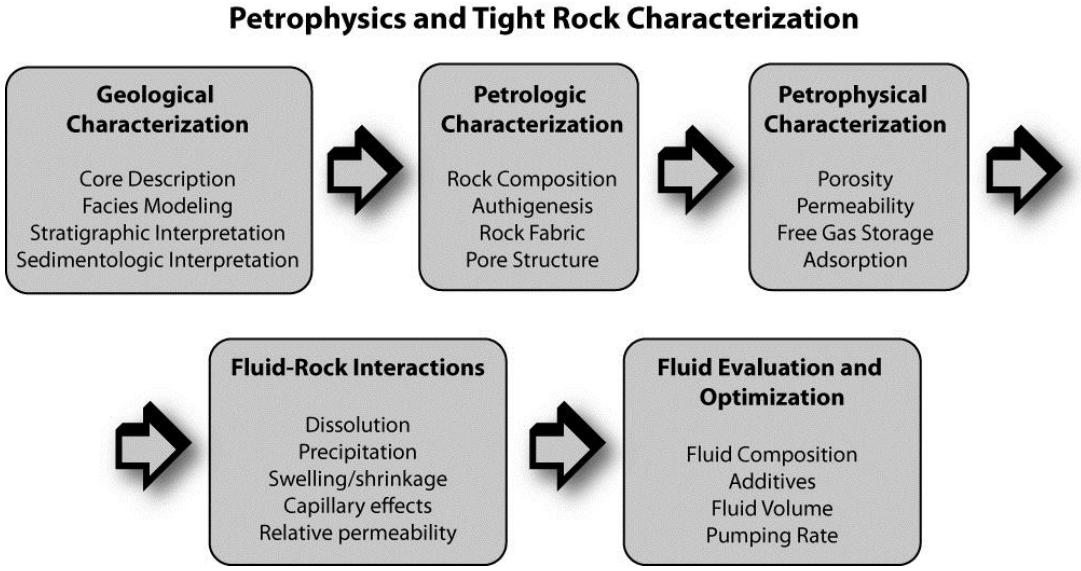

Figure 2.—Diagram showing major topics and workflow of this study.

SECTION A: GEOLOGICAL CHARACTERIZATION:
A.1. GEOLOGICAL CONTROLS OF ROCK PROPERTIES, WOODFORD SHALE, OKLAHOMA

INTRODUCTION

The Woodford Shale is a widely distributed source rock and reservoir that produces large volumes of gas and petroleum liquids across Oklahoma. Because the Woodford Shale formed as a result of deposition of sediments in different tectonic settings and resulting biogenic and depositional processes, the thickness, rock properties and production characteristics are variable and contribute to the uncertainty about what are better reservoir facies and how are they spatially distributed. Within the Arkoma basin of southeastern Oklahoma, the Woodford Shale produces from pervasively silicified mudstone that contains novaculitic chert. In the Ardmore and Marietta basins, southern Oklahoma, most Woodford Shale wells produce from the upper approximately one-third to one-fourth, which is silicified and novaculitic. In the Anadarko basin, similar upper silicified sections of the Woodford Shale are targeted. On the associated shelfal areas of the two major basins, the Anadarko and Arkoma, the Woodford Shale produces, but the controls of production are not well understood.

Much of the uncertainty concerning the best practices for exploration, drilling and completion arises from the limited knowledge of the basic geologic framework for the Woodford Shale, which formed prior to the initiation of uplift and subsidence during the Carboniferous that resulted in the tectonic landscape that presently dominates Oklahoma. While this report focuses on the Woodford Shale, the approach to analyzing the depositional and tectonic history, is applicable to emerging and developing shale plays and is but a

component in the integrated, multidisciplinary approach to shale-gas producibility proposed by Pashin et al. (2011).

PURPOSE

As part of the development of a systematic approach to gas-shale characterization, cores were secured from shale reservoirs within established and potential shale-gas plays in the U.S. However, with the decline in natural gas prices and the resulting reorganization, and in some cases sales of gas-producing properties, access to cores in certain plays was limited. With the ongoing active drilling for Woodford Shale production in Oklahoma, Woodford Shale cores were the most readily available, and least restricted. In addition, cores of the Woodford Shale section were widely distributed, providing samples, that when combined with outcrops, represented settings ranging from the shallow northern Oklahoma shelf to the Southern Oklahoma Aulacogen (SOA) and outer shelf/slope margin of the Ouachita embayment. This research shows how the sedimentary columns associated with these very different tectonic settings were influenced by water depth, degree of water circulation or stratification, and seafloor stability.

A total of nine (7) cores and three (3) outcrops table 1; fig. 1) of the Woodford Shale and equivalent Arkansas Novaculite were described and analyzed. Selected descriptions and analyses of a subset of these cores and outcrops are used to demonstrate changes in depositional facies, composition and rock properties from the more distal settings along the margin of the Ouachita embayment to the proximal settings on the northern shelf of the Oklahoma basin.

Much of the previous work on regional depositional settings of Devonian black shale is from the Appalachian basin (e.g., Rich, 1951; Ettensohn and Elam 1985; Ver Straetan et al., 2011). Studies on the Woodford Shale in Oklahoma have tended to focus source-rock potential or specific plays (Comer, 1992; Blackford, 2007; Caldwell, 2011).

Table1.—Cores and outcrops analyzed in RPSEA study

API Number: core Latitude and Longitude: outcrop	Name	Rock Units	Lithology: Ratio in percent of shale/chert for intact core	Analyses
35-073-24854	Yost 1H-18X	Woodford Shale	95/5	SEM, XRF, Spectral gamma-ray
35-017-24659	Rother 1-H-5X	Woodford Shale	93/7	SEM, XRF, Spectral gamma-ray
15-007-23996	Matthews 2-8H	Woodford Shale	100/0	SEM, XRF, Spectral gamma-ray
35-047-24455	Anderson 12-1	Woodford Shale	90/10	SEM, XRF, Spectral gamma-ray
35-015-20258	Hall 2-B	Woodford Shale	60/40* *estimated: poor core preservation	SEM, XRD, Spectral gamma-ray
35-063-23658	Poe 1-29	Woodford Shale	65/35	SEM, XRF, Spectral gamma-ray
35-119-23842	Jester 1-26	Woodford Shale	100/0	SEM, XRF
36.546164, -94.326153	Jane, MO	Woodford Shale	100/0	SEM, TOC, Spectral gamma-ray
34.374958, -96.110242	Atoka, OK	Arkansas Novaculite	15/85	SEM, Spectral gamma-ray
34.351945, -97.14884	I-35S, OK	Woodford Shale	80/20	SEM, TOC, Spectral gamma-ray

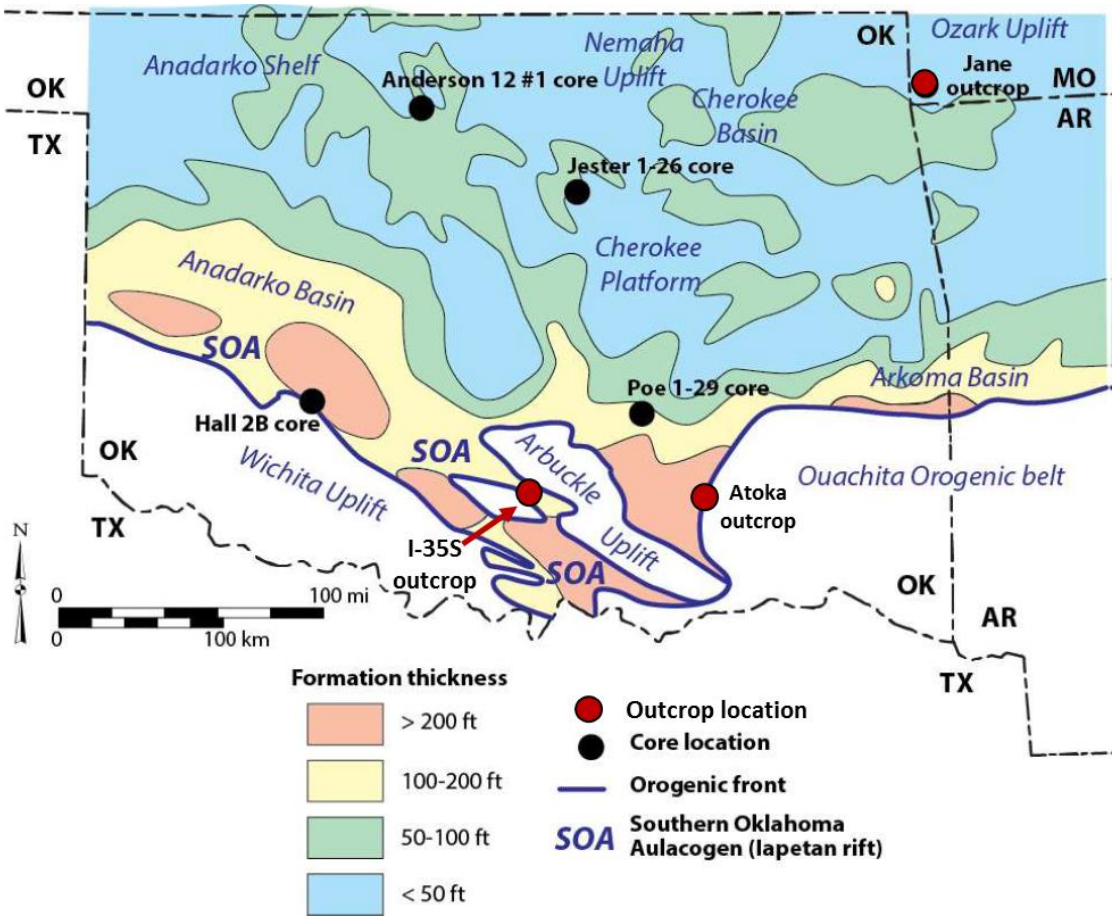

Figure 3.—Generalized map of the Woodford Shale showing locations of cores and outcrops featured in this study (after Comer, 1992).

Studies of Woodford Shale sedimentology and depositional environments include Lambert (1993), Spaw (2013) and Quan et al. (2013). This research addresses the regional depositional and tectonic context of the Woodford Shale and the time-equivalent Arkansas Novaculite in order to assess the influence of depositional setting on sediment composition, syndepositional tectonic deformation, and post-depositional modification, in particular, fracturing and cementation. Core description and thin-section petrography are combined with a number of analytical techniques including trace element geochemistry and scanning electron microscopy to provide insight into the paleoenvironments of the southern Midcontinent during the Devonian to early Mississippian. The long held interpretation that

Devonian black shales, including the Woodford Shale, represent deep-water, totally dysoxic to anoxic deposits has been replaced by interpretations that demonstrate that these shales represent dynamic depositional systems and contain multiple facies, high-energy sedimentary structures, biogenic structures and erosional discontinuities (Pashin and Ettensohn, 1992; Scheiber, 1994; Middleton et al., 2003).

Late Devonian-Early Mississippian black shale is widely distributed across eastern North America. Starting in Late Devonian, organic-rich mud was deposited in a basin that stretched from eastern Canada through the Appalachian foreland and the southern Midcontinent into southwestern U.S. (Ettensohn and Elam, 1985; Ettensohn, 1992). In the Midcontinent, the Woodford Shale and its equivalents (Figure 1) formed in a diverse set of tectonic settings that influenced depositional processes and ultimately composition and fabric, important factors for producibility.

TECTONIC SETTING

The Woodford Shale in Oklahoma accumulated in the cratonic basin called the Oklahoma basin and along the margin of the Ouachita embayment. The axis of the Oklahoma basin followed the trend of the Southern Oklahoma Aulacogen (SOA) and was a depocenter from Cambrian through Carboniferous (Mississippian). As a result, the Woodford Shale generally thickens towards the south toward the axis of the Oklahoma basin and thins to the north. Chert of biogenic origin (i.e. Comer, 1992, Fishman et al., 2010, Cecil, 2016) characterizes the Woodford Shale that formed along the rim of the Ouachita embayment and proximal to the axis of the Oklahoma Basin. Upwelling along the Ouachita embayment formed thick radiolarian chert beds of the Arkansas Novaculite and the thinner novaculitic chert beds in the Woodford Shale more removed from the embayment. The occurrence of

upwelling and associated oxygen minimum zone (OMZ) appears to distinguish Devonian shale of the Midcontinent from that of the Appalachian region (Callner, 2014).

STRATIGRAPHIC SETTING

Woodford Shale outcrops in southern Oklahoma are well studied and the sections shown to be mostly Late Devonian (Famennian), whereas the Arkansas Novaculite spans the time interval from Early Devonian to Mississippian Over, 1992; 2002). The cherty/novaculitic facies of the Woodford Shale, which forms the principal reservoir for vertical gas- and oil-producing wells in southern Oklahoma, is the primary reservoir for the western Arkoma basin Woodford Shale gas play, the first successful non-coalbed methane (CBM) unconventional gas play in the southern Midcontinent. Following the successful western Arkoma shale-gas play, a play developed on the shelf of the Anadarko basin in the chert-rich section of the upper Woodford Shale. This play, coined the CANA play after Canadian County, Oklahoma, produces gas and gas liquids. Additional plays targeting the cherty/novaculitic sections of the Woodford Shale continue to develop in the Ardmore and Marietta basins. These successful Woodford Shale plays combined two important ingredients, brittle silica-rich rocks and sufficient thermal maturity. Because thermal maturity was an important driver for the success of each Woodford Shale play, spatial distribution of the cherty facies and depth of burial within these Carboniferous basins became critical exploration criteria. As a result, understanding the origin of depositional facies and how these facies were influenced by their tectonic context and depositional settings was neglected.

METHODS and TECHNIQUES

Core from four (4) wells and two (2) outcrops in Oklahoma are supplemented with outcrop data from Missouri to form the subset of data sources featured in this report.

Standard core and outcrop descriptions included large- and small-scale descriptions of rock type, color, and sedimentary and biogenic structures including physical sedimentary structures, trace fossils, bioclasts and soft-sediment deformation. Post-depositional alteration including fracturing and cementation were documented with particular attention to the presence of cemented laminae, beds or bands, occurrence and morphology of pyrite and relative abundance of silica spherules, radiolarians, and *Tasmanites*. Over two-hundred petrographic thin sections were used to identify micro-scale sedimentary, biogenic and diagenetic features and classify rock fabric. Samples of interest were ion-milled and examined using scanning-electron microscopy to observe nanoscale features.

Natural gamma-ray spectroscopy for outcrops was collected using portable gamma-ray spectrometers (XP-1316-RS-125/230 or Exploranium GR-320 enviSPEC), while K, U, and Th measurements for core were provided or measured using the portable instrument. All data were plotted and compared with wireline gamma-ray logs for the purpose of correlating core to log and estimating the relative influence of marine and terrestrial sediment sources (Cruse and Lyons, 2004).

Energy-dispersive x-ray fluorescence (XRF) measurements were collected using a Niton™ XL3t GOLDD hand held instrument to establish qualitative estimates of selected trace elements using techniques employed by Rimmer (2004) and Ver Straeten et al. (2011). Elemental ratios were used as proxies for paleo-redox conditions during deposition and compared with values of total organic carbon (TOC) and sedimentary and biogenic features.

RESULTS

As composition and fabric are key factors controlling gas and liquids production from the Woodford Shale, this section provides a summary of each core and outcrop including

characterization of the stratigraphy and sedimentology of each section, followed by the results of the geochemical analyses. Core results are summarized first, followed by outcrop summaries.

ANDERSON 12-1, GARFIELD COUNTY, OKLAHOMA

The Anderson 12-1 core is a continuous core taken to the west of the Nemaha uplift in Garfield County, Oklahoma. The core is 121 feet long, extends from 6,824 ft. to 6,945 ft. (fig. 4) and includes all of the Woodford Shale except the uppermost fourteen feet. The Anderson 12-1 was subdivided based on sedimentary and diagenetic features and compared with the geochemical curves. Nine lithostratigraphic subdivisions were determined that correlated to six chemostratigraphic zones. These in turn were together correlated to the three generalized subdivisions (lower, middle and upper) of the Woodford Shale commonly used by industry.

Description

Interval 1, the lowermost section, extends from 6945 ft. to 6925 ft., and is light-medium gray shale with burrow mottling. It is overlain by interval 2, 6925 to 6923 ft., a siltstone with mud clasts that is in sharp contact with interval 1. Interval 3, 6923 ft. to 6914 ft., is black shale with normally graded silt laminae and concretionary phosphate and pyrite. Interval 3 contains a distinct bone bed of phosphate clasts in burrow mottled siltstone that is capped by a pyrite crust. Interval 3 contains subvertical ptygmatically folded veins of calcite and quartz that are cross cut by planar calcite-cemented fractures (Callner, 2014). Interval 4 from 6914 to 6894 ft. consists of black and gray shale with a mottled texture and few discernible laminae. The lower boundary is sharp with interval 3 and succeeded by a bone bed containing lag of vertebrate skeletal debris. The lag is succeeded by four mm-scale bundled

laminasets containing sub-mm scale horizontal laminae that fine upward. Laminasets are separated by thin dark claystone. Interval 5 extends from 6894 ft. to 6873 ft. and is black shale with fine horizontal laminae, normally and inversely graded laminae and ripple cross-laminae. Interval 6, 6873 ft. to 6862 ft., is black shale with sub-horizontal laminae with silty pyritic laminae and iron sulfide (pyrite/marcasite) concretions. Interval 7 extends from 6862 to 6845 ft. and consists of black shale with subhorizontal and ripple cross-laminae. Thin bands of cryptocrystalline quartz are associated with silty laminae and sub-millimeter spherical pyrite is common (fig. 5). Macroscopic burrows are not evident and an abundance of subhorizontal laminae suggests the interval was not extensively burrowed. Interval 8, 6845-6835 ft. is dark gray to black pyritic shale with horizontal laminae, macroscopic pyritized burrows, isolated skeletal fragments and phosphate nodules. Interval 9, the uppermost unit from 6835 ft. to 6824 ft., is black shale similar to interval 8, but lacks phosphate (fig. 5).

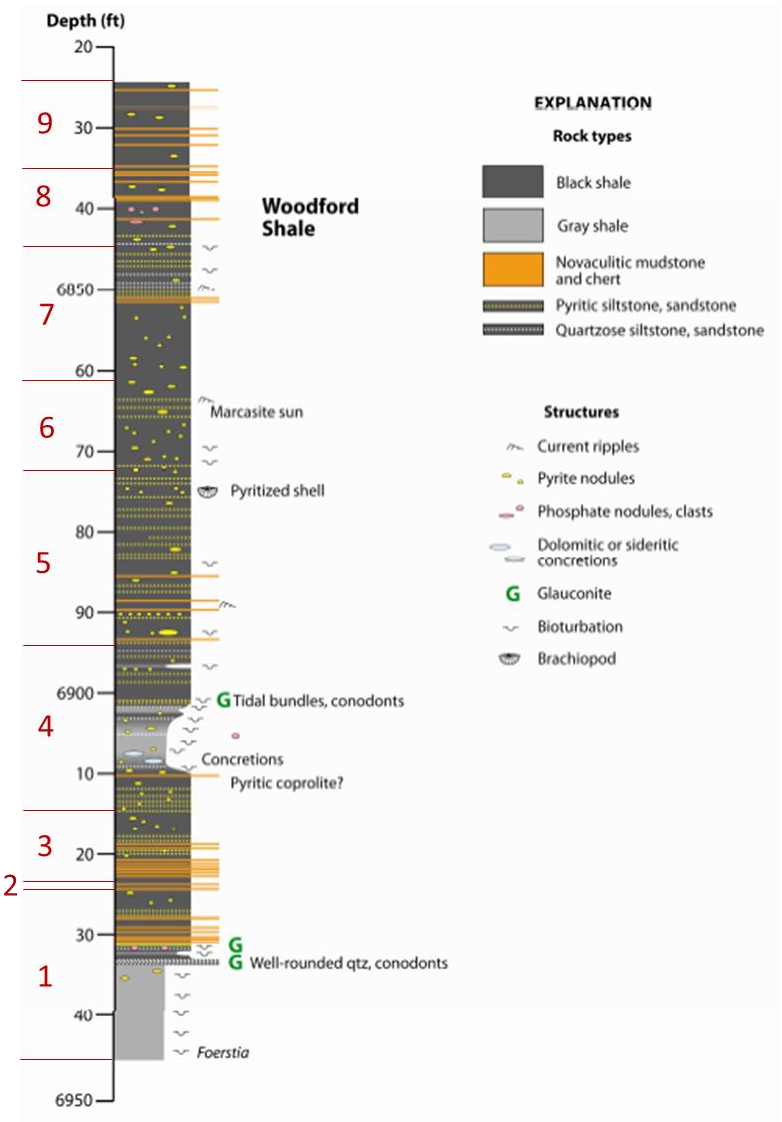

Figure 4.—Petrologic log for the Anderson 21-1 showing lithostratigraphic/chemostratigraphic subdivisions in red. Shale dominates the Woodford Shale section and novaculitic chert make up approximately 10% of the described core. After Callner (2014).

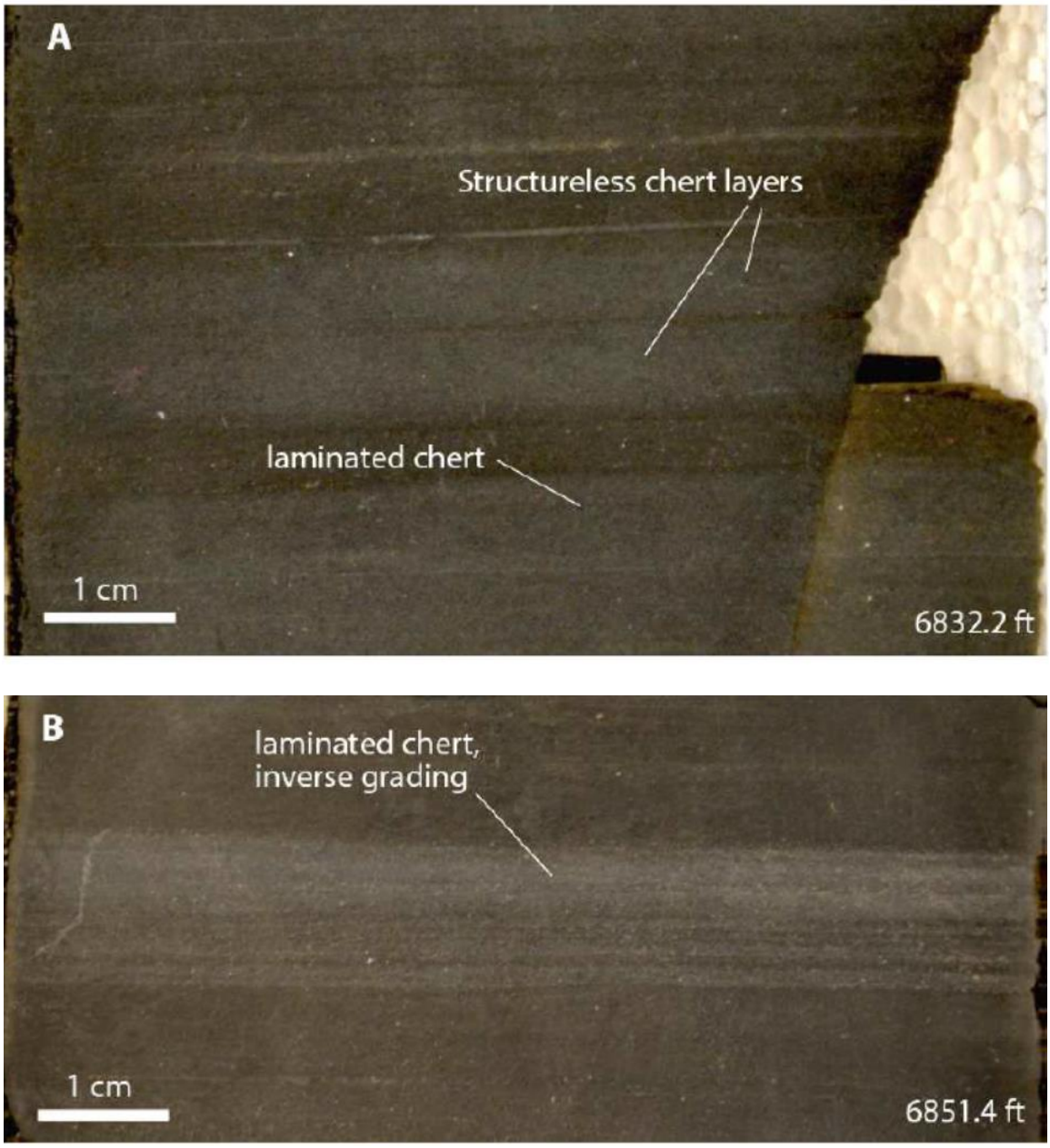

Figure 5. —Laminated chert in the Anderson 12-1. Silica in wells distal to the Ouachita embayment occurs as centimeter-scale chert laminae, which decrease in number and thickness to the north until they are absent. Images from Callner (2014).

(A) Structureless chert layers indicative of deposition in mud flow or diagenetic masking of original structure.

(B) Inversely graded chert laminae suggesting traction current during deposition.

Chemostratigraphy

Chemostratigraphic analysis provided elemental concentrations that were used as proxies to estimate paleoredox conditions. Elemental ratios V/Cr, Ni/Co and V/(V+Ni) were used to determine paleoredox of near-surface and bottom water during deposition (Rimmer, 2004). Concentrations of U, Mo and V were used together to estimate oxygen levels in bottom water or sediment pore water. Bivariate plots of sulfur (wt%) versus iron (wt %) provided an estimate of the degree or pyritization (DOPt) (Berner and Raiswell, 1983). Aluminum was used as the proxy for detrital input and phosphorous an indicator of upwelling or vertebrate skeletal material. Silicon (Si) is a qualitative indicator of increased chert and calcium (Ca) calcite cement or calcareous shale/mudstone.

Chemostratigraphic units were defined based on the relative abundances of Al, Fe, Si, U, P, Mo and V (see fig. 12, Callner, 2014). In the Anderson 12-1 core, chemostratigraphic unit A corresponds with interval 1 and the industry designated lower Woodford interval. Unit A generally has a higher concentration of Al and corresponding lower concentrations of Si, U, Mo and V. Chemostratigraphic unit B corresponds to intervals 2 and 3 and is characterized by a lower concentration of Al and higher concentrations of Si, U, Mo and V. Units C, D, and E, were delineated similarly with C and D appearing to be relatively static, whereas Unit E marks a return to increasing and fluctuating concentrations of Si, U, Mo and V, while the Al concentration decreases. Chemostratigraphic units B through E correlate to the industry designated middle Woodford interval. Unit F correlates to the industry designated upper Woodford and is characterized by decline in Mo, V and U concentrations, an increase in Si, and less fluctuation in elemental concentrations. Chemostratigraphic units B and E are

similar in that U, V and Mo concentrations increase in conjunction with TOC (see Figure 12, Callner 2014).

Elevated degree of pyritization (DOPt) values in the Anderson 12-1 core plot close to the pyrite line indicating the pyrite is the dominant sulfide mineral (Callner, 2014). Paleoredox proxies V/Cr, V/(V+Ni) and Ni/Co indicate fluctuating levels of oxygen during deposition. More oxic intervals have lower disseminated pyrite and obvious bioturbation. Increases in the values of V/Cr, V/(V+Ni) and Ni/Co around depths of 6840 ft. and 6920 ft. coincide with increased TOC, increased U, Mo and V concentrations, decreased Al concentrations, abundant pyrite and preserved laminae, all indicators of decreased oxygen levels to a state of near anoxia (fig. 6).

Hall 2-B: CADDO COUNTY, OKLAHOMA

The Hall 2-B core was recovered from a well in a fault block along the southern margin of the Anadarko Basin in Caddo County, Oklahoma. This vertical Woodford Shale well produced oil and gas from the novaculitic chert zone. The core is 122 feet long, extends from 6,156 ft. to 6,278 ft. and includes the middle and upper intervals of the Woodford Shale and five feet of the overlying Sycamore Limestone. The contact between the Woodford Shale and Sycamore Limestone is marked by a zone of fault gouge (6,162 to 6, 155 feet) containing intensely deformed Woodford and Sycamore strata. Most bedding planes dip at around 20^{o}, although numerous structural panels have dip greater than 50^{o}. Based on geophysical wireline logs, the contact between the upper and middle Woodford zones is approximately 6,238 feet. Since the entire section of the Woodford Shale was not cored or logged, basal bounding stratigraphy is not available for correlation.

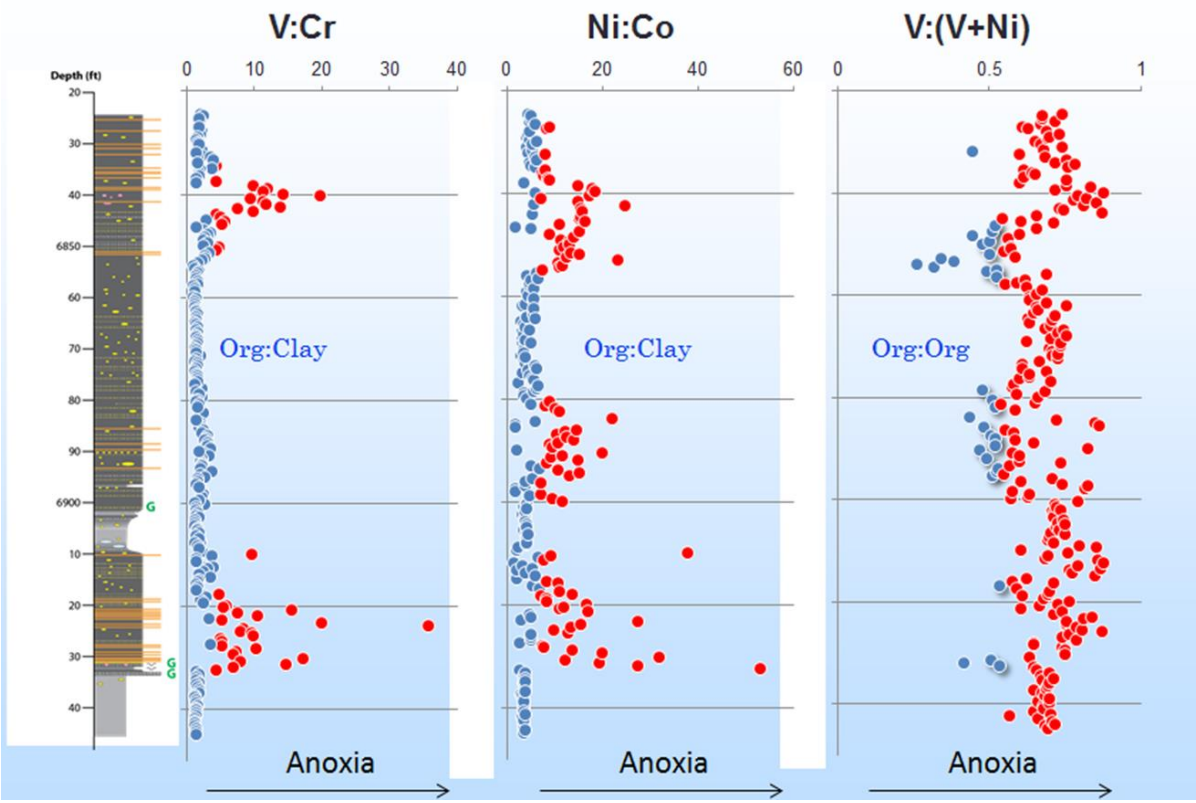

Figure 6. Ratio of selected elements in the Woodford Shale, Anderson, 12-1. The V:Cr and Ni:Co ratios indicate mostly oxygenated water associated with clay flocculation. V:(V+Ni) indicates anoxic water was more common at the water-sediment interface.

Description

The Woodford Shale in the Hall 2-B core consists primarily of laminae to thick beds of chert intercalated with laminae to thin beds of black, fissile shale (fig. 7). The cored interval was divided into five intervals by Callner (2014) based on depositional features and geochemical characteristics. The cored interval exhibits variable dip and evidence of deformation and includes 12 structural panels bounded by faults at the base and angular unconformities at the top. Numerous fractures, often filled with silica or carbonate cement, breccia layers, soft-sediment deformation and syndepositional (growth) faults are evident (figs. 8 and 9) (Callner, 2014). Stratabound fractures are abundant and typically confined to chert beds (fig. 9). Burrowing is less apparent in the Hall 2-B section than in the other

examined Woodford Shale cores. Pyrite and marcasite are present but less common than in other cores, whereas phosphate nodules are abundant (fig. 10).

Chemostratigraphy

The Hall 2-B contains five chemostratigraphic units that generally correspond to lithostratigraphic units (see fig. 16, Callner, 2014). Distinct changes in elemental concentrations of U, Mo and V are not apparent in Hall 2-B. An inverse relationship between Al and Si is evident and attributed to a non-clay source for silicon. Silicon is abundant throughout most of the core, a reflection of the high novaculitic chert content. Pyrite occurs throughout the core, but values for degree of pyritization (DOPt) are low in all but the lowermost section. Values for Ni/Co are consistent with anoxia during deposition of most of the Woodford Shale. High values for V/(V+Ni) indicate even more restricted conditions and possibly euxinia. However, the V/Cr values fall within the dysoxic to suboxic and anoxic range. The scarcity of burrowing in the Hall 2-B core supports the interpretation that during deposition bottom water was oxygen deficient.

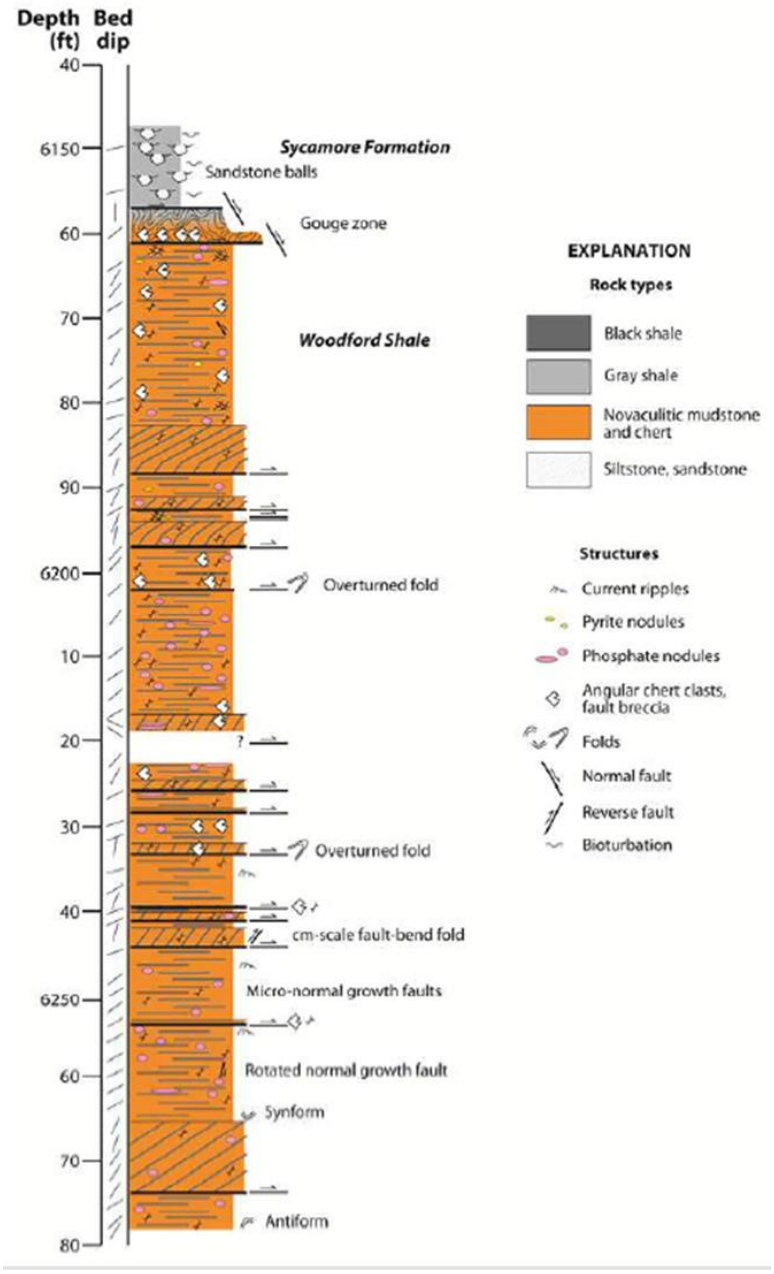

Figure 7.—Petrologic log for the Hall 2-B core that is estimated to be more than 40% novaculitic chert.

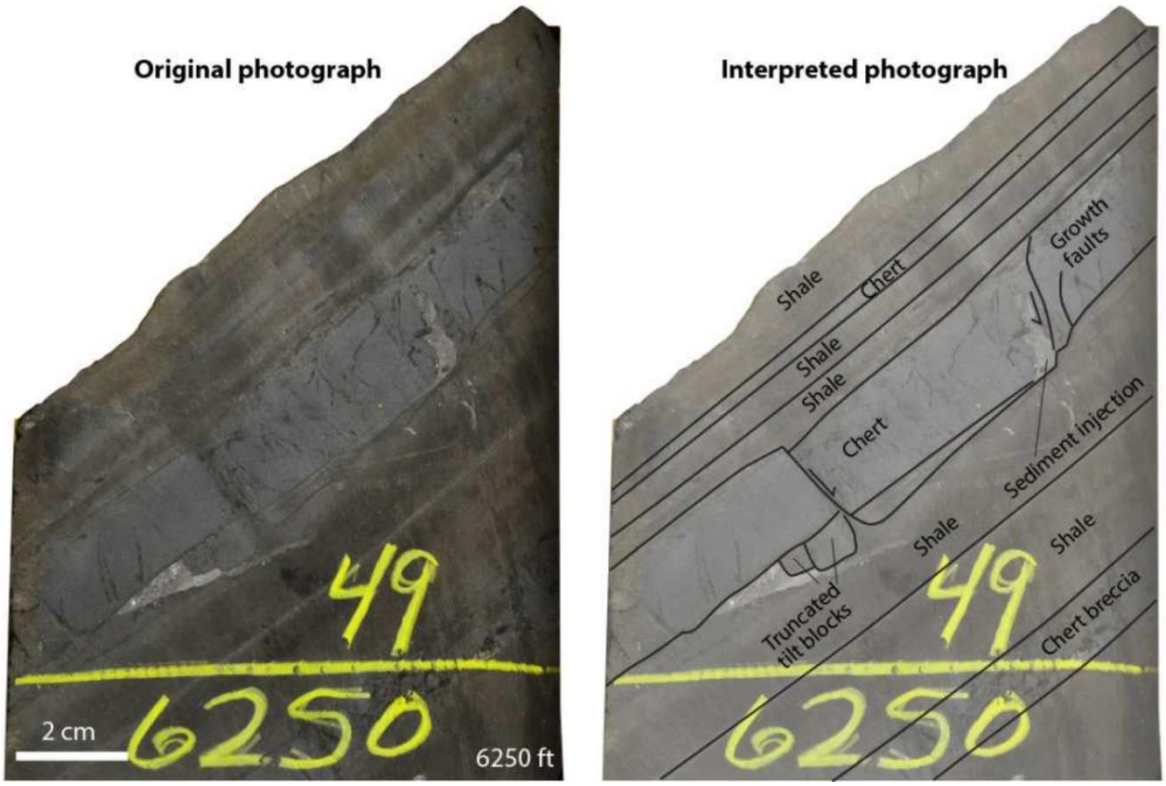

Figure 8.—Normally faulted chert overlain by undeformed chert, Hall 2B core. Note growth of strata in hanging walls of faults. Also note truncated blocks of chert below main chert bed, which indicate significant erosional discontinuities below some chert layers. Syndepositional fault growth, moreover, indicates that chert was deposited by bottom currents rather than simple pelagic sedimentation following phytoplankton blooms.

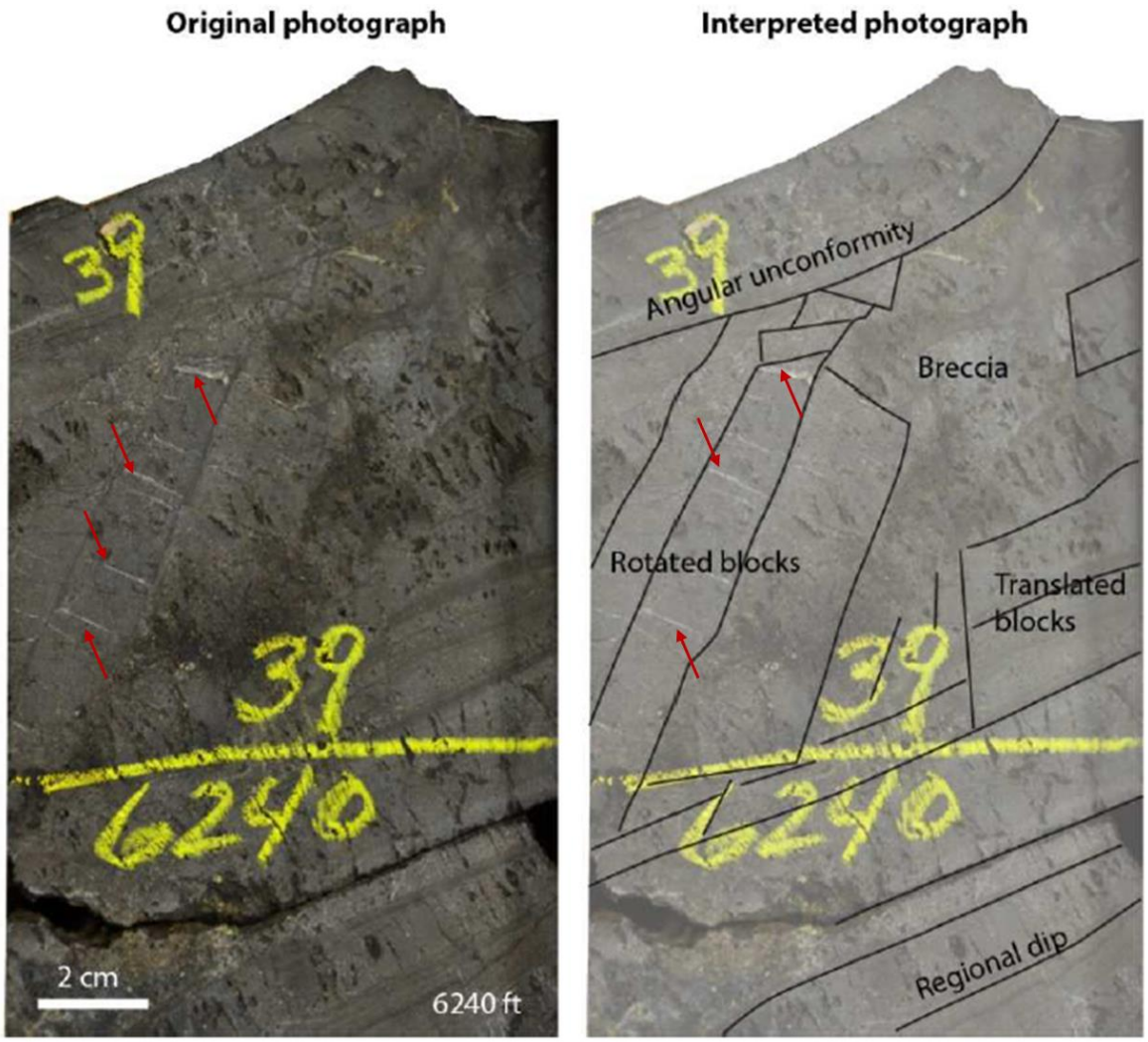

Figure 9.—Rotated chert blocks truncated by angular unconformity in the Hall 2B core. This pattern is interpreted as part of a debris flow or submarine slide deposit. Gently dipping chert beds define regional dip, which developed during the Carboniferous-Permian Wichita orogeny. Red arrows identify stratabound fractures in chert beds.

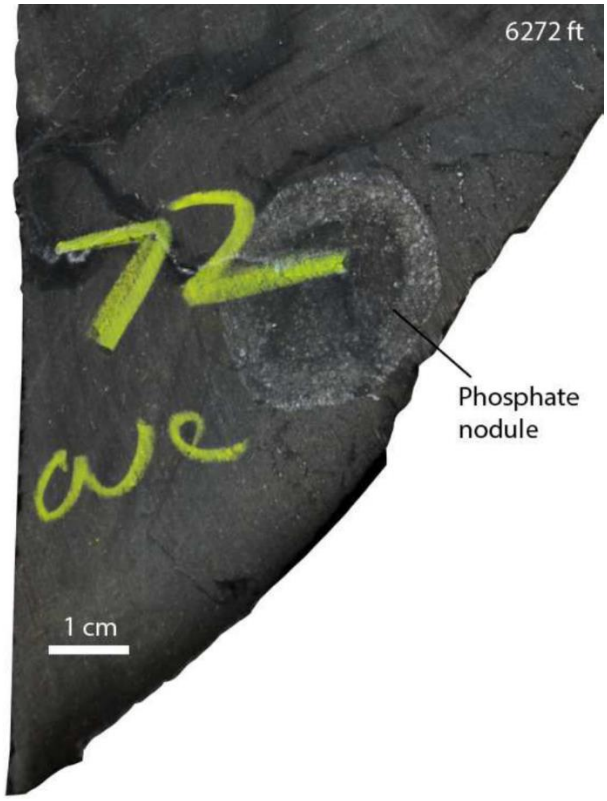

Figure 10.—Subcircular phosphate nodule in bedded chert of the Woodford Shale in the Hall 2B core. Phosphate nodules are interpreted as a product of marine upwelling.in the Ouachita embayment.

POE 1-29, HUGHES COUNTY, OKLAHOMA

The Poe 1-29 core is from the Woodford Shale gas play in the western Arkoma Basin in Hughes County, Oklahoma. The core is 120 feet long, extends from 7,730 ft. to 7,850 ft. and includes all but the lowermost 25 to 30 feet of the Woodford Shale. The Poe 1-29 core includes the upper contact and five feet of the overlying Caney Shale. Seven lithostratigraphic subdivisions of the Woodford Shale were determined that correlated to seven chemostratigraphic zones.

The Woodford Shale in the Poe 1-29 is composed of alternating thin beds of fissile shale and novaculitic chert that form small-scale brittle ductile couplets. The siliceous rocks, which

are mostly novaculitic chert, contain vertical and oblique fractures that are attenuated in adjacent argillaceous beds. The Woodford Shale section is generally dark gray to black with the exception of a few feet of medium to light gray colored strata. The lower portion of the Woodford Shale (7,850 to 7,831 feet) is dark gray to black shale with thin interbeds of novaculitic chert, whereas the upper section from 7,831 to 7,738 feet is medium to dark gray to black and composed primarily of chert (fig. 11).

Description

The Poe 1-29 was subdivided into 7 lithostratigraphic intervals based on sedimentary and diagenetic features (Callner, 2014). Throughout the section, the core contains numerous silica- and calcite-filled fractures, pyrite nodules and laminae, and soft-sediment-deformation features. The chert beds host centimeter-scale silica- and carbonate-filled veins (fig. 12) with most veins being planar and perpendicular to bedding. Ptygmatically folded (fig. 12) and shear veins (fig. 13) also occur as do small-scale normal faults, including growth faults (fig. 13) (Callner, 2014). Marcasite and nodular phosphate occur in the Poe 1-29, as do laminae of pyrite and disseminated pyrite crystals and framboids. The uppermost section of the Woodford consists of alternating beds of clay- and silica-rich mudrock with abundant soft-sediment deformation structures, including isoclinal folds (fig. 14). The contact between the Woodford Shale and overlying Caney Shale is sharp and marked by abundant glauconite and rip-up clasts of Woodford in the basal Caney Shale.

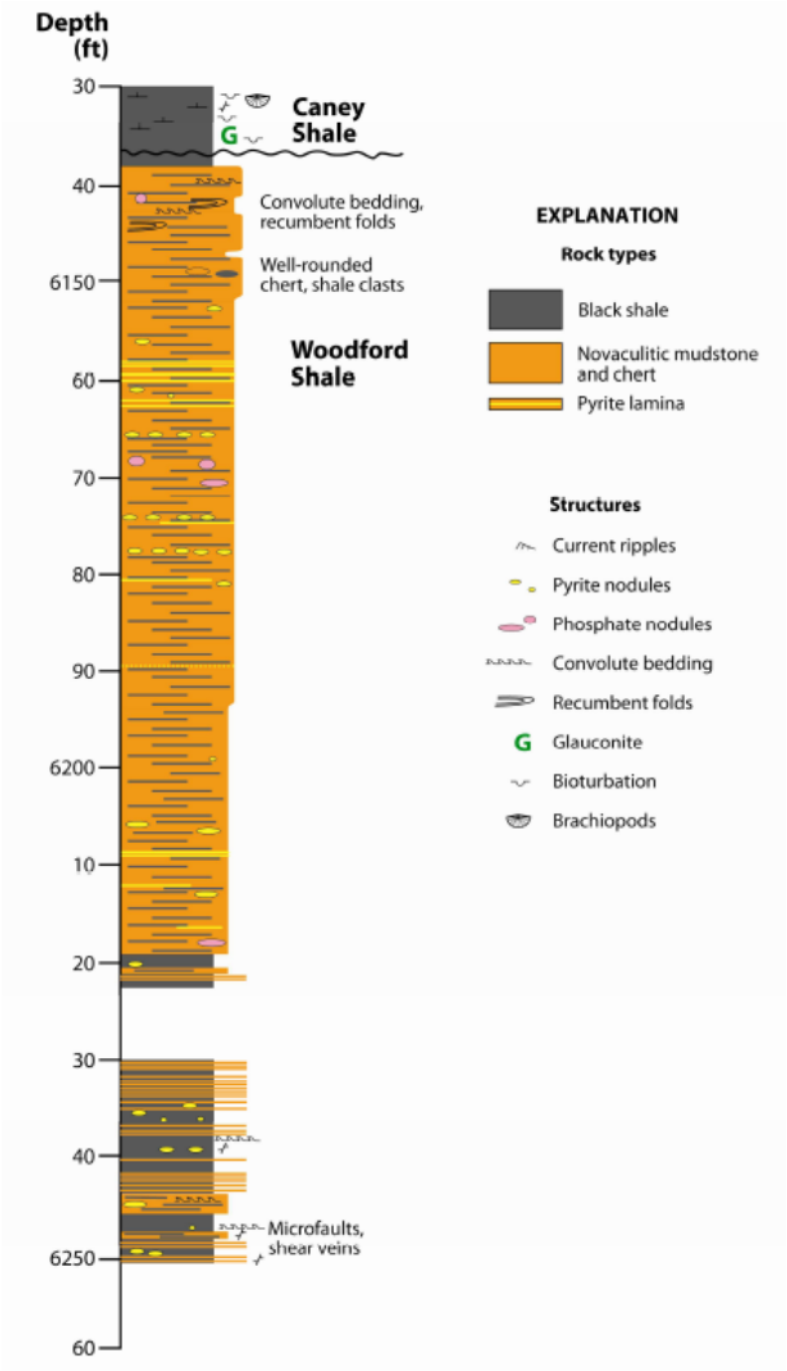

Figure 11.—Petrologic description of the Poe 1-29 core from Callner (2014) showing the abundance of novaculitic chert, which exceeds 35%.

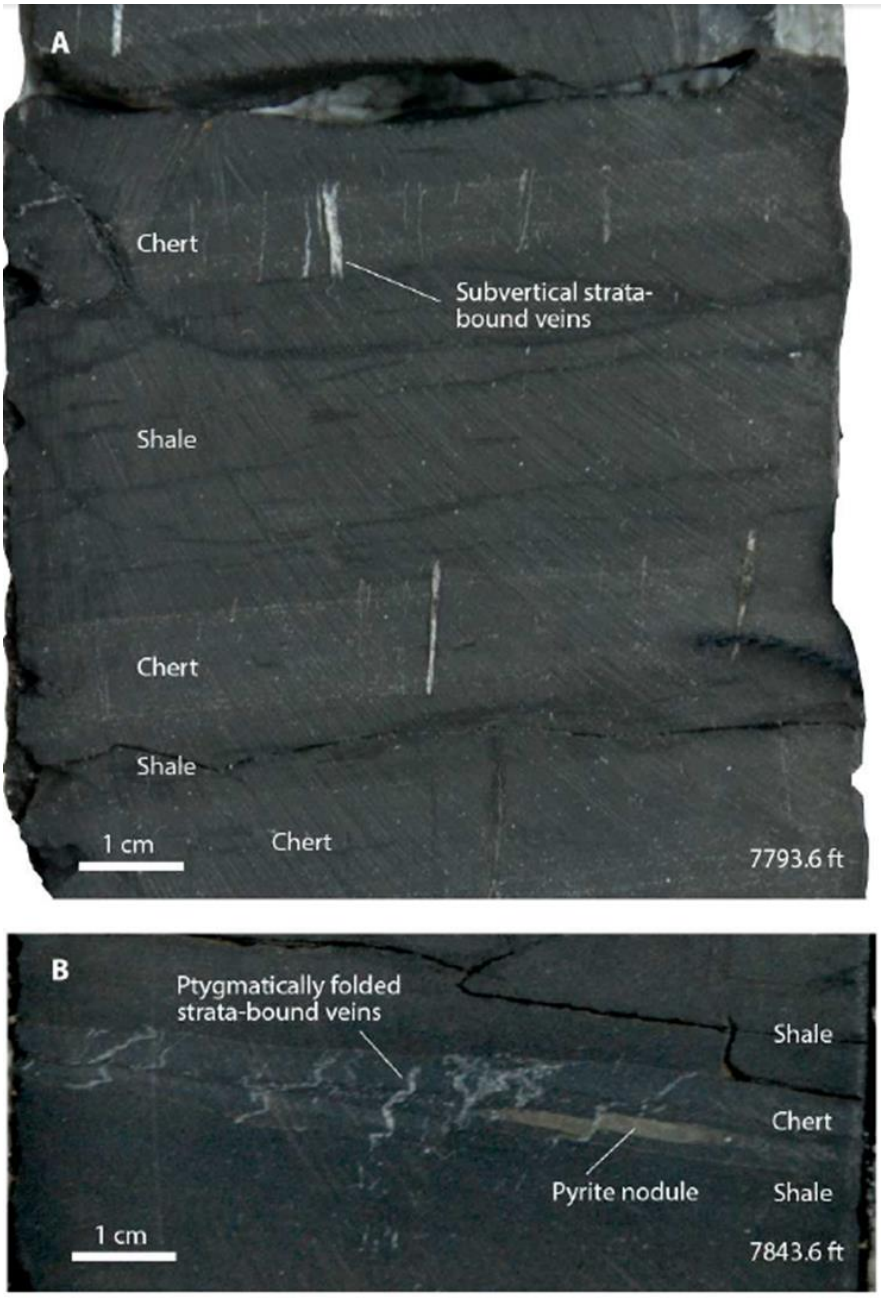

Figure 12.—Strata-bound fractures in silica-rich beds in the Woodford Shale, Poe 1-29 core.
(A) Subvertical veins in novaculitic chert laminae that indicate early tensile stress during burial.
(B) Ptygmatically folded veins indicating fracture was cemented prior to complete compaction. Both subvertical and ptygmatically folded veins terminate in adjacent argillaceous layers.

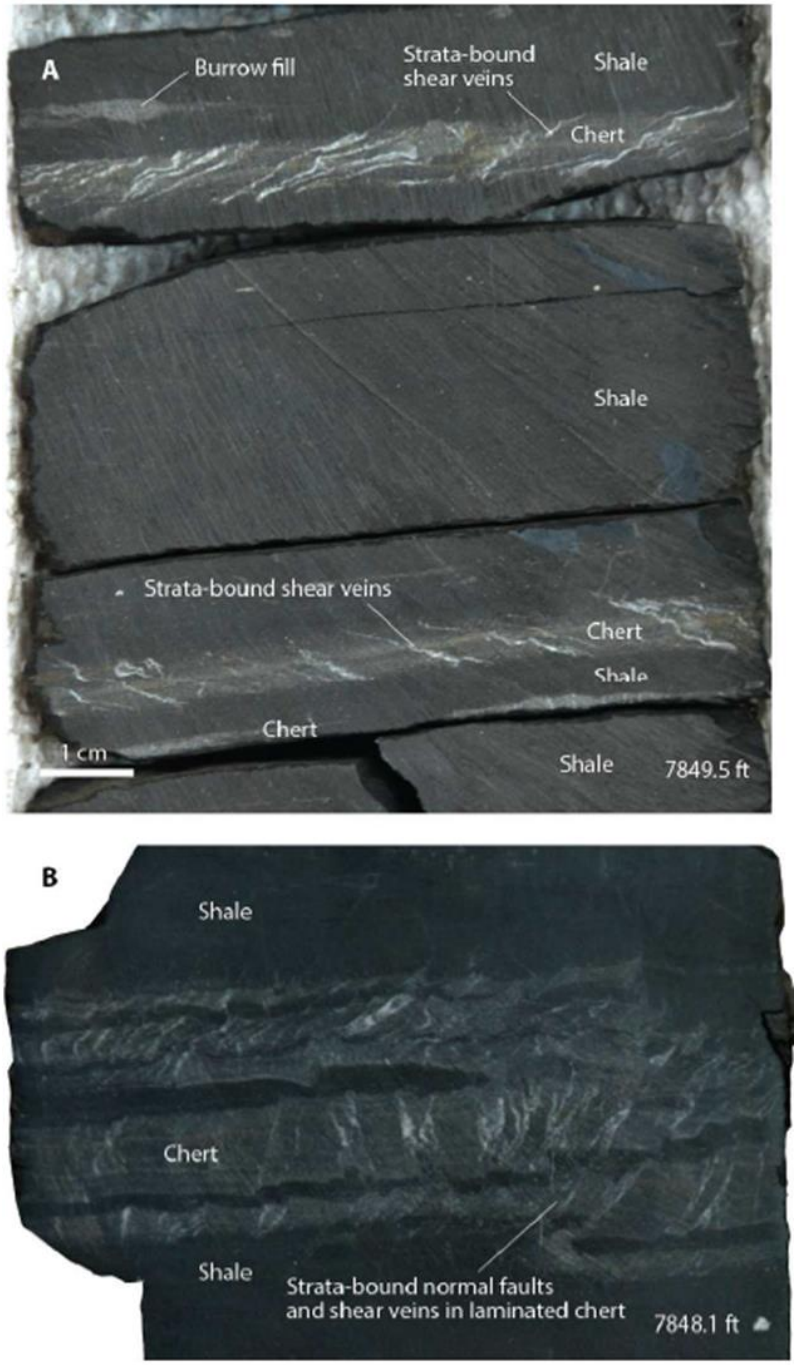

Figure 13.—Strata-bound shear veins in novaculitic chert, Poe 1-29.

(A) Weakly folded shear veins in chert providing evidence for bedding-parallel slip.

(B) Normally faulted chert beds with evidence of syndepositional thickening indicative of extension during deposition and early burial.

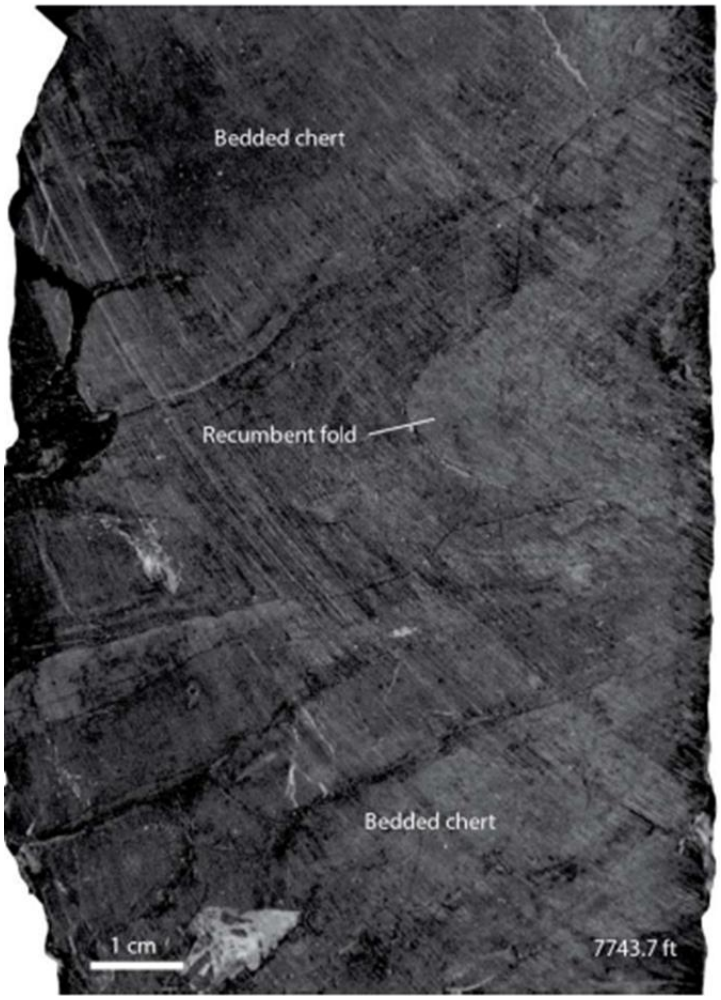

Figure 14.—Recumbent fold near the top of the Woodford Shale in the Poe 1-29 core.

Stratabound veins or cemented fractures dominate the Poe-1-29 core. At hand-specimen scale almost all fractures appear cemented. However, SEM images indicate that seemingly cemented fractures may contain microscale porosity (fig. 15) and as a result contribute to the permeability network and behave as paths of lesser resistance to fracturing fluids during hydraulic stimulation.

Chemostratigraphy

The Woodford Shale in the Poe 1-29 was divided into 6 chemostratigraphic units. The boundaries of these units correlate to boundaries of the lithostratigraphic intervals. Water

oxygenation was estimated using Ni/Co, V/Cr and V/(V+Ni). The Ni/Co ratio indicates much of the Woodford sediment was deposited in oxic conditions with short periods when dysoxic or anoxic conditions prevailed. The lower concentrations of Ni that force the low values for the Ni/Co ratio may have resulted from Ni becoming mobile during catagenesis (Szatmari et al., 2011). The majority of values for V/Cr (2.3-7.9) and V/(V+Ni) (.54-.82) imply dysoxia to anoxia during deposition. Definitive trends of most elements are not evident. Pyrite is not abundant in the Woodford Shale in Poe 1-29 core. DOPt comparisons suggest Fe may be forming other iron-bearing compounds such as siderite and Fe-rich dolomite.

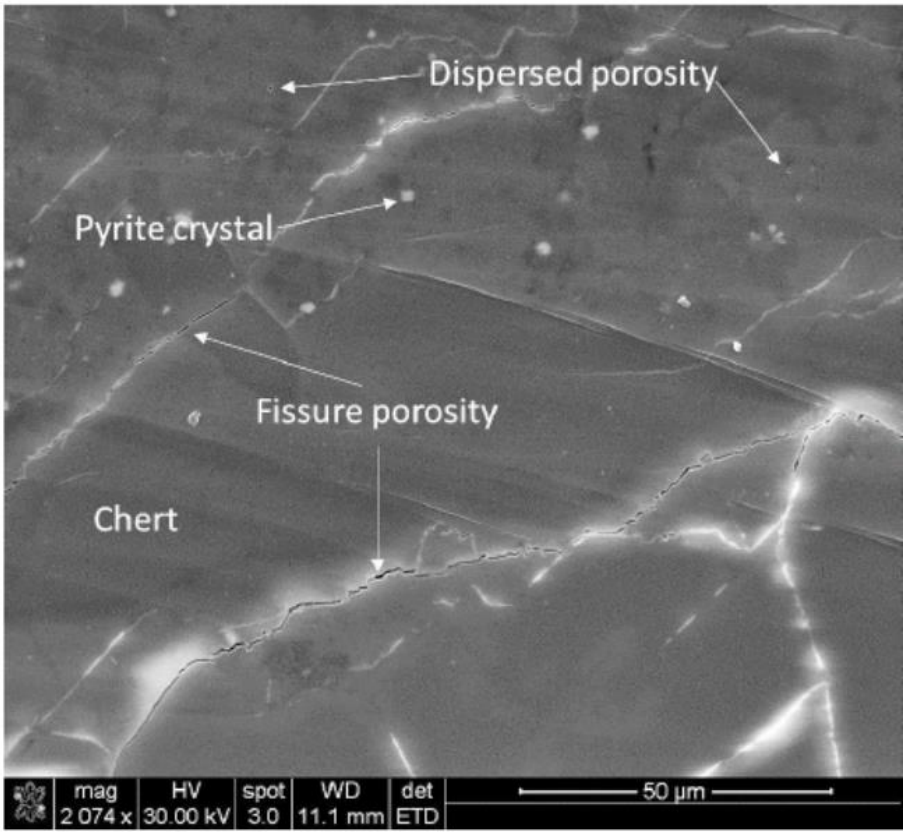

Figure 15.—SEM image showing fissure porosity associated with a partially cemented natural fracture, Poe 1-29. Image from Cecil (2016).

JESTER 1-26: PAYNE COUNTY, OKLAHOMA

The Jester 1-26 core is located in a Woodford Shale producing area east of the Nemaha uplift in Payne County, Oklahoma. The core extends 30 feet from 3,353 to 3,383 feet measure depth, contains 24 feet of Woodford Shale, 6 feet of the overlying Mississippian limestone and was subdivided based on sedimentary and diagenetic features.

Description:

Four sedimentologic/diagenetic intervals were recognized in the Woodford Shale, which is medium gray to black shale with pyritic silty laminae (figs. 16 and 17). The contact between the Woodford Shale and the glauconitic Mississippian limestone is sharp and erosional with weathered clasts of Woodford Shale as inclusions in the glauconitic Mississippian interval immediately above the disconformity.

Chemostratigraphy

Chemostratigraphy was limited to the top 10 feet of the Jester 26-1. The elemental proxies for bottom water redox (Mo, U, and V) increase with gamma-ray values and vary at the inch scale suggesting long term trends of anoxia were not established. Furthermore, the interval with increased values of Mo, U and V is burrowed, which is evidence of oxygenated bottom water.

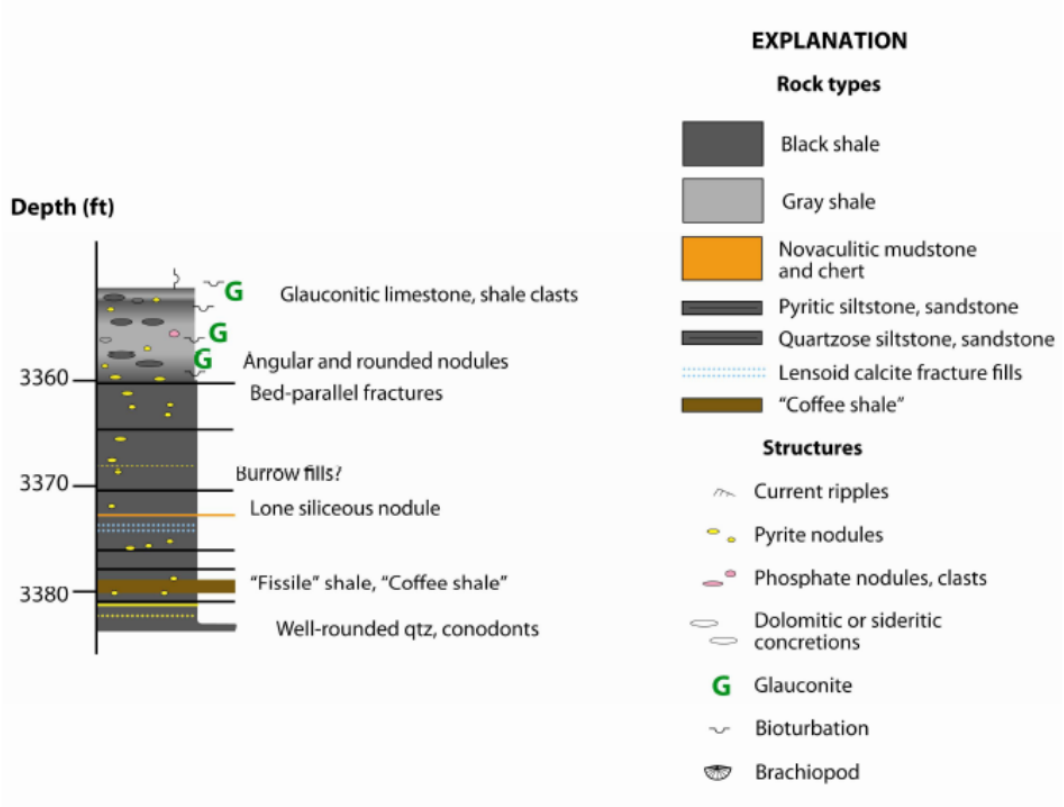

Figure 16.—Petrologic log for the Jester 1-26 showing a shale dominated section without novaculitic chert. From Callner (2014).

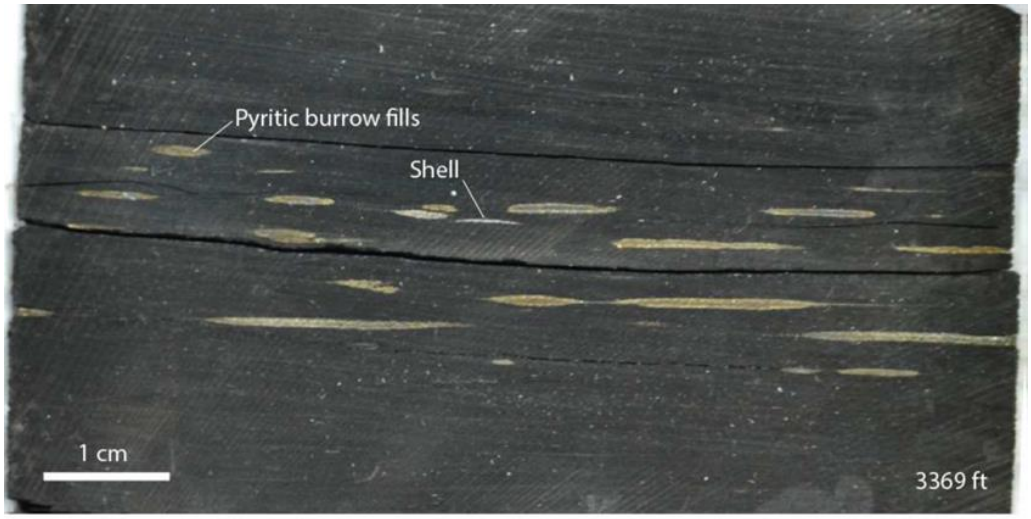

Figure 17.—Image of the Jester 1-26 core from Callner (2014). Invertebrate fossil material (brachiopod shells) and compacted burrows filled with gray shale, siltstone and pyrite are common in laminated Woodford Shale, which represents deposition in oxygenated water.

JANE: MCDONALD COUNTY, MISSOURI

The Jane outcrop is a relatively freshly excavated road cut near the community of Jane in McDonald County, Missouri. Tectonically, the outcrop is on the western flank of the Ozark Uplift and where described consists of approximately 22 feet of Woodford Shale (locally called Chattanooga Shale) and a similar thickness of lower Mississippian section including the Bachelor Formation, Compton Limestone, Northview Shale and Pierson Limestone (figs. 18 and 19)

Description

The lower section of the exposed Woodford Shale consists of seven feet of fissile black shale with pyrite nodules overlain by and in sharp contact with two feet of gray burrowed shale followed by five feet of black silty shale containing abundant current-ripple cross-laminae and burrows in the upper 2 feet (fig. 19). The apparent dip of the ripple foresets indicates flow to the northwest. This interval contains a cm-scale layer of pyrite at 13 feet. The pyrite occurs as nodular and pyritized burrow sheaths, similar to pyrite accumulations described in the Appalachian Basin by Baird and Brett (1986). Oxidation of pyrite in this layer stains the outcrop below orange-brown, creating a stark color contrast with unstained black shale above the pyrite layer (fig. 20).

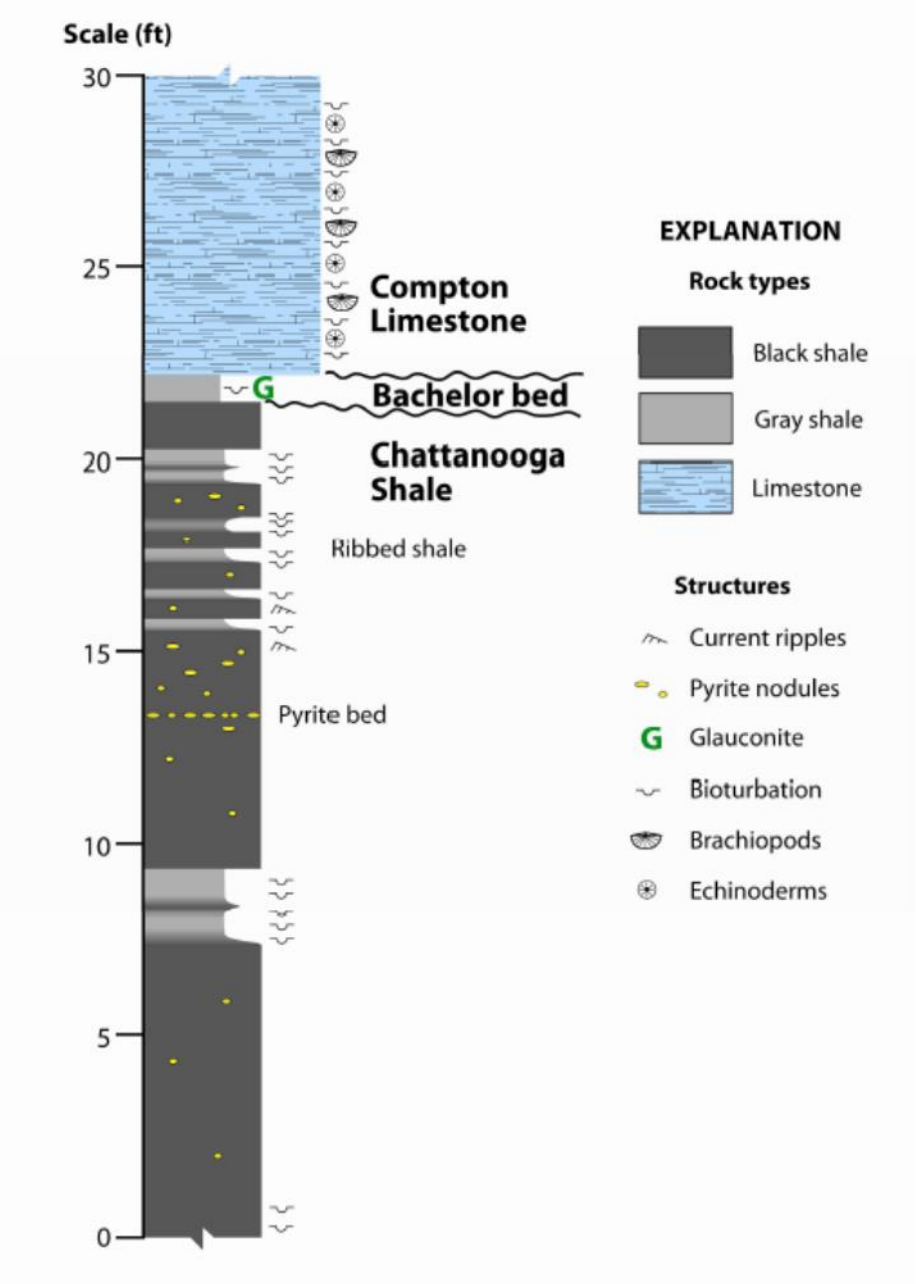

Figure 18.—Measured section of the upper part of the Woodford (Chattanooga) Shale at Jane, Missouri. From Callner (2014).

Figure 19.—Outcrop photo showing dark gray to black and lighter gray beds of the Woodford (Chattanooga) Shale, Jane, Missouri. Person is approximately six (6) feet tall. Oxidation of sulfides in pyrite nodule is responsible for brown stain on black shale toward the middle of the Woodford section. The Jane outcrop is all shale and novaculitic chert and non-skeletal phosphate are not seen.

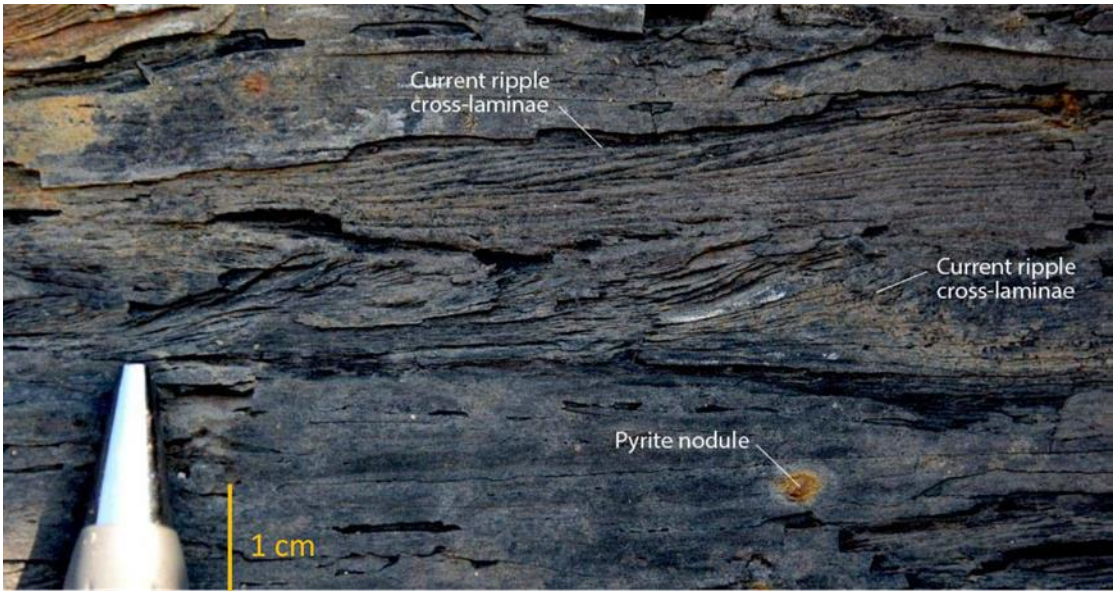

Figure 20.—Current ripple cross-laminae in dark silty shale of the Woodford Shale, Jane, Missouri. Orientation of cross-laminae suggest northerly sediment transport. After Callner (2014).

The upper interval extends from 16 to 22 feet and consists of an alternating series of gray and black shale beds that display a ribbed pattern. The basal gray shale is 1 ft thick. The succeeding black shale beds are typically 4-6 inches thick, whereas gray shale beds are 2-4 inches thick. The upper 2-3 inches of each black shale bed contains burrow filled with lighter-colored gray shale derived from the overlying bed (fig. 21). The basal contacts of gray shale beds are mostly gradational (fig. 21), whereas the top contacts are sharp. The series of black and gray shales is capped by one (1) foot thick black shale, which has sharp contacts with the underlying gray shale and overlying Bachelor Formation, respectively. The Bachelor Formation is the basal unit of the Mississippian limestone section and consists of about 6 inches of calcareous, fossiliferous green glauconitic shale.

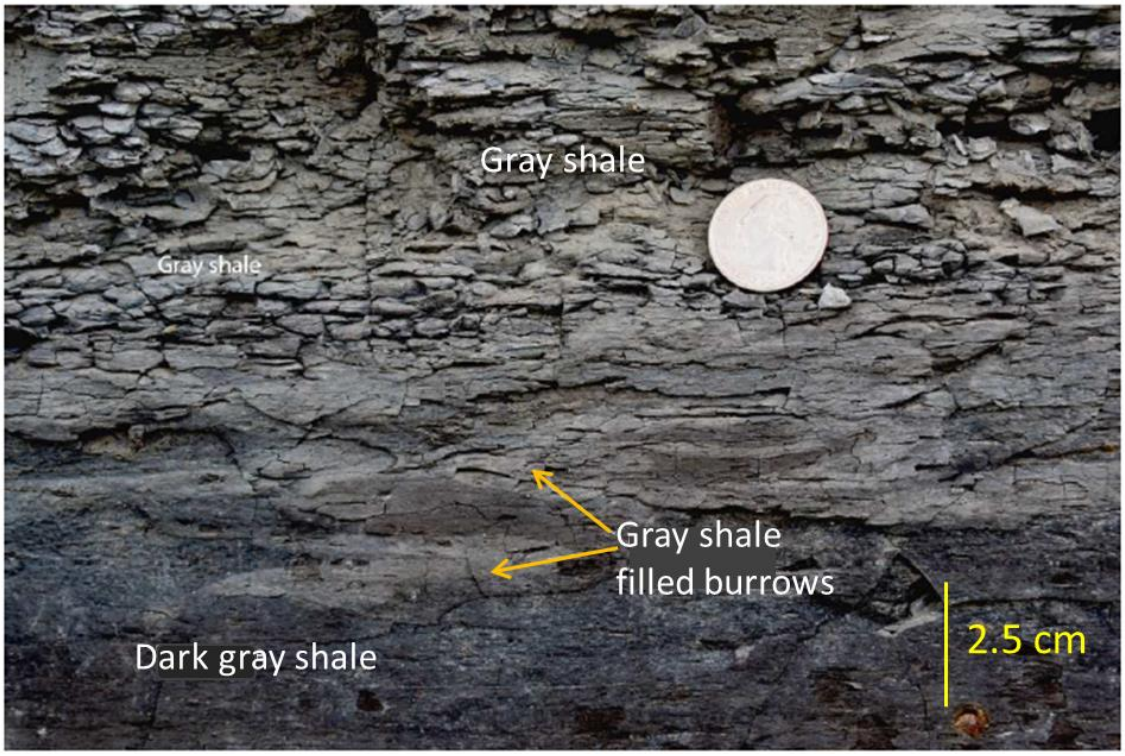

Figure 21.—Detail of transition from dark gray to light gray shale beds, Woodford Shale, Jane Missouri. Burrows in lower bed that filled with the lighter gray mud are integral part of the dark to light shale transition. After Callner (2014).

Chemostratigraphy

The chemostratigraphic survey of the McDonald County outcrop includes a spectral gamma-ray survey and 24 TOC measurements collected by Rivera (2013). XRF data were not collected and inferences concerning sediment sources and bottom water oxygenation are based on sedimentary and biogenic features, U/Th ratios and TOC concentrations. The Th concentration is 5 to 13 ppm greater than U concentration, demonstrating a strong detrital input and location closer to the shoreline than the cores. Thorium concentrations peak in the black shale 9 to 13 feet above the base of the measured section. Values of potassium (K) do not vary much across the outcrop and the TOC content is unusually low for the Woodford Shale, ranging from <1 to1.5% by weight (Rivera, 2013).

I-35S: CARTER COUNTY, OKLAHOMA

The I-35S outcrop is located on the southern flank of the Arbuckle Uplift near Springer, Oklahoma, where the dark-colored Woodford Shale section along the west side of Interstate 35 is approximately 240 feet thick. Both the lower contact with the Hunton Group and the upper contact with greenish-gray shale of the pre-Sycamore beds are exposed. Fay (1989) included the pre-Sycamore shale with the Woodford, which accounts for most of the difference in our measured thickness and 290 feet reported Oklahoma Geological Survey Guidebook 26 (Fay, 1989). Only the top 90 feet were examined in detail as the middle shale-rich section is deeply weathered and covered.

Description

The upper Woodford Shale is dark gray, with dark to light gray novaculitic chert. Fresh surfaces of novaculitic chert feel gritty, but no grains are discernable. The shale intervals tend to be planar to broadly lensoid and range in thickness from laminae to medium beds.

The shale is fissile and internal laminae are on the order of 1 mm thick. The chert layers also range from laminae to medium beds, and tend to thicken upward in section. The chert beds have sharp to gradational contacts, planar to undulatory bedding surfaces and planar to lensoid bed morphology.

Shale and chert layers contain phosphate nodules and lenses that increase in abundance upward in section and range in shape from spherical to oblate or platy. Most nodules are pebble sized and some lenses are up to 3 cm thick and 30 cm in length. Disseminated pyrite crystals and framboids, as well as granule- to pebble-size marcasite nodules occur in shale and chert. Some chert beds appear internally structureless, whereas others are laminated. The laminae are planar to wavy with wavy laminae wrapping around phosphate nodules and lenses (fig. 22).

Chert beds contain open fractures that contribute to free hydrocarbon storage in the Caddo Field approximately 6 miles to the south (Puckette et al., 2013). SEM imaging reveals additional isolated microscale to nanoscale pores (fig. 23).

Chemostratigraphy

The chemostratigraphic survey of the I-35S outcrop includes a spectral gamma-ray survey and 38 TOC measurements collected by Krystyniak (2005). XRF data were not collected and inferences concerning sediment sources and bottom water oxygenation are based on sedimentary and biogenic features, U/Th ratios and TOC concentrations. Uranium concentration average 38 ppm, whereas Th concentrations average 5 ppm.

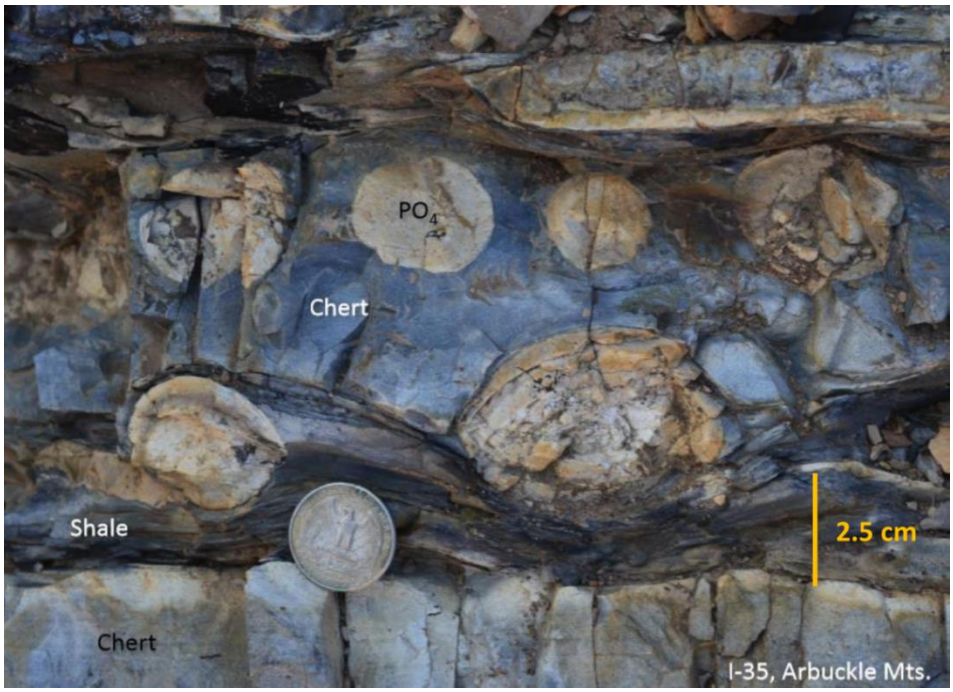

Figure 22.—Abundant phosphate nodules in novaculitic chert, Woodford Shale, I-35S outcrop, Carter County, Oklahoma. Dark gray shale laminae wrap some nodules. Image from Pashin and Callner (2014).

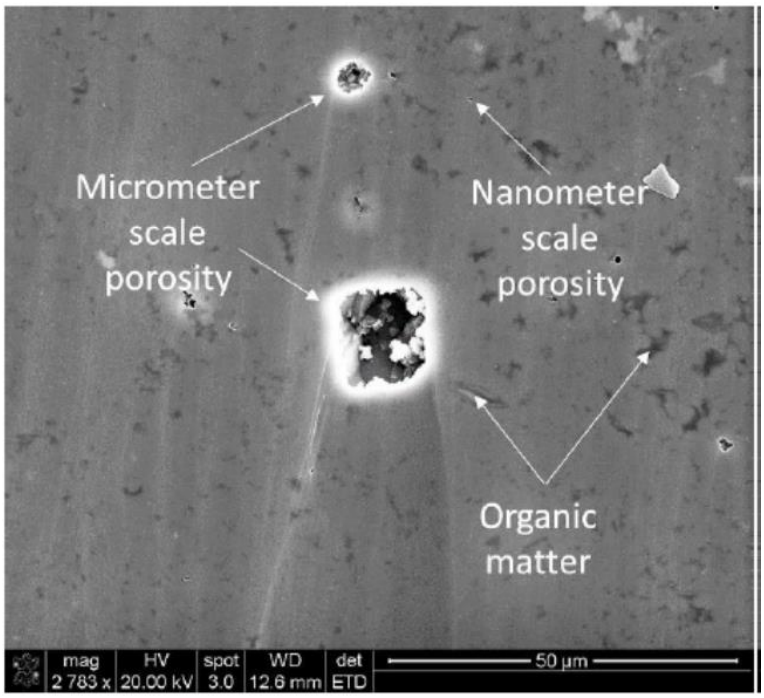

Figure 23.—Backscattered SEM image showing isolated pores in novaculitic chert, I-35S outcrop.

U/Th ratios range from approximately 2 to 53 (fig. 24) with an average of 7.6, indicative of marine-dominated deposition (Paxton et al., 2006). Thirty eight samples have a range of TOC from 0.8 to 17.0 wt%, with an average of 10 wt% (Krystyniak, 2005). The highest TOC values (>14 wt%) correspond with fissile organic-rich shales, whereas the lowest (0.6 to <6 wt%) correspond to siliceous, blocky beds (Krystyniak, 2005).

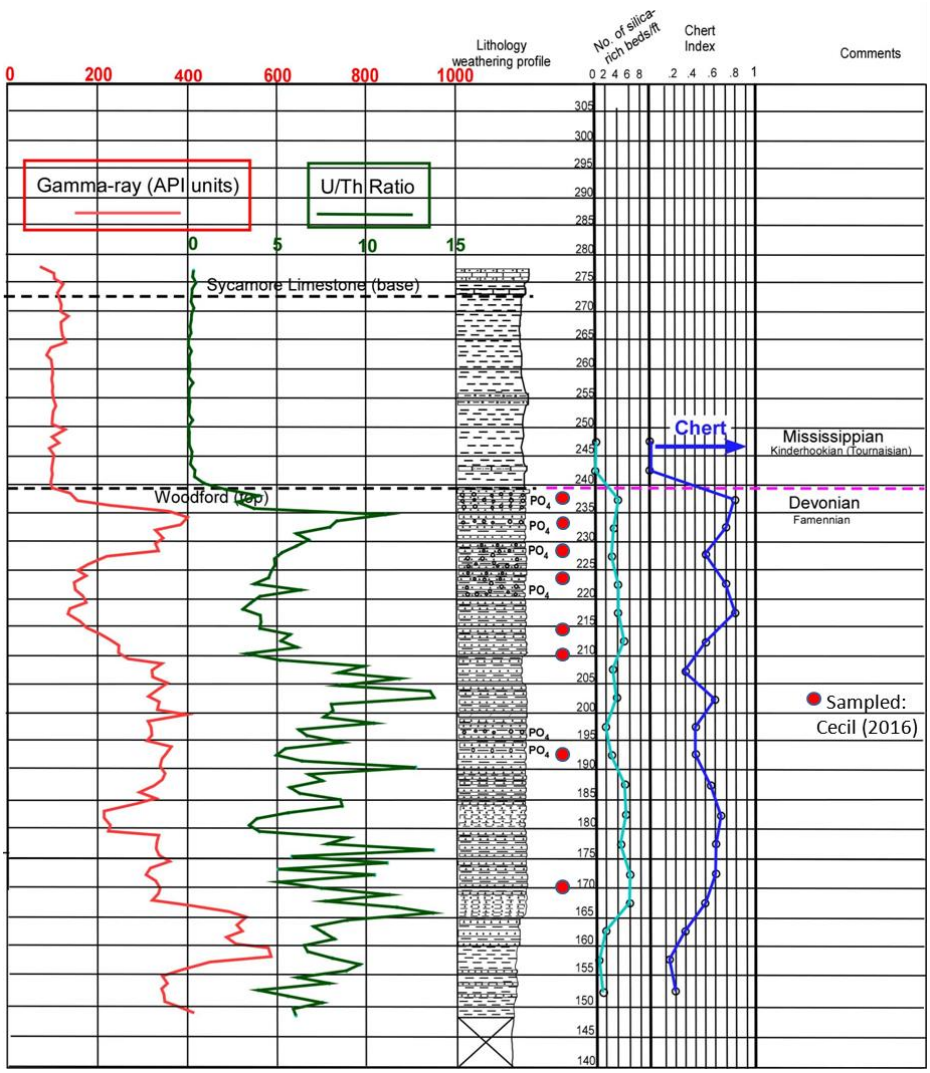

Figure 24.—Measured section for the upper 90 feet of the Woodford Shale and pre-Sycamore beds between top of Woodford Shale and base of Sycamore Limestone. Red line is total gamma-ray in API units. Green line is the U/Th ratio from spectral gamma-ray and red circles are sample locations of Cecil (2016). The light blue line is the average number of chert beds per foot and dark blue total percentage of chert in decimal for the five feet of interest. After Puckette et al. (2013).

ATOKA CHERT PIT: ATOKA COUNTY, OKLAHOMA

The Atoka outcrop of the Arkansas Novaculite is in the fold and thrust belt of the Ouachita orogeny is part of an unusual outlier that exposes pre-orogenic strata cratonward part of the thrust belt. The bedding strikes roughly N. 25^{o} E. and dips approximately 75-80^{o} SE (fig. 25) before overturning in the upper 55 feet to dip approximately 75^{o} SW.

Figure 25.—Steeply dipping interbedded shale and novaculitic chert, Atoka, Oklahoma. Inset shows wider view of the outcrop. Sample locations are shown by colored circles. After Cecil (2016).

Description

The Arkansas Novaculite consists of alternating layers of novaculite chert and fissile shale. The chert is typically dark to medium gray where fresh. Bedding ranges from planar to undulatory, with the chert occurring in laminae to medium beds and the shale occurring in

laminae to thick beds. The shale is dark gray where fresh and weathers to greenish to reddish hues. Shale content increases abruptly in the upper 85 feet of the section (fig. 26). The outcrop is dominated by chert in the lower 253 feet, with the bottom 100 feet being almost 100% novaculite chert. The chert beds, especially in the lower part, exhibit a waxy texture and are internally laminated. Hummocky bedforms are exposed in the middle portion of the section along the bedding plane of steeply dipping chert bed. Chert-rich and dark shale beds some 225 feet above the base contain phosphate nodules that range from platy to spherical in shape and pebble to cobble in size (0.5 – 3.0 in) (fig. 27).

Chemostratigraphy

The Arkansas Novaculite/Woodford Shale section, Atoka chert pit, was scanned using the hand-held gamma-ray spectrometer. The U/Th across the lower 210 feet of novaculitic chert averaged 0.23, evidence of dilution of uranium by silica and/or removal of uranium in oxygenated waters. In contrast, the U/Th for the variegated dark gray to gray-green and red shale and chert from 210 feet to 250 feet was 1.4, well within the expected values for marine-dominated deposition.

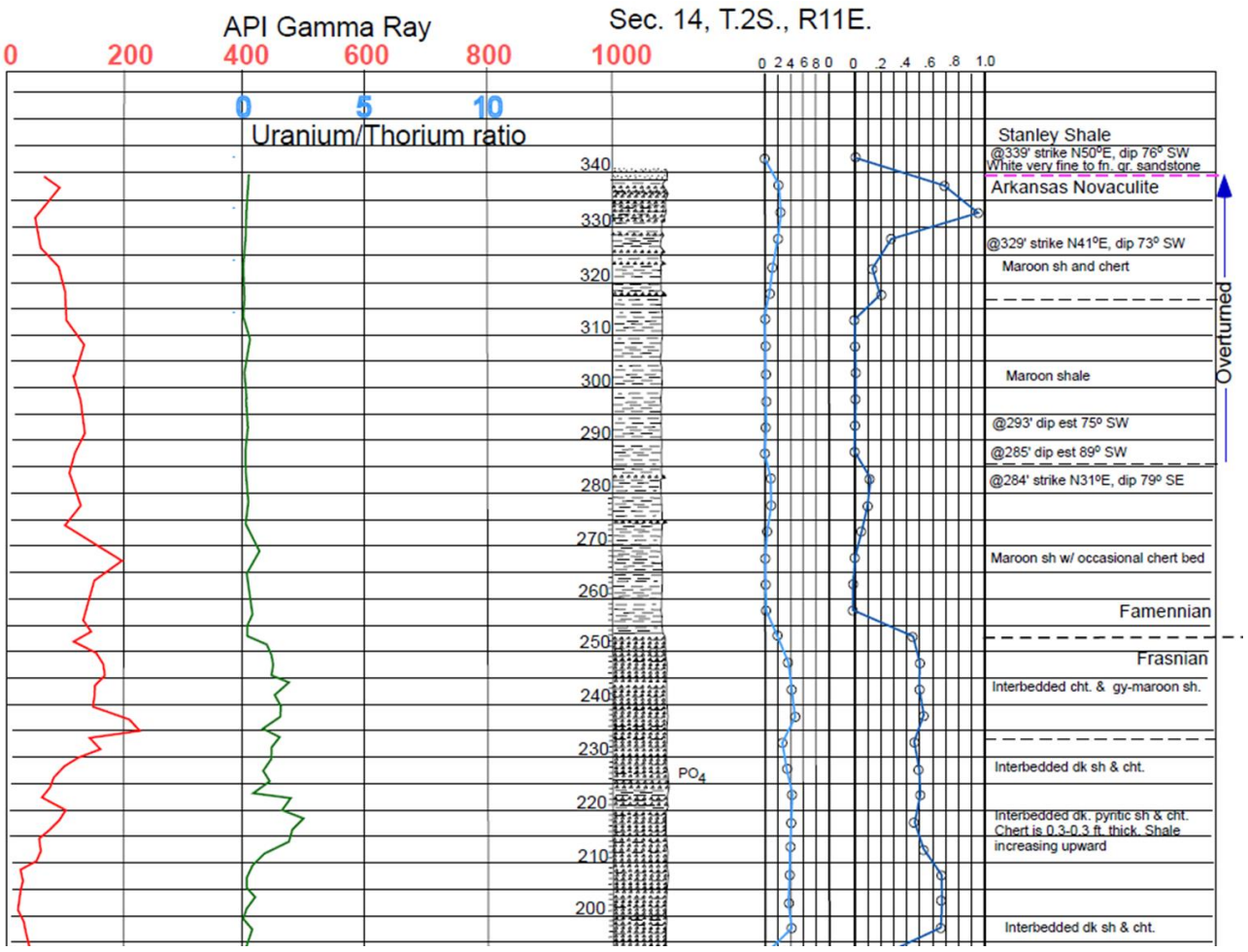

Figure 26.—Measured section for the upper approximately 140 feet of the Arkansas Novaculite at Atoka, Oklahoma. Blue curves to right of the depth track record number of chert beds per five feet and the total chert in decimal across the same interval. Red curve is gamma-ray in API units; green curve U/Th ratio. The upper 87 feet is dominantly shale. The lower 253 feet is overwhelmingly novaculitic chert.

Figure 27.—Abundant phosphate nodules in novaculitic chert bed, Atoka chert pit, Atoka, Oklahoma. From Cecil (2016).

DISCUSSION

Based on Upper Devonian regional paleogeography as interpreted by Heckel and Witzke (1979) and Ettensohn (1997), the McDonald County, Missouri outcrop was proximal to the continental margin that rimmed the north side of the Ouachita embayment (fig. 28). The Woodford Shale sections in Anderson 12-1 and Jester 1-25 cores and the McDonald County outcrop appear to all represent deposition in an inner shelf setting. In contrast, the Hall 2-B and Poe 1-29 cores, and the I-35S outcrop contain novaculitic chert, appear to be strongly influenced by upwelling on the shelf and in the SOA (figs. 28 and 29). The Atoka chert pit outcrop is dominated by novaculitic chert, placing it in a location closest to the upwelling form the Ouachita embayment (figs. 28 and 29). This interpretation is supported by the lithologic, sedimentologic, diagenetic and geochemical data. The relative percentage of novaculitic chert

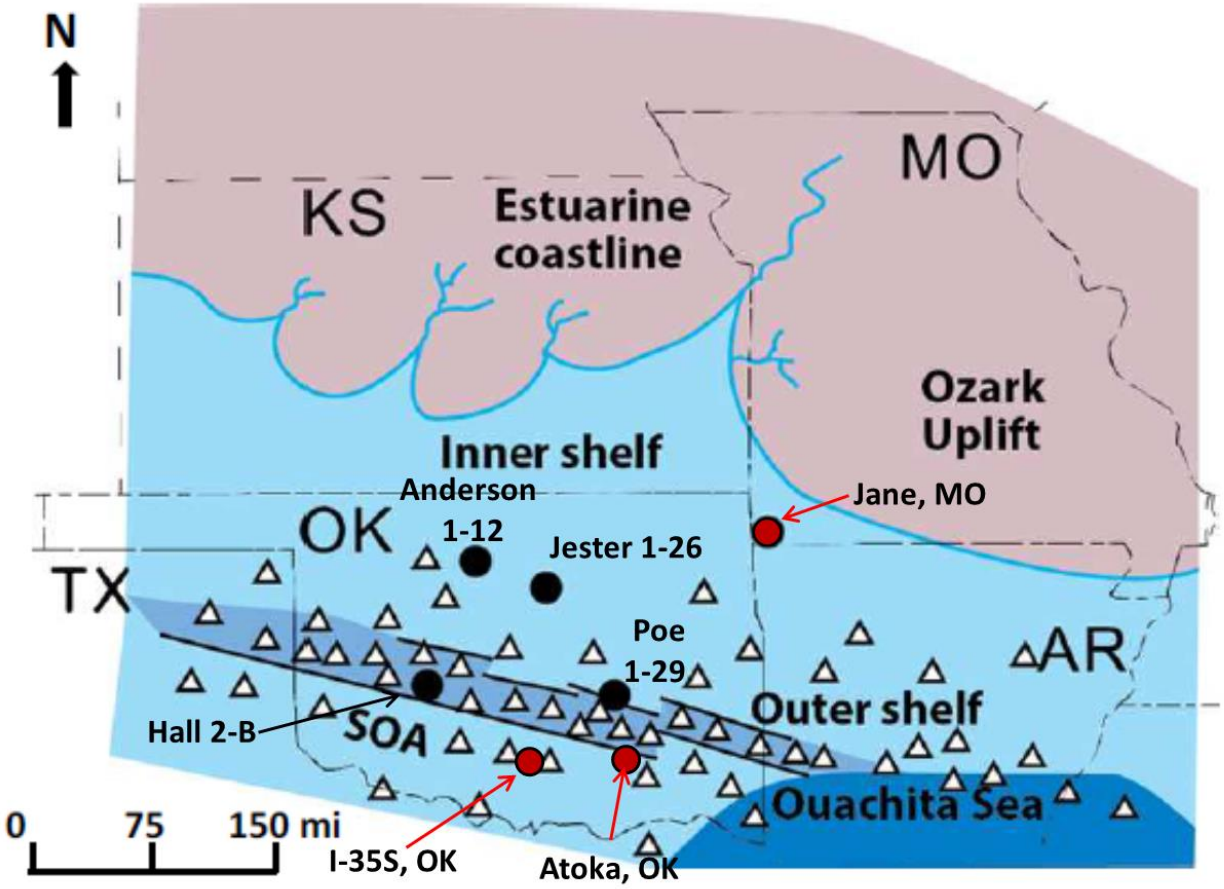

Figure 28.–Paleogeography during Woodford and novaculite deposition. Triangles represent areas of silica deposition that became novaculitic chert. Locations of cores (black circles) and outcrops (red circles) are identified. Chert decreases away from the Ouachita embayment (sea) toward the shelf. Locations of hypothesized faults along the SOA are shown as black lines. After Callner (2014).

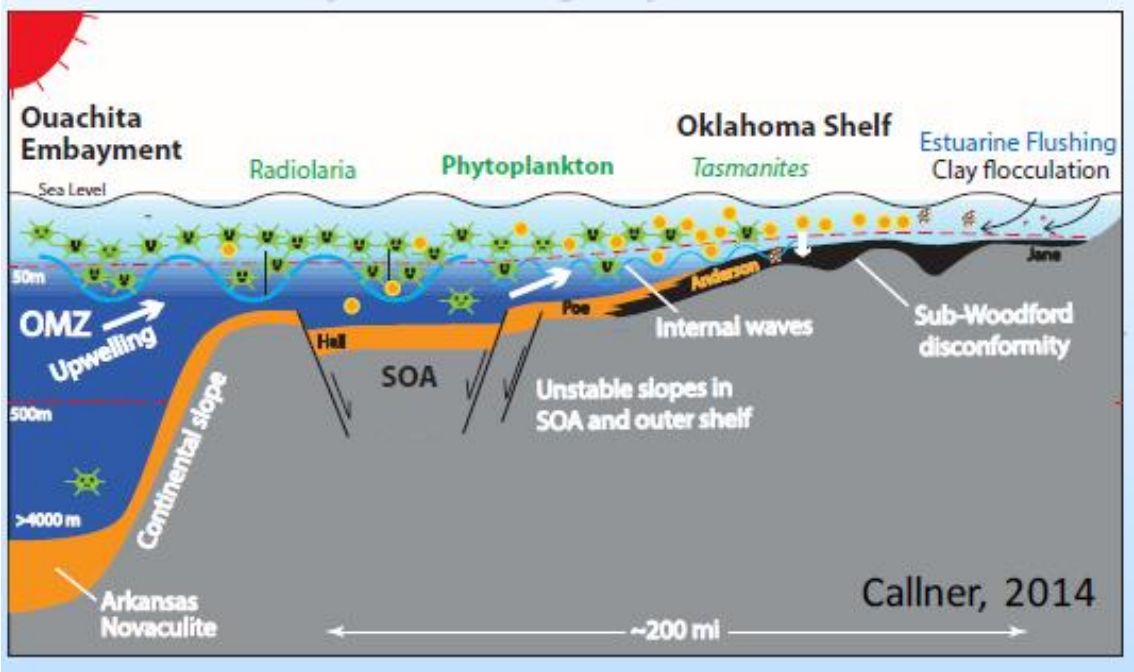

Figure 29.—Diagrammatic cross section showing the hypothesized scenario for the origin of the deposition facies and fabrics evident in the Woodford Shale and Arkansas Novaculite in Oklahoma. OMZ is the oxygen minimal zone, SOA the Southern Oklahoma Aulacogen. The positions of the cores and outcrops included in this report are shown. After Callner (2014).

and diagenetic silica bands and the thickness of chert beds show stratigraphic and geographic variation. Novaculite and chert beds contain preserved silica spherules that can be identified as radiolarians (Figure 30). Originally these beds were likely radiolarian oozes in which the opal-CT was dissolved and reprecipitated as cryptocrystalline quartz (see Roberts and Mittere, 1992).

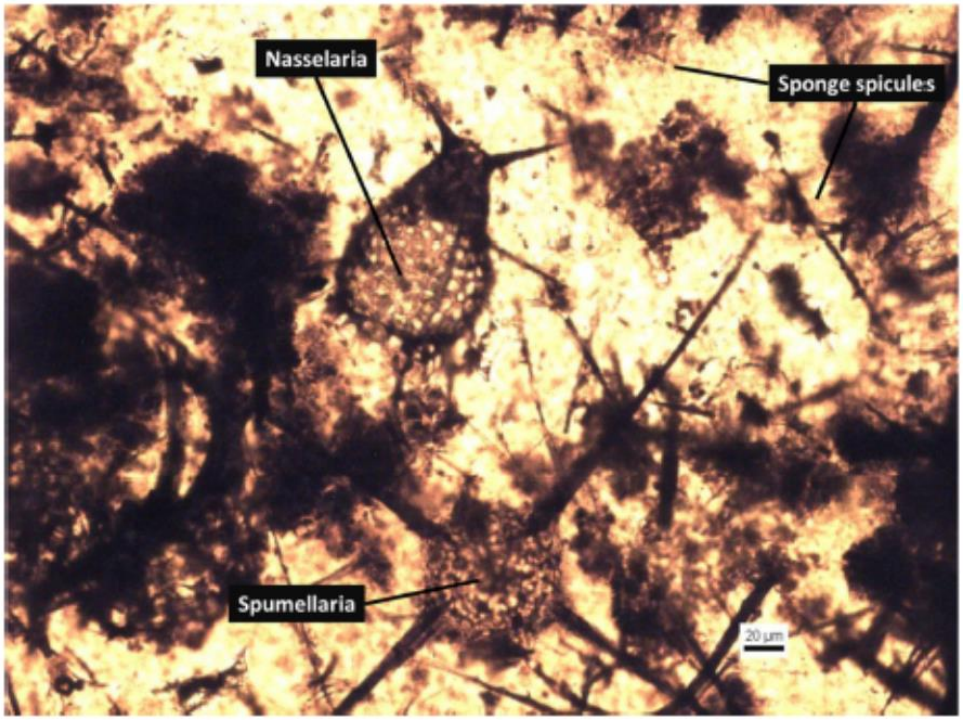

Figure 30.—Thin section photomicrograph showing well preserved Nasselaria and Spumellaria radiolarians and sponge spicules, Hall 2-B core. From Cecil (2016).

When compared to the cored section to the south and west, the Woodford Shale outcrop in McDonald County, Missouri has lowest measured TOC (<1 to 1.5%) indicating lower productivity of organic matter (OM), lower preservation of OM, or higher dilution by detrital silt and clay. High values of Th support the dilution hypothesis, while current ripples and abundant burrowing support oxygentated water and poor preservation. The absence of chert and non-skeletal phosphate indicates that upwelling and the associated radiolarian blooms and phosphate deposition were not effective at this location. Chert and phosphate are common in the Hall 2-B and Poe 1-29 cores in southern Oklahoma (fig. 31), which are proximal to the Ouachita embayment and the SOA. The Poe 1-29 contains evidence for active bottom currents driven by density differences in water masses include ripple cross-laminae, scour surfaces with pyrite lags and normally and inversely silty layers. Horizontal

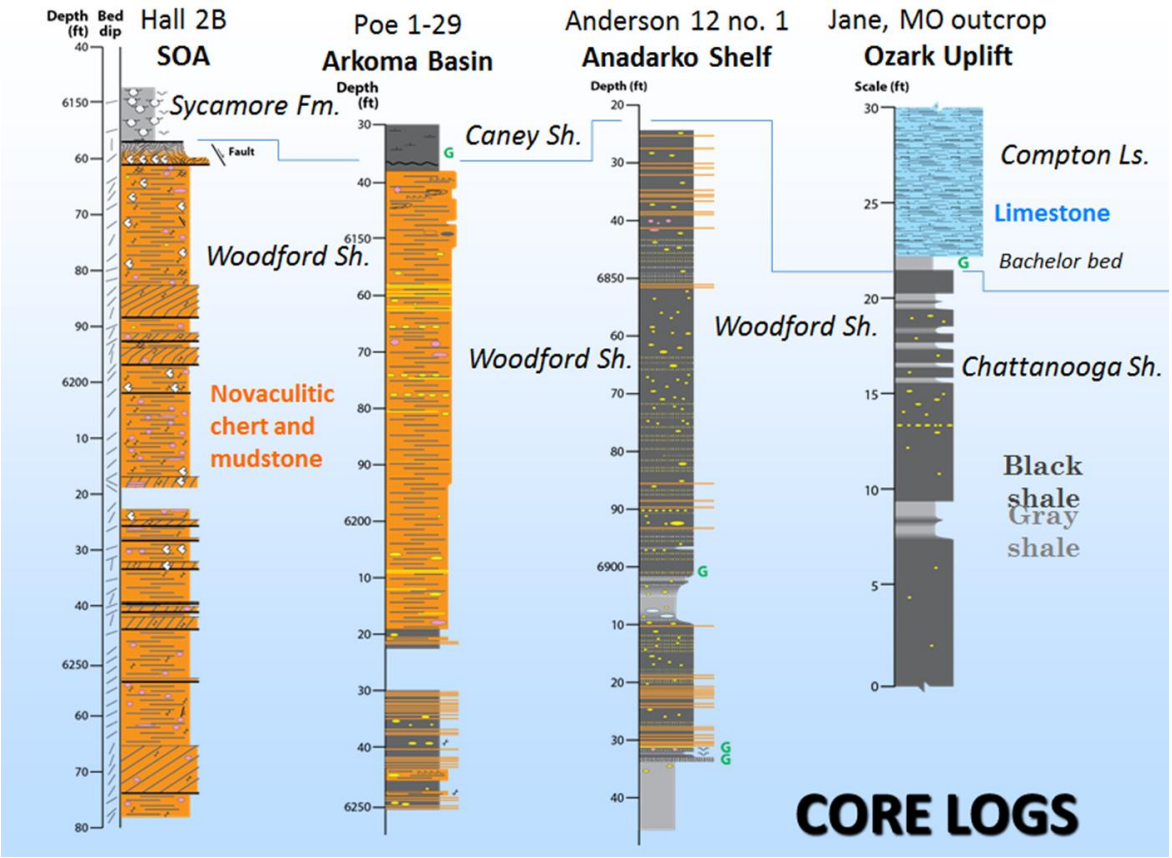

Figure 31.—Cross section illustrating the decrease in chert content in the Woodford Shale distal to the Ouachita embayment and increasing gray shale content in the shelfal position.

lamination is much more common than ripple lamination, but may represent the trailing edges of mud ripples rather than settling from suspension (Schieber and Southard, 2009). The Anderson 12-1 and Jester 1-26 demonstrate the range of depositional processes higher on the continental shelf where the effects of upwelling were apparently less pronounced. The Poe 1-29, by contrast, is the closest of the group to the Ouachita embayment. The Woodford Shale section in this core contains more novaculitic chert and less clay-rich mudstone than the cores and McDonald County, Missouri outcrop (fig. 31). The clay-rich intervals become thinner upward from the base of the core, indicating a decrease in detrital input, and suggesting deposition during transgression. The plot of silica vs aluminum reveals two trends

in the data: a strong inverse relationship implying the Si is biogenic in origin, and a marked increase in Si as Al remains constant. Both trends suggest Si concentration is not coupled to detrital input and the silica is biogenic or diagenetic.

Of the three paleoredox indicators, Ni/Co and V/Cr generally give similar estimates of redox state, whereas V/(V+Ni) typically estimates more restricted conditions. Nickel: cobalt ratios indicate that most of the Woodford Shale in the Poe 1-29 formed under oxic conditions with occasional short periods when either dysoxia or anoxia prevailed. Values for V/Cr are interpreted to indicate conditions were more restricted (suboxic) and V/(V+Ni) indicate greater restriction (anoxia) during deposition. It is possible that different elemental suites originated in different parts of the stratified water column, however values of V/Cr were used to characterize paleo-redox to maintain consistency between cores. Using this indicator, most of the rock in Poe 1-29 was deposited under dysoxic conditions, except for interval 2, which is black shale, and interval 6 (novaculitic chert), during which anoxia prevailed. Though the three proxies (V/Cr,Ni/Co, and V/(V+Ni) give different redox states according to accepted values, they are not inconsistent, but instead are recording different aspects of deposition. For example, V and Cr are bound to clay and can indicate the redox conditions at the site of flocculation/pelletization, whereas organic-bound elements are more likely to indicate water column conditions at the final site of deposition.

All samples collected from the Poe 1-29 were enriched in P, which is consistent with intense upwelling along the margin of the Ouachita embayment (fig. 29). The average enrichment factor for the Poe 1-29 core was 2.46, whereas the inner shelf Anderson 1-12 and Jester 1-26, had enrichment factors for P or 0.06 and 1.08 respectively. These differences are attributed to the inner shelf setting and their position outside the area influenced by

upwelling. Thorium is depleted relative to PAAS across the Woodford Shale in the Poe 1-29 core, indicating the lack of terrestrial sediment input and a predominance of biogenic sediment (fig. 32). The Anderson 1-12 and Jester 1-26 cores, as previously stated, contain Woodford Shale formed inboard of the shelf edge if paleogeographic reconstructions are correct. However, Th is depleted in the Anderson 1-12 and slightly depleted to enriched in the Jester 1-26. Uranium is enriched in both cores, suggesting marine depositional processes dominated and terrestrial influence was limited (fig. 32). In the Anderson 1-12 core, Th concentration increase and U concentrations decrease in intervals 1, 4 and 9. Intervals 1 and 4 are lighter-colored gray shale, whereas interval 9 is dark gray to black. Concentrations of V and Mo are reduced in the same intervals suggesting increased detrital input. TOC correspondingly decreases in intervals 1 and 4, indicating dilution, less production or less preservation.

CONCLUSIONS

The petrologic characterization of the Woodford Shale and Arkansas Novaculite demonstrate the value of integrated datasets in evaluating the regional depositional model for shale gas reservoirs. The Woodford Shale and Arkansas Novaculite example demonstrates that cores and outcrops more proximal to the Ouachita embayment are enriched in biogenic silica and non-skeletal phosphate that accumulated as a result of upwelling from the embayment. In southern Oklahoma, the volume of novaculitic chert is sufficient to generate naturally fractured and brecciated reservoirs that store large volumes of free-state gas. This gas is produced in vertical wells with minimal hydraulic stimulation (Puckette et al., 2013). Chert and non-skeletal phosphate decrease distally to the Ouachita embayment. The Arkansas Novaculite section near Atoka, Oklahoma is greater than 80% novaculitic chert, but

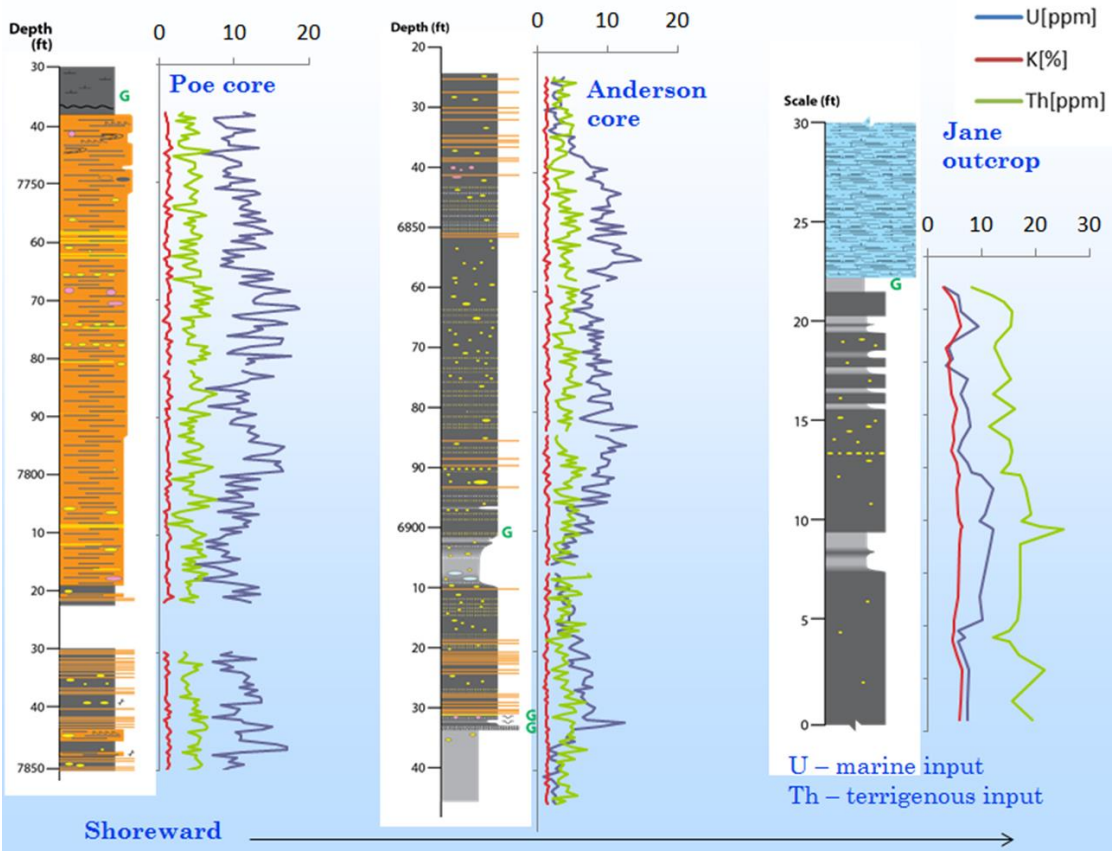

Figure 32. Concentrations of U, K and Th for the Poe 1-29, Anderson 1-12 and Jane outcrop. U:Th ratios indicate the Poe and Anderson sections were dominated by marine biogenic sedimentation. In contrast, the low U:Th ratio in the Woodford Shale at Jane, Missouri indicates a dominance terrestrial sediment source.

contains dark shale with Woodford Shale features. In contrast, the Jester 1-26 core and Jane, Missouri outcrop are devoid or chert and non-skeletal phosphate.

This study shows that the Woodford Shale in tectonically less stable settings such as those associates with the SOA exhibits a variety of deformation features such small scale growth faults, recumbent folds, breccias, shear fractures and dessication fractures that support syndepositional tectonism. Evidence for early cementation of fractures in chert includes ptygmatic fractures deformed during burial compaction.

Shale gas plays in the Woodford Shale depend on brittle rock to provide suitable fabric and composition for gas storage and facture propagation. Understanding the relationship

between facies and shale gas productivity is a key element to successfully exploring and developing these critical resources. Chemostratigraphy is an important tool for interpreting rock composition and origin. Elemental proxies for redox during deposition, TOC and other useful indicators such as U/Th ratios derived from spectral gamma-ray all provide evidence necessary to interpret depositional settings and facies.

A.2. PETROLOGIC AND GEOLOGICAL CHARACTERIZATION OF THE BARNETT SHALE

INTRODUCTION

The Barnett Shale in the Fort Worth basin hosts one of the largest unconventional shale gas plays in North America. Within the central part of the basin, the Barnett is estimated to contain >200 Tcf of gas in place with an estimated 6 to 75 Tcf of undiscovered, technically recoverable gas (Montgomery, 2005; EIA, 2013). Recovery of this undiscovered gas will require continued improvements in geological characterization including thorough petrologic characterization. Petrologic characterization is a key aspect of this project because of the relationship between depositional faces, composition, fabric, and reservoir properties. The petrologic analysis of the Barnett Shale outlined in this report is a component of the larger multidisciplinary effort to evaluate shale reservoirs and facilitate development of additional reserves. This research highlights SEM/EDS mineral and porosity mapping and gives examples that illustrate porosity and permeability values associated with each facies. This study focuses on the Chesapeake Energy, King B 3H core, Tarrant County, Texas (fig. 33). This core is located in the Newark East field, an area of dry gas production. Chesapeake Energy contributed this 400 ft. long core (7180 ft. to 7580 ft.) and accompanying analyses to facilitate increasing the understanding of the relationship between depositional facies, reservoir quality and depositional setting. Furthermore, rock properties were tied to wireline-log signatures to facilitate mapping and delineation of reservoir facies.

PURPOSE

This study is an in-depth analysis of the Barnett Shale in the King B 3H core that is designed to define depositional facies, use these facies and key stratigraphic surfaces to build a depositional models, and relate rock properties of these facies to reservoir quality and

wireline log signatures. The primary objectives of this research were to define and describe lithofacies and associated depositional and diagenetic features, relate these to composition and resulting wireline log signatures, and to define the depositional processes and paleoenvironments in which the Barnett Shale accumulated. The results of this characterization have been synthesized into a conceptual geologic model that can help facilitate continued and more efficient exploration and development of the Barnett Shale.

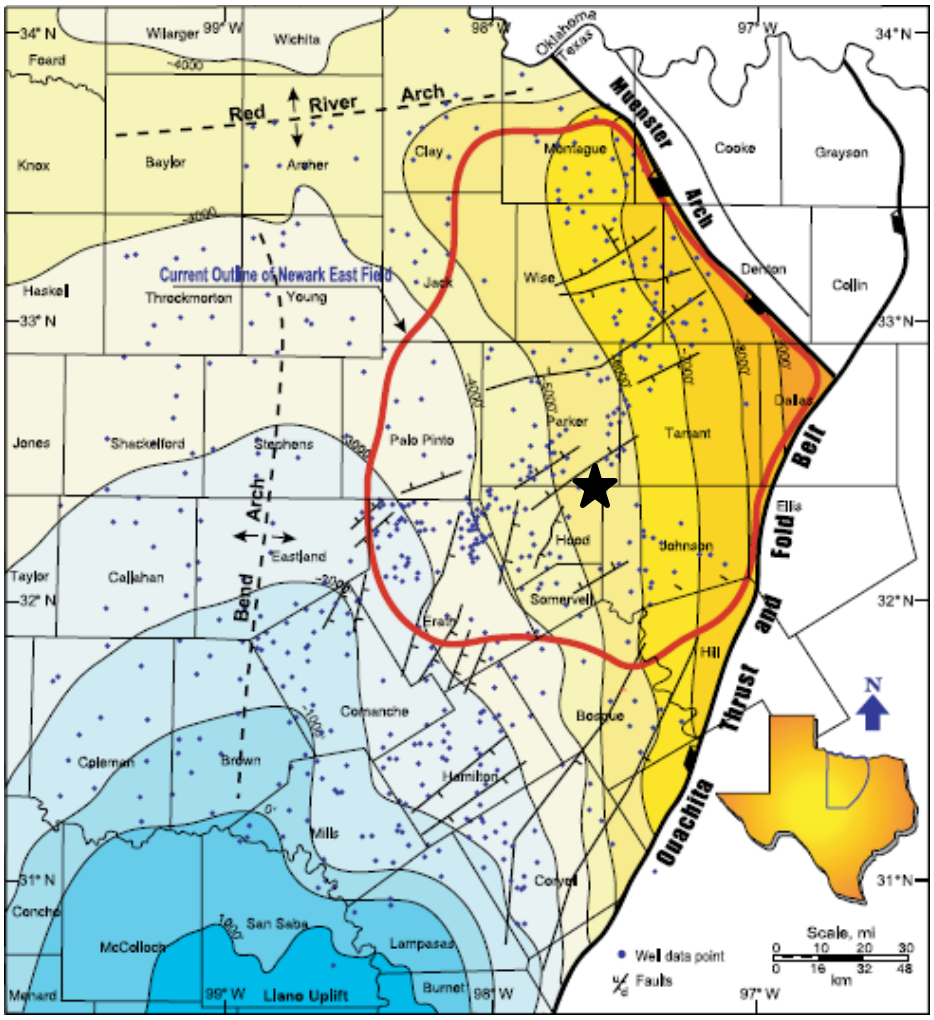

Figure 33.—Regional geology and structure contour map of the base of the Barnett Shale, in the Fort Worth Basin. Contour interval = 1,000 ft. The red line marks the approximate boundary of the Newark East Field. King B 3H well (black star) (modified from Zhao et al., 2007).

METHODS and TECHNIQUES

The objectives of this study include the detailed analysis of the Chesapeake Energy King B 3-H core. Core description was supplemented by the petrographic analysis of 200 thin sections, images acquired by the field emission scanning electron microscope (FESEM), as well as scanning electron microscopy-energy dispersive spectroscopy (SEM-EDS) images. Petrographic data were integrated with wireline log and other petrophysical data, and results of previous Barnett Shale studies to produce a conceptual geologic model. In addition, Chesapeake Energy provided source rock analysis (SRA), tight rock analysis (TRA), composition data from x-ray diffraction (XRD), and over 1,500 core photographs to the project.

RESULTS

PETROLOGY OF BARNETT LITHOFACIES

The siliciclastic mudstone packages and thin carbonate beds that constitute the Barnett Shale were organized into four lithofacies, each containing a distinctive suite of rock types, physical sedimentary structures, biogenic structures, and diagenetic features. These lithofacies are the (1) siliceous mudstone facies, (2) argillaceous mudstone facies, (3) calcareous mudstone facies, and (4) dolomitic mudstone facies (table 2). A detailed description of each facies, its defining properties including sedimentary, biogenic and tectonic structures as well as an interpretation of its context within a sequence stratigraphic framework can be found in Miller (2014).

Table 2.—Characteristics of the generalized depositional facies of the Barnett Shale

Facies	Composition: Representative Sample (XRD)	Porosity & Permeability φ = porosity % k = permeability	TOC %	Comments and Interpretation
Siliceous mudstone	QF = .71 Cl = .27 Ca = .01	φ = 8.3 k = .92 µD	4.4	Spicular and biogenic (radiolarian)-sourced silica. Platy illite shale matrix with cryto-crystalline quartz. Matrix shields interparticle pores from compaction. Porosity and organic matter preserved by packing flaws. Burrows common.
Argillaceous mudstone	QF = .29 Cl = .70 Ca = .01	φ = 7.5 k = .49 µD	7.4	Illite with detrital quartz, plagioclase and organic matter. Dispersed pyrite common. Permeability reduced by more efficient packing and less matrix competence.
Calcareous mudstone	QF = .33 Cl = .37 Ca = .30	φ = 2.7 k = .17 µD	2.2	Significant calcite and dolomite as silt-sized detrital grains and authigenic cement that fills interparticle space and precipitates along grain boundaries. Carbonate cement occludes porosity; reduces organic matter content.
Dolomitic mudstone	QF = .41 Cl = .32 Ca = .27	φ = 3.7 k = .29 µD	2.7	Microcrystalline dolomite instead of rhombohedra. Dolomite preserved as overgrowths on calcite. Tight packing of larger carbonate grains suggests precipitation or mobility shortly after deposition. Cementing of grains occludes porosity; reduces permeability. Pyrite is common.

Siliceous Mudstone Facies

The example siliceous mudstone facies sample is from 7,383.7 feet (fig. 34). The siliceous mudstoned facies is rich in detrital quartz, feldspar (Q+F = 71%) and clay (27%), but contains very little carbonate (1%). Cryptocrystalline silica is the dominant early diagenetic product; other authigenic material includes calcite, dolomite, pyrite and

phosphate. The rock fabric is peloidal to massive and common physical sedimentary structures include horizontal laminae and ripples. Biogenic structures are dominated by burrows and where abundant, give a mottled to nodular texture. The light-colored laminae and burrow fills are mostly silt-sized silica grains, siliceous sponge spicules and plagioclase grains. The cryptocrystalline quartz was likely sourced by dissolution and re-precipitation of opaline tests of radiolarians. Intergranular space generated by packing flaws is partially filled with organic matter that contributes to higher porosity and permeability values associated with this facies.

Argillaceous Mudstone Facies

The representative sample of the argillaceous mudstone facies is from a depth of 7548.8 ft in the basal portion of the lower Barnett. The sampled argillaceous mudstone is rich in clay minerals (70%) with respect to silica (29%) and carbonate (1%). In contrast to the siliceous mudstone lithofacies, cryptocrystalline silica is much less abundant and the matrix is dominated by illite, phosphate and organic matter (fig. 35). The phosphate and organic matter were likely externally sourced from water upwelling on the Barnett shelf. Low pH, reducing bottom water favored phosphate cementation over calcite or dolomite cementation, which is essentially absent. Reducing conditions favored pyrite precipitation as framboids and individual euhedra. Lag deposits containing quartz grains, shell fragments, pyrititized grains, phosphatic oods, and glauconite are interpreted as storm deposits

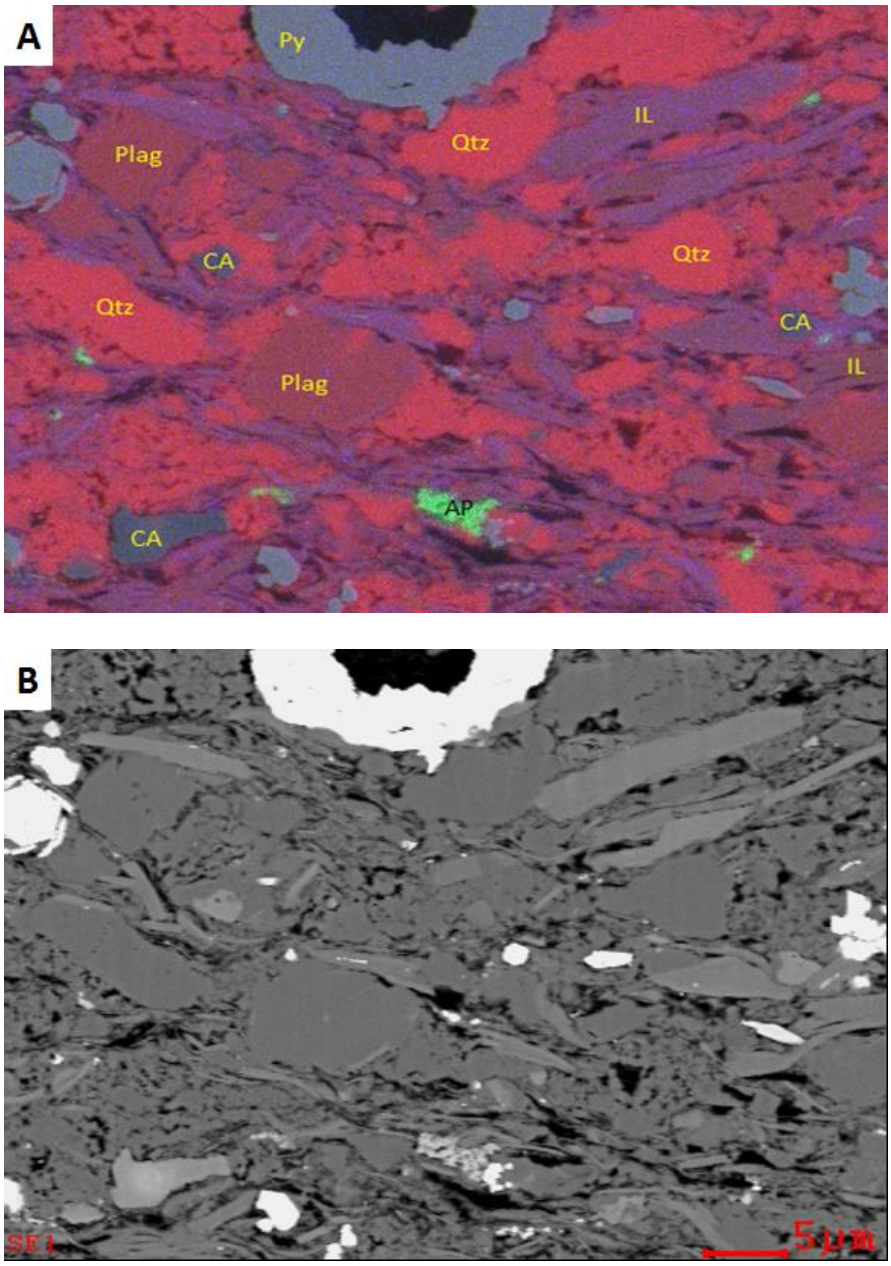

Figure 34.—Images of siliceous mudstone, sample (7,383.72 ft).
(A) EDS color enhanced image of a biogenic silica-rich facies showing quartz occurring as both detrital grains and biogenic silica, forming much of the matrix. Quartz (Qtz), plagioclase (Plag), calcite (CA), illite (IL), apatite (AP), pyrite (Py).
(B) SEM image showing interparticle porosity formed between poorly packed grains contains organic matter (black). Organic matter within pyritized sponge spicule at top of image is also shown in Figure 11.

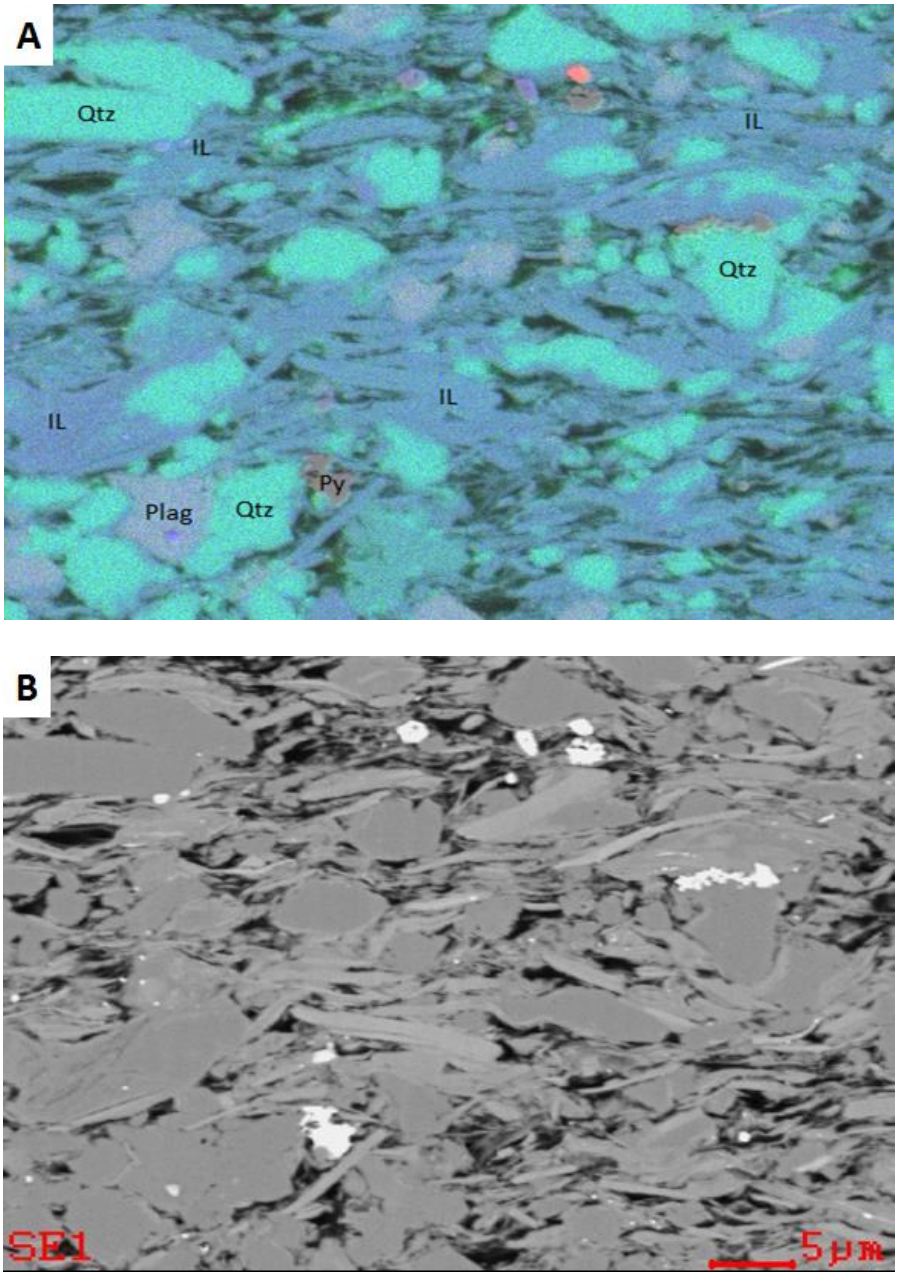

Figure 35..—Images of argillaceous mudstone, sample (7,548.8 ft).
(A) EDS color enhanced image showing quartz grains in a matrix composed predominantly of illite. Quartz (Qtz), illite (IL), plagioclase (Plag) and pyrite (Py).
(B) SEM image showing interparticle porosity filled with organic matter (black) within the matrix. Also note the two forms pyrite both white in color. Individual pyrite euhedra (pe) and framboidal pyrite (fp).

Calcareous Mudstone Facies

The calcareous mudstone sample is from a depth of 7,266.8 ft., which is near the top of the lower Barnett. It consists of interlaminated calcareous and argillaceous shale that is lighter colored than the siliceous and argillaceous mudstone lithofacies. The calcareous mudstone facies contains limestone concretions, argillaceous shale beds, and a graded limestone bed. Based on XRD the representative sample is 37% quartz + feldspar, 33% clay minerals and 30% carbonate. Calcite fills interparticle spaces and precipitates along grain boundaries (fig. 36). As a result, porosity and permeability are reduced significantly and concretionary masses with virtullay no interparticle porosity are common.

Dolomitic Mudstone Facies

The dolomitic mudstone facies is the least common and is interbedded within the previous facies. The representative sample is from 7324.42 ft and contains microcrystalline dolomite rather than larger dolomite rhombohedra. The composition of this sample is 41% Q+F, 32% Cl and 27% Ca, which contains dolomite overgrowths on calcite grains (fig. 37). Dolomitic mudstone beds are typically less than 2 feet thick and easily recognized by their medium to light gray color (Miller, 2014). The dolomite is believed to be authigenic and can occur as dolomitic shale in which clayey matrix is replaced by microcrystalline dolomite (fig. 37) and sand-sized rhombs in argillaceous matrix. Similar to calcite, dolomite cements matrix and greatly reduces interparticle porosity.

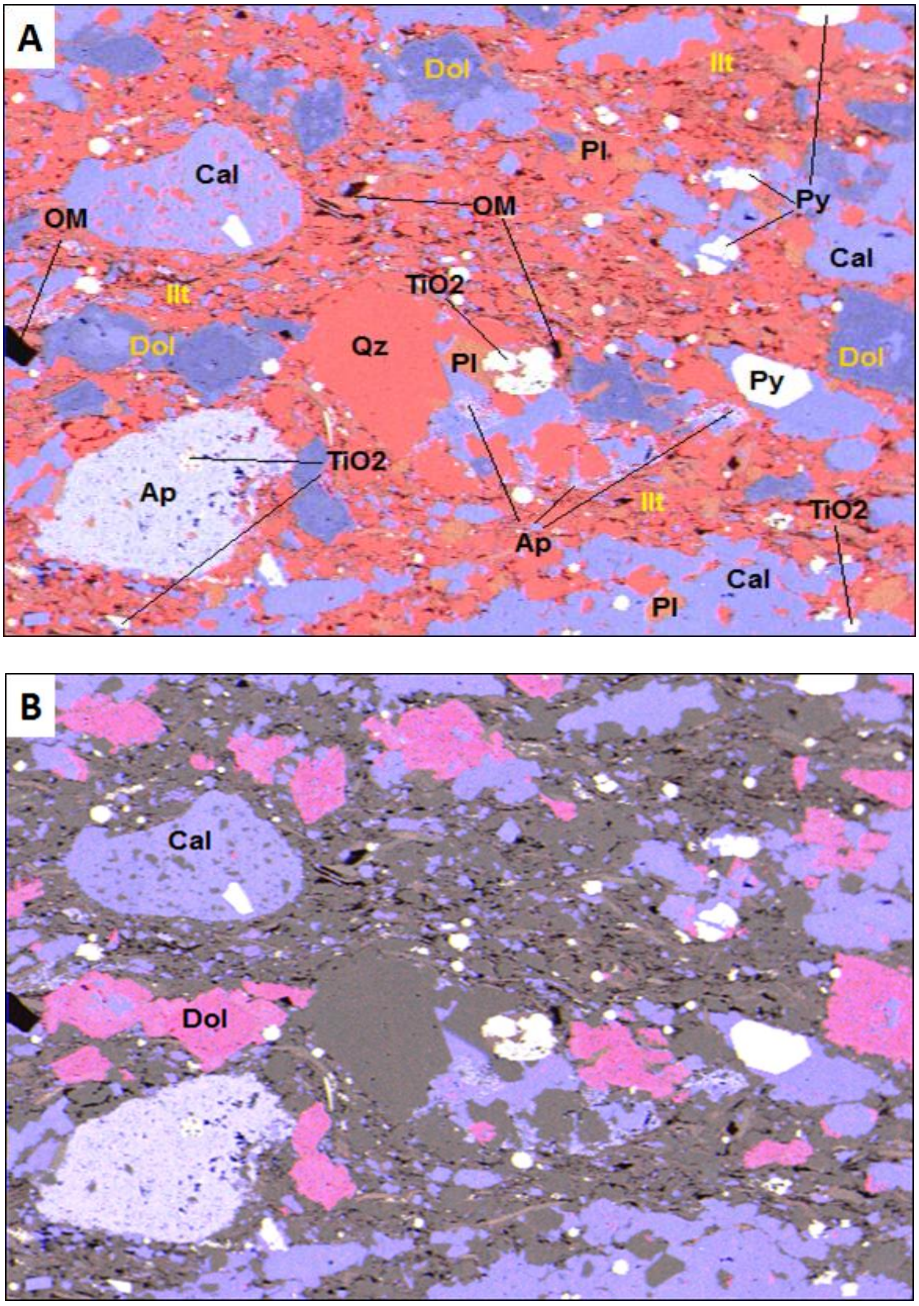

Figure 36.—Images of calcareous mudstone, sample (7,266.8 ft).
(A) EDS color-enhanced image with grains identified, calcite (Cal), organic matter (OM), pyrite (Py), dolomite (Dol), apatite (Ap), quartz (Qz), plagioclase (Pl).
(B) EDS color-enhanced image showing organic matter (black), calcite (purple) and dolomite (pink).

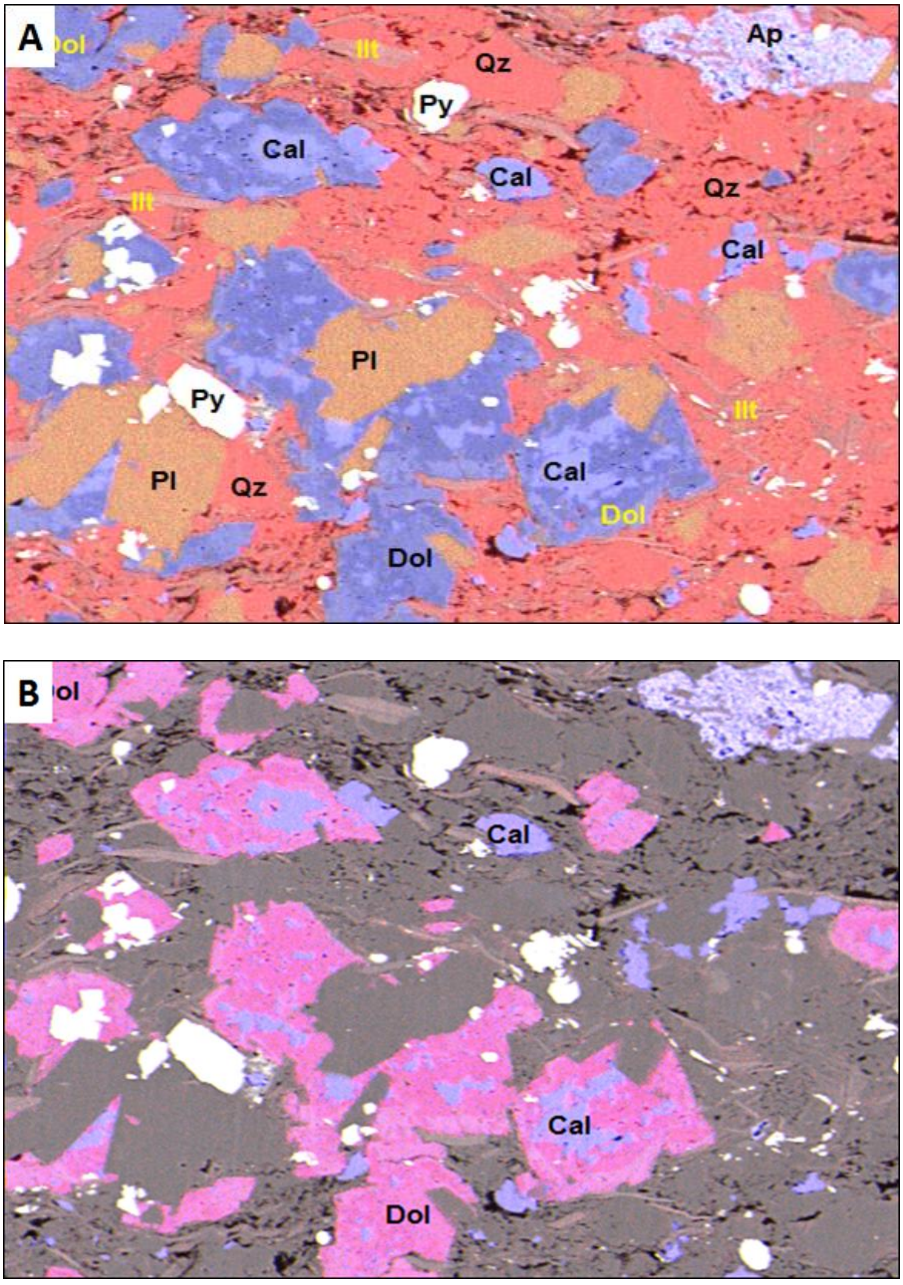

Figure 37.—Images of dolomitic mudstone, sample (7324.42 ft).
(A) EDS color-enhanced image with grains identified, calcite (Cal), organic matter (OM), pyrite (Py), dolomite (Dol), quartz (Qz), plagioclase (Pl), apatite (Ap). Dark material is mostly organic matter.
(B) EDS color-enhanced image with calcite colored purple and dolomite colored pink.

ORGANIC CARBON

The occurrence of organic matter in the Barnett is governed by variables with complex interrelationships. Ultimately, TOC content is controlled by the availability of source organic material and the quality of the original source rocks, which are both primarily governed by geochemical and geothermal kinetics. The total organic carbon (TOC) measured in the King B 3H core ranges from 0.9 to 7.8% (Figure 38). These numbers are consistent with other reported ranges (Jarvie, 2003; Montgomery et al., 2005; Jarvie et al., 2007).

POROSITY

Understanding porosity and its development is a critical element to the petrologic characterization of gas shale reservoirs. Various types of pores were identified in argon-ion milled samples viewed with the field-emission scanning electron microscope (FESEM) (fig. 39). Three types of porosity are common: interparticle/intercrystalline, intrakerogen and intraparticle. The ratio of interparticle porosity to intrakerogen porosity is about 20:80 in most of the Barnett, but in some facies the percentage of interparticle porosity can be as high as 50% (Miller, 2014). Intraparticle porosity was observed locally and accounts for a negligible fraction of the total porosity. The dependence of intrakerogen porosity on interparticle porosity is critical as organic matter is composed of spherical to elliptical particles that accumulated in interparticle space as a colloid-like substance (fig. 39B) (Alcantar-Lopez and Chipera, 2013). The siliceous mudstone facies with its packing flaws provided space for organic matter accumulation. This relationship between the siliceous mudstone facies, porosity, and permeability is critical to the economic success of the Barnett Shale play.

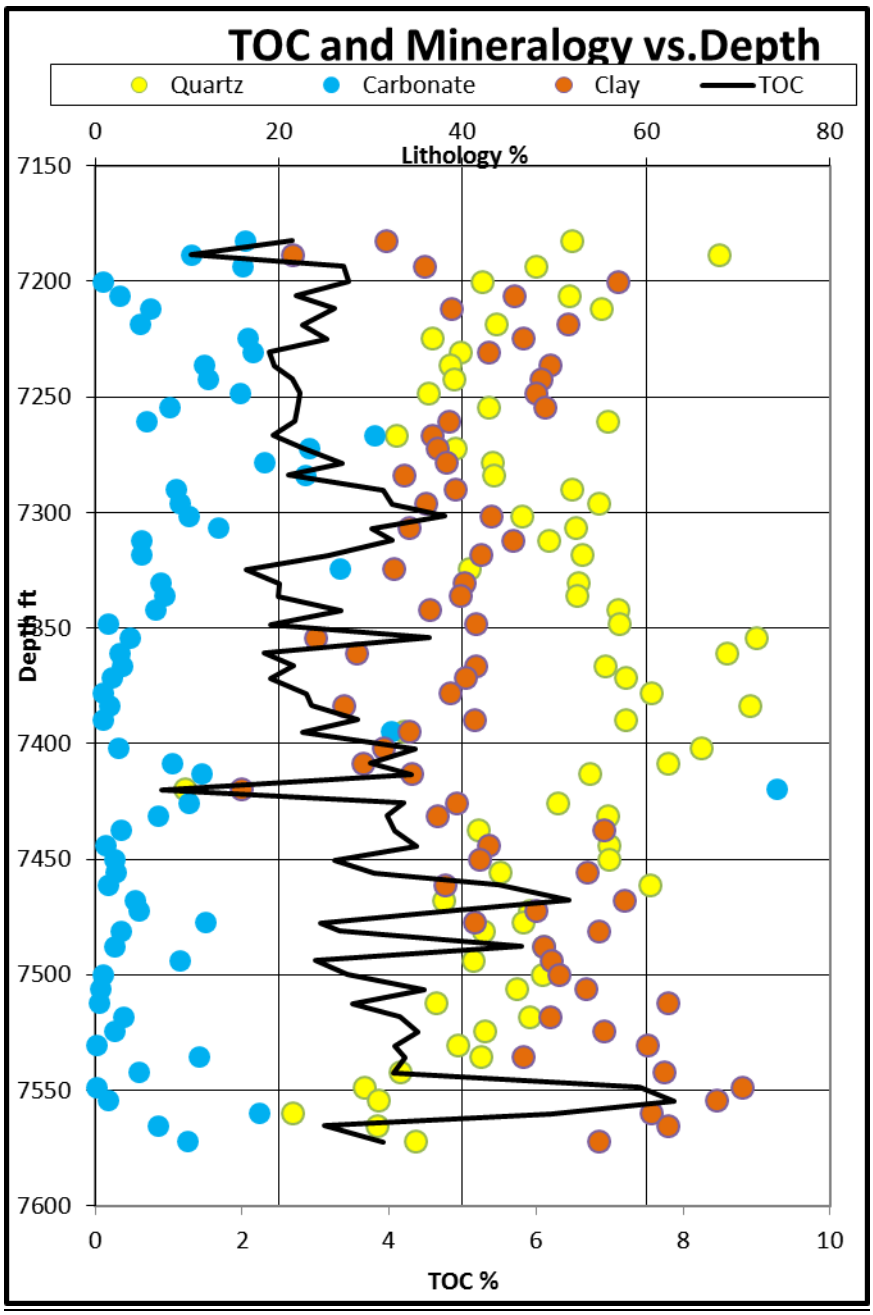

Figure 38.—Graph showing basic mineralogy and TOC in % plotted by depth.

Interparticle/Intercrystalline Porosity

Interparticle porosity occurs in the interstices between mineral grains (figs. 34, 39 & 40). Interparticle porosity is most important in facies containing cryptocrystalline silica (figs. 36A and 41) whose small grains help support the rock framework and protect interparticle pores from being crushed during compaction. Intercrystalline porosity was also observed within pyrite framboids (fig. 40).

Intrakerogen Porosity

Intrakerogen porosity is developed within the organic material (figs. 39 and 42). The common presence of organic matter in open pores and in larger, open, stress-protected pore bodies supports the interpretation that the organic matter was formed within intercrystalline/interparticle space as a colloid-like substance (fig. 39B) (Alcantar-Lopez and Chipera, 2013). Figure 42 shows intrakerogen porosity within organic matter in a fossil fragment. The fossil is the same siliceous sponge spicule replaced by pyrite in Figure 34, an image taken in the siliceous mudstone facies (Miller, 2014).

Intraparticle Porosity

Intraparticle porosity was observed in carbonate grains and diagenetic bodies (figs. 43and 44). Intraparticle porosity is rare, found only in facies with lower porosity and TOC values, and likely does not contribute to permeability.

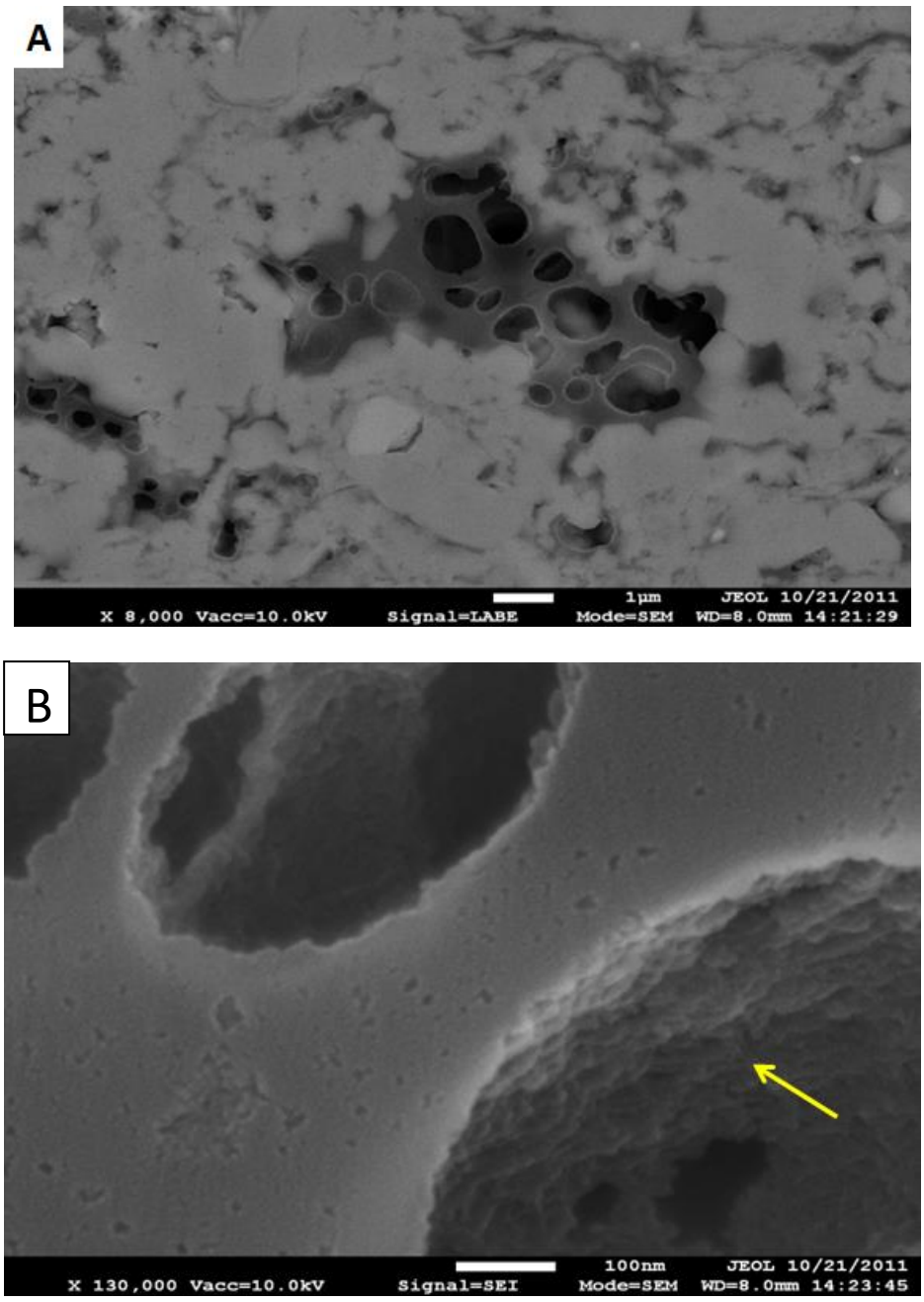

Figure 39.—SEM images of porosity in siliceous mudstone at 7,383.72 feet.

(A) (Low angle backscattered electron) LABE image of siliceous mudstone that shows an area of interparticle porosity within cryptocrystalline silica cement. Interparticle pores are partially filled with organic matter (dark) that exhibits secondary porosity.

(B) (Secondary electron image) SEI image showing the porosity in (A) at 130,000 X, organic matter between intrakerogen pores has colloidal texture (yellow arrow).

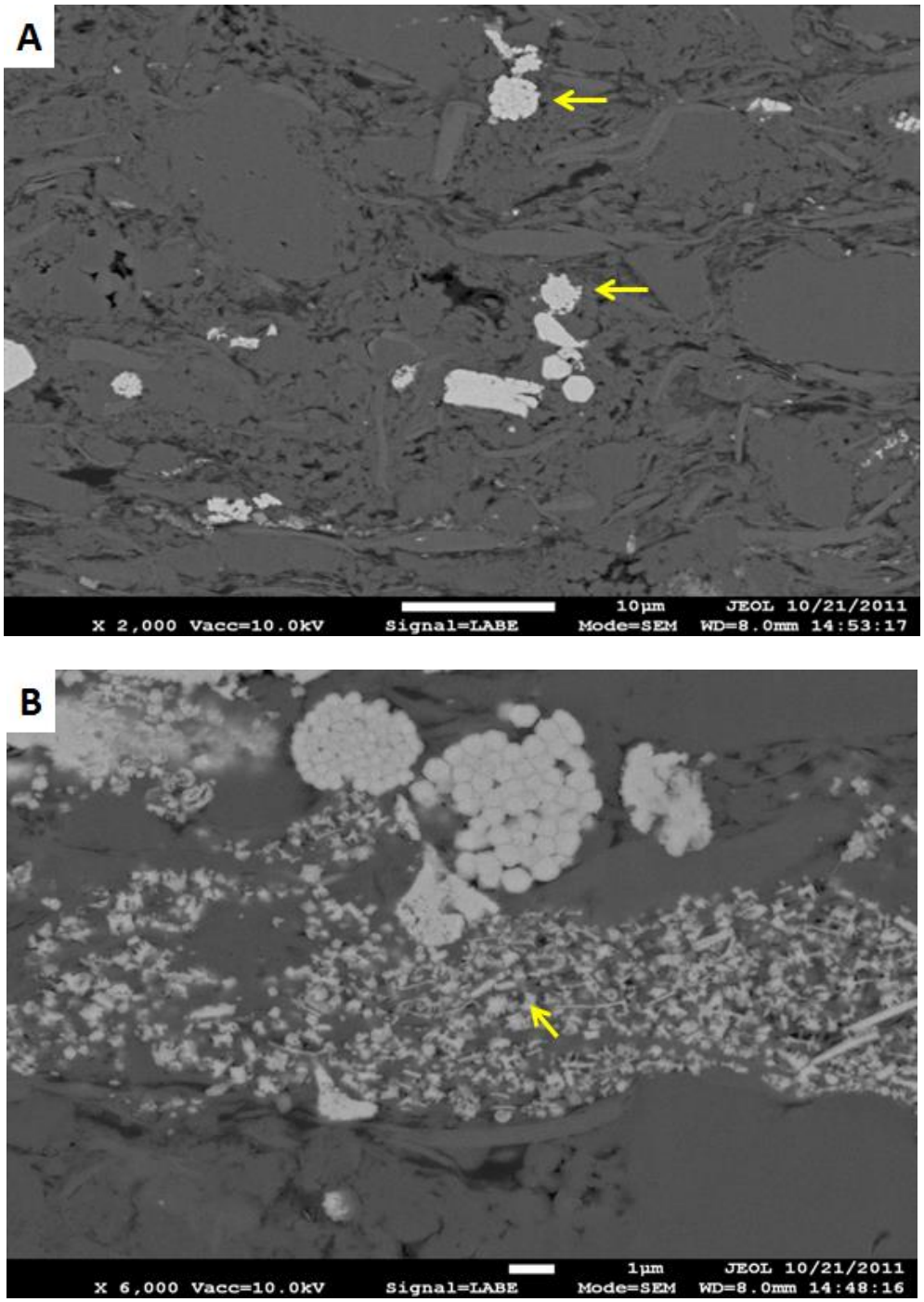

Figure 40.—Images of porosity.

(A) SEM image showing poorly packed grains with interparticle porosity (dark) and framboidal pyrite (light). Arrows identify pyrite framboids. Dark areas are pores that are either open or partially to completely filled with kerogen.

(B) SEM image at higher magnification to show small pores including intercrystalline associated with pyrite that occurs as framboids, isolated euhedra, and pyritized fossil fragments (arrow).

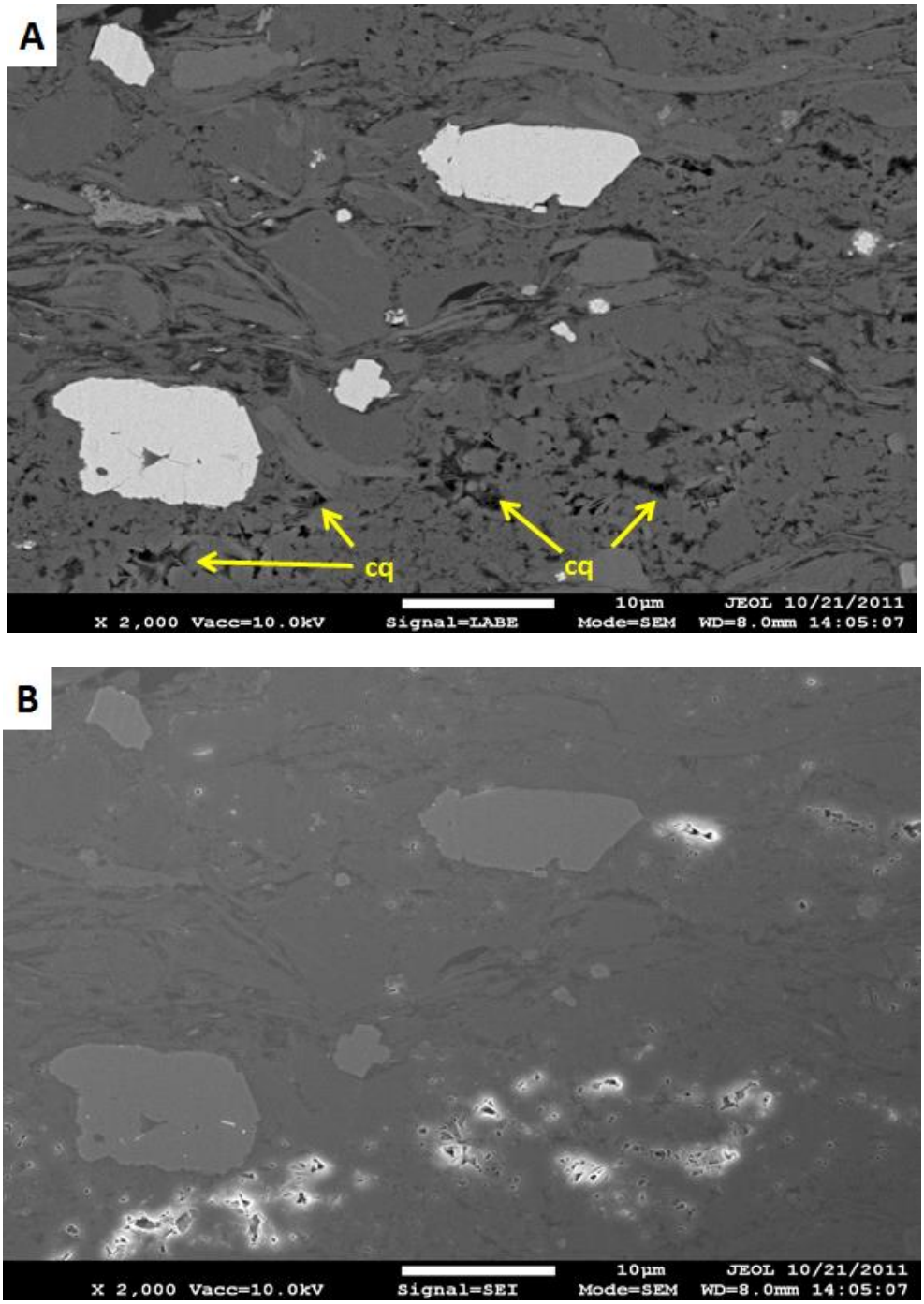

Figure 41.—Images of porosity.

(A) Low angle backscattered electron (LABE) image of siliceous mudstone showing pore spaces preserved by cryptocrystalline quartz cement (cq) in the lower and right side of the image in contrast to the upper left portion of the image that contains detrital quartz and feldspar grains with a mostly argillaceous matrix.

(B) Secondary electron image (SEI) showing interparticle matrix porosity (pores are outlined in white) within the cryptocrystalline quartz cement but almost no interparticle porosity associated with the detrital grains and clay flakes.

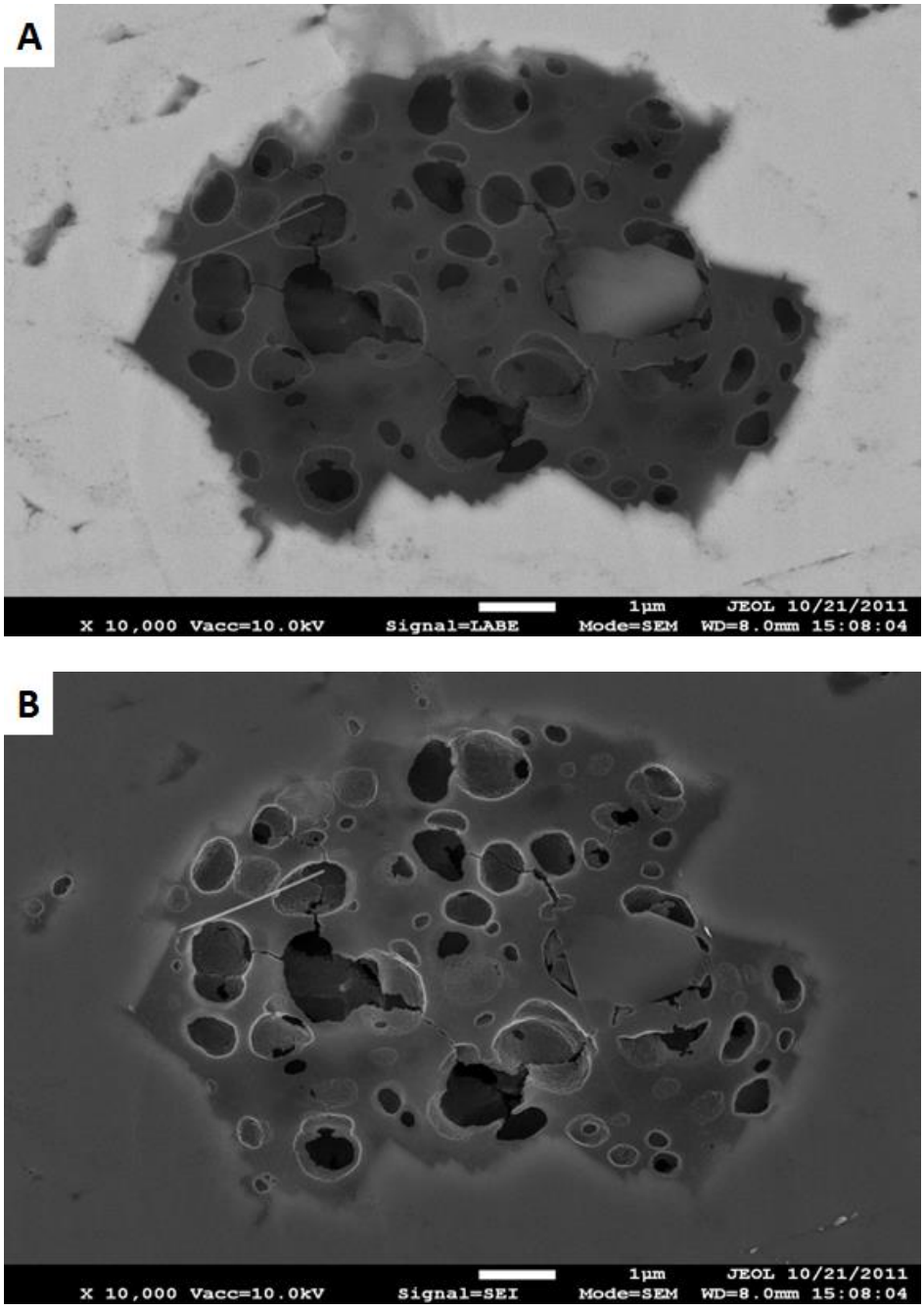

Figure 42.—Images of porosity.

(A) LABE image showing a large pore filled with organic matter inside sponge spicule identified in Figure 3.

(B) SEI image showing the depth of the organic porosity.

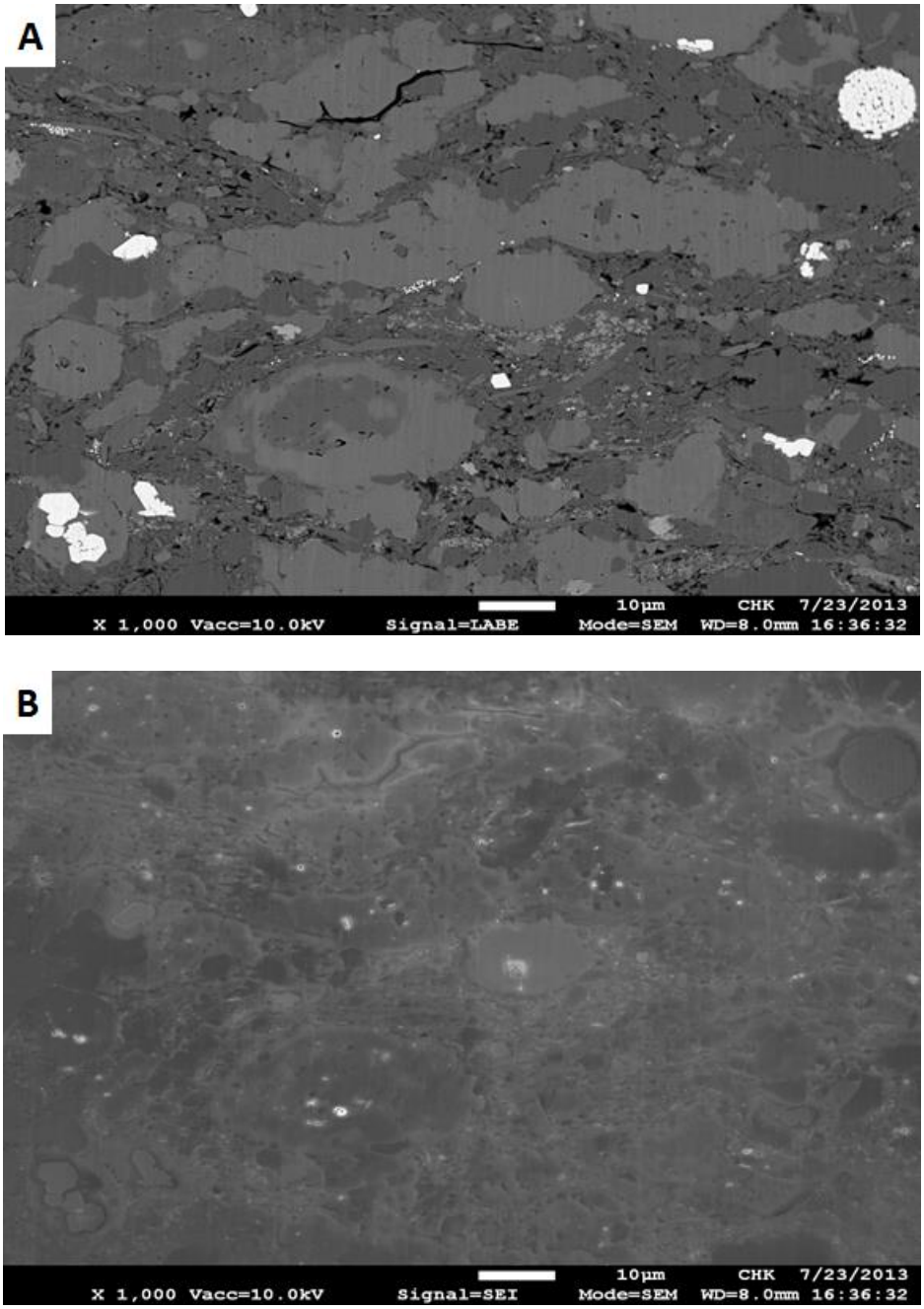

Figure 43.—Images of carbonate mudstone.

(A) LABE image of a carbonate mudstone showing very little porosity or organic material (identified by dark specs) and a very tight matrix

(B) SEI image showing minute amount of porosity (identified by faint white circles) occurring as vacuoles within the larger carbonate grains in this cemented rock.

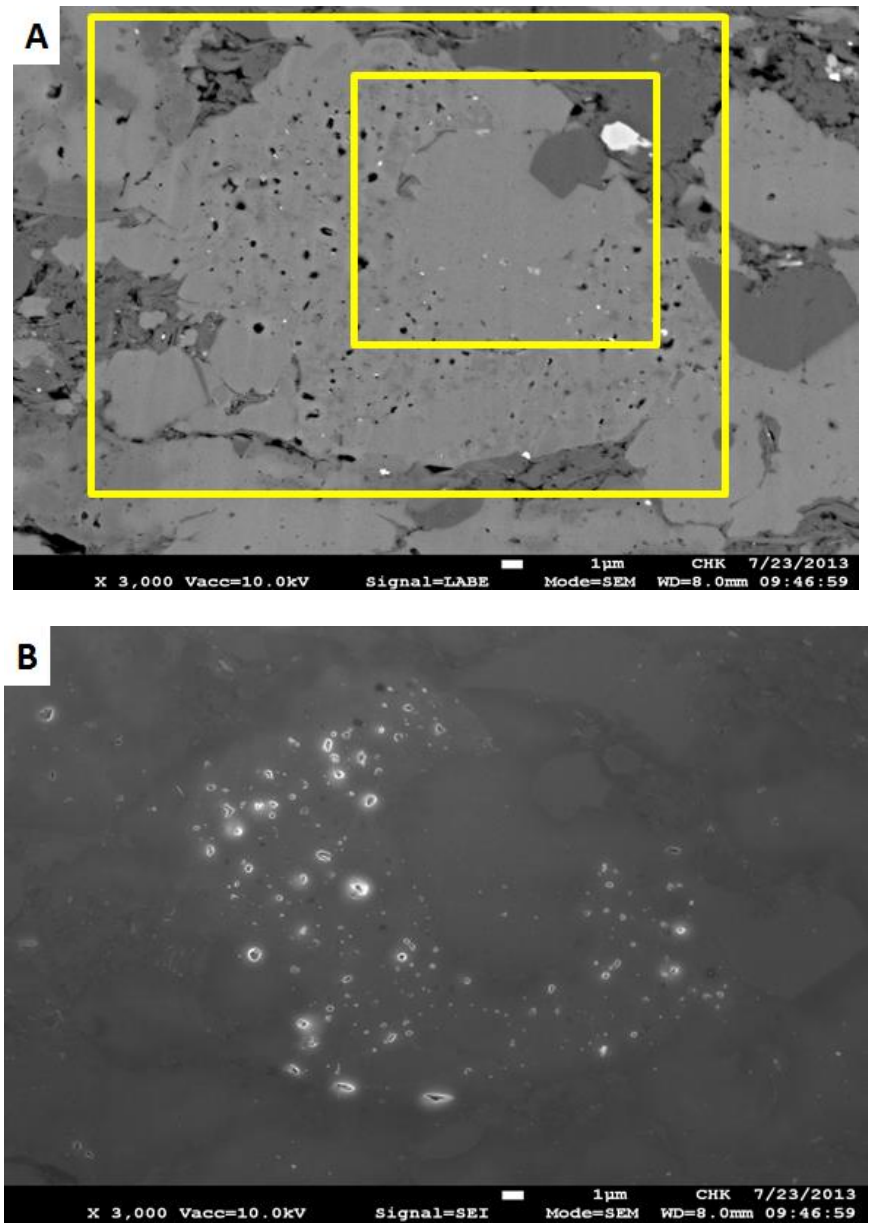

Figure 44.—Images of intracrystalline porosity within a calcite grain with a dolomitic overgrowth.
(A) LABE image showing organic matter in small pores within a portion of the calcite crystal (large yellow box) that is partially dolomitized (smaller yellow box).
(B) SEI image showing small, isolated pores. Also note that the intraparticle porosity occurs overwhelmingly in the calcite portion of the diagenetic body, not in the dolomitic center.

LITHOLOGIC CONTROLS ON POROSITY AND PERMEABILITY

Detrital quartz and feldspar framework grains combined with early diagenetic cryptocrystalline silica contribute to a compaction-resistant framework for the Barnett Shale.

This more rigid framework contributes to overall rock brittleness that facilitates natural fracturing and fracture propagation during hydraulic stimulation. The detrital quartz-feldspar framework favored increased interparticle porosity that is typically partially filled with organic matter. With burial and thermally induced maturation this organic mapper developed the intrakerogen porosity that is crucial the Barnett gas shale play. Milliken et al. (2012) also recognized the role of coarser, quartz and feldspar grains in porosity preservation.

The strong correlation between porosity and permeability is shown in Figure 45. Exact controls and pathways of permeability in the Barnett Shale are not known with certainty, but it is expected that interparticle pores, intrakerogen pores and natural fractures all contribute. The highest permeability occurs in the siliceous mudstone facies that contains higher interparticle porosity, moderate amounts of organic matter whose total volume was likely reduced in part by hydrocarbon expulsion that left intrakerogen pores, and fractures.

When the moving average porosity is plotted against mineralogy, a generalized positive relationship between porosity and quartz is evident (fig. 46). Higher porosity occurs in the siliceous mudstone interval between 7,308 feet and 7,410 feet and tails off in more clay-rich intervals. This plot corroborates the observations from microscopy that detrital quartz and feldspar grains, along with cryptocrystalline quartz provide the framework for preserving interparticle porosity.

The relationship between mineralogy and permeability is more striking as the moving average of quartz exhibits a more positive relationship to permeability (fig. 47) than quartz did with porosity. The highest sustained values for permeability occur between approximately 7,350 and 7, 410 feet, with an overall increase in permeability from around 7,300 feet to 7,410 feet (fig. 44). While permeability and the running average percentage of

quartz exhibit a positive relationship, an inverse relationship exhibits between permeability and clay content.

There appears to be no relationship between the running averages of carbonate and porosity and permeability. However, individual measurements such as the one taken at 7419.9 feet demonstrate that these thin carbonate-enriched intervals can have very low porosity (e.g. 2%) and permeability (e.g. 0.000061mD). When individual measurements of porosity and permeability are compared, a positive correlation and high coefficient of determination are evident (fig. 48) indicating that values for porosity and permeability change together.

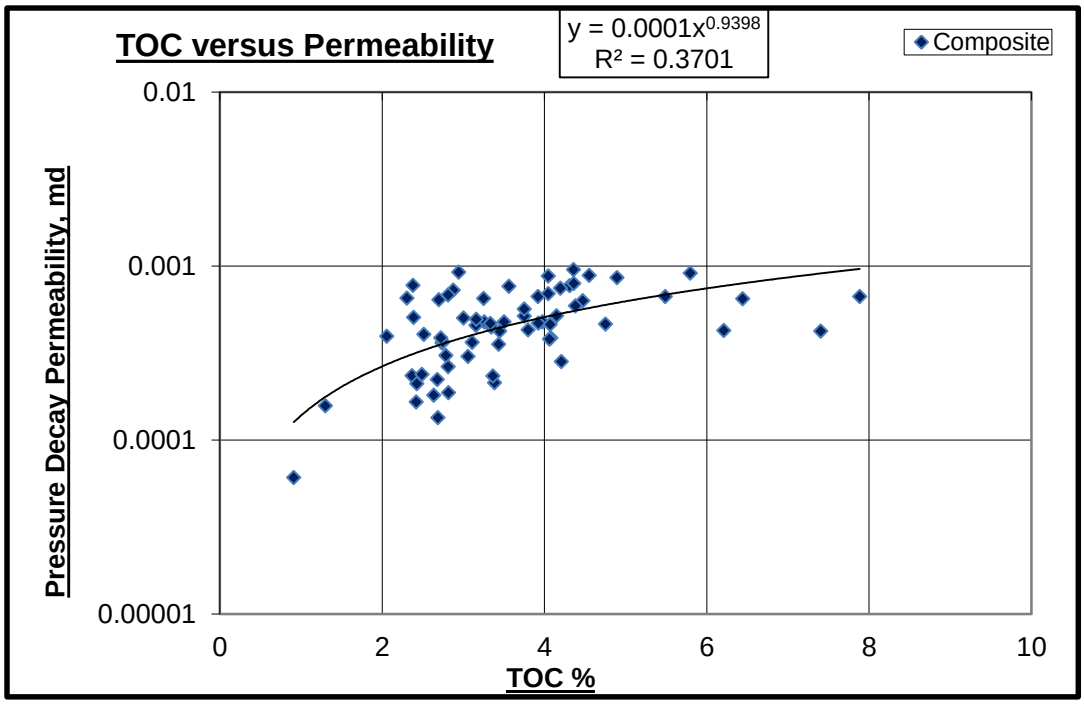

Figure 45.—Scatterplot of TOC versus permeability. Higher values of permeability occur across a range of TOC values, evidence that the TOC in the siliceous mudstone facies could have been reduced by hydrocarbon generation. The resulting intrakerogen pore network, combined with interparticle pores, may give the higher permeability and porosity of this reservoir facies. Higher TOC values in argillaceous mudstone facies follow clay content (Figure 7), but lack the interparticle pores necessary to generate the permeability needed for reservoir facies.

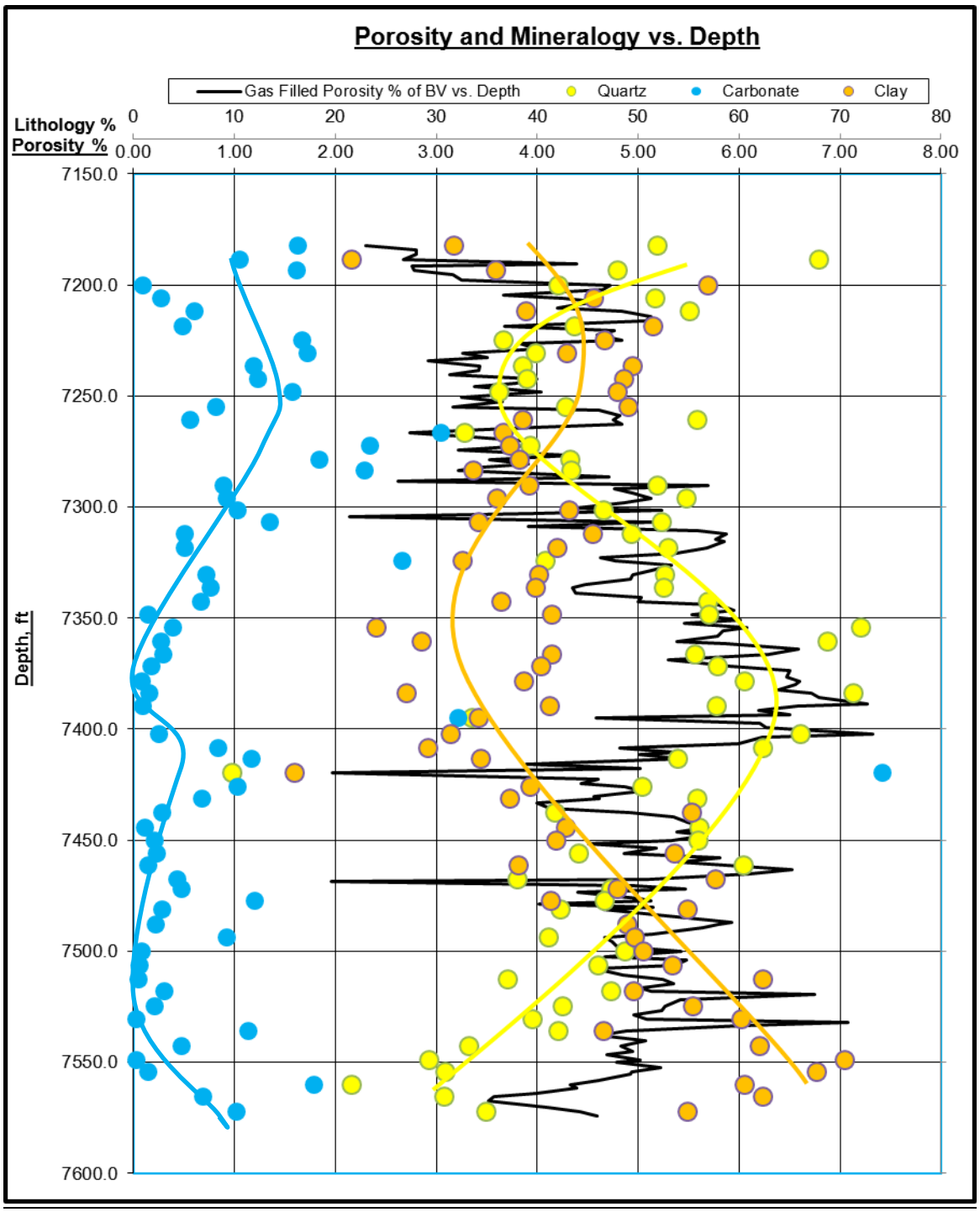

Figure 46.—Graph showing basic mineralogy and porosity plotted against depth. Porosity values exhibit a generalized positive correlation with quartz supporting the observations of the relationship between detrital grains, cryptocrystalline quartz and interparticle porosity.

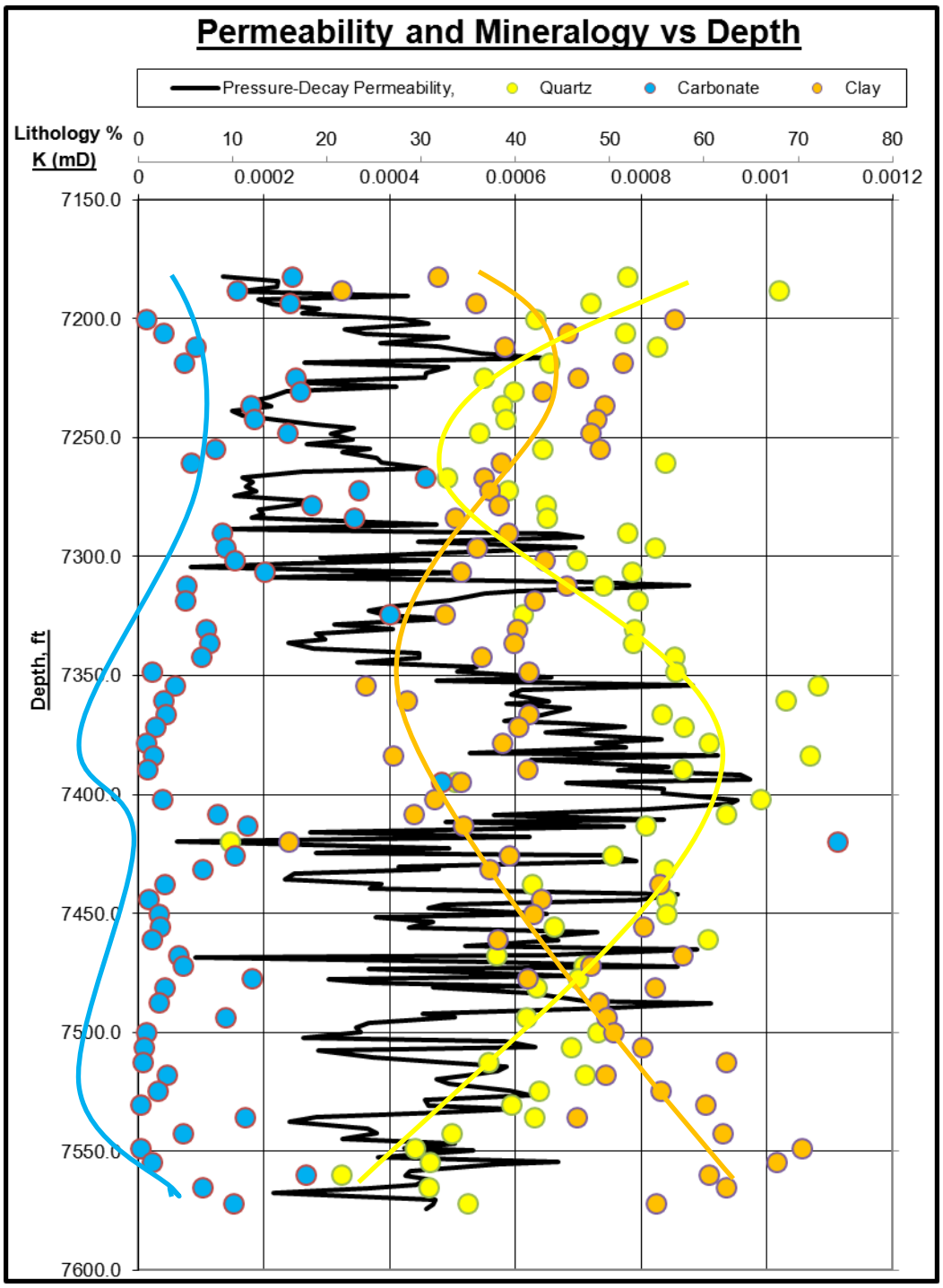

Figure 47.—Graph showing basic mineralogy and permeability plotted against depth. Increased permeability is recognized from approximately 7,350 to 7,440 feet in the silica-rich zone.

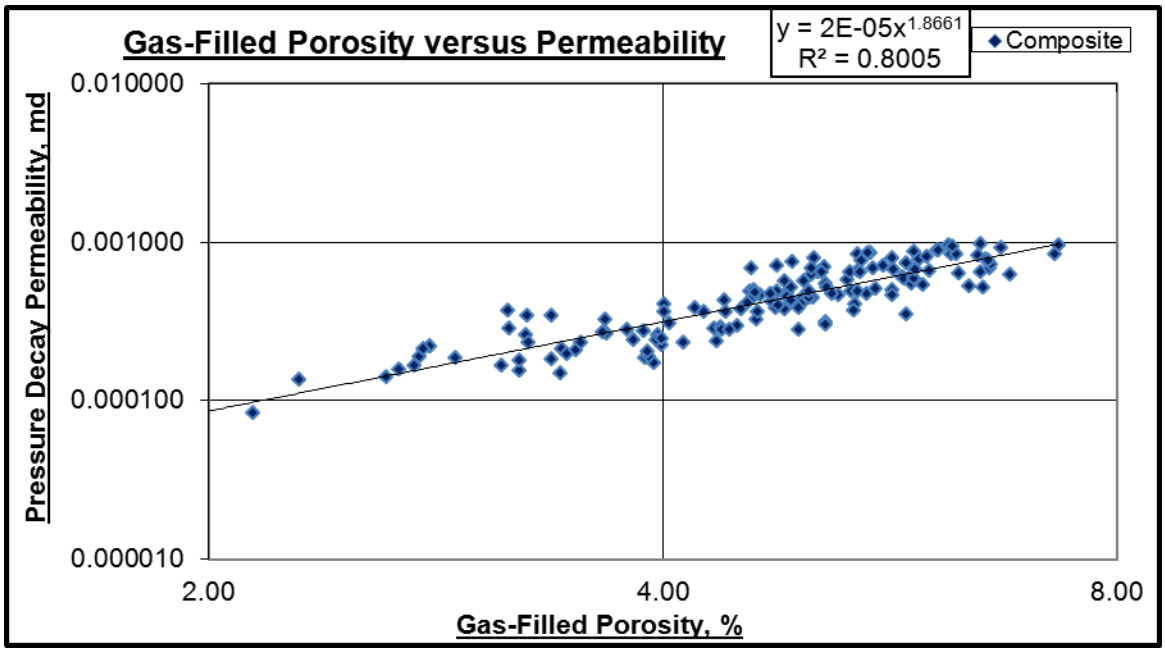

Figure 48.—Graph showing the strong correlation between gas-filled porosity and permeability. The high coefficient of determination ($R^2 = 0.8$) indicates that variance in porosity and permeability values are linked and likely controlled by the same rock properties.

LOG ANALYSIS

An objective of this study was to tie the petrologic characterization to wireline-logs to develop a mapping tool for exploration. Plots comparing rock composition and porosity to wireline-log curves illustrate that relationships exist and that typical wireline-log suites used by industry provide an effective tool for mapping the distribution of reservoir and non-reservoir facies.

The highest gamma-ray responses coincide with lag deposits due to stratigraphic condensation. In the siliceous mudstone section, the gamma-ray response is more consistent as a result of uniform organic matter content and a lack of carbonate beds with low radioactivity that cause sharp decreases in total gamma-ray counts. The lowest gamma-ray values correlate to dolomite beds and calcite-rich concretions. Overall, the gamma-ray curve mimics clay mineral content, increasing when clay mineral content is higher and decreasing

in the siliceous mudstone facies where clay content is reduced (fig. 49). Density logs are influenced by mineral density and the density of organic matter. The siliceous mudstone facies has the lowest bulk density values of approximately 2.4 g/cc when silica >60% (i.e. 7,354.1, 7,383.7, and 7,461.2 ft.) (fig. 50). The highest bulk density value is 2.7 g/cc reported at 7419.9 ft. for the measurement that is >74% carbonate and extremely low porosity (2%). Lower bulk density values for the siliceous mudstone facies are likely a response to both intergranular and intrakerogen porosity. The neutron tool identifies intervals with decreased concentrations of hydrogen, either from the presence of gas in pores or decreased clay content and corresponding decrease in associated bound water. These properties make the combined gamma-ray, density porosity and neutron porosity logs an effective suite for identifying reservoir in the Barnett and similar shales (fig. 51). Photoelectric (PE) curves are density related and provide mineralogical data. Given the PE values for calcite, dolomite and quartz are 5, 3.4 and 1.8, respectively, PE values increases with carbonate content and decrease with increasing quartz content. The interval with the lowest PE response is the siliceous mudstone lithofacies, which contains the highest concentrations of detrital quartz grains and biogenic silica. Carbonate-rich zones are clearly visible on PE logs, which respond positively to increased concentrations of calcite or dolomite (fig. 51). Another useful curve is resistivity, which measures conductivity of the rock and pore fluids, thereby helping distinguish cemented from porous zones and hydrocarbons from briny pore fluids. Utilizing the standard set of gamma-ray, resistivity and density-neutron porosity curves, reservoir facies in the Barnett Shale and similar gas shales can be detected. Compared to argillaceous mudstone facies, siliceous mudstone reservoir facies typically display cleaner (less radioactivity) and consistent gamma-ray values, lower PE values approaching 2.0

barnes/electron, higher resistivity values, lower neutron porosity and higher density porosity values. If the density curve reads higher porosity than the neutron curve (crossover or gas effect), less argillaceous and/or gas-bearing reservoirs is likely. Neutron-density crossover is recognized from approximately 7,365 to 7,415 feet (log depth), which correlates to the siliceous mudstone facies. This interval has the lowest PE values as shown in Figure 49, the lowest bulk density (fig. 50) and highest permeability (fig. 47). Neutron-density crossover correspond to siliceous mudstone facies (yellow boxes) from 7,368 to 7,415 feet (log depth).

GEOLOGICAL CHARACTERIZATION AND DEPOSITIONAL MODEL

A sequence stratigraphy based depositional model was constructed using the observations of depositional facies and stratigraphic surfaces identified in the King B 3H core. The Mississippian section in this core unconformably overlies Ordovician carbonates (Miller, 2014). The flooding of the exposed Ordovician shelf marks the transgressive systems tract and the contact a sequence boundary (fig. 51). The initial Mississippian section is a thin (<3 feet thick) crinoidal limestone. This limestone is succeeded by dark shale formed as the Barnett transgression continued (fig. 52, stages A-C). As the dark, organic-rich sediments accumulated oxygen levels fluctuated due to sea level changes. Periods of dysoxia to anoxia were followed by short periods of adequate bottom water oxygenation to support burrowing infauna (Miller, 2014). Sea level reached a maximum and during the highstand systems tract (fig. 52, stage D), a time of maximum upwelling, biotic bloom in the oxygenated upper water column, and biogenic silica accumulation to form the siliceous mudstone facies (fig. 51). During highstand, upwelling and circulation disrupted stratification, allowing

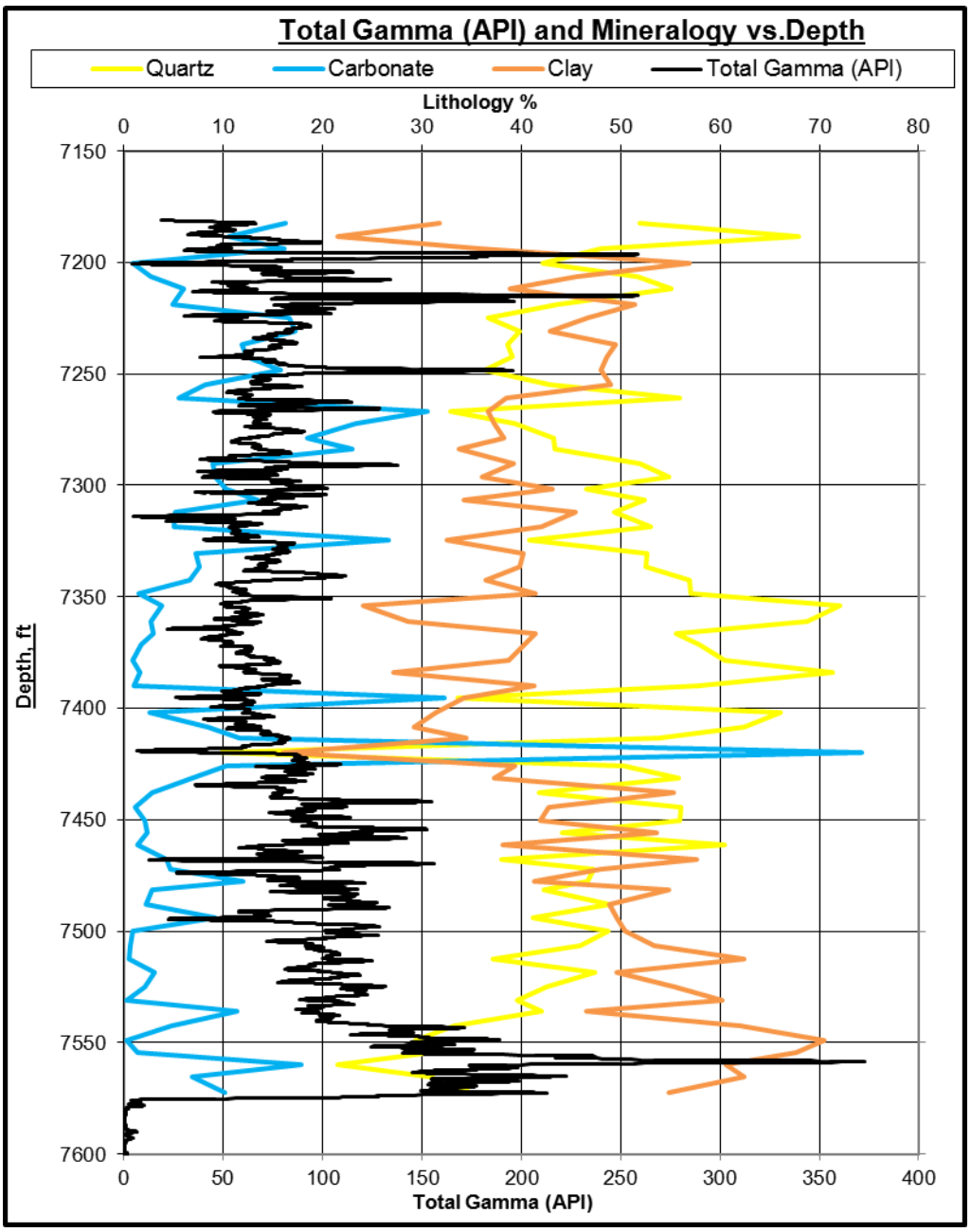

Figure 49.—Graph of mineralogy (quartz, carbonate and clay) and total gamma-ray (API units) plotted against depth. Gamma-ray values follow clay content, increasing in argillaceous facies and decreasing in quartz- and carbonate-rich intervals. From Miller (2014).

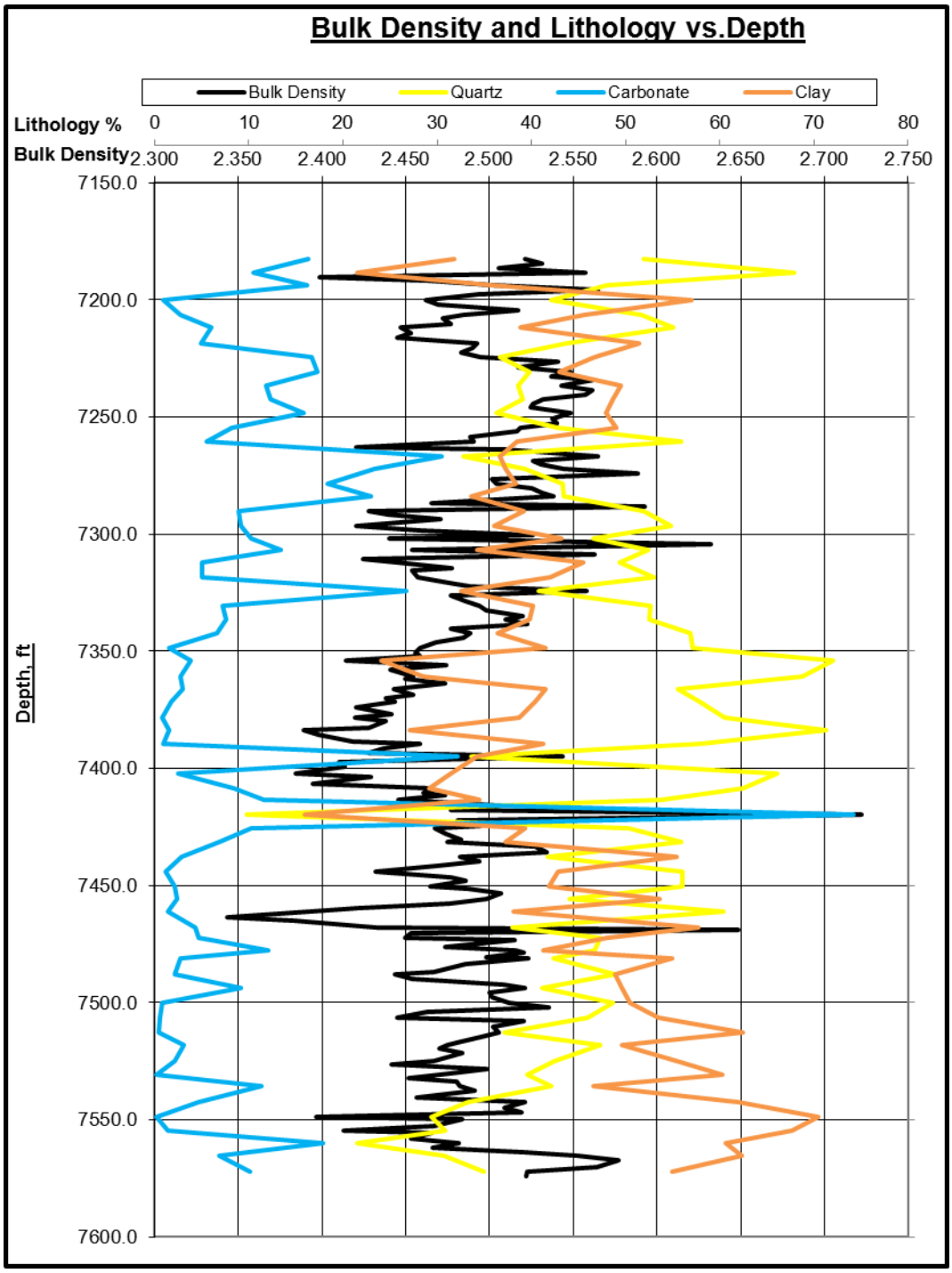

Figure 50.—Quartz, carbonate, clay and bulk density plotted against depth (Miller, 2014). Lower bulk density values (< 2.45 g/cm^3) typically occur in quartz-rich intervals (e.g. 7,310 to 7,410 ft.). The highest bulk density value (2.72 g/cm^3)is associated with the mesasurement at 7419.9 ft. that is > 74% carbonate.

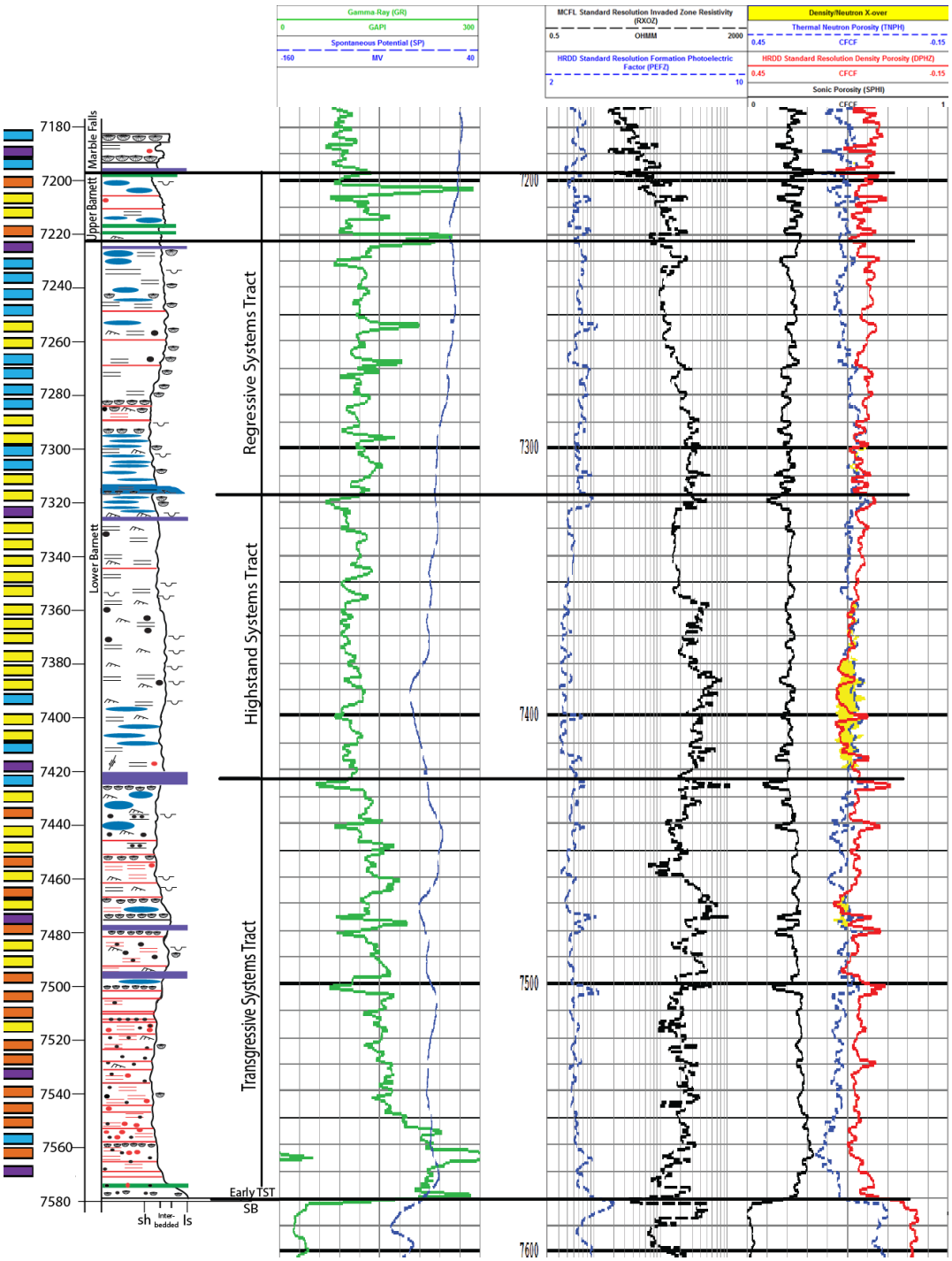

Figure 51.—Composite diagram for the King B 3H core from Miller (2014). Interpretation from left to right: lithofacies (colored boxes), core description, and sequence stratigraphy. Log curves from left to right: gamma-ray (green), spontaneous potential (blue), PE (dark blue dashed), resistivity (black dashed), sonic porosity (black solid), neutron porosity (blue dashed) and density porosity (red solid). Neutron density crossover is shaded yellow. Lower PE values, higher resistivity, and neutron-density

oxygenated bottom water and intermittent benthic colonies as evidenced by abundant burrowing and bioturbation (Miller, 2014). Regression followed the highstand systems tract and the resulting regressive or falling-stage systems tract (fig. 52, stage E) is characterized by the introduction of carbonate (fig. 51) that diluted the silica and clay fractions and reduced TOC. The upper surface of the falling stage systems tract represents a sequence boundary that was succeeded by the Forestburg Limestone in the northern part of the basin. In the King B 3H core the Forestburg Limestone is not present and the sequence boundary was placed along a phosphatic lag deposit (Miller, 2014). The upper Barnett section above this unconformity is similar to the previously described section and culminates at the pre-Marble Falls Limestone (Pennsylvanian) unconformity. A basin-scale model incorporating the sequence boundaries and showing the relationship between the pre-Barnett Ordovician section, lower Barnett, siliceous mudstone facies reservoir zone, Forestburg limestone, upper Barnett and the Marble Falls Limestone is shown in Figure 51 from Miller (2006). This core-, seismic- and wireline log-based model demonstrates basin-scale features that provide geologic context for features observed in the King B 3H core. Regionally the section demonstrates lower Barnett strata onlapping the pre-Barnett (Ellenburger) section, regional thinning of the siliceous zone to the north and south, and truncation of the lower Barnett beneath the sequence boundary (unconformity) below the Forestburg limestone to the north and upper Barnett shale to the south. Above this sequence boundary, a siliceous zone known as the upper Barnett spiculite occurs in a more basinward position to the King B 3H core (fig. 53). This cross section illustrates the importance of geologic characterization and how the lateral distribution of facies, facies stacking patterns, and identifying stratigraphic surfaces in

core, wireline log and/or seismic are all integrated to model the reservoir and predict the distribution of reservoirs and seals.

DISCUSSION

The petrologic and geologic characterization of the Barnett Shale in the King B 3H core illustrates the relationship between depositional facies and reservoir evolution. As the largest volume of porosity is intrakerogen (Miller, 2014), the distribution of organic matter strongly influences permeability and fluid-flow pathways should be greatly influenced, if not controlled, by the three-dimensional arrangement of organic matter grains (Loucks et al., 2009). The correlation between permeability and TOC shown in Figure 45 indicates that the highest permeability does not coincide with the highest values of TOC. This suggests that permeability is not influenced only by the volume of organic matter, but that equally important is the distribution of organic matter within the intercrystalline or interparticle space (Alcantar-Lopez and Chipera, 2013). The organic porosity imaged in core, is consistent in type and volume with previously reported studies (Loucks et al., 2009). The intrakerogen pores are secondary and related to the devolatization of kerogen during catagenesis (Milliken et al., 2012). At the microscale as revealed by SEM images, organic porosity is the most abundant and effective form of porosity and an important vessel for free gas storage in the Barnett Shale. Since organic matter appears to have accumulated as colloidal-like particles in existing pores (Alcantar-Lopez and Chipera, 2013), interparticle porosity was critical for accumulation and perhaps preservation of organic matter. Thus, the productive Barnett Shale gas play required the siliceous mudstone depositional facies with primary interparticle porosity within a rigid and compaction-resistant framework to ensure organic matter deposition.

The siliceous mudstone facies is detectable using industry standard wireline logging suites, thus providing a relatively inexpensive dataset for delineating potentially productive shale gas reservoirs. When the wireline-log dataset is combined with data collected during petrologic and petrophysical characterizations, the combined data becomes a powerful tool for evaluating shale gas plays and exploring for additional gas and liquid hydrocarbon reserves.

Geologic modeling shows that the siliceous mudstone facies formed during the highstand systems tract as a result of phytoplankton bloom and the accumulation of biogenic silica. Interpreting changing sea level and sediment input within a sequence stratigraphic framework is crucial to deciphering the relationship between depositional setting, lithofacies and rock fabric. This combination of geologic and petrologic characterization is necessary to decrease risk and bring marginal gas shale plays to market.

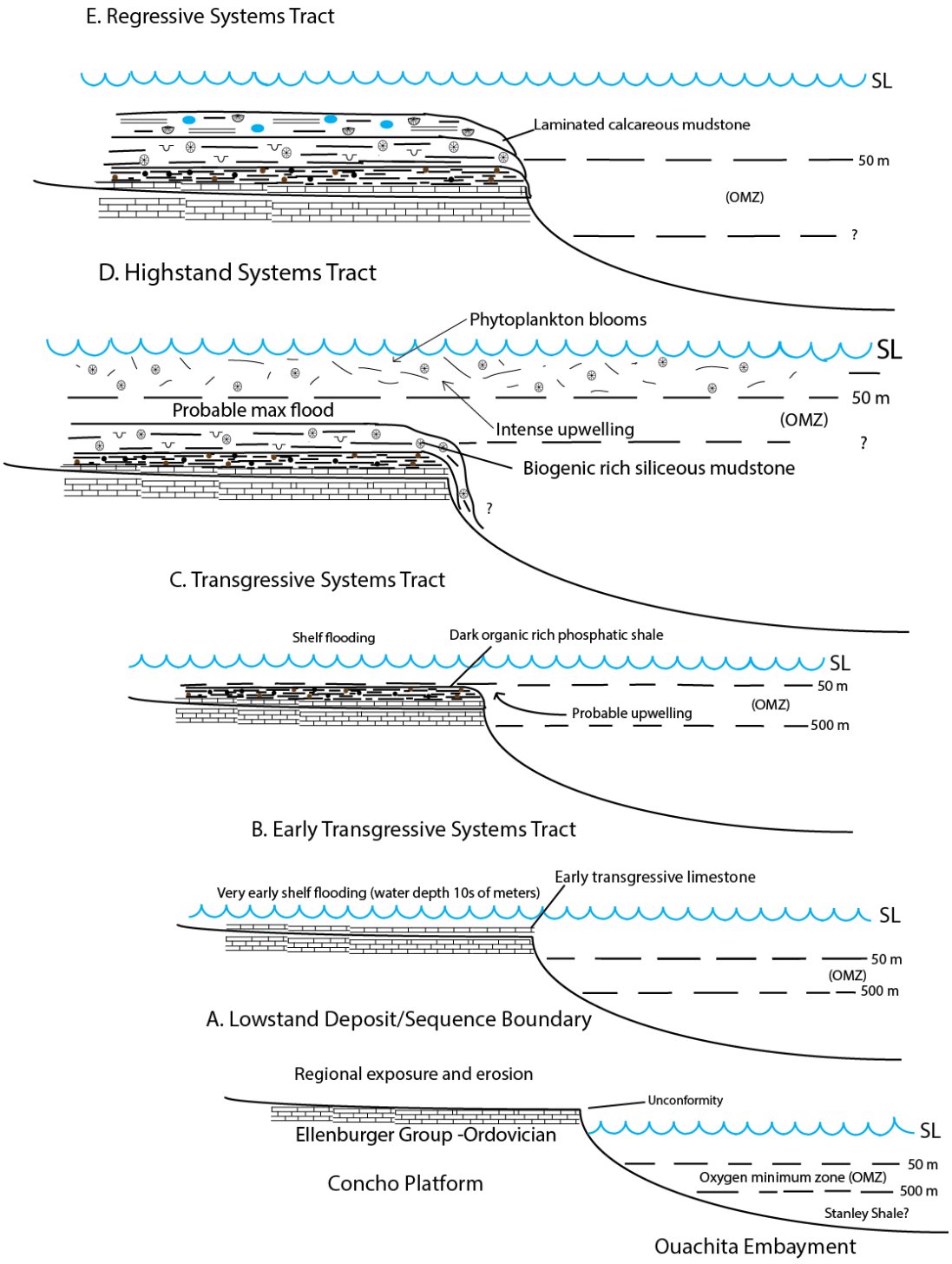

Figure 52.—Schematic diagram of the lower Barnett sequence stratigraphy and depositional model (Miller, 2014). Phytoplankton blooms associated with upwelling during the highstand systems tract produced the biogenic silica crucial for forming the siliceous mudstone reservoir.

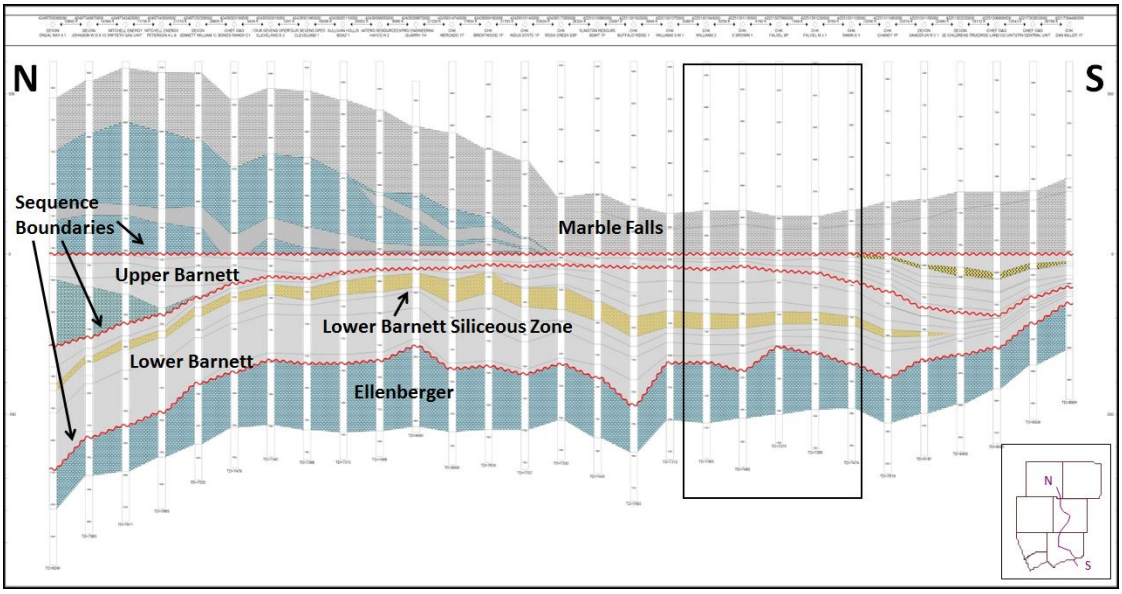

Figure 53.—North to south trending basin-scale cross section showing Barnett sequence boundaries, facies, and approximate location of the King B 3H well (black box) (Modified from Miller, 2006).

CONCLUSIONS

The objective of this study was to determine the lithologic controls on reservoir quality in the Barnett Shale. This was accomplished by analyzing the King B 3H core and utilizing petrographic and petrophysical data sets provided by Chesapeake Energy to build depositional and sequence stratigraphic models to predict reservoir quality.

Core analysis led to the definition of four main lithofacies; siliceous mudstone, argillaceous mudstone, calcareous mudstone, and dolomitic mudstone. Each lithofacies represented an end-member of the quartz-carbonate-clay tertiary diagram except for diagenetic dolomite. The lithofacies show a mixture of detrital and authigenic constituents that each correlate to a specific depositional environment.

The rock fabric and porosity was analyzed using FESEM images. Intrakerogen porosity was found to be the most important type of porosity because of the abundance of secondary pores that formed during catagenesis. These pores appear to be the principal source of

permeability in the reservoir facies, but without an abundance of primary, interparticle porosity for organic matter to accumulate in, the secondary intrakerogen porosity would not exist. Thus, productive Barnett Shale required primary interparticle porosity, sufficient organic matter and stability during burial, compaction, and diagenesis.

The siliceous mudstone facies contained the highest porosity and permeability as well as the most efficient fabric for the creation and preservation of primary interparticle porosity. A by-product of this semi-rigid framework is mechanically brittle strata that provide the best interval to land a well bore in and propagate hydraulic fractures. This fabric is the result of the combined effects of detrital quartz and feldspar grains and cryptocrystalline quartz cement that provide a rigid, compaction-resistant matrix.

Organic carbon was identified in every facies in the Barnett, but was found to show significant vertical variability. The vertical distribution of TOC is a function of organic matter production, destruction, and dilution. These three variables and the relationships between them are tied to depositional environments and the unique conditions that produce them. After producing the sequence stratigraphic model, the vertical distribution of TOC and stacking patterns of source rocks can be quantified and even predicted.

Well logs were analyzed and correlated to lithofacies. In the Barnett Shale tying log data to core is critical because of the heterogeneity both laterally and vertically. Each lithofacies was found to exhibit a distinct set of log characteristics that could be used to develop a predictive model. The siliceous mudstone facies can be identified by low gamma-ray values, low PE values, higher resistivity, and neutron-density porosity crossover.

The upper and lower Barnett each represents a second order sequence. The sequence is identified by exposure or erosion at the sequence boundary followed by a thin transgressive

muddy limestone. As transgression progressed, the shelf flooded and organic-rich phosphatic argillaceous mud was deposited. The following highstand is characterized by nutrient-rich upwelling and production of large amounts of organic matter. This results in a silica rich facies and the geochemical conditions to precipitate cryptocrystalline quartz that was shown to be essential to reservoir quality in the Barnett Shale. During the regressive systems tract, sea level fell and calcareous mud was deposited that was diluted of silica and TOC. This sediment became the calcareous mudstone facies of the Barnett Shale that represents the poorest reservoir quality.

Sequence stratigraphic surfaces and lithofacies identified in core were integrated and placed in the context of a basin-scale model. This model demonstrates erosional and onlapping relationships between strata, and facies stacking patterns. These basin scale trends can be combined with higher resolution petrologic characterization to create effective models to predict distribution of reservoirs and seals.

A.3. PETROLOGIC CHARACTERIZATION USING MICRO X-RAY COMPUTED TOMOGRAPHY (CT) COUPLED WITH SCANNING ELECTRON MICROSCOPY (SEM)

INTRODUCTION

Shale samples from several Paleozoic formations in southeastern and south-central United States were analyzed to establish rock fabric, physical sedimentary and biogenic features, body fossils, diagenetic minerals, fractures and faults. Qualitatively, CT facilitated the characterization of heterogeneity and a variety of depositional, diagenetic and structural features. Quantitatively, data from CT was used to calculate volumetric percentages of porosity and mineral constituents (Powers, 2015). Scanning electron microscopy with energy dispersive spectroscopy (SEM/EDS) data were collected from the same samples scanned using micro CT analysis. The micro CT was used to locate areas of samples in which the microfabric could be further resolved and analyzed using SEM. EDS allowed for rapid and straightforward determination of mineral composition. This work demonstrates the utility of integrating CT and SEM/EDS analyses to interpret microstructure and thereby improving interpretation of sedimentologic, structural and petrologic features.

METHODS

A total of 30 shale samples from nine different cores in four basins (Anadarko, Arkoma, Black Warrior and Appalachian) and the Appalachian Thrust Belt (fig. 54; table 3) were scanned using a Zeiss Xradia VersaXRM 410 CT scanner using parameters (scan size, energy and time) customized for the individual sample. Reconstructed CT scans were used to identify areas of interest for microfabric analyses. A total of 11 argon-ion milled and 3

freshly broken surface samples were observed and analyzed using a FEI Quanta 600 SEM/EDS unit.

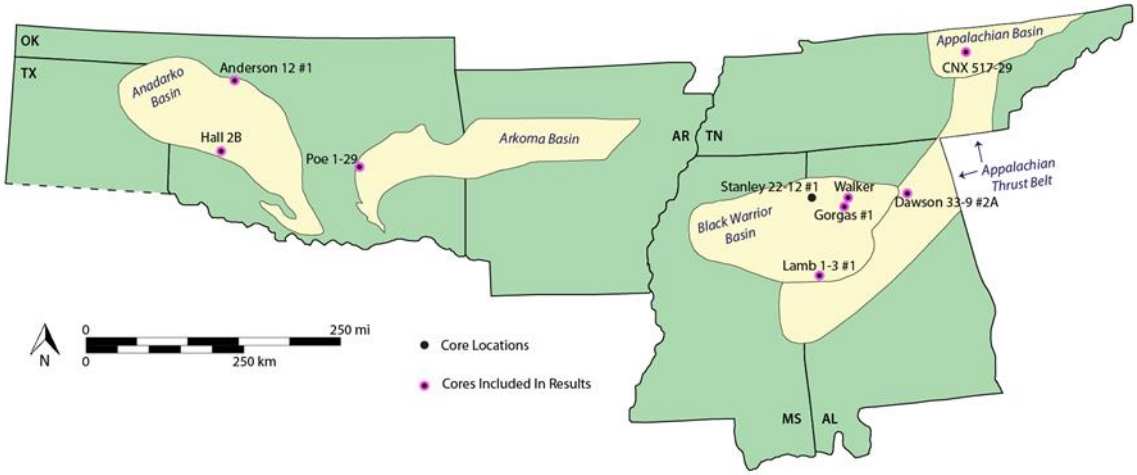

Figure 54.— Generalized map from Powers (2015) showing the locations of cores used in this study.

Table 3.—Well locations and the formations analyzed with their corresponding ages. Note: Only samples from well names with asterisks are featured in this report.

Core Data			
Age	**Formation**	**Well Name**	**Location**
Pennsylvanian	Pottsville Formation	* Gorgas #1	Walker County, AL
Mississippian	Floyd tongue of Bangor Limestone	* Walker	Walker County, AL
	Pride Mountain Formation	Stanley 22-12 #1	Lamar County, AL
Devonian	Woodford Shale	* Hall 2B	Caddo County, OK
		* Poe 1-29	Hughes County, OK
		* Anderson 12 #1	Garfield County, OK
	Chattanooga Shale	* CNX 517-29	Campbell County, TN
		* Lamb 1-3 #1	Greene County, AL
Cambrian	Conasauga Formation	* Dawson 33-9 #2A	St. Clair County, AL

XMReconstructor software was used to reconstruct scans by stitching individual radiographs to generate CT slices. The number of slices generated for each scan ranged from 950 to 1004. Reconstructions were performed by manually entering inputs that corrected for sample shifting or beam hardening during a scan. Reconstructed scans were used to gather both qualitative and quantitative data using two different software packages. A density filter was used to highlight sedimentary structures, fossils, mineral components and grains. Image analysis software called ImageJ was used to calculate volumetric percentages of mineral constituents and fracture porosity by segmenting gray values using hand-selected histogram cutoffs.

RESULTS

Selected examples from the nine cores are used to demonstrate the results of the CT and SEM/EDS analyses. Included are description and basic interpretation of the tomographs and image micrographs. Results are listed stratigraphically beginning with the oldest unit, the

CONASUAGA FORMATION: DAWSON 33-9 NO. 2A CORE

The Dawson 33-9 core comes from the Big Canoe Creek Field, St. Clair County, Alabama. One sample from a depth of 7,565.7 ft. was CT-scanned. The sample is from a weakly deformed block in the Conasuaga shale and is laminated shale with mostly sand- to granule-size pyrite nodules. An unusual "carbonate" nodule in the upper part of the sample was imaged (fig. 55). The CT scan shows that the interior of the nodule is less dense than the outside, suggesting it is composed of clay instead of carbonate. The nodule contains a network of microburrows that appear to be filled with a denser material (carbonate). The interior also contains pyrite nodules that image brightly (Powers, 2014). The margin of the

nodule becomes a carbonate lamina, a feature common to the Conasuaga (Pashin et al., 2012). Dispersed throughout the rest of the

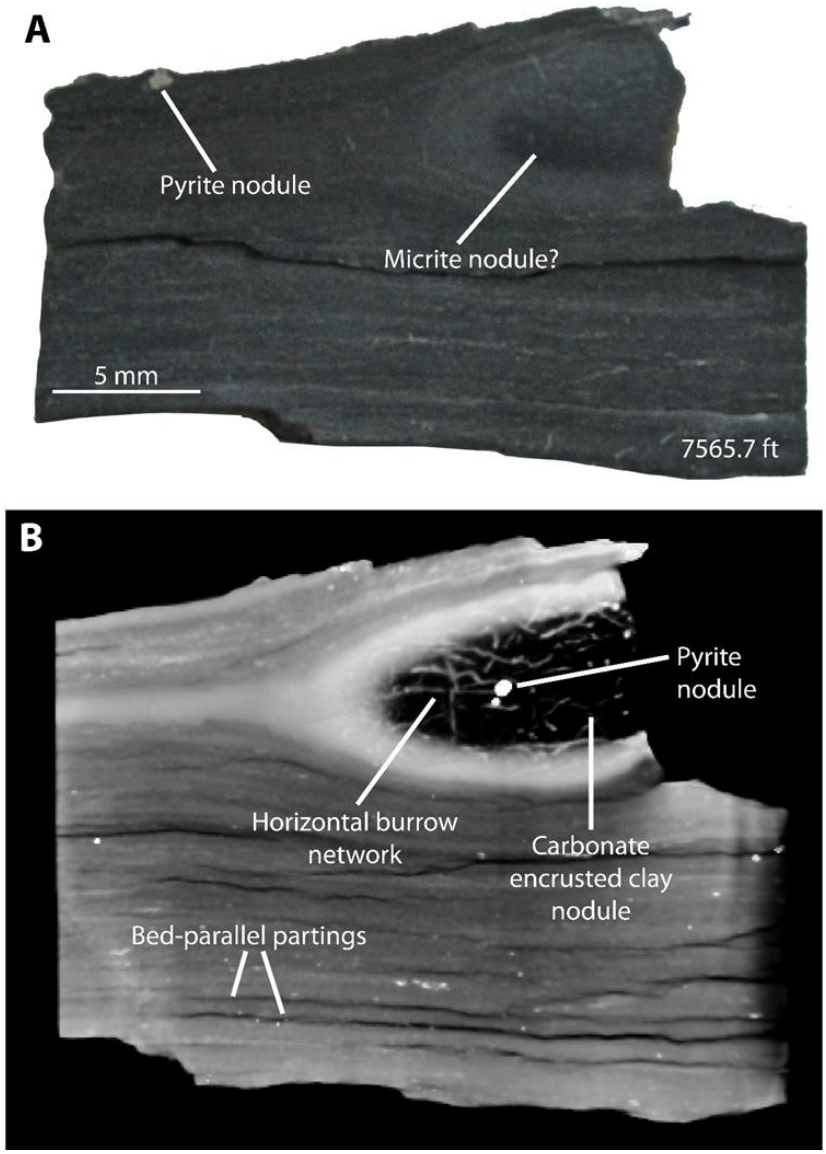

Figure 55.—Photograph and corresponding tomograph of Dawson 38-9 #2A core, 7,565.7 ft.
(A) Black shale containing a pyrite nodule and what appears to be a micrite nodule encrusted in carbonate.
(B) Black shale with a carbonated encrusted low-density nodule containing horizontal carbonate-filled burrows and pyrite nodules. Bed-parallel partings, demonstrating the high fissility of the shale, and indiscernible bright grains are present throughout the sample.

sample are numerous clay laminae, bed partings, and unidentified bright particles that the SEM image shows as carbonate grains and pyrite framboids (fig. 56).

CHATTANOOGA SHALE: LAMB 1-3 NO. 1; CNX 517-29

Five samples from the Chattanooga Shale in the Lamb 1-3 and CNX 517-29 cores were photographed and CT-scanned. Four samples were taken from the Lamb 1-3 at depths of 9,167.5 ft., 9,173.5 ft., 9,180 ft., and 9,192.5 ft. The sample of the Chattanooga Shale taken at 9,167.5 ft. was chosen to test the efficacy of scanning whole core on the XRadia VersaXRM 410 instrument, which can physically accommodate large samples, but only image a small area (5 cm x 4 cm x 4 cm) at a given time. The resulting tomograph illustrates problem encountered when larger core-size samples are imaged (fig. 57). While pyrite grains and argillaceous and silty layers were observed, the information revealed using tomography is limited. Beam hardening artifacts within the tomograph overshadow useful data as adsorbed x-rays result in bright spots and edges. Furthermore, the loss of energy toward the center of the core causes it to appear dull or less dense, when in reality the core is similar density throughout.

The sample of Chattanooga Shale from 9,173.5 ft. is black shale with subvertical fractures. Applying a glow density filter to CT scan of a volume of this sample reveals the internal geometry of overlapping, subvertical, mineralized fractures (fig. 58).

A sample from 9,192.5 was scanned for 12.5 hours with the intent of determining which features could be resolved near the resolution limits of the scanner. Voxel resolution was 900nm and the corresponding CT slice diameter 900 um for the tomograph. A microfracture

and high-density mineral particles were easily recognized (fig. 56), but porosity was not resolved.

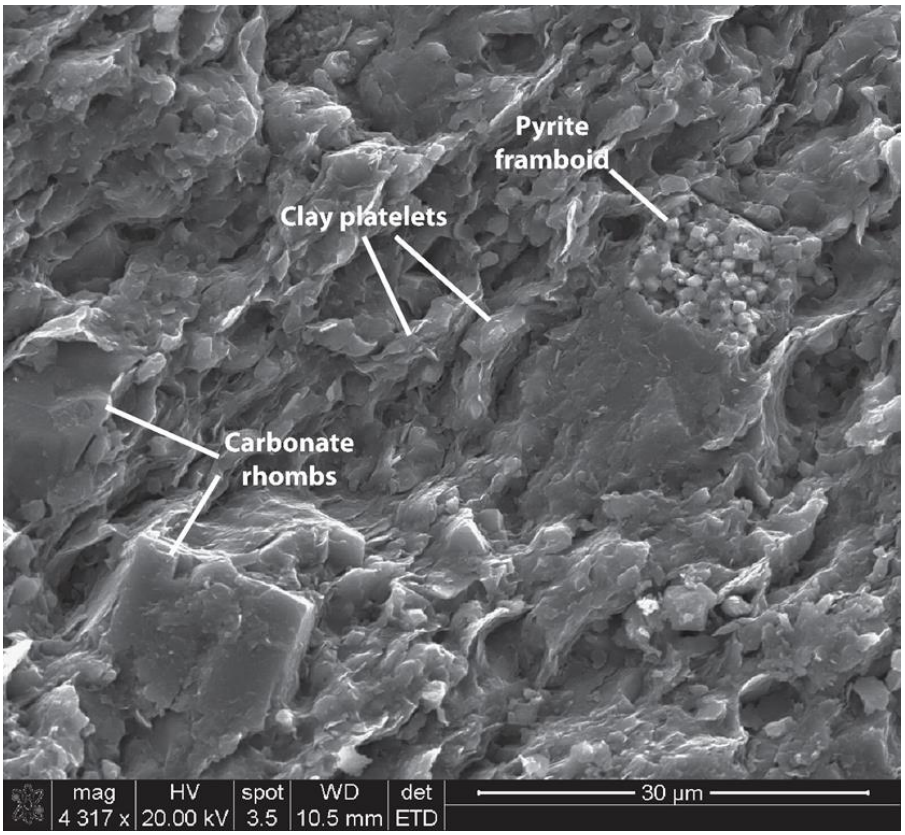

Figure 56.—SEM ETD image of microfabric from a freshly broken sample of Conasauga Shale in the Dawson 33–9 #2A core, 7,565.7 ft. A pyrite framboid and carbonate rhombs are preserved in a matrix of platy illite with poorly aligned and folded clay platelets.

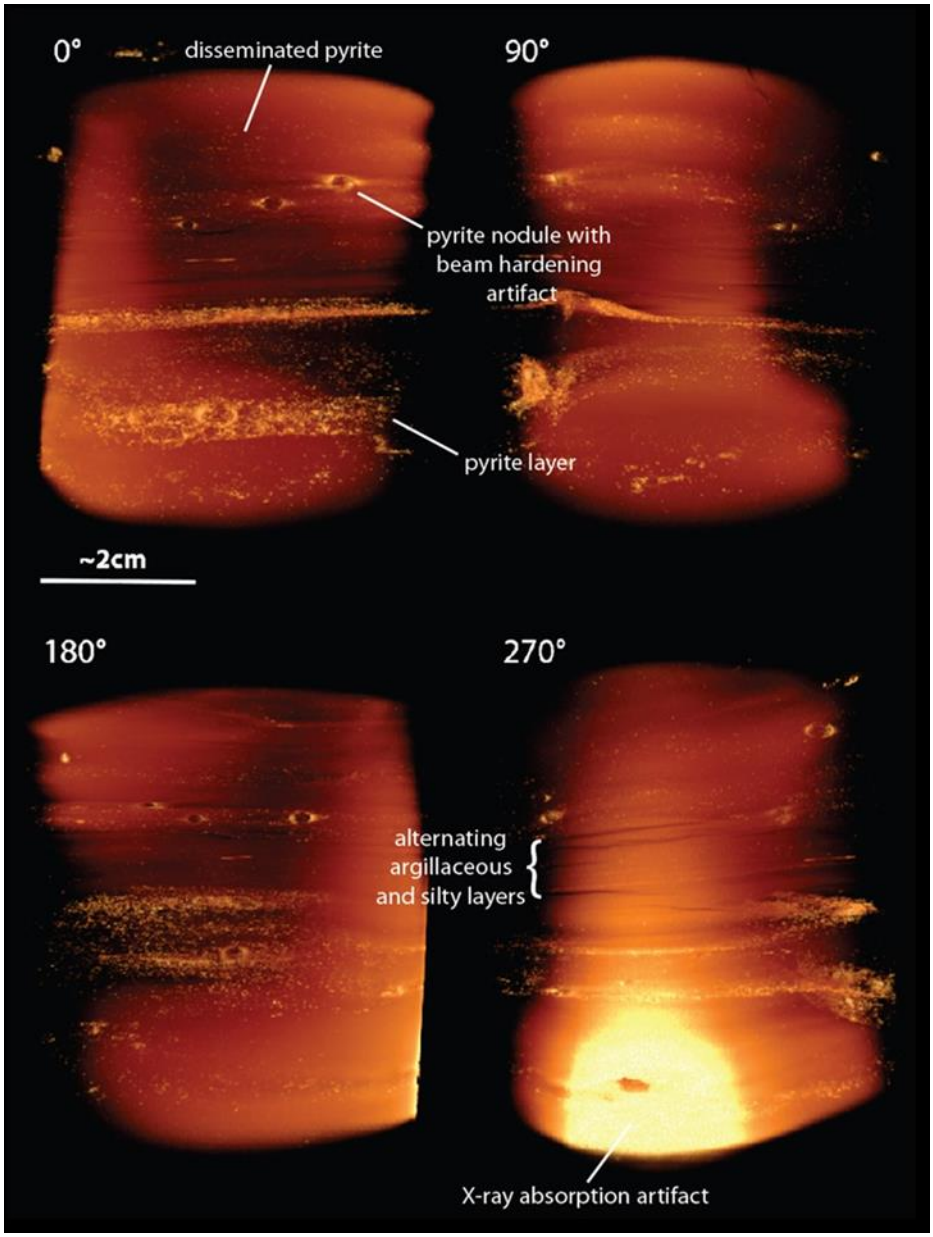

Figure 57.—Glow density filtered tomograph presented at four different angles, Lamb 1-3 #1 core, 9,167.5 ft. At 0°, pyrite can be seen in several different forms; disseminated grains, nodules and laminae. The nodules have significant beam hardening artifacts, as indicated by their edges being much brighter than their centers. At 270°, there is another beam hardening artifact where the edge of the sample absorbed a large amount of x-rays, making it appear much brighter than the rest of the sample. Alternating argillaceous and silty layers can also be observed at this angle.

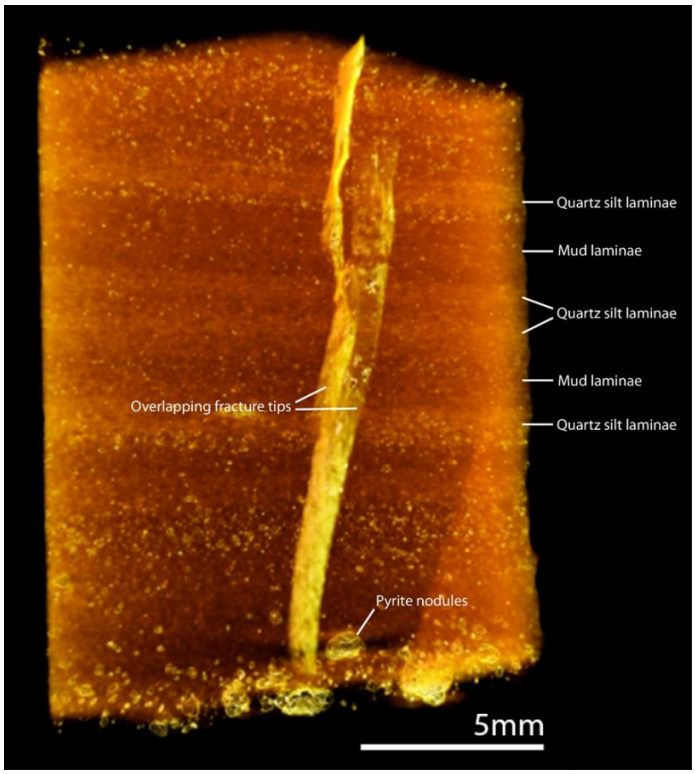

Figure 58.—Glow density filtered tomograph of overlapping mineralized fracture tips, Lamb 1-3 #1 core, 9,173.5 ft. Note alternating mud and quartz silt laminae and pyrite nodules are prevalent throughout.

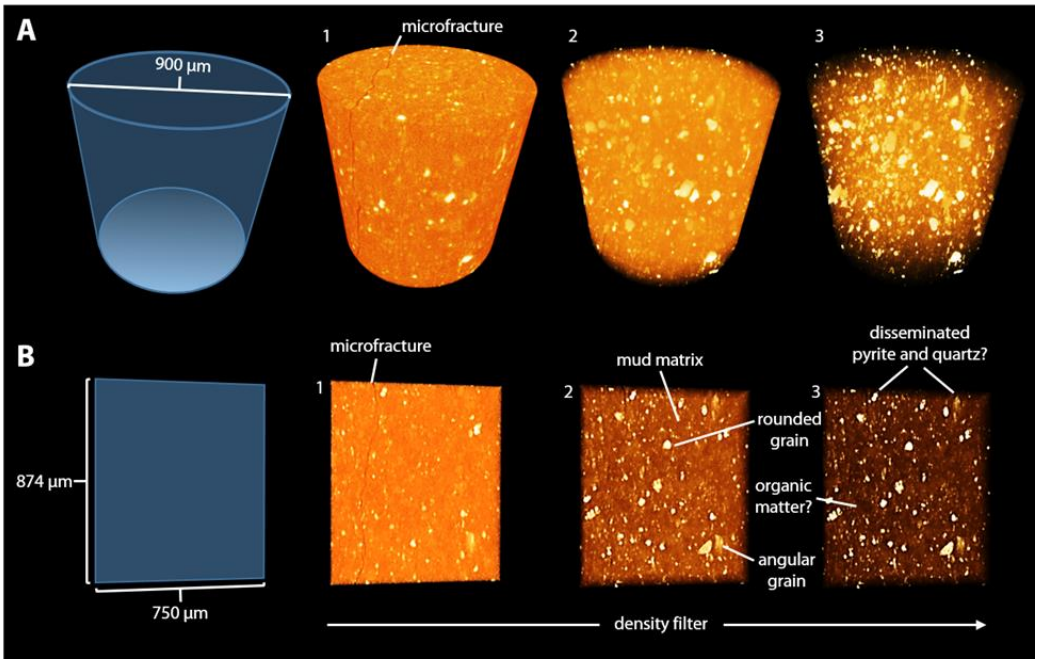

Figure 59.—Glow density filtered full volume tomograph and CT slice, Lamb 1-3 #1 well, 9,192.5 ft.
(A) Tomograph of the entire volume progressively filtered to isolate high density material.
(B) CT slice progressively filtered to isolate high density material.

After successfully imaging fractures ona small scale in sample 9,192.5 ft, a larger and more fractured sample from 9,180 ft was analyzed. This sample is black shale with a normal faulted novaculitic chert lamina with stratabound jointing and pyrite accumulations (fig. 60).

The tomograph for sample 9,180 ft revealed much the internal fracture geometry and variability of fracture and fault mineralization (fig. 61). The normal faulted novaculitic chert lamina displays three different types of strata-bound joints. One joint offset by the fault is mineralized by silica. The other two joints are filled with silica and clay and have pyrite accumulations in the clayey beds at each end. The CT scanner not only imaged joints visible on the surface, but also microfractures that were not readily visible. Other internal features were silica fault gouge and disseminated pyrite, mineral components whose identification was aided by the sample photograph, XRD results and thin section petrography.

CHATTANOOGA SHALE: CNX 517-29

One sample of the Chattanooga Shale was taken at 3,200 ft. from the CNX 517-29 core. This sample is black shale with pyrite laminae and alternating silt and mud laminae (fig. 62). The tomograph of the 3,200 ft. sample revealed a great deal more useful information than the photograph. The tomograph captured additional laminae of quartz silt and mud, more pyrite nodules and more importantly, a partially mineralized fracture plane (fig. 63) that was not expressed on the core surface. The irregular distribution of mineralization along the fracture, lends credence to the interpretation that fluids could be transmitted along the plane.

WOODFORD SHALE

The Woodford Shale is world-class petroleum source rock as well as the principal shale reservoir target in the southern Midcontinent. Seven samples from three Woodford Shale cores (Hall 2-B, Anderson 12-1, and Poe 1-19) were scanned. These samples were chosen to

display the variability of the Woodford Shale across the Anadarko and Arkoma basins (Powers, 2015).

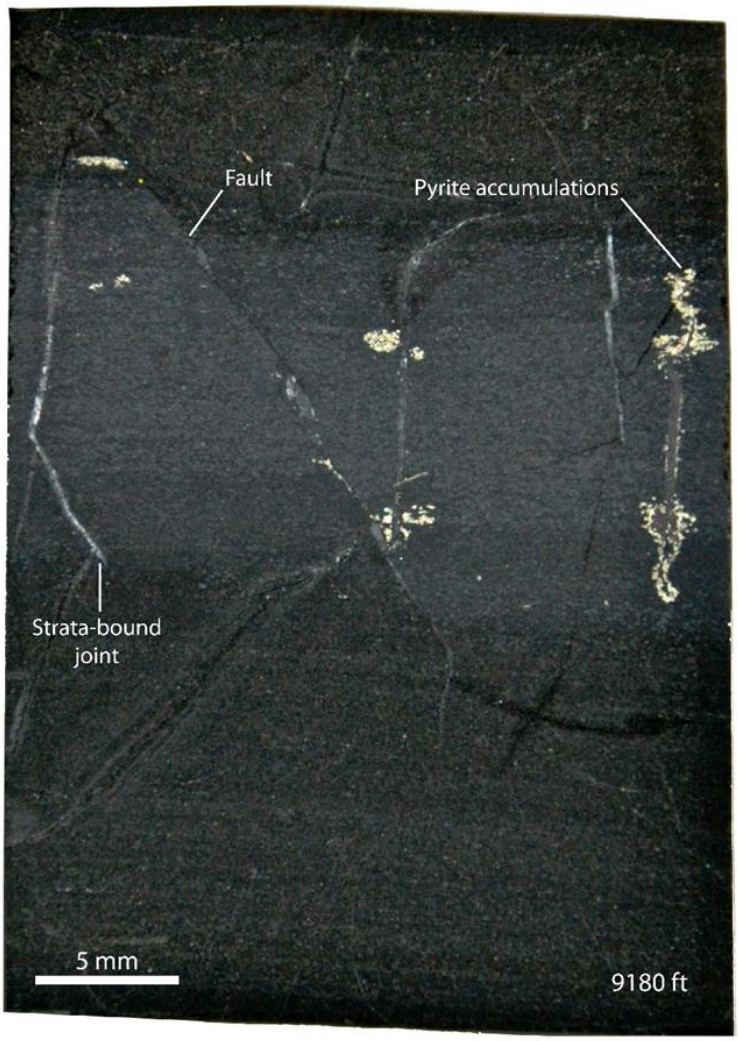

Figure 60. —Photograph of black shale with a normal faulted novaculitic chert lamina with strata-bound jointing and pyrite accumulations, Lamb 1-3 #1 well, 9,180 ft. Note silica/carbonate and clay cement along some of the fractures.

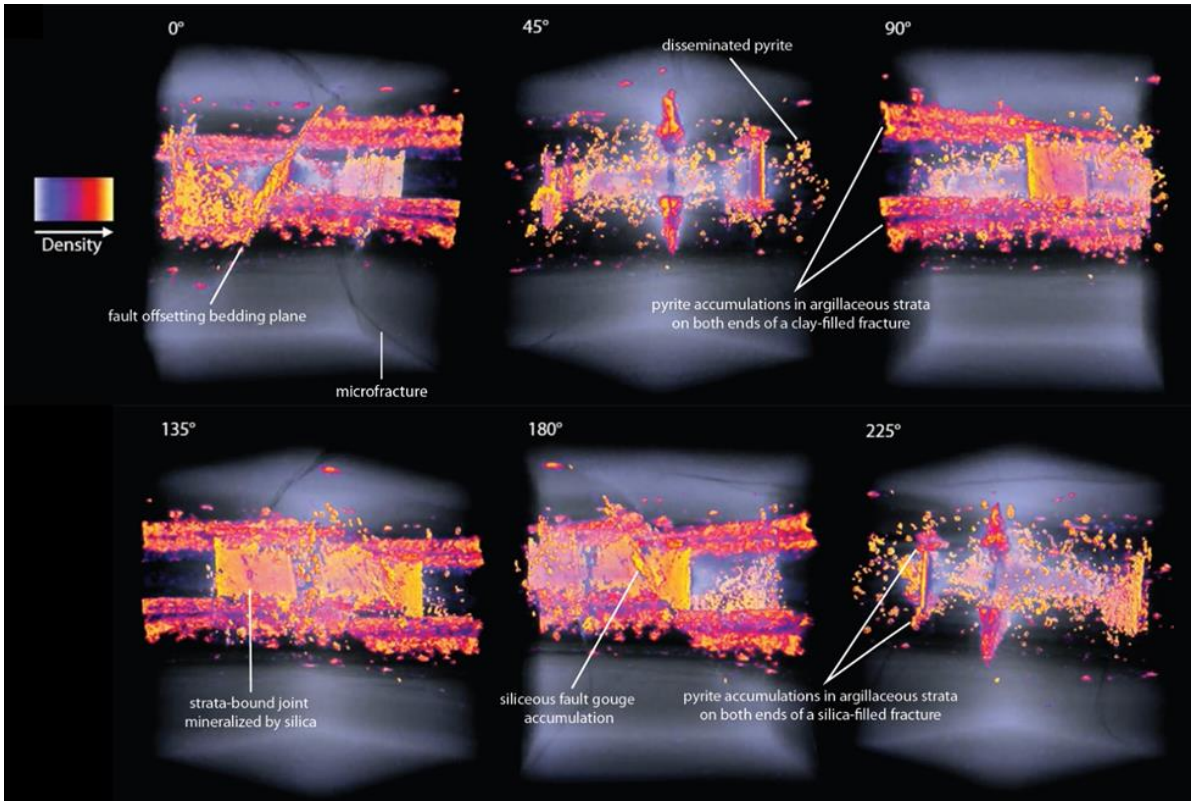

Figure 61.—Temperature density filtered tomograph presented at six different angles, Lamb 1-3 #1 well, 9,180 ft. The features imaged include: a mineralized normal fault and fault gouge (180°), a strata-bound joint mineralized by silica and offset by the fault (135°), pyrite accumulations on both ends of a clay-filled joint offset by the fault (90°), a clay filled fracture and disseminated pyrite (45°).

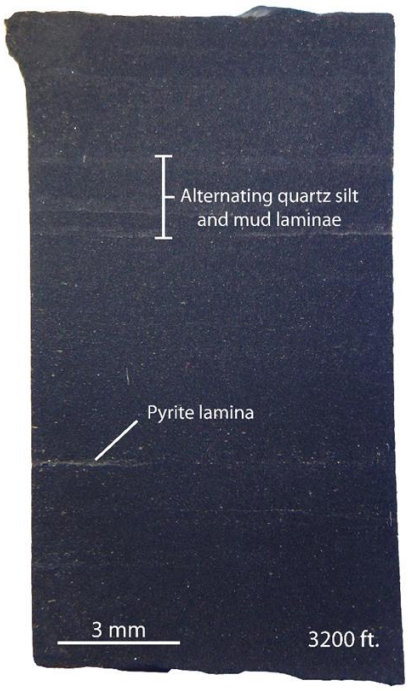

Figure 62. Photograph of black shale with pyrite lamina and alternating quartz silt and mud laminae, CNX 517-29 core, 3,200 ft.

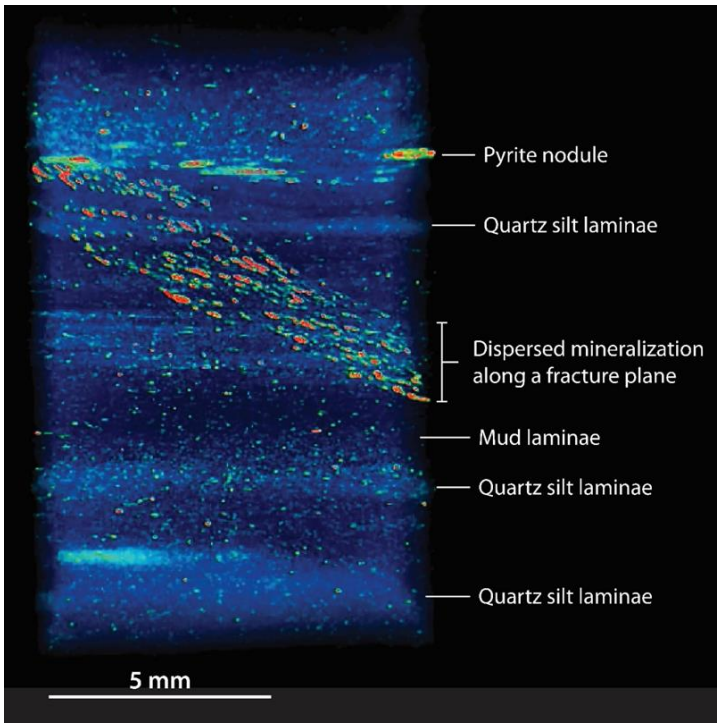

Figure 63. Hue ramp density filtered tomograph of Chattanooga Shale, CNX 517-29 core, 3,200 ft. Numerous pyrite nodules and quartz silt and mud laminae are imaged. A dipping fracture plane with patchy cement cross cuts the sample.

Woodford Shale: Anderson 12-1

Three samples were chosen for the Anderson 12-1 core: 6,839.8 ft., 6,843.6 ft. and 6,900.7 ft. The sample from 6,839.8 ft. is black shale containing phosphate nodules coated with pyrite and calcite (fig. 64). The interior was CT-scanned and inspected by applying a gray ramp

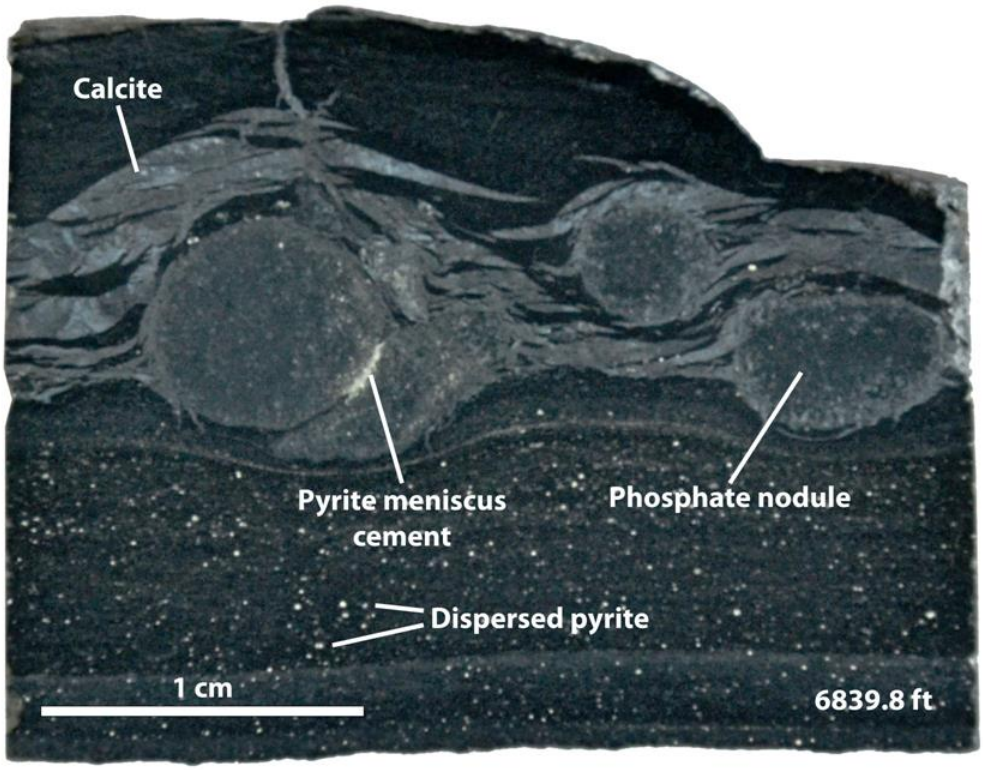

Figure 64. Photograph of black shale containing phosphate nodules coated with pyrite and calcite, Anderson 12-1 core, 6,839.8 ft. Note dispersed pyrite in lower part of sample.

density filter to the tomograph (fig. 65). Lower-density material was filtered, revealing the spatial distribution and morphology of phosphate nodules. Meniscus cement is evident between nodules and internal mineralogy is imaged. For closer inspection of the interiors of

phosphate nodules, a CT slice was examined, which revealed possible nucleation of nodules around pyrite nodules and litho- or bioclasts (fig. 65).

The sample taken from 6,843.6 ft. is black shale containing sulfide that displays several morphologies. CT scanning revealed the presence of marcasite (Figure 65), a reactive form of iron sulfide that can oxidize within months after a core is cut. The sample taken from

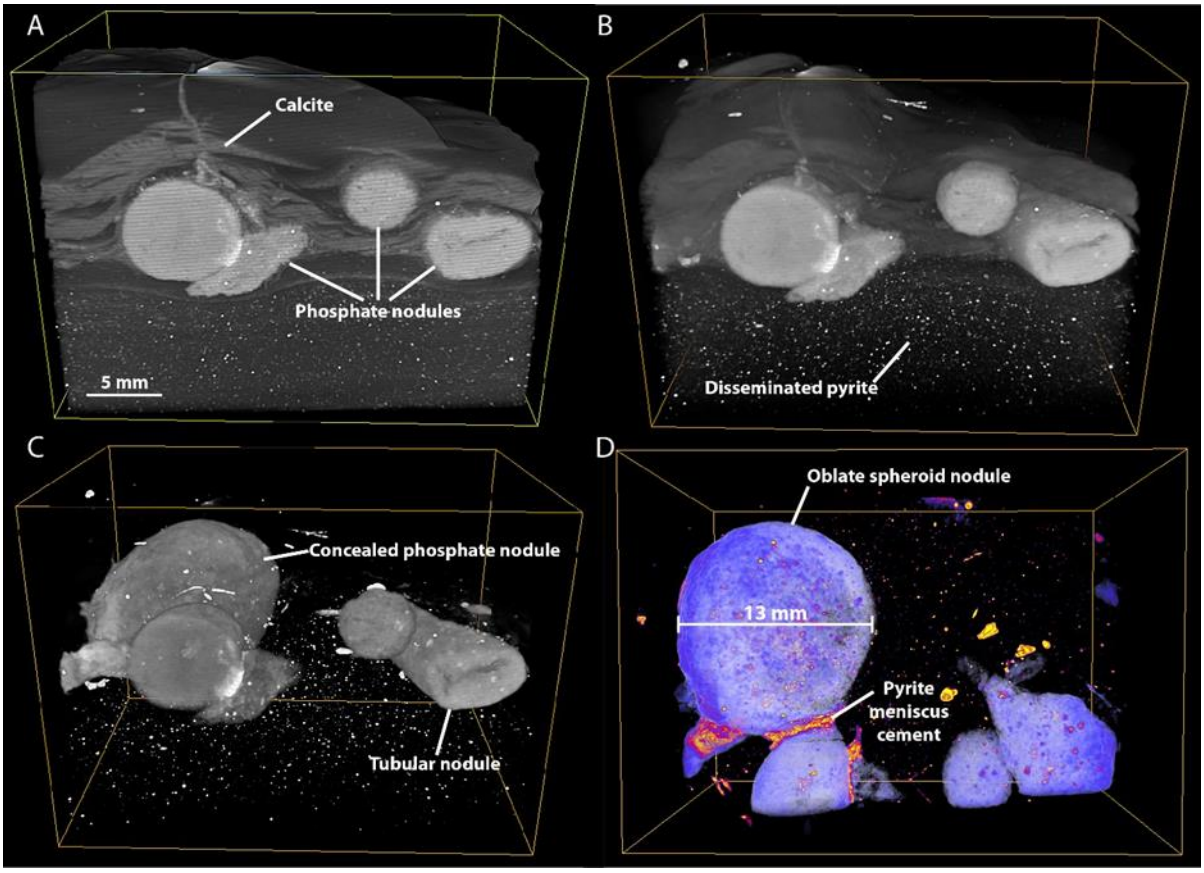

Figure 65.—Gray ramp and temperature density filtered tomograph, Anderson 12 no. 1 core, 6,839.8 ft.

(A-C) Gray ramp density filter applied to the tomograph filters the low density material and leaves the phosphates nodules and disseminated pyrite. The largest phosphatenodule in the sample is revealed, and the filter also allows for determining nodule shapes.

(D) A temperature density filtered view of the sample down the XY plane allows for measuring nodule diameters and observations of meniscus cement and mineral constituents within the nodules.

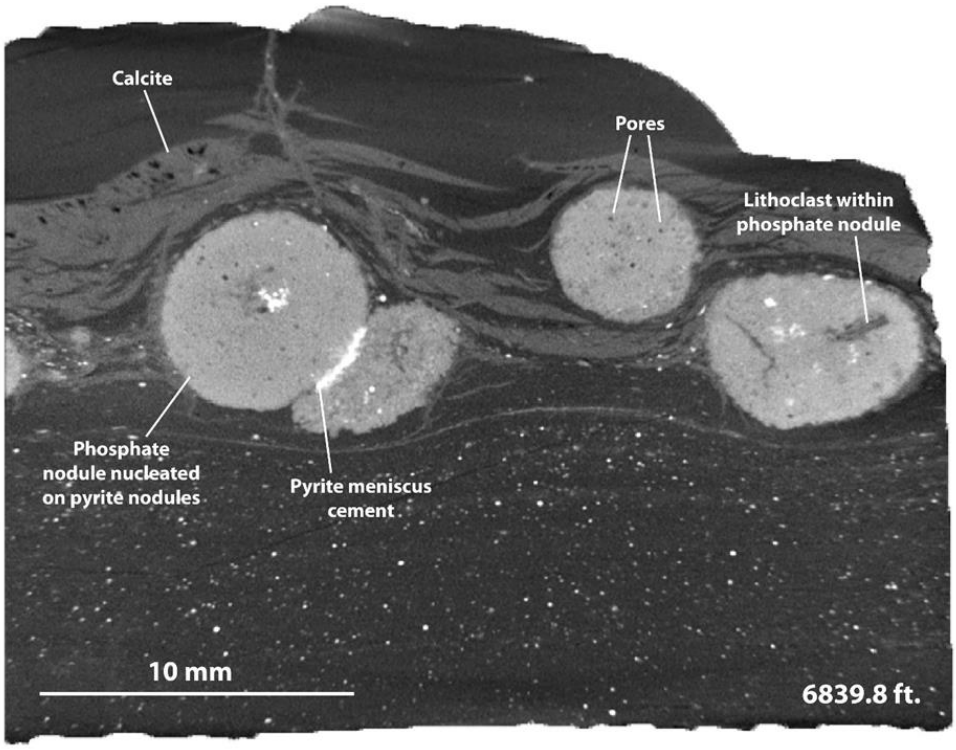

Figure 66.—CT slice showing calcite coatings and inclusions in the interior of the phosphate nodules, Anderson 12-1 core, 6,839.8 ft. Inclusions include pyrite grains and a lithoclast. There also appears to be micro-porosity within all nodules.

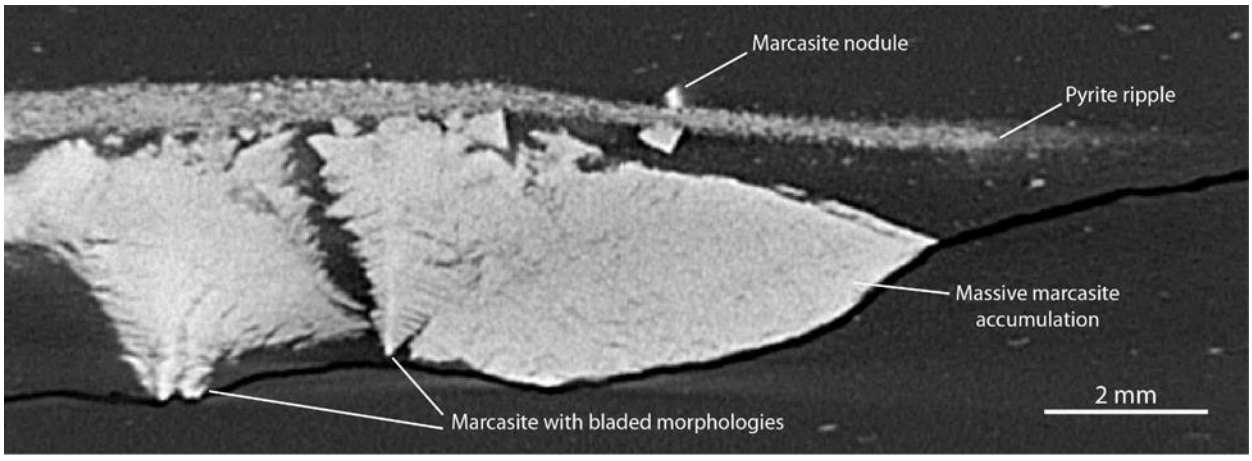

Figure 67.—CT slice showing a pyrite ripple with various forms of marcasite above and below, Anderson 12-1 core, 6,843.6 ft. Sulfide is nodular above the ripple and forms large nodules with bladed crystals below.

6,900.7 ft. is black shale with an unusual lag bed as well as laminasets composed of siltstone-shale couplets (fig. 68). A cropped tomograph of this sample proved revealing in that the lag bed contains phosphate and glauconite clasts, detrital quartz grains, conodont elements, and sparse vertebrate debris (fig. 69). Cyclic variation of pyrite and quartz silt content is suggestive of spring-neap tidal cycles. SEM micrographs of an argon-ion milled sample show aspects of the fabric and porosity that below the limit of resolution by CT scanning. The sample microfabric contains detrital quartz grains and a variety of pyrite forms in a matrix of clay mineral platelets aligned to bedding (fig. 70). Pyrite occurs as framboids, nodules, euhedral crystals and dispersed grains. Organic matter fills void space and lines clay minerals, pyrite and detrital quartz grains. Porosity occurs as fissure porosity along the boundary between organic matter and mineral grains and as intraparticle pores in quartz grains (fig. 71). Honeycomb- or sponge-like porosity is not evident in the organic matter due to the low thermal maturity of this sample from northern shelf of the Anadarko basin.

Woodford Shale: Poe 1-29

Two samples were analyzed for the Poe 1-29 core: 7,843.7 ft. and 7,848 ft. The 7,843.7 ft. sample contains black shale with pyrite nodules and veins and chert laminae hosting ptygmatic folds (fig. 72). A density filtered CT slice reveals interlaminated siliceous and argillaceous layers (fig. 73) that are not apparent in Figure 72. Contrarily, the thicker chert laminae are not as obvious in the CT scan. Imaging the interlaminated varve-like layers demonstrates the capability of CT analysis to detect sedimentary features that would have otherwise gone undetected. With the importance of biogenic siliceous oozes to silica mineralization, increased brittleness, and propensity for forming natural or hydraulically induced fractures, the value of CT analysis should not be understated.

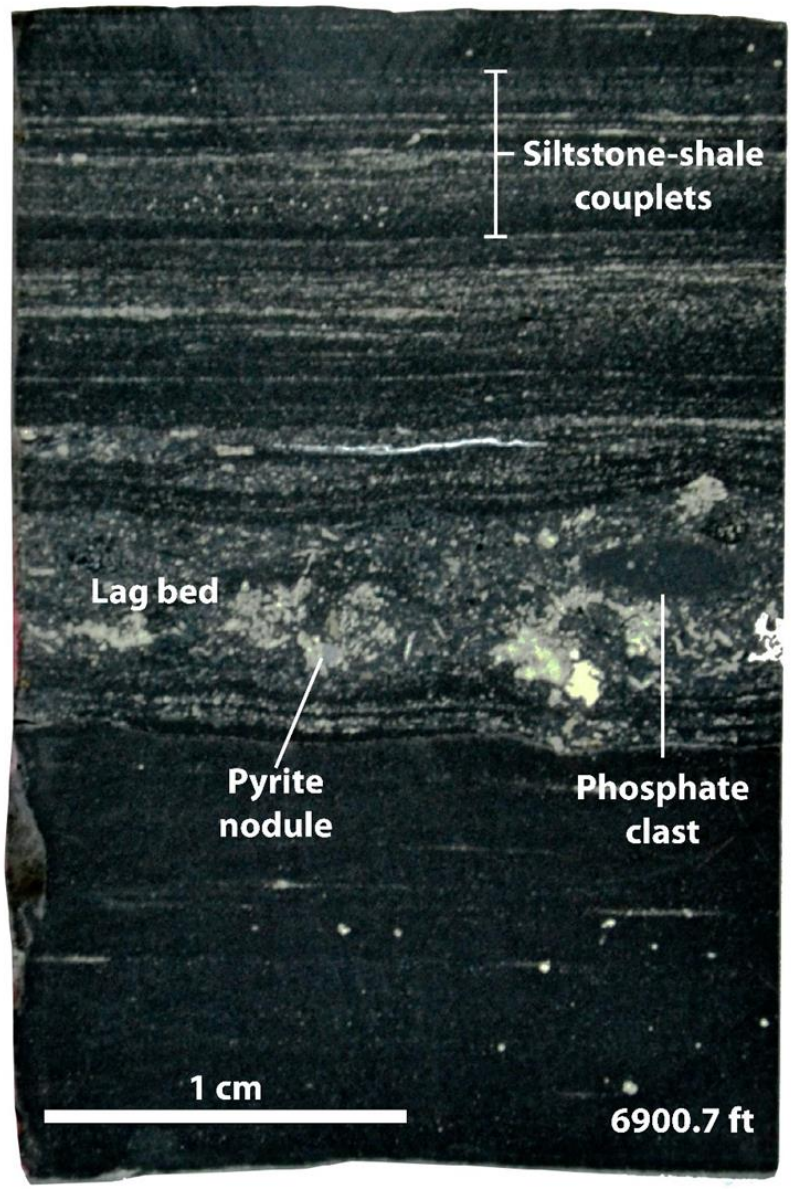

Figure 68.—Photograph of black shale containing a thin lag bed and bundled siltstone-shale couplets, Anderson 12 no. 1 core, 6,900.7 ft. The lag bed is pyritic and includes lithoclasts of phosphate and glauconite, as well as abundant conodont elements.

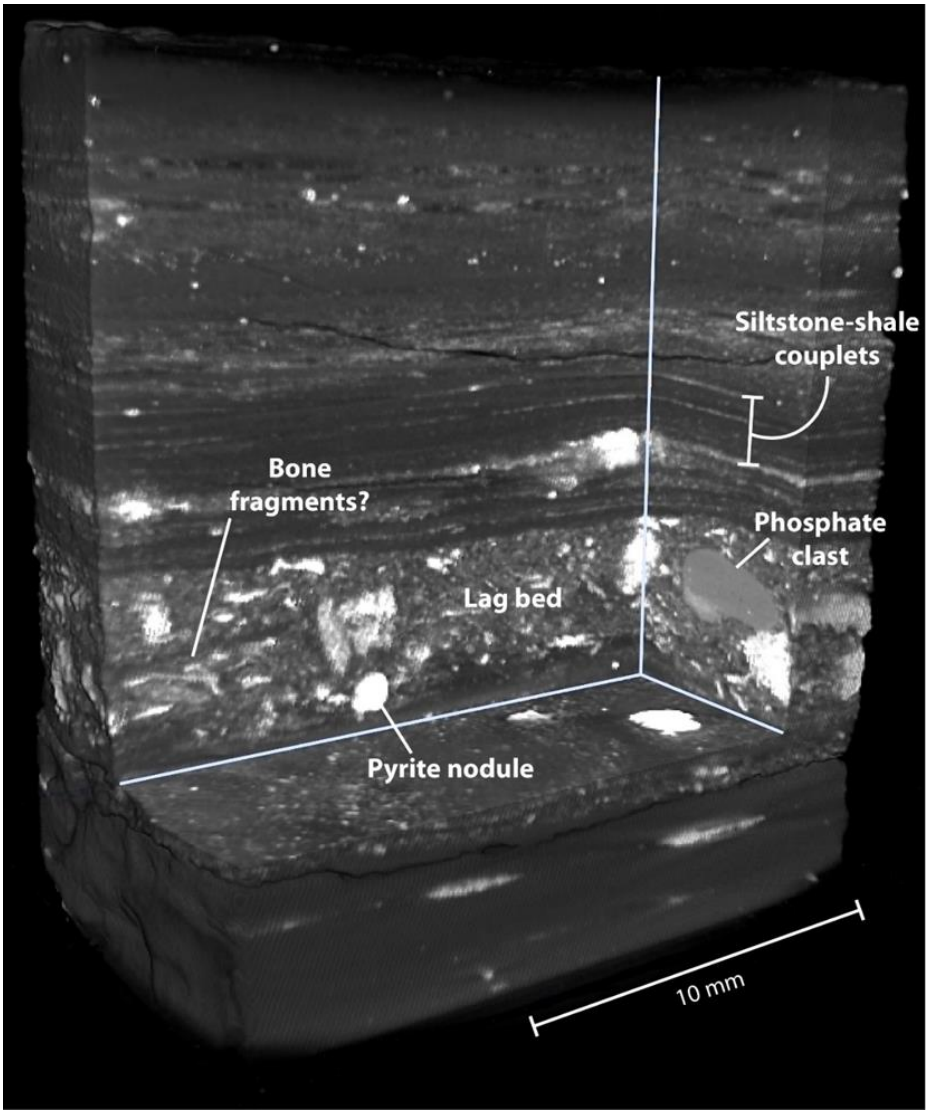

Figure 69.—Gray ramp density filtered cropped tomograph, Anderson 12 no. 1 core, 6,900.7 ft. Cropping the tomograph exposed the internal fabric of the rock. Siltstone-shale couplets appear blurry. Lag constituents are readily identified.

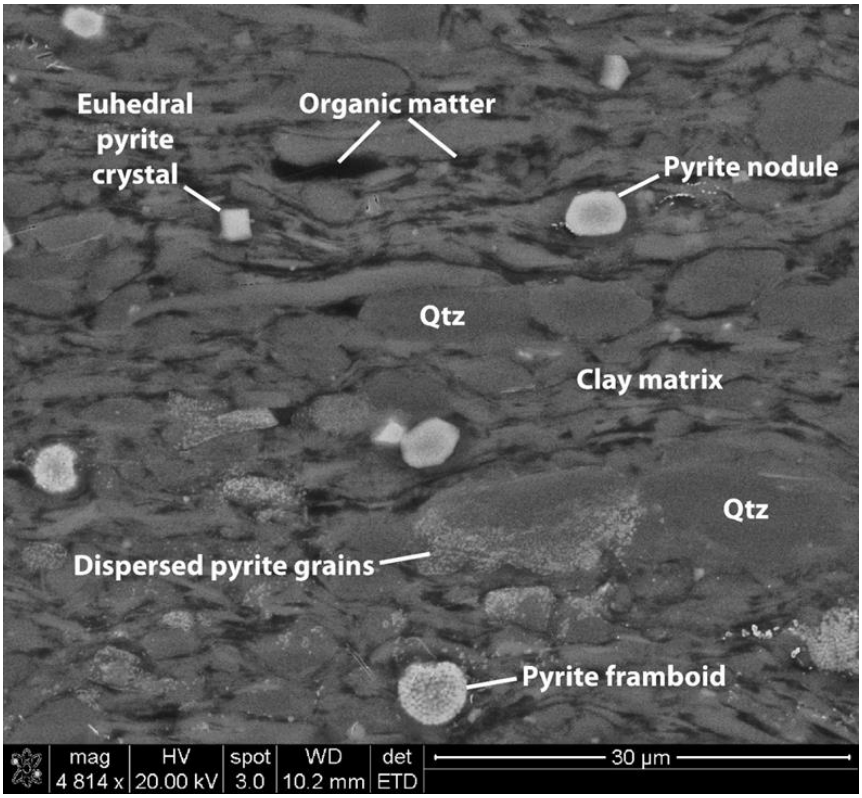

Figure 70.—SEM ETD image of microfabric from an argon ion milled sample of Woodford Shale in the Anderson 12 no. 1 core, 6,893 ft. Microfabric shows diverse pyrite forms, detrital quartz, and a clay matrix of clay platelets aligned to bedding. Organic matter lines the mineral constituents.

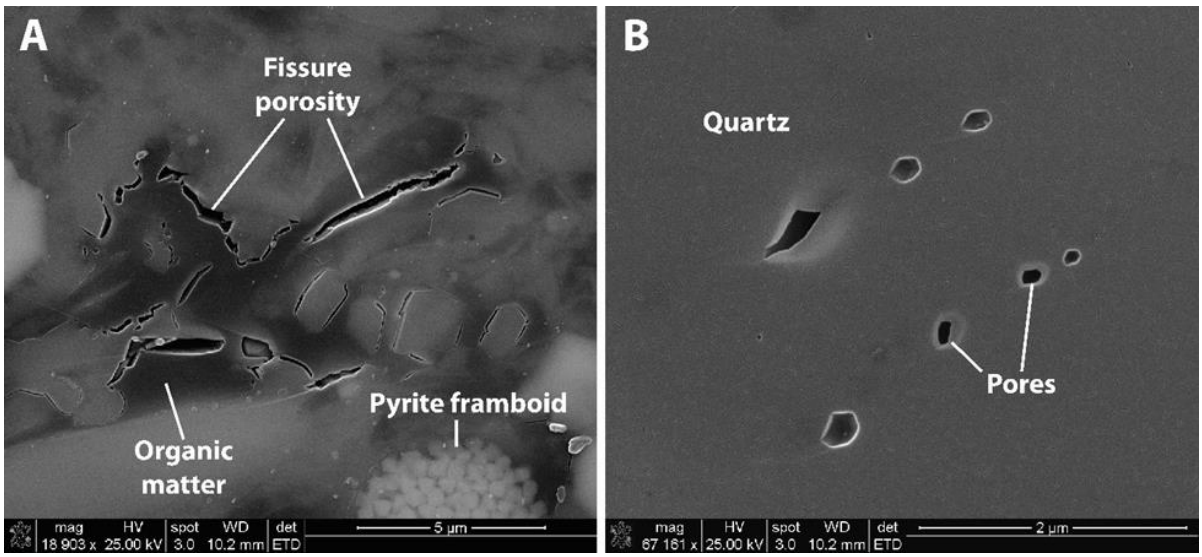

Figure 71.—SEM ETD images of pores from an argon ion milled sample of Woodford Shale in the Anderson 12 no. 1 core, 6,893 ft.
(A) Fissure porosity is observed in organic matter along mineral grain boundaries.
(B) Intragranular, nanometer-scale pores in a quartz grain.

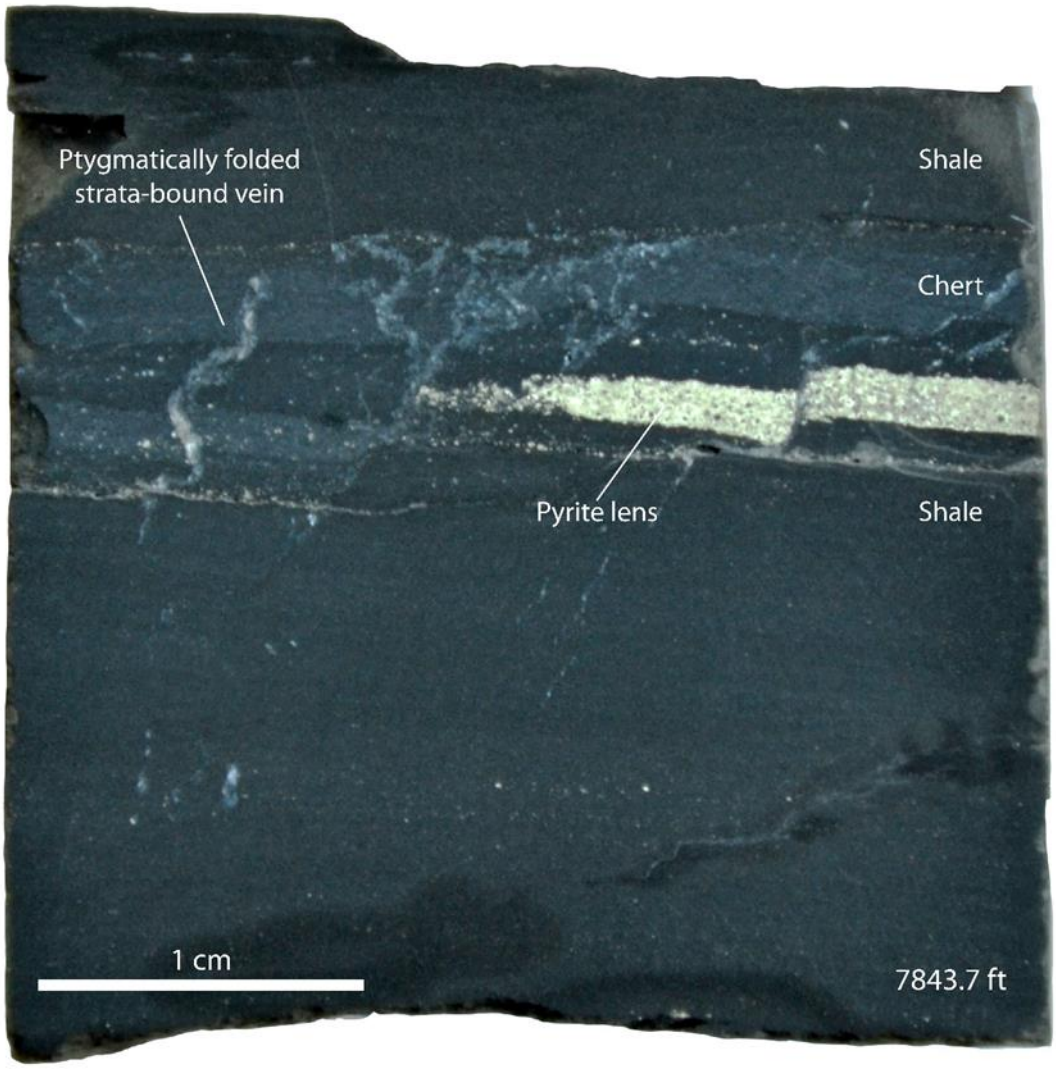

Figure 72.—Photograph black shale with chert laminae, Poe 1-29 core, 7,843.7 ft. Note complexly folded strata-bound veins and faulted pyrite lens.

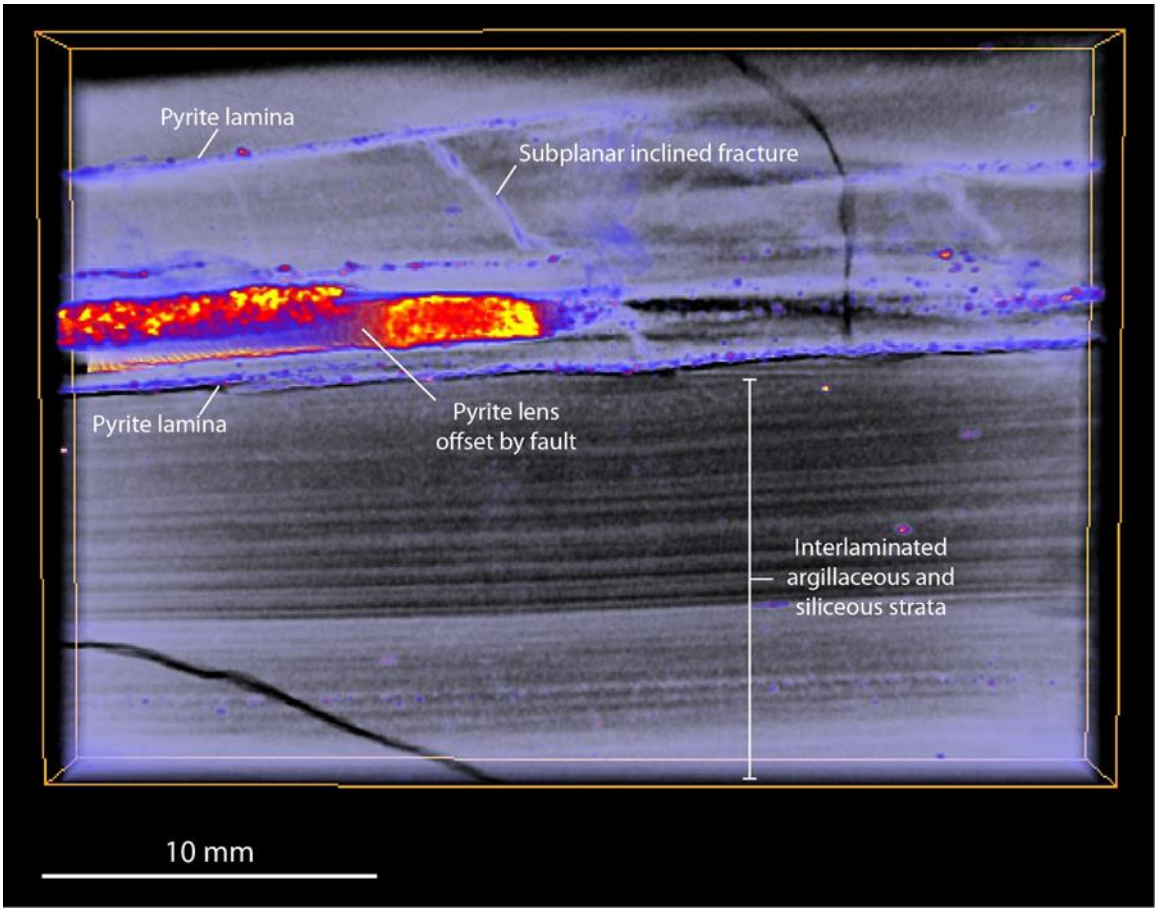

Figure 73.—Temperature density filtered cropped tomograph of Woodford Shale, Poe 1-29 core, 7,843.7 ft. Pyrite laminae and nodules and a subplanar inclined fracture occur within the chert laminae. Thinly interlaminated argillaceous and siliceous laminae are present that were not evident in Figure 67.

The sample taken at 7,848 ft. was CT scanned to reveal the geometry of microfaults and shear veins, as well as rock fabric (fig. 74). The tomograph shows the intensity of strata-bound extensional faulting and shear veins in chert that are mostly undetected in the 2-d core photograph.

Woodford Shale: Hall 2-B

The Hall 2-B core was sampled at depths of 5,899 ft. and 6,178.5 ft. to illustrate the fabric of the fractured and brecciated Woodford section. The CT slice displays several features, including

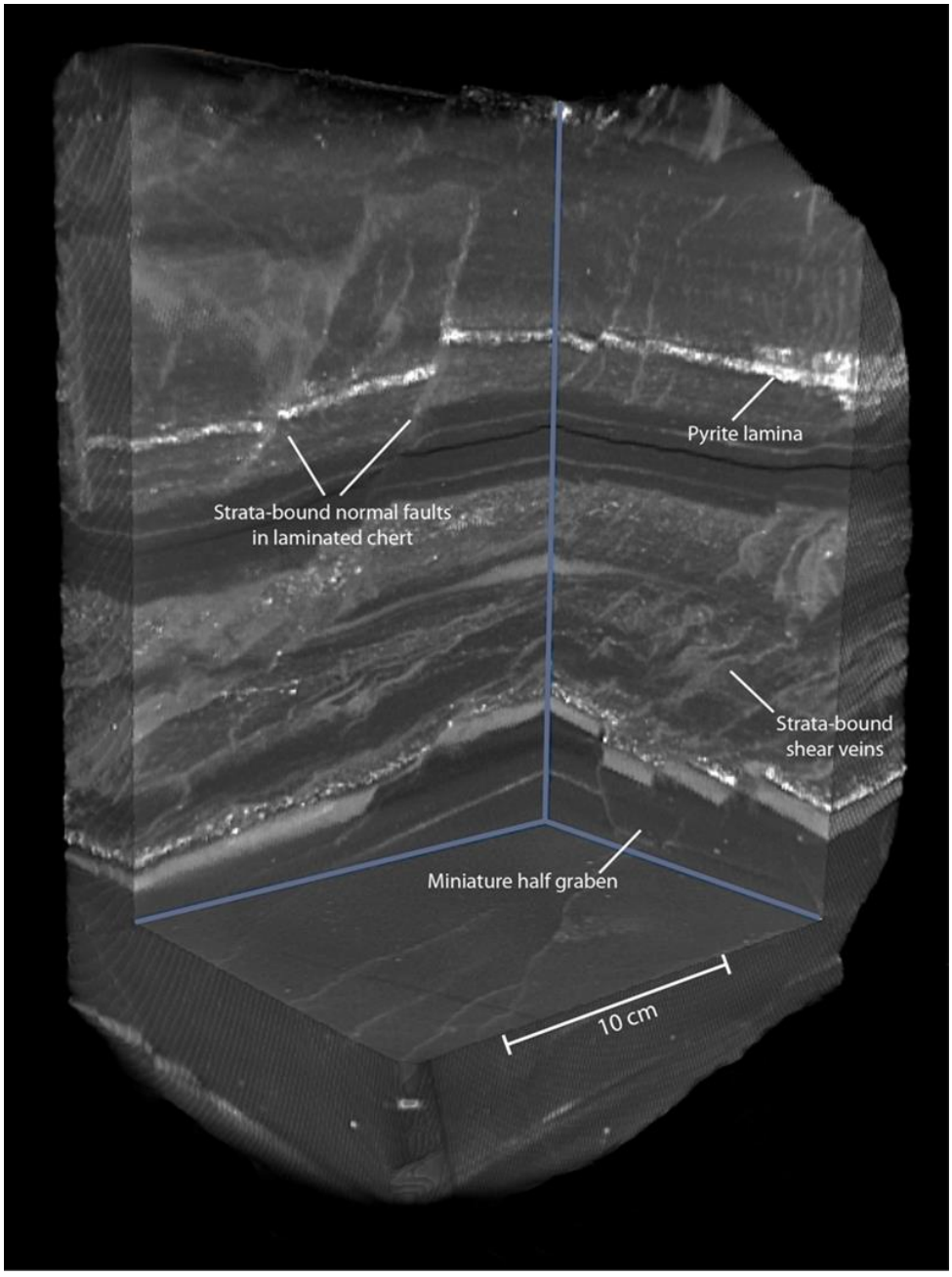

Figure 74. Gray ramp density filtered cropped tomograph of Woodford Shale, Poe 1-29 core, 7,848 ft. Normal faults and shear veins are largely bound within the laminated chert. A miniature half graben is preserved in the lower part of the sample.

pyrite nodules and subrounded to angular chert clasts in a shale matrix, two sets of quartz veins dipping at 10^{o} and 40^{o}, respectively, and a network of fracture porosity (Powers, 2015). By segmenting veins and open fractures via histogram cutoffs, three-dimensional renderings

were generated (fig. 75). Though many microfractures were not detected in the CT slice, the volumetric percentage of open fracture porosity was quantified using ImageJ software (fig. 76).

The chert portion of the sample from 6,178.5 ft. was argon-ion milled and examined using SEM/EDS. The microfabric exhibits fissure porosity in organic matter (fig. 77) similar to that observed in the Anderson 12-1.

DISCUSSION

In this study, the utility of micro-CT scanning for geologic investigations was examined and demonstrated. In addition to illustrating the usefulness of CT scanning in imaging rock features, operational considerations relating to imaging resolution, scanning arifacts, sample size and sample composition were considered.

SAMPLE SIZE

Results demonstrate that sample size is a crucial consideration for scan quality when using the micro-CT scanner. While whole core samples can be scanned, only a small volume, approximately 5cm in height, 4 cm wide and 4 cm thick, can be imaged and the volume of material outside that sample window attenuates the x-ray beam and lowers the contrast. In addition, scanning a volume within a whole core-size sample requires maximum x-ray energy (150 kV) to penetrate the material. This, too, lowers the contrast of the scan. Scan time can be greatly reduced by using small samples, and the resolution of the resulting tomograph is much higher. In addition, contrast is higher in small samples because there is less material to penetrate. Moreover, less x-ray energy is required to scan small samples. While smaller samples will yield high resolution and high contrast scans, the best strategy is to tailor sample size to the scale of what is desired to be imaged.

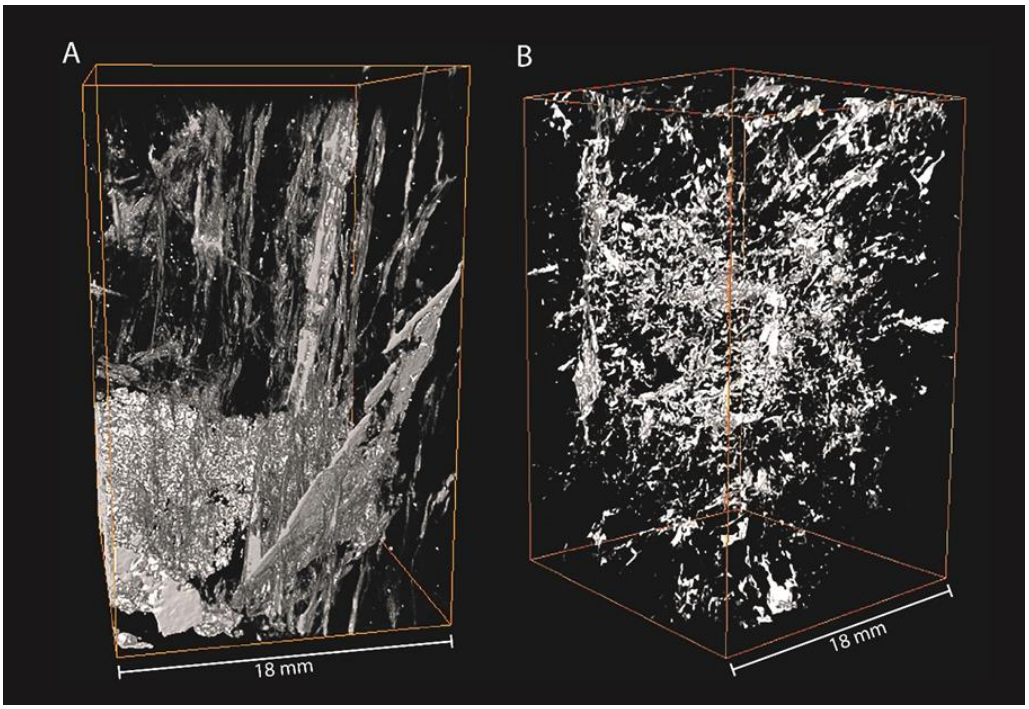

Figure 75. Three-dimensional renderings displaying the interconnectivity of the fracture networks, Hall 2B core, 5,899 ft. (A) Two sets of quartz veins, dipping 50° and 80°, are preserved. (B) Open fractures appear as discontinuous pockets of porosity throughout the sample. The extraction failed to image interconnecting hairline fractures with aperture below the voxel resolution of 31 µm.

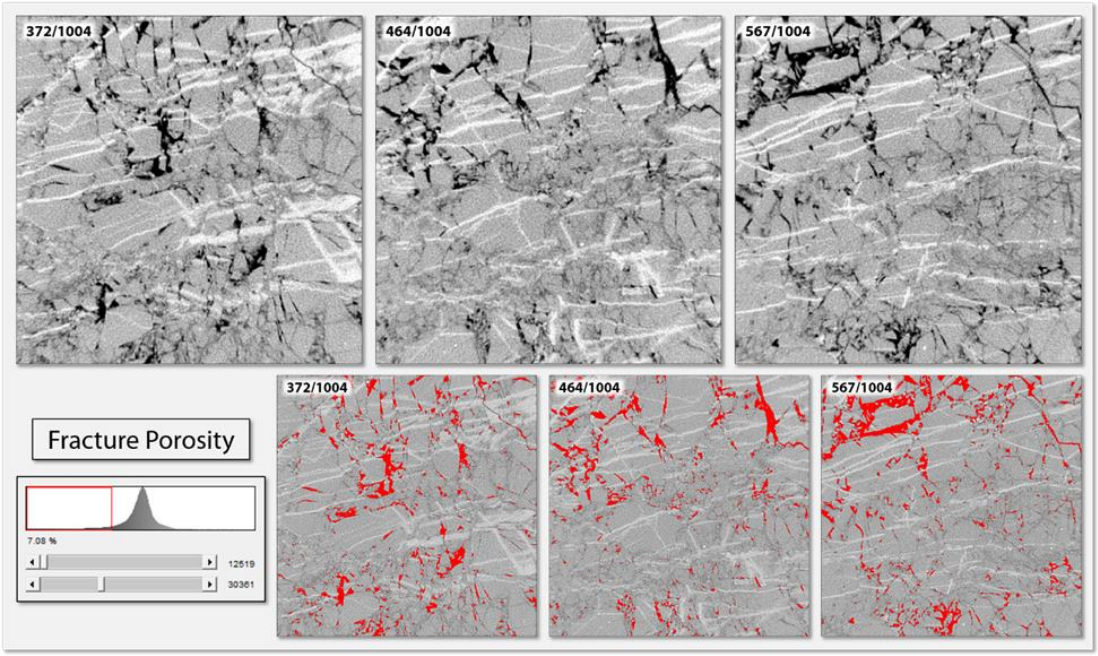

Figure 76. CT slices showing raw images and volumetric segmentation for porosity determination (highlighted in red), Hall 2B core, 5,899 ft. CT slices on the top correspond to the segmented images on the bottom and were used as visual references when applying the histogram cutoffs for segmentation (lower left).

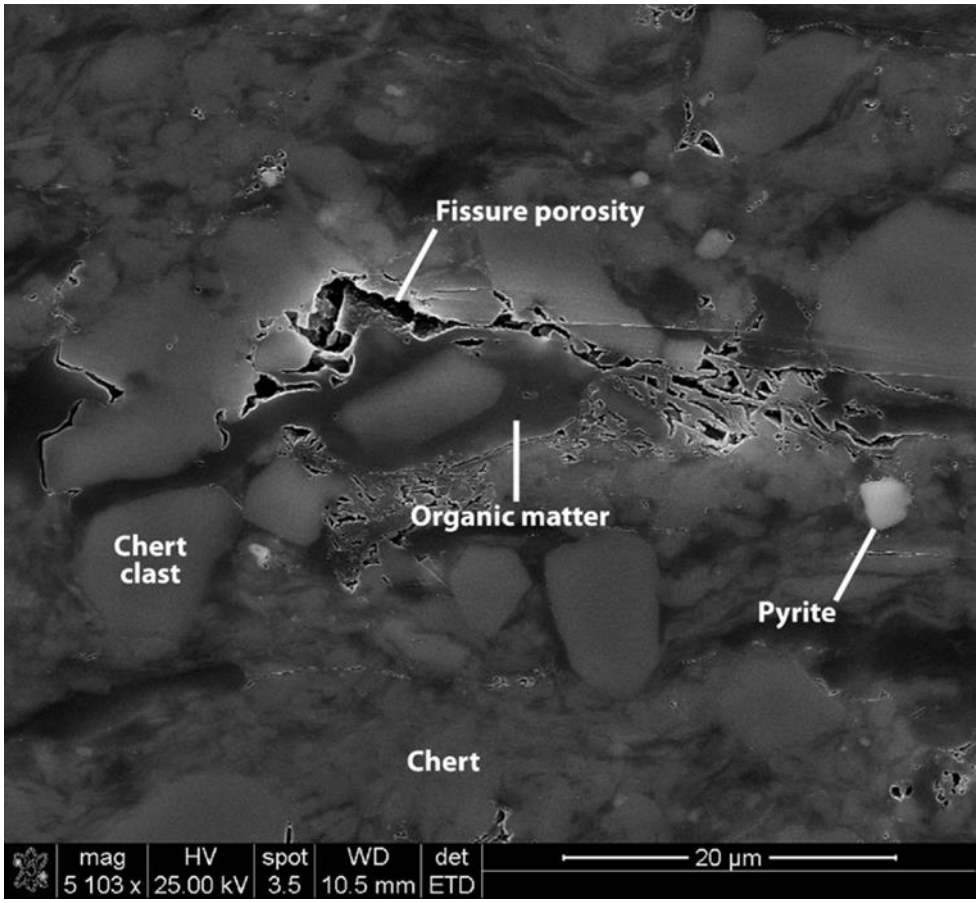

Figure 77. SEM ETD image of pores from an argon ion milled sample of Woodford chert, Hall 2B core, 6,178.5 ft. Fissure porosity in organic matter along the boundaries chert particles.

SCANNING ARTIFACTS

Another problem encountered during scanning large samples is beam hardening, which causes the edges of an object to appear brighter than the center, even if the material is internally homogeneous (see fig. 57). Partial volume effects, which occur when a voxel volume comprises more than one constituent is another x-ray artifact. Unlike beam hardening, partial volume effects can enhance the quality of an image by highlighting features, like microfractures, that are below the voxel resolution of the scan. However, the downside to this effect is that it can lead to erroneous volumetric determinations involving

objects at the sub-voxel scale. Micron-scale mineral grains are difficult to image, and particles need to occupy many voxels to avoid blurry edges.

SAMPLE COMPOSITION

Density contrast is the key to CT imaging and rocks with low density variability such as low porosity carbonates and evaporites may not image well. Adequate density contrast within a sample opens the door for several applications. If compositional data are available, a semi-quantitative estimation of the volumetric percentage of the known constituents is achieved by segmenting scans via gray value histogram cutoffs (fig. 78). This estimated composition using this quick-look method can be improved via the marriage of CT and EDS map datasets using a method called TACCo (Tomography Assisted Chemical Correlation) (Hu et al., 2014). Also, volumetric percentages can be converted to weight percent and molar fractions so that geochemical analysis can be performed. Segmentation of gray values also enables the user to isolate and inspect features of similar density (figs.79 and 80). In Figure 80, gray values allow imaging of Mississippian marine fossils in the Floyd tongue of the Bangor Limestone recovered in the Walker core. However, it is important to note that even if a feature is resolvable, it must have a distinctive gray value to be segmented. This issue was encountered when calculating the percentage of fracture porosity in the Hall 2-B

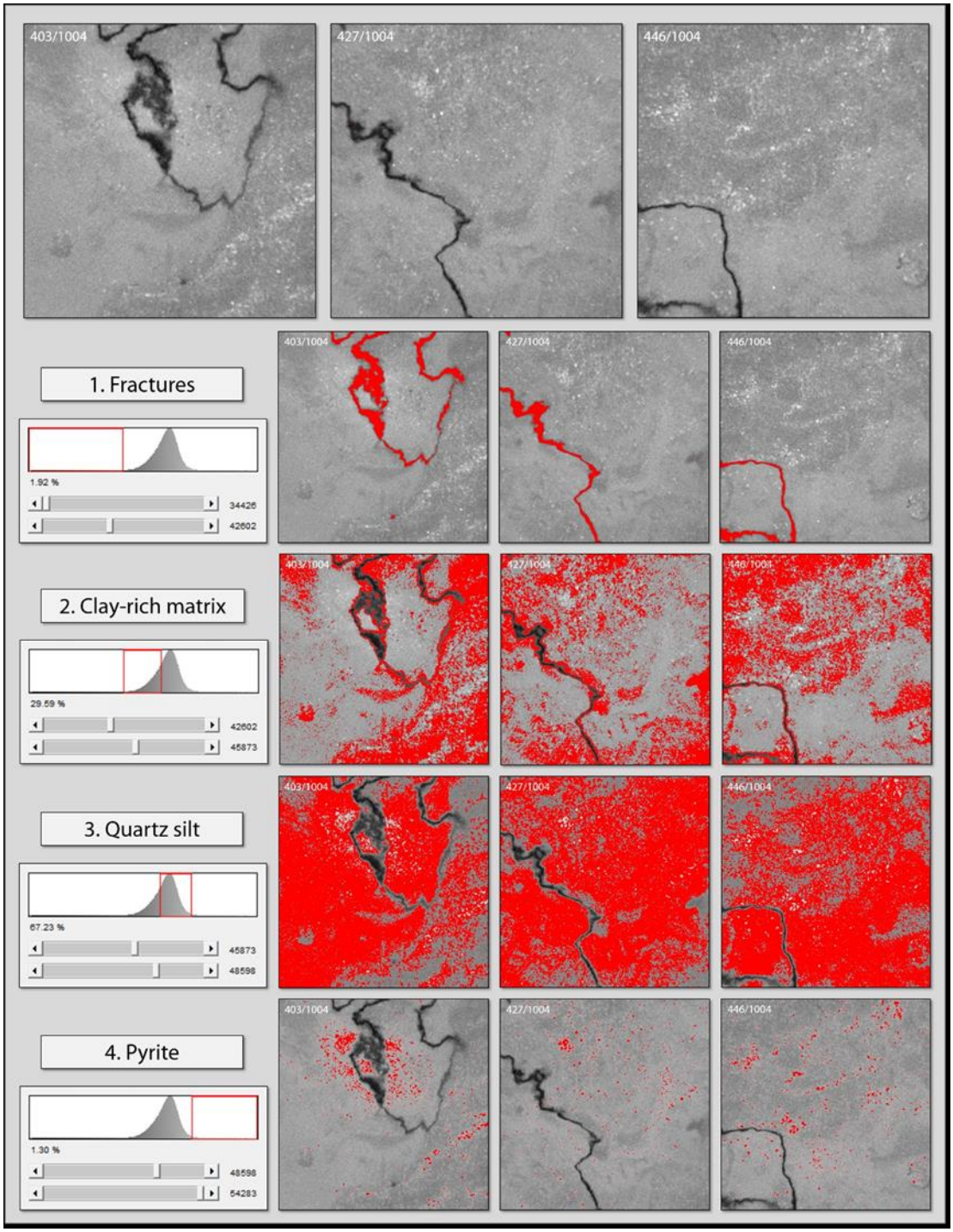

Figure 78.—Analysis used to determine volumetric percentages of fracture space, argillacous mud, quartz silt, and pyrite in a Pottsville shale-siltstone sample from the Gorgas no. 1 core. The tomograph was segmented using gray-scale histogram cutoffs to identify major sample constituents.

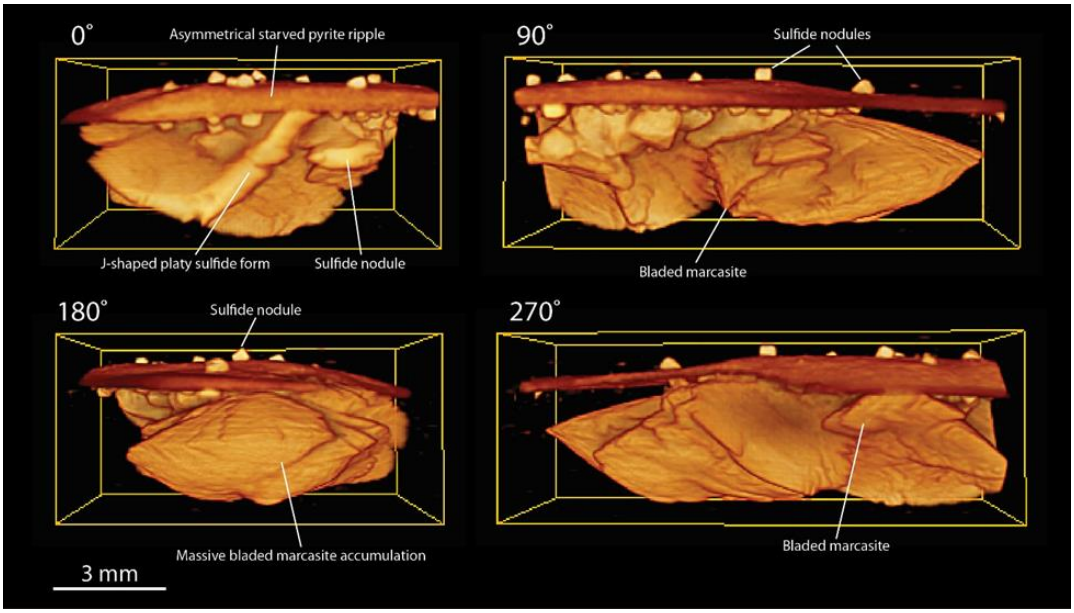

Figure 79.—Glow density filtered tomograph presented at four different angles, Anderson 12- 1 core, 6,843.6 ft. Pyrite appears as an asymmetrical starved ripple. Sulfide nodules are seen above and below the ripple. The largest sulfide nodules contain platy and bladed crystals, indicating formation of marcasite.

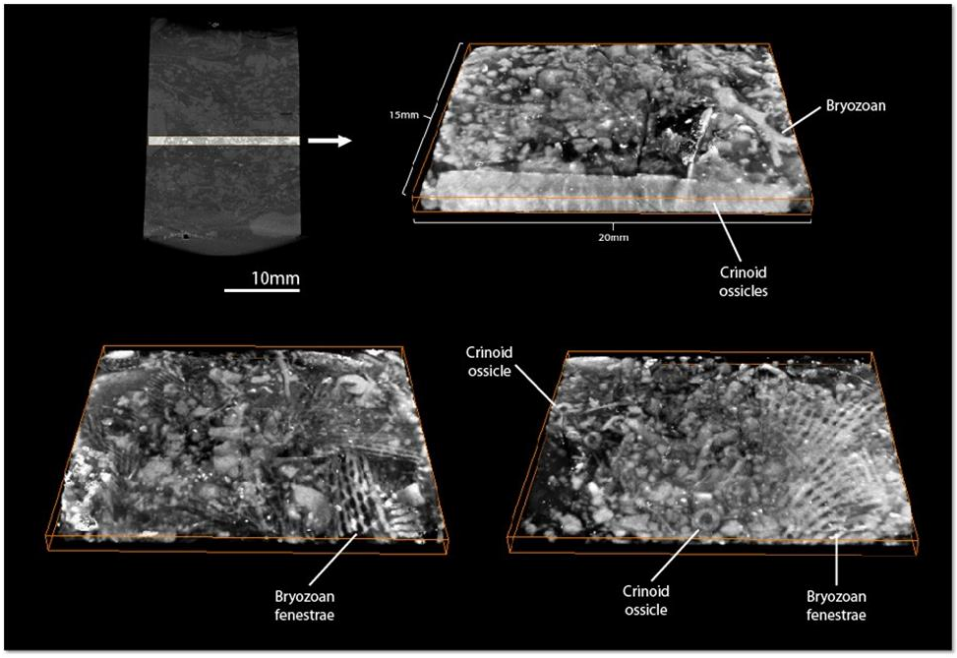

Figure 80.—Three gray ramp density filtered cropped tomographs of Mississippian fossils, Walker core, 2,619 ft. The tomograph has been cropped to reveal bryozoans and crinoids in three dimensions. This demonstrates the utility of the micro-CT as a tool for paleontologic and taphonomic analysis.

core (fig. 73). In the Hall 2-B samples, gray values for hairline fractures matched gray values of the rock matrix and were not effectively imaged.

IMAGING RESOLUTION

The maximum voxel resolution of the CT scanner used in this study is 100 nm. To obtain that resolution while maintaining an adequate density contrast, sample size must be approximately 0.2 mm in height, 0.1 mm wide and 0.1 mm thick. However, preparing a geologic specimen with those dimensions compromises sample integrity. A more realistic maximum voxel resolution for a geologic sample, while maintainin specimen integrity, is approximately 500 nm. The image quality of a CT slice at maximum resolution is much less than that of an SEM micrograph due to the blurry edges caused by partial volume effects. As a result, the smallest pore diameter that can be resolved using the micro CT is approximately 3 μm.

Rock fabric

Micro-scale observations of rock fabric rely on density differences. The simplest observation made from the CT scans was the recognition of dense mineral grains because of their bright appearance, which reflects a high degree of x-ray attenuation. Common minerals with higher densities than clay minerals include pyrite, quartz, carbonate and phosphate, with pyrite and detrital quartz being most common and easily recognized at the micro-scale (fig. 59). While dense minerals are easily imaged, they can be difficult to differentiate because of the similar gray values assigned to them by the imaging software. Grain shape, size, roundness and sorting were also observable (figs. 59 and 81). In addition to dense mineral grains, clay matrix was readily observed due to its lower density. It also appears that

imaging of organic matter may be possible (fig. 59). In several cases, pore types were identified in CT slices and volumetrics

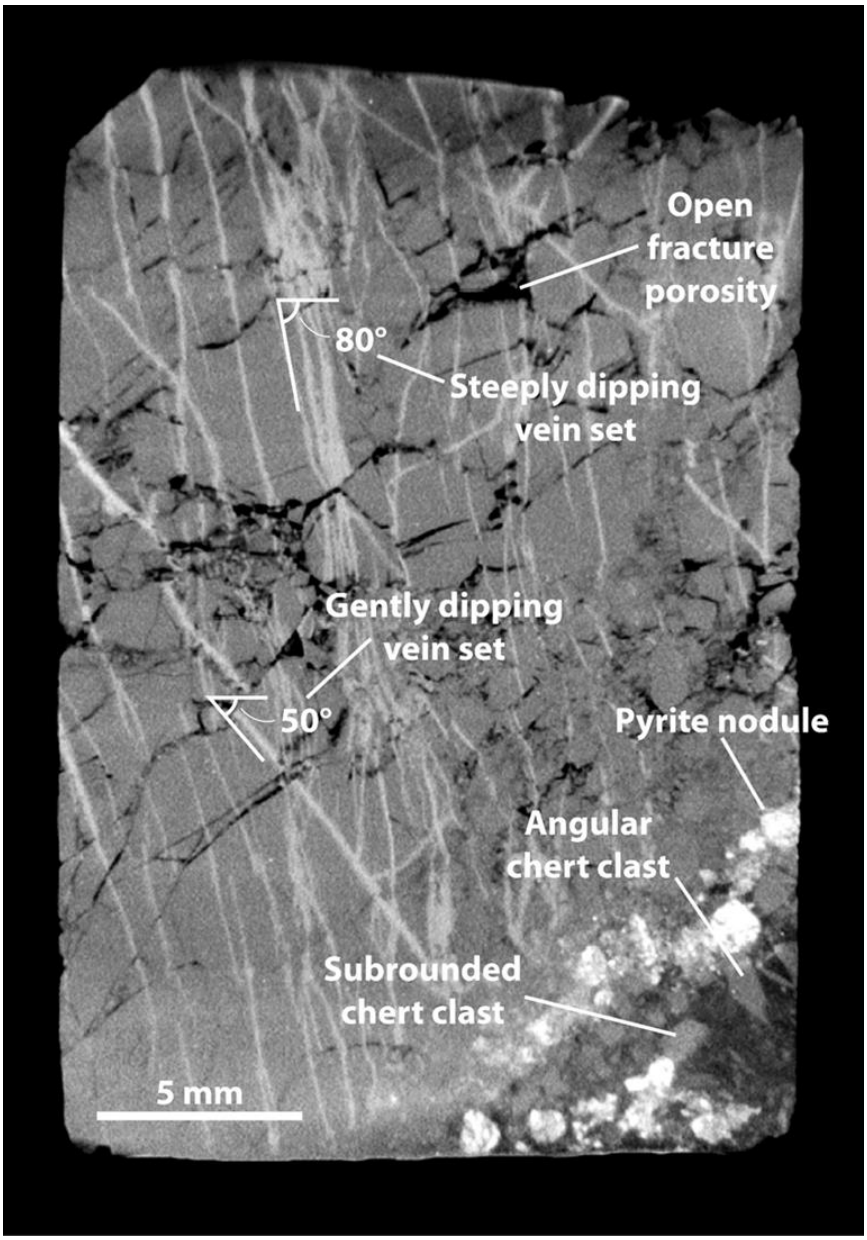

Figure 81.—CT slice showing two sets of quartz veins, open fracture porosity, subrounded to angular chert clasts and pyrite nodules, Hall 2B core, 5,899 ft.

for fracture pores were calculated from one of the Hall 2-B core samples, although some fractures below the resolution limit of the instrument were not included in the calculation (fig. 76).

SEDIMENTARY AND BIOGENIC STRUCTURES

Physical sedimentary structures were recognized where density contrast is present. Ripple-cross laminae and alternating mud and silt laminae were observed that were otherwise undetected (e.g., figs. 72 and 73). The limitation of sample size for the instrument precludes imaging physical structures larger than a few centimeters, such as large scale cross-strata. In addition to physical structures, several biogenic structures were imaged with micro-CT scanning. A horizontal burrow network filled with dense material was observed within a mud-rich nodule in a sample of Conasauga Shale (fig. 62). Other biogenic structures worth imaging include trace-fossil associations (e.g., *Skolithos, Cruziana, Zoophycos* and *Nereites*), tracks and trails.

Body fossils

One of the advantages that CT scanning of rocks provides is the ability to view slices of the rock that are parallel, perpendicular, or even oblique to bedding. By looking parallel to bedding planes, flattened fossils are more readily recognized (fig. 82). Fossil assemblages can also be viewed by cropping thicker slices from a tomograph and filtering out the lower density phases, leaving only the fossils (fig. 80). It is important to note that CT scanning has proven itself to be just as effective for imaging low-density fossils, such as carbonized plants (Kvale, 2014). The potential to image biogenic structures and non-destructively extract a high resolution 3-D image of a fossil from the interior of a rock sample has innumerable applications to systematic paleontology, taphonomy and paleoecology.

DIAGENETIC FEATURES

CT scanning also proved useful for imaging diagenetic features. The most common diagenetic sedimentary structures in shaly sequences are concretionary (e.g. nodules) (Potter and Pryor, 1980). Numerous phosphate nodules were imaged in a Woodford Shale sample from the

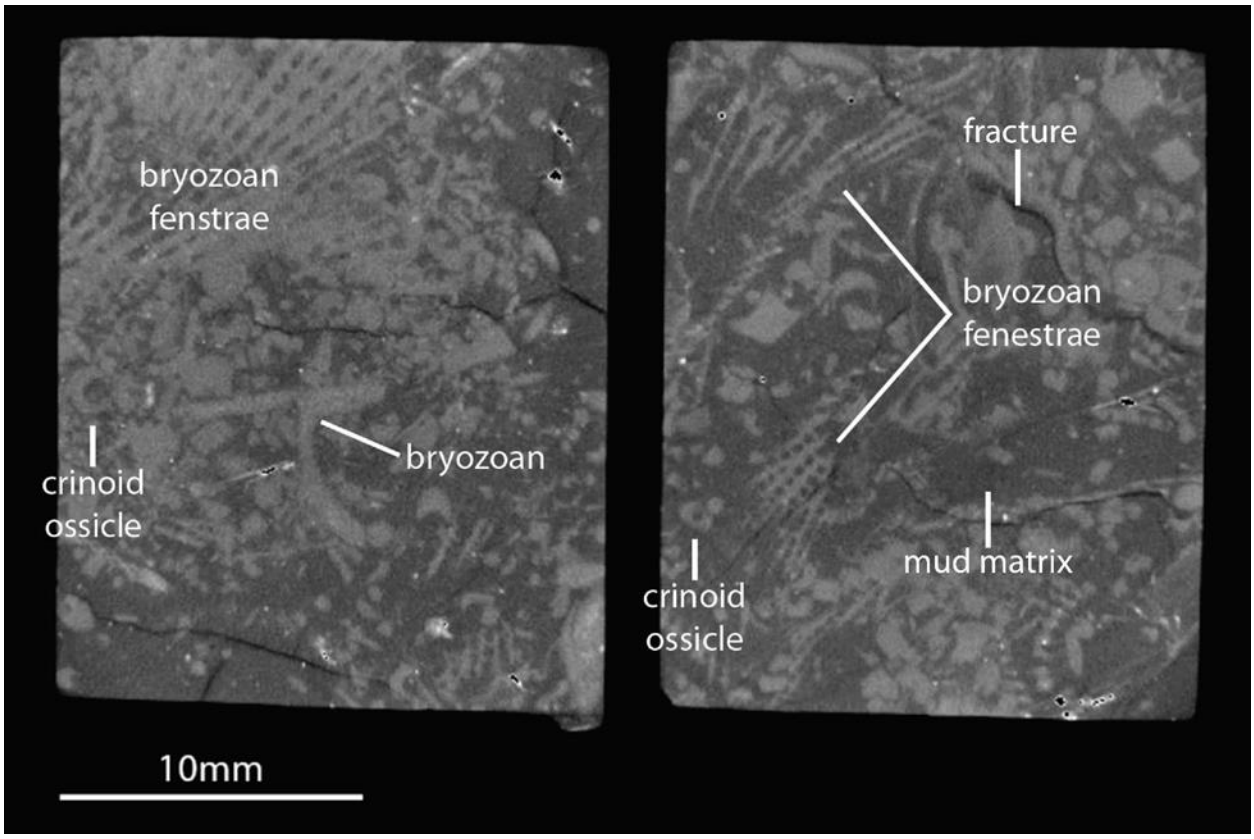

Figure 82. CT slices of fossils in the XY plane, Mississippian (Floyd tongue of Bangor Limestone) Walker core, 2,619 ft. Fenestrate bryozoa and crinoid ossicles are easily identified. In addition to fossils, irregular fractures and the mud matrix are imaged. Black areas that appear to be pores are high density material (pyrite) that was poorly imaged because of unresolved reconstruction errors.

Anderson 12-1 core, and the ability to slice, filter, and density map enabled characterization of basic diagenetic relationships (figs.77 and 78).

Pyrite is a common product of early diagenesis in organic-rich sediment (Berner, 1984; Taylor and Macquaker, 2000). Various pyrite morphologies and textural features have been

used to infer geochemical and paleoenvironmental conditions (Schieber and Baird, 2001; Passier et al., 1997). Pyrite, in various forms, was imaged with the CT scanner and SEM in every sample analyzed (e.g., figs. 57, 58 and 79). Other diagenetic features imaged with the micro-CT unit include partially and fully-cemented fractures (figs. 63 and 74) and pores. Organic-matter pores were only imaged using SEM (figs. 71 and 77), but altogether imaging of diagenetic structures with micro-CT was successful and could be added as another investigative approach to their systematic study.

FRACTURES AND FAULTS

The CT scanner proved to be an excellent tool for the analysis of faulting and fracturing where density contrasts generated by mineralization along the fault or fracture plane are detected. The smallest resolvable fracture apertures observed from a CT scan ranged from 1 – 2 μm (fig. 83). Smaller fracture apertures will undoubtedly be resolvable as micro-CT imaging resolution advances. Both mineralized and open fractures were imaged is samples of the Hall 2-B core, sample, and their cross-cutting relationships allowed for determining structural chronology (fig. 81). Histogram cutoffs allowed for segmentation of various fracture types and enabled 3D renderings of fracture networks to be generated for visualization purposes (fig. 75). When fracture porosity is resolvable, a volumetric calculation is also possible (fig. 76). In addition to structural chronology and fracture composition, identification of fracture geometry and interconnectivity of fracture networks is another powerful use of CT scanning. Determination of fracture geometry and interconnectivity was achieved by applying a density filter to a tomograph.

SEM-EDS

Observation of rock microfabric in a CT slice or tomograph is an effective way to identify areas to characterize further with the SEM. Argon ion milling samples made microfabric characterization much easier, as it produced high quality surfaces with minimal artifacts. SEM proved to be an excellent tool for observation of pores, sulfide morphology, fossils, mineralgrains, and fracture-filling cement. SEM, coupled with EDS, allowed for rapid and straightforward determination of those mineral grains. Together, CT and SEM/EDS data

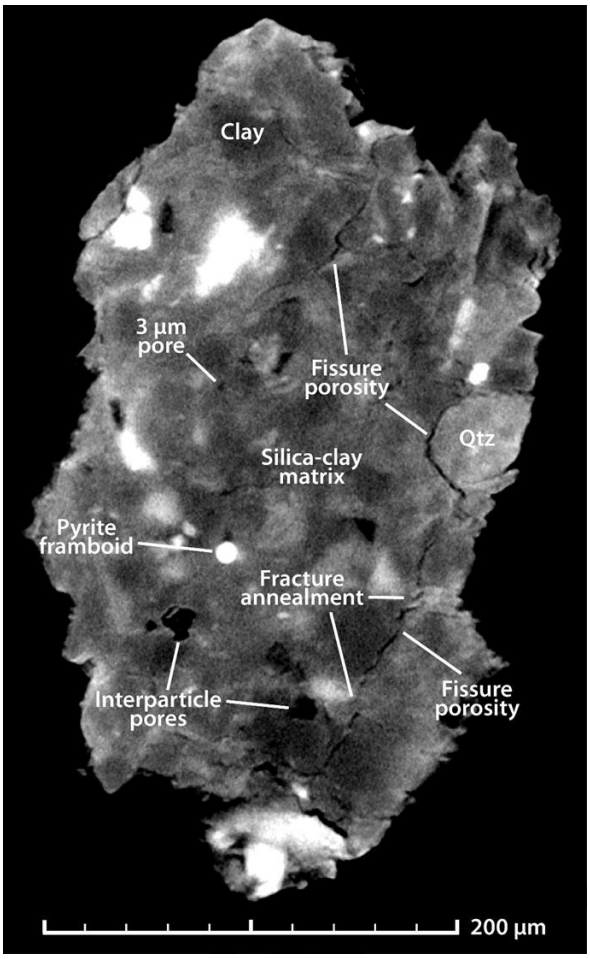

Figure 83. CT slice, Pennsylvanian (Pottsville) Gorgas no. 1 core sample showing microfabric. Porosity types imaged are fissure and interparticle porosity, with the smallest resolvable pore measuring 3 µm in diameter. Porosity was identified by the true black gray value assigned to it. Mineral constituents include quartz grains and pyrite bodies in a clay-silica matrix.

complemented each other very well. While CT was used to pinpoint areas for further high quality imaging and analysis, the data gathered from those areas with SEM/EDS was used to supplement interpretations made from the lower resolution CT data. The two datasets can work seamlessly together and thoroughly bridge the gap from micro- to nano-scale observations.

CT STRATEGY AND WORKFLOW

Micro- CT scanning has proven to be a very useful tool for shale characterization. Yet, a CT scanning workflow for rock imaging and analysis has not been firmly established. This is because micro-CT scanning of geological media is in its infancy. The following paragraph outlines a generalized step-by-step process for CT scanning rocks that is designed to benefit future investigators (fig. 84).

Using core descriptions and other data as a guide, an area with distinctive features (e.g., sedimentary structures, fossils, diagenetic structures, etc.) is chosen for closer inspection via CT analysis. Using a precision saw with a diamond blade, a sample is cut from the core slab, with the dimensions tailored to what is attempting to be imaged. The sample is then mounted in the scanner and scanning conditions are determined. After scanning, the scan file is processed to eliminate sample shifting and beam hardening. Reconstructed CT slices are generated and a continuous stack of the slices can be created to make a 3-D volume. Image software can then be used to perform qualitative inspections and quantitative operations on the reconstructed sample. Samples can be viewed as 2-D slices in the XY, XZ and YZ directions. Samples can also be viewed in full or cropped 3-D volumes. Density filters enable the user to highlight various features. Applying cutoffs to a histogram of a scans gray

values allows the user to isolate features of interest and visualize them in 3-D. Volumetric calculations can also be performed with histogram cutoffs.

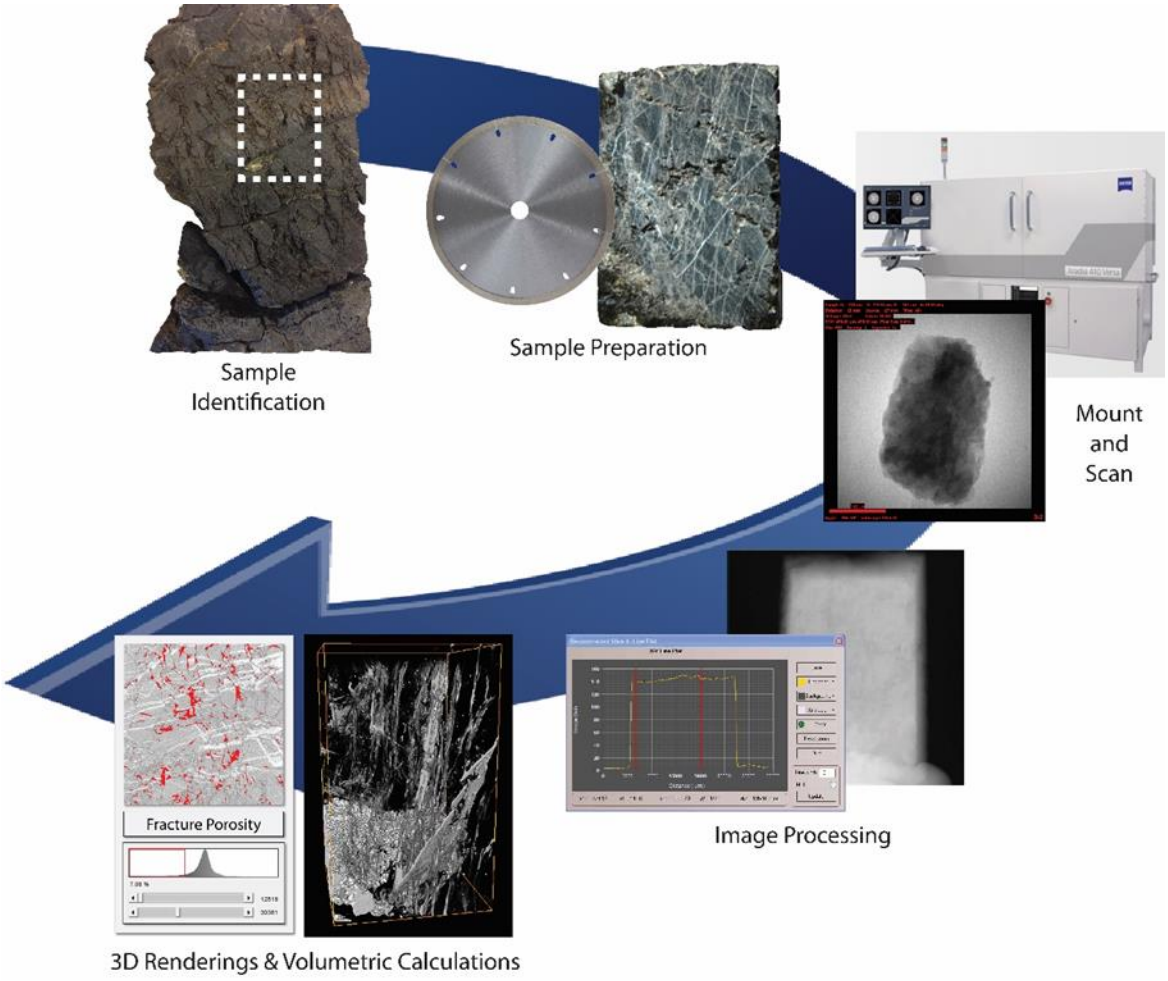

Figure 84. CT scanning strategy outlining the steps from sample identification to qualitative and quantitative data gathering.

While micro-CT has proven itself to be a useful tool in the field of shale research, it is but one component of the systematic approach that is required to adequately study shale. A robust workflow (fig. 85) that covers a large scale of observations must be implemented to in order to understand the characteristics and origin of shale. Micro-CT scanning makes a great addition to this type of workflow because it helps bridge gaps among different analyses. Conversely, interpretation of CT scan results is informed by the data gathered from other

analytical tools. With CT being an evolving technology, data gathered from micro-CT analysis will only improve with time. Higher magnification objectives will allow for improved resolution. Also, a wider range of x-ray energy will enable larger samples to be scanned while maintaining adequate contrast, serving to enhance the contrast of scans on very small samples. Higher resolution and enhanced contrast will greatly improve geologic investigations.

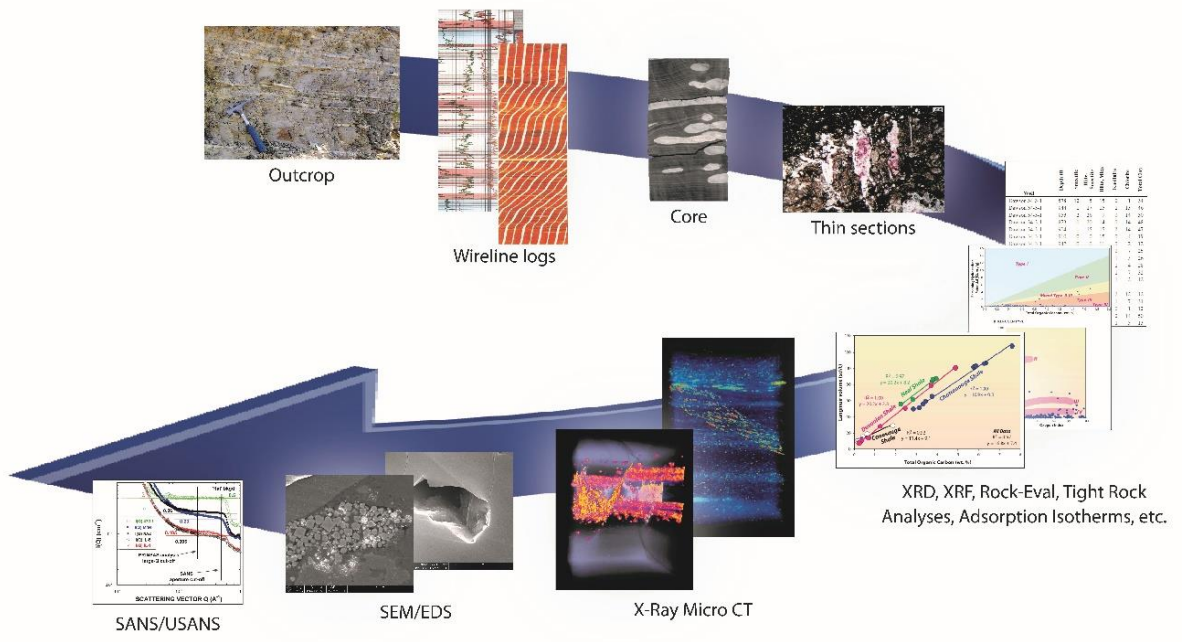

Figure 85. Integrated workflow for shale from megascopic to nano-scale data analysis.

CONCLUSIONS

Shale is of enormous economic importance because it has sourced the majority of the world's hydrocarbons, forms the majority of the world's reservoir seals and has now emerged as a world-class reservoir rock. Nonetheless, shale is amongst the least understood of all sedimentary rock types (Wignall, 1994). A major reason for the lack of understanding of argillaceous rocks is difficulty of analysis. Micro-CT analysis is a technique for visualizing

features in the interior of opaque solid objects, and for obtaining digital information on their 3-D geometries and properties. It requires relatively little sample preparation and is a powerful extension to traditional petrographic analysis, as it allows observations and measurements to be extended into three dimensions. Even at its simplest, data can be visualized to observe texture and structure in sedimentary rocks. Micro-CT differs from conventional medical CAT-scanning in its ability to resolve details as small as 0.1 μm in size, even when imaging objects consisting of high density materials. Due to its origin outside of the earth sciences, exploring applications to geological problems is still in its infancy.

A variety of major rock features were observed using micro-CT scanning. Micro-scale observations of rock fabric were made that include mineral grains, matrix materials, and pores. Physical sedimentary structures like laminae and ripples were imaged. In addition, biogenic sedimentary structures, including trace fossils and body fossils, also were imaged. Diagenetic features were observed, such as phosphate nodules and a range of sulfide forms. Lastly, fracture and fault geometry was easily discerned for both open and mineralized fracture and fault networks.

In addition to the unparalleled qualitative data that can be gathered through two- and three-dimensional observations, CT is also a very powerful method for semi-quantitative analysis. Using image analysis software, volumetric data can be collected. This is demonstrated by the percentage of fracture porosity and mineral constituent volumes that were estimated in this study. While volumetrics for porosity were not calculable from the shale samples that were scanned in this study, the ability of the machine to resolve ≥ 3 μm

pores may be of interest to geoscientists interested in performing porosity studies on macroporous sedimentary rocks.

SEM/EDS data from this study were used in concert with the CT data that was gathered. The CT was used for identifying locations in which the microfabric could be further analyzed using SEM. SEM proved to be an excellent tool for observation of pores, sulfide morphologies, fossils and mineral grains, and the high resolution of the SEM images relative to the CT scans provided a wealth of information that was instrumental for the interpretation of the CT data. EDS, moreover, allowed for rapid identification of minerals by determining major element composition.

While the work here demonstrated the power of integrating CT into argillaceous rock analysis, there are still several limitations of the instrument. Resolution of the machine that was used is limited to 1/1,000th the cross-sectional diameter of the scan. Finite resolution can cause blurring of material boundaries. As such, a high resolution scan with high contrast requires small samples. Accordingly, the greatest significance should be placed on the amount of contrast a scan will generate, as it determines the overall quality of a scan. A long scan can be performed on a small volume within a large sample to obtain high resolution, but large samples requires high x-ray energy and long scan times that may not be practical. And the higher the x-ray energy, the less contrast a scan will yield. With less contrast, a lower number of gray values will be derived, and rock features will be muted.

Experience with the Xradia VersaXRM 410 indicates that sample size should be tailored to what is attempted to be imaged. Not all features within a rock have sufficiently large attenuation contrast for effective imaging. Although a sedimentary structure may exist within a rock, it will appear homogenous if there is no density contrast. For example, while

calcareous fossils in argillaceous matrix were imaged effectively, they may not have been resolvable had they been preserved in limestone. Lastly, CT produces large volumes of data (gigabytes to terrabytes) and requires large storage devices and considerable computing power for visualization and quantitative analysis.

While these may be pitfalls in modern CT analysis, they undoubtedly will be areas of future advancement, as CT is an evolving technology. Overall, this study has demonstrated the usefulness of incorporating CT analysis into shale studies by exhibiting the wide variety of observations that can be made. Micro-CT provides a nondestructive way to image shale samples in three dimensions and facilitates in the identification of heterogeneity and inspection of sedimentary features (e.g., rock fabric, physical and biogenic sedimentary structures, diagenetic structures, fractures, and faults). By observing these characteristics, how microfabric relates to macrostructure, sedimentary processes, and tectonic processes can be determined. In addition to shale studies, this work provides a foundation for applying CT analysis to studies of other rock types.

REFERENCES

Alcantar-Lopez, L. and S. J. Chipera, 2013, Improving our understanding of porosity in Source rock reservoirs through advanced imaging techniques: Unconventional Resources Technology Conference (URTeC), unpaginated CD-ROM, 2013.

Baird, G.C., and Brett C.E., 1986, Erosion on an anaerobic seafloor: significance of reworked pyrite deposits from the Devonian of New York state: Paleogeography, Palaeoclimatology, Palaeoecology, p. 157-193.

Berner, R. A., 1984, Sedimentary pyrite formation: an update: Geochimica et Cosmochimica Acta, v. 48, p. 605-615.

Berner, R. A., and Raiswell, R., 1983, Burial of organic carbon and pyrite sulfur iron Sediments over Phanerozoic time: a new theory, Geochim. Cosmochim. Acta, v. 47, p. 855-862.

Blackford, M.A., 2007, Electrostratigraphy, thickness and petrophysical evaluation of the Woodford Shale, Arkoma Basin, Oklahoma: unpublished M.S. thesis, Oklahoma State University, 94 p.

Caldwell, C. D., 2011, Lithostratigraphy of the Woodford Shale, Anadarko Basin, west-Central Oklahoma, in Oklahoma Geological Survey Workshop, Shales Moving Forward.

Callner, S.A., 2014, An integrated approach to understanding sedimentary structures and depositional processes in Devonian-Mississippian black shale: the Woodford Shale and associated strata in the southern midcontinent: unpublished M.S. thesis, Oklahoma State University, 90 p.

Cecil, K.A, 2016, Origin and characterizaiton of Devonian-Mississippian novaculitic chert in Oklahoma; unpublished M.S. thesis, Oklahoma State University, 154 p.

Comer, J.B., 1992, Organic geochemistry and paleogeography of Upper Devonian formations in Oklahoma and western Arkansas, in K.S. Johnson and B.J. Cardott (eds.), Source rocks in the southern Midcontinent, 1990 symposium: OGS Circular no. 93, p. 70-93.

Cruse, A.M. and Lyons, T.W., 2004, Trace metal records of regional paleoenvironmental variabiltiy in Pennsylvanian (Upper Carboniferous) black shales: Chemical Geology, v. 206, no. 3-4, p. 319-345.

Energy Information Agency (EIA), 2013, Shale oil and shale gas resources are globally abundant: Washington, D.C., U.S. Department of Energy, v. 2014.

Ettensohm, F.R., 1992, Controls on the origin of the Devonian-Mississippian oil and gas shales, east-central United States: Fuel, v. 71, no. 12, p. 1487-1492.

Ettensothn, F.R. and Elam, T.D., 1985, Defining the nature and location of a Late Devonian-Early Mississippian pycnocline in eastern Kentucky: Geological Society of America Bulletin, v. 96, no. 10, p. 1313-1321.

Fay, R.O., 1989, Geology of Arbuckle Mountains along Interstate 35, Carter and Murray counties, Oklahoma: Oklahoma Geological Survey, Guidebook 26, 59 p.

Fishman N., Ellis, G.E., Pasxton, S.T., Abbott, M.M. and Boehlke, A.R., 2010, From Radiolarian ooze to reservoir rocks: microporosity in chert beds in the Upper Devonian-Lower Missisippian Woodford Shale, Oklahoma: AAPG Search and Discovery Article 10268, 18 p.

Heckel, P.H., and Witzke, B.J., 1979, Devonian world paleogeography determined from distribution of carbonate and related lithic, paleoclimatic indicators: Special Papers in Paleontology, v.23, p. 99-123.

Hu, Q., Ley, M.T., Davis, J., Hanan, J.C., Frazier, R., and Zhang, Y., 2014, 3D chemical segmentation of fly ash particles with X-ray computed tomography and electron probe microanalysis: Fuel, v. 116, p. 229-236.

Jarvie, D.M., R. J. Hill, T. E. Ruble, and P. R.M., 2007, Unconventional shale-gas systems: The Mississippian Barnett Shale of north-central Texas as one model for thermogenic shale-gas assessment: AAPG Bulletin, v. 91, p. 475–499.

Jarvie, D.M., 2003, The Barnett Shale as a model for unconventional shale gas exploration, Humble Geochemical Services; Division of Humble Instruments & Services, Inc., p. 7-26.

Krystyniak, A. M., 2005, Outcrop-based gamma-ray characterization of the Woodford Shale of south-central Oklahoma: unpublished M.S. thesis, Oklahoma State University, 160 p.

Kvale, E., 2014, Depositional implications of museum-quality terrestrial ferns in deep water Wolfcamp Formation: Denver, Unconventional Resources Technology Conference Proceedings, unpaginated.

Lambert, M.W., 1993, Internal stratigraphy and organic facies of the Devonian-Mississippian Chattanooga (Woodford) Shale in Oklahoma and Kansas: AAPG Special Volume, Source Rocks in a Sequence Stratigraphic Framework, p. 163-176.

Loucks, R.G., R.M. Reed, S. C. Ruppel, and D.M. Jarvie, 2009, Morphology, genesis, and distribution of nanometer scale pores in mudstones of the Mississippian Barnett Shale: Journal of Sedimentary Research, v. 79, p. 848–861.

Middleton, G., Church, M.J., Coniglio, M., Hardie, L.A., and Longstaffe, F.J., 2003,

Encylopaedia of Sediments and Sedimentary Rocks, Kluwer Academic Publishers, 928 p.

Milliken, K. L., P. K. Papazis, R. J. Day-Stirrat, and C. Dohse, 2012, Carbonate lithologies of the Mississippian Barnett Shale, in J. Breyer, ed., Shale reservoirs: Giant resources for the 21st century: AAPG Memoir 97, p. 290–321.

Miller, B., 2014, Lithologic Characterization of the Barnett Shale: Controls on Reservoir Quality: unpublished M.S. thesis, Oklahoma State University, 112 p.

Miller, J., 2006. Chesapeake's Integrated Workflow. ed. Tulsa Geological Society Meeting. March 6, 2006. Tulsa Oklahoma.

Montgomery, S. L., D. M. Jarvie, K. A. Bowker, and R. M. Pollastro, 2005, Mississippian Barnett Shale, Fort Worth Basin, north-central Texas: Gas-shale play with multitrillion cubic foot potential: AAPG Bulletin, v. 89, p. 155–175.

Over, D.J. 1992, Conodonts and the Devonian-Mississippian boundary in the upper Woodford Shale, Arbuckle Mountains, south-central, Oklahoma: Journal of Paleontology, v. 66, p. 293-311.

Over, D.J., 2002, Conodonts and age of depositional sequences in the Chattanooga Shale, Upper Devonian, southern Appalachian basin, eastern U.S.: Strata (Eighth International Conodont Symposiu-ECOS VIII), v. 12, p. 51.

Pashin, J.C., and Ettensohn, F.R., 1992, Palaeoecology and sedimentology of the dysaerobic Bedford fauna (late Devonian), Ohio and Kentucky (USA): Palaeogeography, Palaeoclimatology, Palaeoecology, v. 91, no.1-2, p. 21-34.

Pashin, J.C., Kopaska-Merkel, D.C., Arnold, A.C., and McIntyre, M.R., 2011, Geological foundation for production of natural gas resources from diverse shale formations: Sugarland, Texas, Research Partnership to Secure Energy for America, Final Report, 156 p.

Pashin, J.C., Kopaska-Merkel, D.C., Arnold, A.C., McIntyre, M.R., and Thomas, W.A., 2012, Gigantic, gaseous mushwads in Cambrian shale: Conasauga Formation, southern Appalachians, USA: International Journal of Coal Geology, v. 103, p. 70-91.

Pashin, J.C., and Callner, S.A., 2014, Paleoceanographic and estuarine influence on sedimentation in an unconventional source rock-reservoir system: Devonian shale of the southern Midcontinent, USA: Eastern Unconventional Oil and Gas Symposium, Lexington, Kentucky.

Passier, H.F., Middelburg, J.J., de Lange, G.J., and Böttcher, M.E., 1997, Pyrite contents, microtextures, and sulfur isotopes in relation to formation of the youngest eastern Mediterranean sapropel: Geology, v. 25, p. 519-522.

Potter, P.E., Maynard, J.B., and Pryor, W.A., 1980, Sedimentology of Shale: Study Guide and Reference Source: New York, Springer-Verlag, 303 p.

Powers, M.R., 2015, Exploring micro x-ray computed tomography coupled with scanning electron microscopy as tools for Paleozoic shale studies: unpublished M.S. thesis, Oklahoma State University, 108 p.

Puckette, J., Boardman, D. R., and Watney, W.L., 2013, Woodford Shale: correlating rock properties in outcrop and core with wireline log characteristics: AAPG Search and Discovery, Article no. 50885.

Quan, T.M., Adigwe E.N., Riedeinger, N., and Puckete, J., 2013, Evaluating nitrogen isotopes as proxies for depositional environmental conditions in shales: Comparing the Caney and Woodford shales in the Arkoma basin, Oklahoma: Chemical Geology, v. 360, p. 231-240.

Rich, J.L., 1951, Three critical environments of deposition and criteral for recogonition of rocks deposited in each of them: Geol. Society of America Bulletin, v. 62, p. 1-19.

Rimmer, S.M., 2004, Geochemical paleoredox indicators in Devonian-Mississippian black shales, central Appalachian basin (USA): Chemical geology, v. 206, p. 373-391.

Rivera, K.T., 2013, Geologic controls on nitrogen isotopes in marine black shale: a case study of the Woodford Shale, Anadarko basin, Oklahoma, USA: unpublished M.S. thesis, Oklahoma State University, 129 p.

Roberts, C.T., and Mitterer, R.M., 1992, Laminated black shale-bedded chert cyclicity in the Woodford Formation, southern Oklahoma, in K.S. Johnson and B.J. Cardott (eds.), Source rocks in the southern Midcontinent, 1990 symposium: Oklahoma Geological Survey, Circular 93, p. 330-336.

Schieber, J., 1994, Evidence for high-energy events and shallow-water deposition in the Chattanooga Shale, Devonisn, central Tennessee, USA: Sedimentary Geology, v.. 93, p. 193-208.

Schieber, J., and Baird, G., 2001, On the origin and significance of pyrite spheres in Devonian black shales of North America: Journal of Sedimentary Research, v. 71, p. 155-166.

Schieber, J., and Southard, J.B., 2009, Bedload transport of mud by floccule ripples-direct observation of ripple migration processes and their implications: Geology, v. 37., p. 483-486.

Spaw, J.M., 2013, Microfacies analysis: an integrated petrologic approach to characterizing

mudrock heterogeneity, in AAPG Unconventional Resources Technology Conference, Denver, Colorado, p. 7.

Taylor, K.G., and Macquaker, J.H.S., 2000, Early diagenetic pyrite morphology in a mudstone-dominated succession: the Lower Jurassic Cleveland Ironstone Formation, eastern England: Sedimentary Geology, v. 131, p. 77-86.

Ver Straeten, C.A., Brett, C.E., and Sageman, B.B., 2011, Mudrock sequence stratigraphy: a multi-proxy (sedimentological, paleobiological and geochemical) approach, Devonian, Appalachian basin: Palaeogeography, Palaeoclimatology, Palaeoecology, v. 304, no.1, p. 54-73.

Wignall, P.B., 1994, Black shales: Oxford, Oxford University Press, 127 p.

Zhao, H., N. B. Givens, and J. B. Curtis, 2007, Thermal maturity of the Barnett Shale determined from well-log analysis: AAPG Bulletin, v. 91, p. 535–749.

PETROLOGIC CHARACTERIZATION: GAS SHALES BLACK WARRIOR BASIN AND APPALACHIAN THRUST BELT

GEOLOGICAL SURVEY OF ALABAMA

Berry H. Tew, Jr
State Geologist

Petrophysics and Tight Rock Characterization for the Application of Improved Stimulation and Production Technology in Shale

FINAL REPORT

OPEN-FILE REPORT 1603

Reporting Period: June 27, 2013-June 26, 2016

by

David C. Kopaska-Merkel, Guohai Jin, Jamekia Dawson, and Denise J. Hills

Geological Survey of Alabama
P.O. Box 869999, Tuscaloosa, AL 35486-6999

Prepared for the Research Partnership to Secure Energy for America (RPSEA) under Subcontract AA-5-49123

Tuscaloosa, Alabama
2016

EXECUTIVE SUMMARY

Shale gas development is taking place in multiple Paleozoic formations in the Black Warrior basin (BWB) and the Appalachian thrust belt of Alabama. Development of these reservoirs has been slowed by uncertainty about best practices for exploration, drilling, and well completion. The diversity of these formations, which range in age from Cambrian to Mississippian, provides an excellent opportunity to examine shale formations with a wide range of reservoir properties in varied geologic settings. Shale formations in Alabama pose a broad range of technical challenges, many of which relate to insufficient characterization of the regional geologic framework, in addition to an inadequate understanding of the fundamental geologic controls governing the producibility of shale gas. To facilitate the development of shale gas reservoirs in the region, this study employs a systematic, multidisciplinary approach to the evaluation of shale reservoirs. Key geologic variables addressed are stratigraphy, sedimentology, structure, petrology, geochemistry, and fracture analysis.

This current study builds upon results of an initial study completed in 2011. Between the two studies, a total of 17 cores were described and/or analyzed using standard geological and petrophysical techniques, such as scanning electron microscopy (SEM), as well as newer methods of focused ion beam (FIB) and discrete fracture network (DFN) analyses. Regional field data were also incorporated into our analyses. This study built on the earlier study by describing one Cambrian core and eight Mississippian cores; conducting SEM analyses on six Cambrian and 39 Mississippian samples; conducting FIB analyses on two Mississippian samples; and developing DFN models based on two Devonian cores and field observations.

Stratigraphy and sedimentology are important because many of the fundamental characteristics of shale are determined in the original depositional environment. Alabama shale reservoirs were deposited in euxinic sedimentary basins that were influenced by the development of cratonic carbonate ramps and orogenic foreland basins. Numerous sedimentary processes were active in these basins, and secular variation of physical, geochemical, and biological processes resulted in complex stratigraphic architecture and heterogeneous reservoir quality, which are important considerations for shale gas development. Folding and faulting affect the geometry and continuity of reservoirs, and fracturing affects subsurface flow and the applicability of completion technology to shale formations. The BWB and Appalachian thrust belt contain a spectrum of extensional and compressional tectonic structures, and these structures are expressed differently in each target shale formation.

Petrology and geochemistry are important for characterizing reservoir quality. All shale formations studied contain a broad suite of detrital and authigenic minerals. Rock fabric was influenced by sedimentation, diagenesis, and hydrocarbon generation, and the degree of alignment of platy clay minerals appears to reflect structure and basin hydrodynamics. Detrital and authigenic minerals, moreover, affect shale geomechanics and the applicability of hydraulic fracturing technologies.

Fractures in shale commonly create preferential paths of fluid flow. The permeability of a fracture is usually much greater than that of the rock matrix and consequently the fluid will flow preferentially through the fracture network, providing the fractures are extensively interconnected. Accurate modeling of effective permeability of fractured reservoirs has been a challenging task, but it is important because fracture networks in reservoirs may

significantly alter reservoir hydrologic properties. DFN modeling can provide valuable insights into fractured-reservoir characterization. Our work shows that in systems with moderately and highly directionally concentrated fractures, such systems can be treated as anisotropic homogeneous media. Hydraulic fracturing in such systems will be most effective if the orientation of the hydraulic fracture is perpendicular to the mean direction of the natural fracture set. In contrast, the fracture-permeability tensor has to be computed for each element for fluid flow and transport modeling in systems with randomized fracture orientations. In such systems, there is no preferred direction for a hydraulic fracture to be most effective, due to the interconnected pathways of the natural fracture network. Application of these DFN modeling technique to the Devonian Chattanooga Shale suggests that there is no preferred orientation of hydraulic fractures required for maximum performance.

CONTENTS

FIGURES

TABLES

VIDEOS

(in file/on CD)

1. FIB serial sections of sample from 3,700 ft., OGB PN 13979, Mississippian Floyd/Neal Shale. 60 images are 167 nm apart. Secondary electrons.
2. FIB serial sections of sample from 3,700 ft., OGB PN 13979, Mississippian Floyd/Neal Shale. 60 images are 167 nm apart. Backscatter electrons.
3. FIB serial sections of sample from 3,723.4 ft., OGB PN 13979, Mississippian Floyd/Neal Shale. 50 images are 198 nm apart. Secondary electrons.
4. FIB serial sections of sample from 3,732.4 ft., OGB PN 13979, Mississippian Floyd/Neal Shale. 50 images are 198 nm apart. Backscatter electrons.

APPENDIX FIGURES

INTRODUCTION

The Black Warrior basin (BWB) and Appalachian thrust belt of Alabama contain diverse emerging shale gas plays in Cambrian, Siluro-Devonian, and Mississippian strata (fig. 1). Development of these reservoirs has been slowed by uncertainty about best practices for exploration, drilling, and well completion. A large part of this uncertainty stems from limited knowledge of the basic geologic framework of the targeted shale formations. This uncertainty is compounded by major differences of composition, thickness, geometry, and fracture architecture between the emerging shale reservoirs of the BWB and Appalachian thrust belt and the established shale reservoirs in other regions.

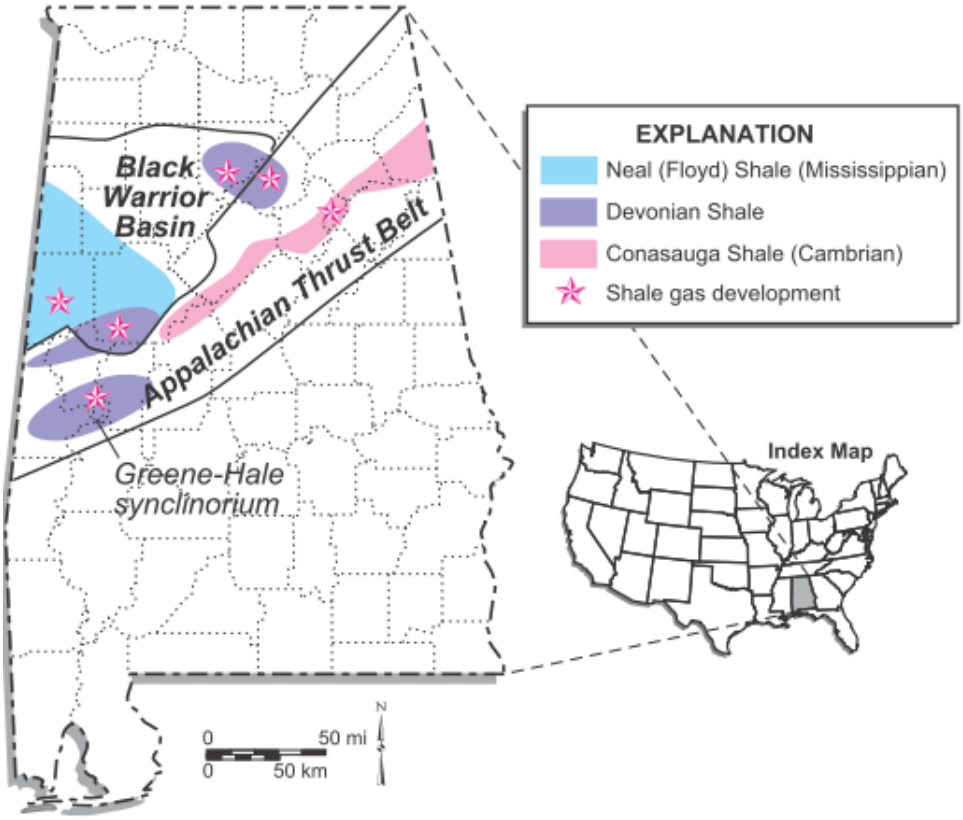

Figure 1.—Generalized map showing location of shale-gas development areas in Alabama.

Unconventional gas plays require an integrated, multidisciplinary approach to exploration and development, yet broadly applicable geologic models of resource distribution and producibility analogous to those for coalbed methane reservoirs (e.g., Pashin and others, 1991; Ayers and Kaiser, 1994; Pashin, 2007; Pashin and Groshong, 1998; Scott, 2002) are just beginning to be developed for shale gas reservoirs (e.g., Hill and Jarvie, 2007; Ross and Bustin, 2008). Shale formations in Alabama pose a broad range of technical challenges, many of which relate to insufficient characterization of the regional geologic framework, in addition to an inadequate understanding of the fundamental geologic controls governing the producibility of shale gas. Therefore, a need exists to develop integrated geologic models for the emerging shale plays of the BWB and Appalachian thrust belt that take into account the broad range of reservoir types and reservoir conditions (fig. 2). This type of approach has been applied to coalbed methane reservoirs of the BWB, where an industry that was initially limited by technological and

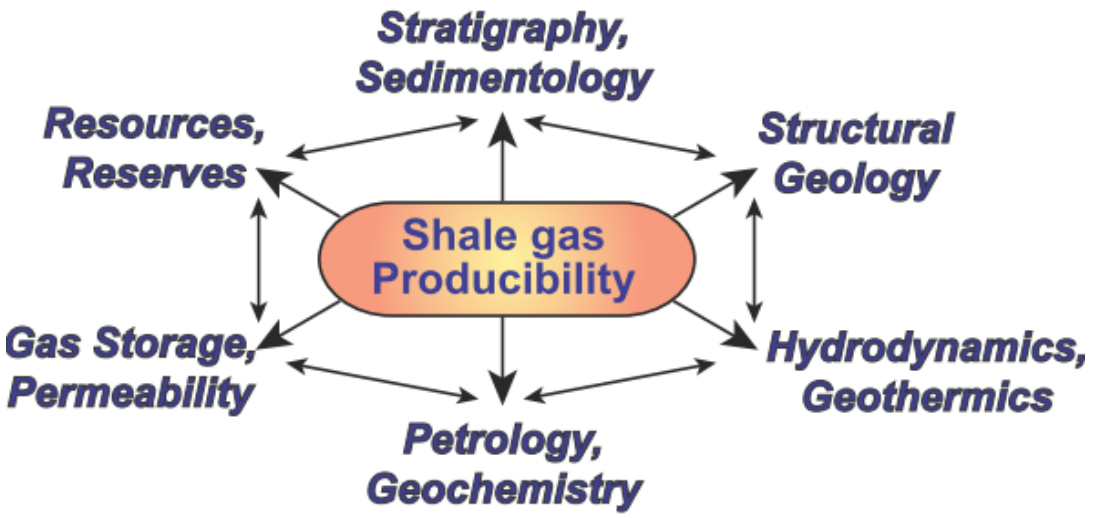

Figure 2.— Conceptual model of shale-gas producibility based on key geologic variables.

economic impediments now ranks third globally in cumulative coalbed gas production (Pashin and others, 1991; Pashin and Hinkle, 1997; Pashin, 2010). Applying a similar multidisciplinary approach to gas shale reservoirs is assisting the natural gas industry by providing new insights on the distribution and producibility of shale gas resources (Pashin, 2008, 2009; Pashin, Carroll, and others, 2010; Pashin, Grace, and others, 2010) (fig. 2). This approach affords flexibility that can be applied to a spectrum of emerging and frontier gas-shale plays, thereby increasing the efficiency of exploration and development programs.

A key aspect in this approach will be advanced and accurate characterizations of fractured shale units, as it is widely acknowledged that fractures in shale commonly create preferential paths of fluid flow. The permeability of a fracture is usually much larger than that of the rock matrix and consequently the fluid will flow preferentially through the fracture network, providing the fractures are extensively interconnected (Lee and others, 2001). The permeability of fractured rock is a nonlinear function of matrix permeability, fracture density and transmissivity, fracture orientation and interconnection, and the statistical distribution of length and orientation of the fractures (Dershowitz, 1985; Long and others, 1985; Anderson and Dverstrop, 1987; Cacas and others, 1990). Accurate modeling of effective permeability of fractured reservoirs has been a challenging task because fracture networks in reservoirs may significantly alter reservoir hydrologic properties. Due to the widespread occurrence of fracture networks and the common practice of hydraulic fracturing in tight rocks such as shales, it is of vital importance to characterize the nature of fracture networks in fractured shale reservoirs and to investigate how it can be used to optimize hydraulic fracturing.

PURPOSE

To assist in the development of emerging gas-shale plays in Alabama, the Geological Survey of Alabama completed an initial study that provides a geologic foundation for

exploration and development (Pashin and others, 2011). The current study was conducted to build on results of that earlier study of potential gas-shale reservoirs in Alabama (fig. 1). These studies employed an integrated approach that draws on a spectrum of geologic disciplines (fig. 2). The general approach of the current study is to systematically evaluate reservoir potential by detailed petrophysical characterization and characterization of the fluid-rock interactions of the shale formations.

Between the two studies, a total of 17 cores were described and/or analyzed (table 1). Of these, eight cores (all assigned to the Mississippian System) were described as part of the current study (fig. 3). Six of these eight cores, along with two cores described but not analyzed in the previous study, were analyzed using a scanning electron microscope (SEM). These analyses include samples from the Cambrian (one core, six samples; tables 1, 2) and Mississippian systems (seven cores, 39 samples; tables 1, 2). An additional analytical technique became available, focused ion beam (FIB) serial sectioning, which made it possible to examine pore-system topology in 3D. An appendix includes graphic core logs of cores described that are not figured in the main body of this report nor in Pashin and others (2011) including the two cores used for discrete fracture network models. Cores are referred to by Alabama Oil and Gas Board permit number (OGB PN); well names can be found in tables 1 and 2.

Additionally, we used our previously developed technique (Jin, 2013; Jin and Pashin, 2013) of fracture permeability characterization, which takes advantage of discrete fracture networks (DFN). We investigated the impact of fracture properties such as orientation, size, and connectivity on the orientation of hydraulically driven fractures. Core data from two Devonian

Table 1.—Cores described during two RPSEA studies (this study; Pashin and others, 2011). Locations of the wells can be found on figure 3. "Figure" refers to the figure of the graphic core log as cited in this report. Additional detail for the SEM and FIB analyses can be found in table 2.

OGB PN	Well Name	Figure	Rock Unit(s)	Dominant rock types	% of total, shale and mudstone	SEM, FIB, DFN analyses
1160	James B. Hill #1	26	Bangor	Lime mudstone	2	SEM
3074	Bonzell McGee 13-8 #1	27	Lewis	Shale	97	None
3518	ARCO/Anschutz Alabama Property Co. 15-11 #1	14	Conasauga	Pyritic shale	100	SEM
3707	Cobb 30-12 #1	35	Parkwood, *Millerella*	Lime mudstone	39	SEM
3939[a]	Burke 27-9 #1	A2	Chattanooga	--	--	SEM
4054	Patterson 20-5 #1	28	Parkwood, Lewis	Fossiliferous shale	80	SEM
4305	Spann 10-13 #1	29	Lewis	Fossiliferous shale	77	SEM
4801	Arthur 11-13 #1	30	Lewis	Lime mud-wackestone	30	SEM
5198	Z.D. Vick 30-9 #1	31	Lewis	Lime mudstone	33	None
5321	Stanley 22-12 #1	32	Lewis, Pride Mountain	Pyritic shale	90	SEM
13979[a]	Richards 35-2 #1	25	Floyd (Neal)	—	—	SEM; FIB
14045[a]	O'Bryant 6-15 #1	A6	Floyd (Neal), Bangor, Lewis	—	—	None
14065[a]	Exum Trust 16-6 #1	A7	Floyd (Neal)	—	—	None
14673[a]	Bayne Etheridge 36-9 #1	A3	Chattanooga	—	—	SEM; DFN
15075B[a]	Weyerhaeuser No. 2-43-2402 #1	A5	Chattanooga	—	—	SEM
15270[a]	Dawson 33-09 #2A	A1	Conasauga	—	—	SEM
15668[a]	Lamb 1-3 No.1	A4	Chattanooga	—	—	SEM; DFN

[a] Originally described in Pashin and others (2011).

wells from the BWB, along with regional field data from our previous studies, have been used for investigation of fracture properties and for DFN modeling realizations. Fracture permeability from the generated DFN models has been analyzed to determine the existence of representative equivalent volume (REV) with respect to the fracture stochastic properties. DFN models with various patterns have been established to investigate how the fracture orientation and connectivity will influence the hydraulic fracture pathways.

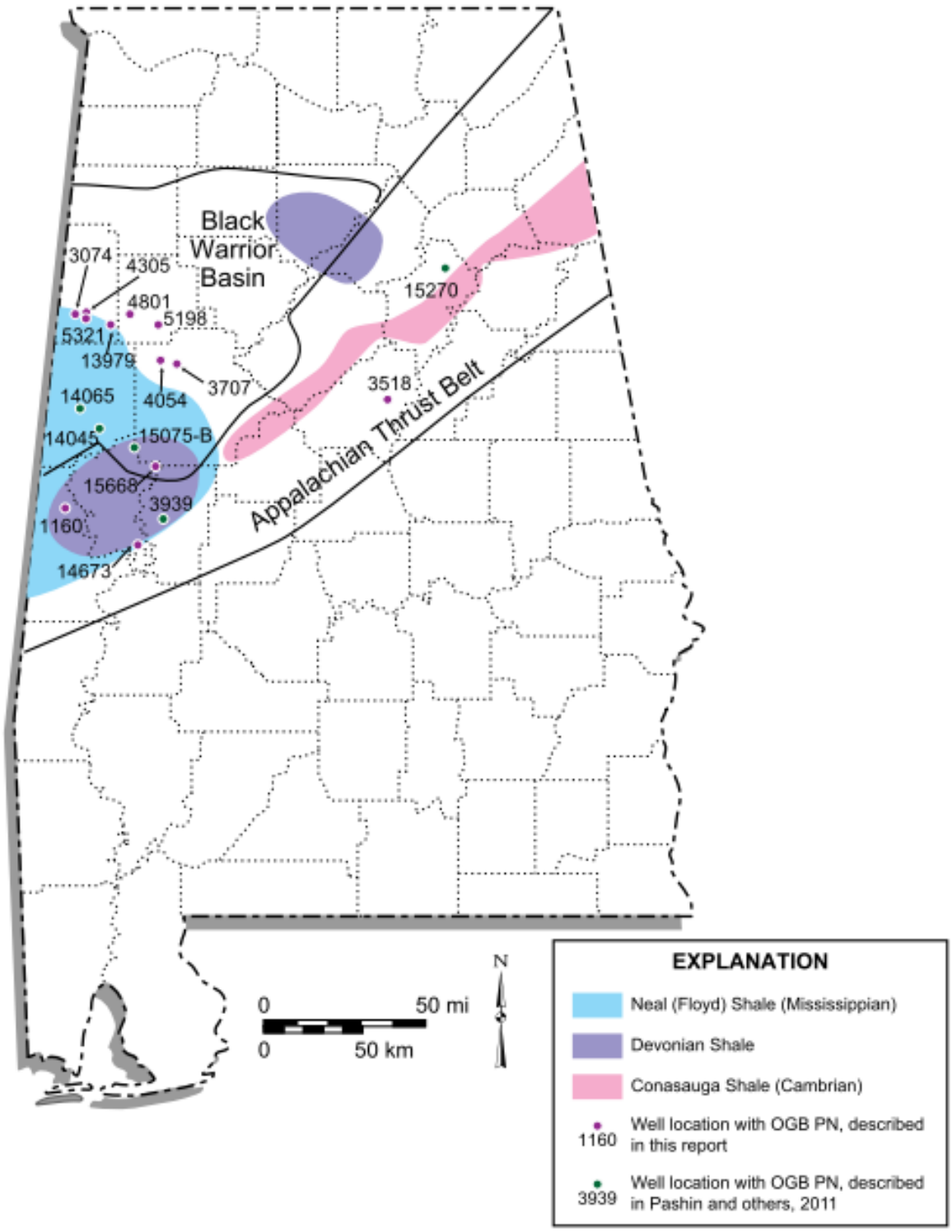

Figure 3.—Map showing approximate locations of wells referred to in this report (see table 1).

Table 2.—Samples analyzed using an SEM

OGB PN	Well Name	Depth (ft)	System	Rock Unit
1160	James B. Hill #1	5,220-5,221	Mississippian	Bangor
3518	ARCO/Anschutz Alabama Property Co. 15-11 #1	14,170	Cambrian	Conasauga
		14,174	Cambrian	Conasauga
		14,182.3	Cambrian	Conasauga
		14,192	Cambrian	Conasauga
		14,192.9	Cambrian	Conasauga
		14,197.4	Cambrian	Conasauga
3707	Cobb 30-12 #1	3,984	Mississippian	Parkwood
3939[a]	Burke 27-9 #1	10,303.3	Devonian	Chattanooga
		10,307.8	Devonian	Chattanooga
		10,317	Devonian	Chattanooga
		10,340.4	Devonian	Chattanooga
		10,354.9	Devonian	Chattanooga
4054	Patterson 20-5 #1	3,763	Mississippian	Parkwood
		4,486	Mississippian	Lewis
		4,493.1	Mississippian	Lewis
		4,600	Devonian?	?
4305	Spann 10-13 #1	4,597	Mississippian	Lewis
		4,605	Mississippian	Lewis
4801	Arthur 11-13 #1	3,113.8	Mississippian	Lewis
		3,122	Mississippian	Lewis
5321	Stanley 22-12 #1	4,649	Mississippian	Lewis, Pride Mountain
		4,661.8	Mississippian	Lewis, Pride Mountain
		4,667	Mississippian	Lewis, Pride Mountain
		4,667.1	Mississippian	Lewis, Pride Mountain
13979[b]	Richards 35-2 #1	3,700	Mississippian	Floyd/Neal
		3,732.4	Mississippian	Floyd/Neal
14045[a]	O'Bryant 6-15 #1	6,974.5	Mississippian	Parkwood
		7,123.1	Mississippian	Neal
14673[a]	Bayne Etheridge 36-9 #1	8,317	Devonian	Chattanooga
		8,327	Devonian	Chattanooga
		8,444	Devonian	Chattanooga
15075[a]	Weyerhaeuser No. 2-43-2402	8,011.4	Mississippian	Floyd
		8,031.6	Mississippian	Floyd
		8,034.9	Mississippian	Floyd
		8,039.3	Mississippian	Floyd
		8,046	Mississippian	Floyd
		8,211.9	Devonian	Chattanooga
		8,227.6	Devonian	Chattanooga
15270[a]	Dawson 33-09 #2A	7,540.3	Cambrian	Conasauga
		7,544.2	Cambrian	Conasauga
		7,558.8	Cambrian	Conasauga
		7,575	Cambrian	Conasauga
15668[a]	Lamb 1-3 #1	9,022.3	Mississippian	Floyd
		9,190.8	Devonian	Chattanooga

[a] Scanning electron microscope analyses reported by Pashin and others (2011)
[b] Focused ion beam analyses also conducted

GEOLOGIC SETTING

Fine-grained sedimentary rocks that are rich in organic matter are the focus for shale gas development and are important as both source rocks and reservoir seals. The first recorded

production in the Appalachian region occurred a century and a half ago in Kentucky (Nuttall and others, 2009). Since then, hydraulic fracturing technology developments have facilitated high production rates (Hill and Jarvie, 2007).

Black shale forms under low-energy conditions associated with the accumulation of fine-grained sediment and the reducing conditions required for the preservation of organic matter. Organic-rich shale accumulates in dynamic environments with diverse sedimentary processes (e.g., Schieber and others, 1998). Shale formations being developed in Alabama are no exception (Pashin, 2008, 2009; Pashin, Grace, and others, 2010; Pashin and others, 2011).

STRATIGRAPHIC SETTING

Shale plays in the BWB and the Appalachian thrust belt include units in the Conasauga Formation, Chattanooga Shale, and the Floyd (Neal) Shale. The Middle-Upper Cambrian Conasauga Formation is composed of shale, limestone, and dolostone and was deposited on a carbonate ramp (Astini and others, 2000; Thomas and others, 2000). The productive black shale facies contains abundant nodules and thin beds of microcrystalline limestone (Pashin, 2008) and was deposited in a graben that formed during late Precambrian-Early Cambrian Iapetan rifting and was deformed into giant shale masses during late Paleozoic Appalachian thrusting (Thomas, 2001; Thomas and Bayona, 2005) (fig. 4). The landmark discovery of gas in the Conasauga Formation by Dominion Exploration and Production, Incorporated, resulted in the first commercial gas production from shale in Alabama and the establishment of Big Canoe Creek Field, Alabama's only shale gas field. Further, the Conasauga is geologically the oldest and most structurally complex shale from which production of natural gas has been established.

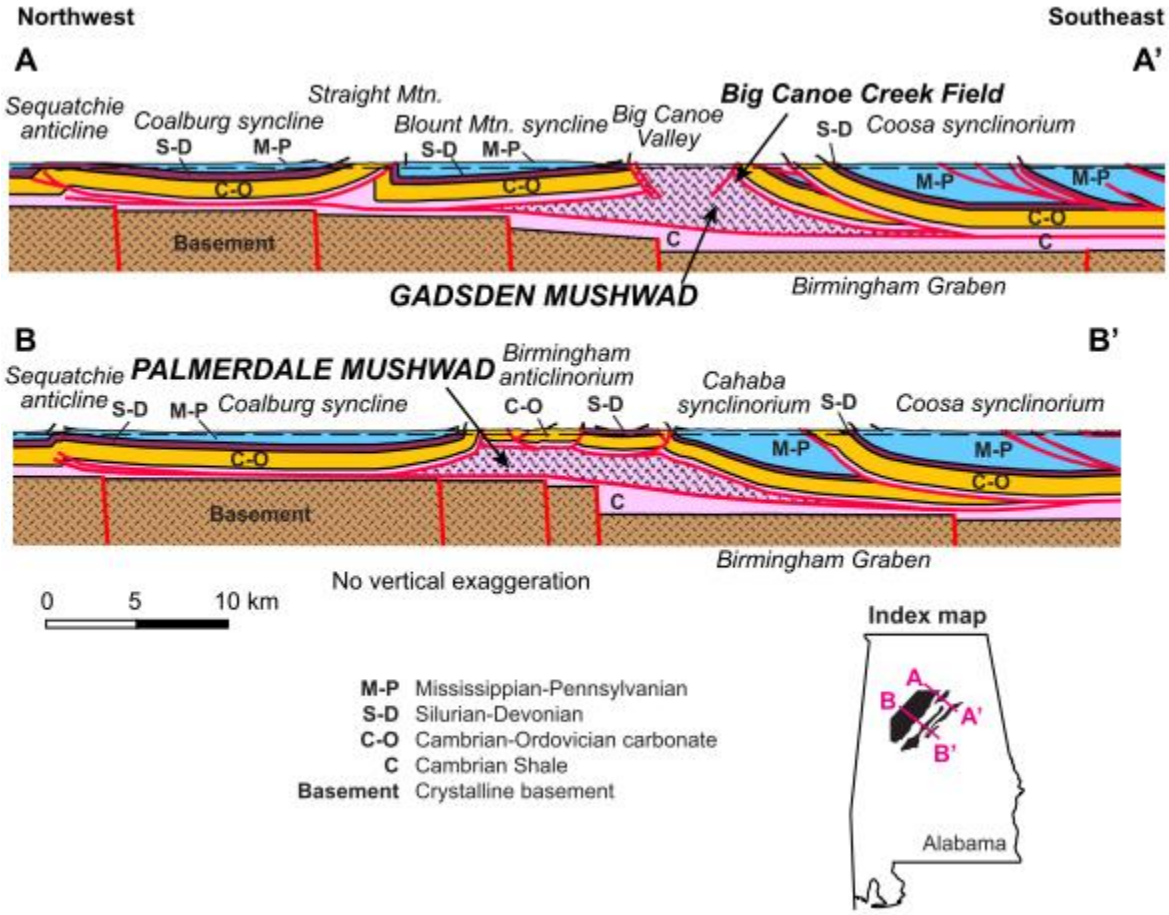

Figure 4.—Balanced structural cross sections of the southern Appalachian thrust belt in Alabama (modified from Thomas and Bayona, 2005).

Development has been focused on the widespread Devonian shale in the BWB and Appalachian thrust belt of Alabama (fig. 1). The Chattanooga Shale is of Middle to Late Devonian age and is the most widespread black shale unit in Alabama. Equivalent stratigraphically to the Ohio Shale of the Appalachian basin, the Antrim Shale of the Michigan basin, and the Woodford Shale of the southern Midcontinent region, which have produced gas for many years, the Chattanooga Shale has been interpreted as a euxinic basin facies that was deposited in a cratonic extension of the Acadian foreland basin (Pashin, Carroll, and others, 2010) (fig. 5). The Chattanooga is being developed in the BWB along the frontal structures of the Appalachian thrust belt (Pashin, 2008, 2009; Pashin, Carroll, and others, 2010; Haynes and

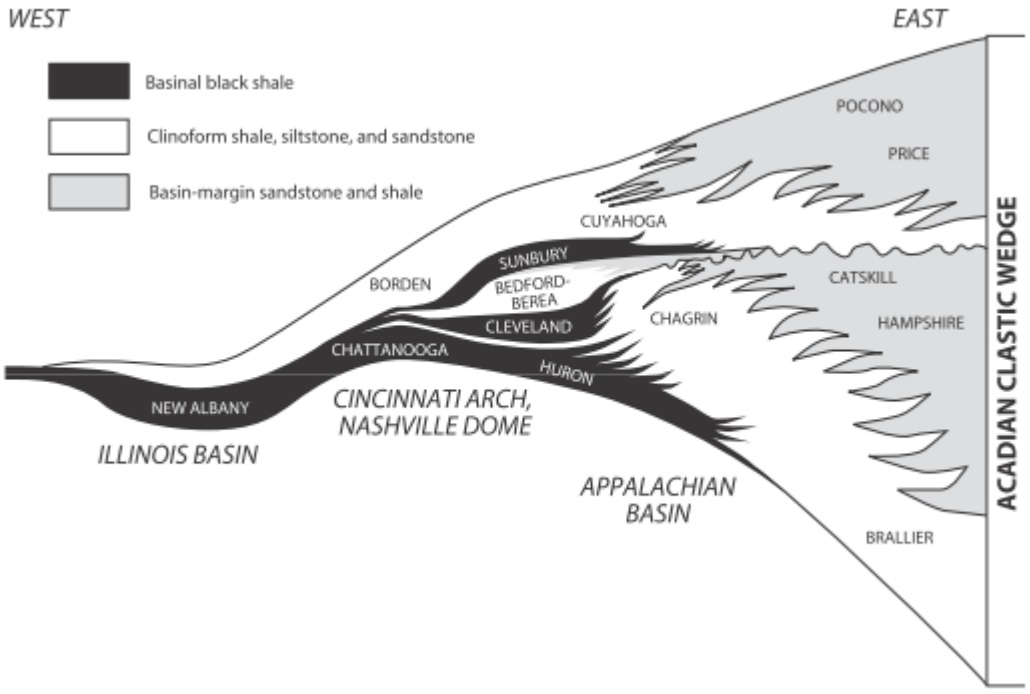

Figure 5.—Regional cross section showing the relationship of the Chattanooga Shale and correlative black shale formations to the Acadian clastic wedge (modified from Pashin and Ettensohn, 1995).

others, 2010). In the interior of the thrust belt below the Gulf Coastal Plain, potential has been recognized in a thick section of organic-rich shale that is interpreted to be of Silurian-Devonian age and includes Chattanooga equivalents (Pashin, Carroll, and others, 2010; Pashin, Grace, and others, 2010).

The Mississippian Neal (Floyd Shale) (fig. 5) has long been recognized as containing the principal source beds for conventional hydrocarbons in the BWB (e.g., Carroll and others, 1995) and is a stratigraphic equivalent of the established gas shale reservoirs of the Barnett Shale of the Fort Worth basin and the Fayetteville Shale of the Arkoma basin. The complex facies relationship with a large number of siliciclastic and carbonate units in the Floyd Shale, leading to a varied suite of rock types, has caused some confusion in exploration and development. While the Floyd primarily consists of organic-lean gray shale and limestone in most of the basin, there is organic-rich black shale (called the Neal by drillers) restricted to the southwestern part of the

basin, where the shale was deposited in slope and basin environments (e.g., Cleaves and Broussard, 1980; Pashin, 1993, 1994). The Neal has been the subject of most exploration activity as it has the greatest gas potential. However, some wells have been drilled in search of gas in organic-lean facies of the Floyd.

TECTONIC SETTING

Since folding, faulting, and fracturing are basic controls on the geometry, continuity, and permeability of shale formations, shale gas reservoirs in Alabama are being developed in diverse tectonic settings. In the BWB, for example, development is focused on an extensional tectonic setting in which strata are subhorizontal and are weakly deformed. In the Appalachian thrust belt, by comparison, shale gas is being developed in a compressional tectonic setting in which strata are folded and faulted. Paleozoic strata of the BWB and the Appalachian thrust belt are exposed in the northeastern part of the study area. In the southwestern part, however, these strata are concealed below Cretaceous strata of the Gulf of Mexico basin, which dip gently southwestward, lack significant folds and faults, and overlie the Paleozoic section with angular unconformity.

The BWB, a late Paleozoic foreland basin that formed adjacent to the juncture of the Appalachian and Ouachita orogenic belts (Thomas, 1977, 1988), developed on the Alabama Promontory, a protuberance of the Laurentian continental platform that formed during late Precambrian-Cambrian Iapetan rifting. A structural homocline that dips southwest toward the Ouachita orogen, the BWB is broken by numerous northwest-striking faults (e.g., Thomas, 1988; Pashin and Groshong, 1998) (fig. 6). Some faults have traces that extend for tens of miles and have displacement exceeding 1,000 ft. Superimposed along the southeast margin of the homocline, Appalachian folds and thrust faults strike northeast. Ouachita orogenesis was initiated along the southwest margin of the promontory during Mississippian time (Thomas,

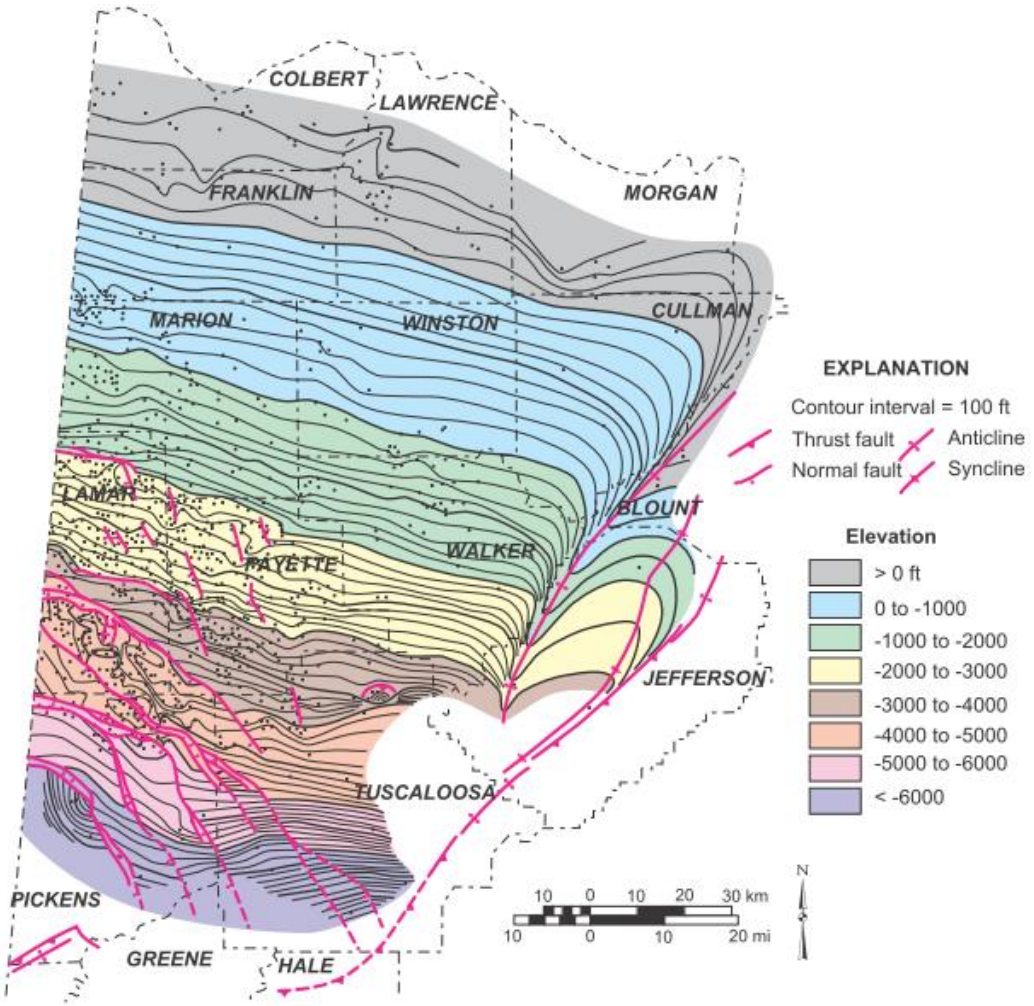

Figure 6.—Structural contour map of the top of the Tuscumbia Limestone in the Black Warrior basin of Alabama (modified from Pashin, 1993).

1977). The BWB can be considered to be mainly an Ouachita foreland basin, and major Appalachian thrust and sediment loads did not impinge on the southeastern part of the basin until Early Pennsylvanian time (Pashin, 2004). However, evidence exists for a Devonian (Acadian) subsidence event along the southeastern margin of the promontory (Pashin, Carroll, and others, 2010).

The gently dipping strata of the BWB are separated from igneous-metamorphic rocks of the Appalachian orogen by the Appalachian thrust belt, which is composed of deformed pre-orogenic carbonates of Cambrian through Mississippian age and synorogenic siliciclastic rocks

of Upper Mississippian and Lower Pennsylvanian age (e.g., Thomas, 1985; Thomas and Bayona, 2005) (figs. 4, 7). Shale gas exploration has been concentrated in the frontal part of the thrust belt, which is dominated by thin-skinned deformation in which Paleozoic strata have been translated northwestward above a basal detachment in Cambrian shale (Rodgers, 1950; Thomas, 1985). The geomechanically weak lithotectonic unit of Cambrian shale, including the Conasauga

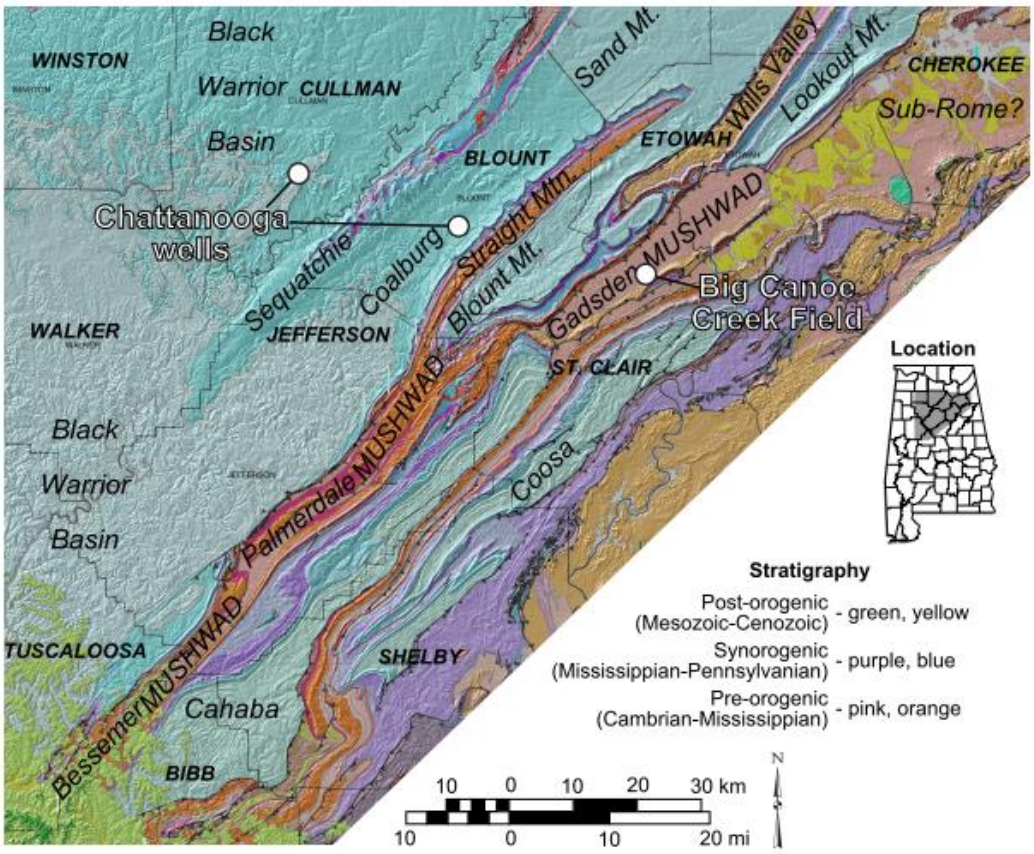

Figure 7.—Geologic map of frontal Appalachian structures showing areas of shale gas development (modified from Pashin, 2008, 2009).

Formation, not only hosts the basal detachment, but is in places duplicated into giant antiformal stacks that are locally thicker than 12,000 ft. (Thomas, 2001). By contrast, the pre-orogenic carbonate section is a stiff mechanical layer that hosts frontal and lateral thrust ramps that dictate structural geometry above the basal detachment, with secondary detachments developed locally in the Silurian-Devonian section (Thomas and Bayona, 2005). The synorogenic siliciclastic

section, a weak geomechanical unit, was transported cratonward along with the pre-orogenic carbonates and locally hosts upper level and secondary detachments (Thomas, 1985; Pashin and Groshong, 1998; Thomas and Bayona, 2005). This mechanical stratigraphy has resulted in a distinctive suite of faults, folds, and fracture systems that should be taken into consideration when formulating shale gas development strategies.

ANALYTICAL METHODS

The basic materials employed in this research include outcrops and cores. Methods range from standard stratigraphic, sedimentologic, and structural procedures for rock description to SEM analysis and SEM-FIB milling, employed to characterize petrology and permeability, to DFN modeling for investigation of fracture properties.

STRATIGRAPHY AND SEDIMENTOLOGY

We described eight Mississippian cores, of which seven contain at least 10 ft. of siliciclastic mudstone or shale (table 1). These intervals range (in core) from 10 to 56 ft. in length and 30 to 100 percent of the core. Mudstone and shale layers in these cores are interbedded with lime mudstone (Dunham, 1962) and sandstone, as well as minor conglomerate and siltstone. Cores are stored at the Geological Survey of Alabama and are accessible to the public. Cores were measured with ruler and tape, and rock types, grain size, color, and sedimentary structures were described. Occurrences of trace fossils and body fossils were recorded. Faults and fractures also were identified and described. Core data are displayed as graphic logs.

Preliminary petrologic observations were made from slabbed cores as they were described, and billets of representative samples were cut to make thin sections so that rock fabric and mineralogy could be analyzed. However, intensely fissile or fractured shale could not be sampled in this way, and so the thin section collection is biased toward competent shale samples. Thin sections were prepared to standard 30 micrometer (μm) thickness, stained with Alizarin red

S for calcite and sodium cobaltinitrite for potassium feldspar, and examined with a petrographic microscope. Typical and diagnostic features were identified and documented using digital microphotography.

FRACTURE ANALYSIS AND MICROSTRUCTURE

The novel method for characterization of fracture permeability using DFN models has been employed for this study to facilitate shale-gas-reservoir characterization (Clark and others, 2013; Jin, 2013; Jin and Pashin, 2013). This method fully utilizes the stochastic properties of individual fractures, resulting in scale-independent models. Core data from two Devonian wells from the BWB, along with regional field data from our previous studies, have been used for investigation of fracture properties and for DFN modeling realizations. Fracture permeability from the generated DFN models has been analyzed to determine the existence of representative equivalent volume (REV; also, representative element volume) with respect to the fracture stochastic properties. DFN models with various patterns have been established to investigate how the fracture orientation and connectivity will influence the hydraulic fracture pathways.

The effective fracture permeability is defined for a medium that is statistically homogeneous on a large scale beyond a minimum volume (Pouya and Fouche, 2009). This volume at which the fracture permeability first ceases to vary is the representative equivalent volume (REV) (fig. 8). The REV of a fractured medium can be calculated by measuring the average permeability of increasing volumes of rock until the value does not change significantly with the change of rock volume. However, this is no guarantee of the existence of a REV for every fracture system. With increasing size of the element volume, the equivalent permeability tends towards the effective permeability if it exists (Pouya and Fouche, 2009).

DFN modeling is a stochastic modeling approach using the probabilistic density functions of fracture geometry, dimension, and transmissivity from individual fractures. The

fracture statistics can be collected and inferred from field investigations, well logs, and/or core analyses. The method was introduced in the early 1980s and has been continuously developed afterwards with many applications in civil, environmental and reservoir engineering (Long and others, 1982; Dershowitz and Einstein, 1988). Multiple realizations of a DFN model can be

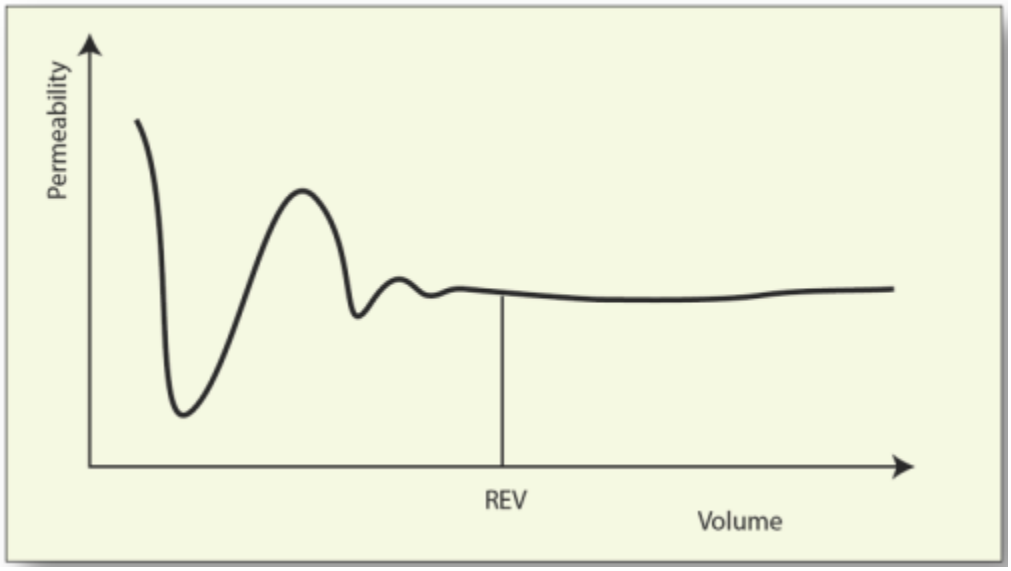

Figure 8.—Effective permeability of fractured media.

stochastically generated if the statistics of populations of fracture orientation, size, and aperture are known. Flow modeling is therefore conducted by treating each generated fracture individually in a discretized modeled domain. Theoretically the DFN approach is the most accurate model predicting fluid flow and transport through fractured geometric media. However, it has inherent disadvantages: its computation-intensive nature and extreme difficulty of domain discretization, which severely limit its practical applications to problems with hundreds of thousands of fractures, and the continuum model with equivalent properties becomes more practical and attractive.

A new approach and workflow is used in this study to calculate the effective permeability of fractured networks which integrates the DFN method while honoring the geometrical pattern

of each individual fracture based on previous studies. A full permeability matrix can be expressed as a second rank tensor. Each fracture is defined as a finite crack with two parallel plates. The permeability of a fracture obeys the "cubic" law which has been widely accepted for Newtonian flow. A permeability tensor of a fracture is defined as:

$$K_f = \frac{A_f}{V} \bullet \frac{b^3}{12} \bullet \begin{bmatrix} 1-n_1n_1 & -n_1n_2 & -n_1n_3 \\ -n_1n_2 & 1-n_2n_2 & -n_2n_3 \\ -n_1n_3 & -n_2n_3 & 1-n_3n_3 \end{bmatrix} \qquad (1)$$

where:

K_f = concentration parameter
A_f = area of the fracture
b = aperture
V = volume of element containing the fracture
n = the normal to the fracture plane.

It can be seen from equation 1 that the permeability tensor is composed of three terms, namely the fracture size, aperture, and orientation. The equivalent permeability of an element is the sum of the permeability tensors of each fracture contained in equation 1.

In order to stochastically characterize the fractured reservoirs, we have established a workflow that was based on our past research experience (fig. 9). This workflow allows us to quickly evaluate the equivalent fracture permeability base on multiple realizations of a DFN

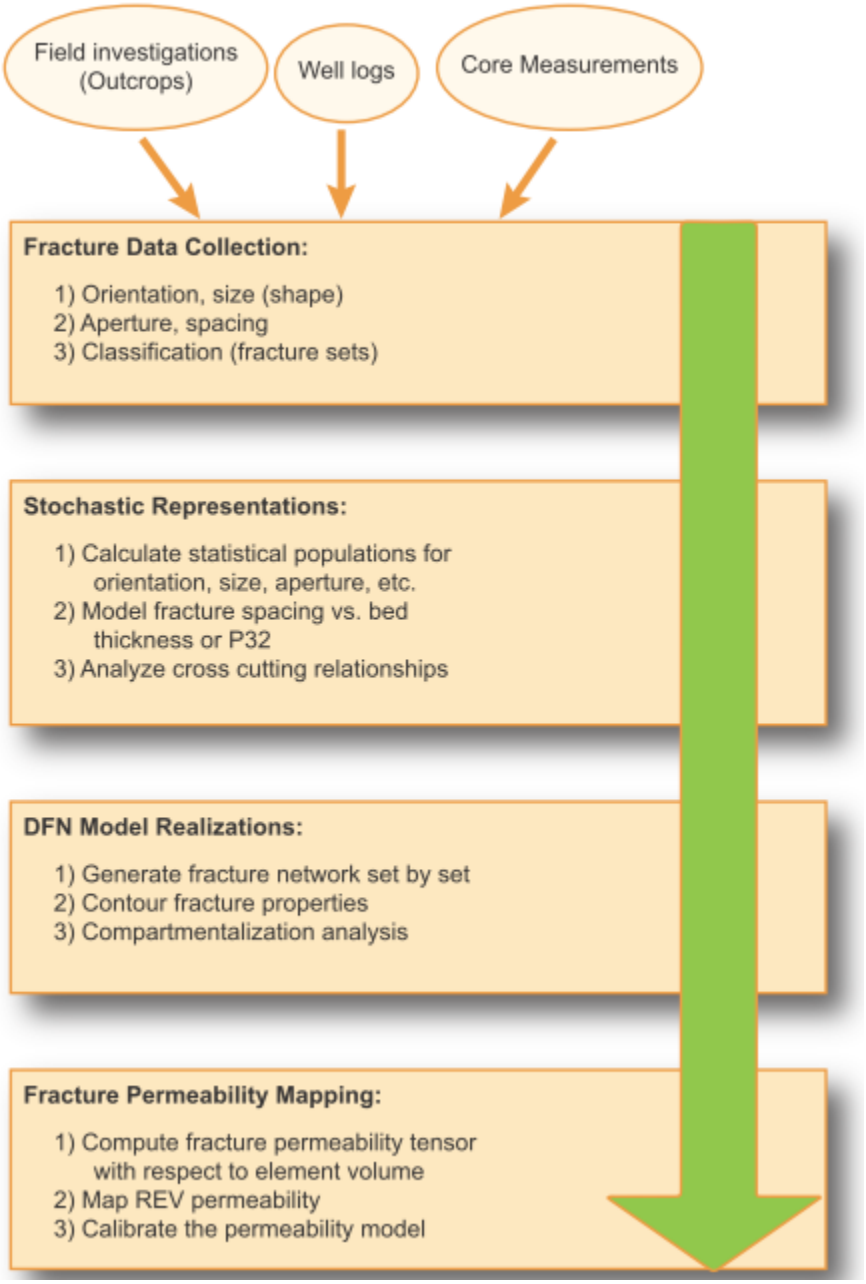

Figure 9.—Workflow for characterizing fracture permeability for fractured-reservoir characterization.

model and to optimize the grid size of the model to achieve accurate yet computationally less intensive modeling for multiphase flow problems.

ROCK FABRIC, PETROLOGY, GEOCHEMISTRY, AND PORE SYSTEMS

Rock fabric and pore systems from 23 samples of eight cores were examined using two SEMs at the Central Analytical Facility of the University of Alabama (CAF-UA) (table 2; fig. 3).

Selected samples were broken from cores, and rough surfaces were examined with a JEOL 7000 field emission SEM. The secondary-electron detector is familiar to most users of SEMs, revealing micro- and nanotopography of samples. The backscatter detector responds differently to minerals composed of lighter or heavier elements. Heavy minerals, such as pyrite, are brighter in this view than are lighter minerals, such as calcite. An INCA probe attached to the JEOL was used to analyze elemental composition of individual particles or crystals. Samples were viewed at operating voltages of 15 or 20 kiloelectronvolts (keV) at a working distance of 10 μm. One of the goals of the SEM study was to use digital photography and energy dispersive x-ray analysis to investigate and document the size, shape, fabric, and chemical composition of gas shale and its constituent particles. In many samples, laminae much thinner than 1 millimeter (mm) were observed.

Rock fabric and pore-system topology were studied by means of serial sectioning using an FIB. These analyses were performed on a Tescan Lyra FIB-FESEM (Field Emission SEM) at the CAF-UA. We chose the edges of thin shale flakes and milled rectangular pedestals up to about 10 μm on a side and up to about 10 μm high (fig. 10), using a beam current of 4.8 to 5.2 nanoamps (nA) intensity. The pedestals were then polished using a beam current of 2.5 nA and finished with a beam of 644 picoamps (pA) using a 2 μm polishing depth. The pedestals are surrounded by gutters about 6 μm wide (fig. 10), so that material ablated from the pedestal will not be redeposited on the pedestal itself. Slices 33 nanometer (nm) thick for the sample from 3,700 feet, OGB PN 13979, and 66 nm for the sample from 3,732.4 feet, OGB PN 13979, were sequentially removed from the top of the pedestal; after each pass the new surface was photographed twice, using secondary and backscattered electrons. The result is a set of hundreds of photographs documenting the appearance of evenly spaced surfaces. Because only pores are

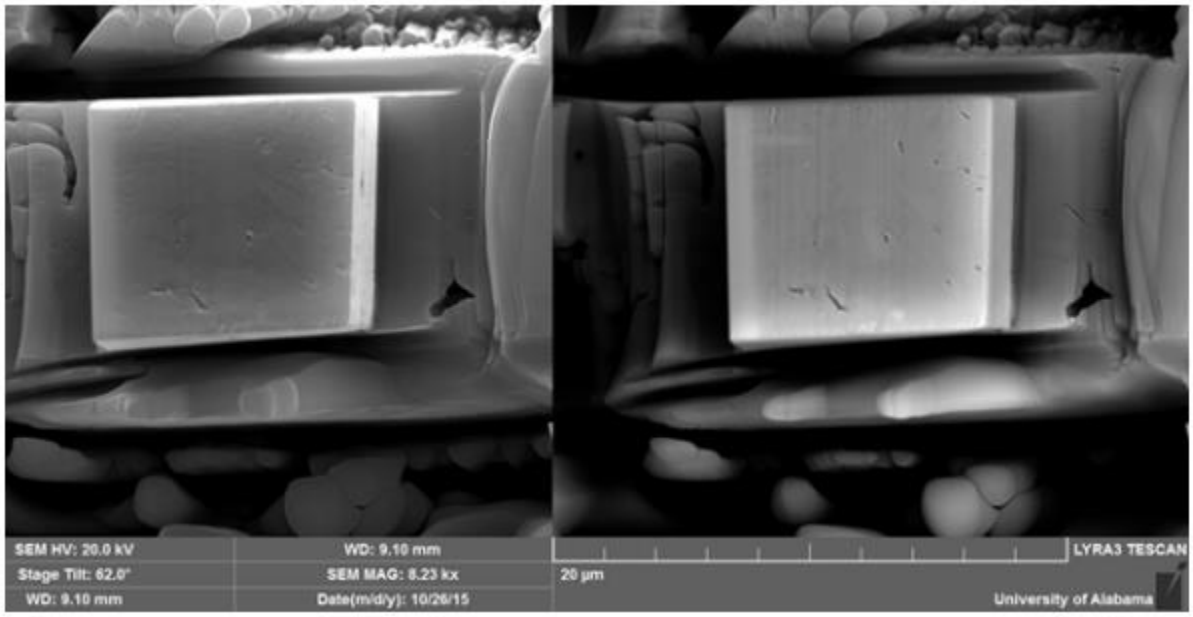

Figure 10.— Pedestal in shale, shaped for Focused Ion Beam (FIB) 3D analysis; Mississippian Floyd Shale, sample from 3,700 ft., OGB PN 13979. Note gutter around pedestal. Secondary electron image on the left, backscatter electron image on the right. Scale 20 µm.

black in secondary-electron view, this is the best view for examining pore systems (fig. 11). The succession of images provides a visual record of the 3D pore network. It takes several hours, or more, to shape the pedestal, and several more hours to destroy it, one thin slice at a time. Consequently, a relatively small number of samples could be studied this way. Animations of FIB images are presented as videos 1 through 4.

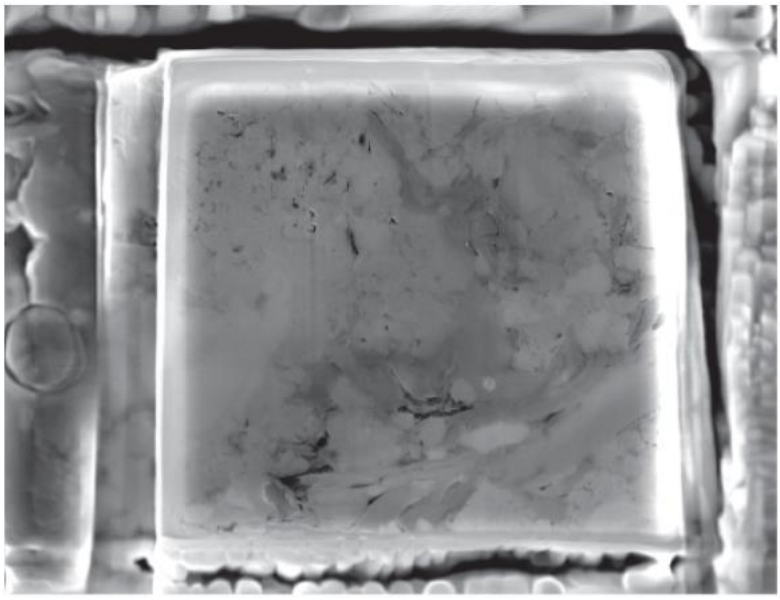

Figure 11.—Polished porous surface of pedestal in shale, prepared for Focused Ion Beam (FIB) 3D analysis.

RESULTS

STRATIGRAPHY AND SEDIMENTOLOGY

Many key characteristics of shale, such as bulk composition, bed thickness patterns, and continuity are determined largely in the original depositional environment, and so stratigraphy and sedimentology are critical component of exploration and development strategies. In Alabama, Paleozoic gas shale is marine, and grades laterally into various carbonate and coarser siliciclastic deposits. In the following sections, the stratigraphic and sedimentologic characteristics of each formation are discussed to highlight regional correlation, diagnostic rock types and sedimentary structures, as well as the types of sedimentary processes that were active during deposition.

CONASAUGA FORMATION

The Conasauga Formation constitutes a thick succession of shale, limestone, and dolostone containing a diverse suite of depositional facies (Butts, 1910, 1926; Astini and others, 2000; Thomas and others, 2000) (fig. 12). The Conasauga gradationally overlies the Lower

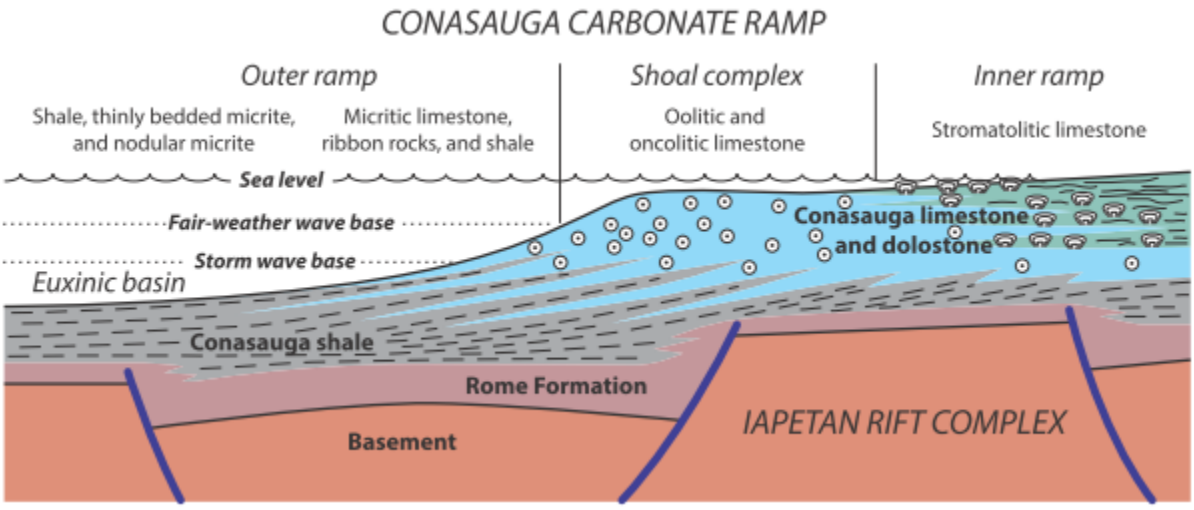

Figure 12.—Generalized depositional model of the Conasauga Formation in Alabama (modified from Markello and Read, 1982; Astini and others, 2000).

Cambrian Rome Formation, which contains interbedded shale, siltstone, sandstone, and limestone, including redbeds, which help distinguish Rome shale from Conasauga shale. The Middle to Upper Cambrian Conasauga has a stratigraphic thickness ranging from 1,500 to 3,000 ft. in Alabama, although tectonic deformation has created shale masses locally thicker than 12,000 ft. (Thomas and Bayona, 2005) (fig. 4). The Conasauga is overlain conformably by Upper Cambrian chert and dolostone of the Copper Ridge Dolomite, the basal unit of the Knox Group. It is stratigraphically complex (Butts, 1910, 1926, 1927; Osborne and others, 2000), and in general, shale predominates in the lower part of the formation, with limestone and dolostone predominate above. Thus, the Conasauga is a giant shoaling-upward succession in which subtidal shale passes into ramp carbonates (Astini and others, 2000).

A Conasauga core, OGB PN 3518 (ARCO/Anschutz Alabama Property Co. 15-11 #1) (fig. 3), consists of gray calcareous shale with lime-mudstone laminae (fig. 13). SEM analysis used to study the pore system and rock fabric of six samples from this core (table 2) revealed several noteworthy features.

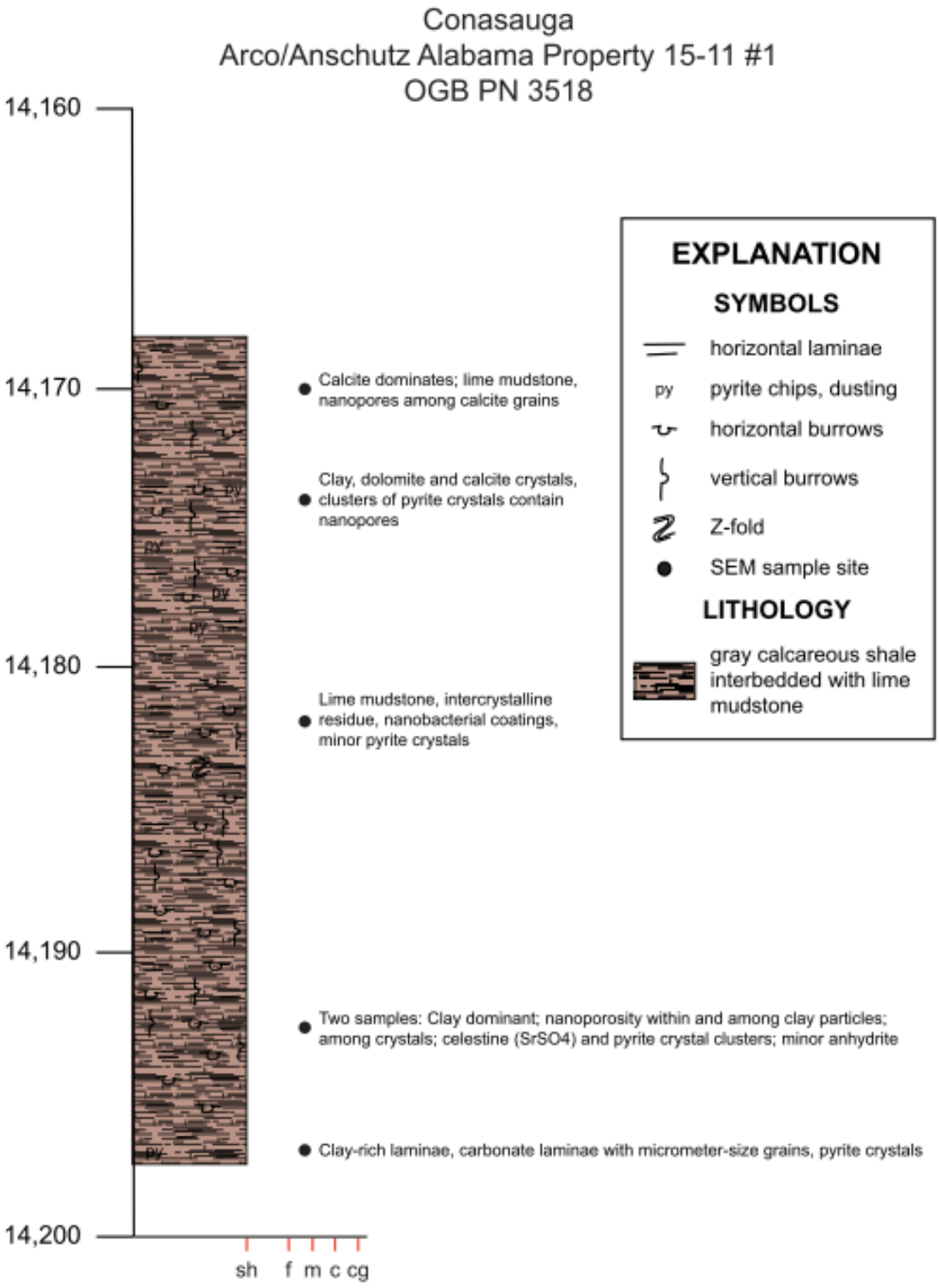

Figure 13.—Graphic core log of Cambrian Conasauga Formation, OGB PN 3518 (ARCO/Anschutz Alabama Property Co. 15-11 #1 well).

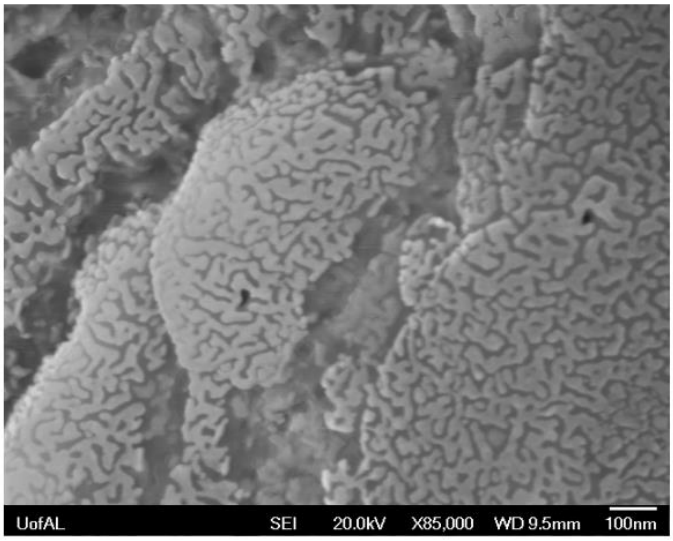

Figure 14.—Anastomosing ridges on the surface of a calcite crystal, interpreted as a possible trace of nanobacterial growth, lime mudstone lamina; Cambrian Conasauga Formation, sample from 14,182.3 ft., OGB PN 3518. SEM secondary electron image, scale 100 nm.

One of two samples of lime mudstone exhibited anastomosing ridges on the surfaces of carbonate particles. The ridges are tens of nanometers wide (fig. 14). Similar features have been interpreted as having been formed by nanobacteria (R. L. Folk, personal communication, 1990; Folk and Lynch, 1997, Folk and Chafetz, 2000), although Kirkland and others (1999) suggested that the inferred nanofossils do not record the sizes and shapes of organisms. Nanobacteria (bacteria smaller than 1 μm in diameter) have long been suggested to be involved in carbonate deposition. They are now widely believed to occur in human and other mammalian kidneys (Kajander and Çiftçioglu, 1998; Khullar and others, 2004) and other organs, as well as in soils (Lysak and others, 2013). However, Cisar and others (2000), for instance, reported evidence that nanobacteria-like objects may have been made by larger bacteria or in other ways. Despite more than two decades of study, the existence of nanobacteria is still hotly debated. Nonetheless, it is generally agreed that nanobacteria-like objects result from biologic activity. This may result in residual organic material trapped in some carbonate laminae. Other samples from this and other cores we studied (table 1) did not show any nanobacteria-like objects. A sample from another

lime mudstone lamina in this core consisted of anhedral calcite particles with smooth surfaces (fig. 15).

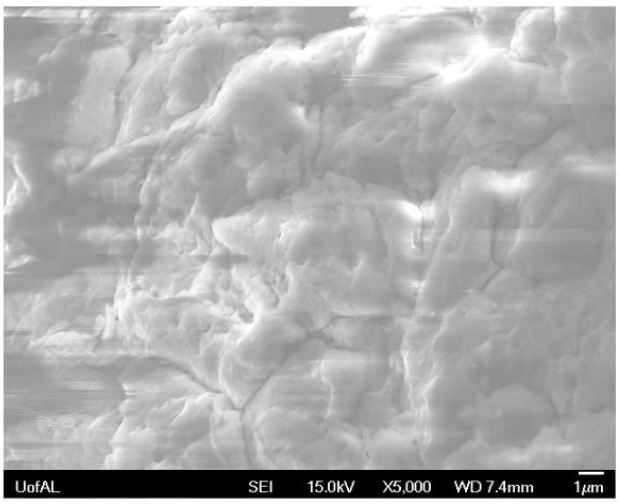

Figure 15.—Calcite crystals with smooth surfaces, Cambrian Conasauga Formation, sample from 14,170 ft., OGB PN 3518. SEM secondary electron image; scale 1 μm.

Four shale samples were examined from this core. One contained clusters of acicular crystals of celestite (also called celestine). The clusters are up to about 5 μm across (fig. 16).

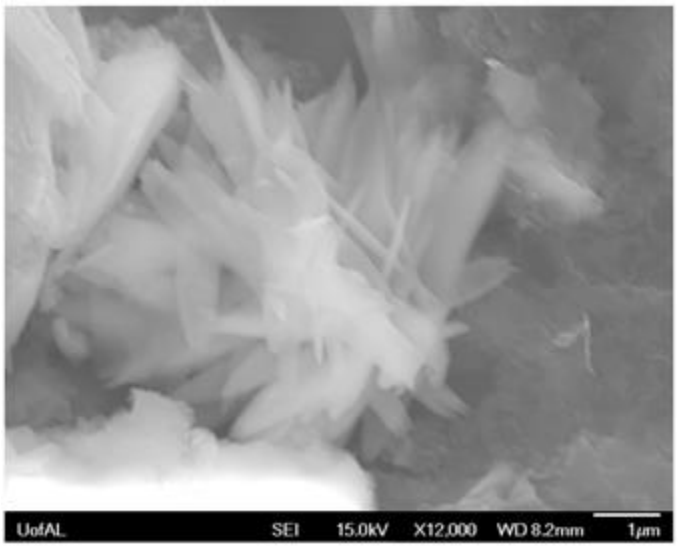

Figure 16.—Cluster of celestite (strontium sulfate) crystals, Cambrian Conasauga Formation, sample from 14,192 ft., OGB PN 3518. SEM secondary electron image; scale 1 μm.

Celestite (strontium sulfate) generally occurs with evaporite minerals, such as halite and anhydrite. Minor amounts of anhydrite were associated with the celestite crystals in this core. The rare presence of evaporite minerals within the shale suggests transient hypersalinity of pore waters, though it is not clear when these conditions occurred. The celestite may have formed syndepositionally or at any later time when pores were open.

All shale samples contain pyrite crystals in loose clusters up to about 10 μm across (fig. 17). The crystals range from well-formed bipyramids to spheroidal anhedra, ranging in size from 200 to 500 nm in long dimension. There are no framboids, which usually form syndepositionally in the water column. The clusters we observed are diagenetic and formed in place before lithification. They contain intercrystalline porosity partly occluded by illite crystals, which have the form of thin discoidal flakes (fig. 17).

Graphic core logs of additional Conasauga wells are presented in figure A1 and plate 1 in Pashin and others (2011).

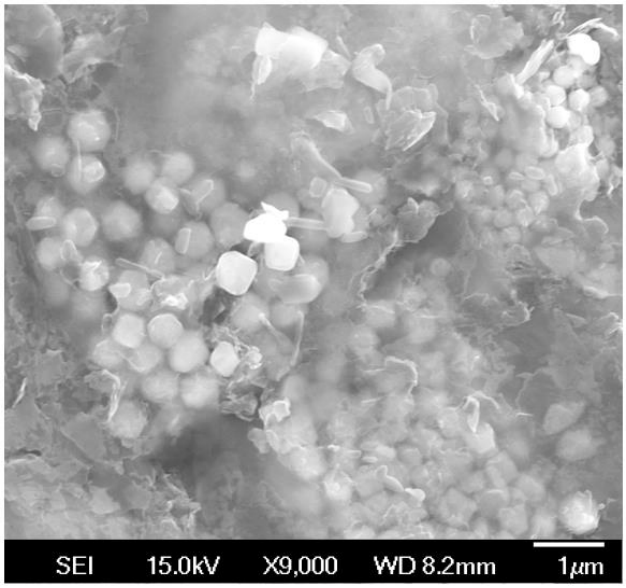

Figure 17.—Clusters of pyrite crystals, each homogeneous in crystal size, and containing potato-chip-shaped illite crystals, Cambrian Conasauga Formation, sample from 14,192 ft., OGB PN 3518. SEM secondary electron image, scale 1 μm.

DEVONIAN SHALE

No Devonian cores were examined for this study. Previous work on the Chattanooga and other Devonian shales was presented by Pashin and others (2011); see also Appendix figures A2 through A5.

MISSISSIPPIAN SHALE

The Upper Mississippian Floyd Shale is an equivalent of the prolific Barnett Shale of the Fort Worth basin and the Fayetteville Shale of the Arkoma basin. The Floyd has thus been the subject of intense interest for shale gas exploration. The Floyd is dominated by shale and limestone and extends from the Appalachian thrust belt of Georgia through the BWB of Alabama and Mississippi (Thomas, 1972). Usage of the term, Floyd, can be confusing. The type Floyd Shale of Georgia includes strata equivalent to the Tuscumbia Limestone. In Alabama and Mississippi, the Floyd is above the Tuscumbia, Pride Mountain Formation, or Hartselle Sandstone, and below the first sandstone in the Parkwood Formation (fig. 18).

Importantly, most Floyd facies are not prospective as gas reservoirs. Drillers have long recognized a resistive, organic-rich shale interval in the lower part of the Floyd Shale that is called informally the Neal shale (Cleaves and Broussard, 1980; Pashin, 1994). In addition to being the probable source rock for conventional oil and gas (Telle and others, 1987; Carroll and others, 1995), the Neal has the greatest potential as a shale-gas reservoir in the Mississippian section of Alabama and Mississippi.

The Neal is developed mainly in the southwestern part of the BWB and is in facies relationship with strata of the Pride Mountain Formation, Hartselle Sandstone, Bangor Limestone, and Parkwood Formation (fig. 5). In cores, the Neal is a black shale that superficially resembles the Chattanooga Shale. The shale is silty and is commonly calcareous, and internal

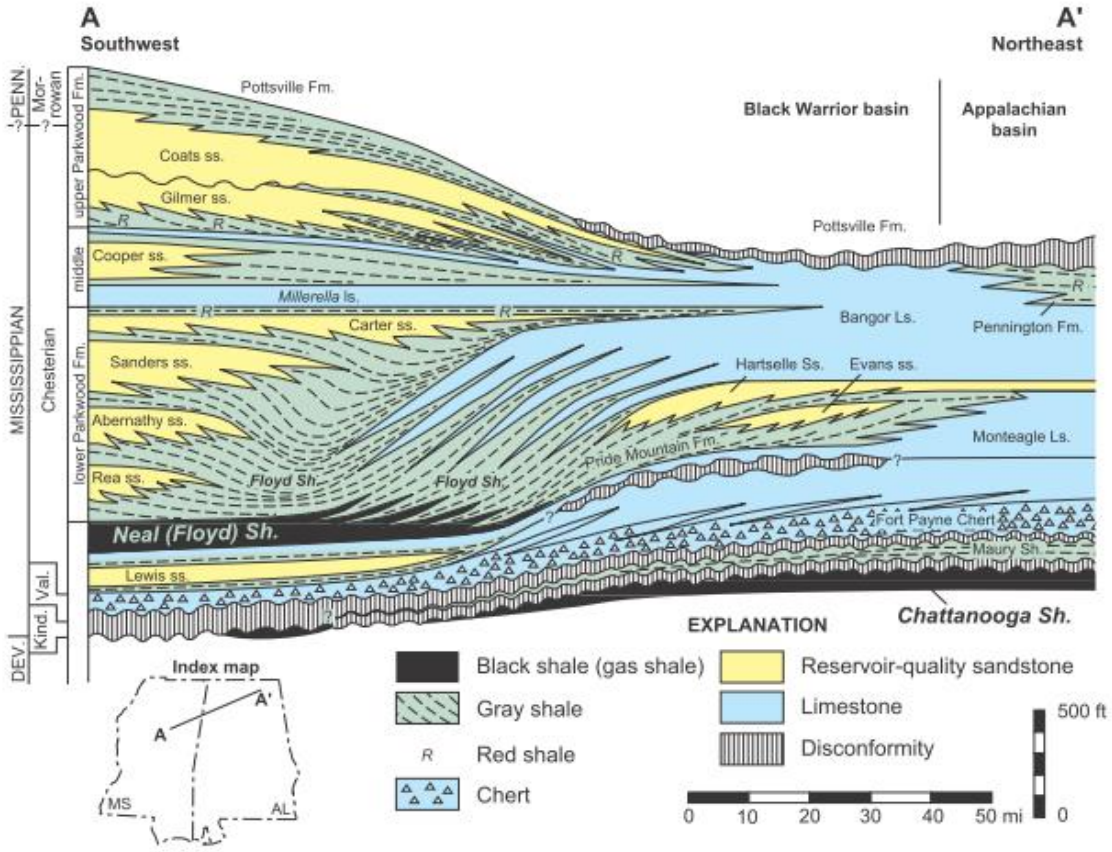

Figure 18.—Regional cross section showing facies relationships in Devonian-Mississippian strata of the Black Warrior basin (modified from Pashin, 1994).

laminae are more difficult to distinguish than in the Chattanooga. The Neal is laminated to thick bedded and contains thin interbeds of limestone and siltstone, which tend to be wavy and lenticular and contain ripple cross-laminae (fig. 19). These interbeds are abundant in the clinoform shale and are less abundant farther south where the shale exhibits a fondoform stratal geometry. The high-resistivity shale that is so distinctive in well logs is difficult to distinguish from low resistivity intervals by color alone. However, low-resistivity shale tends to be less fissile and more distinctly bioturbated; it contains a more diverse fauna that includes brachiopods, mollusks, and echinoderms. Well logs demonstrate that as shale resistivity

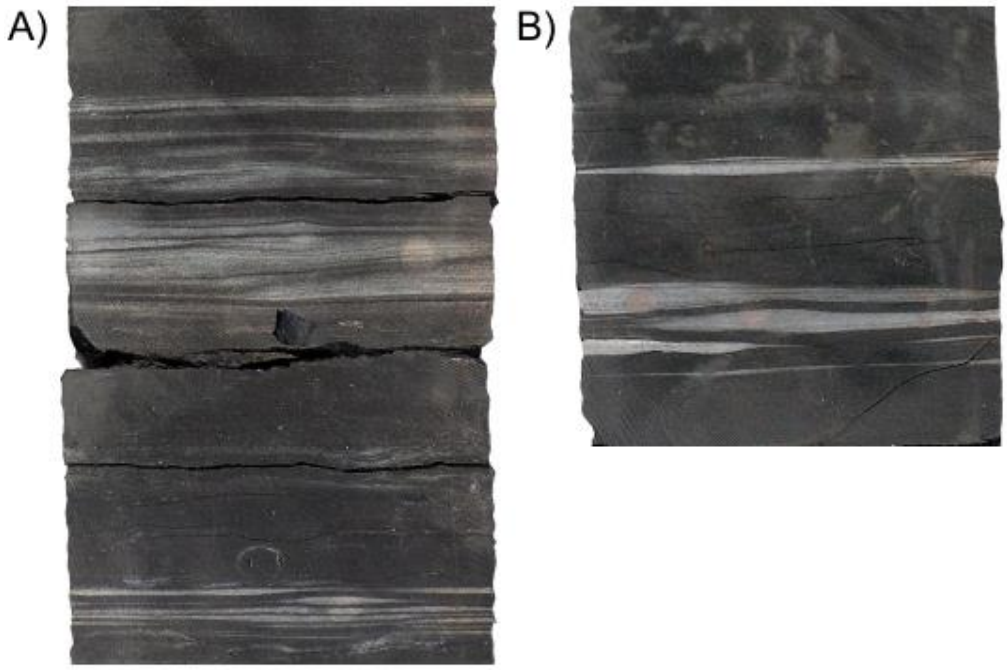

Figure 19.—Photos of Neal shale from OGB PN 14065. (A) Shale with wavy- and lenticular-bedded siltstone, 6,565.7 ft. (B) wavy-bedded limestone in shale, 6,569.6 ft.

increases, radioactivity also increases. Conversely, bulk density and density porosity decrease as resistivity increases. In addition, high-resistivity intervals are less prone to caving during drilling.Pashin (1993, 1994) interpreted the Neal as an oxygen-deficient basin deposit (fig. 20) that formed during the early stages of the Ouachita orogeny. Correlation of the Neal with equivalent strata indicates a close relationship between the internal stratigraphy of the shale and that of equivalent shale, sandstone, and limestone units that were deposited to the northeast in nearshore environments (fig. 20). Progradational gray shale-sandstone packages were deposited during highstands, whereas the Hartselle Sandstone and many of the carbonate intervals were deposited during marine transgressions. Correlation of these deposits with black shale suggests that most of the low-resistivity shale was deposited during highstand events and that the resistive shale includes highstand and transgressive deposits.

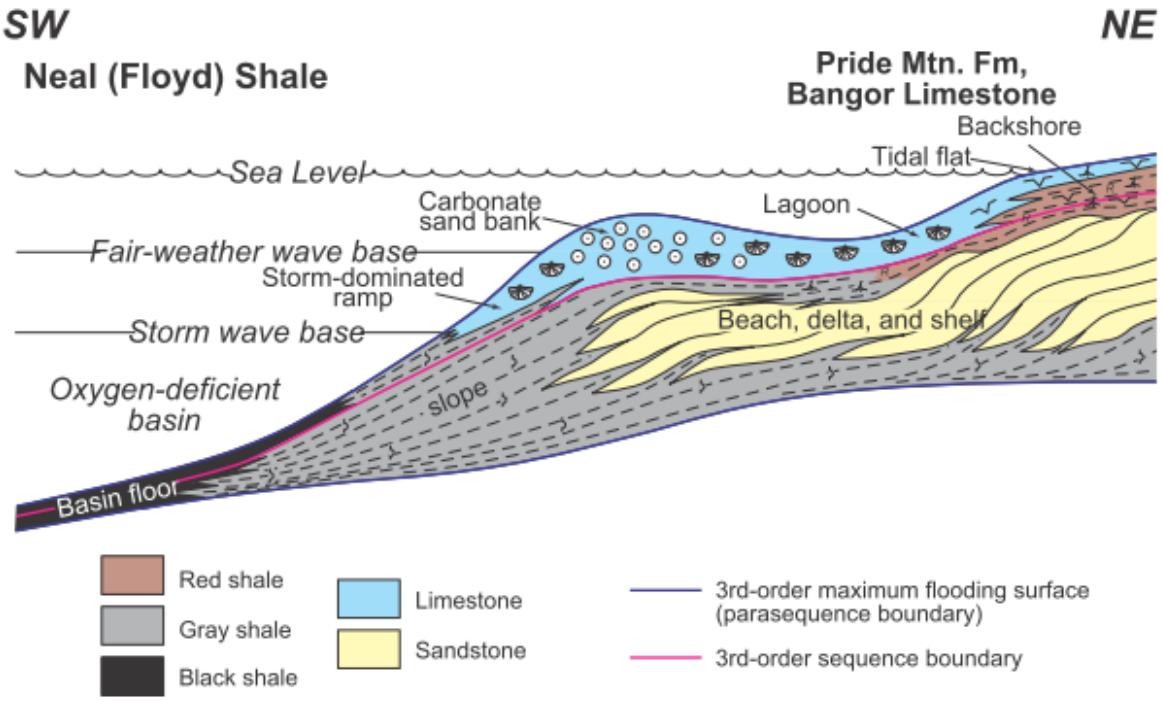

Figure 20.—Depositional model of an idealized third-order parasequence in Upper Mississippian strata of the BWB (modified from Pashin, 1994).

The Neal shale is thickest (200 to 350 ft.) in a belt extending from west-central Lamar County to southwestern Fayette County (fig. 21). This thick shale corresponds with the clinoform shale facies that was deposited on the distal slope of the Bangor carbonate ramp. The shale thins northeastward to less than 50 ft. as it intertongues with the Bangor. To the southwest, the shale has a fondoform geometry and is typically between 100 and 250 ft. thick.

The Neal shale and equivalent strata can be subdivided into three major stratigraphic intervals, and isopach maps of these intervals define the depositional framework and illustrate the stratigraphic evolution of the BWB in Alabama (Pashin, 1993, 2008). The first interval includes strata equivalent to the Pride Mountain Formation and the Hartselle Sandstone and thus shows the early configuration of the Neal basin (fig. 22). The Pride Mountain-Hartselle interval is thought to contain barrier-strandplain deposits (Cleaves and Broussard, 1980; Thomas and

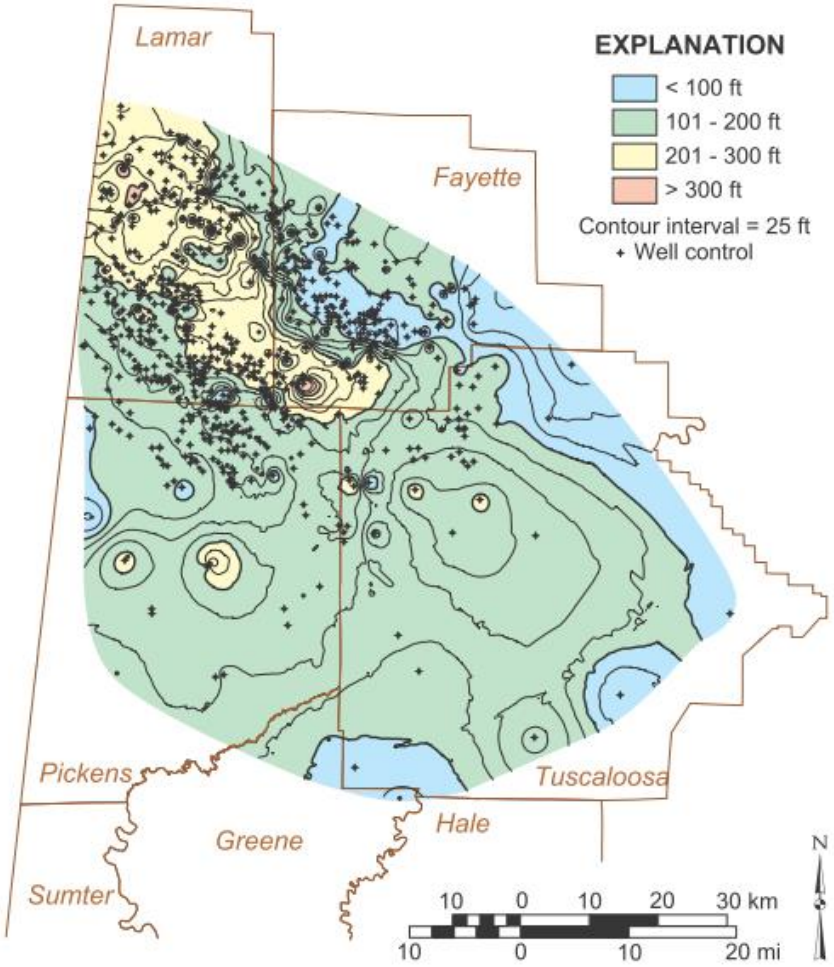

Figure 21.—Isopach map of the Neal (Floyd) shale in the BWB of Alabama.

Mack, 1982). Isopach contours define the area of the barrier-strandplain system in the northeastern part of the basin, and closely spaced contours where the interval is between 25 and 225 ft. thick define a southwestward slope that turns sharply and faces southeastward in western Marion County. The black shale facies of the Neal is in the southwestern part of the map area and is thinner than 25 ft.

The second interval includes strata equivalent to the main part of the Bangor Limestone (fig. 23). A generalized area of inner ramp carbonate sedimentation is defined in the northeastern part of the map area where the interval is thicker than 300 ft. Muddy, outer-ramp facies are

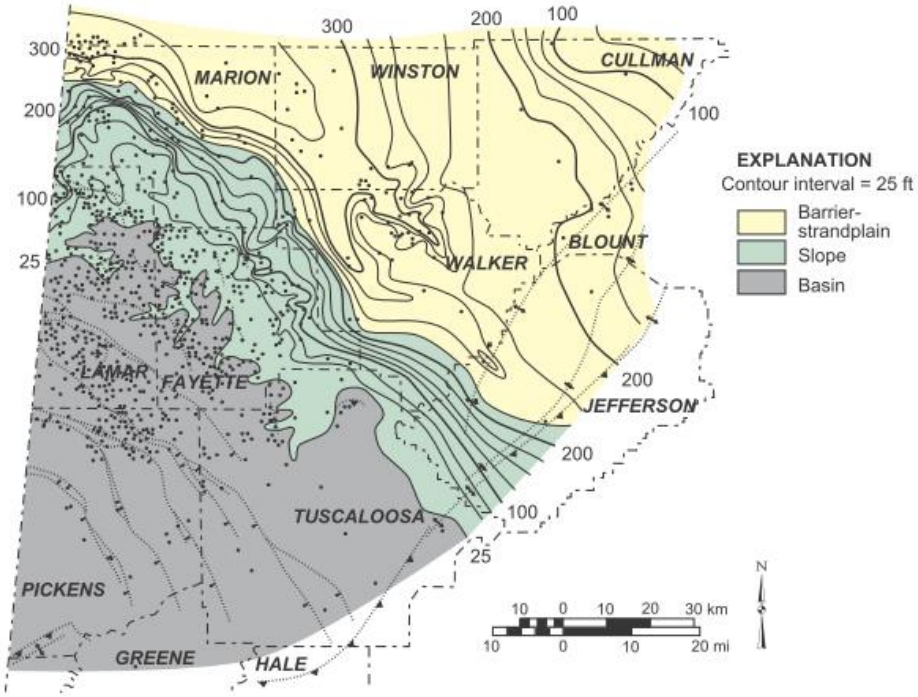

Figure 22.—Isopach map of the Pride Mountain Formation, Hartselle Sandstone, and equivalent strata in the Neal shale in the BWB of Alabama (modified from Pashin, 1993).

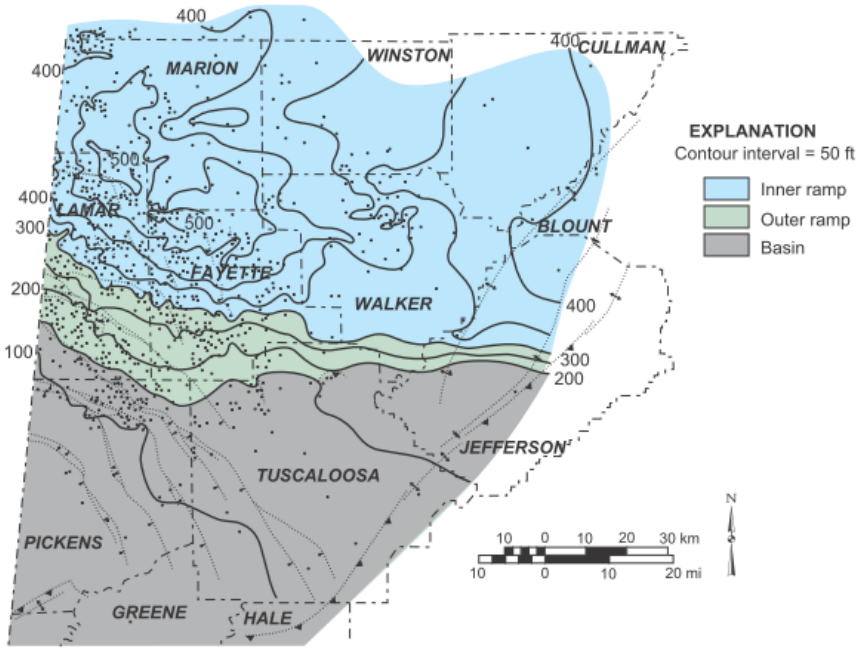

Figure 23.—Isopach map of the Bangor Limestone and equivalent strata in the Neal shale of the BWB in Alabama (modified from Pashin, 1993).

concentrated where this interval thins from 300 to 150 ft. and includes clinoform strata of the Neal shale. A basinal region, where the shale has a fondoform geometry, is marked by widely spaced contours where the shale is thinner than 200 ft. This interval contains the vast majority of the prospective Neal reservoir facies, and the isopach pattern indicates that the slope prograded more than 25 miles southwestward during Bangor deposition.

The final interval includes strata equivalent to the lower Parkwood Formation and the basal part of the *Millerella* limestone (fig. 24). The lower Parkwood separates the Neal shale and the main part of the Bangor Limestone from carbonate-dominated strata of the middle Parkwood Formation. The lower Parkwood is a succession of siliciclastic deltaic deposits that prograded onto the Bangor ramp in the northeastern part of the study area and into the Neal basin in the southern part. This section contains the most productive conventional reservoirs in the BWB (Cleaves, 1983; Pashin and Kugler, 1992; Mars and Thomas, 1999). The lower Parkwood is thinner than 25 ft. above the inner Bangor ramp and includes a variegated shale interval

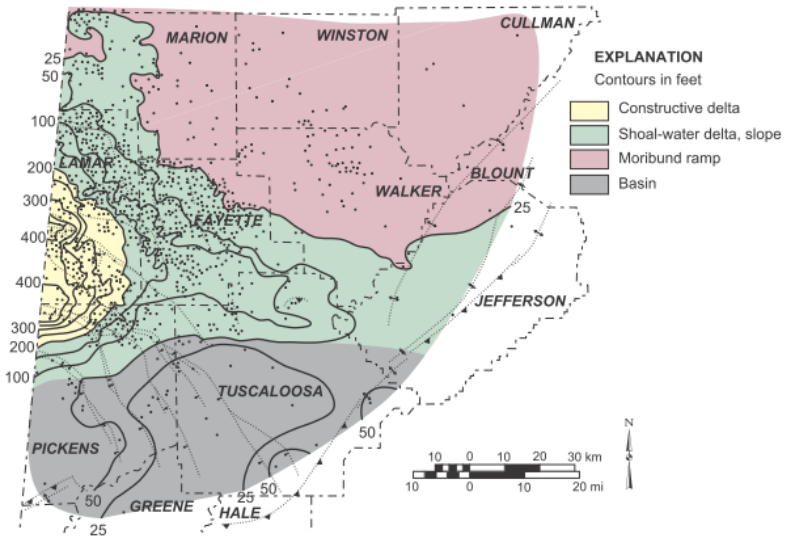

Figure 24.—Isopach map of the lower Parkwood Formation and equivalent strata in the Neal shale of the BWB in Alabama (after Pashin, 1993).

containing abundant slickensides and calcareous nodules, which indicate exposure and vertic soil formation. The area of deltaic sedimentation is where the lower Parkwood is thicker than 50 ft. and includes constructive deltaic facies in the Neal basin and destructive, shoal-water deltaic facies along the margin of the Bangor ramp. In the southern part of the study area, the 50-foot contour defines a remnant of the Neal basin that persisted through lower Parkwood time. Here, Neal strata equivalent to the middle Parkwood merge with the main black shale body, and this is where most gas exploration has taken place in the Neal shale.

Even though the Neal is the only Mississippian unit that is recognized to be a potential shale-gas reservoir, we used the SEM to examine other Mississippian shale units (table 2). This was done for comparison purposes and in case shale-gas reservoirs are found in these formations in the future. Eight Mississippian cores were described for this study (table 1; fig. 3). The units sampled include the Bangor Limestone, Lewis shale, *Millerella* shale, and Parkwood Formation. All but one of these cores contain substantial shale intervals. The Floyd was not penetrated by any of the eight Mississippian cores described here, but see Pashin and others (2011), and figures A5 through A7. The Floyd in OGB PN 13979 (fig. 25) was studied by us using a FIB-FESEM (see methods section, and later section for results).

BANGOR LIMESTONE

The upper Bangor is predominantly limestone, but the lower Bangor contains considerable amounts of shale. The Bangor was cored in OGB PN 1160 (James B. Hill #1) (fig. 26). The cored interval consists of lime mudstone with scattered beds of shale, siliciclastic mudstone, and sandy limestone. Examination of one SEM sample from a thin shale bed dominated by illite revealed fine calcite debris as well as authigenic quartz, pyrite, and albite. The detrital calcite indicates that areas of siliciclastic mud on the seafloor were relatively small

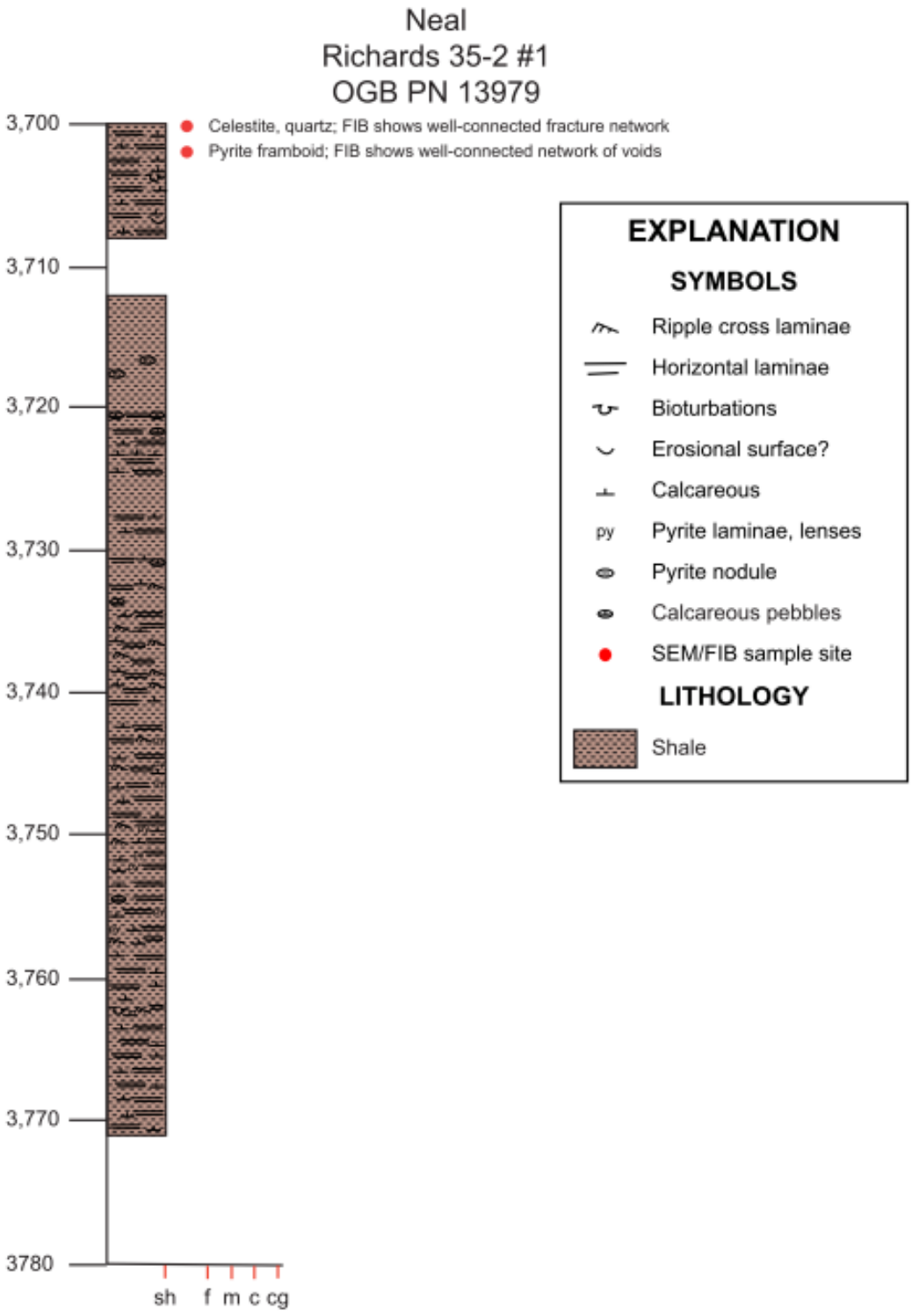

Figure 25.—Graphic core log of Mississippian Floyd Shale, OGB PN 13979 (Richards 35-2 #1).

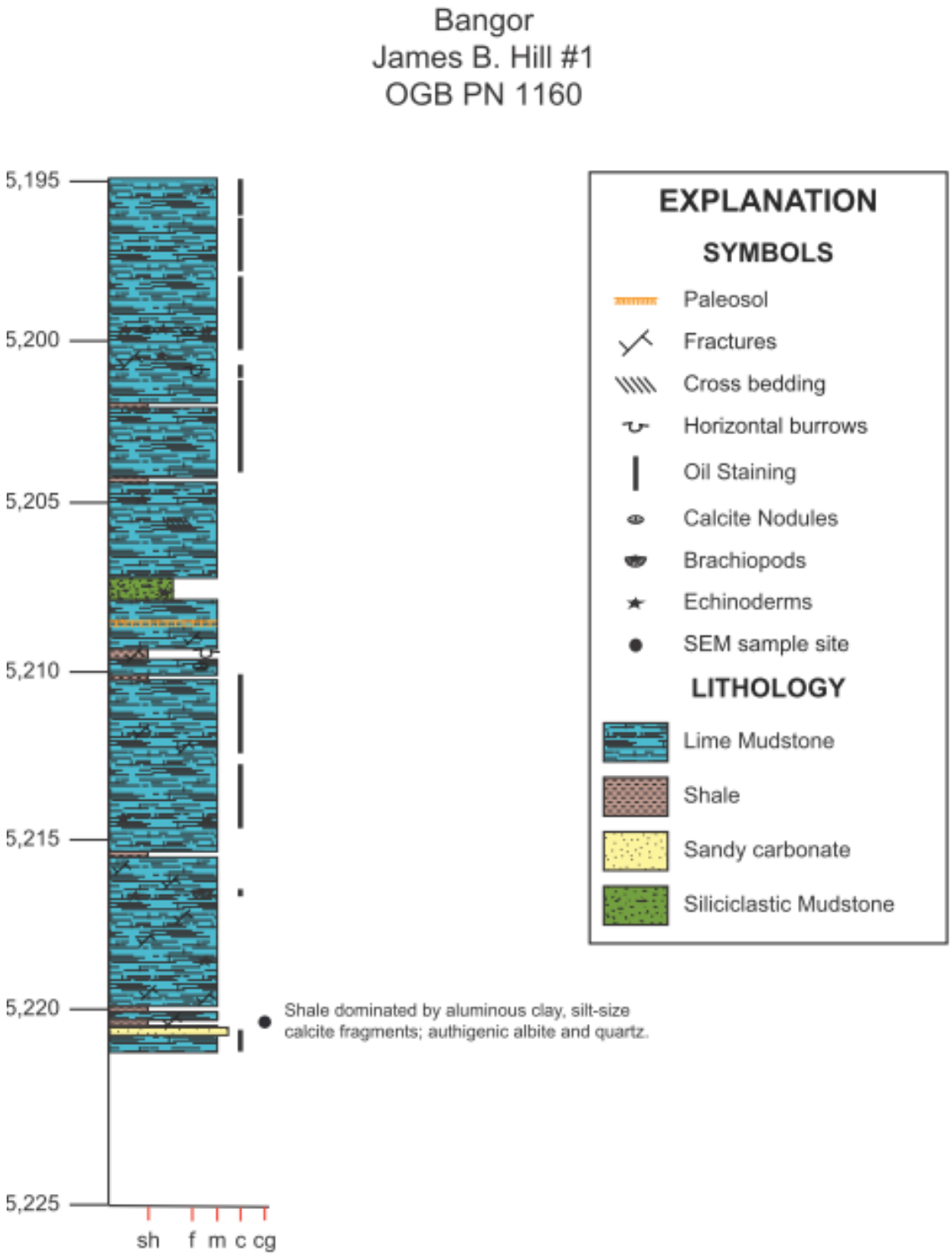

Figure 26.—Graphic core log of Mississippian Bangor Limestone, OGB PN 1160 (James B. Hill #1).

and that lime mud was exposed nearby. Pore fluids were at times acidic and oxygenated, and at other times reducing.

LEWIS SHALE

The Lewis (an informal and highly variable unit in the lower Pride Mountain Formation) was cored in six wells: OGB PN 3074 (Bonzell McGee 13-8 #1), OGB PN 4054 (Patterson 20-5 #1), OGB PN 4305 (Spann 10-13 #1), OGB PN 4801 (Arthur 11-13 #1), OGB PN 5198 (Z.D. Vick 30-9 #1), and OGB PN 5321 (Stanley 22-12 #1) (table 1; figs. 27 through 32 respectively). SEM samples were examined from cores of OGB PN 4054, OGB PN 4305, OGB PN 4801, and OGB PN 5321 (table 2).

The core from OGB PN 3074 (fig. 27) is dominated by shale, with a few intervals up to 2 ft. thick of siliciclastic mudstone and sandstone. Echinoderms and brachiopods were observed here and there in the shale, as is common in the Lewis. This core shows considerable staining by sulfur minerals, perhaps caused by oxidation of pyrite after the core was collected.

The lower part of the core from OGB PN 4054 (fig. 28) is assigned to the Lewis. Here, the Lewis consists of illitic/chloritic clay shale with a limestone bed about 2.5 feet thick, calcareous nodules, and scattered brachiopod shells. Possible fungal borings (fig. 33) suggest subaerial exposure.

In OGB PN 4305 the Lewis (fig. 29) consists of illitic/chloritic clay shale, with loose clusters of pyrite crystals (visible with the SEM), abundant masses (<10 μm) of ~1-μm anhedral-subhedral crystals of iron sulfate, iron oxide, quartz, and sprays of authigenic anhydrite laths. Iron sulfate is found in oxidation zones where iron minerals like pyrite were common. The location of this well at the edge of the Neal depocenter makes exposure and soil formation unlikely, leaving the abundance of oxidized minerals in this core something of a puzzle. It could

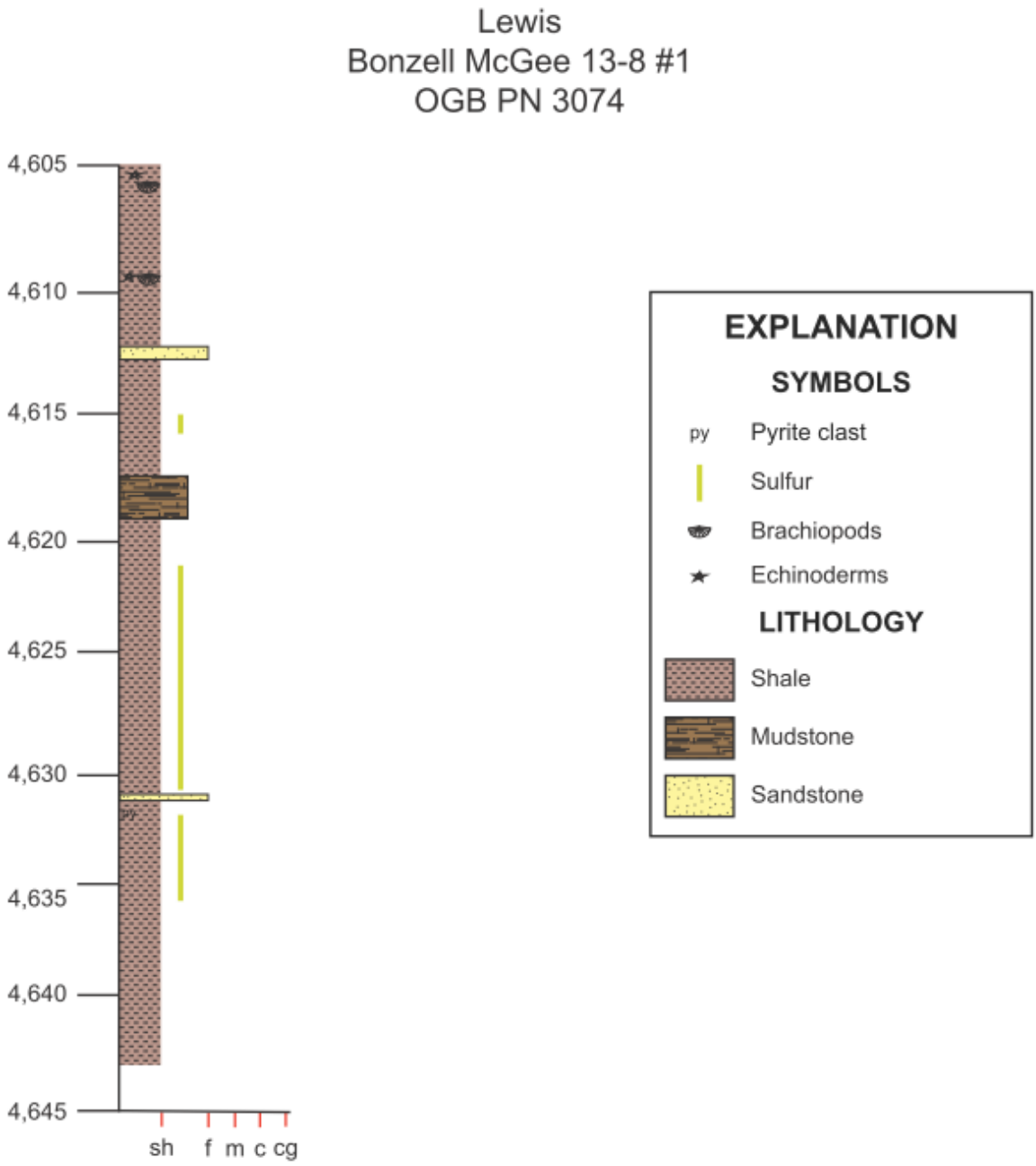

Figure 27.—Graphic core log of the Mississippian Lewis shale (an informal unit), OGB PN 3074 (Bonzell McGee 13-8 #1).

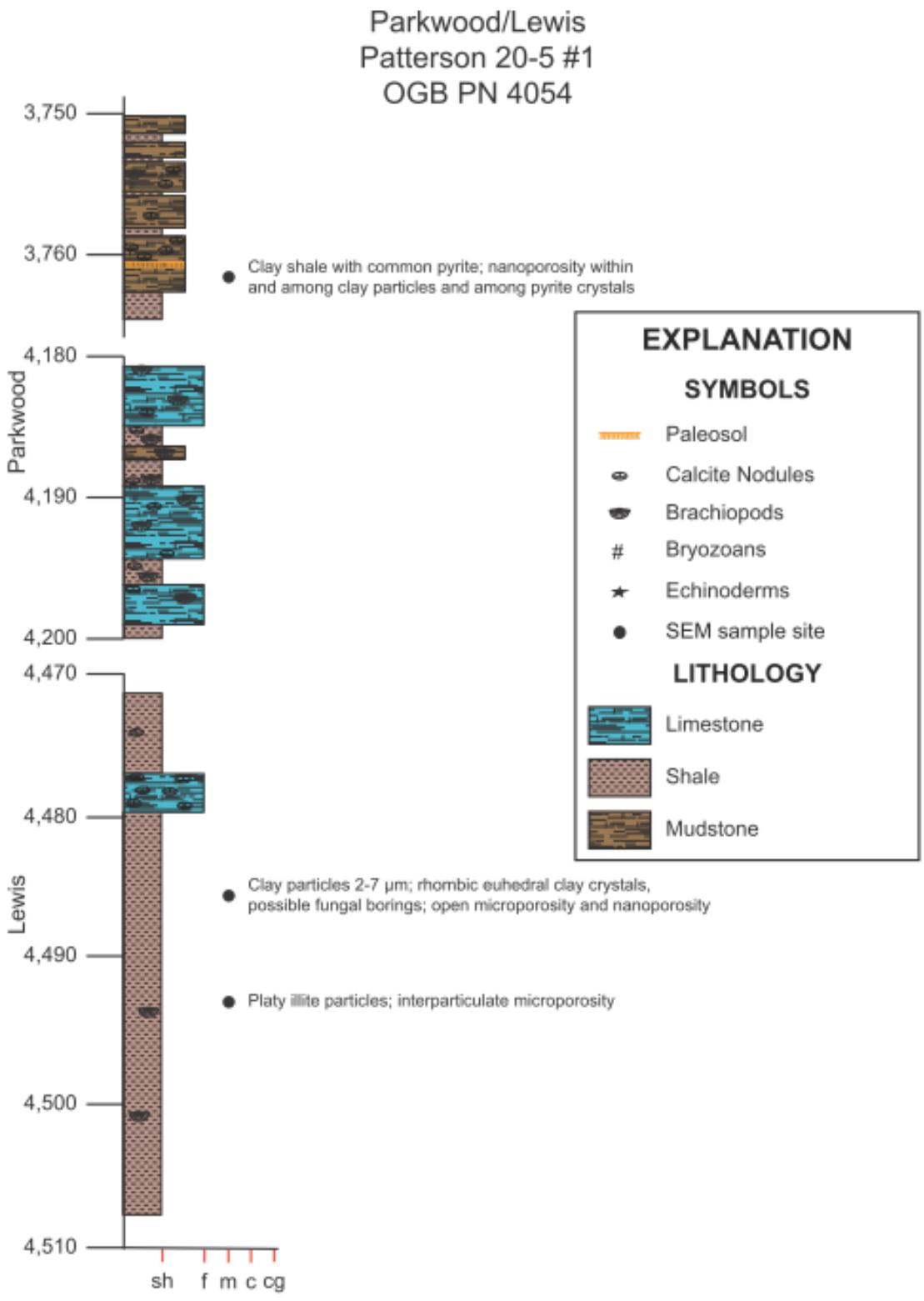

Figure 28.—Graphic core log of the Mississippian Lewis shale (an informal unit) and the Mississippian Parkwood Formation, OGB PN 4054 (Patterson 20-5 #1).

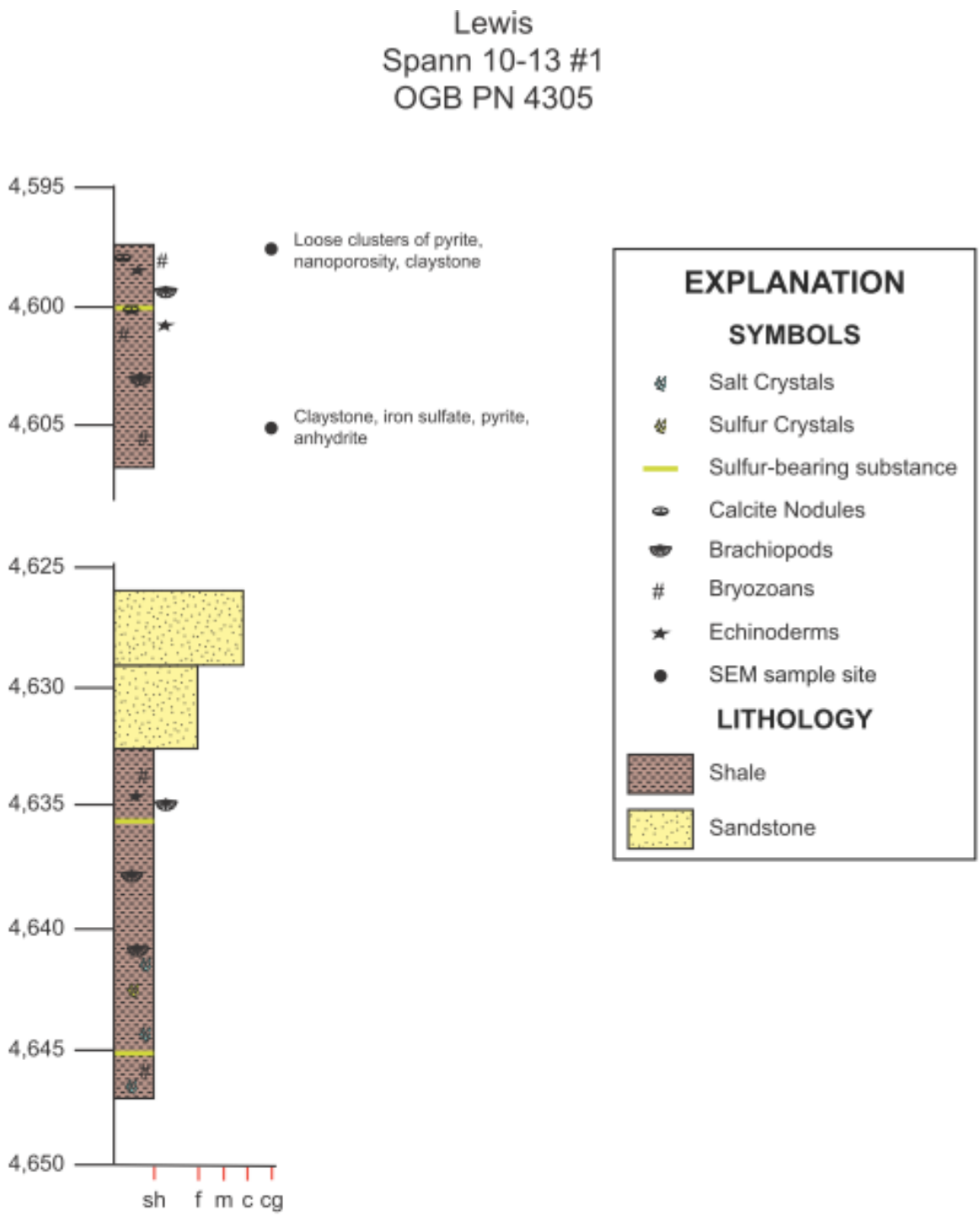

Figure 29.—Graphic core log of the Mississippian Lewis shale (an informal unit), OGB PN 4305 (Spann 10-13 #1).

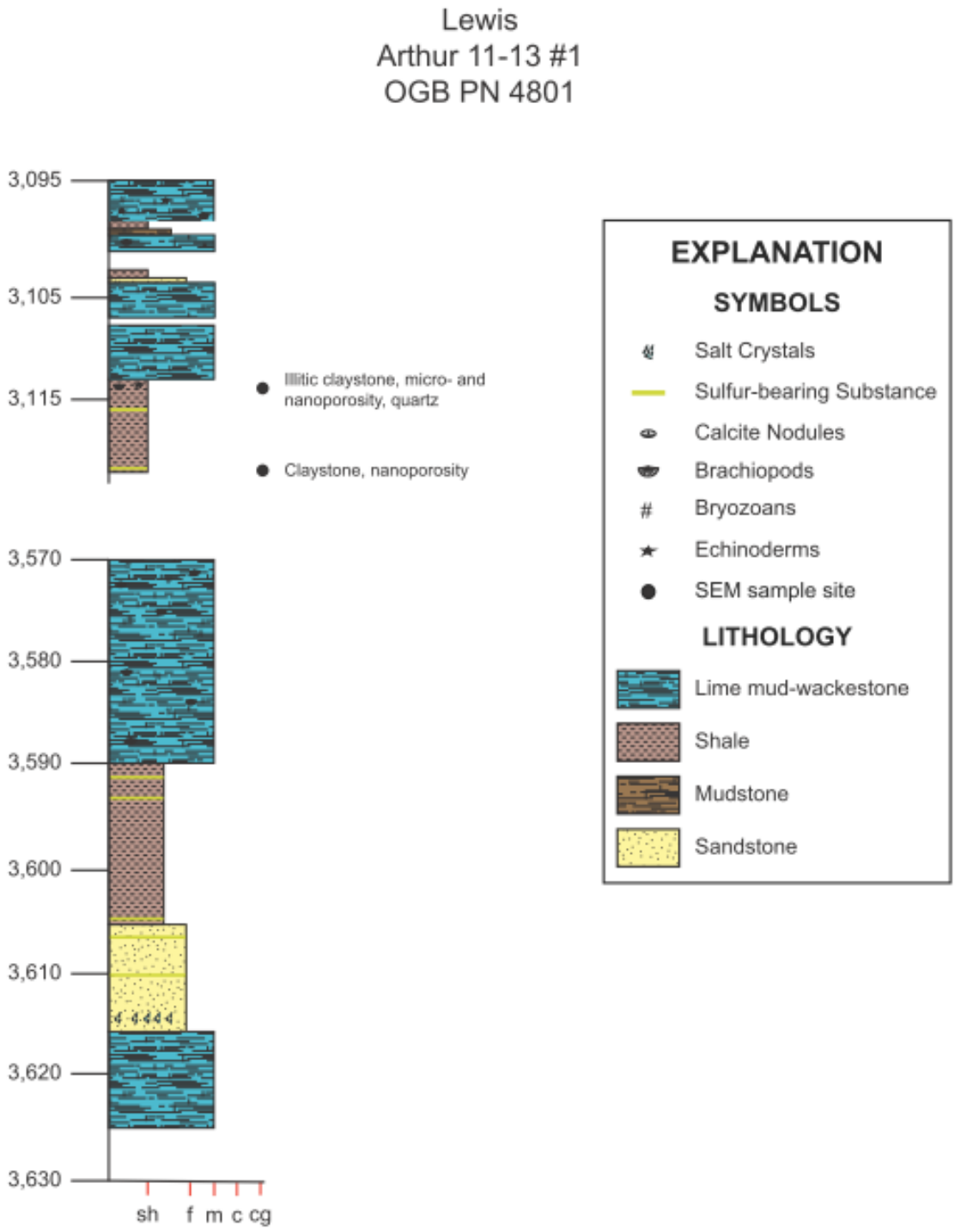

Figure 30.—Graphic core log of the Mississippian Lewis shale (an informal unit), OGB PN 4801 (Arthur 11-13 #1).

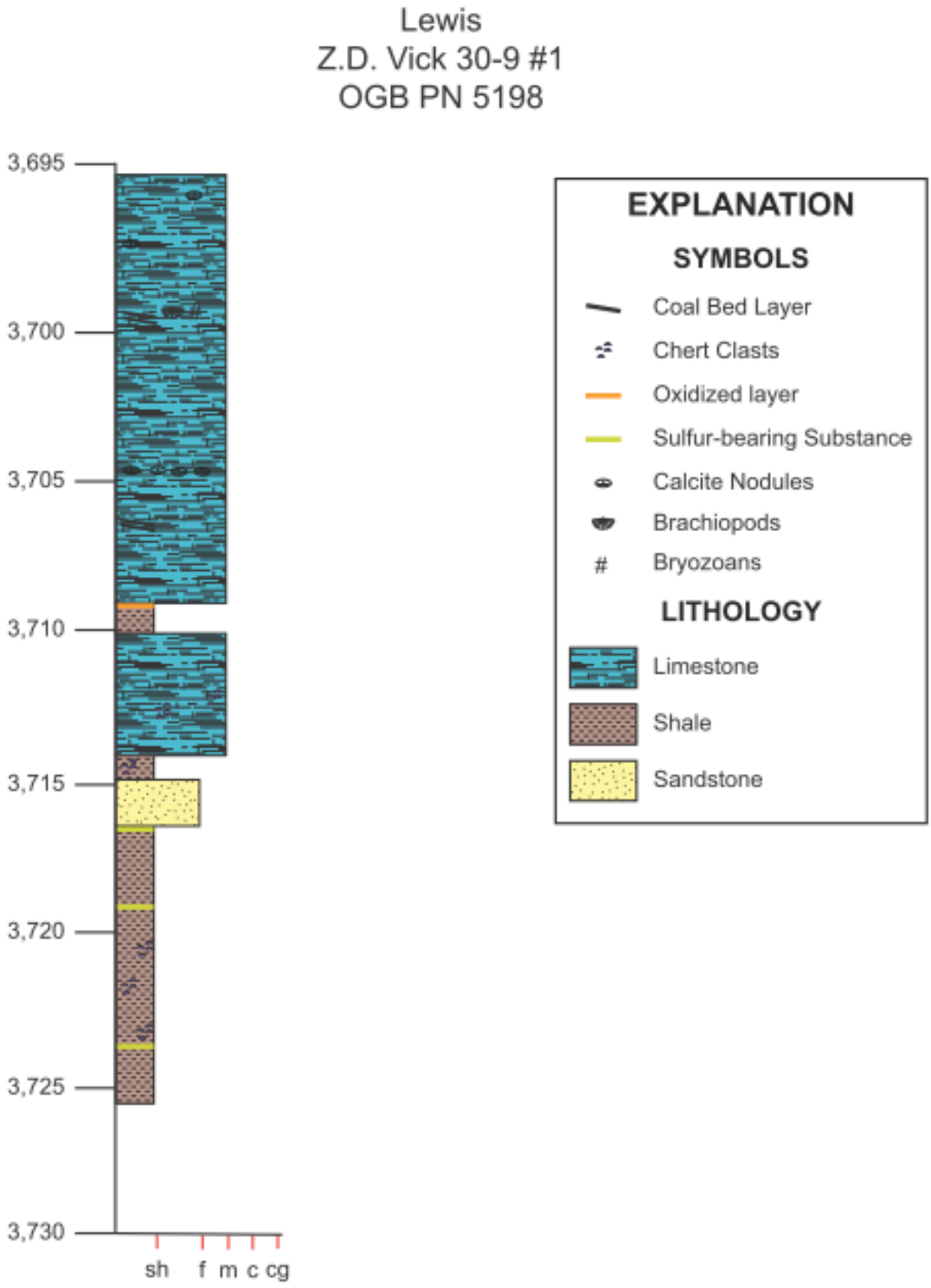

Figure 31.—Graphic core log of the Mississippian Lewis shale (an informal unit), OGB PN 5198 (Z.D. Vick 30-9 #1).

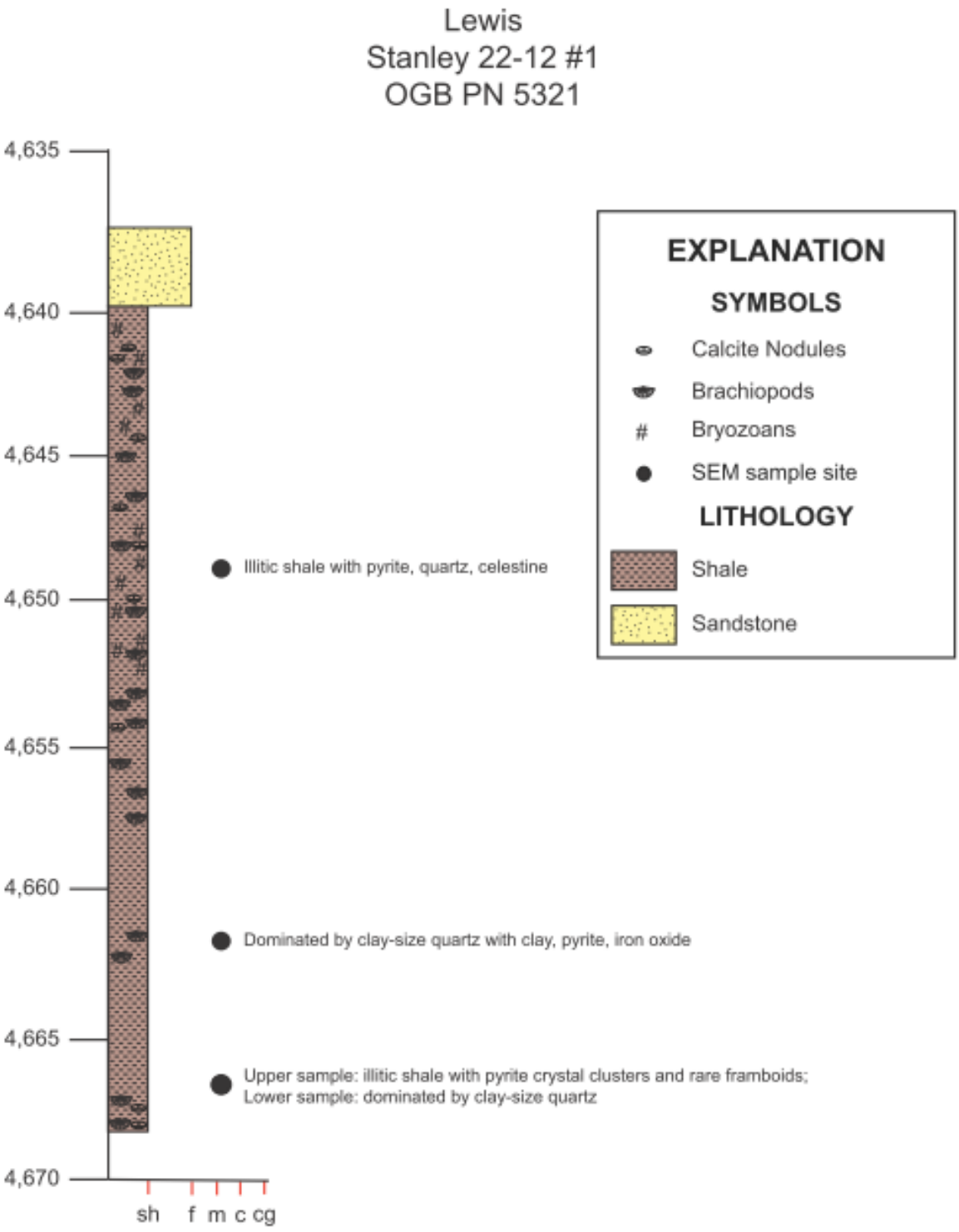

Figure 32.—Graphic core log of the Mississippian Lewis shale (an informal unit), OGB PN 5321 (Stanley 22-12 #1).

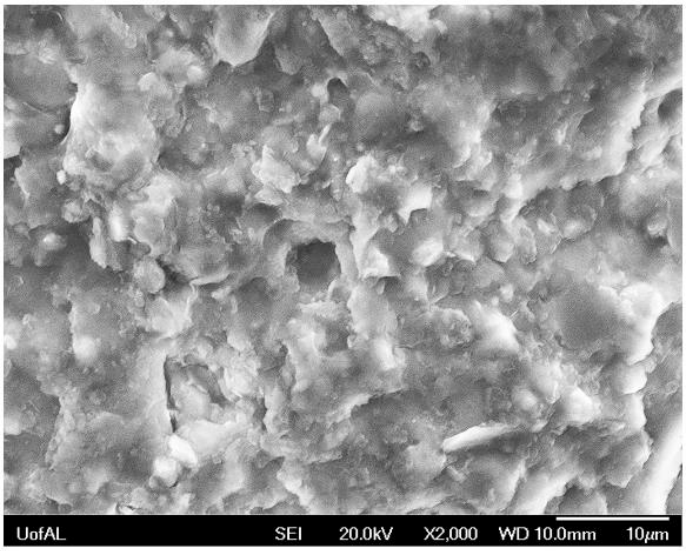

Figure 33.—Possible fungal boring in Mississippian Lewis shale (an informal unit); sample from 4,486 ft., OGB PN 4054 (Patterson 20-5 #1). SEM image, scale 10 μm; see figure 29.

be that oxidized formation waters reached the basinal location of OGB PN 4305 via the thick sandstone unit not far below the SEM sample containing the iron sulfate and other oxidized materials.

The Lewis in OGB PN 4801 (fig. 30) is dominated by fossiliferous wackestone and clay shale, which may reflect its relatively proximal location. Quartzitic illite/chlorite clay from this core contains symmetrical objects about 5 μm across (visible using the SEM) composed of quartz grains (fig. 34); these may be microfossils. Another sample from the same core consists of relatively pure clay shale. The abundant limestone was not sampled.

The Lewis in the core from OGB PN 5198 is dominated by lime mudstone and lesser shale (fig. 31). Chert clasts and calcite nodules are common at certain horizons. No samples from this core were examined with the SEM, due to its proximal calcareous character and position on the basin-marginal slope (figs. 5, 24).

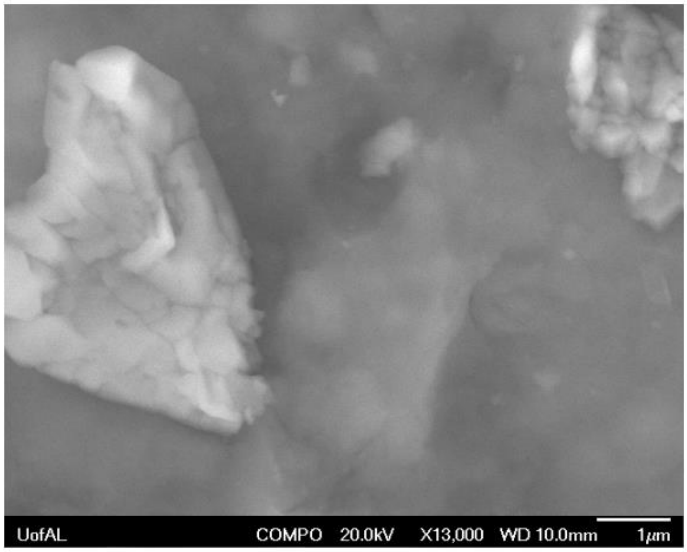

Figure 34.—Siliceous microfossil, heart shaped, in Mississippian Lewis shale (an informal unit); sample from 3,113.8 ft, OGB PN 4801 (Arthur 11-13 #1). SEM backscatter electron image, scale 1 μm.

In the core from OGB PN 5321, the Lewis is dominated by illitic/chloritic shale (fig. 32). However, two out of four laminae that were analyzed with the SEM are dominated by clay-sized quartz. These layers may be distal turbidites or storm deposits. The upper 18 ft. of cored shale come from a fossiliferous facies that is markedly different from underlying strata. The fossiliferous unit contains the evaporite celestite. (Evaporites also were observed in OGB PN 4305, located close by in a similar paleogeographic setting at the edge of the Neal basin.) Underlying strata contain laminae of clay-size quartz, iron oxide, and rare pyrite framboids. This core records wide swings in groundwater chemistry, in contrast to more consistently reducing conditions indicated by black shale of the Neal (Pashin and others, 2011).

In summary, the Lewis shale in these six cores appears relatively homogeneous to the eye, but evidence of hypersaline pore waters, influx of oxidized iron minerals, and distal event deposits show that the shale facies of the Lewis is more complex than it seems. If gas-reservoir facies are discovered in the Lewis, their thickness, quality, and distribution will be variable and complex.

PARKWOOD FORMATION

The Parkwood Formation *sensu stricto* was cored in OGB PN 3707 and OGB PN 4054 (figs. 28 and 35, respectively). Interbedded shale and lime mudstone dominate the lower Parkwood core; a shallower core is all shale. A single SEM sample from the shallower core in OGB PN 3707 is illitic/chloritic shale with pyrite, quartz coated with clay, rutile, and possible potassium feldspar. The Parkwood in OGB PN 4054 was also sampled once for the SEM (table 2). It consists of illitic/chloritic shale containing pyrite and other, less common, minerals. In this core a lower part is dominated by fossiliferous limestone units a few feet thick, with thinner interbedded shale layers. The upper part of the core is dominated by siliciclastic mudstone (which is where the SEM sample came from) with thinner shale interbeds. This shallower cored interval contains numerous calcite nodules, but not near the sampled site.

FRACTURE ANALYSIS AND MICROSTRUCTURE

DFN MODELS FROM FRACTURED DEVONIAN CHATTANOOGA SHALE

FRACTURE DATA FROM CORES

The Chattanooga Shale is the most widespread black shale unit in Alabama and thus is selected for the fractured-network modeling study. The fractures and their properties were investigated from the two wells in the area with cores available for direct observation for the shale unit, namely OGB PN 14673 and OGB PN 15668 (fig. 3, tables 3, 4; figs. A3, A4). The observed fractures from both wells in the Chattanooga Shale are essentially perpendicular to bedding and were shear fractures. The average virtual angles between fractures and bedding planes from the OGB PN 15668 well is 88.1º and 88.4º from OGB PN 14673. They were also

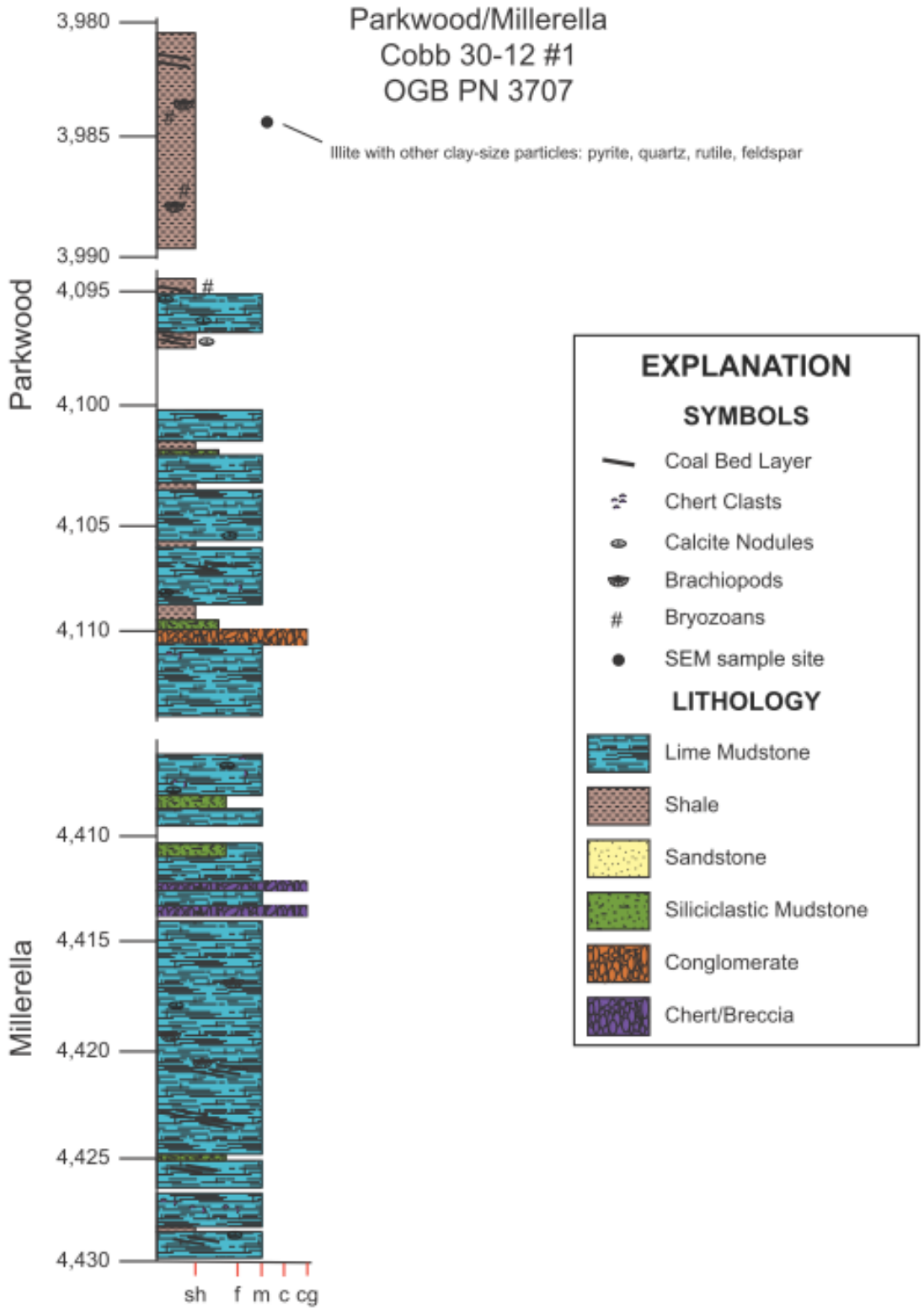

Figure 35.—Graphic core log of Mississippian Parkwood Formation, OGB PN 3707 (Cobb 30-12 #1).

strata-bound fractures as observed in cores. These basic features of observed fractures were consistent with our field and core observations in the Pottsville Formation in the same area. It can be inferred that fractures in Devonian shales were of the same origin as those from the Pottsville Formation in the BWB.

The aperture for each fracture in the cores also was measured (tables 3, 4). While the average fracture aperture value for the OGB PN 15668 is only 0.079 mm, it is 0.234 mm for OGB PN 14673. The considerable difference in apertures of the two wells most likely reflects regional variation of fracture properties.

Table 3.—Fractures observed in cores from OGB PN 15668

Depth Interval (ft)	Virtual Dip	Aperture (mm)	Fracture Type	Confidence
9,134.50 – 9,136.50	90	0.095	S	10
9,140.50 – 9,144.00	88	0.050	S	10
9,144.00 – 9,145.00	85	0.050	S	10
9,147.50 – 9,149.90	90	0.075	S	10
9,159.20 – 9,161.00	90	0.115	S	10
9,162.00 – 9,175.00	90	0.095	S	10
9,181.00 – 9,182.50	90	0.062	S	10
9,184.00 – 9,185.50	85	0.075	S	10
9,186.00 – 9,188.00	85	0.095	S	10

Table 4.—Fractures observed in cores from OGB PN 14673

Depth Interval (ft)	Virtual Dip	Aperture (mm)	Fracture Type	Confidence
8,319.00 – 8,320.00	90	0.062	S	10
8,420.00 – 8,422.00	85	0.175	S	10
8,423.00 – 8,424.00	85	0.175	S	10
8,435.00 – 8,437.00	90	0.062	S	10
8,442.00 – 8,446.00	90	0.750	S	10
8,450.00 – 8,452.00	90	0.115	S	10
8,456.00 – 8,458.00	90	0.265	S	10
8,458.00 – 8,462.00	90	0.265	S	10

DFN MODELS FOR THE CHATTANOOGA SHALE

Based on the assumption of the same structural origin of fractures in the Chattanooga Shale as those from the Pottsville Formation, we constructed basic fracture-network models using stochastic properties of the fractures from field observations previously made by Pashin and others (2004, 2008). Two DFN scenarios are explored: a single northeast-oriented fracture set (system), and a system fracture set intersected by a crossing fracture set. The stochastic parameters used for DFN model realizations for those two scenarios are shown in tables 5 and 6, respectively.

In order to understand the impact of the degree of preferred orientation of a fracture set on hydraulic fracturing, we have used several concentration parameters of fracture orientation for construction of DFN models in the single fracture-set scenario. It is commonly assumed that the orientation of natural fractures in a set obeys the spheric normal distribution (von-Mises distribution), and that the concentration parameter (K) measures the concentration (a reciprocal measure of dispersion) of fracture orientation, in which a larger K value represents a more concentrated fracture distribution. We have used three K values, 10, 500, and 1,500, to construct three DFN models on the single-fracture scenario.

Table 5.—Stochastic parameters for single fracture set (system) DFN models. A 16-m-interval (-3,200 m to -3,216 m) was used for a northeast fracture set.

Mean Direction		P32	Aperture Mean (m)	Size (m)	Termination %
Strike	Dip				
40	88.5	0.20	1.52E-04	150	0

Table 6.—Stochastic parameters for two fracture set (system) DFN model. A 16-m-interval (-3,200 m to -3,216 m) was used for both fracture sets.

Northeast Fracture Set						Southeast Fracture Set					
Mean Direction		P32	Aperture* mean (m)	Size (m)	Termination %	Mean Direction		P32	Aperture mean (m)	Size (m)	Termination %
Strike	Dip					Strike	Dip				
40	88.5	0.20	1.52E-04	150	0	130	90	0.1	1.50E-04	50	100

HYDRO-FRACTURING PATHWAY ANALYSES FROM SINGLE FRACTURE SET DFN MODELS

Fracture-permeability characterization and hydraulic-fracturing pathway analysis was performed in single-fracture-set DFN models. The pathway of a hydraulic fracture is defined as the number of fractures penetrated directly by the hydraulic fracture and the fracture(s) being interconnected with the penetrated fractures. Theoretically, the larger the fractures being penetrated or interconnected, the larger the pathway a hydraulic fracture will own, and hence, the more fluid it can transport.

DFN MODELS WITH HIGHLY CONCENTRATED FRACTURES

We began with the simplest, a highly concentrated DFN model with a concentration-parameter (K) value of 1,500 (fig. 36). This DFN model visually represents an almost parallel-oriented fracture set with very few fracture intersections (no interconnectivity among fractures). A 3-D view of the DFN model with fractures color-contoured by apertures (fig. 37) shows that

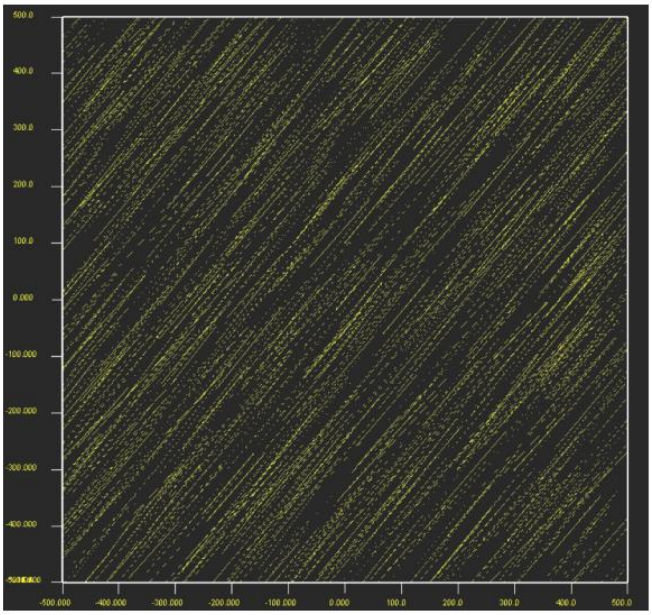

Figure 36.—Map view of a single fracture set DFN model, K = 1,500. The x and y axes are for east and north coordinates in meters.

the majority of fractures are much narrower than the average. Fracture interconnectivity analysis for the DFN model reveals that there is little reservoir compartmentalization (fig. 38). The oblate shapes of compartments (fig. 38) resulted from the highly concentrated fractures.

Fracture-permeability modeling for this DFN model indicates that the magnitude for each component of the permeability tensor varies significantly when the element modeling size is less than 150 m, which suggests that the fractured shale reservoirs are quite heterogeneous (fig. 39). One implication of the high heterogeneity of permeability with elements of this size is that one has to treat each element with a separate permeability tensor for in-fluid transport modeling. For the element size of 200 to 400 m, the permeability tensors reveal a stable range, indicating an REV exists. Thus, the fractured-shale reservoir can be treated as an effectively homogeneous medium for fluid-transport modeling.

In modeling pathways of a hydraulic fracture (HF), we designed a series of HFs 10^{o} apart in strike (orientation) in order to analyze the effects of HF orientation on the pathways (fig. 40). Pathway analysis of hydraulic fracturing in the single fracture set of the highly concentrated DFN model shows that HF has the maximum number of pathways and penetrated fractures with its strike being in a range of 110º to 140º (fig. 41). Given that mean fracture orientation (strike) is 40^{o}, hydraulic fracturing clearly becomes most effective when it is designed to be perpendicular to the preferred orientation of natural fractures. When the HF is more closely aligned with the fractures both the pathways and number of fractures being penetrated will be progressively reduced. Hydraulic fractures become least effective if their orientation is parallel to the strike of the fracture set (fig. 41).

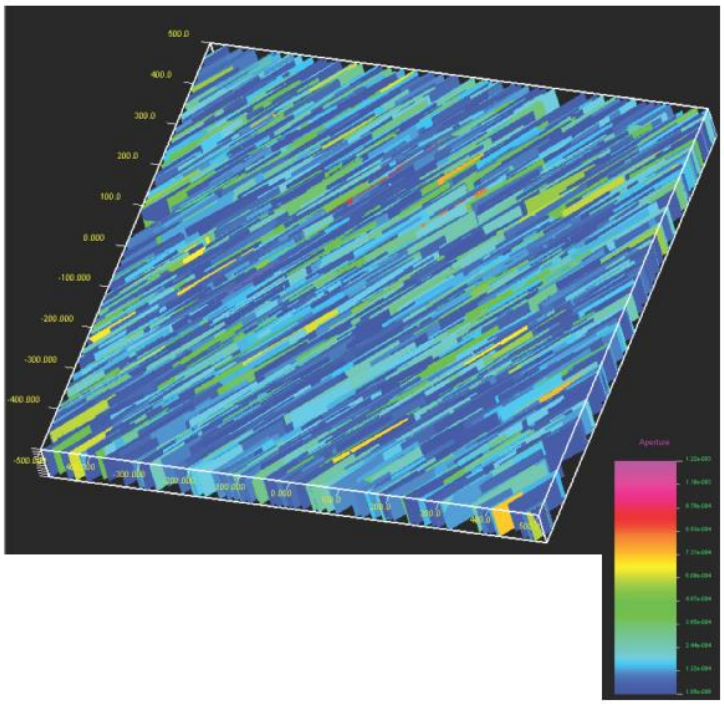

Figure 37.—Single set DFN model, K = 1,500 with color contours of fracture aperture. The x and y axes are for east and north coordinates in meters.

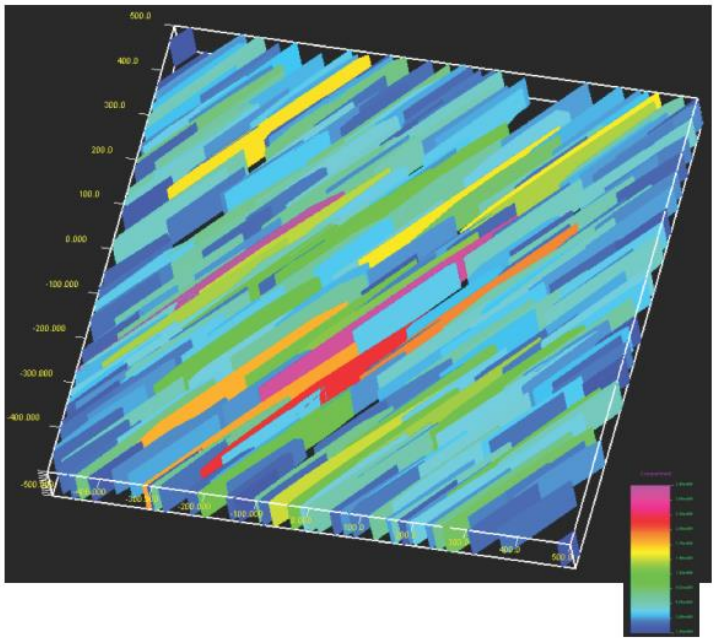

Figure 38.—Compartments color contoured by volume for single fracture set DFN model, K=1,500. The x and y axes are for east and north coordinates in meters.

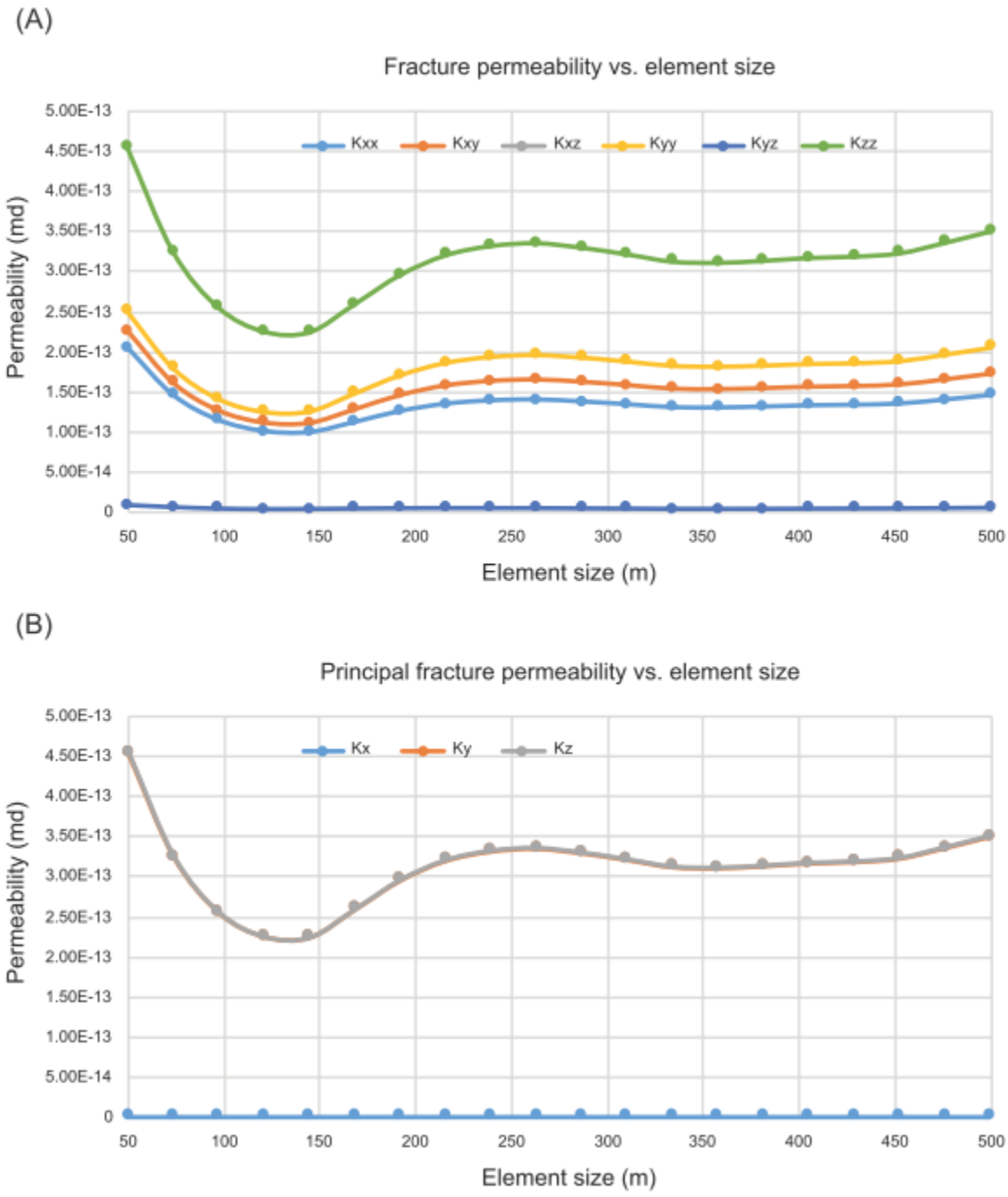

Figure 39.—Fracture permeability vs. element size, K = 1,500.

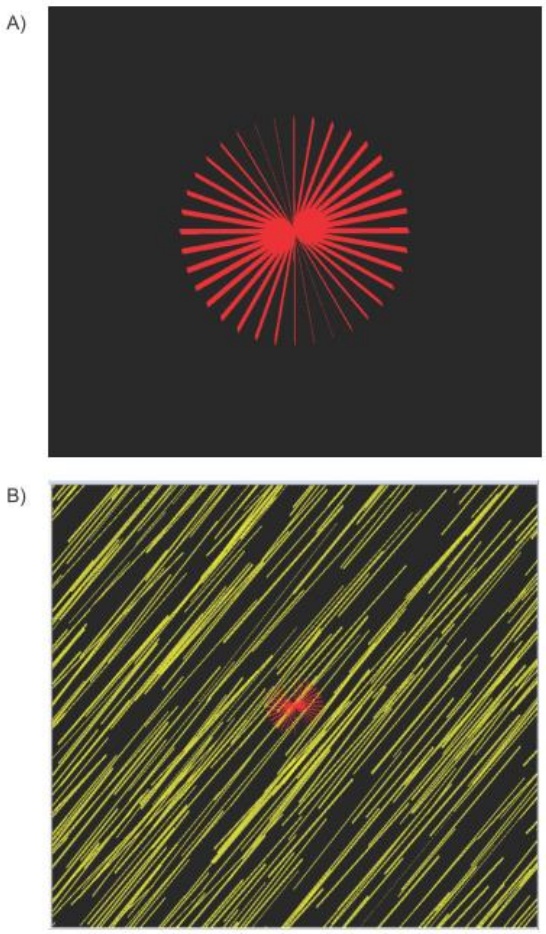

Figure 40.—Implementation of hydraulic fractures in a DFN model.

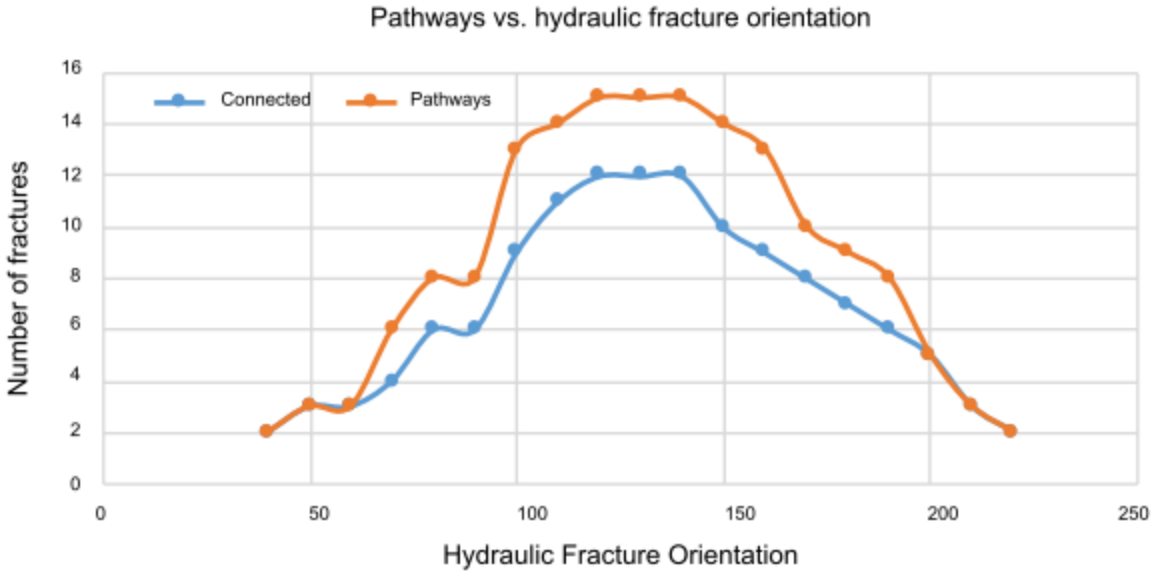

Figure 41.—Pathway analysis of hydraulic fracture in a single set DFN model, K = 1500.

DFN MODELS WITH MODERATELY CONCENTRATED FRACTURES

A DFN model with moderately concentrated fractures can be generated when the concentration parameter K is set to be 500 (fig. 42). Fracture orientation has some degree of randomization resulting in a fair number of natural fractures intersecting natural fractures in this DFN model. The contour of fracture apertures of such a DFN model is very similar to the previous model, indicating that the majority of the fractures have lower than the mean aperture (fig. 43). The compartmentalization of such a DFN model also reveals that most compartments formed by intersecting fractures are northeast-oriented (fig. 44).

Fracture permeability mapping for the DFN model with moderately concentrated fracture orientation is shown in figure 45. The principal permeability tensors with respect to the element size suggest that an REV exists with the element size larger than 250 meters (m). Therefore, the fractured-shale reservoir can be effectively treated as an anisotropic homogeneous medium under that modeling size.

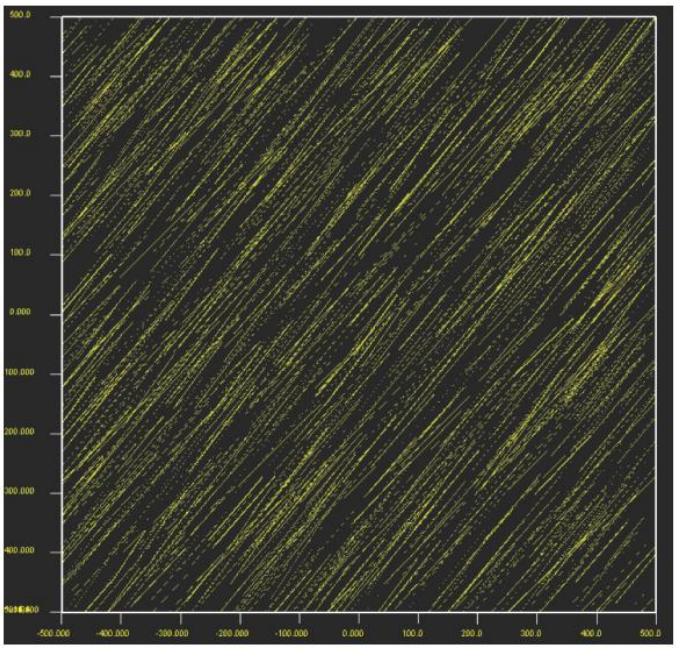

Figure 42.—Map view of a single fracture set DFN model, K = 500. The x and y axes are for east and north coordinates in meters.

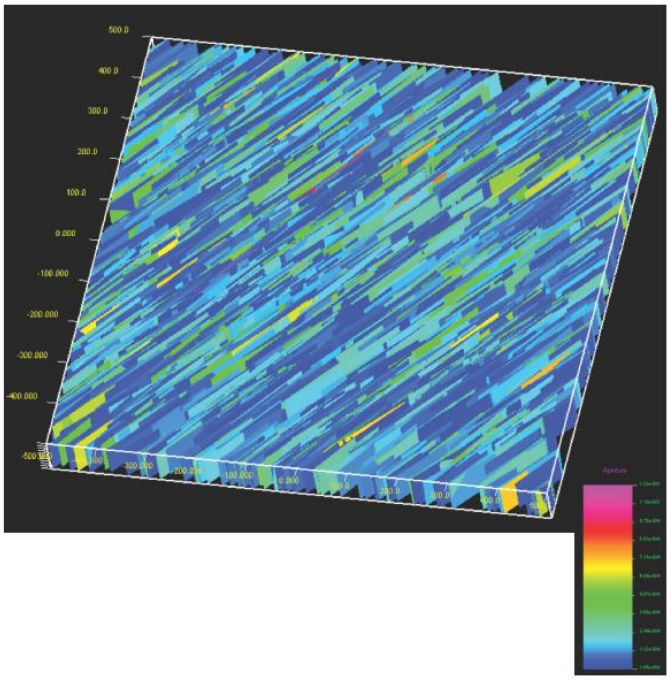

Figure 43.—Single set DFN model, K = 500 with colored contours indicating fracture aperture. The x and y axes are for east and north coordinates in meters.

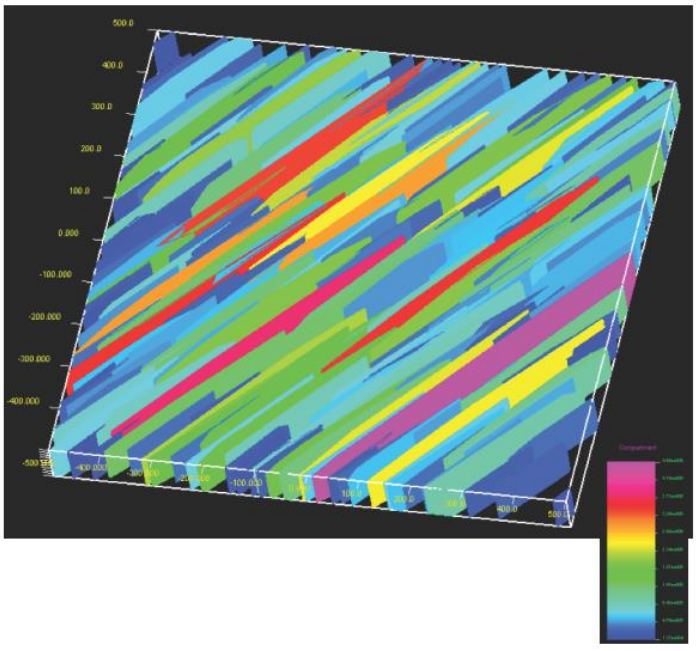

Figure 44.—Compartments color contoured by volume for single fracture set DFN model, K=500. The x and y axes are for east and north coordinates in meters.

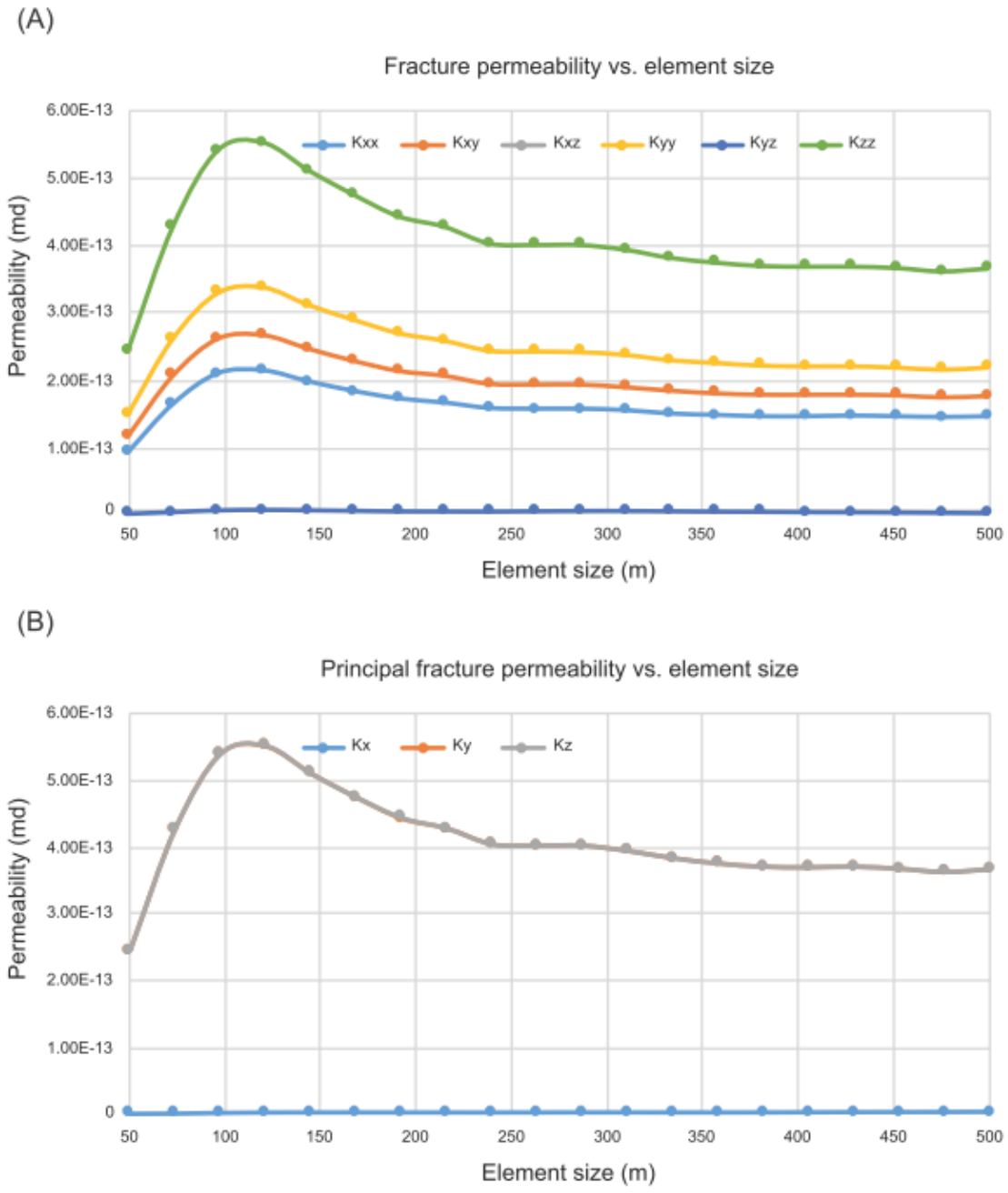

Figure 45.—Fracture permeability vs. element size, K = 500.

The number of fractures directly intersected and the number of fractures interconnected (pathways) peak when a hydraulic fracture is oriented around 100º to 150º (fig. 46). The stochastic mean strike of the fracture set is 40º, which indicates that hydraulic fracturing will be

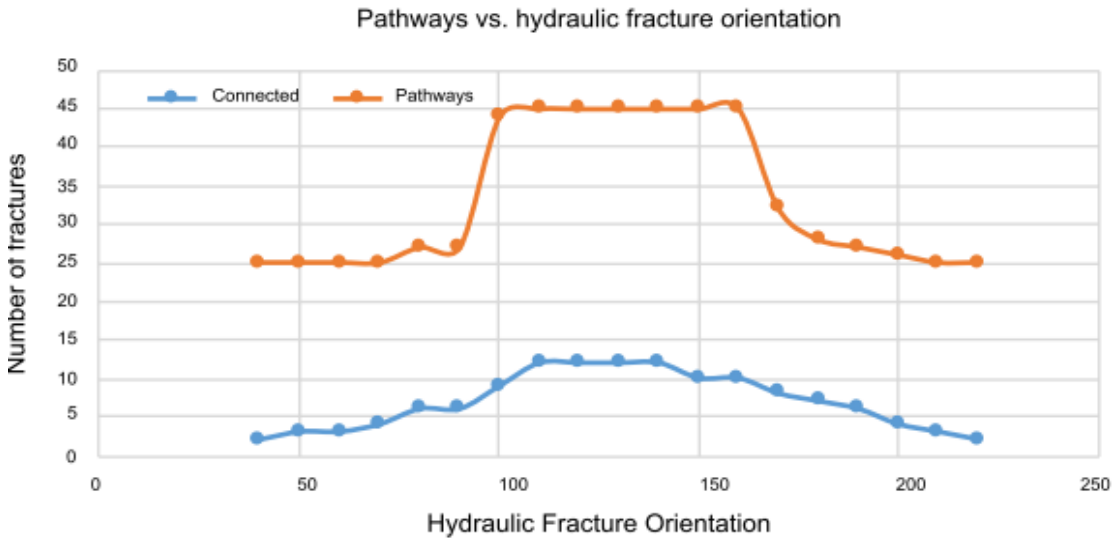

Figure 46.—Pathway analysis of hydraulic fracture in a single set DFN model, K = 500.

most effective if it is designed with the orientation perpendicular to the mean fracture strike. Although this is similar to the previous model, there are some critical differences. In the previous DFN model with highly concentrated fracture orientation, the difference between the number of fractures and the number of fractures interconnected by the hydraulic fracture was negligible. In this intermediate case, it is quite significant, which implies it is more critical to generate hydraulic fractures perpendicular to the mean fracture orientation.

DFN MODELS WITH RANDOMIZED FRACTURES

A more or less randomized fracture network can be generated when K is set to a small value, for example, K < 100. A DFN model with K = 10 shows that most fractures lack a preferred direction and thus tend to be interconnected (fig. 47). A fracture aperture contour map (fig. 48) reveals the same characteristics as the previous models because the same stochastic distribution is assigned to the apertures. Compartmentalization analysis, however, suggests a significant difference (fig. 49). A first order, massive compartment is formed with interconnected

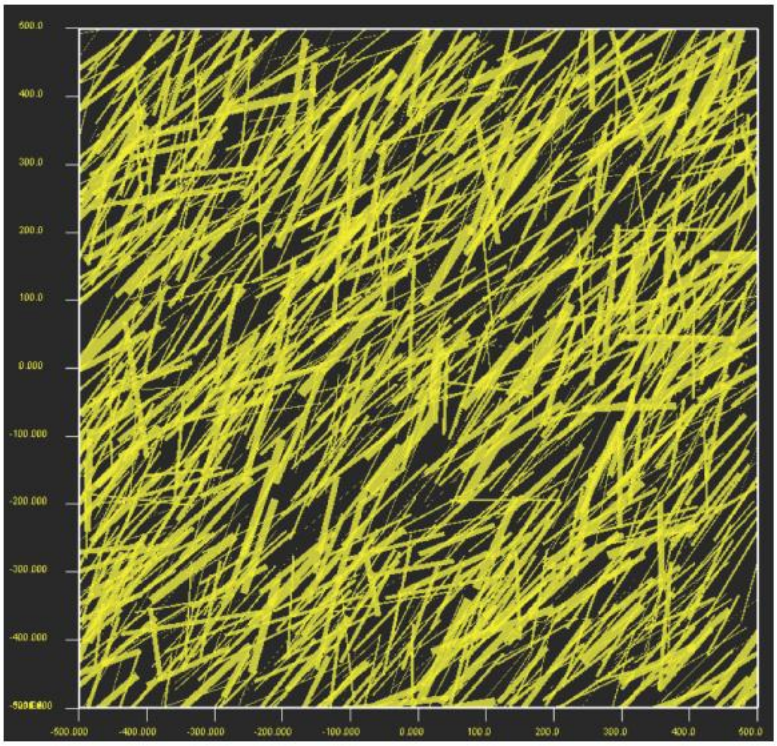

Figure 47.—Map view of a single fracture set DFN model, K = 10. The x and y axes are for east and north coordinates in meters.

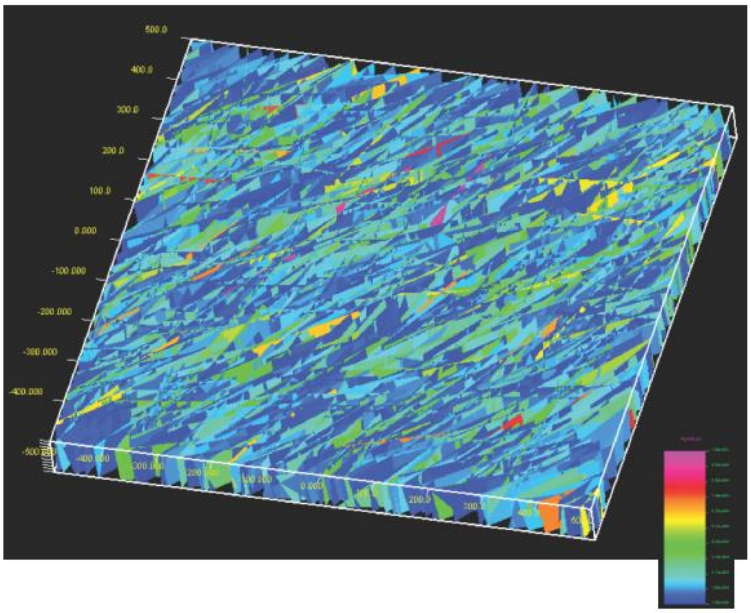

Figure 48.—Single fracture set DFN model, K = 10, with contours of fracture aperture. The x and y axes are for east and north coordinates in meters.

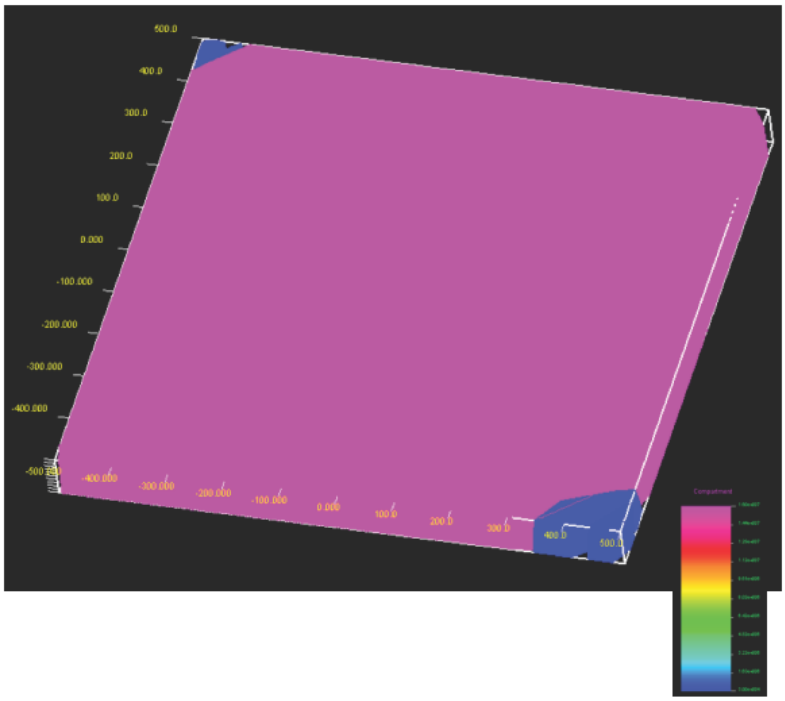

Figure 49.—Compartments color contoured by volume for single fracture set DFN model, K=10. The x and y axes are for east and north coordinates in meters.

fractures which covers almost the entire volume of the model. Second-order compartments with small volumes also exist but are much less common than in the previous two DFN models.

Fracture-permeability analysis suggests a unique feature of this model. The fracture permeability increases with the element size all the way up to the entire model, which indicates that there is no REV (fig. 50). In such a DFN model, the fractured reservoir has to be treated as an anisotropic heterogeneous medium for fluid transport modeling because there is no specific representative permeability value which could be used for every element at any given scale. This could be due to a fracture network that is not densely developed enough for the reservoir to be homogeneously fractured. Therefore, the fracture permeability has to be computed for each individual element for accurate and realistic fluid modeling.

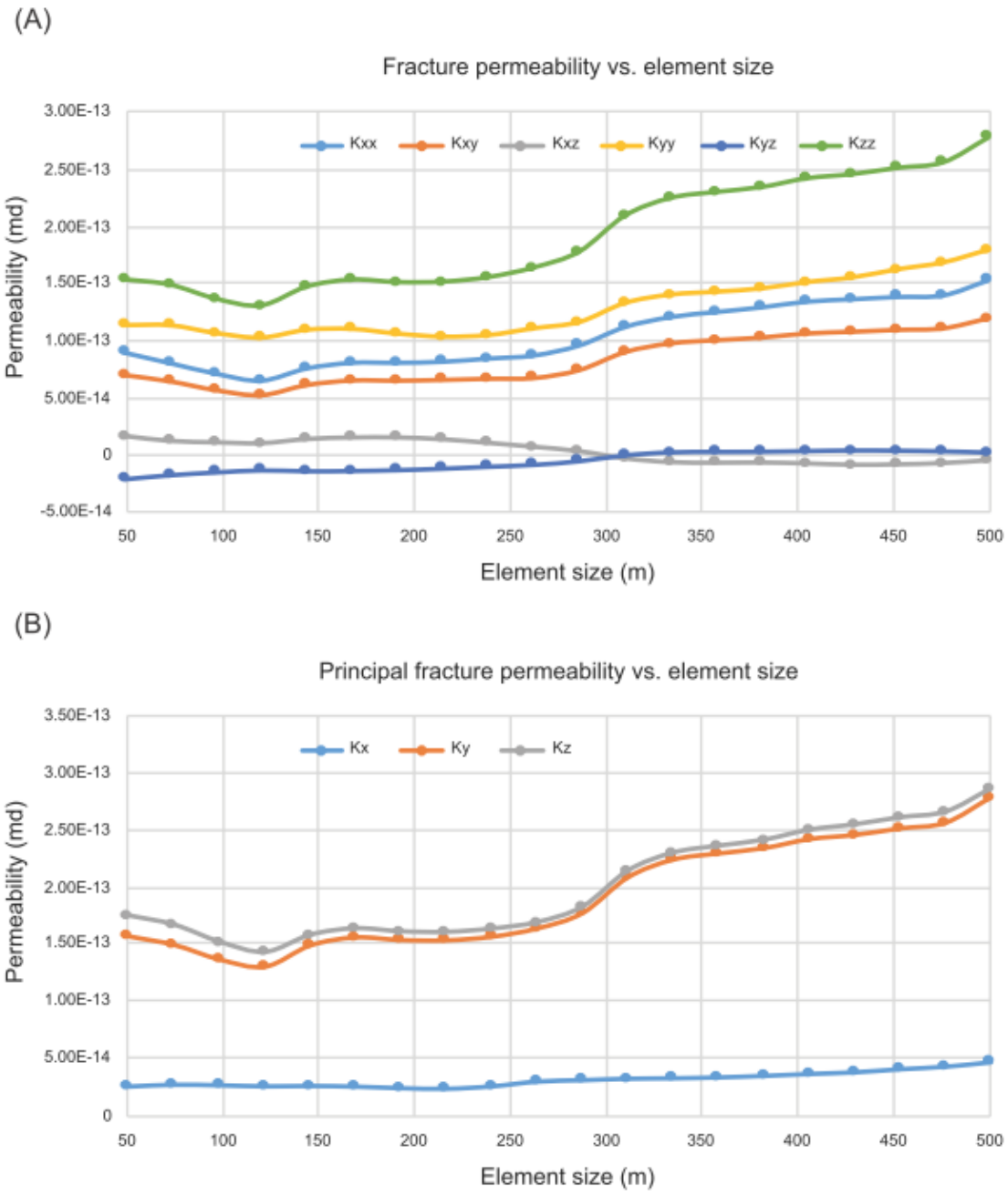

Figure 50.—Fracture permeability vs. element size, K = 10.

The pathway analysis suggests that there is no preferred hydraulic fracture orientation for optimal effectiveness (fig. 51). The number of interconnected fractures becomes very large due to the randomness of fracture orientations, and retains virtually the same value regardless of hydraulic fracture orientation. Moreover, the difference between the directly

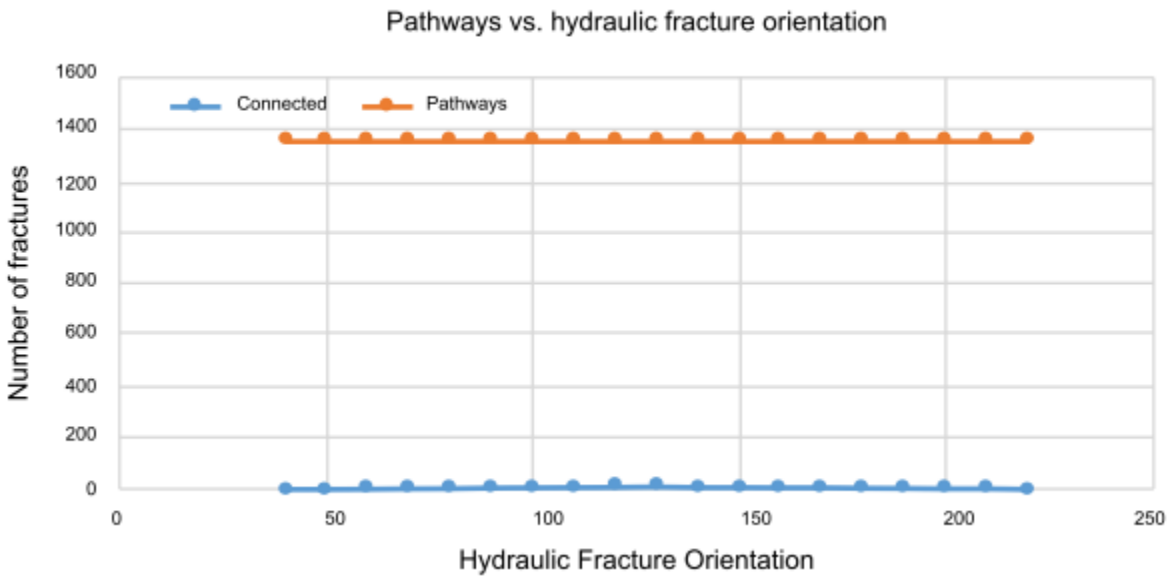

Figure 51.—Pathway analysis of hydraulic fracture in a single set DFN model, K = 10.

intersected fractures and the pathways is significant. Thus, it appears that hydraulic fracturing in a randomized fractured reservoir will be most effective, with virtually no preferred orientation required.

HYDRAULIC FRACTURING ANALYSIS FOR DEVONIAN CHATTANOOGA SHALE

A DFN model based on the core data and regional field data available for the Devonian Chattanooga Shale in the BWB was generated, with a primary fracture set predominantly oriented NE-SW, and a virtually perpendicular NW-SE oriented fracture set with 100% termination rate (fig. 52). The two fracture sets are both strata-bound and vertically (perpendicular to bedding) oriented. The apertures of the fractures are assumed to obey the exponential law, which indicates that a majority of fractures have aperture values less than the mean (fig. 53). The DFN model for the Chattanooga Shale suggests significant compartmentalization, with compartments of various sizes (fig. 54).

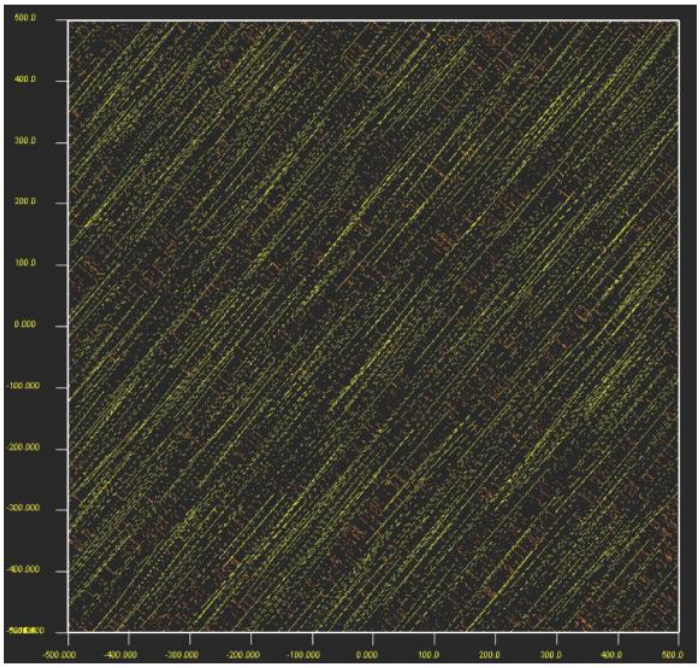

Figure 52.—DFN model for Devonian Chattanooga Shale. The x and y axes are for east and north coordinates in meters.

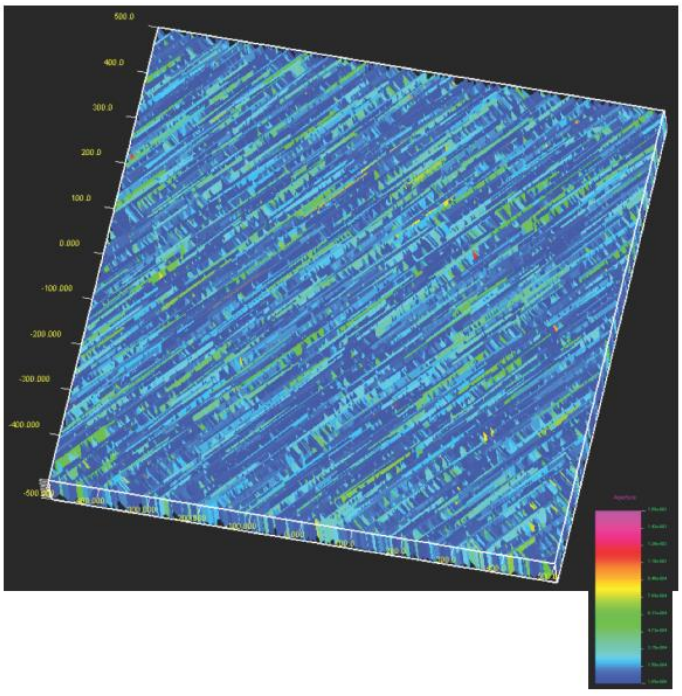

Figure 53.—Fracture networks color contoured by aperture for Chattanooga Shale. The x and y axes are for east and north coordinates in meters.

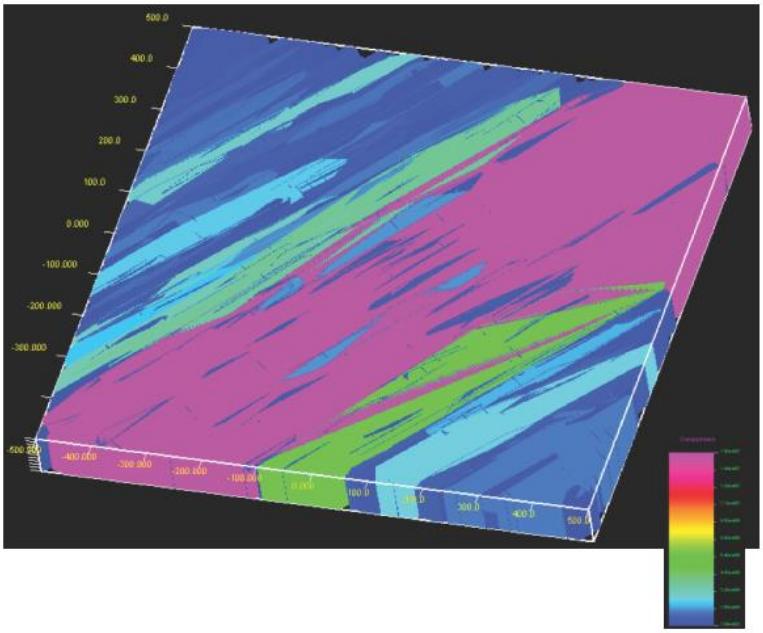

Figure 54.—Compartments color contoured by volume for Chattanooga Shale. The x and y axes are for east and north coordinates in meters.

Fracture permeability analysis based on the DFN model has been performed for various element sizes. There exists an REV at an element size larger than 150 m in the DFN model for the Devonian shale in the BWB (fig. 55), which is similar to results found for the Knox Group in the region (Clark and others, 2013; Jin, 2013). This indicates that the fractured shale reservoir can be treated as an anisotropic but homogeneous medium for fluid flow and transport modeling at such an element size. For example, the principal permeability tensor is calculated as:

$$K = \begin{bmatrix} 1.35E-13 & 0 & 0 \\ 0 & 2.28E-13 & 0 \\ 0 & -n_2 n_3 & 3.62E-13 \end{bmatrix} \qquad (2)$$

with the associated axial directions:

$$\begin{bmatrix} V_x \\ V_y \\ V_z \end{bmatrix} = \begin{bmatrix} -0.76053 & 0.649 & -0.0198 \\ -0.64913 & -0.76078 & 3.6E-5 \\ 0.01506 & -0.0129 & -0.9998 \end{bmatrix} \qquad (3)$$

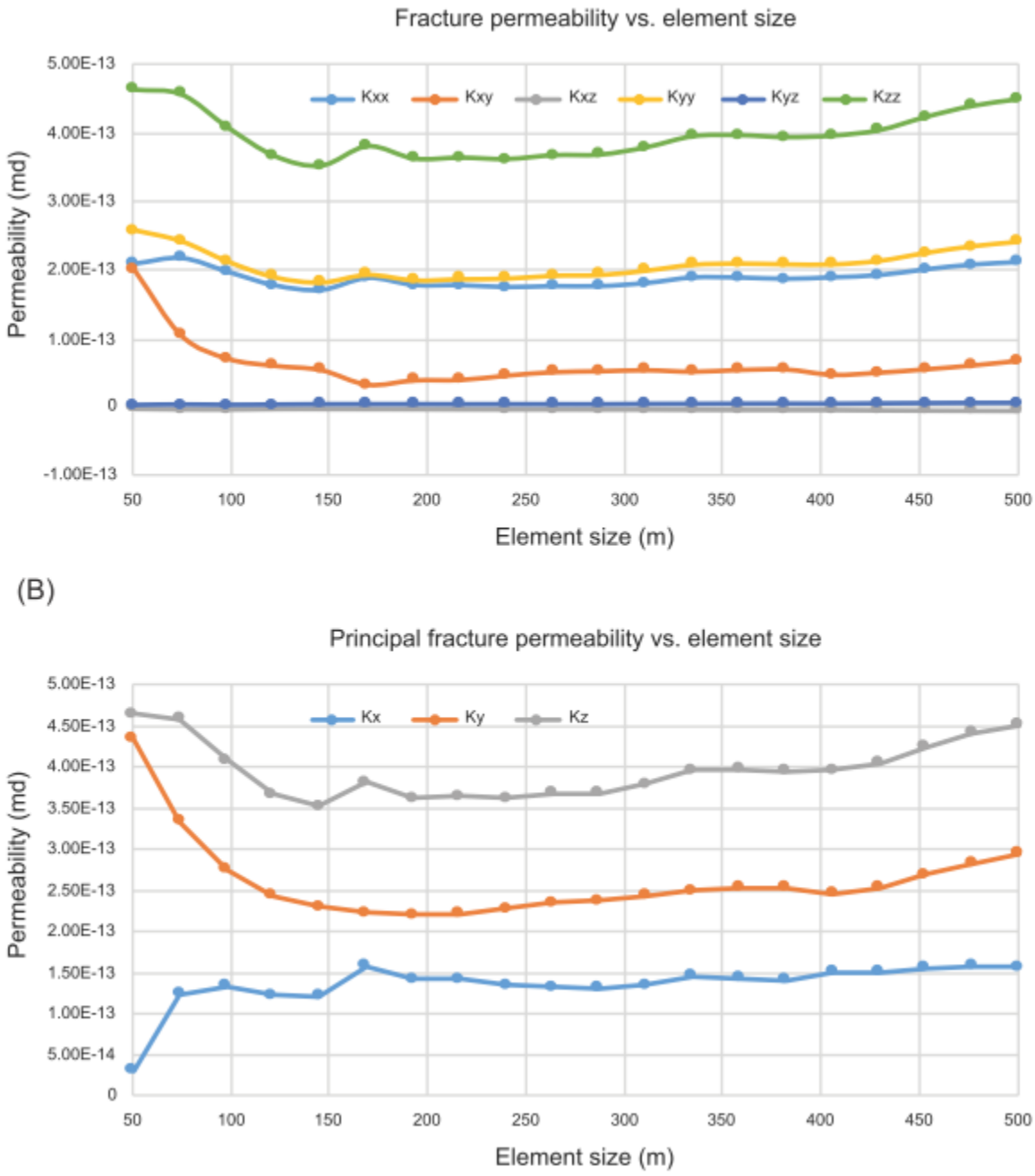

Figure 55.—Fracture permeability analysis for Chattanooga Shale.

The principal permeability tensor defined by equations 2 and 3 suggests an oblate (dish-shaped) ellipsoid standing vertically and elongated to the northeast, which indicates it is aligned with the regional preferred orientation of the system fracture set.

The pathway analysis of hydraulic fracturing from such a DFN model for the Devonian Chattanooga Shale suggests there is virtually no preferred orientation of hydraulic fractures required for maximum performance. The number of fractures interconnected by a hydraulic fracture is constant as long as it is not aligned with the system fractures (fig. 56). This result aligns with the previous single-set DFN model with randomized orientations (fig. 51), indicating that a cross-set DFN model is hydraulically equivalent to a randomized oriented DFN model in that they both provide continuous interconnected fracture pathways.

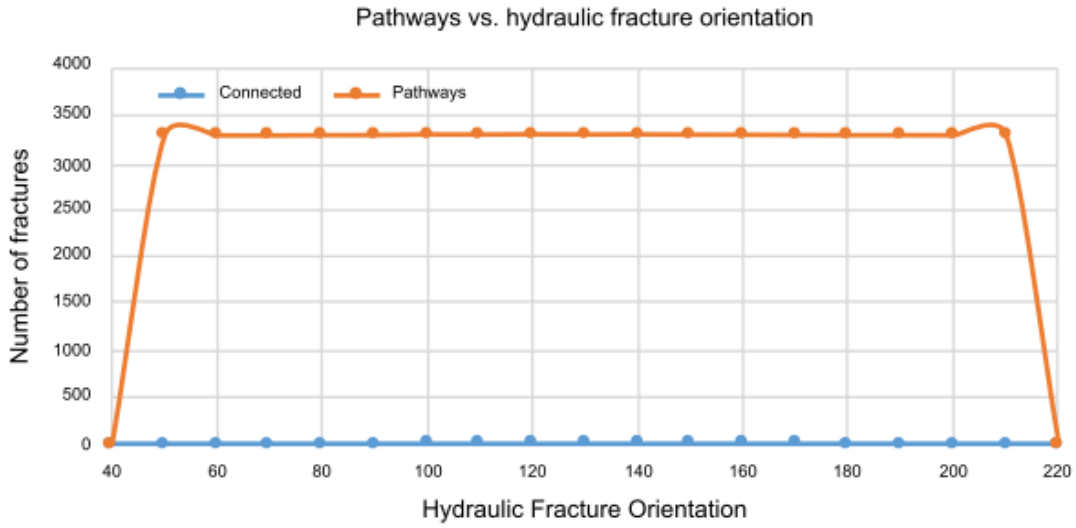

Figure 56.—Pathway analysis of hydraulic fracturing for Chattanooga Shale.

PETROLOGY AND GEOCHEMISTRY

DETRITAL COMPOSITION

Previous work on the detrital composition of Cambrian, Devonian, and Mississippian shale units in Alabama was reported by Pashin and others (2011). To their descriptions, a few observations may be added based on SEM study of Mississippian samples. Parkwood shale is similar to that of the Floyd (Pashin and others, 2011), consisting of detrital illite and chlorite,

with minor quartz. We did not observe organic material like that common in the Neal (organic-rich facies of the Floyd; Pashin and others, 2011), which suggests the Parkwood is not a promising target for gas exploration in Alabama.

The Lewis is a highly variable unit at the base of the Pride Mountain Formation. We examined samples of shale beds in the Lewis. In OGB PN 4054, Lewis shale is dominated by illite and chlorite with little admixture of other detrital minerals or organic matter. One sample included minor authigenic anhydrite, which could have formed syndepositionally. In OGB PN 4305, iron sulfate indicates an oxidation zone; this may be debris remobilized from the nearby shelf to the northeast. That is more likely than prolonged subaerial exposure at this basinal site in Lamar County (fig. 3). Shale from OGB PN 4801 contains abundant silt- and clay-size quartz, but this may be authigenic. In OGB PN 5321 the Lewis contains the typical clay shale, but also quartzose claystone relatively free of clay minerals. These laminae may be distal event deposits, like turbidites or other gravity-flow deposits. We did not observe fragments of organic material. Because the Lewis is thin, heterogeneous, and organic-lean, it is not likely to produce commercial quantities of gas in Alabama.

AUTHIGENESIS

Diagenesis of shale results from an interplay of sediment characteristics and the evolving physico-chemical environment. Physical diagenesis involves rotation and compaction of particles, and expulsion of water. Chemical diagenesis is dominated by the formation of new minerals and the cementation of existing components to form solid rock. Authigenesis is the formation of new rock components, such as crystals, after deposition. These processes can have sweeping effects on pore systems.

Well-formed crystals of illite and other clay minerals, which tend to be thin but broad, are good at blocking pores. However, there is little evidence in the samples we examined of clay

crystals growing into pores. The most obvious exception is within pyrite crystal clusters (fig. 17), with little effect on fluid flow (because the clusters are small and widely spaced).

Petrophysical characteristics of uncommon quartzose clay- or siltstone laminae in Lewis shale are not well known. This deserves more study if gas reservoirs are discovered in the Lewis, as these laminae could become conduits for fluid flow or barriers to it, depending on the scope of cementation. By contrast, highly visible authigenic components such as pyrite or celestine crystal clusters do not have much effect on the movement of water or gas. This is because they are small and widely spaced. Fluids moving in or out of these crystal clusters travel great distances among clay particles, which controls their large-scale movement.

There does not seem to be any evidence for large-scale occlusion of pores by diagenetic crystal growth. Most micropores and nanopores are among or within clay particles or crystals.

MICROFABRIC

CAMBRIAN

Anastomosing ridges on the surfaces of clay-size calcite crystals in a lime mudstone lamina in core from OGB PN 3518 suggest that the surfaces had been colonized by nanobacteria (fig. 14). This distinctive surface texture was observed on numerous calcite particles in this specimen, but on no other samples examined for this project, including two other samples of lime mudstone from the Conasauga in this well. This kind of surface texture was not reported by Pashin and others (2011), further indicating that it is uncommon in Alabama Paleozoic shale units.

Conasauga shale in this well is dominated by clay fragments oriented in all different directions (fig. 57). This indicates deposition with little subsequent reorientation under the pressure of overlying sediment. Unlike younger Paleozoic shale units in Alabama, Conasauga shale is relatively free of coarser siliciclastic debris (Pashin and others, 2011).

Carbonate layers consist of anhedral fitted particles of calcite (fig. 15). Loose clusters of pyrite are characterized by homogeneous crystal sizes, although clusters of finer and coarser crystals are often adjacent to one another (fig. 17). This suggests repeated pyrite precipitation in the same areas at different rates.

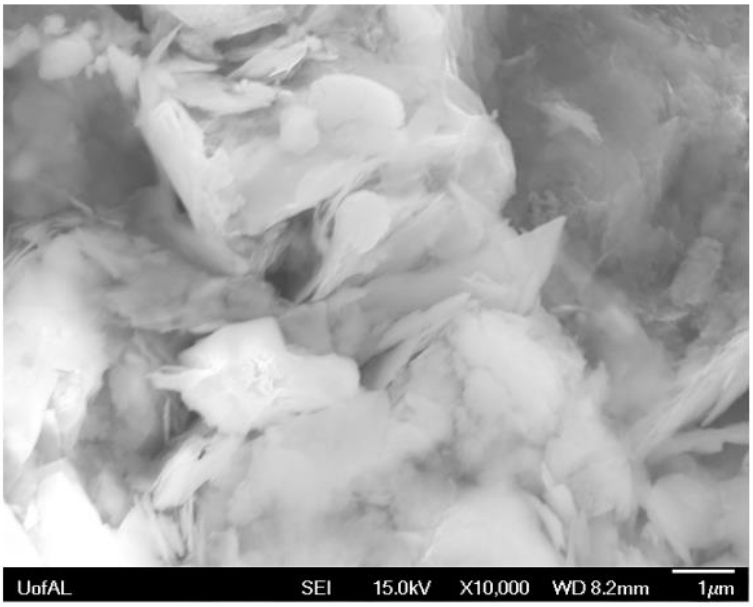

Figure 57.—Intercrystalline microporosity in loose illite fabric in clay shale, Cambrian Conasauga Formation; sample from 14,192 ft., OGB PN 3518 (ARCO/Anschutz Alabama Property Co. 15-11 #1). SEM secondary electron image, scale 1 μm.

MISSISSIPPIAN

BANGOR LIMESTONE

We studied one Bangor core, from OGB PN 1160 (fig. 26), and examined a single sample with the SEM (depth 5,220-5,221 ft.). This sample consists primarily of clay-size calcite anhedra. These are in places fitted, and in places separated by voids (fig. 58). The particles, as well as the spaces between them, have complex shapes.

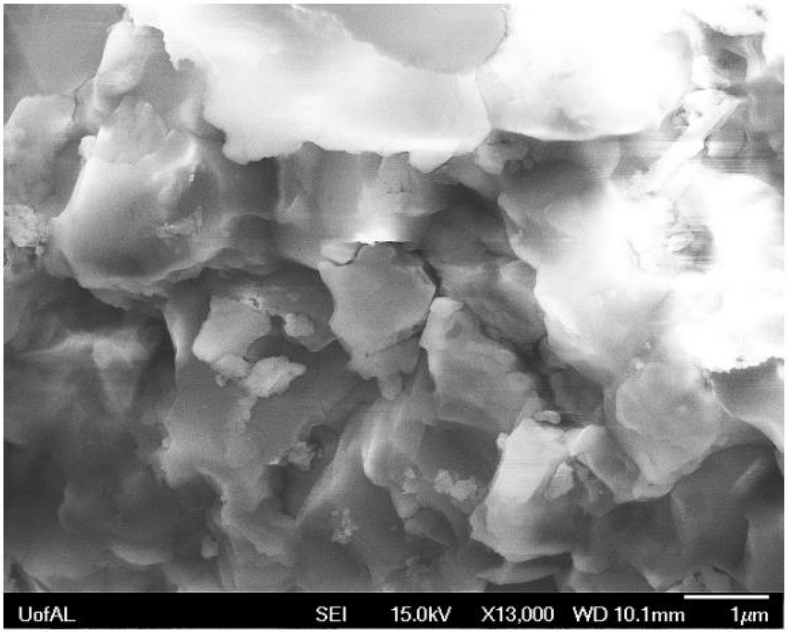

Figure 58.—Nanoporosity among calcite anhedra in Bangor lime mudstone; sample from depth 5,220-5,221 ft., OGB PN 1160 (James B. Hill #1). SEM secondary electron image, scale 1 μm.

FLOYD (NEAL) SHALE

The Neal facies of the Floyd Shale is the only Mississippian unit in Alabama that is thought likely to contain commercial quantities of gas hosted by shale. Neal cores were described as part of the study conducted by Pashin and others (2011) (fig. 25; figs. A6, A7); we examined three samples of a Neal core (OGB PN 13979; fig. 25) with two different SEMs as part of this study. The samples that we examined using FIB (3700 and 3732.4 feet, table 2) show well-connected micro- and nanoporosity (videos 1 through 4). Pores are smaller but better connected in the shallower sample, which did not appear to differ to the naked eye. Permeability values of these two intervals have not been measured.

LEWIS SHALE

Several SEM samples give us a good understanding of Lewis microfabric (table 2). Lewis shale is dominated by platy clay particles, most of clay size and a few slightly larger. Because the particles are mostly subhorizontal, there is only room for small pores. A possible fungal

boring normal to bedding (fig. 33) probably formed relatively recently, and in any case such pores appear to be quite uncommon, as we observed only one. This is the only unit in which we observed true pyrite framboids (fig. 59). They are rare, even here, in contrast to the Neal and Chattanooga shales (Pashin and others, 2011). Framboids commonly form in the water column, unlike loose crystal clusters, which always form in place in sediment. Thus, framboids indicate conditions conducive to preservation of organic matter in the lower part of the water column, or in unlithified sediment (Sawlowicz, 1993; Wilkin and Barnes, 1997); crystal clusters always indicate shallow-groundwater conditions. We did not observe significant amounts of organic material in the Lewis. However, the Lewis is heterogeneous, and it may contain more organic material elsewhere.

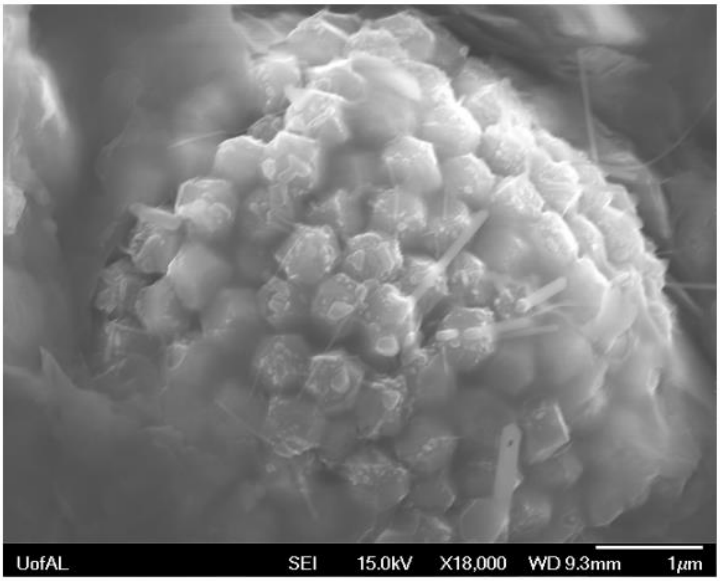

Figure 59.—Pyrite framboid in Lewis shale (an informal unit), composed of pyritohedrons; sample from 4,667 ft., OGB PN 5321 (Stanley 22-12 #1). SEM secondary electron image, scale 1 μm.

PARKWOOD FORMATION

Two samples from the Parkwood were examined via SEM (table 2). One sample of shale in OGB PN 3707 (fig. 35) consists of relatively equant clay- and silt-size particles (fig. 60). Another sample, from OGB PN 4054 (fig. 28), contains large fragments of organic material (fig.

61), but otherwise consists of the same kind of matrix. Both samples are dominated by clay, but contain a variety of other minerals. These few observations add little to our understanding of the Parkwood.

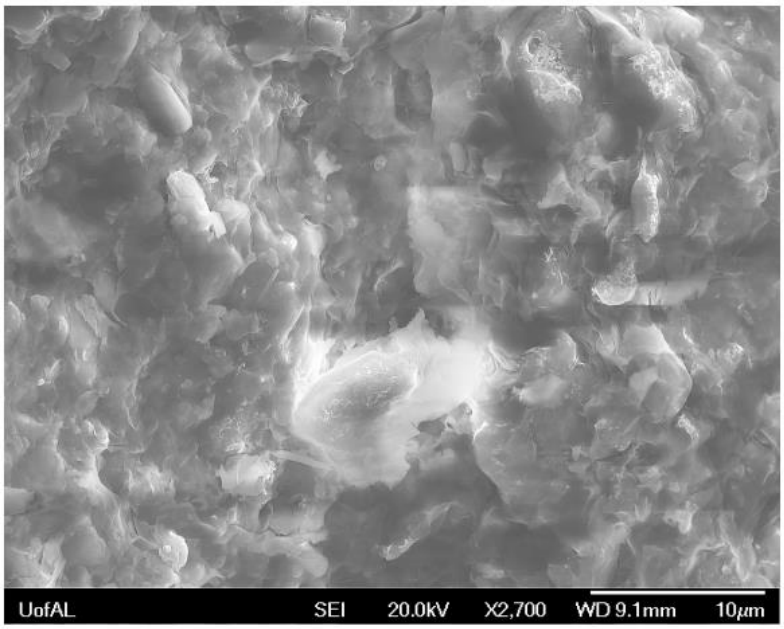

Figure 60.—Equant clay particles in Parkwood Formation; sample from 3,984 ft., OGB PN 3707 (Cobb 30-12 #1). SEM secondary electron image, scale 10 μm.

MICROPOROSITY

CAMBRIAN

The Conasauga Formation, the only unit currently producing hydrocarbons from shale in Alabama, was described in Pashin and others (2011); see also figure A1. For the present study, an SEM was used to investigate composition, rock fabric, and porosity in this unit. OGB PN 3518 (fig. 13) was examined using an SEM, revealing intercrystalline nano- and microporosity

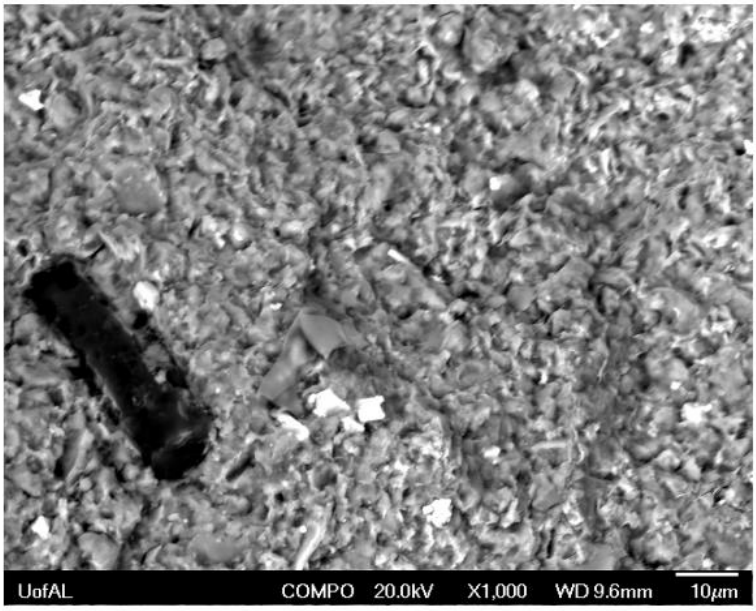

Figure 61.—Organic-rich clay particle (dark color), Mississippian Parkwood; sample from 3,763 ft., OGB PN 4054 (Patterson 20-5 #1). SEM backscatter electron image, scale 10 μm.

among clay flakes (fig. 57) and within splayed clay books in clay shale. Nano- and microporosity within pyrite crystal clusters (not framboids) is clearly visible but not volumetrically significant. Lime mudstone layers were found to be essentially nonporous. Argillaceous microcrystalline dolostone contains minor crystal-moldic microporosity, but is an uncommon rock type in the Conasauga.

MISSISSIPPIAN

The Floyd (Neal) Shale, a primary target of shale-gas exploration in Alabama, and studied by Pashin and others (2011), received further scrutiny as part of this project. Three samples of shale from OGB PN 13979 (table 2; fig. 25) were analyzed with the SEM, and two of them were serially sectioned with FIB. Serial sectioning allows visual representation of the shapes and connectivity of pores (videos 1 through 4). Two samples were analyzed so that the results could be compared, giving an idea of within-group variation in pore-system topology.

The sample from 3,700 feet in OGB PN 13979 consists of dark gray shale in an interval containing numerous lime-mudstone laminae. Most voids rim particles and are well-connected at the scale of analysis (video 1, secondary electrons), which was approximately a cube 10 μm on a side (fig. 10). Pyrite crystal clusters contain nanoporosity (fig. 17), but seem to have no effect on the pore system at this scale (bright objects in video 2, backscatter electrons). This is because, compared to the connected voids, pyrite crystal clusters are small and widely spaced. They can make a small contribution to effective porosity where they are intersected by fractures. Because the videos include every fifth recorded surface, the frames show surfaces that are 330 nm apart.

The sample from 3,732.4 feet in OGB PN 13979 also comes from a dark shale with lime-mudstone laminae (fig. 25). At the scales of naked-eye to thin-section examination, these two samples come from lithologically nearly identical locations. Nevertheless, the sample from 3,700 ft. is far more porous and permeable than the sample from 3,732.4 ft. The micro- and nanoscale pore systems at these two depths are radically different. Pore systems are not homogeneous at the scale of meters in these fine-grained rocks. In the absence of permeable systems of fractures (natural or otherwise), pore-system heterogeneity is important.

Other Mississippian units that we sampled are not known to contain sufficient quantities of organic material to become shale-gas reservoirs. However, some do have micro- and nano-scale pore systems. These include the Lewis and Parkwood. For instance, the intracrystalline nanoporosity in partially crushed illite crystals (OGB PN 5321, fig. 62) and the interparticle nanoporosity (OGB PN 4054, fig. 63) can be significant. A possible fungal boring normal to bedding probably formed relatively recently, and in any case such pores appear to be uncommon. The Lewis is heterogeneous, and it may contain very different pore systems elsewhere. One sample of Parkwood shale in OGB PN 3707 (fig. 35) may contain significant interparticle

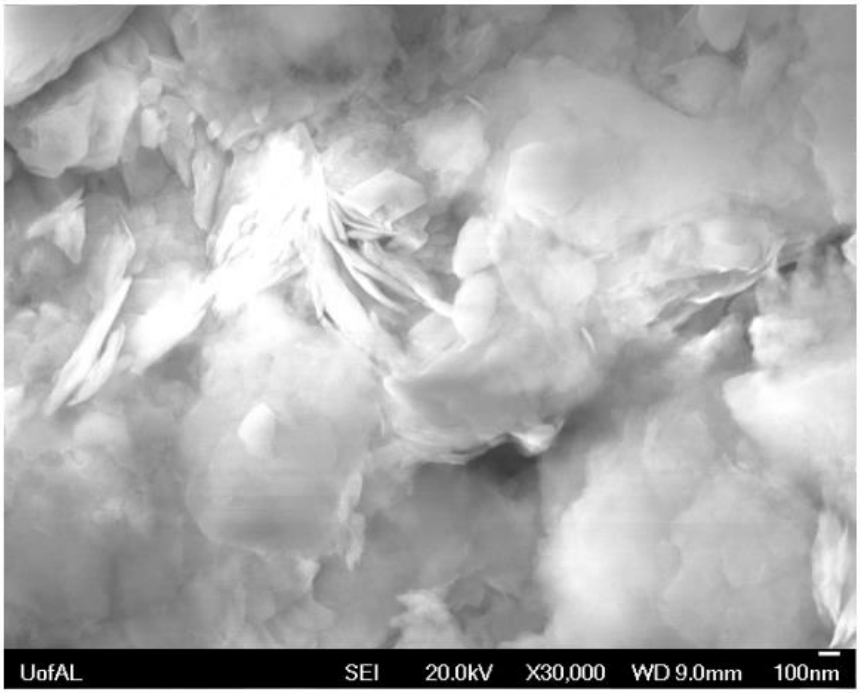

Figure 62.—Nanoporosity within partially crushed illite crystals, Mississippian Lewis shale (an informal unit); sample from 4,667 ft., OGB PN 5321 (Stanley 22-12 #1). SEM secondary electron image, scale 100 nm.

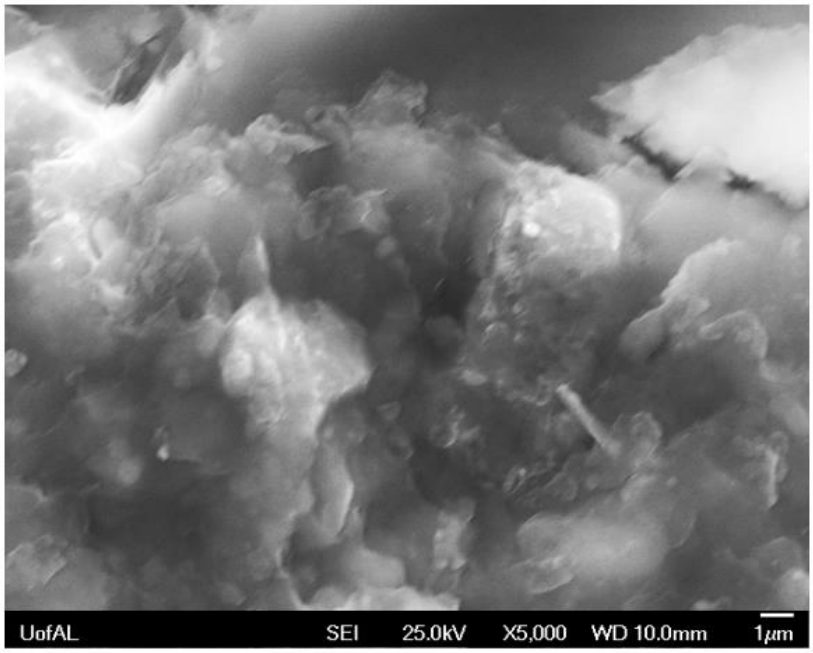

Figure 63.—Interparticle nano- and microporosity, Mississippian Lewis shale (an informal unit); sample from 4,486 ft., OGB PN 4054 (Patterson 20-5 #1). SEM secondary electron image, scale 1 μm.

nanoporosity (fig. 60). Another sample, from OGB PN 4054, shows little discernible microporosity, but contains large fragments of organic material (fig. 61) and also may contain nanoporosity. Perhaps the Parkwood has both porosity and gas in some places.

CONCLUSIONS

Core descriptions and SEM studies confirm that the Mississippian Neal black-shale facies of the Floyd Shale is the only Paleozoic shale unit with known shale-gas potential in Alabama. Other Mississippian units, notably the Parkwood and the Lewis, younger and older than the Neal, respectively, are locally porous and permeable. These units may contain commercial quantities of shale gas if sufficient organic material is present. However, the relative scarcity of organic debris and early-formed pyrite in these gray shales, as revealed by SEM analysis, does not indicate the presence of potential gas-prone facies where the Lewis and Parkwood have been cored. All available cores of these units have been examined (Pashin and others, 2011; this report), but they are too few for definitive conclusions. The abundance, distribution, and other characteristics of organic material in the Lewis and Parkwood are not yet known in sufficient detail to rule out the possibility of shale-gas resources occurring locally in either formation.

The use of FIB permits serial sectioning of areas that are just a few micrometers across. This technique will permit 3D mapping of pore systems, which could allow estimation of properties such as permeability and tortuosity of pore systems. This kind of analysis also will allow 3D element and mineral mapping at the same scale.

The DFN technique can provide valuable insights into fractured-reservoir characterization. In DFN models with moderately and highly directionally concentrated fractures, there exists an REV for fracture-permeability characterization, which indicates the fractured reservoirs represented by such DFN models can be treated as anisotropic homogeneous media. A DFN model with randomized fracture orientations, on the other hand, lacks an REV for

fracture characterization. Therefore, the fracture-permeability tensor has to be computed from each element for fluid flow and transport modeling. In DFN models with highly or moderately directionally concentrated fractures, hydraulic fracturing will be most effective if the orientation of the hydraulic fracture is perpendicular to the mean direction of the natural fracture set. In a DFN model with randomized fracture orientations, there exists no preferred direction for a hydraulic fracture to be most effective, thanks to the interconnected pathways of the natural fracture network.

Fracture permeability mapping can be extrapolated to reservoir scale from commonly limited surface and well/core data. In the BWB, the Devonian Chattanooga Shale was selected for fractured-reservoir characterization and hydraulic-fracturing optimization analysis. Our studies indicate that the Chattanooga Shale is highly fractured, with most fractures perpendicular to bedding with smooth surfaces, suggesting a structural origin. Fracture-permeability and hydraulic-fracturing pathway analysis of the Devonian Chattanooga Shale suggest that an REV does exist for fluid flow and transport modeling at element sizes larger than 200 m. At such an element size, the fractured-shale reservoir can be represented by anisotropic homogeneous media defined by a principal permeability tensor. Hydraulic-pathway analysis indicates that hydraulic fracturing can be equally effective for hydrocarbon fluid/gas exploration as long as its orientation is not aligned with that of the regional system fractures.

ACKNOWLEDGMENTS

The following current and former staff of the Geological Survey of Alabama (GSA) contributed materially to this research: Levi Crooke, Steve Mann, and Ashley Quarles. Johnny Goodwin and Rich Martens of the University of Alabama Central Analytical Facility were a great help with data collection and training of GSA staff.

REFERENCES CITED

Anderson, J., and Dverstrop, B., 1987, Conditional simulation of fluid flow in three-dimensional networks of discrete fractures: Water Resources Research, v. 23, no. 10, p. 1876-1886, doi:10.1029/WR023i010p01876.

Astini, R. A., Thomas, W. A, and Osborne, W. E., 2000, Sedimentology of the Conasauga Formation and equivalent units, Appalachian thrust belt in Alabama, *in* Osborne, W. E., Thomas, W. A., and Astini, R. A., eds., The Conasauga Formation and equivalent units in the Appalachian thrust belt in Alabama: Tuscaloosa, Alabama Geological Society 31st Annual Field Trip Guidebook, p. 41-71.

Ayers, W. B., Jr., and Kaiser, W. A., eds., 1994, Coalbed methane in the Upper Cretaceous Fruitland Formation, San Juan Basin, Colorado and New Mexico: Texas Bureau of Economic Geology Report of Investigations 218, 216 p.

Butts, Charles, 1910, Description of the Birmingham Quadrangle, Alabama: U.S. Geological Survey Geologic Atlas, Folio 175, 24 p.

___1926, The Paleozoic rocks, *in* Adams, G. I., Butts, Charles, Stephenson, L. W., and Cooke, C. W., Geology of Alabama: Alabama Geological Survey Special Report 14, p. 40-230.

___1927, Bessemer–Vandiver folio: U.S. Geological Survey Geologic Atlas, Folio 221, 22 p.

Cacas, M. C., Ledoux, E., de Marsily, G., Title, B., Barbreau, A., Durand, E., Feuga, B., and Peaudecerf, P., 1990, Modeling fracture flow with a stochastic discrete fracture network: Calibration and validation 1, Flow model: Water Resources Research, v. 26, no. 3, p. 479-489, doi:10.1029/WR026i003p00479.

Carroll, R. E., Pashin, J. C., and Kugler, R. L., 1995, Burial history and source-rock characteristics of Upper Devonian through Pennsylvanian strata, Black Warrior basin, Alabama: Alabama Geological Survey Circular 187, 29 p.

Cisar, J. O., Xu, D.-Q., Thompson, John, Swaim, William, Hu, Lan, and Kopecko, D. J., 2000, An alternative interpretation of nanobacteria-induced biomineralization: Proceedings of the National Academy of Sciences, v. 97, no. 21, p. 11511-11515, doi:10.1073/pnas.97.21.11511.

Clark, P. E., Pashin, J. C., Carlson, E. S., Goodliffe, A. M., McIntyre-Redden, M. R., Jin, G., Mann, S. D., and Thompson, M., 2013, Site characterization for CO_2 storage from coal-fired power facilities in the Black Warrior Basin of Alabama: Final Report, U.S. Department of Energy Award DEFE0001910, 219 p.

Cleaves, A. W., 1983, Carboniferous terrigenous clastic facies, hydrocarbon producing zones, and sandstone provenance, northern shelf of Black Warrior basin: Gulf Coast Association of Geological Societies Transactions, v. 33, p. 41-53.

Cleaves, A. W., and Broussard, M. C., 1980, Chester and Pottsville depositional systems, outcrop and subsurface, in the Black Warrior basin of Mississippi and Alabama: Gulf Coast Association of Geological Societies Transactions, v. 30, p. 49-60.

Dershowitz, W. S., 1985, Rock joint system: Cambridge, Massachusetts Institute of Technology, Ph.D. dissertation, 918 p.

Dershowitz, W. S., and Einstein, H. H., 1988, Characterizing rock joint geometry with joint system models: Rock Mechanics and Rock Engineering, v. 21, no. 1, p. 21-51.

Dunham, R. J., 1962, Classification of carbonate rocks according to depositional texture, *in* Ham, W. E., ed., Classification of carbonate rocks: American Association of Petroleum Geologists Memoir 1, p. 108-121.

Folk, R. L., and Chafetz, H. S., 2000, Bacterially induced microscale and nanoscale carbonate precipitates, *in* Riding, R. E., and Awramik, S. M., eds., Microbial sediments: Springer-Verlag, p. 40-49.

Folk, R. L., and Lynch, F. L., 1997, Nanobacteria are alive on Earth as well as Mars: *in* Conference on Instruments, methods, and missions for the investigation of extraterrestrial microorganisms, San Diego, California, July 11, 1997, Proceedings: San Diego, Calif., SPIE, v. 3111, p. 406, doi:10.1117/12.278795.

Haynes, C. D., Malone, P. G., and Camp, B. S., 2010, Exploration of the shallow Chattanooga Shale in north central Alabama, *in* Symposium on International Coalbed and Shale Gas: Tuscaloosa, Alabama, 2010 International Coalbed and Shale Gas Symposium Proceedings, Paper 1015, 16 p.

Hill, R. J., and Jarvie, D. M., eds., 2007, Barnett Shale: American Association of Petroleum Geologists Bulletin, v. 91, no. 4, p. 399-622.

Jin, G., 2013, A novel approach to characterization of effective permeability for naturally fractured reservoirs [abs.]: Abstract H53A-1402 presented at 2013 Fall Meeting of the American Geophysical Union, San Francisco, California.

Jin, G., and Pashin, J. C., 2013, Multiphase flow modeling of CO_2 injected into deep saline fractured reservoirs in Knox Group, Black Warrior Basin, Alabama [abs.]: Geological Society of America Abstracts with Programs, v. 45, no. 7, p. 750.

Kajander, E. O., and Çiftçioglu, Neva, 1998, Nanobacteria: An alternative mechanism for pathogenic intra- and extracellular calcification and stone formation: Proceedings of the National Academy of Sciences, v. 95, no. 14, p. 8274–8279.

Khullar, Madhu, Sharma, S. K., Singh, S. K., Bajwa, P., Sheikh, F. A., Relan, V., and Sharma, M., 2004, Morphological and immunological characteristics of nanobacteria from human renal stones of a north Indian population: Urological Research, v. 32, no. 3, p. 190-195, doi:10.1007/s00240-004-0400-3.

Kirkland, B. L., Lynch, F. L., Rahnis, M. A., Folk, R. L., Molineux, I. J., and McLean, R. J. C., 1999, Alternative origins for nannobacteria-like objects in calcite: Geology, v. 27, p. 347-350, doi:10.1130/0091-7613(1999)027<0347:AOFNLO>2.3.CO;2.

Lee, S. H., Lough, M. F., and Jensen, C. L., 2001, Hierarchical modeling of flow in naturally fractured formations with multiple length scales: Water Resources Research, v. 37, no. 3, p. 443-455, doi:10.1029/2000WR900340.

Long, J. C. S., Remer, J. S. , Wilson, C. R. , and Witherspoon, P. A., 1982, Porous media equivalents for networks of discontinuous fractures: Water Resources Research, v. 18, no. 3, p. 645-658, doi:10.1029/WR018i003p00645.

Long, J. C. S., Gilmour, P., and Witherspoon, P. A., 1985, A model for steady fluid flow in random three-dimensional networks of disc-shaped fractures, Water Resources Research, v. 21, no. 8, p. 1105-1115, doi:10.1029/WR021i008p01105.

Lysak, L. V., Kadulin, M. S., Konova, I. A., Lapygina, E. V., Ivanov, A. V., and Zvyagintsev, D. G., 2013, Population number, viability, and taxonomic composition of the bacterial nanoforms in iron-manganic concretions: Eurasian Soil Science, v. 46, no. 6, p. 668-675, doi:10.1134/S1064229313060069.

Markello, J. R., and Read, J. F., 1982, Upper Cambrian intrashelf basin, Nolichucky Formation, southwest Virginia Appalachians: American Association of Petroleum Geologists Bulletin, v. 66, no. 7, p. 860-878.

Mars, J. C., and Thomas, W. A., 1999, Sequential filling of a late Paleozoic foreland basin: Journal of Sedimentary Research, v. 69, no. 6, p. 1191-1208, doi:10.2110/jsr.69.1191.

Nuttall, B. C., Drahovzal, J. A, Eble, C. F., and Bustin, R. M., 2009, Regional assessment of organic-rich gas shales for carbon sequestration: an example from the Devonian shales of the Illinois and Appalachian basins, Kentucky, *in* Grobe, M., Pashin, J. C., and Dodge, R. L., eds., Carbon dioxide sequestration in geological media: State of the science: American Association of Petroleum Geologists Studies in Geology 59, p. 173-190.

Osborne, W. E., Thomas, W. A., Astini, R. A., and Irvin, G. D., 2000, Stratigraphy of the Conasauga Formation and equivalent units, Appalachian thrust belt in Alabama, *in* Osborne, W. E., Thomas, W. A., and Astini, R. A., eds., The Conasauga Formation and equivalent units in the Appalachian thrust belt in Alabama: Tuscaloosa, Alabama, Alabama Geological Society 37th Annual Field Trip Guidebook, p. 1-17.

Pashin, J. C., 1993, Tectonics, paleoceanography, and paleoclimate of the Kaskaskia sequence in the Black Warrior basin of Alabama, *in* Pashin, J. C., ed., New Perspectives on the Mississippian System of Alabama: Tuscaloosa, Alabama, Alabama Geological Society 30th Annual Field Trip Guidebook, p. 1-28.

___1994, Cycles and stacking patterns in Carboniferous rocks of the Black Warrior foreland basin: Gulf Coast Association of Geological Societies Transactions, v. 44, p. 555-563.

___2004, Cyclothems of the Black Warrior basin in Alabama: eustatic snapshots of foreland basin tectonism, *in* Pashin, J. C., and Gastaldo, R. A., eds., Sequence stratigraphy, paleoclimate, and tectonics of coal-bearing strata: American Association of Petroleum Geologists Studies in Geology 51, p. 199-217.

___2007, Hydrodynamics of coalbed methane reservoirs in the Black Warrior Basin: key to understanding reservoir performance and environmental issues: Applied Geochemistry, v. 22, no. 10, p. 2257-2272, doi:10.1016/j.apgeochem.2007.04.009.

___2008, Gas shale potential of Alabama, *in* Symposium on International Coalbed and Shale Gas: Tuscaloosa, Alabama, 2008 International Coalbed and Shale Gas Symposium Proceedings, Paper 0808, 13 p.

___2009, Shale gas plays of the southern Appalachian thrust belt, *in* Symposium on International Coalbed and Shale Gas: Tuscaloosa, Alabama, 2009 International Coalbed and Shale Gas Symposium Proceedings, Paper 0907, 14 p.

___2010, Mature coalbed natural gas reservoirs and operations in the Black Warrior basin of Alabama, *in* Reddy, K. J., ed., Coalbed natural gas: Energy and environment: Haupage, New York, Nova Science Publishers, p. 31-57.

Pashin, J. C., Carroll, R. E., McIntyre, M. R., and Grace, R. L. B., 2010, Geology of unconventional gas plays in the southern Appalachian thrust belt: Society for Sedimentary Geology (SEPM) Guidebook, Field Trip 7, American Association of Petroleum Geologists Annual Conference and Exposition, New Orleans, Louisiana, 86 p.

Pashin, J. C., and Ettensohn, F. R., 1995, Reevaluation of the Bedford-Berea sequence in Ohio and adjacent states: forced regression in a foreland basin: Geological Society of America Special Paper 298, 68 p., doi:10.1130/SPE298.

Pashin, J. C., Grace, R. L. B., and Kopaska-Merkel, D. C., 2010, Devonian shale plays in the Black Warrior basin and Appalachian thrust belt of Alabama, *in* Symposium on International Coalbed and Shale Gas: Tuscaloosa, Alabama, 2010 International Coalbed and Shale Gas Symposium Proceedings, Paper 1016, 20 p.

Pashin, J. C., Grace, R. L. B., and Kopaska-Merkel, D. C., 2011, Geological foundation for production of natural gas from diverse shale formations: Tuscaloosa, Alabama Geological Survey, topical report prepared for the Research Partnership to Secure Energy for America (RPSEA) under Subcontract 07122-17, 120 p.

Pashin, J. C., and Groshong, R. H., Jr., 1998, Structural control of coalbed methane production in Alabama: International Journal of Coal Geology, v. 38, no. 1-2, p. 89-113, doi:10.1016/S0166-5162(98)00034-2.
Pashin, J. C., and Hinkle, F., 1997, Coalbed methane in Alabama: Alabama Geological Survey Circular 192, 71 p.
Pashin, J. C., Jin, G., and Payton, J. W., 2004, Three-dimensional computer models of natural and induced fractures in coalbed methane reservoirs of the Black Warrior basin: Alabama Geological Survey Bulletin 174, 62 p.
Pashin, J. C., Jin, G., Zheng, C., Chen, S., and McIntyre, M. R., 2008, Discrete fracture networks for risk assessment of carbon sequestration in coal: Final technical report, U.S. Department of Energy, National Energy Technology Laboratory, Award DE-FC26-05NT42435, 118 p.
Pashin, J. C., and Kugler, R. L., 1992, Delta-destructive spit complex in Black Warrior basin: facies heterogeneity in Carter sandstone (Chesterian), North Blowhorn Creek oil unit, Lamar County, Alabama: Gulf Coast Association of Geological Societies Transactions, v. 42, p. 305-325.
Pashin, J. C., Ward, W. E., II, Winston, R. B., Chandler, R. V., Bolin, D. E., Richter, K. E., Osborne, W. E., and Sarnecki, J. C., 1991, Regional analysis of the Black Creek-Cobb coalbed-methane target interval, Black Warrior basin, Alabama: Alabama Geological Survey Bulletin 145, 127 p.
Pouya, A., and Fouche, O., 2009, Permeability of 3D discontinuity networks: new tensors from boundary-conditioned homogenization: Advances in Water Resources, v. 32, p. 303-314, doi:10.1016/j.advwatres.2008.08.004.
Rodgers, John, 1950, Mechanics of Appalachian folding as illustrated by the Sequatchie anticline, Tennessee and Alabama: American Association of Petroleum Geologists Bulletin, v. 34, no. 4, p. 672-681.
Ross, D. J. K., and Bustin, R. M., 2008, Characterizing the shale gas resource potential of Devonian-Mississippian strata in the Western Canada sedimentary basin: Application of an integrated formation evaluation: American Association of Petroleum Geologists Bulletin, v. 92, p. 87-125, doi:10.1306/09040707048.
Sawlowicz, Z., 1993, Pyrite framboids and their development: a new conceptual mechanism: Geologische Rundschau, v. 82, no. 1, p. 148-156, doi:10.1007/BF00563277.
Schieber, J., Zimmerle, W., and Sethi, P. S., 1998, Shales and mudstones: Stuttgart, Germany, E. Schweizerbart Verlagsbuchhandlung, 2 v., 680 p.
Scott, A. R., 2002, Hydrogeologic factors affecting gas content distribution in coal beds: International Journal of Coal Geology, v. 50, p. 363-387, doi:10.1016/S0166-5162(02)00135-0.
Telle, W. R., Thompson, D. A., Lottman, L. K., and Malone, P. G., 1987, Preliminary burial-thermal history investigations of the Black Warrior basin: implications for coalbed methane and conventional hydrocarbon development, *in* Symposium on Coalbed Methane: Tuscaloosa, Alabama, 1987 Coalbed Methane Symposium Proceedings, p. 37-50.
Thomas, W. A., 1972, Mississippian stratigraphy of Alabama: Alabama Geological Survey Monograph 12, 121 p.
___1977, Evolution of Appalachian-Ouachita salients and recesses from reentrants and promontories in the continental margin: American Journal of Science, v. 277, no. 10, p. 1233-1278, doi:10.2475/ajs.277.10.1233.

___1985, Northern Alabama sections, *in* Woodward, N. B., ed., Valley and Ridge thrust belt: balanced structural sections, Pennsylvania to Alabama: University of Tennessee Department of Geological Sciences Studies in Geology 12, p. 54-60.

___1988, The Black Warrior basin, *in* Sloss, L. L., ed., Sedimentary cover—North American craton: Geological Society of America, The Geology of North America, v. D-2, p. 471-492.

___2001, Mushwad: Ductile duplex in the Appalachian thrust belt in Alabama: American Association of Petroleum Geologists Bulletin, v. 85, no. 10, p. 1847-1869.

Thomas, W. A., Astini, R. A., Osborne, W. E., and Bayona, G., 2000, Tectonic framework of deposition of the Conasauga Formation, *in* Osborne, W. E., Thomas, W. A., and Astini, R. A., eds., The Conasauga Formation and equivalent units in the Appalachian thrust belt in Alabama: Tuscaloosa, Alabama, Alabama Geological Society 37th Annual Field Trip Guidebook, p. 19-40.

Thomas, W. A., and Bayona, G., 2005, The Appalachian thrust belt in Alabama and Georgia: thrust-belt structure, basement structure, and palinspastic reconstruction: Alabama Geological Survey Monograph 16, 48 p.

Thomas, W. A., and Mack, G. H., 1982, Paleogeographic relationship of a Mississippian barrier-island and shelf-bar system (Hartselle Sandstone) in Alabama to the Appalachian-Ouachita orogenic belt: Geological Society of America Bulletin, v. 93, no. 1, p. 6-19, doi:10.1130/0016-7606(1982)93<6:PROAMB>2.0.CO;2.

Wilkin, R. T., and Barnes, H. L., 1997, Pyrite formation in an anoxic estuarine basin: American Journal of Science, v. 297, no. 6, p. 620-650, doi:10.2475/ajs.297.6.620.

APPENDIX

GRAPHIC CORE LOGS FOR CORES PREVIOUSLY DESCRIBED BUT NOT PUBLISHED

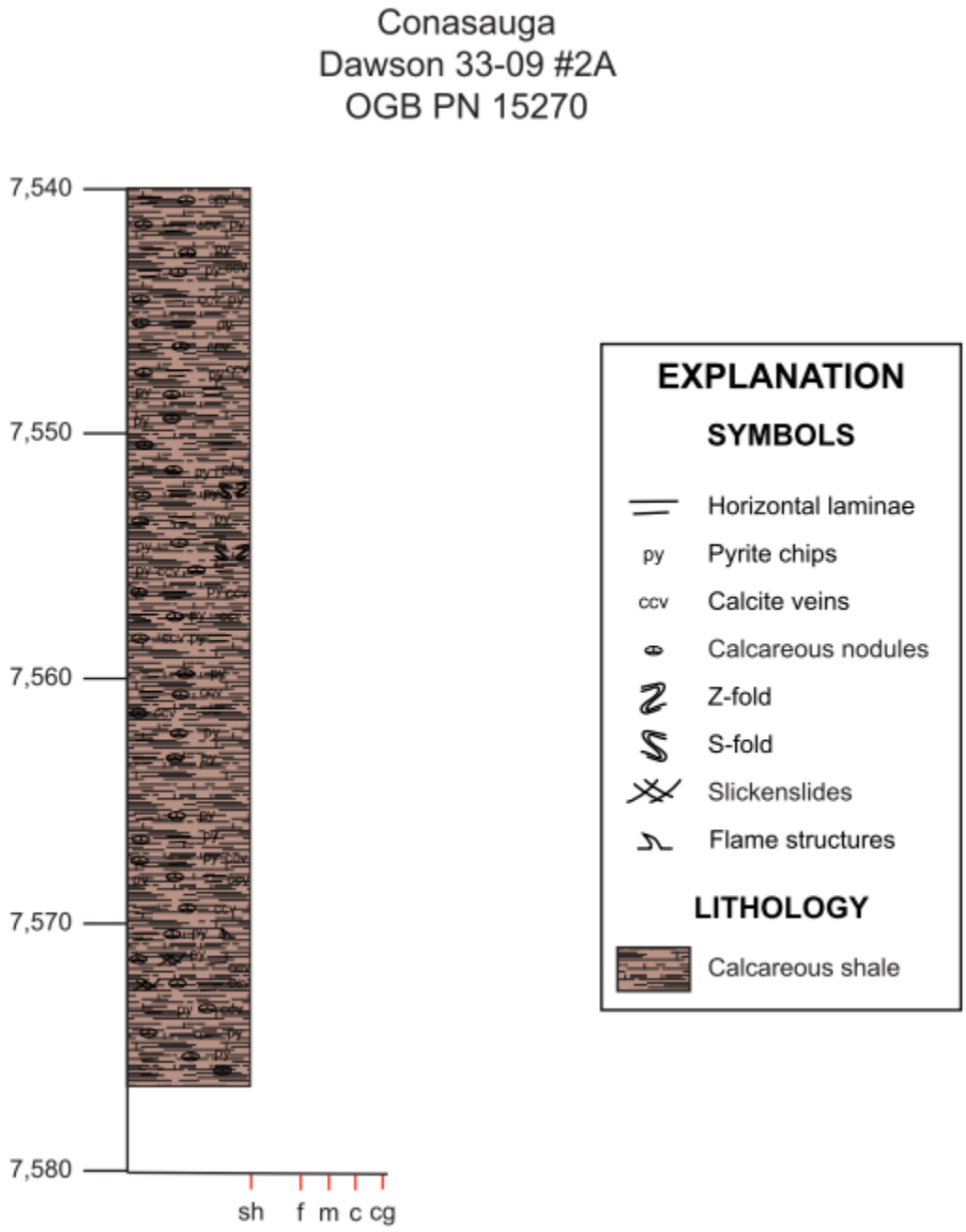

Figure A1.—Graphic core log of the Cambrian Conasauga shale, OGB PN 15270 (Dawson 33-09 #2A).

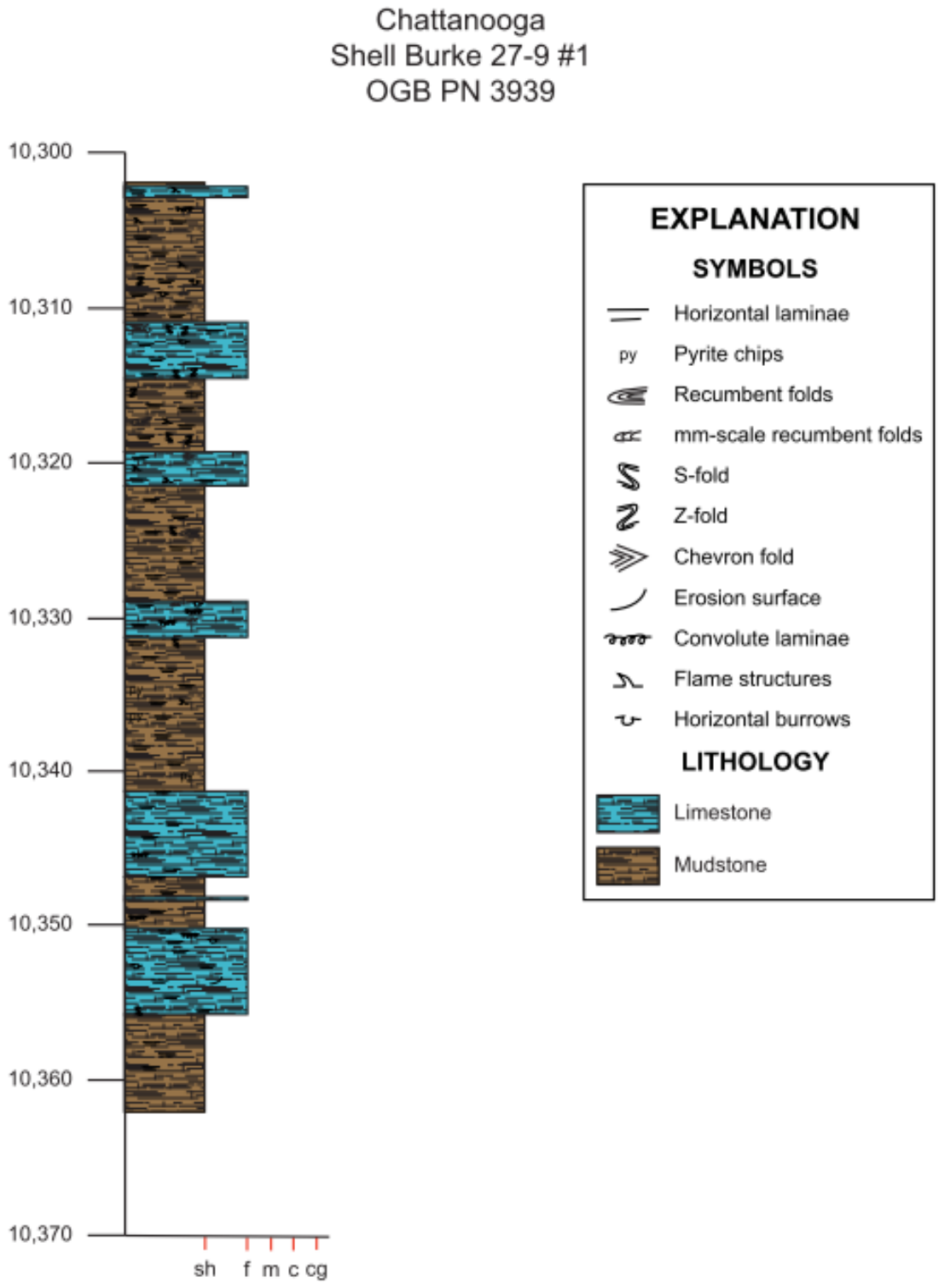

Figure A2.—Graphic core log of the Devonian Chattanooga shale, OGB PN 3939 (Shell Burke 27-9 #1).

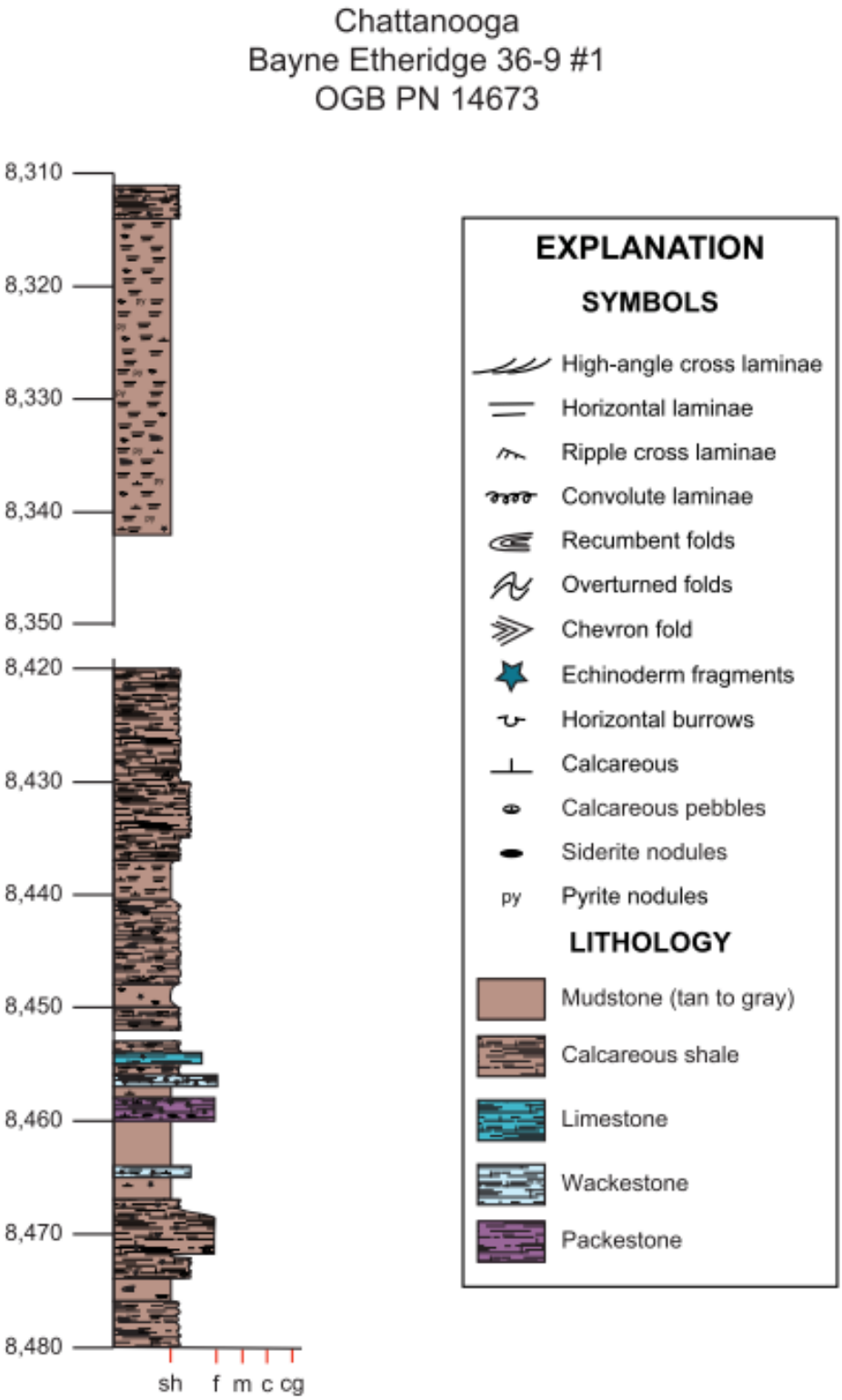

Figure A3.—Graphic core log of the Devonian Chattanooga shale, OGB PN 14673 (Bayne Etheridge 36-9 #1).

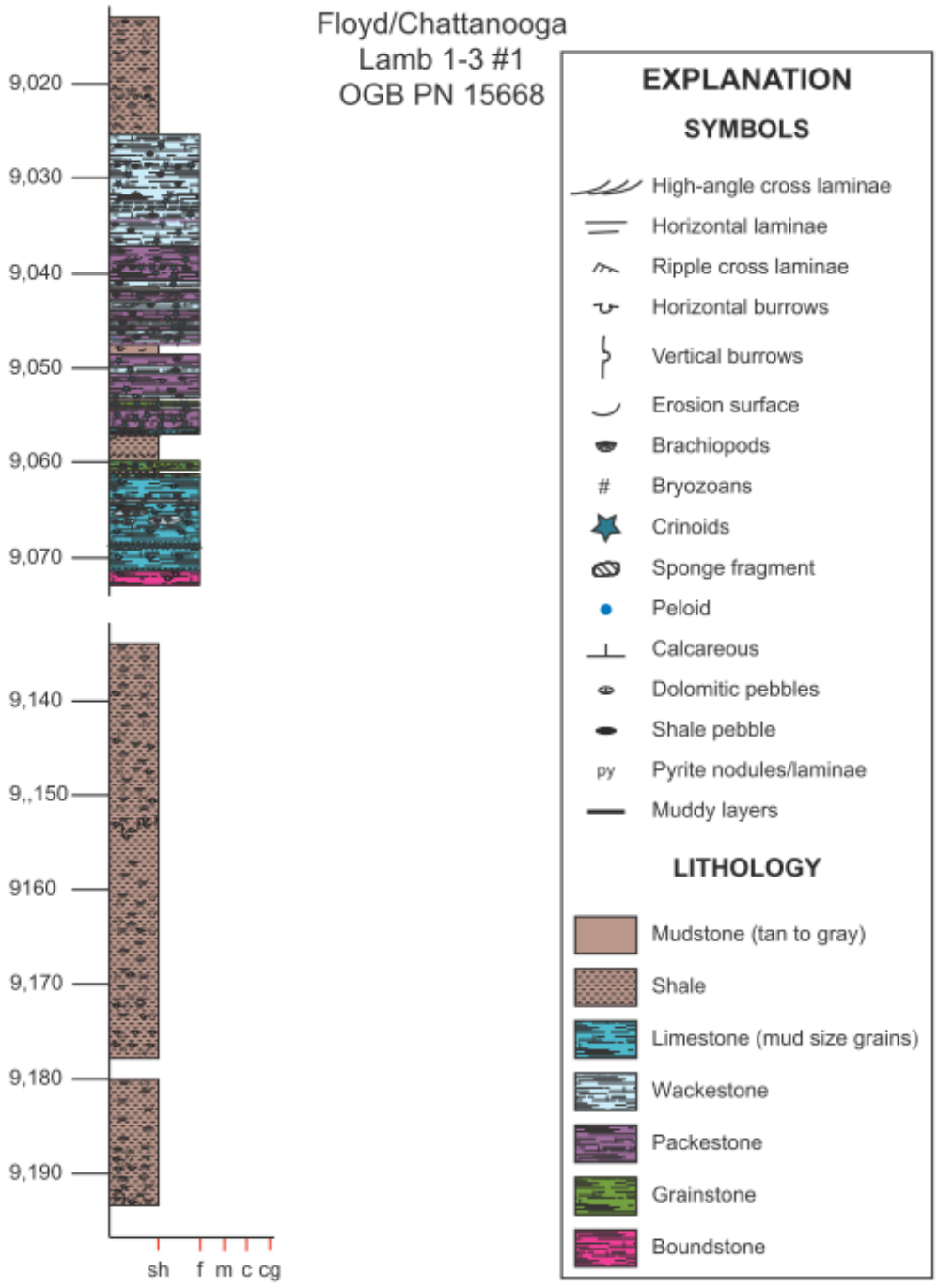

Figure A4.—Graphic core log of the Devonian Chattanooga shale, OGB PN 15668 (Lamb 1-3 #1).

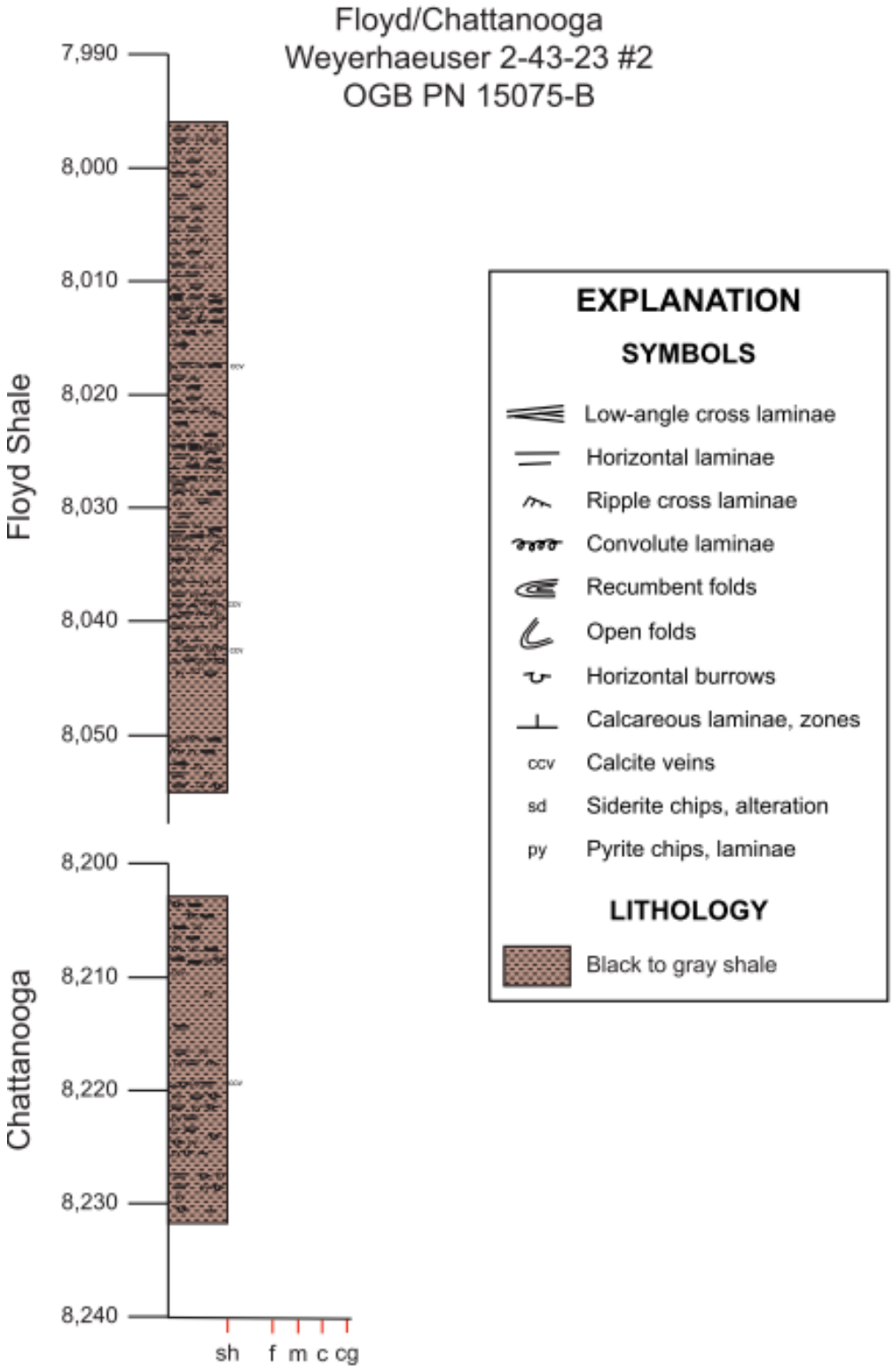

Figure A5.—Graphic core log of the Devonian Chattanooga and Mississippian Floyd shales, OGB PN 15075B (Weyerhaeuser No. 2-43-2402 #1).

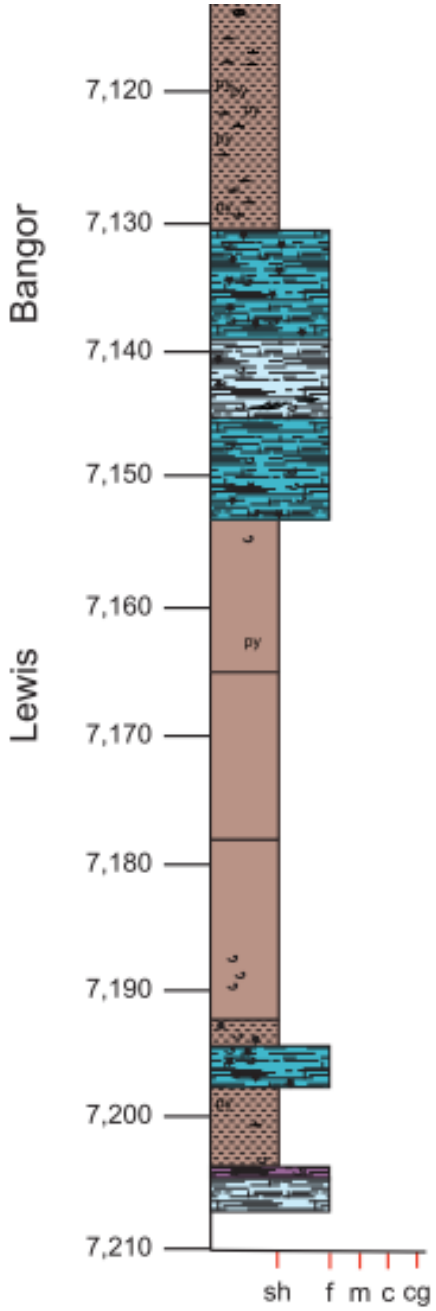

Figure A6.—Graphic core log of the Mississippian Neal shale, Bangor limestone, and Lewis shale (an informal unit), OGB PN 14045 (O'Bryant 6-15 #1). Part 1—lower section.

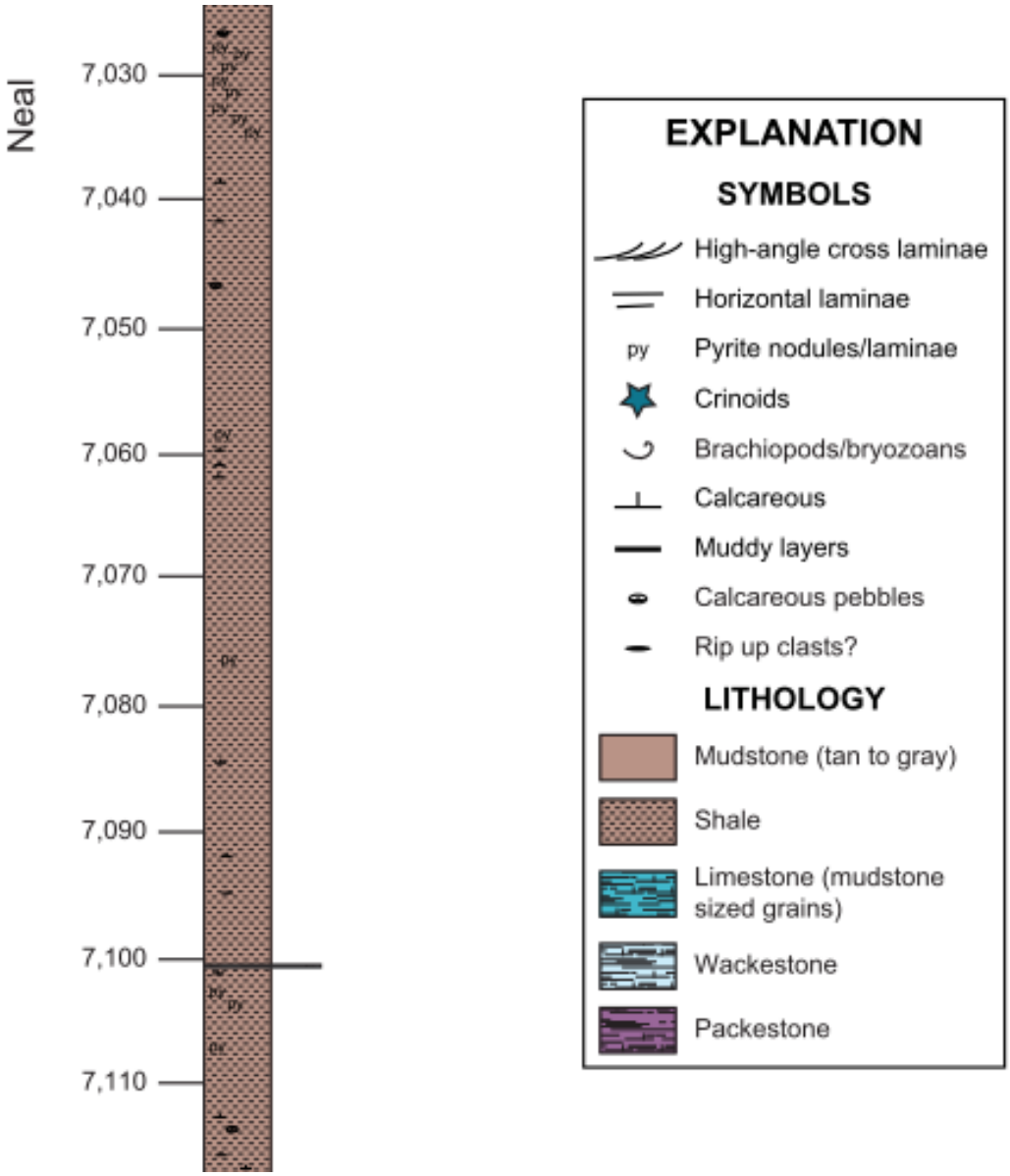

Figure A6.—Graphic core log of the Mississippian Neal shale, Bangor limestone, and Lewis shale (an informal unit), OGB PN 14045 (O'Bryant 6-15 #1). Part 2 —middle section.

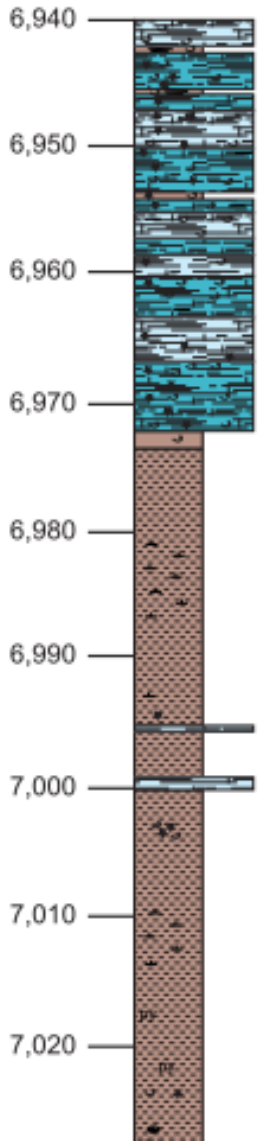

Figure A6.—Graphic core log of the Mississippian Neal shale, Bangor limestone, and Lewis shale (an informal unit), OGB PN 14045 (O'Bryant 6-15 #1). Part 3 —upper section.

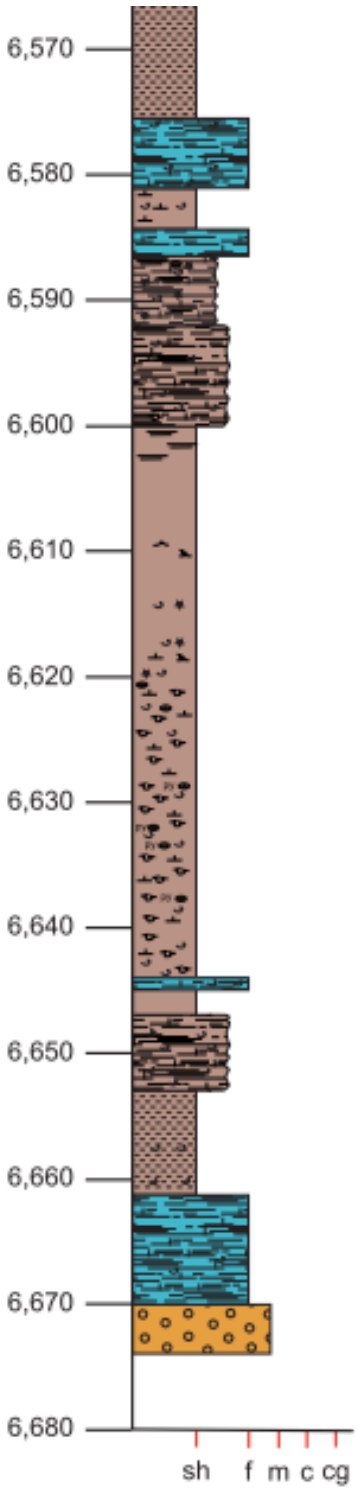

Figure A7.—Graphic core log of the Mississippian Neal shale, OGB PN 14065 (Exum Trust 16-6 #1). Part 1 —lower section.

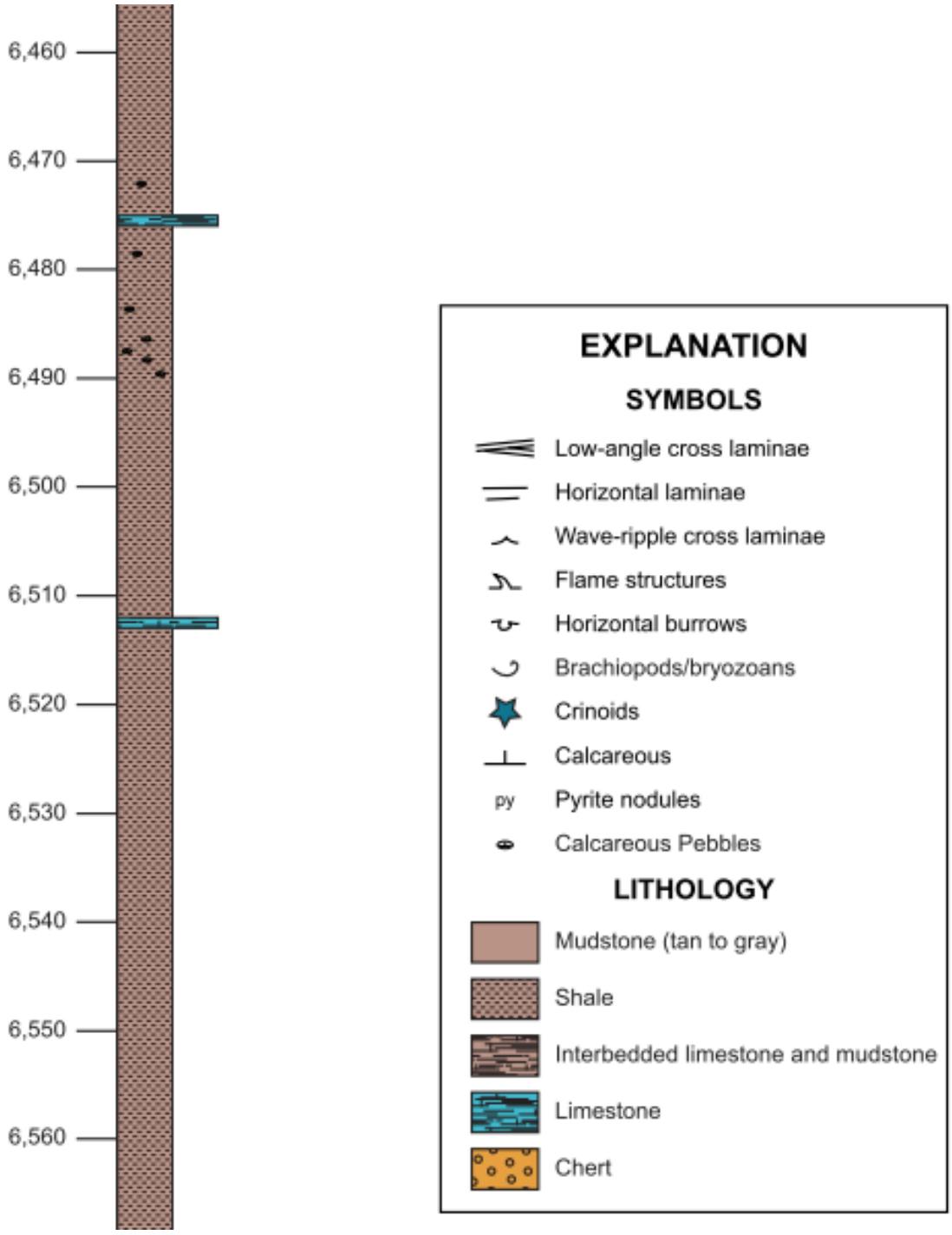

Figure A7.—Graphic core log of the Mississippian Neal shale, OGB PN 14065 (Exum Trust 16-6 #1). Part 2 —middle section.

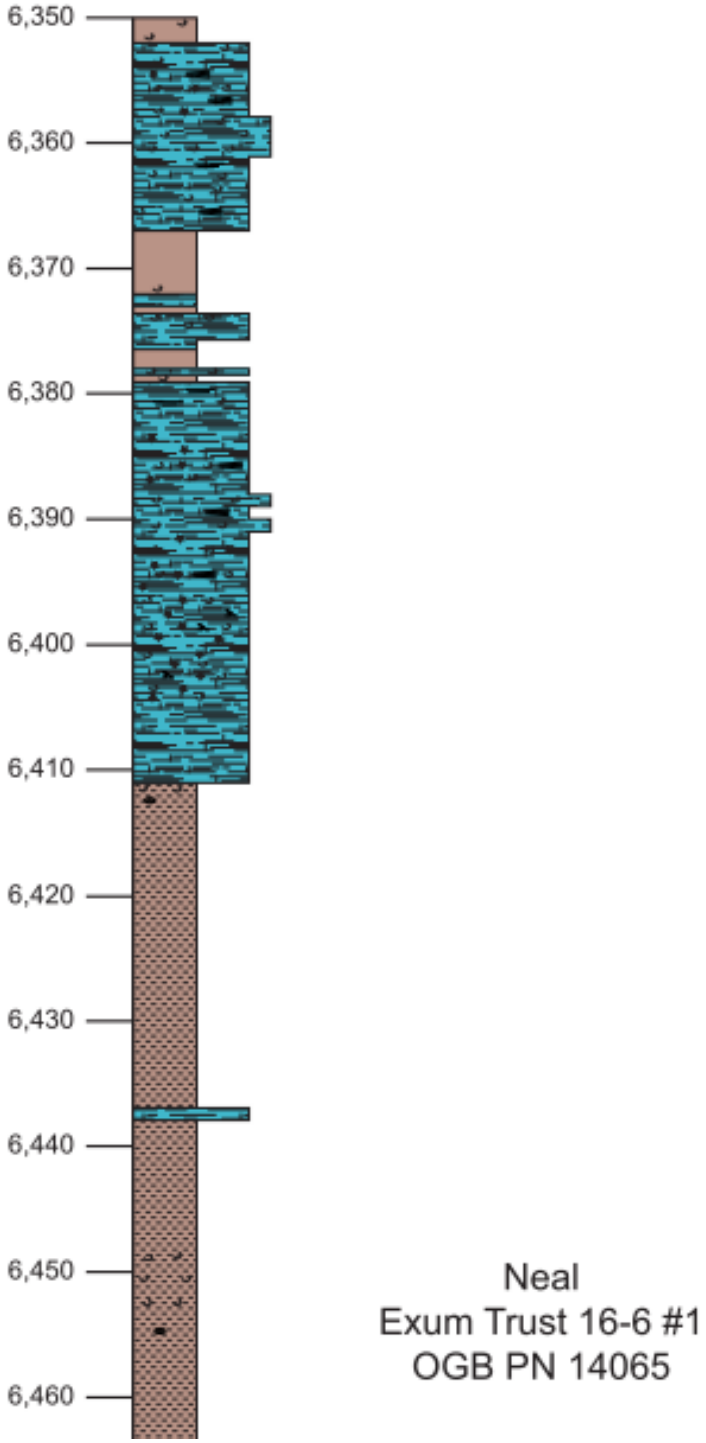

Figure A7.—Graphic core log of the Mississippian Neal shale, OGB PN 14065 (Exum Trust 16-6 #1). Part 3 —upper section.

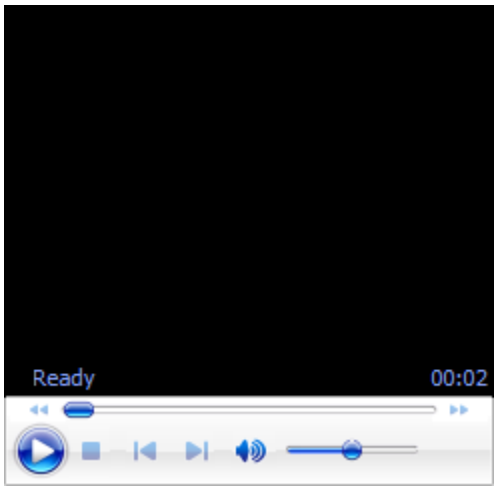

video_1_PN13979_d3700_FIB_secondary_electrons

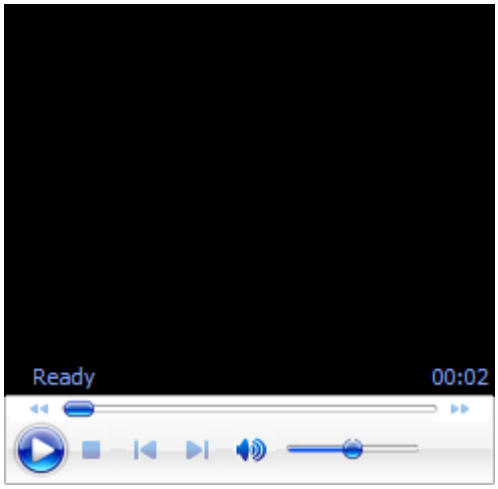

Video_2_PN13979_d3700_FIB_backscatter

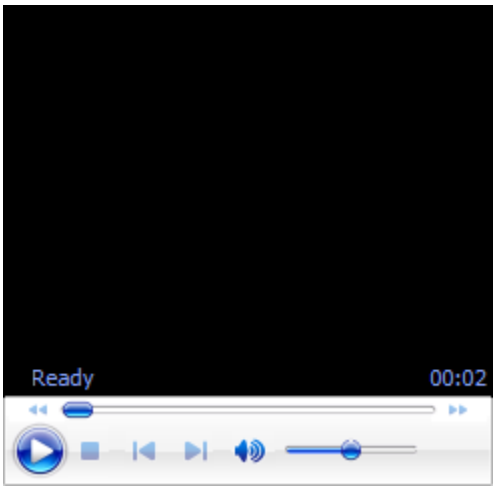

Video_3_PN13979_d3732_FIB_secondary_electrons

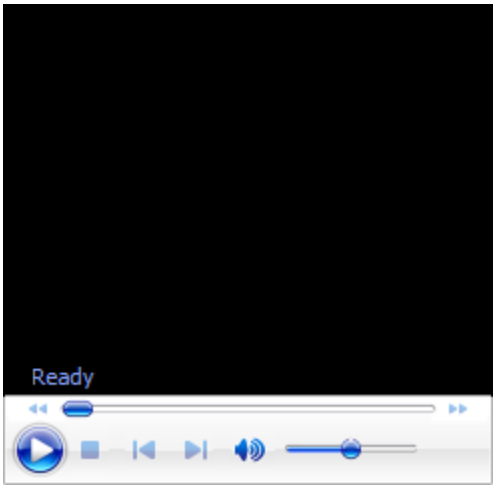

Video_4_PN13979_d3732_FIB_backscatter

SECTION C: PETROPHYSICAL CHARACTERIZATION: POROSITY, PERMEABIITY, FREE GAS STORAGE AND ADSORPTION

UNIVERSITY OF ALABAMA AT BIRMINGHAM

Petrophysics and Tight Rock Characterization for the Application of Improved Stimulation and Production Technology in Shale

FINAL REPORT

Reporting Period: June 27, 2013- June 26, 2016

by

Peter M. Walsh
Michael J. Hannon, Jr.

Prepared for the Research Partnership to Secure Energy for America (RPSEA) under Contract 11122-63

Birmingham, Alabama
2016

PERMEABILITY OF A FRACTURE IN THE PRESENCE AND ABSENCE OF A WETTING PHASE AND THE EFFECT OF CONFINING AND PORE PRESSURES ON MATRIX PERMEABILITY TO GAS

CONTENTS

FIGURES

TABLES

1. Permeability of a Fracture to Gas in the Absence of a Wetting Phase

1.1. Introduction

Measurement of the permeability of a shale sample containing fractures is complicated by the high gas flow velocities that may occur in fractures having micrometer-size and larger apertures, resulting in contributions from inertial effects to the observed pressure gradients. An analysis by Zhengwen Zeng and Reid Grigg, at New Mexico Tech, provides a method for treatment of this problem (Zeng and Grigg, 2006). Their theoretical analysis and procedure for data reduction were applied to the interpretation of measurements of gas flow and pressure in a fractured sample of Woodford Shale.

1.2. Measurement of the Apparent Permeability

The sample of Woodford Shale is shown in Figure 1. Its dimensions and the conditions during measurements of its permeability are given in Table 1. The axis of the cylinder is parallel to the bedding plane. A fracture running the entire length of the core divides the sample into two separate pieces, held together by transparent tape in the photo. Several notches are visible on the near end of the plug in the photo, but none of them, except the one accompanying the fracture, extends far into the sample.

Figure 1.—Woodford Shale sample containing a fracture running the length of the cylinder. The axis of the cylinder is parallel to the bedding plane. The sample is wrapped with transparent tape to hold its two halves together.

The measurements of permeability were made using the Core Lab/TEMCO triaxial core holder in the laboratory at UAB. The set-up of the equipment is shown in Figure 2. The measurements were made on the as-received samples, without extraction, drying, or other pretreatment. Permeability was measured by steady flow of N_2 at room temperature (19.2 to 22.1 ^{o}C) and at pressures from 0.44 to 1.47 MPa, absolute (49 to 198 psig) on the upstream face of the core. Pressures at the outlet from the core varied from 0.10 to 1.34 MPa, absolute (0 to 180 psig). The pressure drop was controlled using a metering valve at the outlet from the core holder. The flow rate of gas through the sample was measured by timing the displacement of a soap film in a graduated tube (Teledyne Hastings Mini-Flo Calibrator, Model HBM-1A). The confining pressure, both axial and radial, was 3000 psig.

Table 1.—Properties of the Woodford Shale Sample and the Conditions and Result of the Measurements of Permeability.

Sample No.	2-18 OSU
Origin	Woodford
Depth	11,669.4 ft
Orientation	axis parallel to bedding
Diameter	0.02506 m
Length	0.03371 m
Condition of sample	as received
Fluid	N_2 gas
Temperature	19.2 - 22.1 °C
Sample inlet pressure	0.44 to 1.47 MPa, absolute 49 to 198 psig
Sample outlet pressure	0.10 to 1.34 MPa, absolute 0 to 180 psig
Axial and radial confining pressures	3000 psig
Average permeability of the rock matrix and fracture by the method of Zeng and Grigg (2006), Figure 4	$(3.0 \pm 0.2) \times 10^{-15}$ m^2 3.1 ± 0.2 millidarcy

Permeability was determined using the following equation accounting for deviation from ideal-gas behavior of N_2 under the conditions of the measurements (Walsh et al., 2013):

$$k = \frac{\frac{\dot{m}}{W}\frac{\mu L}{A}}{\frac{P_{in}-P_{out}}{B_V} - \frac{RT}{B_V^2}\ln\frac{1+\frac{B_V P_{in}}{RT}}{1+\frac{B_V P_{out}}{RT}}} \quad (1)$$

where:

A cross-section area of the sample perpendicular to the flow direction, m^2
B_V second volume Virial coefficient (Sengers et al., 1972), m^3/kmol
k coefficient of permeability, m^2
L length of the sample, m
$\dot{m}$ mass flow rate, kg/s
P_{in} absolute pressure at the inlet to the sample, Pa
P_{out} absolute pressure at the outlet from the sample, Pa
R universal gas constant, = 8314.46 J/(kmol·K)
T absolute temperature, K
W molecular weight, kg/kmol
μ absolute viscosity at the temperature and mean pressure in the sample (Lemmon et al., 2013), Pa·s

Equation (1) was used to determine the effective permeability from measurements of inlet and outlet pressures, the volumetric flow rate at ambient conditions, temperature in the core, the dimensions of the sample, the value for the second Virial coefficient of N_2 at the temperature in the core (Sengers et al., 1972), and values for the gas density at ambient conditions and viscosity at the temperature and mean pressure in the core (Lemmon et al., 2013). The correction applied using Equation (1) is not so important in the case of N_2, but it can be significant for gases deviating more strongly from ideal behavior, such as CO_2.

Five to seven measurements of the flow rate were made at each pressure. In a conventional method for determining permeability by steady flow of gas, such as ASTM D4525-13e1 (ASTM, 2013), measurements of the apparent permeability over a range of pressures are plotted versus the reciprocal of the mean absolute pressure in the sample and extrapolated to 1/pressure = 0, to correct for the Klinkenberg effect or slip, when the mean free path of gas molecules is comparable to pore diameters in the rock (Klinkenberg, 1941; Collins, 1961; API, 1998; ASTM, 2013). The results of the application of this procedure to the measurements are shown in Figure 3. There are two sets of measurements over the range of mean pressures from 0.27 to 0.62 MPa (24 to 75 psig) and two sets of measurements over the range from 0.45 to 1.41 MPa (50 to 189 psig). As shown in the figure, the permeabilities determined by extrapolation of the measurements in the two ranges of mean pressure are not consistent. A possible explanation is contributions from inertial effects associated with high-velocity flow in the fracture.

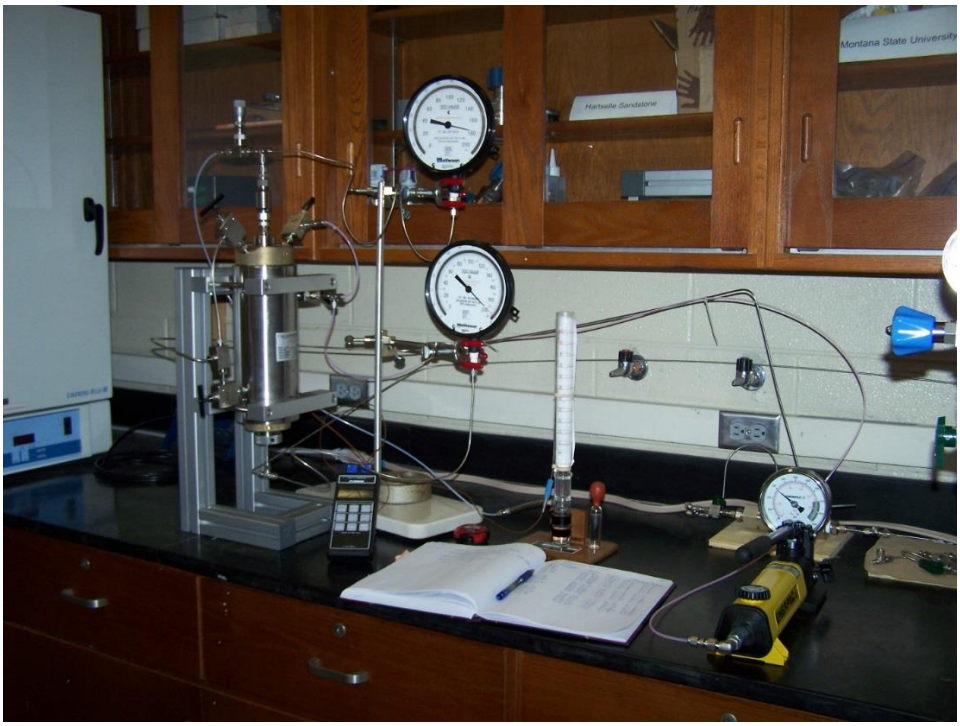

Figure 2.—Triaxial core holder, inlet and outlet pressure gauges, thermocouple readout, flowmeter, and confining pressure pump and gauge in the arrangement for measurement of permeability by steady flow of nitrogen.

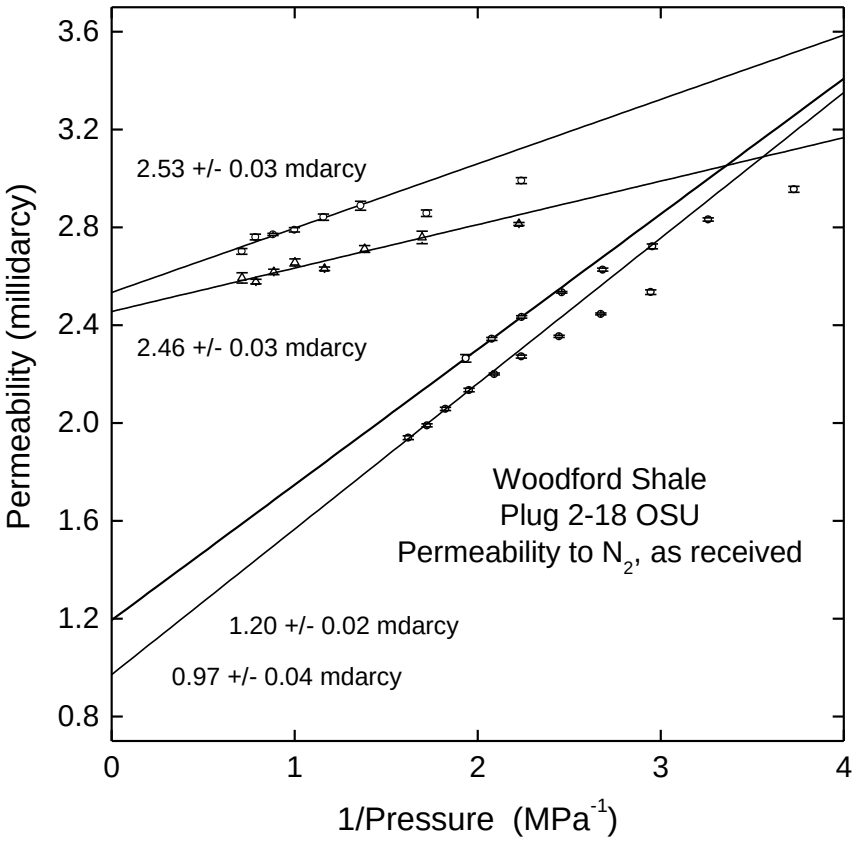

Figure 3.—Apparent permeability of the fractured Woodford Shale plug shown in Figure 1, determined by steady flow of nitrogen. The mean nitrogen pressures in the sample during the two upper sets of measurements were in the range from 0.45 to 1.41 MPa (50 to 189 psig) and during the two lower sets of measurements, in the range from 0.27 to 0.62 MPa (24 to 75 psig).

1.3. Correction for Inertial Effects

Zhengwen Zeng and Reid Grigg, at New Mexico Tech, derived a method to account for effects of non-Darcy flow on permeability at high gas velocity, using the Forchheimer Equation (Zeng and Grigg, 2006; Forchheimer, 1901):

$$-\frac{dP}{dz} = \frac{\mu v}{k} + \beta \rho v^2 \tag{2}$$

Integration of Equation (2) leads to a linear equation:

$$y = \frac{1}{k} + \beta x \tag{3}$$

with $y = \frac{WA(P_{in}^2 - P_{out}^2)}{2ZRT\mu L\, \rho_0 Q_0}$ and $x = \frac{\rho_0 Q_0}{\mu A}$,

where:

A cross-section area of the sample perpendicular to the flow direction, m^2
k coefficient of permeability, m^2
L length of the sample, m
P absolute pressure, Pa
Q volumetric flow rate, m^3/s
R universal gas constant, = 8314.46 J/(kmol·K)
T temperature, K
v superficial velocity, m/s
W molecular weight, kg/kmol
z axial coordinate, m
Z compressibility factor, -
β "non-Darcy" coefficient, m^{-1}
μ absolute viscosity at the temperature and mean pressure in the sample (Lemmon et al., 2013), Pa·s
ρ fluid density, kg/m^3

Subscripts

in at the inlet
out at the outlet
o condition in the flowmeter

A plot of Equation (3) has slope, β, and intercept, $1/k$.

The measurements of nitrogen flow through the Woodford Shale sample are presented in Figure 4 as points defined by Zeng and Grigg's *x* and *y*. The four sets of data are now in good agreement. The average permeability of the rock matrix and fracture, parallel to bedding, from the values of the intercepts in the figure, is $(3.0 \pm 0.2) \times 10^{-15}$ m^2, or 3.1 ± 0.2 millidarcy.

Under the simplifying assumptions that the permeability of the rock matrix is small and the walls of the fracture are smooth parallel plates, the aperture of the fracture is estimated to be approximately 10 μm.

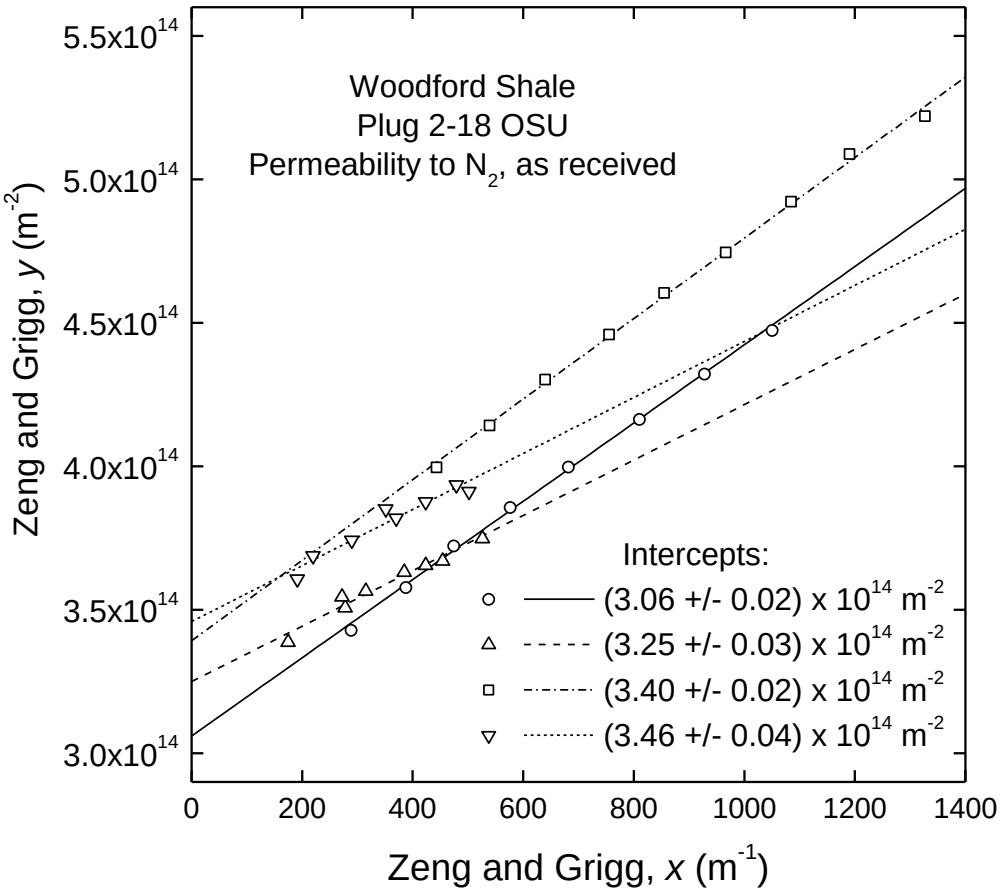

Figure 4.—Plot of the measurements shown in Figure 3 as points defined by Zeng and Grigg's *x* and *y*, according to Equation (3).

2. Breakthrough Pressure and Effective Permeability of a Fracture to Gas in the Presence of a Wetting Phase

2.1 Introduction

The "minimum capillary displacement pressure" and effective permeability are the experimental results of the method developed by A. Hildenbrand and coworkers at RWTH Aachen University, for quantitative assessment of the permeability to gas, of brine-saturated fine-grained rocks (Hildenbrand et al., 2002, 2004). The minimum capillary displacement pressure is found by saturating a core with brine, applying a pressure difference across the sample greater than the breakthrough pressure, and allowing capillary flow through the sample to bring the upstream to downstream pressure difference to equilibrium. The effective permeability can be determined as a function of time, or the pressure difference, from the rate of change in pressure and the volume of the upstream or downstream chamber.

2.2. Minimum Capillary Displacement Pressure

The measurements were made using the fractured Woodford Shale sample shown in Figure 1, following the permeability measurements described in Section 1. The conditions during the measurements of minimum capillary displacement pressure and effective permeability are given in Table 2. The setup for the measurements, using the Core Labs/TEMCO triaxial core holder, is similar to that shown in Figure 2, but without the flowmeter.

The sample was first saturated with brine (10 wt% KCl) by filling the cavity above the sample, which becomes the downstream volume during the measurements, with brine, and applying a steady, regulated high pressure of nitrogen over the brine, until brine flowed out from the other end of the plug. Nitrogen at constant pressure, above the anticipated breakthrough pressure, was then applied to the upstream (lower) end of the plug, with the downstream (upper) end at atmospheric pressure. The valves on the upstream and downstream sides were then closed, sealing the cavities on both ends.

Two determinations of the minimum capillary displacement pressure were performed, at initial pressure differences across the sample plug of 0.539 MPa (78 psi) and 1.375 MPa (199 psi). The time dependence of the pressure drop across the brine-saturated plug is shown in Figures 5a and 6a. Of the two runs, the more informative one was at the lower pressure, shown in Figure 5a, which provided better resolution of the changes in pressure. The following discussion focuses on that case.

Just after the upstream and downstream cavities are sealed, at time = 0, the initial rise in downstream pressure is slow because the brine saturation of the rock is high. As brine is displaced and drained from the fracture and largest pores connecting the upstream and downstream faces, the permeability of the sample to the gas increases and the rate of rise in downstream pressure increases, eventually passing through a maximum at the minimum brine saturation reached under the conditions of the measurement. After passing through the maximum effective permeability, as the pressure difference across the sample continues to decrease, the direction of brine migration reverses and brine is reimbibed, first into the smallest or narrowest of the open, gas-filled passages connecting the upstream and downstream faces of the sample. The process of reimbibition continues in progressively larger passages, until the

largest open passages in the fracture connecting the upstream and downstream faces close, cutting off flow of gas through the sample. The residual pressure difference, corresponding to the capillary pressure in the narrowest passage in the highest conductivity path through the fracture, is the "minimum capillary displacement pressure."

The instantaneous effective permeability during drainage and reimbibition of the brine is given by (Hildenbrand et al., 2002):

$$k_{eff} = -\frac{2\,\mu\,L\,V_1}{A\,(P_1^2 - P_2^2)}\,\frac{\Delta P_1}{\Delta t} \tag{4}$$

where:

A cross section area of the sample perpendicular to the flow direction, m^2
k_{eff} effective permeability to gas in the presence of the wetting phase, m^2
L length of the sample, m
P_1 instantaneous absolute pressure in the upstream chamber, Pa
P_2 instantaneous absolute pressure in the downstream chamber, Pa
V_1 volume of the upstream chamber, m^3
Δt time interval corresponding to the change in upstream pressure, ΔP_1, s
μ absolute viscosity of N_2 at the temperature and mean pressure of the test (Lemmon et al., 2013), Pa·s

The minimum capillary displacement pressure is equivalent to the breakthrough pressure, above which capillary flow of gas will occur through a rock initially saturated with the wetting phase, given sufficient time. The measurement is an alternative to the traditional method of determining breakthrough pressure by increasing the pressure of gas on one face of a brine-saturated plug in small increments, until breakthrough is observed. The traditional method tends to overestimate the breakthrough pressure, because there can be a long lag time before gas appears on the downstream side of a plug, even at upstream pressures well above the pressure ultimately identified as the true breakthrough pressure. In the presence of the fracture, the minimum capillary displacement pressures are relatively low: 0.0209 MPa (3.03 psi) and 0.0171 MPa (2.48 psi) at the lower and higher initial pressure differences, shown in Figures 5a and 6a, respectively.

The dependence of the effective permeability on time is shown in Figures 5b and 6b. In the lower pressure case (Figure 5b), the maximum effective permeability, where the brine saturation of the sample is lowest, is 0.14 ± 0.01 millidarcy, approximately 1/20th of the absolute permeability of the rock (3.1 millidarcy). In the higher pressure run (Figure 6b), the maximum effective permeability is 0.28 millidarcy, twice as great as in the lower pressure case because, at the higher pressure drop, brine is drained from a larger fraction of the continuous passages and pores connecting the upstream and downstream faces of the sample.

Table 2.—Woodford Shale Sample: Conditions and Results of the Measurements of Minimum Capillary Displacement Pressure and Effective Permeability.*

Property	Lower Pressure Trial	Higher Pressure Trial
Non-Wetting Fluid	N_2	N_2
Wetting Fluid	Brine, 10 wt% KCl	Brine, 10 wt% KCl
Temperature	21.0 - 22.3 ^{o}C	19.9 - 23.1 ^{o}C
Initial Pressure Difference	0.539 MPa 78 psi	1.375 MPa 199 psi
Axial and Radial Confining Pressures	3000 psig	3000 psig
Minimum Capillary Displacement Pressure, P_{mcdp}	0.0209 MPa 3.03 psi	0.0171 MPa 2.48 psi
Maximum Effective Permeability, $k_{eff,max}$	0.14 ± 0.01 millidarcy	0.28 millidarcy
Pressure drop at the Maximum Effective Permeabilty, P_{max}	0.272 MPa 39.5 psi	0.548 MPa 79.5 psi

*The origin, dimensions, and condition of the sample are given in Table 1.

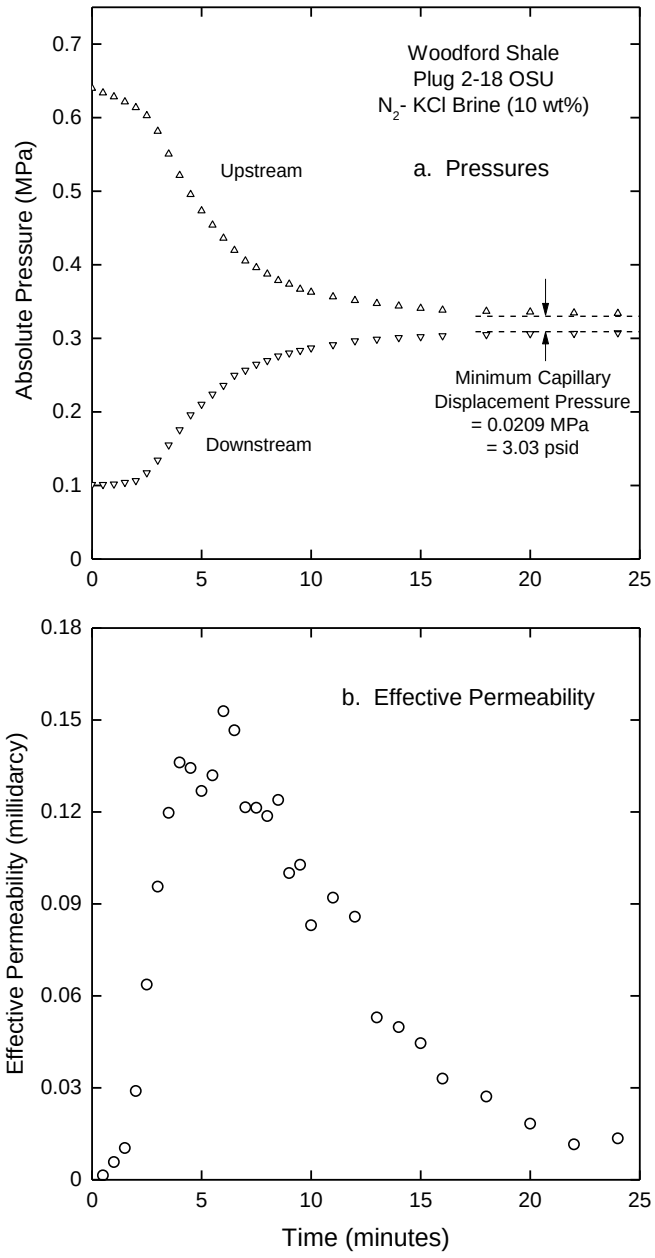

Figure 5.—Approach to the minimum capillary displacement pressure and determination of the effective permeability of the fractured Woodford Shale plug.

a. Pressures upstream and downstream from the sample versus time, starting at initial pressures of 0.640 MPa (78 psig) and 0.101 MPa (0 psig), upstream and downstream, respectively. Both chambers, upstream and downstream from the sample, are closed. The minimum capillary displacement pressure, 0.0209 MPa (3.03 psi), was measured at times of 60, 75, 90, and 105 minutes.

b. Effective permeability versus time, first increasing as brine is displaced, increasing the gas saturation, passing through a maximum at the highest gas and lowest brine saturations reached under the conditions of the measurement, then decreasing as brine is reimbibed and closes off the smallest of the open continuous channels or pores, then finally, at the minimum capillary displacement pressure, closing the narrowest aperture in the highest conductivity path through the fracture connecting the upstream and downstream faces of the sample.

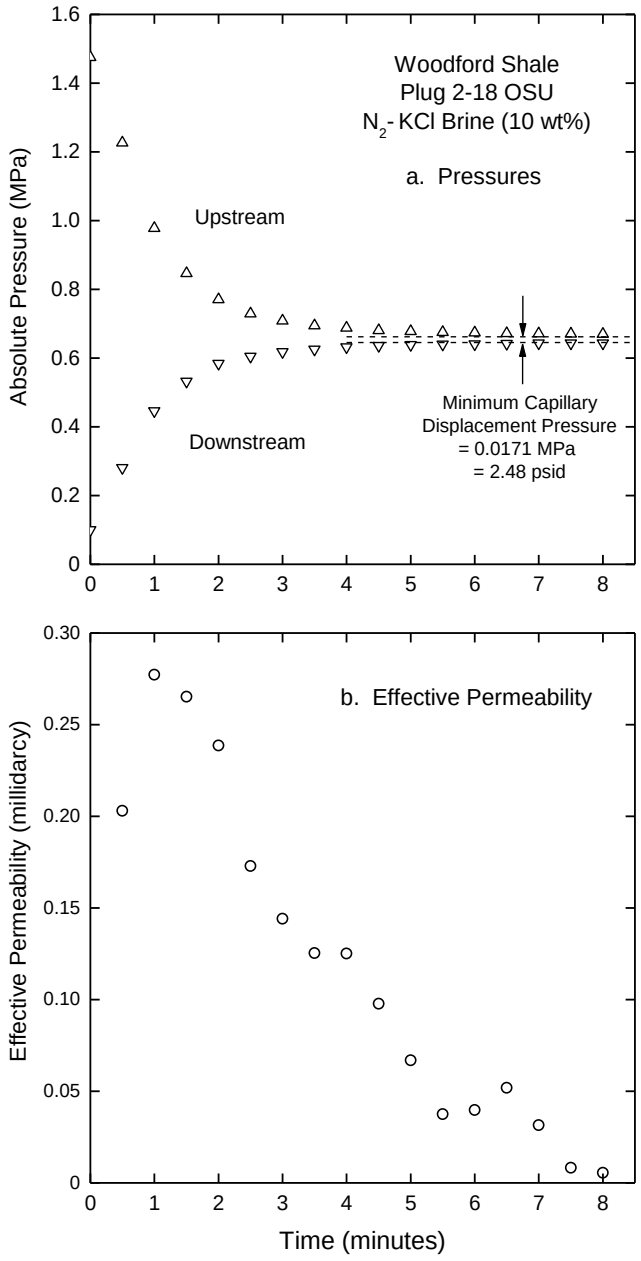

Figure 6.—a. Approach to the minimum capillary displacement pressure, and b. Effective permeability of the fractured Woodford Shale sample following the imposition of a 1.375 MPa (199 psi) pressure drop across the brine-saturated plug. In the presence of the higher pressure drop, brine is drained from the fracture more quickly and completely, increasing the maximum effective permeability by a factor of two compared with the lower pressure case shown in Figure 5b.

2.3. Effective Permeability versus Pressure

The effective permeabilities, from Figures 5b and 6b, are plotted versus the corresponding upstream to downstream pressure differences, from Figures 5a and 6a, in Figures 7 and 8, respectively.

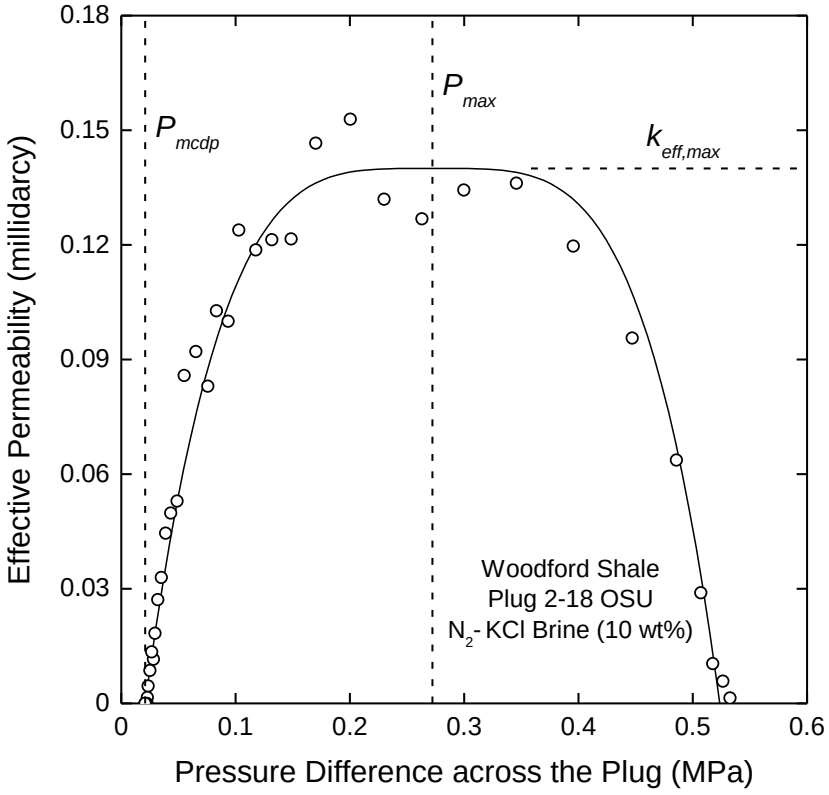

Figure 7.—Dependence of the effective permeability of the brine-saturated Woodford Shale plug on pressure difference, following breakthrough, from the measurements shown in Figures 5a and 5b. The effective permeability varies from 0 at the minimum capillary displacement pressure, P_{mcdp}, to a maximum of 0.14 ± 0.01 millidarcy near P_{max} = 0.272 MPa. The curve fit to the measurements is Equation (5), with the value of the exponent n = 4.

The dependence of the effective permeability on the pressure difference, above the minimum capillary displacement pressure, has a characteristic symmetric shape described by

$$k_{eff} = k_{eff,max}\left[1 - \left(\frac{|P_{max} - P|}{P_{max} - P_{mcdp}}\right)^n\right] \tag{5}$$

where:

k	coefficient of permeability, m^2 or darcy
P	pressure difference, Pa

Subscripts

eff	effective (permeability)

max maximum (effective permeability or pressure at the maximum effective permeability)
mcdp minimum capillary displacement pressure

In a brine-saturated formation, the pressure difference, P in Equation (5), is the difference between the pore pressure and the local hydrostatic pressure. The effective permeability of a rock is zero for a pressure difference less than the minimum capillary displacement pressure. Above the minimum capillary displacement pressure, the effective permeability is expected to increase with increasing pressure up to a maximum value, $k_{eff,max}$, at the maximum pressure difference, P_{max}, present in, or imposed upon, the formation. If the irreducible brine saturation were reached, the effective permeability would be expected to remain at the maximum value with further increase in excess gas pressure above P_{max}, following the horizontal dashed line labeled $k_{eff,max}$ in Figures 7 and 8. As excess gas pressure decreases from P_{max}, the effective permeability is expected to follow the left branch of the curves shown in Figures 7 and 8 down to the minimum capillary displacement pressure, where the gas flow would be shut off.

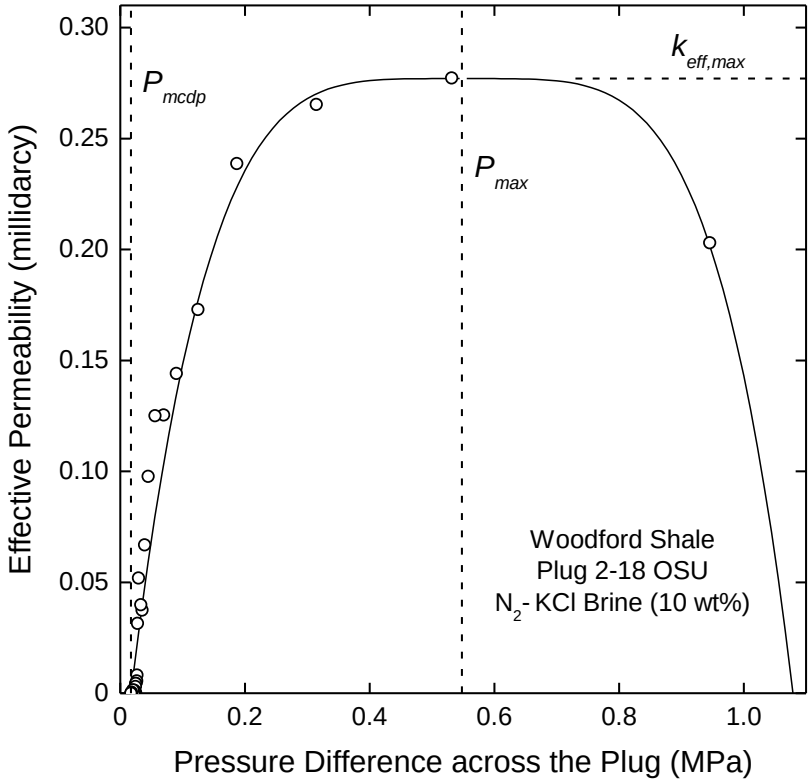

Figure 8.—Dependence of the effective permeability of the brine-saturated Woodford Shale plug on the pressure difference across the sample, following breakthrough, from the measurements shown in Figures 6a and 6b. The effective permeability varies from 0 at the minimum capillary displacement pressure, P_{mcdp}, to a maximum of 0.28 millidarcy near P_{max} = 0.548 MPa. The curve fit to the measurements is Equation (5), with the value of the exponent n = 4.5.

Equation (5) provides a relation with which to estimate the effective permeability as a function of pressure, accompanied by drainage or imbibition of brine, but additional work is needed to determine the dependence of the irreducible brine saturation and maximum effective permeability on pressure.

3. Effect of Confining and Pore Pressures on the Matrix Permeability of the Barnett Shale

3.1. Introduction

To be useful for the simulation of production from gas shale reservoirs, measurements of the permeability of shale samples should reproduce the effective stress state in the formation under consideration. Heller, Vermylen, and Zoback (2014) made a thorough study of the effects of confining pressure and pore pressure on the permeability of gas shales from the Barnett, Eagle Ford, Marcellus, and Montney shale reservoirs. They were able to correlate permeability, over wide ranges of confining and pore pressures, with an effective stress, σ_{eff}, given by

$$\sigma_{eff} = P_{conf} - \chi P_{pore} \tag{6}$$

where P_{conf} and P_{pore} are the confining and pore pressures, respectively, and χ is the "effective stress coefficient for permeability" (Heller et al., 2014). According to these authors, "χ determines the relative sensitivity of permeability to changes in confining pressure and pore pressure." The permeabilities of the gas shales studied by Heller and coworkers were all correlated using values of χ less than 1, showing that the shales are more sensitive to changes in confining pressure than to changes in pore pressure.

Bhandari, Flemings, Polito, Cronin, and Bryant (2015) reviewed investigations of matrix permeability of gas shales and the dependence of permeability on "simple effective stress" ($P_{conf} - P_{pore}$) and orientation of the direction of flow with respect to bedding. These authors concluded, from their review of the data, that "it is difficult to find a definite answer regarding the primary controls of permeability and regarding permeability anisotropy and stress dependence." From their own study of Barnett Shale samples, Bhandari and coworkers inferred that the observed permeability anisotropy (parallel vs. perpendicular to bedding) is due to stratigraphic layering and that multiscale permeability (pressure pulse decay occurring on different time scales) is due to "millimeter-scale interbeds of more permeable, organic-rich material with less permeable, more siliceous material."

Because the confining and pore pressures are among the conditions having the greatest impact on the apparent permeability of gas shales, an investigation of the effect of the pressures was undertaken to examine the sensitivity of the apparent permeability of the Barnett Shale to effective stress and the time dependence of the response of its permeability to change in effective stress.*

* In what follows we use the term "effective stress" for the simple effective stress, or difference between confining and pore pressures, $P_{conf} - P_{pore}$.

3.2. Variation of Confining Pressure at Fixed Pore Pressure

A photograph of the sample is shown in Figure 9 and its dimensions are given in Table 3. The sample is thin for two reasons: first, because the shale fractures very readily at weak layers into thin disks when cutting plugs with a core sampling bit, and second, because the permeability of the rock is so low that measurements of the flow through it would be difficult, were the sample much longer.

The conditions under which the measurements were made are summarized in Table 3. Permeability was determined using helium under conditions of steady flow, with high pressure on one end of the sample and atmospheric pressure at the outlet from the sample. This has the disadvantage that the effective stress changes significantly over the length of the sample, complicating the construction of a quantitative model for the effect of effective stress on permeability. However, our objective here is illustration of the importance of the pressures. In practice one would reproduce the overburden and gas pressures in the formation of interest as closely as possible and, for the present application, pressure-pulse decay measurements are preferable to steady flow (Heller at al., 2014).

Figure 9.—Barnett Shale sample. The axis of the cylinder is perpendicular to the bedding plane.

Five sequences of measurements were performed during which the mean pore pressure was fixed and confining pressure was varied stepwise, beginning at a low pressure. The pressure was first increased then decreased, stepwise, to observe the dependence of permeability on effective stress and the response of permeability to the direction of change in stress. The results are shown in Figure 10.

The sequence of measurements began at the lowest mean pore pressure, 200 psig, shown in Figure 10a. The very first measurements are those shown by the three black open triangles, at the top left. With the pore pressure fixed, the confining pressure was first set at 800 psig, then increased to 1200 and 1600 psig. In response to the increase in effective stress, the permeability decreased from 0.27 to 0.12 microdarcy.

Table 3.—Properties of a Barnett Shale sample and the
Conditions during Measurements of Permeability versus Effective Stress.

Sample No.	FWB1 OSU
Origin	Fort Worth Basin
Depth	7553.3 ft
Orientation	axis perpendicular to bedding
Diameter	0.02568 m
Length	0.01051 m
Condition of sample	cut dry from larger sample, as received
Fluid	He gas
Temperature	21.5 – 23.8 ^{o}C
Sample inlet pressure	2.86, 8.37, and 13.9 MPa, absolute (400, 1200, and 2000 psig)
Sample outlet pressure	0.1 MPa, absolute (0 psig)
Axial and radial confining pressures*	5.62 to 33.2 MPa, absolute (800 to 4800 psig)
Range of apparent permeability, Figure 10	(1.3 to 30) x 10^{-20} m^2 (0.014 to 0.30 microdarcy)

*Confining pressure was always at least 2.76 MPa (400 psi) greater than the sample inlet pressure.

The next measurements in the sequence are those shown in Figure 10b, at a mean pore pressure of 600 psig. In the first set of measurements in Figure 10b, the confining pressure was increased from 1600 to 4000 psig with the corresponding permeabilities shown by the upward-facing triangles. The permeability decreased from 0.09 to 0.025 microdarcy. Reversing the process and decreasing the confining pressure from 4000 back down to 1600 psig produced the permeabilites shown by the downward-facing triangles. The response to decreasing confining pressure is slower, and on arriving back at the confining pressure of 1600 psig, the permeability is only 0.042 microdarcy, less than half of the value at the same confining pressure at the outset.

Measurements at the highest mean pore pressure, 1000 psig, are shown in Figure 10c. The confining pressure began at 2400 psig and was increased to 4800 psig. Permeability, shown by the upward facing triangles, decreased from 0.037 to 0.017 microdarcy. Decreasing the confining pressure back to 2400 psig returned the permeability to 0.026 microdarcy, equal to 70% of the initial permeability at that confining pressure.

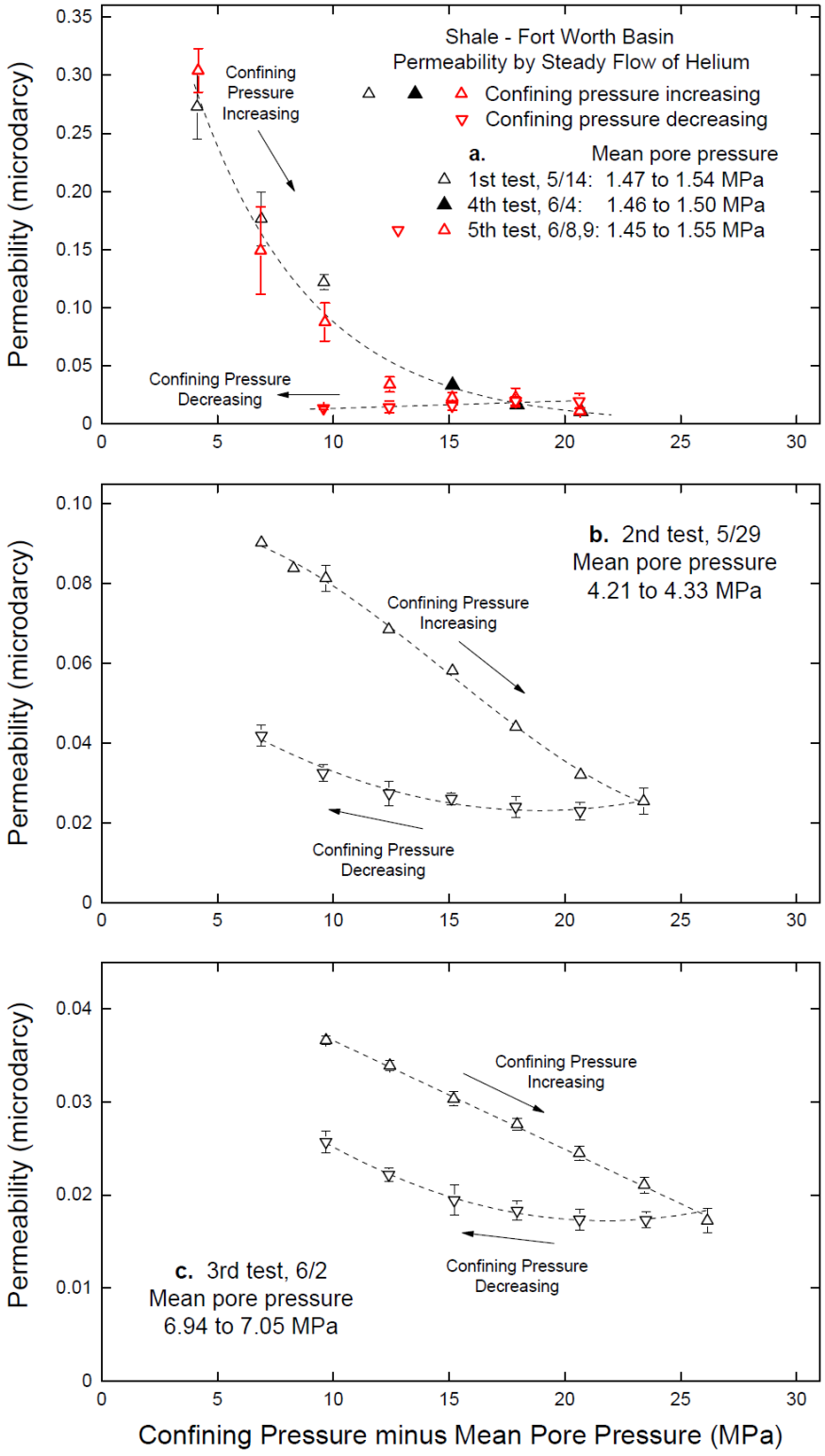

Figure 10.—Permeability of the Barnett Shale sample versus mean effective stress.
a. Confining pressure 5.62 to 22.2 MPa (800 to 3200 psig), mean pore pressure 1.5 MPa (200 psig).
b. Confining pressure 11.1 to 27.7 MPa (1600 to 4000 psig), mean pore pressure 4.3 MPa (600 psig).
c. Confining pressure 16.6 to 33.2 MPa (2400 to 4800 psig), mean pore pressure 7.0 MPa (1000 psig).

To determine whether the effects of high confining pressures on permeability were accumulating, the mean pore pressure was returned to 200 psig, as in the first condition investigated. The first confining pressures tested were 2400, 2800, and 3200 psig, toward the upper end of the range of confining pressures investigated. The corresponding values for the permeability are 0.034, 0.017, and 0.011 microdarcy, shown as black filled triangles at the bottom right in Figure 10a. The last two values, at the two highest confining pressures (data points hidden behind red triangles), are much lower than the values for the permeability from the 3rd test at the same effective stress, shown in Figure 10c. For example, at the effective stress of 20.7 MPa (3000 psi) during the 3rd test, we have a confining pressure of 4000 psig and a mean pore pressure of 1000 psig, for a mean effective stress of 3000 psi. The permeability in this case, with confining pressure increasing, is 0.024 microdarcy. In the 4th test, shown in Figure 10a, we have, at the effective stress of 20.7 MPa (3000 psi), a confining pressure of 3200 psig, a mean pore pressure of 200 psig, a mean effective stress of 3000 psi, and a permeability of 0.011 microdarcy, less than half of the permeability at the higher confining and mean pore pressures. Apparently, comparing these two particular cases, lower mean pore pressure is more detrimental to permeability than high confining pressure, when confining pressure is increasing. The reverse is true, for the sample under consideration, at the mean effective stress of 9.65 MPa (1400 psi). At this condition high confining pressure is more detrimental to permeability than low mean pore pressure, when confining pressure is increasing.

It was not possible to obtain a satisfactory correlation of all of the measurements using Equation (6) with a single value for the effective stress coefficient, χ, as had been done very successfully by Heller, Vermylen, and Zoback (2014) for Barnett, Eagle Ford, Marcellus, and Montney shales. This may be due, at least in part, to the very wide range of pore pressures in the sample during the measurements reported here. The range of pore pressures varies from the sample inlet pressure down to atmospheric pressure, causing the effective stress to vary over a wide range and increasing the effective permeability due to the Klinkenberg effect toward the outlet from the sample.

3.3. Response of Permeability to Changes in Pressure

As shown in Figure 10, permeability responds more quickly to changes in effective stress when confining pressure increases than it does when confining pressure decreases, indicating that the closure of pores with increasing effective stress occurs more rapidly than the recovery of pore structure with decreasing effective stress. A series of measurements was made to examine the time dependence of permeability following a reduction in effective stress. The permeability was again determined by steady flow of helium.

At the beginning of the test, the sample had been in the core holder for three days under a confining pressure of 11.1 MPa (1600 psig) and with the gas in its pores at atmospheric pressure. The confining pressure was first increased to 16.65 MPa (2400 psig), followed immediately by an increase in the mean pore pressure to 4.23 MPa (600 psig, with inlet at 1200 psig and outlet at atmospheric pressure). The dependence of permeability on time is shown in Figure 11a on a linear time scale, and in Figure 11b as a function of the logarithm of time. The first six data points on the log plot are based on individual measurements of the helium flow rate. The later data points are averages of from four to eight measurements of the flow rate.

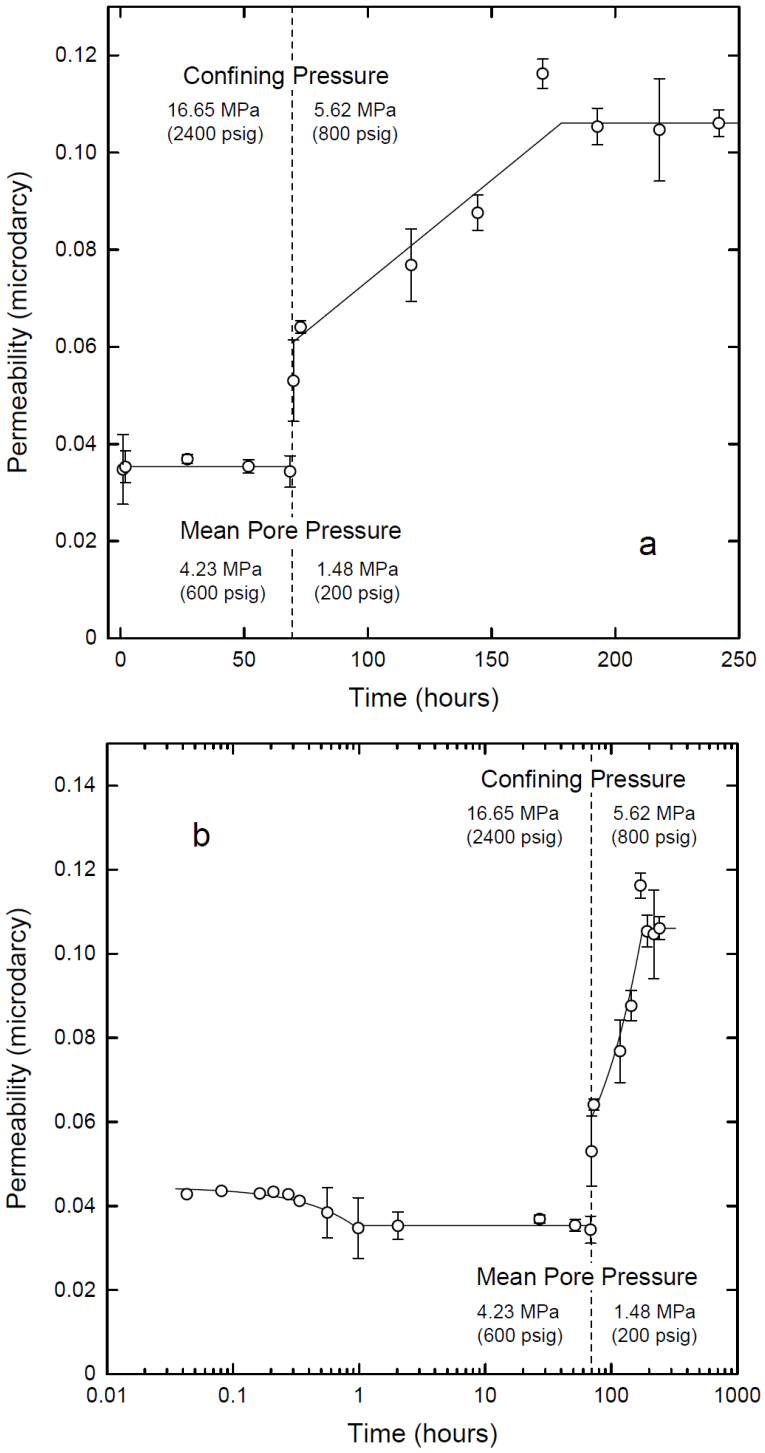

Figure 11.—Response of the permeability of a Barnett Shale sample to helium gas following a decrease in confining pressure from 16.65 MPa (2400 psig) to 5.62 MPa (800 psig) and a simultaneous decrease in mean pore pressure from 4.23 MPa (600 psig) to 1.48 MPa (200 psig).

a. Linear time scale.

b. Logarithmic time scale to show the early time behavior in response to the initial adjustment of confining pressure from 11.1 MPa (1600 psig) to 16.65 MPa (2400 psig) and increase in mean pore pressure from atmospheric to 4.23 MPa (600 psig), including some additional measurements at early times.

As shown on the log plot, Figure 11b, permeability responded very quickly to the initial change in pressures, arriving after 2.6 minutes at a value only 21% higher than the ultimate value established at the new condition. The permeability drifted slowly downward during the first hour, arriving at a value that remained constant, within the uncertainty of the measurements, for the next 68 hours.

Seventy hours after the first adjustment of the pressures, the mean pore pressure was reduced to 1.48 MPa (200 psig, with inlet at 400 psig and outlet at atmospheric pressure) and the confining pressure was reduced to 5.62 MPa (800 psig). As shown in Figures 11a and b, there was first a very rapid increase in permeability, by a factor of 1.7, followed by a much slower, roughly linear increase, by another factor of 1.7, over the next 120 hours. Following this slow adjustment of permeability, it remained constant, within the uncertainty of the measurements, over the next 50 hours.

This example illustrates the complexity of the dependence of apparent permeability of a Barnett Shale sample on overburden pressure, pore pressure, and their histories. Differences in the responses of the mineral structure and hydrocarbon porosity to changes in the pressures are expected to be among the effects responsible for the observed behavior (Heller, Vermylen, and Zoback, 2014; Bhandari, Flemings, Polito, Cronin, and Bryant, 2015).

Conclusions

The analysis by Zeng and Grigg (2006) based on the Forchheimer equation successfully accounted for inertial effects on the pressure gradient arising from high velocity gas flow through a sample of Woodford Shale containing a single fracture. The approach succeeded in unifying four sets of steady flow permeability measurements, whose apparent absolute permeabilities, obtained by extrapolation of the graphs of apparent permeability versus 1/pressure, were in poor agreement, ranging from 0.97 to 2.53 millidarcy. Zeng and Grigg's method produced an absolute permeability for the four sets of measurements of 3.1 ± 0.2 millidarcy, consistent with correction for inertial effects on the pressure gradient in the fracture. Under the assumption that the permeability of the rock matrix is negligible and the walls of the fracture are smooth parallel plates, the average aperture of the fracture was estimated to be approximately 10 μm.

The method developed by Hildenbrand and coworkers (2002, 2004) for determination of the gas breakthrough pressure of a brine-saturated rock was also applied to the fractured Woodford Shale sample. The measurement is called, by its authors, the "minimum capillary displacement pressure," because the critical pressure is found by applying a pressure difference greater than the breakthrough pressure to a fully-brine-saturated rock, causing pores and fractures to drain and allowing gas to flow through the sample. As the pressure drop across the sample decreases, it reimbibes the brine, beginning with the smallest open passages through the sample, and comes to equilibrium at the pressure difference equal to the capillary pressure at the smallest aperture in the highest conductivity path through the sample, the same path along which gas flow begins, when the process is reversed. The minimum capillary displacement pressure is the excess pressure, over hydrostatic, at which gas flow through the fracture would cease, as the pressure driving the flow declines. It is low for the fractured shale, as expected. Two determinations produced values of 0.0209 and 0.0171 MPa (3.03 and 2.48 psi), when the initial pressure differences across the sample were 0.539 MPa (78 psi) and 1.375 MPa (199 psi), respectively.

The maximum effective permeability, at the maximum gas saturation and minimum brine saturation, when the direction of brine migration changes from drainage to imbibition, increased by a factor of two, from 0.14 to 0.28 millidarcy, with a factor of two increase in the pressure drop across the sample at the maximum permeability, from 0.272 to 0.548 MPa (39.5 to 79.5 psi). A function fit to the dependence of effective permeability on pressure drop suggests that it would be useful in the simulation of gas flow in the presence of a wetting phase, but additional work is needed to establish the dependence of irreducible brine saturation and maximum effective permeability on pressure, for gas and the rock and wetting phases of interest.

The dependence of the permeability of the Barnett Shale on confining and pore pressures was examined by varying the confining pressure at fixed mean pore pressures, using helium. The permeabilities are presented as functions of the difference between the confining and pore pressures, or effective stress. At a mean pore pressure of 1.5 MPa (200 psig) increasing the effective stress from 4.14 MPa (600 psi) to 20.7 MPa (3000 psi) reduced the permeability of the shale to helium by a factor of 26, from 0.29 to 0.011 microdarcy. At higher pore pressure the sensitivity to increasing effective stress was less. At a mean pore pressure of 7.0 MPa (1000 psig) increasing the effective stress from 9.65 MPa (1400 psi) to 26.2 MPa (3800 psi) reduced the permeability by only a factor of 2, from 0.037 to 0.017 microdarcy. Permeability responded more quickly to increases in confining pressure than to decreases in confining pressure.

The time dependence of permeability was recorded over a period of 10 days, following a decrease in confining pressure from 16.65 MPa (2400 psig) to 5.62 MPa (800 psig) and simultaneous decrease in mean pore pressure from 4.23 MPa (600 psig) to 1.48 MPa (200 psig). An almost instantaneous increase in permeability, by a factor of 1.7, was followed by a slower increase, by another factor of 1.7, over the next 120 hours, after which the permeability remained constant until the end of the observations 50 hours later. The response of permeability to changes in pressure evidently consists of structural changes of at least two types or in two materials, such as the mineral fabric and the hydrocarbons.

References

American Petroleum Institute, "Recommended Practices for Core Analysis," Recommended Practice 40, 2nd ed., February 1998.

American Society for Testing and Materials, "Standard Test Method for Permeability of Rocks by Flowing Air," D4525-13e1, ASTM International, West Conshohocken, PA, 2013, with editorial corrections, February 2014.

Bhandari, A. R., P. B. Flemings, P. J. Polito, M. B. Cronin, and S. L. Bryant, "Anisotropy and Stress Dependence of Permeability in the Barnett Shale," *Transport in Porous Media*, **2015**, *108*, 393-411.

Collins, R. E., *Flow of Fluids through Porous Materials*, PennWell Publishing Co., Tulsa, OK, 1961, pp. 50-51.

Forchheimer, P., "Wasserbewegung durch Boden," *Zeitschrift des Vereins Deutscher Ingenieure*, **1901**, *45*, 1782-1788.

Heller, R., J. Vermylen, and M. Zoback, "Experimental investigation of matrix permeability of gas shales," *AAPG Bulletin*, **2014**, *98*, 975-995.

Hildenbrand, A., S. Schlömer, and B. M. Krooss, "Gas breakthrough experiments on fine-grained sedimentary rocks," *Geofluids*, **2002**, *2*, 3-23.

Hildenbrand, A., S. Schlömer, B. M. Krooss, and R. Littke, "Gas breakthrough experiments on pelitic rocks: comparative study with N_2, CO_2 and CH_4," *Geofluids*, **2004**, *4*, 61-80.

Klinkenberg, L. J., "The Permeability of Porous Media to Liquids and Gases," *Drilling and Production Practice*, American Petroleum Institute, Washington, DC, 1941, pp. 200-213.

Lemmon, E. W., M. L. Huber, and M. O. McLinden, "REFPROP Reference Fluid Thermodynamic and Transport Properties," NIST Standard Reference Database 23, Version 9.1, Applied Chemicals and Materials Division, U.S. Department of Commerce, 2013.

Sengers, J. M. H. L., Klein, M., and Gallagher, J. S., "Pressure-Volume-Temperature Relationships of Gases; Virial Coefficients," Section 4i in: Gray, D. E. (Ed.), *American Institute of Physics Handbook*, 3rd ed., McGraw-Hill, New York, 1972, pp. **4**-204 to **4**-221.

Walsh, P. M., R. A. Esposito, K. Theodorou, M. J. Hannon, Jr., A. D. Lamplugh, and K. M. Ellison, "Recovery Act: Geologic Sequestration Training and Research," Final Scientific/Technical Report, DOE Award No. DE-FE0002224, Submitted by the University of Alabama at Birmingham, December 17, 2013.

Zeng, Z., and R. Grigg, "A Criterion for Non-Darcy Flow in Porous Media," *Transport in Porous Media*, **2006**, *63*, 57-69.

NEW EXPERIMENTAL METHOD: FULL IMMERSION PRESSURE-PULSE DECAY

Michael J. Hannon, Jr.

CONTENTS

FIGURES

TABLES

1. Introduction

An alternative is proposed to the conventional pressure-pulse decay method for determining the permeability of a cylindrical rock sample. The proposed method has the advantage that permeabilities in both the axial and radial directions in the sample are determined in a single test on a single cylindrical core sample. From a test on a core plug cut perpendicular to the bedding plane, the proposed method provides permeabilities parallel and perpendicular to bedding without having to perform measurements on separate samples. The method is described as "Full Immersion Pressure-Pulse Decay."

*****The work described in this section was also supported, in part, by the Alabama Power Company and Southern Company, under the project entitled, "Geologic Carbon Sequestration: Caprock Integrity Laboratory;" by the National Energy Technology Laboratory, under Award Number DE-FE0002224, entitled, "Recovery Act: Geologic Sequestration Training and Research;" by Advanced Resources International, under Award Number DE-FE0010554 from the National Energy Technology Laboratory, entitled, "Commercial Scale CO_2 Injection and Optimization of Storage Capacity in the Southeastern United States;" and by Montana State University, under Award Number DE-FE0004478 from the National Energy Technology Laboratory, entitled, "Advanced CO_2 Leakage Mitigation using Engineered Biomineralization Sealing Technologies."

†A Patent Cooperation Treaty Application for this technology was filed by the UAB Research Foundation on May 7, 2016.

For experimental testing of the proposed technique, core samples from an outcrop formation were provided by Weatherford Laboratories. Measurements using the full immersion technique are compared with permeabilites determined by Weatherford using the methods established by long experience in their laboratories. The author is grateful to Patrick Lasswell and Keegan Gallaher of Weatherford Laboratories for providing the rock samples and measurements of their permeability.

2. Experiment

A pressure vessel was designed and fabricated to house a cylindrical core sample and expose the sample to fluid over its entire outer surface, as shown in Figure 1. The cell and associated valves and tubing were placed in a water bath inside an incubator that maintained the temperature constant to within ± 0.5 °C. In its present configuration the sample cannot be subjected to axial or radial confining stresses. For each sample, a series of experiments was performed with helium gas at four different initial pressures, ranging from approximately 250 to 1000 psia. The gas was first introduced into the space surrounding the sample, between the outer surface of the sample and the inner wall of the pressure vessel, and allowed to fill the pore space in the sample at an initial equilibrium pressure, p_0. The pressure in the volume surrounding the sample was then quickly increased, by just under 10% of the initial equilibrium pressure, to the "pulse" pressure, p_p, and the pressure vessel was closed. The pressure in the space surrounding the sample was recorded as the gas fills the pore volume in the rock. The effect of temperature fluctuations on the pressures was small. Examples of the time dependence of the pressure for two of Weatherford Laboratories' samples, UAB-3 and UAB-4, at four different initial pressures, and comparison with the best fits of the flow model to the data, are shown in Figures 2 and 3. The two sets of measurements chosen as the examples are those on the samples having the lowest (UAB-3) and highest (UAB-4) permeabilities, among the four samples tested.

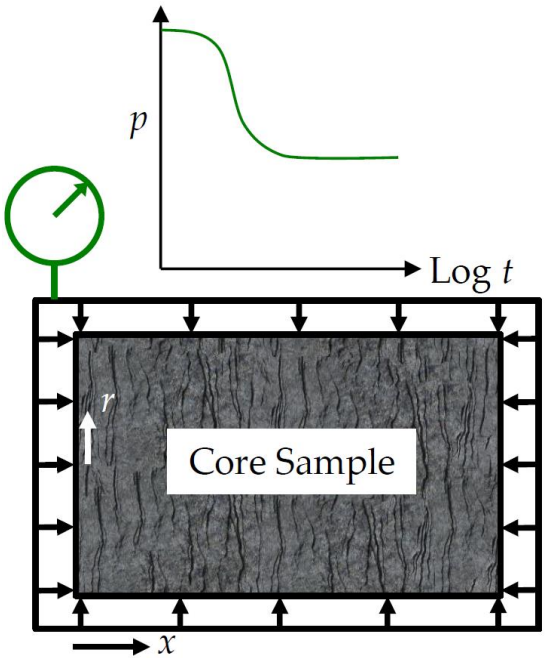

Figure 1.Pressure-pulse decay with a cylindrical rock sample exposed to fluid over its entire surface.

Moving averages of the pressure were calculated while recording the data and again during post-processing, providing a set of 500 data points for comparison with the model. The resolution of the data is increased at higher pressures and at later times. Because the inversion procedure employs a weighted-least-squares approach, data at early times and low pressures (due to sensor accuracy) are given lowest priority, resulting in small characteristic differences between the measurements and the model at early times, following the initial transient.

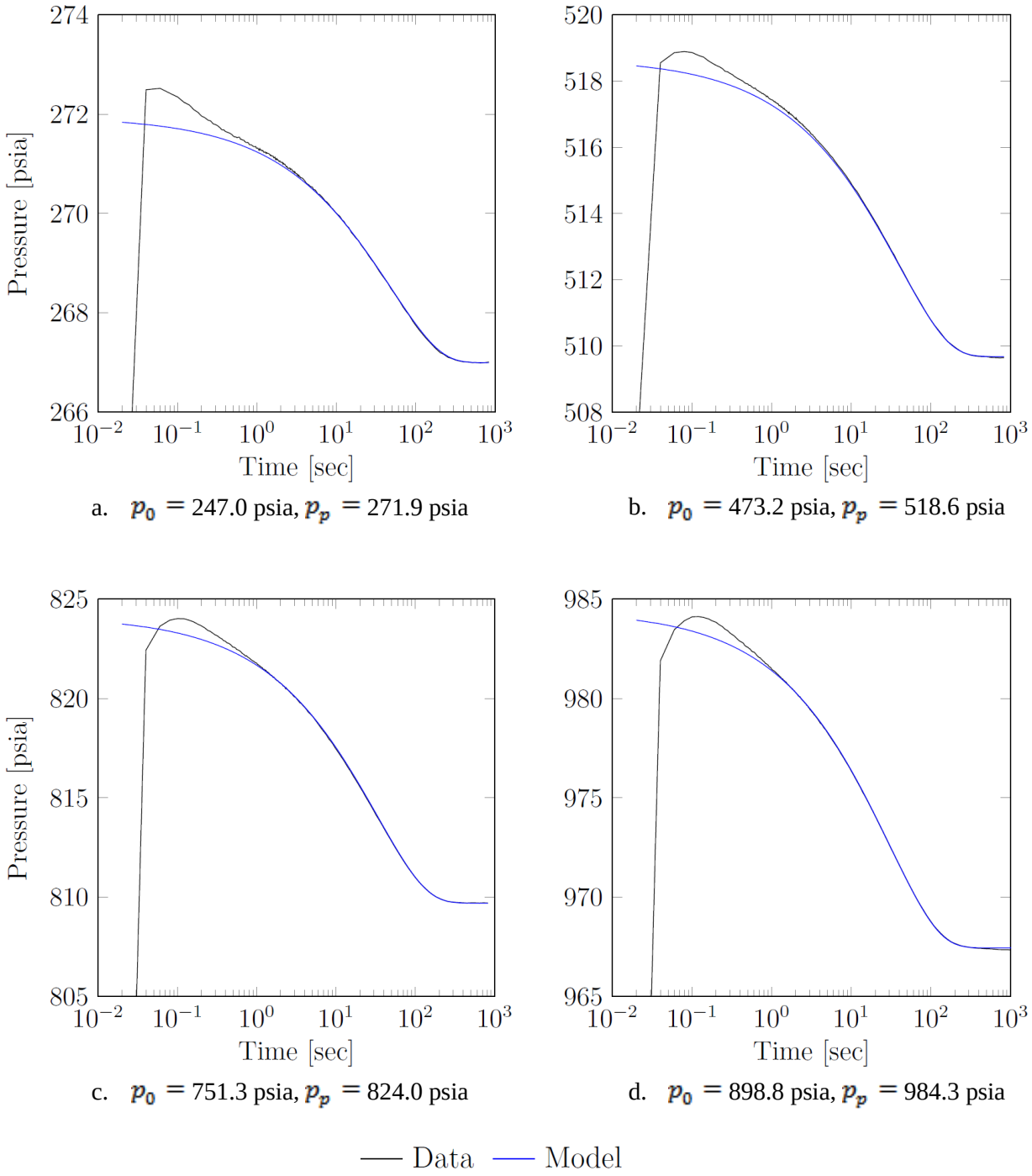

a. p_0 = 247.0 psia, p_p = 271.9 psia

b. p_0 = 473.2 psia, p_p = 518.6 psia

c. p_0 = 751.3 psia, p_p = 824.0 psia

d. p_0 = 898.8 psia, p_p = 984.3 psia

Figure 2. History match between model and data for sample UAB-3.

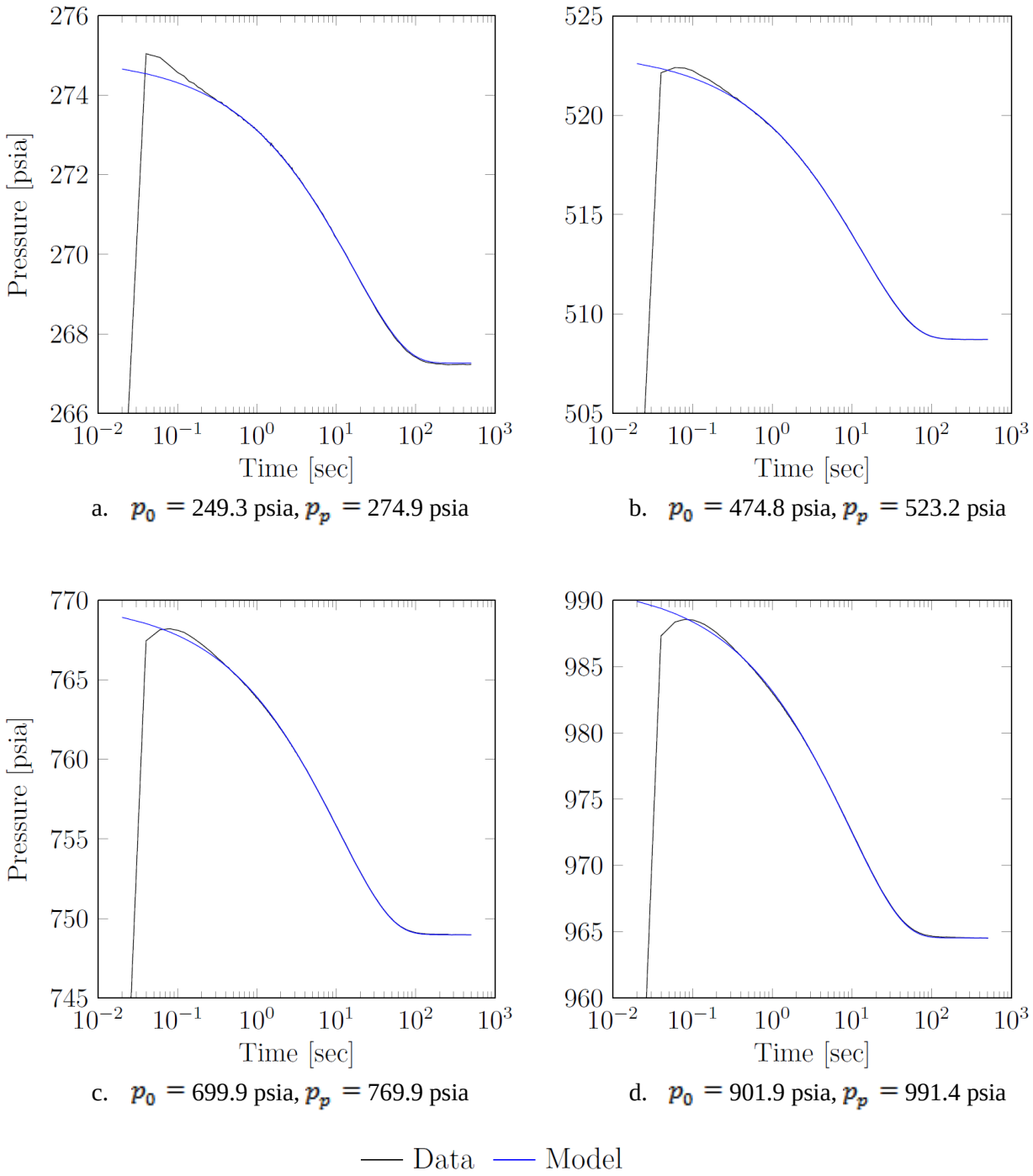

a. p_0 = 249.3 psia, p_p = 274.9 psia

b. p_0 = 474.8 psia, p_p = 523.2 psia

c. p_0 = 699.9 psia, p_p = 769.9 psia

d. p_0 = 901.9 psia, p_p = 991.4 psia

Figure 3. History match between model and data for sample UAB-4.

3. Flow Model

Applying a pressure pulse to the entire outer surface area of the sample, as shown in Figure 1, yields pressure gradients oriented along the principal axes, x and r, restricting flow to only those directions. This simplifies the governing equations of motion, producing an axisymmetric flow model for comparison with experimental data. Assuming that the fluid travels along axisymmetric flow paths, the governing equation of motion, in terms of the non-dimensional pseudo-pressure, p_D^*, and pseudo-time, $t_{D,R}^*$, defined by Haskett, Narahara, and Holditch (1988), becomes:

$$\frac{\partial p_D^*}{\partial t_{D,R}^*} = \frac{\mu c}{(\mu c)_{ref}} \frac{\partial p_D^*}{\partial t_{D,R}} = \frac{1}{r_D} \frac{\partial p_D^*}{\partial r_D} + \frac{\partial^2 p_D^*}{\partial r_D^2} + \lambda_x^2 \frac{\partial^2 p_D^*}{\partial x_D^2} \tag{1}$$

Because its solution will be approximated numerically, the equation of motion is written in both the standard time domain t, to facilitate comparison with experimental data, and in the pseudotime domain t^*, for comparison with analytical models. The time constant τ_R,

$$\tau_R = \frac{n(\mu c)_{ref} R^2}{k_r} \tag{2}$$

normalizing the temporal coordinate, is based on the sample radius R and its permeability in the radial direction, k_r. Flow in the radial direction is expected to dominate, because the radius of a sample plug is typically shorter than half its length and the permeability in the radial direction, in a plug cut perpendicular to the bedding plane, is expected to be higher than in the axial direction.

The axial coordinate x is normalized by half the length of the sample: $x_D \equiv 2x/L$. The dimensionless parameter, λ_x^2, defined by Equation 3, contains the ratio of axial (perpendicular to bedding) to radial (parallel to bedding) permeability and the dimensions of the sample. It is written in this form to preserve the convention adopted in previously-derived analytical models for other scenarios involving multiple permeabilities.

$$\lambda_x^2 \equiv \frac{k_x}{k_r} \left(\frac{D}{L}\right)^2 \tag{3}$$

Equation 4 defines the initial pressure disturbance in the reservoir space ($r_D = 1,\ x_D = 0$) applied to the the initial equilibrium pressure state within the pore space ($0 \le r_D < 1,\ 0 < x_D \le 1$).

$$p_D^*(r_D, x_D, t_{D,R} = t_{D,R}^* = 0) = \begin{cases} 0, & 0 \le r_D < 1, 0 < x_D \le 1 \\ 1, & r_D = 1, x_D = 0 \end{cases} \tag{4}$$

The boundary conditions describe the absence of flow across the inner boundaries (axis and center plane) of the sample (Equation 5) and provide a material balance between gas in the reservoir space and the mass flow of gas through the outer surface of the sample (Equation 6).

$$\left.\frac{\partial p_D^*}{\partial r_D}\right|_{r_D=0} = \left.\frac{\partial p_D^*}{\partial x_D}\right|_{x_D=1} = 0 \tag{5}$$

$$\frac{\gamma}{2}\frac{\partial p_D^*}{\partial t_{D,R}^*}\bigg|_{\substack{r_D=1\\x_D=0}} = \frac{\gamma}{2}\frac{\mu c}{(\mu c)_{ref}}\frac{\partial p_D^*}{\partial t_{D,R}}\bigg|_{\substack{r_D=1\\x_D=0}} = \lambda_x^2\int_0^1 \frac{\partial p_D^*}{\partial x_D}\bigg|_{x_D=0} r_D\, dr_D - \int_0^1 \frac{\partial p_D^*}{\partial r_D}\bigg|_{r_D=1} dx_D \qquad (6)$$

A numerical discretization scheme was employed to determine an approximate solution of Equations 1 to 6. Using this solution, the dependence of reservoir pressure ($p_D^*|_{r_D=1,x_D=0}$) on time for various values of λ_x^2 and γ is shown in Figure 4. The cases of $\lambda_x^2 = 0$ (shown as solid black lines) are produced using the previously-derived analytical model for the radial flow problem, in good agreement with the numerical solution for the axisymmetric model. In all cases, the ratio of reservoir volume to pore volume, γ, determines the final equilibrium pressure of the test, and the normalized permeability ratio λ_x^2 determines the deviation of the pressure-response curve from the radial-flow solution. The effect of λ_x^2 on the flow model is investigated more thoroughly in the following sections.

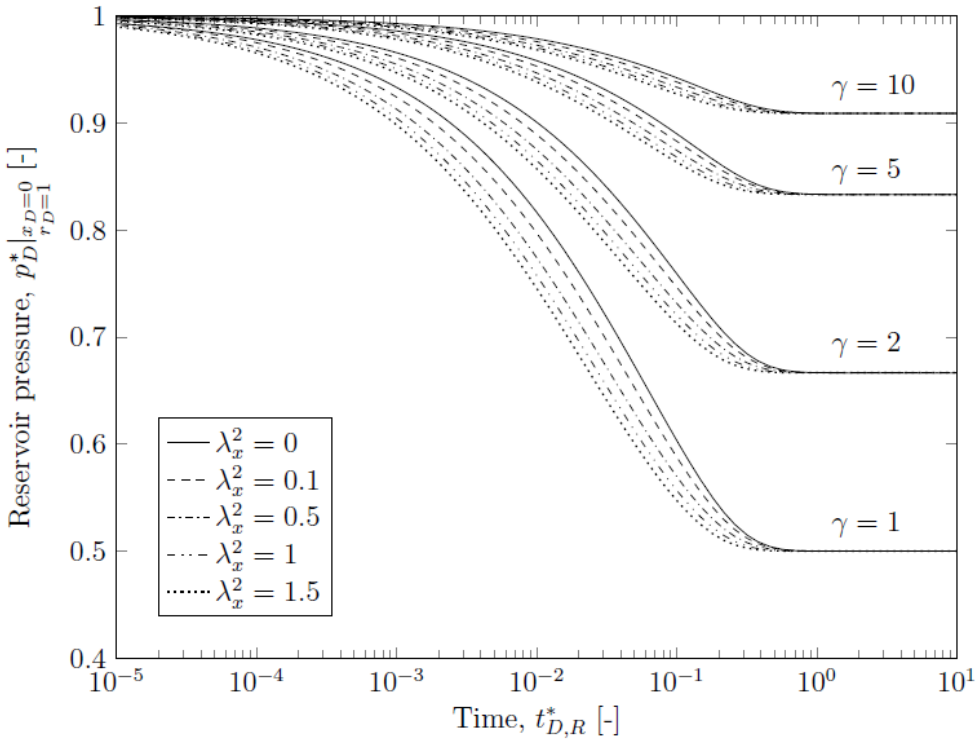

Figure 4. Dependence of reservoir pressure on time during an axisymmetric fully-immersed pressure-pulse decay with varying permeability ratio, λ_x^2, and ratio of reservoir volume to pore volume, γ.

Several effects associated with the initial step change in pressure cause the experimental data to deviate from the model at early times. These include temperature changes due to the Joule-Thomson effect and adiabatic expansion of the gas, and the time required for the gas to fill the space in the cell surrounding the sample. Ambient temperature changes and leakage of the gas around the O-rings and fittings cause deviations of the late-time behavior from the model prediction. The analysis procedure discounts the temperature changes and fill time by ignoring the first second of pressure data and treating the initial pulse pressure p_p as a fitting parameter. Numerical compensation for leakage is done using a linear fit to a portion of the late-time data. The leak rates ranged from 0.03 to 0.5 psi/hr from the small volume of gas in the cell. Due to the short duration of the tests, typically 500 to 1000 s, leakage at these rates was negligible.

Properties of the gas were obtained from the NIST REFPROP database (Lemmon, Huber, and McLinden, 2013) at the average temperature recorded during each test.

Adjustment of the initial pulse pressure, porosity, absolute axial and radial permeabilities, and axial and radial Klinkenberg coefficients to obtain the optimum fit of the model to the pressure measurements produced the calculated time-dependent pressures compared with the measurements in Figures 2 and 3 and the values for porosity, permeabilities, and Klinkenberg coefficients given in Table 1.

4. Test of the Full Immersion Method

Data from the four tests at different pressures were fit simultaneously to the flow model, treating the apparent radial permeabilities k_r, parallel to bedding, and apparent axial permeabilities k_x, perpendicular to bedding, as constants for each test. These values varied from test to test according to Equations 7 and 8, accounting for slip (Klinkenberg, 1941). The subscript ∞ indicates absolute (or liquid) permeability, and b is the Klinkenberg coefficient.

$$k_r = k_{\infty,r}\left(1 + \frac{b_r}{p_{ref}}\right) \tag{7}$$

$$k_x = k_{\infty,x}\left(1 + \frac{b_x}{p_{ref}}\right) \tag{8}$$

The reference pressure p_{ref} for each test was assigned the average value over the duration of the test and the porosity n was assumed to be the same for all tests performed on the same sample.

4.1. Parameter Estimation

The procedure followed by the parameter estimator for the fully-immersed flow scenario is outlined in Figure 5. The algorithm invokes the analytical solution for radial flow to provide educated initial parameter estimates before refining them with the more computationally intensive full-immersion model. In most porous materials investigated using this technique, it is likely for the flow to occur predominantly in the radial direction. This is due both to the higher expected radial permeability ($k_r > k_x$) as well as the higher efficiency for radial flow to infiltrate a standard-sized cylindrical sample. As a result, the analytical and computationally efficient radial-flow model provides useful initial estimates of the parameters. Final parameter estimates are then determined by the degree to which the experimental data deviate from the radial-flow model. Limitations are also placed on parameter estimates to ensure $k_r > k_x$ while approaching the solution.

The flow diagram presented in Figure 5 outlines the algorithm employed to determine the reservoir to pore volume ratio γ, the radial flow time constant τ_R, and the normalized axial to radial permeability ratio λ_x^2, based on data from a single experiment. Measured quantities are denoted by the superscript $\widehat{\ }$, and parameter estimates are denoted by the superscript $\widetilde{\ }$. The raw pressure traces are transformed to the dimensionless pseudo-pressure and pseudo-time domains to provide the initial estimates of $\widetilde{\tau_R}$, $\tilde{\gamma}$, and $\widetilde{p_p^*}$ using the analytical radial flow model. From that point, while pressure data remain as normalized pseudo-pressures, the numerical

model outputs values of p_D^* in the original time domain, t. Using a sufficiently small value of λ_x^2 as an initial guess, along with the initial estimates of the remaining parameters, updated estimates of all parameters are determined by fitting the model at a coarse spatial resolution to the data. Estimates are updated in the numerical model with increasing spatial resolution until a fit to the data is acquired at sufficiently high spatial resolution, resulting in the final estimates of parameters $\widetilde{\tau_R}$, $\widetilde{\lambda_x^2}$, $\tilde{\gamma}$, and $\widetilde{p_p^*}$.

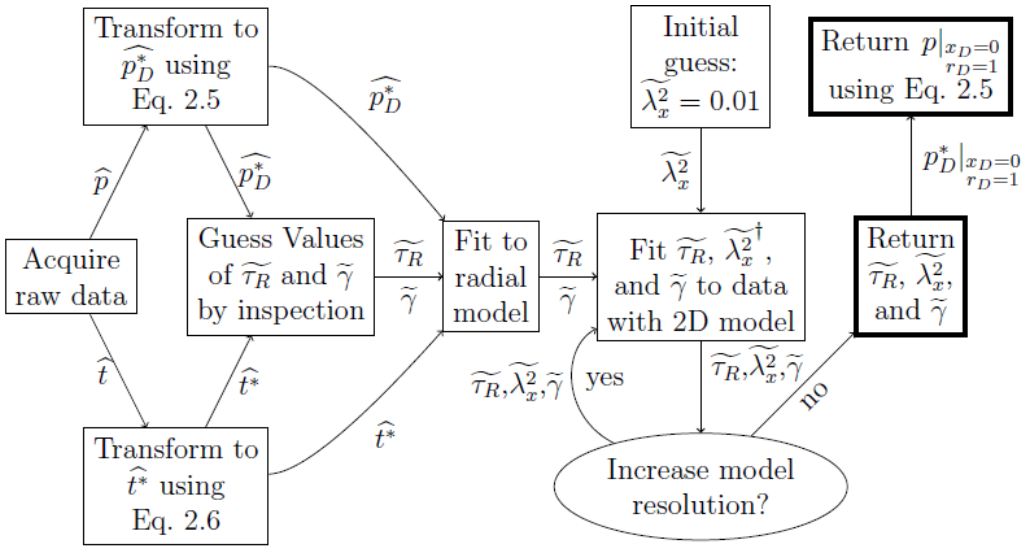

† Changes in estimated values of $\widetilde{\lambda_x^2}$ limited to ensure $k_x < k_r$.

Figure 5. Parameter estimation algorithm for analysis of the data from a single full immersion pressure pulse decay experiment. Analogous schemes are employed for simultaneous analysis of multiple tests on the same sample, accounting for the Klinkenberg effect at different reference pressures.

The resulting parameter estimates for each of the four core samples, UAB-1 to UAB-4, from Weatherford Laboratories, are given in Table 1, with estimates of their uncertainty. Uncertainty in the results for $k_{\infty,x}$ and b_x is much greater than the uncertainty in the values for $k_{\infty,r}$ and b_r, whose uncertainty is much greater than that in the estimates for porosity, *n*.

4.2. Comparison with Measurements by Weatherford Laboratories

Klinkenberg plots relating apparent permeabilities (k_r, shown in red, and k_x, shown in blue) to inverse pressure, for each sample, are shown in Figure 6. The results are compared with independent assessments of k_x performed by Weatherford Laboratories using nitrogen gas at a pressure of 60 psig, shown by the blue X symbols (Keegan Gallaher, Weatherford Laboratories, personal communication, February 17, 2016). The averages of the axial permeabilities determined by the full immersion method, shown by the blue dashed lines on the Klinkenberg plots, are slightly higher than the measurements by Weatherford Laboratories. The largest deviation was observed for sample UAB-4, in Figure 6d, where the full immersion measurement is 1.62 times the measurement at Weatherford Laboratories. In all cases, Weatherford Laboratories' values fall well within the uncertainty limits of the full immersion results. Contributing to the differences between the measurements may be the difference in confining

stresses in the two experiments. Weatherford Laboratories' measurements were made with the sample subjected to a net confining stress of 500 psi, while the full immersion tests were performed with the samples under no net confining stress.

Table 1.
Properties of Rock Samples Provided by Weatherford Laboratories for the
Blind Test of Full Immersion Pressure-Pulse Decay.
Measurements using helium gas.

Core	Diameter D, inch	Length L, inch	Porosity n, %	Radial Direction: Absolute Permeability $k_{\infty,r}$, nanodarcy	Radial Direction: Klinkenberg Coefficient b_r, psi	Axial Direction: Absolute Permeability $k_{\infty,x}$, nanodarcy	Axial Direction: Klinkenberg Coefficient b_x, psi
UAB-1	1.490	0.940	$4.85^{+0.05\%}_{-0.05\%}$	$88.7^{+9.06\%}_{-8.31\%}$	$476^{+26.4\%}_{-20.9\%}$	$14.3^{+86.0\%}_{-46.3\%}$	$4020^{+154\%}_{-60.7\%}$
UAB-2	1.498	0.980	$6.75^{+0.06\%}_{-0.06\%}$	$225^{+5.76\%}_{-5.44\%}$	$397^{+19.2\%}_{-16.1\%}$	$23.1^{+74.8\%}_{-42.8\%}$	$3860^{+97.2\%}_{-49.3\%}$
UAB-3	1.476	0.993	$4.70^{+0.05\%}_{-0.05\%}$	$67.6^{+8.96\%}_{-8.22\%}$	$540^{+23.5\%}_{-19.0\%}$	$5.39^{+214\%}_{-68.1\%}$	$6160^{+264\%}_{-72.5\%}$
UAB-4	1.490	0.999	$7.59^{+0.04\%}_{-0.04\%}$	$306^{+11.1\%}_{-9.96\%}$	$424^{+30.8\%}_{-23.6\%}$	$57.2^{+80.8\%}_{-44.7\%}$	$2260^{+116\%}_{-53.6\%}$

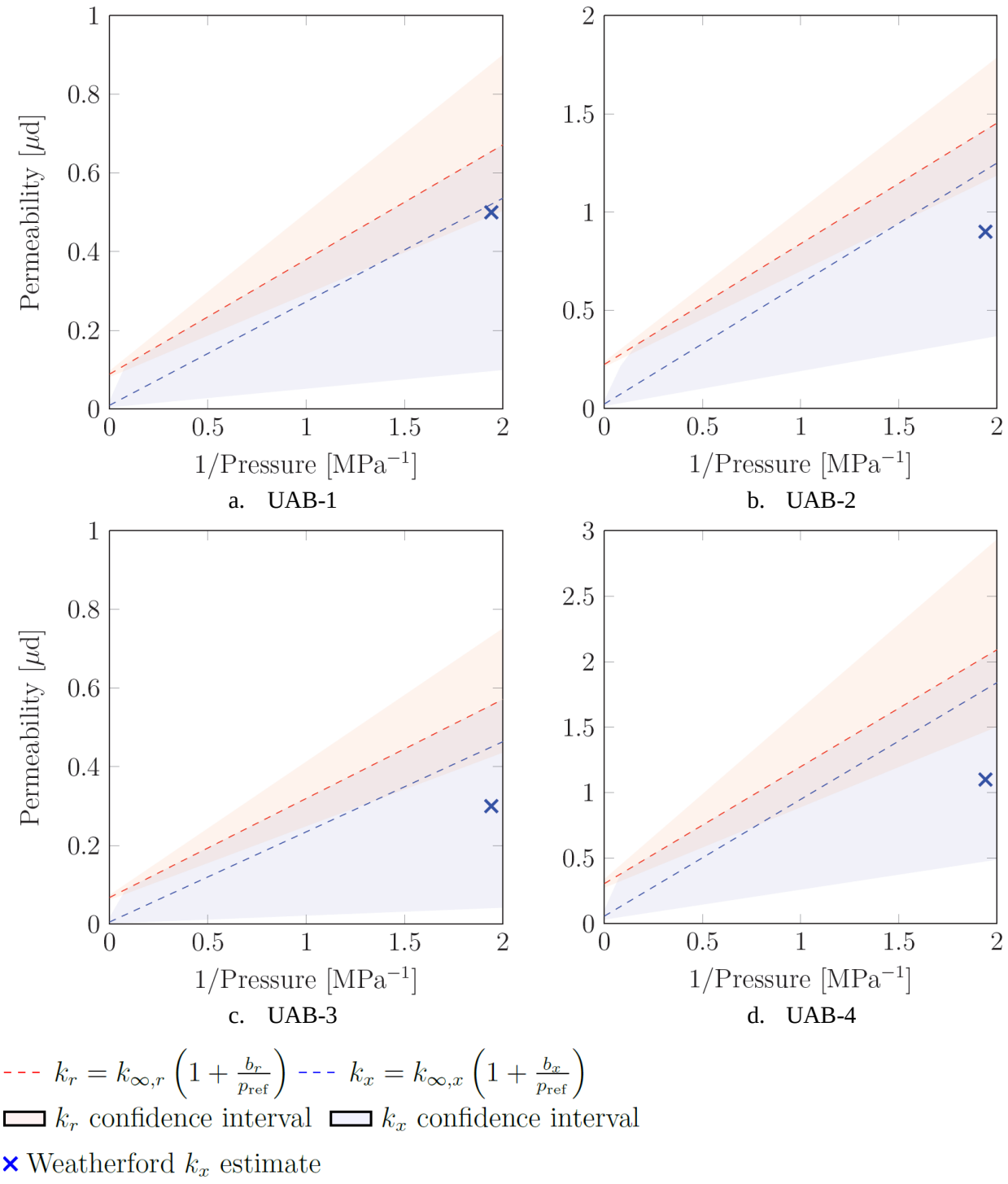

Figure 6. Klinkenberg plots of apparent permeabilities to helium, parallel and perpendicular to bedding, for four cylindrical samples provided by Weatherford Laboratories.

Red dash: full immersion measurements of radial permeability with uncertainty (pink shading).

Blue dash: full immersion measurements of axial permeability with uncertainty (blue shading).

Blue X: Weatherford Laboratories' measurements using nitrogen at a net confining stress of 500 psi (Keegan Gallaher, Weatherford Laboratories, personal communication, February 17, 2016).

The large uncertainties in the values for k_x and b_x are indicated by the large confidence intervals (shown in blue shading) of the apparent permeability perpendicular to bedding, compared with the narrower confidence intervals for k_r and b_r (shown in pink shading), parallel to bedding. In the data analysis, the upper bounds of permeabilities perpendicular to bedding were constrained to be less than those parallel to bedding. Given the good agreement between the model and experimental data, shown in Figures 2 and 3, such large uncertainties can only arise from parameter correlation. For a given experiment, such correlation effects are manageable as long as the factor $(k_x/k_r)(D/L)^2$ remains less than 1. Prior to the tests, the experimental apparatus and sample geometry were chosen in anticipation of apparent permeability ratios k_x/k_r remaining well under this limit at all test pressures. It appears that the mechanism driving the ratio down is the large Klinkenberg coefficient b_x. If so, lower ratios are only encountered at sufficiently high pore pressure, above the 1000 psia maximum pressure rating of the present test cell.

These full immersion tests provide accurate estimates of k_r, but can only provide estimates of upper and lower bounds on k_x. There are several strategies that would narrow the confidence intervals. Listed in order of increasing difficulty, with the least difficult to implement first, the greatest contributions to uncertainty can be alleviated by:

1. Accounting for non-linear trends in apparent permeability (i.e., Knudsen diffusion).
2. Decreasing the diameter-to-length ratio, D/L, of the sample.
3. Performing tests at higher pressure (above the rated maximum pressure of the present apparatus).
4. Performing unidirectional tests for calibration.

5. Measurements of Permeability of Shale

The first application of the full immersion method was to measurement of the axial and radial permeabilities of a sample of Barnett Shale from the Fort Worth Basin. The sample was 2 inches in diameter and 1 inch long, with its axis perpendicular to bedding. Tests were performed at four pressures using helium gas. The record of pressure versus time for a test having pulse pressure of 937.5 psia and reference (average) pressure of 934.2 psia, the highest of the four pressures run, is shown in Figure 7. The duration of the test for this low permeability rock was approximately 14 hours, compared with the tests on higher permeability samples, shown in Figures 2 and 3, which lasted only 8 to 17 minutes. The results of the simultaneous measurements of permeability parallel and perpendicular to bedding are presented in Table 2.

A Klinkenberg plot of the axial and radial permeabilities versus $1/p_{ref}$ is shown in Figure 8. The extrapolation to $1/p_{ref} = 0$ provides estimates of absolute permeabilities of 51.4 ± 38.5 and 22.5 ± 13.4 picodarcy, parallel and perpendicular to bedding, respectively.

The dimensions of the test cell and sample plug were chosen to optimize the precision of the determination of both permeabilities, with the expectation that the ratio of permeabilities, k_r/k_x, would be equal to or greater than about 10. The results of the present tests indicate a ratio of 3. The uncertainty in the measurements is expected to be lower in tests on samples 1 inch, instead of 2 inches, in diameter.

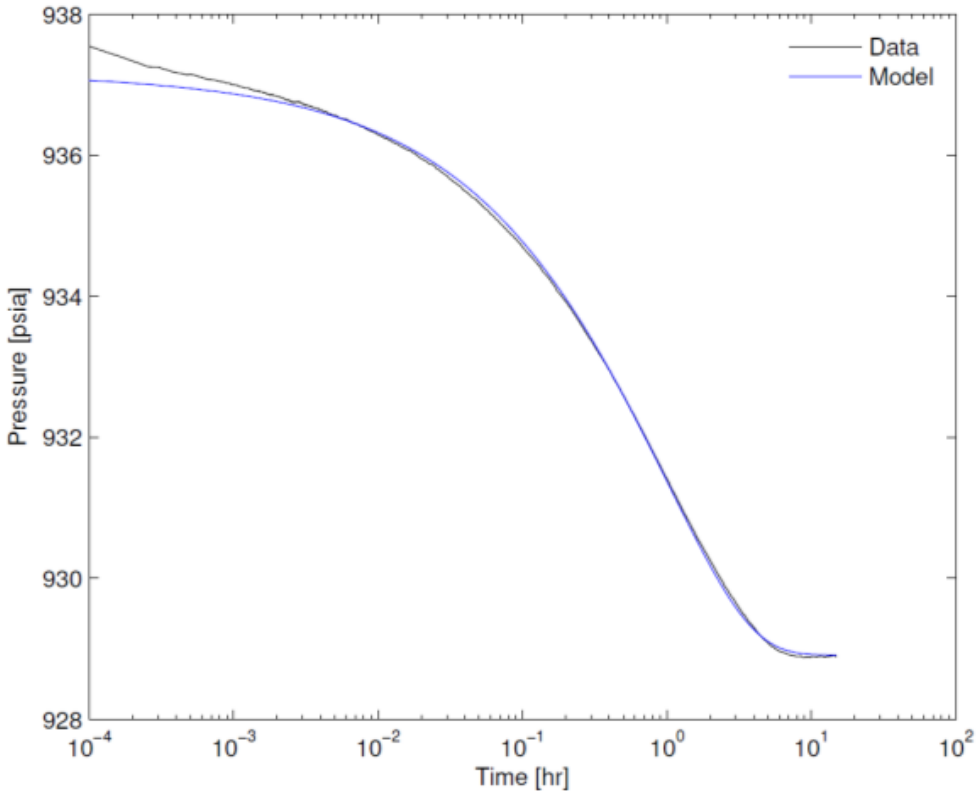

Figure 7. Record of pressure versus time, shown in black, during a full immersion pressure-pulse decay measurement of the axial and radial permeabilities to helium of Barnett Shale sample. The axis of the cylindrical core is perpendicular to bedding. The permeabilities determined from the best fit of the model, shown in blue, to the measurements are 0.595 and 0.199 nanodarcy, parallel and perpendicular to bedding, respectively.

Table 2.
Shale Sample from the Fort Worth Basin.
Permeabilities to Helium Gas Parallel and Perpendicular to Bedding
Determined Simultaneously by Full Immersion Pressure-Pulse Decay.*

Average Pressure, p_{ref} (psia)	Permeability: Parallel to Bedding, k_r (nanodarcy)	Permeability: Perpendicular to Bedding, k_x (nanodarcy)
274.9	1.880	0.621
574.7	0.965	0.324
788.6	0.657	0.222
934.2	0.595	0.199

*Porosity of the shale was determined to be 1.74 ± 0.05%.

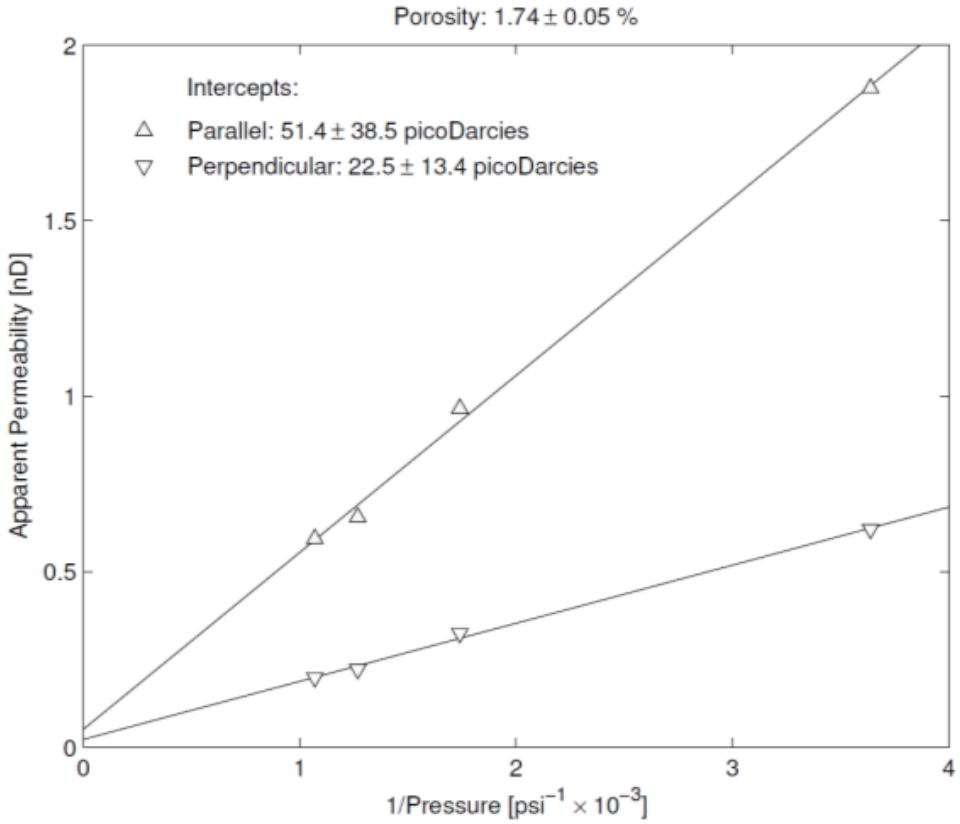

Figure 8. Klinkenberg plot of the apparent permeabilities to helium, parallel and perpendicular to bedding of the Barnett Shale versus the reciprocal of the average pressure, $1/p_{ref}$, and extrapolation to $1/p_{ref} = 0$ for determination of absolute permeabilities. It is expected that the uncertainty in the extrapolated values can be minimized by using a smaller diameter sample plug, so the characteristic times for flow in the axial and radial directions are farther apart.

A test on the Barnett Shale was also run using methane gas, with the result shown in Figure 9. Agreement between the model and measurements is not as good as in the test shown in Figure 7, with helium. A possible explanation is that the time dependence of the pressure is distorted, compared with that associated with purely capillary flow, by the adsorption of methane in the hydrocarbon present in the rock. The permeabilities determined by the best fit of the model to the data are: parallel to bedding, k_r = 51.5 picodarcy, and perpendicular to bedding, k_x = 18.0 picodarcy, both an order of magnitude smaller than the corresponding values for helium, in Table 2, at p_{ref} = 788.6 psia. The porosity determined using methane, 1.78%, is in good agreement with the value of 1.74% determined using helium.

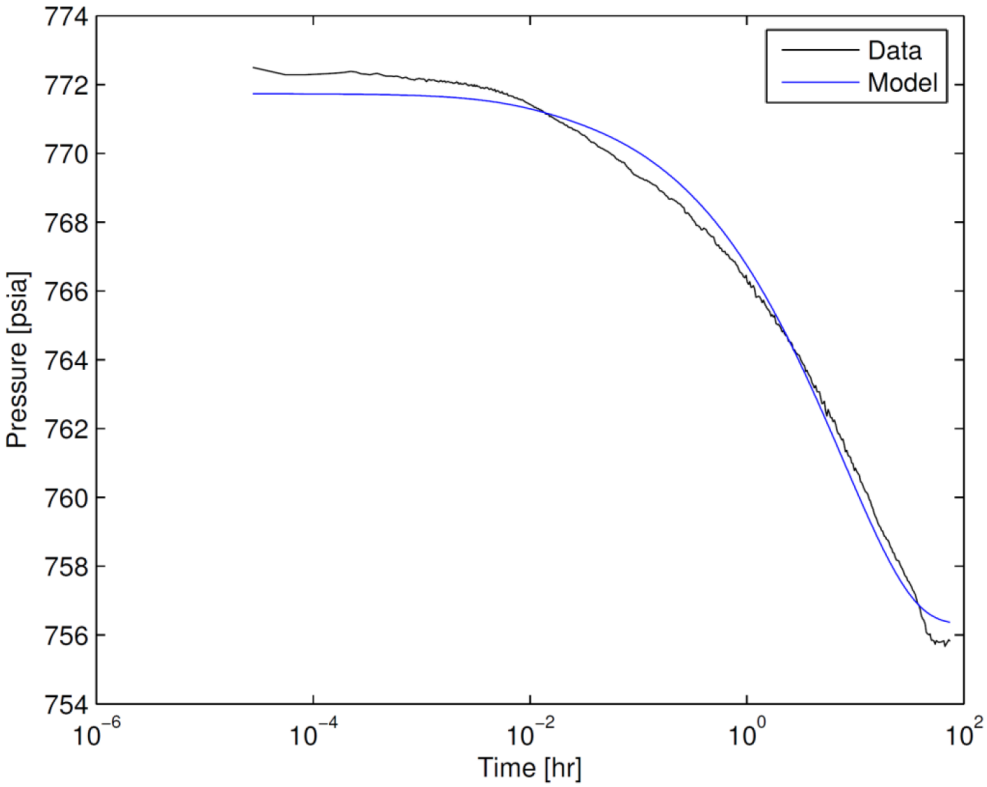

Figure 9. Record of pressure versus time, shown in black, during a full immersion pressure-pulse decay measurement of the axial and radial permeabilities to methane of a Barnett Shale sample. The sample is the same one whose pressure pulse decay response to helium is shown in Figure 7. The permeabilities determined from the best fit of the model, shown in blue, to the measurements are 51.5 and 18.0 picodarcy, parallel and perpendicular to bedding, respectively.

6. Conclusions

A new method for determination of the permeability of intact cylindrical rock samples has been developed, in which the rock is exposed to a permeating gas over all of its surface. The new technique, called "full immersion pressure-pulse decay," has the advantage that permeabilities in both axial and radial directions in a sample can be determined in a single experiment. For a sample plug cut perpendicular to bedding, this permits the permeabilities parallel and perpendicular to bedding to be determined simultaneously, on the same sample.

The theory was first developed, followed by design of the experiment, then derivation of a procedure for inversion of the data to determine porosity and the permeabilites. A blind test was conducted using samples generously provided by Weatherford Laboratories. The permeabilities measured by the full immersion technique were slightly larger than those measured at Weatherford Laboratories, using their standard methods. For the sample having the largest deviation between the results from the two laboratories, the axial permeability determined by full immersion was 1.62 times the value determined by Weatherford Laboratories, so agreement between the two methods was good. The differences between the results from the two laboratories may be explained by the fact that in the tests at Weatherford the samples were under

a confining stress of 500 psi, while in the tests by full immersion pressure-pulse decay the samples were under no confining stress.

The first application of the full immersion pressure-pulse decay method was the measurement of porosity and permeability to helium of a sample of Barnett Shale from the Fort Worth Basin. Measurements at four different average pore pressures in the range from 275 to 934 psia produced apparent permeabilities in the range from 0.6 to 1.9 nanodarcy parallel to bedding and from 0.2 to 0.6 nanodarcy perpendicular to bedding. Klinkenberg plots of the apparent permeabilites versus the reciprocal of the mean pore pressure and extrapolation to high pressure gave absolute permeabilities of 51.4 ± 38.5 and 22.5 ± 13.4 picodarcy parallel and perpendicular to bedding, respectively. It is expected that the uncertainty in the measurements can be minimized by adjusting the diameter to length ratio of the sample, so the characteristic times for flow in the axial and radial directions are farther apart.

A full immersion pressure-pulse decay measurement on the sample of Barnett Shale was also performed using methane gas. While it was possible to extract porosity and permeabilities from the data, the fit of the model to the pressure decay was not as good as for the test using helium, perhaps because the time dependence of the pressure was distorted, compared with that associated with purely capillary flow, by adsorption of methane in the organic material in the rock. The permeabilities determined by the best fit of the model to the data were: parallel to bedding, k_r = 51.5 picodarcy, and perpendicular to bedding, k_x = 18.0 picodarcy, both an order of magnitude smaller than the corresponding values for helium. However, the porosity determined using methane, from the difference between the initial pressure and the ultimate equilibrium pressure at long times, was in good agreement with the value determined using helium.

Nomenclature

b	Klinkenberg coefficient, psi or Pa
c	compressibility of the fluid, Pa^{-1}
D	diameter of cylindrical sample, inch or m
k	permeability, darcy or m^2
L	length of cylindrical sample, inch or m
n	porosity, dimensionless
NIST	National Institute of Standards and Technology
p	pressure, psi or Pa
r	radial position, inch or m
R	radius of cylindrical sample, inch or m
t	time, s or hour
x	axial position, inch or m
γ	ratio of reservoir volume to pore volume, dimensionless
λ_x^2	product of the ratio of axial to radial permeability and the diameter to length ratio squared, = $(k_x/k_r)\cdot(D/L)^2$, Equation 3, dimensionless
μ	dynamic viscosity, Pa·s

τ characteristic time, s

Subscripts

D dimensionless
p pulse (pressure, after the step change)
r radial direction, parallel to bedding plane
R referring to the radius of the cylindrical sample
ref reference (pressure)
x axial direction, perpendicular to bedding plane
o initial (pressure, before the step change, or "pulse")
∞ absolute (permeability)

Superscript

* transformed pseudo variable
$\frown$ measured quantity
$\sim$ parameter estimate

References

Haskett, S. E., Narahara, G., Holditch, S., A Method for Simultaneous Determination of Permeability and Porosity in Low-Permeability Cores, *SPE Formation Evaluation*, Vol. 3, Issue 3, 1988, pp. 651-658.

Klinkenberg, L. J., The Permeability of Porous Media to Liquids and Gases, *Drilling and Production Practice*, American Petroleum Institute, Washington, DC, 1941, pp. 200-213.

Lemmon, E. W., Huber, M. L., McLinden, M. O., REFPROP Reference Fluid Thermodynamic and Transport Properties, NIST Standard Reference Database 23, Version 9.1, Applied Chemicals and Materials Division, U.S. Department of Commerce, 2013.

OKLAHOMA STATE UNIVERSITY

Petrophysics and Tight Rock Characterization for the Application of Improved Stimulation and Production Technology in Shale

FINAL REPORT

Reporting Period: June 27, 2013- June 26, 2016

by

Sayeed Mohamed
Robert L. Robinson, Jr.
Pongtorn Charoensuppanimit
Agelia M. Abudour

School of Chemical Engineering

Prepared for the Research Partnership to Secure Energy for America (RPSEA) under Contract 11122-63

Stillwater, Oklahoma
2016

CONTENTS

TABLES

FIGURES

1. Executive Summary

Shale is an important source of natural gas, and the recovery of natural gas from such unconventional reservoirs has increased considerably in the U.S. Shale reservoirs may also offer carbon dioxide (CO_2) sequestration potential. Since a large portion of the gas in shale reservoirs exists in an adsorbed state, modeling of gas adsorption behavior is needed for generating reliable gas-in-place estimates as well as in evaluating CO_2 sequestration potential. Reliable adsorption data measured at reservoir conditions and an accurate adsorption model are two important requirements for describing gas adsorption behavior on shales. To date, high-pressure gas adsorption data on shales are limited, and this is especially true for CO_2 adsorption at higher pressures.

In this work, we have measured adsorption of methane, nitrogen and CO_2 on three shale samples from the Woodford and Caney shale plays in the U.S. Two of the samples were Woodford Shale from Payne and Hancock counties and the third sample was Caney Shale. Pure-gas adsorption was measured at 328.2 K and pressures up to 12.4 MPa. Results indicate that at about 7 MPa, the adsorption ratio of nitrogen, methane and CO_2 are about 1: 2.9: 6.1 for the Woodford Shale from Payne County, 1: 3.0: 12.8 for the Woodford Shale from Hancock County and about 1: 3.5: 30.1 for the Caney Shale. Our results also showed that adsorption capacities of these gases appear to be related with total organic carbon content (TOC) of these shales. In addition, CO_2 preferential adsorption over methane on the shales was stronger for samples with higher ash content, indicating that mineral matter is an important contributing factor in the CO_2 adsorption capacity of shales.

The simplified local-density (SLD) model was used to represent the adsorption data obtained in this work. The SLD modeling results indicate that the adsorption data were represented within the experimental uncertainties. Overall, the percentage average absolute deviations for methane, nitrogen and CO_2 adsorption on the three shales were about 7%. In addition, the SLD model surface areas and solid-solid interaction parameters appear related to TOC content of shales. However, additional adsorption data on shales, as well as detailed surface characterization of

such samples, will be necessary for developing a generalized, predictive adsorption model for shale gas systems.

2. Conclusions

Methane, nitrogen and CO_2 adsorption was measured on Woodford Shale samples from Payne and Hancock counties and Caney shale. For each shale sample, CO_2 had the highest adsorption capacity and nitrogen the lowest. CO_2 adsorption was 2.1 to 8.6 times higher than methane adsorption on these samples. Adsorption capacity was related to the total organic carbon content of these samples. Further, as ash content or mineral matter content increased on a sample, the preferential adsorption of CO_2 over methane also showed an increase.

The SLD model described the gas adsorption data on these shales within the experimental uncertainty. Two of the SLD model parameters, i.e., surface area and ε_{ss}/k appear related to the TOC of the shale samples. This highlights the importance of obtaining more detailed shale surface characterization since this may provide the basis for SLD model parameter generalizations in future studies.

3. Background

Recent advances in horizontal drilling and hydraulic fracturing has stimulated the recovery of natural gas from shale reservoirs.[1] Among shale reservoirs in the U.S., Woodford and Caney shales contain significant amounts of technically recoverable natural gas.[2] A recent study reported that the Woodford Shale is ranked among the top five U.S shale plays that produce natural gas commercially.[3]

In addition to natural gas interests, numerous studies have evaluated the potential of shale reservoirs for possible use as CO_2 geological sinks. Nuttall, et al. [4] estimated the CO_2 sequestration capacity in Devonian black shales and Big Sandy gas field in Kentucky and their results indicate that large amounts of CO_2 can be stored in these shale plays. Kang, et al. [5] presented mass-transport paths and mechanisms for CO_2 uptake in shales and identified that

micropores in organic matter acted as molecular sieves that allowed only linear molecules such as CO_2 to access their pore space. Recently, Tao and Clarens [6] used a computational method based on the kinetics of mass transport to estimate CO_2 sequestration capacity and time required to fill up a Marcellus shale reservoir with CO_2. The results obtained from their computational work reveal that fractured shales may store a large amount of CO_2. Further, Tao and coworkers noted that despite low permeability, the fractured shale can sequester CO_2 approximately five times faster than the time that the reservoir would require for completion of the methane recovery process.

As outlined above, shale reservoirs have gained significance as a result of their abundant natural gas content and their potential for CO_2 sequestration. Since shale reservoirs generally contain large amounts of adsorbed gas, the modeling of adsorption behavior is essential for obtaining reliable gas-in-place estimates and designing CO_2 sequestration processes in these reservoirs. Two important elements for modeling gas adsorption behavior are (1) adsorption data measured at reservoir operating temperatures and pressures and (2) a reliable model capable of describing accurately the adsorption behavior over wide pressure and temperature ranges.

Previous Experimental Studies

Recent studies have presented adsorption data on shales and the focus in these studies have been primarily on effect of shale composition and maturity on the adsorption of methane. For example, Beaton, et al. [7] measured adsorption of methane on shale samples from the Duvernay, Muskwa, Banff and Exshaw formations. Zhang, et al. [8] investigated effects of organic-matter type and thermal maturity on methane adsorption on diverse shales. Wang, et al. [9] measured methane adsorption capacity on Paleozoic shales from the Sichuan basin, China and investigated the effect of TOC and clay mineral content on adsorption capacity of methane. Rexer, et al. [10] measured adsorption of methane and pore characteristics on oil-window immature and gas-window mature samples from the Posidonia shale formation. Rexer and coworkers found that apart from primary adsorption on organic carbon, methane adsorption on mineral content was significant on relatively dry shales. Gasparik, et al. [11] investigated constituents in Paleozoic and Mesozoic shales that control methane storage in these organic-rich shales. Hu, et al. [12] studied the effect of thermal maturity induced by hydrous pyrolysis on methane adsorption on Woodford

shale. Tan, et al. [13] evaluated the gas potential of a shale formation from Yangtze platform in China by measuring adsorption capacities of methane on shales extracted from the platform.

To date, few studies have provided adsorption capacity of CO_2 on shales. Nuttall, Eble, Drahovzal and Bustin [4] reported methane and CO_2 adsorption on New Albany and Ohio shales. Busch, et al. [14] studied CO_2 storage potential on Muderong shale and Weniger, et al. [15] measured adsorption of methane and CO_2 on coal and shale samples from the Paraná Basin. Chareonsuppanimit, et al. [16] measured methane, nitrogen and CO_2 adsorption on the New Albany shale. Khosrokhavar, et al. [17] presented data for the adsorption of methane and CO_2 on carboniferous shale.

Previous Models for Adsorption

Several adsorption models have been used with varying success for modeling gas adsorption on shales. These models include the modified Langmuir model[8, 10-13, 15], Ideal-Adsorption Solution (IAS) Theory, Dubinin-Radushkevich (D-R) adsorption model and Two-Dimensional EOS model.[18] Among these adsorption models, the simplified local-density (SLD) model has been successful in describing gas adsorption on activated carbons, coals and shales[16]. Further, the SLD model parameters were generalized successfully based solely on surface characterization information.[19] In continuation of our earlier efforts [16], the SLD model was used in the present work.

Accordingly, this project aims to provide the following contributions on shale gas adsorption:

1. Enrich the adsorption data of CO_2 at high pressures, which is useful for the evaluation of CO_2 sequestration potential in shales.
2. Enrich the adsorption data of N_2, which can be beneficial for the enhanced gas recovery processes in shales.

3. Investigate the relation between adsorption behavior and shale composition such as TOC content, ash content, etc.

4. Investigate the relation between the SLD model parameters and the shale composition and assess the potential for generalized model predictions.

4. Experimental Methods and Procedures

The experimental method used in this study is based on the volumetric method and has been described in several of our previous studies[16, 20-22]. For completeness, the essential details of the measurement method and data reduction procedures used in this study are outlined below.

Figure 1 presents a schematic of the adsorption measurement apparatus. The apparatus is contained in an air bath maintained at constant temperature. The equilibrium cell contains the shale sample and the cell is under partial vacuum at the start of the experiment. For measurements on moist adsorbent samples, there is a potential for the loss of moisture from the sample when placed under vacuum. To avoid loss of moisture from the sample, the vacuum pressure applied to the sample was limited and maintained above the vapor pressure of water vapor at the temperature used for measuring the isotherms (328.2 K). Further, in order to test for possible loss of moisture and volatile organics, the shale sample was carefully weighed before and after the adsorption isotherm experiments. No appreciable loss of mass was detected from the sample, indicating that there was very little (if any) change in composition of the adsorbent sample.

Helium was used to determine the void volume, V_{void}, in the equilibrium cell. The void volume can be calculated as:

$$V_{void} = \frac{\left(\frac{P\Delta V}{ZT}\right)_{pump}}{\left(\frac{P_2}{Z_2 T} - \frac{P_1}{Z_1 T}\right)_{cell}} \qquad (1)$$

where ΔV is the volume of the helium injected, Z_1 and Z_2 are the compressibility factors of helium. The subscripts 1 and 2 refer to cell conditions before and after the helium injection,

respectively. The void volume was measured at 328.2 K and at different pressures up to 12.4 MPa. The void volume calculated from measurements over this range of pressures varied less than 0.3 cm^3.

Once void volume was determined, the adsorption of pure methane, nitrogen and CO_2 was measured using similar injection procedures. Specifically, a known quantity, n_{inj}, of gas is injected into the equilibrium cell. Then, knowing the unadsorbed amount of gas in the bulk gas phase in the cell, n^{Ex}_{unads}, the excess adsorption, n^{Ex}_{ads}, is determined as follows:

$$n^{Ex}_{ads} = n_{inj} - n^{Ex}_{unads} \qquad (2)$$

In the above equation, the amount of gas injected into the cell can be calculated as:

$$n_{inj} = \left(\frac{P\Delta V}{ZRT}\right)_{Pump}, \qquad (3)$$

and the amount of unadsorbed gas is determined after equilibrium is attained in the cell as:

$$n^{Ex}_{unads} = \left(\frac{PV_{void}}{ZRT}\right)_{Cell} \qquad (4)$$

where P is the gas pressure at equilibrium. The equilibrium in the cell was indicated when no pressure changes were observed for a period of 12 hours. Further, all adsorption measurements were performed when the system was found free of leaks for a period of 24 hours under helium pressure test of 12.4 MPa.

The temperatures in the cell and pump were measured with RTDs that were calibrated using a reference thermometer. Pressure was measured using the STJE pressure transducers, which were calibrated using a deadweight tester with a calibration standard traceable to NIST. The experimental uncertainties were estimated as: temperature, 0.1 K; pressure, 6.9 kPa; and injected gas volume, 0.02 cm^3. The uncertainties in the amount adsorbed at a given pressure, as will be presented later, were estimated using multivariate error propagation.

The compressibility factors for methane, nitrogen and CO_2 were calculated from reference equations of state[23-25], whereas the compressibility factor for helium was calculated with an expression based on experimental data reported elsewhere[26].

Materials

Gases used in this work had purities of 99.99%. The shale samples were provided by Dr. James Puckette from the School of Geology, Oklahoma State University. The Woodford shale from Payne County was retrieved at 4250 feet below the surface, the Woodford shale from Hancock County was retrieved at about 17,730 feet below the surface, and the Caney shale was retrieved at 7366-7377 feet below the surface. The samples were pulverized and stored carefully in an inert environment to avoid possible oxidation. Adsorption isotherms were measured on the "as-received" samples without any further drying of the sample. Table 1 presents the compositional analysis of the shale samples in this study. The analysis was conducted by Huffman Laboratories, Colorado. The Woodford shale from Payne county contains about 8.5% total organic carbon (TOC), 1% moisture and 84% ash content, the Woodford shale from Hancock county contains about 6.4% TOC, 0.8% moisture and 86% ash and the Caney shale contains about 2% TOC, 1.7% moisture and 92% ash. Although several other types of shale characterization can be obtained, we have focused on characterization that is more *relevant* to describing adsorption on shales. In a previous work[19], we have shown that adsorption model parameters can be generalized successfully in terms of compositional characterization listed in Table 1. We anticipate undertaking similar model-parameter generalization for shales when sufficient data become available.

Gas Solubility in Water

Equation (2) was extended to account for the solubility of gas in water, n_{sol}:

$$n_{ads}^{Ex} = n_{inj} - n_{unads}^{Ex} - n_{sol} \qquad (5)$$

The following expression was used to estimate the solubility of methane and nitrogen in water:

$$x_{gas} = \frac{P}{a + bP + cP^2} \qquad (6)$$

Table 2 presents the parameters values used in Equation (6). The solubility of CO_2 was estimated based on the following expression:

$$x_{CO2} = \frac{P}{a + (b_1 + b_0 T)P + (c_1 + c_0 T)P^2} \qquad (7)$$

The amount of CO_2 dissolved in water can then be given as

$$n_{sol} = \frac{x_{co_2} n_{water}}{(1 - x_{co_2})} \qquad (8)$$

Since x_{CO2} is small, the above equation can be further simplified as:

$$n_{sol} \approx x_{co_2} n_{water} \qquad (9)$$

where n_{water} is the number of moles of water present in the shale sample.

Table 3 lists the values of parameters in Equation (7). The inclusion of a term for solubility of gas in water lowers the excess adsorption estimated from Equation (5). In this study, we have used the "conventional" method of data reduction described above. In particular, the method includes an assumption that water present in the shale sample remains adsorbed during the experiment. In addition, the bulk gas-phase is considered to be free from water vapor. In an earlier study, we have investigated a different method that accounts for the presence of water in different phases and presented an approach for modeling the competitive adsorption of gas/water mixtures[27].

Since the two Woodford shale samples contained only small amounts of moisture, the correction for gas solubility in water was quite small. However, the moisture content in the Caney shale was higher than the Woodford shales. The higher presence of moisture does affect the

dissolution of CO_2 in water. The difference in calculated amounts of gas adsorbed ranged from 10-15% for this shale sample.

5. Model Development

Simplified Local-Density Model

In the SLD model, the adsorbent is assumed to be composed of rectangular-shaped slit pores and an adsorbed molecule exhibits interactions with the two walls of the adsorbent. The SLD model was first developed by Rangarajan, et al. [28] In our previous works [19, 29], we have described in detail the model equations and algorithm for the SLD model. For this reason, only an overview is included below.

Using the equality of chemical potential for the bulk and adsorbed fluid and accounting for the gas-solid interactions, the following equilibrium relationship is obtained for adsorption:

$$f_{ff}(z) = f_{bulk}\exp\left(-\frac{\Psi^{fs}(z) + \Psi^{fs}(L-z)}{kT}\right) \qquad (10)$$

where k is the Boltzmann's constant. For

The excess adsorption (n^{Ex}) is obtained from the SLD model using the following relation:

$$n^{Ex} = \frac{A}{2}\int_{\frac{3}{8}\sigma_{ff}}^{L-\frac{3}{8}\sigma_{ff}} (\rho(z) - \rho_{bulk})\,dz \qquad (11)$$

where "A" is the accessible surface area of an adsorbent for a given adsorbate. For the fluid-solid interaction, $\Psi^{fs}(z)$, we employed Lee's potential[30]:

$$\Psi^{fs}(z) = 4\pi\rho_{atoms}\varepsilon_{fs}\sigma_{fs}^2\left(\frac{\sigma_{fs}^{10}}{5(z')^{10}} - \frac{1}{2}\sum_{i=1}^{4}\frac{\sigma_{fs}^4}{(z'+(i-1)-\sigma_{ss})^4}\right) \qquad (12)$$

$$\varepsilon_{fs} = \sqrt{\varepsilon_{ff}\times\varepsilon_{ss}} \qquad (13)$$

where ε_{fs} and ε_{ss} are the fluid-solid and solid-solid interaction energy parameters, respectively, and ρ_{atoms} = 0.382 atoms/Å^2. Here, the fluid-solid molecular diameter, σ_{fs} and z' are defined as:

$$\sigma_{fs} = \frac{\sigma_{ff} + \sigma_{ss}}{2} \qquad (14)$$

$$z' = z + \frac{\sigma_{ss}}{2} \qquad (15)$$

The parameters σ_{ff} and σ_{ss} represent the molecular diameter of the adsorbing gas and the carbon interplanar distances, respectively. The carbon interplanar distance was assumed to be that of graphite, 0.335 nm[31] and values of σ_{ff} and ε_{ff} were adopted from the literature.[32]

Modeling Methodology

The SLD model contains three parameters, namely, accessible surface area, A_i, solid-solid interaction energy, ε_{ss}/k, and the slit length, L. There is only one parameter that is specific to an adsorbing gas. Thus, the inclusion of more than one gas in the model regressions adds only one additional parameter (the accessible surface area, A_i) for each gas. The model parameters were determined by simultaneous regression of adsorption data for methane, nitrogen and CO_2.

The objective function used in the model regressions was the weighted root-mean-squared (WRMS) expressed as:

$$WRMS = \sqrt{\frac{\sum_{i=1}^{NPTS} \left(\frac{n_{cal} - n_{exp}}{\sigma_{exp}}\right)_i^2}{NPTS}} \qquad (16)$$

where n_{cal} and n_{exp} are the calculated and experimental excess adsorption, respectively, σ_{exp} is estimated experimental uncertainties in the adsorption data and NPTS is number of data points.

The model results are evaluated in terms of the following statistics:

Percentage average-absolute deviation:

$$\%AAD = \frac{\sum_{i=1}^{NPTS} \left| \frac{n_{cal} - n_{exp}}{n_{exp}} \right|_i}{NPTS} \times 100\% \quad (17)$$

Root-mean-squared error:

$$RMSE = \sqrt{\frac{\sum_{i=1}^{NPTS} (n_{cal} - n_{exp})_i^2}{NPTS}} \quad (18)$$

Weighted average-absolute deviation:

$$WAAD = \frac{\sum_{i=1}^{NPTS} \left| \frac{n_{cal} - n_{exp}}{\sigma_{exp}} \right|_i}{NPTS} \quad (19)$$

6. Results and Discussion

6.1 Experimental results

Methane, Nitrogen and CO_2 Adsorption Isotherms

Adsorption of gases on Woodford shales from Payne and Hancock counties and Caney shale were measured using the high-pressure adsorption apparatus. In the following discussion, "Woodford Payne" refers to the Woodford shale from Payne County and "Woodford Hancock" refers to the Woodford shale from Hancock County. Tables 4(a)-(c) present the adsorption data

for methane, nitrogen and CO_2 on these shales. The tables provide the pressure, excess adsorption and expected experimental uncertainty for each data point. As stated earlier, these uncertainties were calculated using standard multivariate propagation of errors.[16] The average experimental uncertainties for the adsorption of methane, nitrogen and CO_2 are, respectively, 0.0067, 0.0058 and 0.0260 mmol/g on the Woodford Payne, 0.0062, 0.0051 and 0.0241 mmol/g on the Woodford Hancock and 0.0069, 0.0057 and 0.0268 mmol/g on the Caney shale.

Figures 2(a)-(c) present the adsorption isotherms for methane, nitrogen and CO_2 on the Woodford Payne, the Woodford Hancock and the Caney shales, respectively. Error bars on each data point are the expected experimental uncertainty. As shown in these figures, the methane and nitrogen adsorption isotherms exhibited the characteristic Type I isotherm whereas the CO_2 isotherms exhibited a characteristic cusp-like curve with a maximum excess adsorption at a pressure of about 9.7 MPa.

Effect of Total Organic Carbon Content on Gas Adsorption

To compare the excess adsorption of the three gases, the adsorption ratios at about 7 MPa were determined for each shale. The $N_2/CH_4/CO_2$ ratios were 1/2.9/6.1 on the Woodford Payne, 1/3.0/12.8 on the Woodford Hancock and 1/3.5/30.1 on the Caney shale. These ratios show that CO_2 was higher adsorbing gas on these shales. This may be attributed to (1) hydrogen bond formed between organic functional groups (i.e., hydroxyl and carboxylic groups) and CO_2[33] and (2) porous organic matter in shales that acts as a molecular sieve, which allows only a linear molecule such as CO_2 to access the pores. [5] The adsorption of CO_2 was 2.1 to 8.6 times higher than methane adsorption on these samples. The higher adsorption of CO_2 than methane was also observed in previous studies on shales[15, 16]. Thus, these experimental results indicate a strong preference of shale samples for adsorbing CO_2 compared to methane, which may be useful for CO_2 storage potential in these shale reservoirs.

Figures 3(a)-(c) provide comparison of adsorption on the three shales for methane, nitrogen and CO_2, respectively. As shown in these figures, Woodford Payne has the highest adsorption capacity and Caney shale has the lowest adsorption capacity for each adsorbed gas. Among these shale samples, Woodford Payne also has the highest total organic carbon (TOC) content and

Caney shale has the lowest TOC content as evident from Table 1. Since adsorption occurs primarily on active sites containing organic carbon[4], shales that have a higher TOC content are expected to have larger adsorption capacity, which is consistent with the experimental results presented here.

To investigate the general trend between TOC content and adsorption capacity, the excess adsorption at about 9.7 MPa was chosen to represent the adsorption capacity of each isotherm from Tables 4(a)-(c). For illustration purposes, Figure 4 presents the trends in adsorption capacities at 9.7 MPa with TOC content for the three shales. The excess adsorption values of the three gases at about 9.7 MPa increase almost linearly as a function of TOC content.

Effect of Ash Content on Gas Adsorption

As shown in Figures 3(a)-(c), Caney shale with the highest ash content had the lowest gas adsorption capacities and vice-versa for the Woodford Payne. This trend was expected since ash and TOC contents present in these shales vary inversely, as listed in Table 1. In fact, our previous study[16] has also shown that adsorbents that have higher ash content appear to have lower gas adsorption capacity. Typically, ash content is an indicator of mineral matter which is a hydrophilic adsorption site[13]. However, recent works have reported adsorption of non-polar gases such as methane[34] and CO_2[14] on mineral-matter-rich rocks. Since mineral matter is a major component in ash content, effect of ash content or mineral matter on gas adsorption behavior merits further study. Specifically, it appears important to determine whether methane or CO_2 is the more preferred adsorbate on mineral matter.

Table 5 lists the excess adsorption of methane and CO_2 on mineral-matter-rich rocks (Kaolinite and Illite) at about 7 MPa. The methane adsorption was obtained from Ji, Zhang, Milliken, Qu and Zhang [34] and adsorption of CO_2 was obtained from Busch, Alles, Gensterblum, Prinz, Dewhurst, Raven, Stanjek and Krooss [14] The CO_2/CH_4 ratios shown in Table 5 were determined based on two assumptions: (1) the effect of minor temperature difference (5 K difference) between the two sources on gas adsorption can be neglected and (2) the rock samples from Busch, Alles, Gensterblum, Prinz, Dewhurst, Raven, Stanjek and Krooss [14] were assumed to

contain only pure Illite and Kaolinite. The methane adsorption on samples from Ji, Zhang, Milliken, Qu and Zhang [34] (95 wt.% Kaolinite and 99 wt.% Illite rock samples) was normalized by the percentage weight of mineral matter (i.e. mmol/g Kaolinite and mmol/g Illite basis). As shown in Table 5, CO_2 adsorption was 2.4 to 8.8 times higher than methane adsorption, indicating that CO_2 was adsorbed preferentially on mineral matter relative to methane. Such preference of mineral matter for adsorbing CO_2 may be explained by the considerable polarity of the CO_2 quadrupole as it interacts with the polar sites contained within mineral matter.

Table 6 presents ash content and CO_2/CH_4 adsorption ratios at 7 MPa. As shown in the table, the CO_2/CH_4 ratio increases as ash content increases. This trend may be explained by a combination of two factors: (1) since CO_2 adsorbs on mineral matter more than methane, the corresponding reduction in CO_2 adsorption with increasing ash content is lower than that of methane and (2) since methane adsorbs primarily on organic carbon, the adsorption of methane decreases as ash content increases. Shales are generally rich in ash content, which can be approximately 60-90% of their total weight. This indicates that shale reservoirs with higher ash content may serve as potential CO_2 sequestration sites.

6.2 SLD Modeling Results

The SLD model's capability to describe the adsorption data on shales in this study was evaluated. Table 7 lists the regressed model parameters. In the table, the differences in the surface areas of the gases reflect the varying accessibilities of the adsorbent surface for the three gases. For each shale sample, the accessible surface area for CO_2 was the highest and nitrogen had the lowest surface area derived from the model regressions. Thus, these surface areas were consistent with the adsorption capacities on shales, where CO_2 adsorption was the highest and nitrogen the lowest adsorption capacity.

Table 8 presents the model statistics for these systems. As evident from the table, the SLD model was capable of describing the gas adsorption data on these shale samples within the experimental uncertainties. In particular, the overall %AADs for Woodford Payne, Woodford Hancock and

Caney shales were 6.6%, 8.3% and 6.8%, respectively. The data representation for nitrogen adsorption on Woodford Hancock and Caney shales at 2.9 MPa yielded anomalously high percentage errors due to extremely low (close to zero) adsorbed amounts. Therefore, these data were excluded from the modeling analysis and the statistics in Table 8. For illustration purposes, Figures 2(a)-(c) present the model results for methane, nitrogen and CO_2 adsorption on the three shales.

Figures 5(a)-(c) present the resulting deviations from the SLD model. For adsorption on the three samples, about 88% of the data for methane, 74% of the data for nitrogen and 83% of the data for CO_2 were represented within 10% deviation. Overall, 81% of the total data were represented within 10% deviation. Thus, the SLD model was found capable of describing the adsorption data on these shales.

Figures 6(a)-(b) show the trends between SLD model parameters and TOC content. As shown in Figure 6(a), the surface area for each gas appears to be approximately linear with TOC of these samples. Since the SLD model surface area represents the adsorption capacity on shales, the results in Figure 6(a) are consistent with the relation between adsorption capacities and TOC illustrated earlier in Figure 4. Figure 6(b) shows the trend between ε_{ss}/k and TOC. In the SLD model, the ε_{fs}/k is a geometric mean of $\varepsilon_{ss}/_{k}$ and ε_{ff}/k. Since the fluid-fluid energy parameter is independent of the adsorbent, the higher values of ε_{ss}/k signify stronger *fluid-solid* interactions. Thus, shales that have higher TOC content also exhibit larger ε_{ss}/k.

The results shown in Figures 6(a)-(b) illustrate some general trends in the SLD model parameters as a function of shale properties such as TOC content. In an earlier study[19], we developed a generalized adsorption model capable of predicting gas adsorption on *coals* based on adsorbent characterization. The results presented in the current study indicate that a similar modeling capability on shales appears possible. However, at the time of this writing, there appear to be limited datasets on shales that contain *both* adsorption and surface characterization information. Therefore, additional data will be necessary before a generalized model can be developed for shale gas systems.

7. References

1. EIA, Natural Gas Gross Withdrawals and Production, U.S. Energy Information Administration. http://www.eia.gov/dnav/ng/ng_prod_sum_dcu_NUS_m.htm. Released October 2014. **2014**.

2. Cardott, B. J., Woodford Shale: From Hydrocarbon Source Rock to Reservoir. AAPG Woodford Shale Forum. **2013**.

3. EIA, Outlook for U.S. shale oil and gas. http://www.eia.gov/pressroom/presentations/sieminski_01042014.pdf. **2014**.

4. Nuttall, B. C.; Eble, C. F.; Drahovzal, J. A.; Bustin, M. *Analysis of Devonian Black shales in Kentucky for potential carbon dioxide sequestration and enhanced natural gas production*; University of Kentucky: Lexington, Kentucky, 2005.

5. Kang, S. M.; Fathi, E.; Ambrose, R. J.; Akkutlu, I. Y.; Sigal, R. F., Carbon Dioxide Storage Capacity of Organic-Rich Shales. **2011**.

6. Tao, Z.; Clarens, A., Estimating the Carbon Sequestration Capacity of Shale Formations Using Methane Production Rates. *Environmental Science & Technology* **2013,** 47, (19), 11318-11325.

7. Beaton, A. P.; Pawlowicz, J. G.; Anderson, S. D. A.; Berhane, H.; Rokosh, C. D. *Total organic carbon and adsorption isotherms of the Duvernay and Muskwa formations in Alberta:shale gas data release*; Energy Resources Conservation Board, ERCB/AGS: Edmonton, Alberta, 2010; p 33.

8. Zhang, T.; Ellis, G. S.; Ruppel, S. C.; Milliken, K.; Yang, R., Effect of organic-matter type and thermal maturity on methane adsorption in shale-gas systems. *Organic Geochemistry* **2012,** 47, (0), 120-131.

9. Wang, S.; Song, Z.; Cao, T.; Song, X., The methane sorption capacity of Paleozoic shales from the Sichuan Basin, China. *Marine and Petroleum Geology* **2013,** 44, (0), 112-119.

10. Rexer, T. F.; Mathia, E. J.; Aplin, A. C.; Thomas, K. M., High-Pressure Methane Adsorption and Characterization of Pores in Posidonia Shales and Isolated Kerogens. *Energy & Fuels* **2014,** 28, (5), 2886-2901.

11. Gasparik, M.; Bertier, P.; Gensterblum, Y.; Ghanizadeh, A.; Krooss, B. M.; Littke, R., Geological controls on the methane storage capacity in organic-rich shales. *International Journal of Coal Geology* **2014,** 123, (0), 34-51.

12. Hu, H.; Zhang, T.; Wiggins-Camacho, J. D.; Ellis, G. S.; Lewan, M. D.; Zhang, X., Experimental investigation of changes in methane adsorption of bitumen-free Woodford Shale with thermal maturation induced by hydrous pyrolysis. *Marine and Petroleum Geology* **2014,** 59, (0), 114-128.

13. Tan, J.; Weniger, P.; Krooss, B.; Merkel, A.; Horsfield, B.; Zhang, J.; Boreham, C. J.; Graas, G. v.; Tocher, B. A., Shale gas potential of the major marine shale formations in the Upper Yangtze Platform, South China, Part II: Methane sorption capacity. *Fuel* **2014,** 129, (0), 204-218.

14. Busch, A.; Alles, S.; Gensterblum, Y.; Prinz, D.; Dewhurst, D. N.; Raven, M. D.; Stanjek, H.; Krooss, B. M., Carbon dioxide storage potential of shales. *International Journal of Greenhouse Gas Control* **2008,** 2, (3), 297-308.

15. Weniger, P.; Kalkreuth, W.; Busch, A.; Krooss, B. M., High-pressure methane and carbon dioxide sorption on coal and shale samples from the Paraná Basin, Brazil. *International Journal of Coal Geology* **2010,** 84, (3–4), 190-205.

16. Chareonsuppanimit, P.; Mohammad, S. A.; Robinson Jr, R. L.; Gasem, K. A. M., High-pressure adsorption of gases on shales: Measurements and modeling. *International Journal of Coal Geology* **2012,** 95, (0), 34-46.

17. Khosrokhavar, R.; Wolf, K.-H.; Bruining, H., Sorption of CH4 and CO2 on a carboniferous shale from Belgium using a manometric setup. *International Journal of Coal Geology* **2014,** 128–129, (0), 153-161.

18. Clarkson, C. R.; Haghshenas, B., Modeling of Supercritical Fluid Adsorption on Organic-Rich Shales and Coal. In Society of Petroleum Engineers: 2013.

19. Mohammad, S. A.; Chen, J. S.; Robinson, R. L.; Gasem, K. A. M., Generalized Simplified Local-Density/Peng−Robinson Model for Adsorption of Pure and Mixed Gases on Coals. *Energy & Fuels* **2009,** 23, (12), 6259-6271.

20. Hall, F.; Zhou, C.; Gasem, K. A. M.; Robinson, R. L., Jr. , Adsorption of Pure Methane, Nitrogen, and Carbon Dioxide and Their Binary Mixtures on Wet Fruitland Coal. In *SPE Eastern Regional Conference & Exhibition, SPE Paper 29194*, Charleston, S.C., 1994.

21. Sudibandriyo, M.; Pan, Z.; Fitzgerald, J. E.; Robinson, R. L., Jr.; Gasem, K. A. M., Adsorption of Methane, Nitrogen, Carbon Dioxide, and Their Binary Mixtures on Dry Activated Carbon at 318.2 K and Pressures up to 13.6 MPa. *Langmuir* **2003,** 19, (13), 5323-5331.

22. Mohammad, S. A.; Chen, J. S.; Fitzgerald, J. E.; Robinson, R. L.; Gasem, K. A. M., Adsorption of Pure Carbon Dioxide on Wet Argonne Coals at 328.2 K and Pressures up to 13.8 MPa. *Energy & Fuels* **2009,** 23, (2), 1107-1117.

23. Angus, S.; Armstrong, B.; de Reuck, K. M., *International Thermodynamic Tables of the Fluid State-5: Methane*. Pergamon Press: New York 1978.

24. Angus, S.; de Reuck, K. M.; Armstrong, B., *International Thermodynamic Tables of the Fluid State-6: Nitrogen*. Pergamon Press: New York, 1979.

25. Span, R.; Wagner, W., A New Equation of State for Carbon Dioxide Covering the Fluid Region from the Triple Point Temperature to 1100 K at Pressures up to 800 MPa. *J. Phys. Chem. Ref. Data* **1996,** 25, 1509-1590.

26. McCarty, R. D. *Thermophysical Properties of Helium-4 from 2 to 1500 K with Pressures to 1000 Atmospheres*; NBS Technical Note 631; U.S. Dept of Commerce 1972.

27. Mohammad, S. A.; Gasem, K. A. M., Modeling the Competitive Adsorption of CO2 and Water at High Pressures on Wet Coals. *Energy & Fuels* **2012,** 26, (1), 557-568.

28. Rangarajan, B.; Lira, C. T.; Subramanian, R., Simplified local density model for adsorption over large pressure ranges. *AIChE Journal* **1995,** 41, (4), 838-845.

29. Fitzgerald, J. E.; Robinson, R. L.; Gasem, K. A. M., Modeling High-Pressure Adsorption of Gas Mixtures on Activated Carbon and Coal Using a Simplified Local-Density Model. *Langmuir* **2006,** 22, (23), 9610-9618.

30. Lee, L. L., *Molecular Thermodynamics of Non-ideal Fluids*. Butterworth: Stoneham, MA 1988.

31. Subramanian, R.; Pyada, H.; Lira, C. T., Engineering model for adsorption of gases onto flat surfaces and clustering in supercritical fluids. *Industrial & Engineering Chemistry Research* **1995,** 34, (11), 3830.

32. Reid, R. C.; Prausnitz, J. M.; Poling, B. E., *The Properties of Gases and Liquids*. McGraw-Hill New York, 1987.

33. Huang, X.; Chu, W.; Sun, W.; Jiang, C.; Feng, Y.; Xue, Y., Investigation of oxygen-containing group promotion effect on CO2–coal interaction by density functional theory. *Applied Surface Science* **2014,** 299, (0), 162-169.

34. Ji, L.; Zhang, T.; Milliken, K. L.; Qu, J.; Zhang, X., Experimental investigation of main controls to methane adsorption in clay-rich rocks. *Applied Geochemistry* **2012,** 27, (12), 2533-2545.

8. Tables

Table 1.—Compositional Analyses of Shale Samples

Analyses	Woodford Payne Shale	Woodford Hancock Shale	Caney Shale
Dry-ash-free basis			
Carbon %	56.0	56.0	32.1
Hydrogen %	7.3	5.5	9.8
Oxygen %	0.6	10.9	31.8
Sulfur %	34.3	25.3	22.5
As-received basis			
Moisture %	0.98	0.84	1.67
TOC %	8.49	6.38	2.23
Volatile Matter %	11.9	11.6	6.6
Ash %	83.57	85.72	91.74

Table 2.—Parameters for Methane and Nitrogen Solubility in Water

Constant	Units of Constant	Methane	Nitrogen
a	MPa	5302.07	10204.24
b	-	150.4	127.3
c	1/MPa	-0.78	-0.09

Table 3.—Parameters for CO_2 Solubility in Water

Constant	Value	Units of Constant
a	272.21	MPa
b_1	-332.637	-
b_0	1.06683	1/K
c_1	19.18	1/MPa
c_0	-0.05609	1/(MPa K)

Table 4(a).—Excess Adsorption of Methane, Nitrogen and CO_2 on Woodford Shale from Payne County at 328.2 K

CH_4			**N_2**			**CO_2**		
Pressure (MPa)	**Excess Adsorption (mmol/g)**	**σ Excess Adsorption* (mmol/g)**	**Pressure (MPa)**	**Excess Adsorption (mmol/g)**	**σ Excess Adsorption* (mmol/g)**	**Pressure (MPa)**	**Excess Adsorption (mmol/g)**	**σ Excess Adsorption* (mmol/g)**
2.77	0.0382	0.0046	2.82	0.0078	0.0039	2.72	0.0932	0.0246
4.57	0.0545	0.0051	4.24	0.0139	0.0042	4.16	0.1169	0.0242
5.57	0.0603	0.0054	5.60	0.0181	0.0047	5.56	0.1337	0.0239
6.92	0.0676	0.0060	7.04	0.0234	0.0053	6.94	0.1437	0.0237
8.36	0.0716	0.0067	8.48	0.0265	0.0059	8.29	0.1546	0.0239
9.72	0.0737	0.0075	9.73	0.0286	0.0065	9.66	0.1616	0.0251
11.07	0.0751	0.0086	11.07	0.0297	0.0071	10.70	0.1565	0.0276
12.43	0.0771	0.0094	12.43	0.0306	0.0085	11.84	0.1490	0.0350

*Absolute uncertainty in excess adsorption

Table 4(b).—Excess Adsorption of Methane, Nitrogen and CO_2 on Woodford Shale from Hancock County at 328.2 K

CH_4			**N_2**			**CO_2**		
Pressure (MPa)	**Excess Adsorption (mmol/g)**	**σ Excess Adsorption (mmol/g)**	**Pressure (MPa)**	**Excess Adsorption (mmol/g)**	**σ Excess Adsorption (mmol/g)**	**Pressure (MPa)**	**Excess Adsorption (mmol/g)**	**σ Excess Adsorption (mmol/g)**
2.90	0.0128	0.0045	2.79	0.0010	0.0035	2.87	0.0607	0.0224
4.37	0.0198	0.0048	4.19	0.0037	0.0038	4.23	0.0838	0.0221
5.75	0.0256	0.0052	5.56	0.0060	0.0042	5.61	0.1054	0.0218
6.97	0.0291	0.0057	7.06	0.0097	0.0048	7.04	0.1232	0.0217
8.39	0.0328	0.0063	8.32	0.0111	0.0053	8.47	0.1390	0.0219
9.70	0.0377	0.0069	9.73	0.0134	0.0059	9.80	0.1487	0.0230
11.19	0.0379	0.0077	11.08	0.0142	0.0064	10.92	0.1452	0.0254
12.41	0.0397	0.0084	12.48	0.0150	0.0071	12.34	0.1371	0.0348

Table 4(c).—Excess Adsorption of Methane, Nitrogen and CO_2 on Caney Shale at 328.2 K

CH_4			**N_2**			**CO_2**		
Pressure (MPa)	**Excess Adsorption (mmol/g)**	**σ Excess Adsorption (mmol/g)**	**Pressure (MPa)**	**Excess Adsorption (mmol/g)**	**σ Excess Adsorption (mmol/g)**	**Pressure (MPa)**	**Excess Adsorption (mmol/g)**	**σ Excess Adsorption (mmol/g)**
2.86	0.0028	0.0050	2.86	0.0003	0.0039	2.88	0.0434	0.0255
4.25	0.0060	0.0053	4.20	0.0013	0.0043	4.22	0.0621	0.0251
5.67	0.0090	0.0058	5.59	0.0023	0.0047	5.60	0.0773	0.0248
6.99	0.0107	0.0063	6.97	0.0030	0.0052	6.95	0.0918	0.0246
8.38	0.0119	0.0070	8.34	0.0035	0.0058	8.32	0.1036	0.0247
9.74	0.0128	0.0077	9.72	0.0041	0.0065	9.72	0.1182	0.0259
11.10	0.0137	0.0084	11.10	0.0043	0.0071	10.65	0.1130	0.0280
12.48	0.0138	0.0094	12.48	0.0044	0.0078	11.61	0.1073	0.0357

Table 5.—Excess Adsorption Ratio of CO_2 and Methane on Illite and Kaolinite

Adsorbate	**Temperature (K)**	**Excess Adsorption at about 7 MPa on Mineral Matter (mmol/g Mineral)**		**Reference**
		Illite	**Kaolinite**	
CH_4	323.5	0.044	0.063	[34]
CO_2	318.2	0.388	0.149	[14]
CO_2:CH_4		8.8	2.4	

Table 6.—Excess Adsorption Ratio of CO_2 and Methane on Brazilian, Woodford and Caney Shales

Sample	**Temperature (K)**	**Characterization**		**Adsorption at about 7 MPa (mmol/g shale)**			**Reference**
		TOC (%)	**Ash (%)**	**CH_4**	**CO_2**	**CO_2:CH_4**	
117/118*	318.2	21.1	67.2	0.2231	0.3359	1.5	Weniger, Kalkreuth, Busch and Krooss [15]
181*		11.1	81.7	0.0999	0.2863	2.9	
114*		1.7	93.1	0.0461	0.2412	5.2	
Woodford Payne	328.2	8.5	83.6	0.0676	0.1437	2.1	This Work
Woodford Hancock		6.4	85.7	0.0291	0.1232	4.2	
Caney		2.2	91.7	0.0107	0.0918	8.6	

*These samples are shales from Rio Bonito formation, Brazil

Table 7.—SLD Model Parameters for Methane, Nitrogen and CO_2 Excess Adsorption on Woodford Shales from Payne and Hancock Counties and Caney Shale

Parameter	**Woodford Payne**	**Woodford Hancock**	**Caney**
CH_4 Surface Area (m^2/g)	16.8	7.9	3.3
N_2 Surface Area (m^2/g)	8.7	4.2	1.6
CO_2 Surface Area (m^2/g)	20.0	16.4	15.1
ε_{ss}/k (K)	5.1	3.4	2.6
Slit Length L (nm)	1.04	1.32	1.33

Table 8.—SLD Model Statistics for Methane, Nitrogen and CO_2 Excess Adsorption on Woodford Shales from Payne and Hancock Counties and Caney Shale

Adsorbate	**Woodford Payne**			**Woodford Hancock**			**Caney**		
	%AAD*	**RMSE***	**WAAD***	**%AAD**	**RMSE**	**WAAD**	**%AAD**	**RMSE**	**WAAD**
CH_4	4.6	0.0032	0.4	2.7	0.0010	0.1	4.8	0.0008	0.1
N_2	6.9	0.0013	0.2	18.5	0.0018	0.4	10.7	0.0004	0.1
CO_2	8.3	0.0136	0.4	5.1	0.0071	0.2	5.2	0.0047	0.2
Overall	**6.6**	**0.0081**	**0.4**	**8.3**	**0.0043**	**0.2**	**6.8**	**0.0028**	**0.1**

*%AAD is percentage absolute-average deviation in excess adsorption, RMSE is root-mean-squared error presented in mmol/g and WAAD is weighted absolute-average deviation in excess adsorption where the assigned weights were experimental uncertainties in adsorption data.

9. Figures

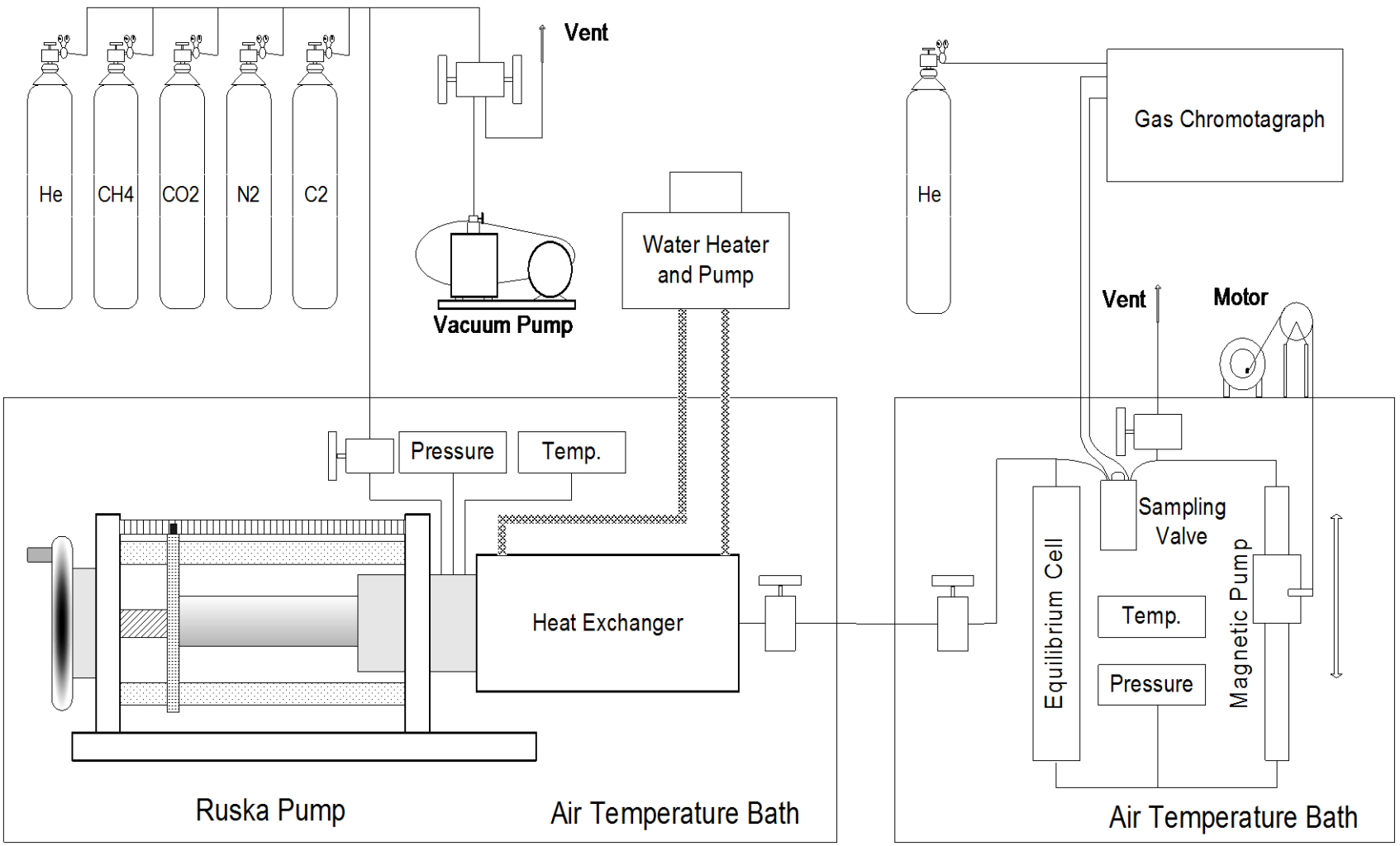

Figure 1.—Experimental Setup for Measuring Gas Adsorption

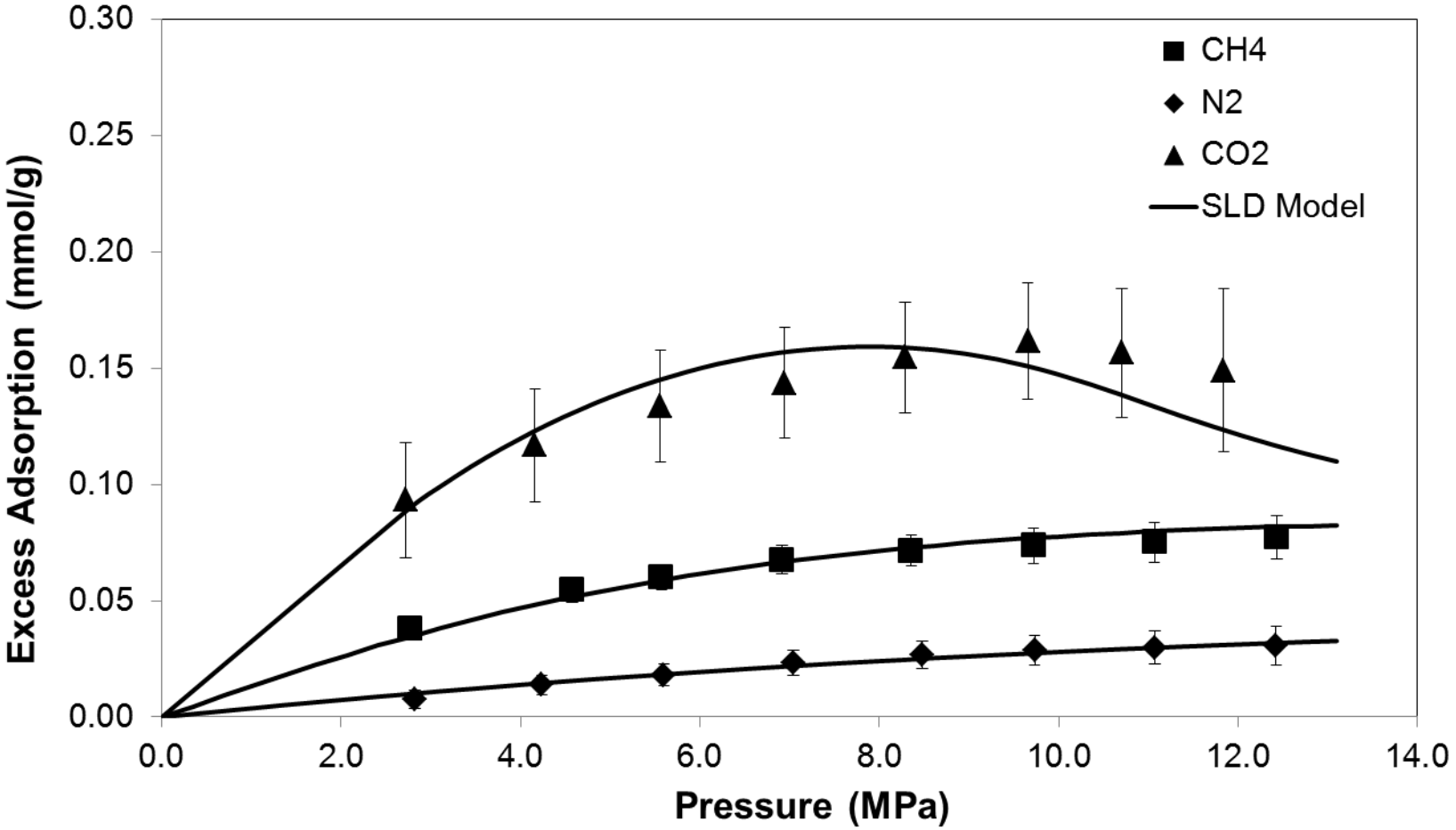

Figure 2(a).—Adsorption of Methane, Nitrogen and CO_2 on Woodford Shale from Payne County at 328.2 K

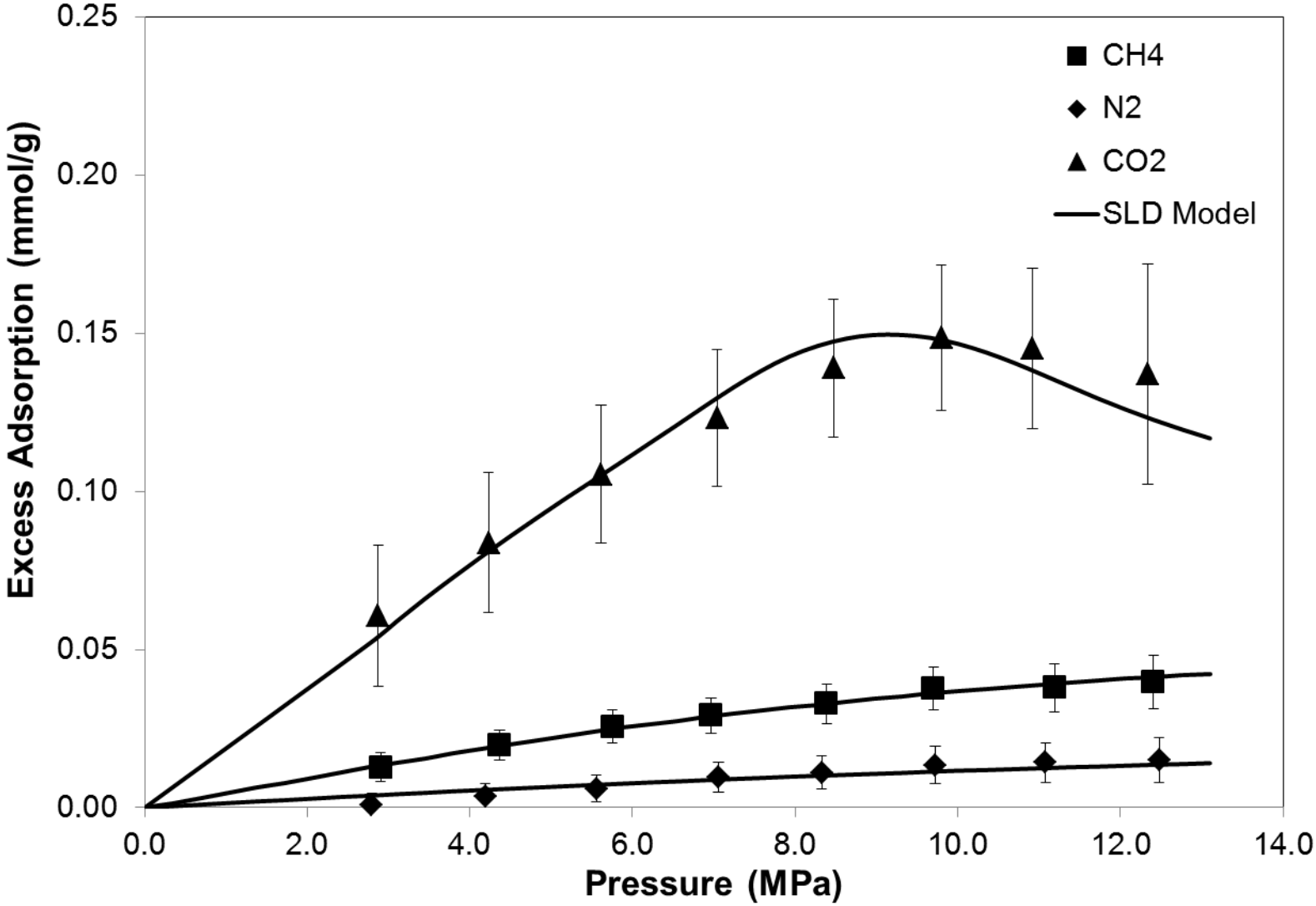

Figure 2(b).—Adsorption of Methane, Nitrogen and CO_2 on Woodford Shale from Hancock County at 328.2 K

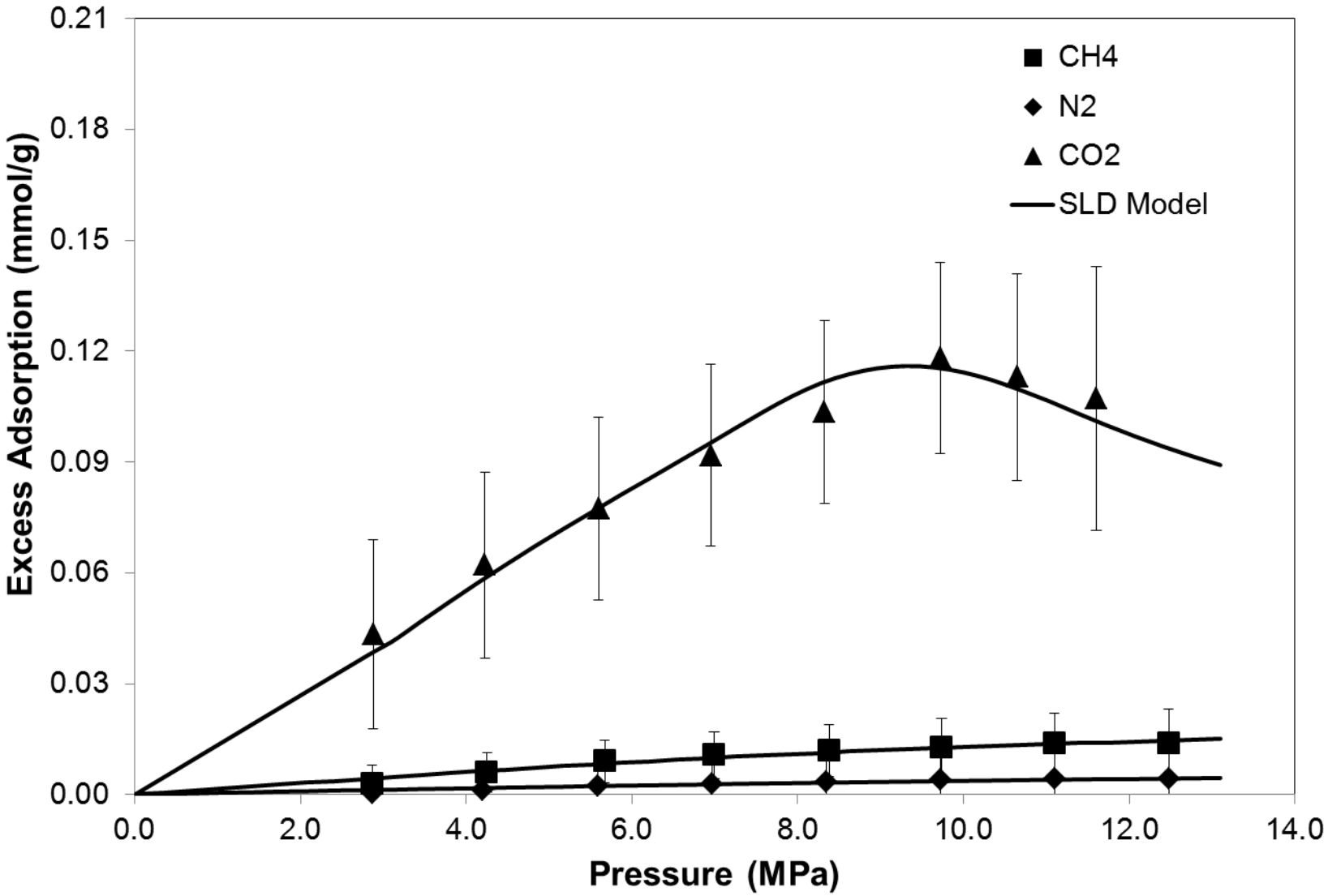

Figure 2(c).—Adsorption of Methane, Nitrogen and CO_2 on Caney Shale at 328.2 K

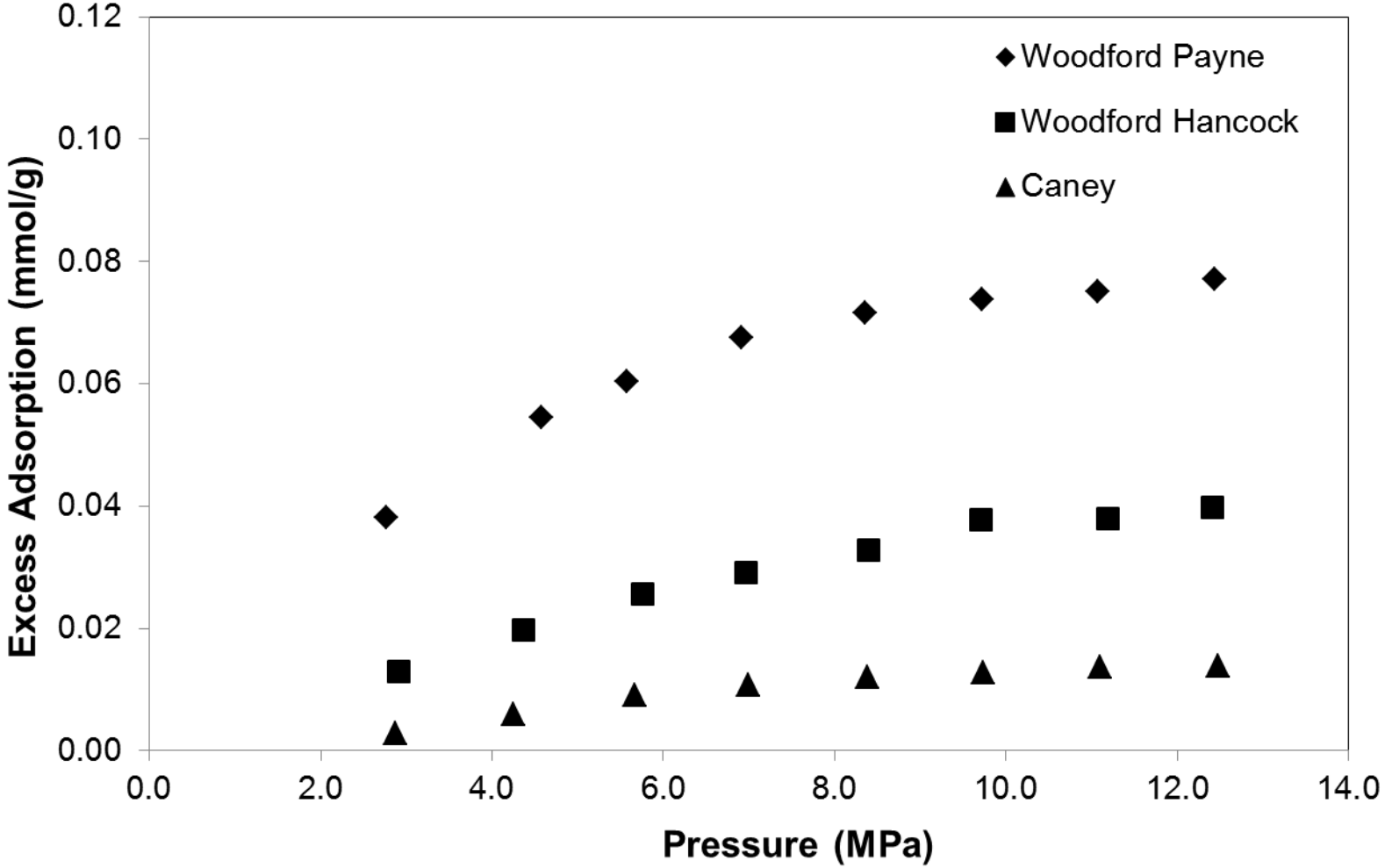

Figure 3(a).—Comparison of Methane Adsorption on Woodford Shale samples from Payne and Hancock Counties and Caney Shale at 328.2 K

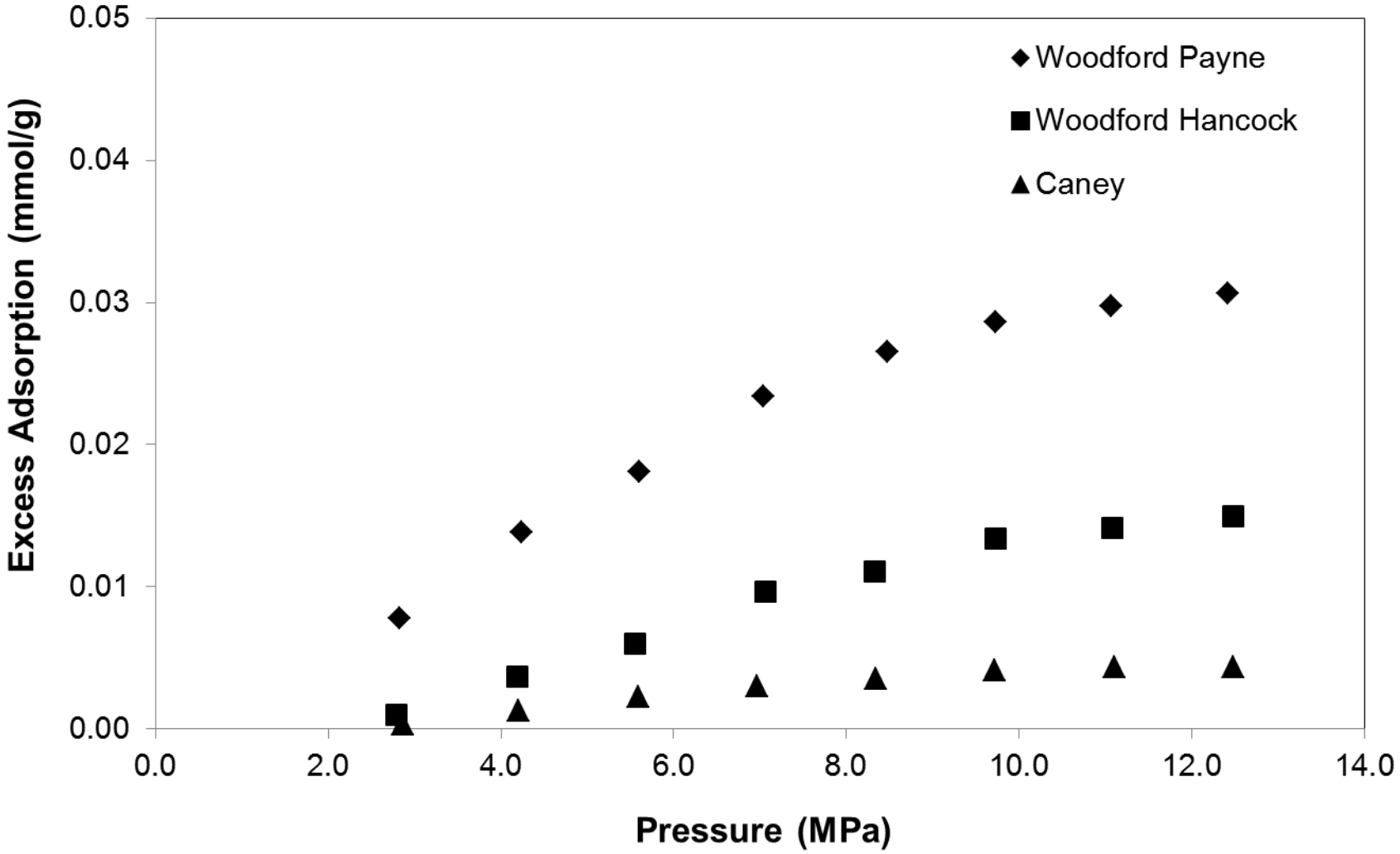

Figure 3(b).—Comparison of Nitrogen Adsorption on Woodford Shales from Payne and Hancock Counties and Caney Shale at 328.2 K

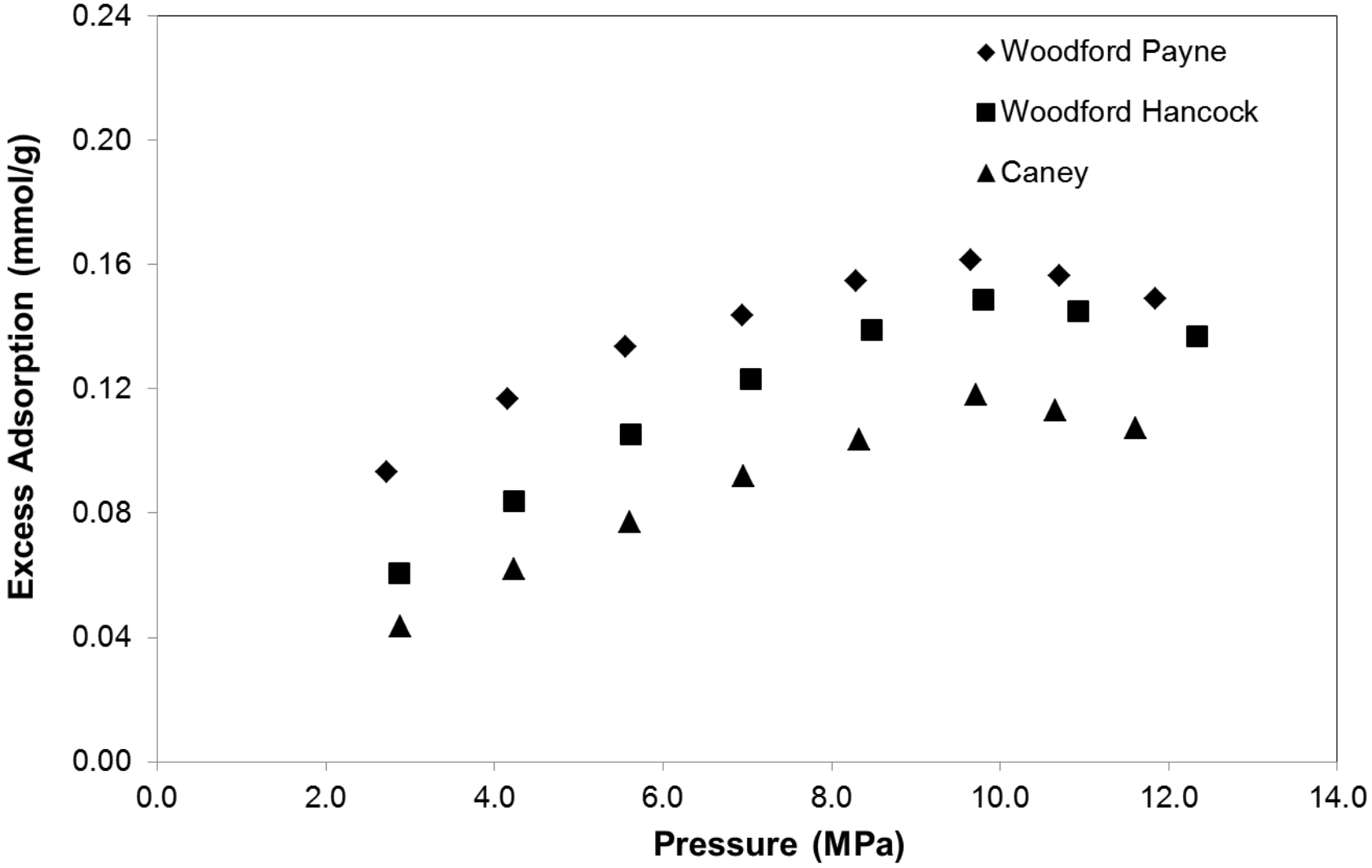

Figure 3(c).—Comparison of CO_2 Adsorption on Woodford Shales from Payne and Hancock Counties and Caney Shale at 328.2 K

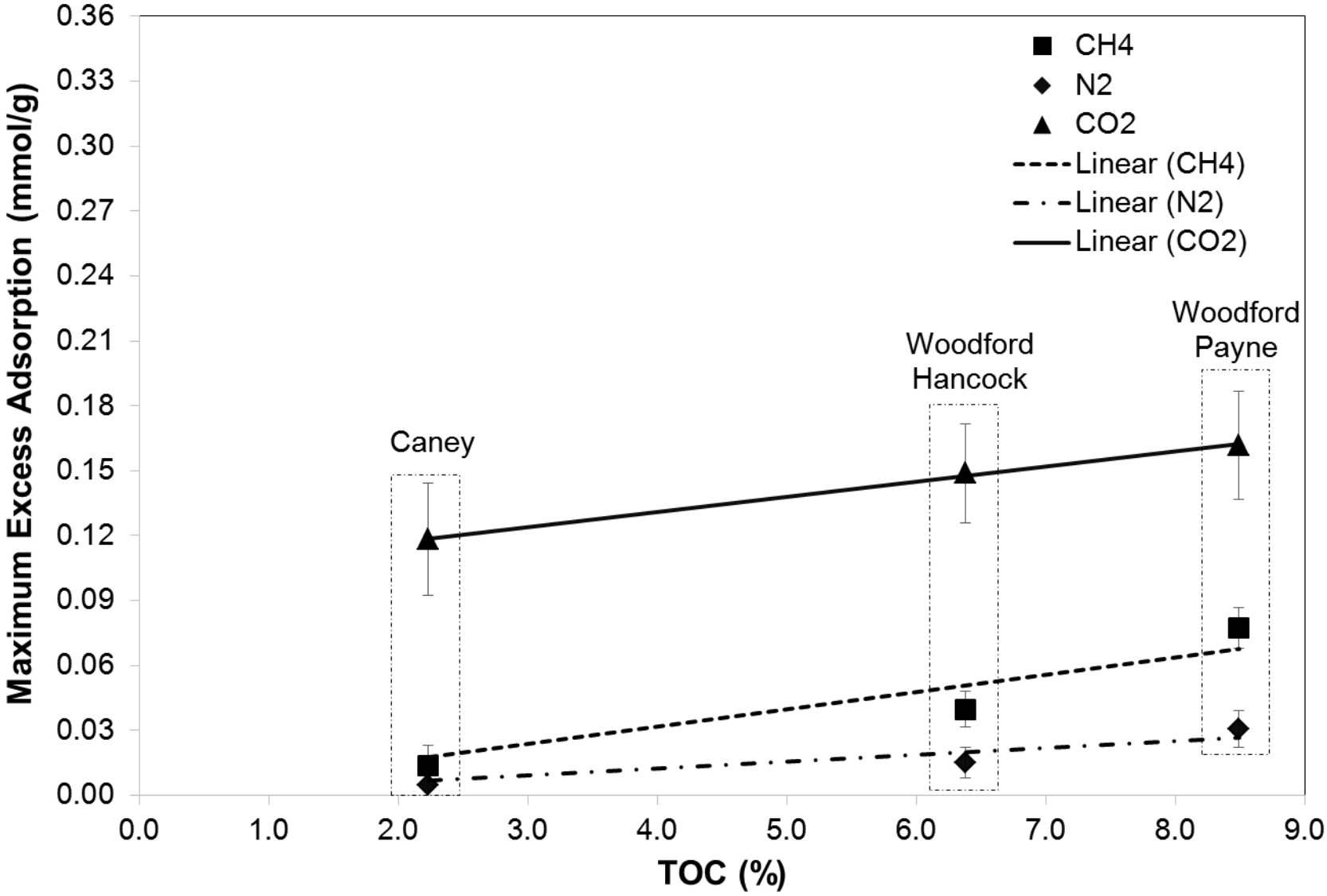

Figure 4.—Maximum Excess Adsorption Capacity vs TOC for Methane, Nitrogen and CO_2 at 328.2 K

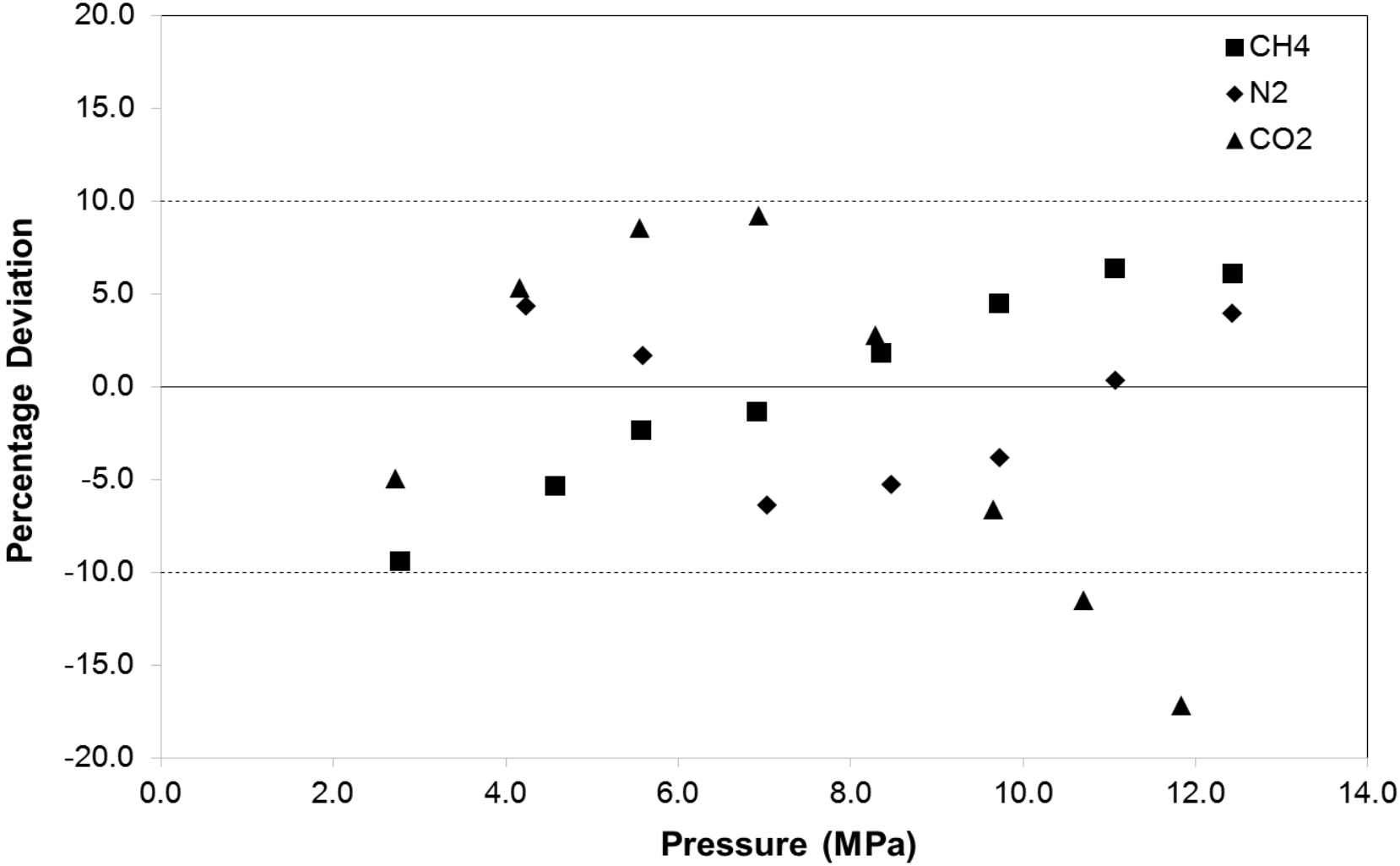

Figure 5(a).—Percentage Deviation of SLD Model Representations for Methane, Nitrogen and CO_2 Adsorption at 328.2 K on Woodford Shale from Payne County

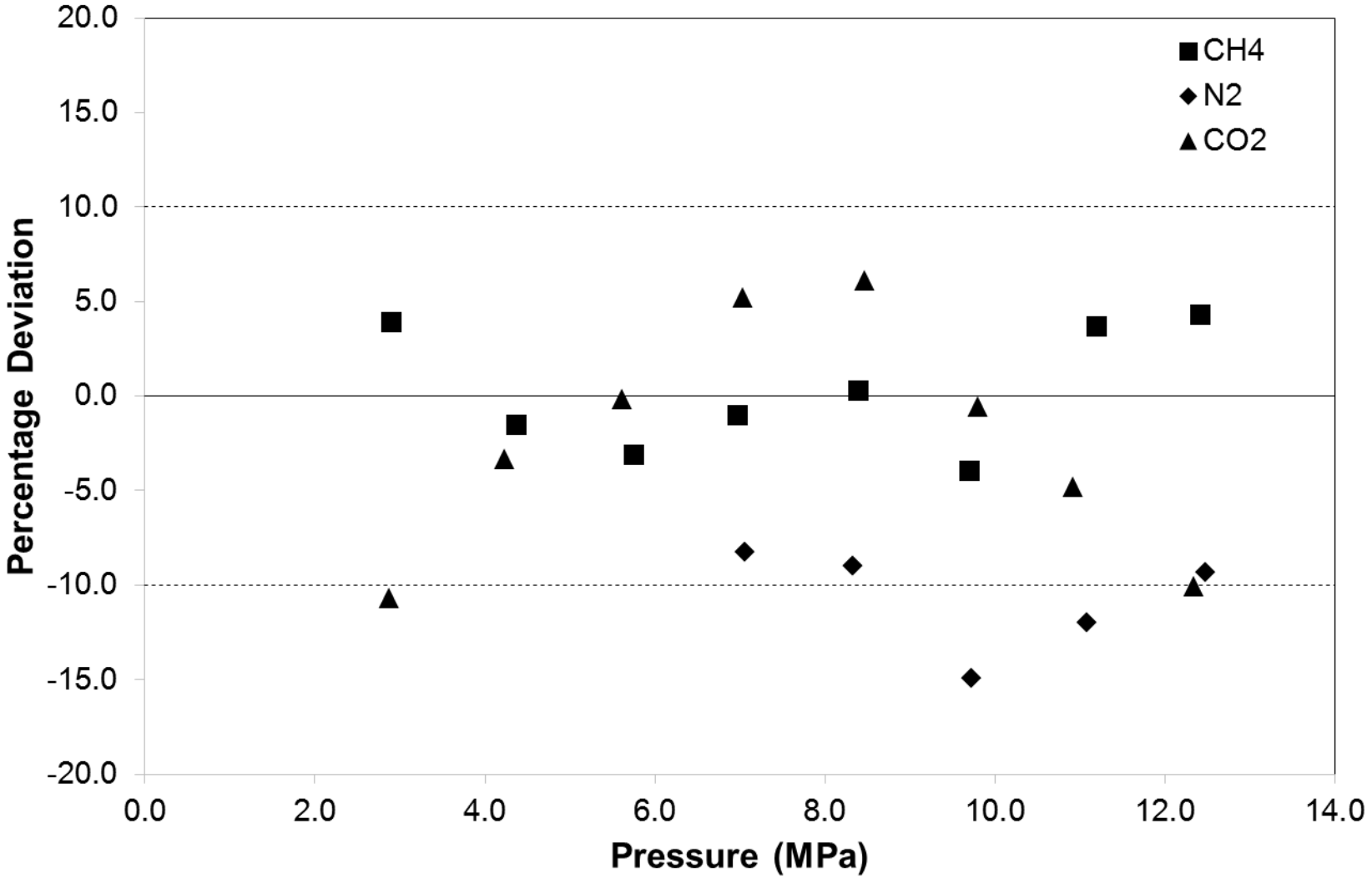

Figure 5(b).—Percentage Deviation of SLD Model Representations for Methane, Nitrogen and CO_2 Adsorption at 328.2 K on Woodford Shale from Hancock County

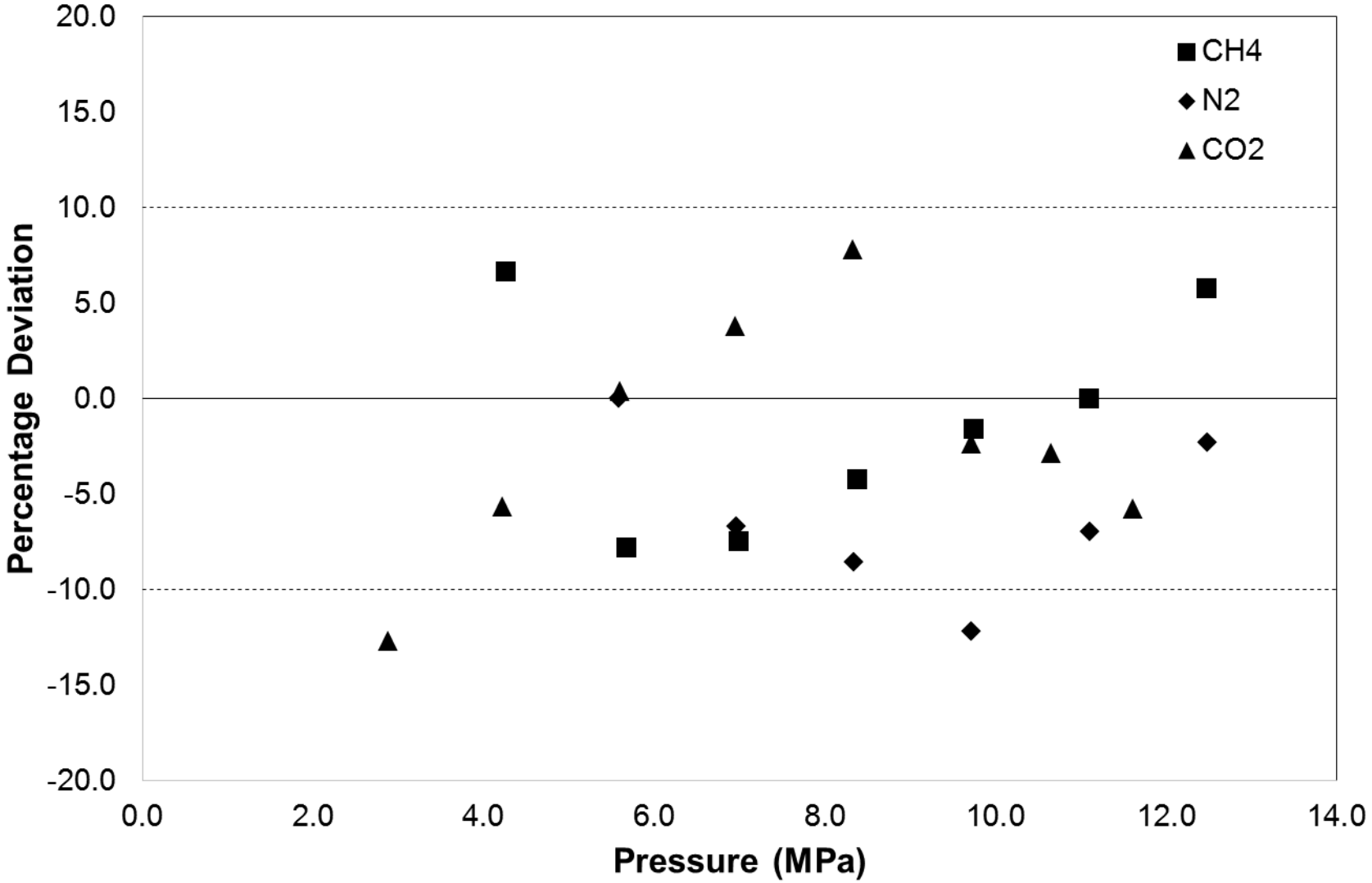

Figure 5(c).—Percentage Deviation of SLD Model Representations for Methane, Nitrogen and CO_2 Adsorption at 328.2 K on Caney Shale

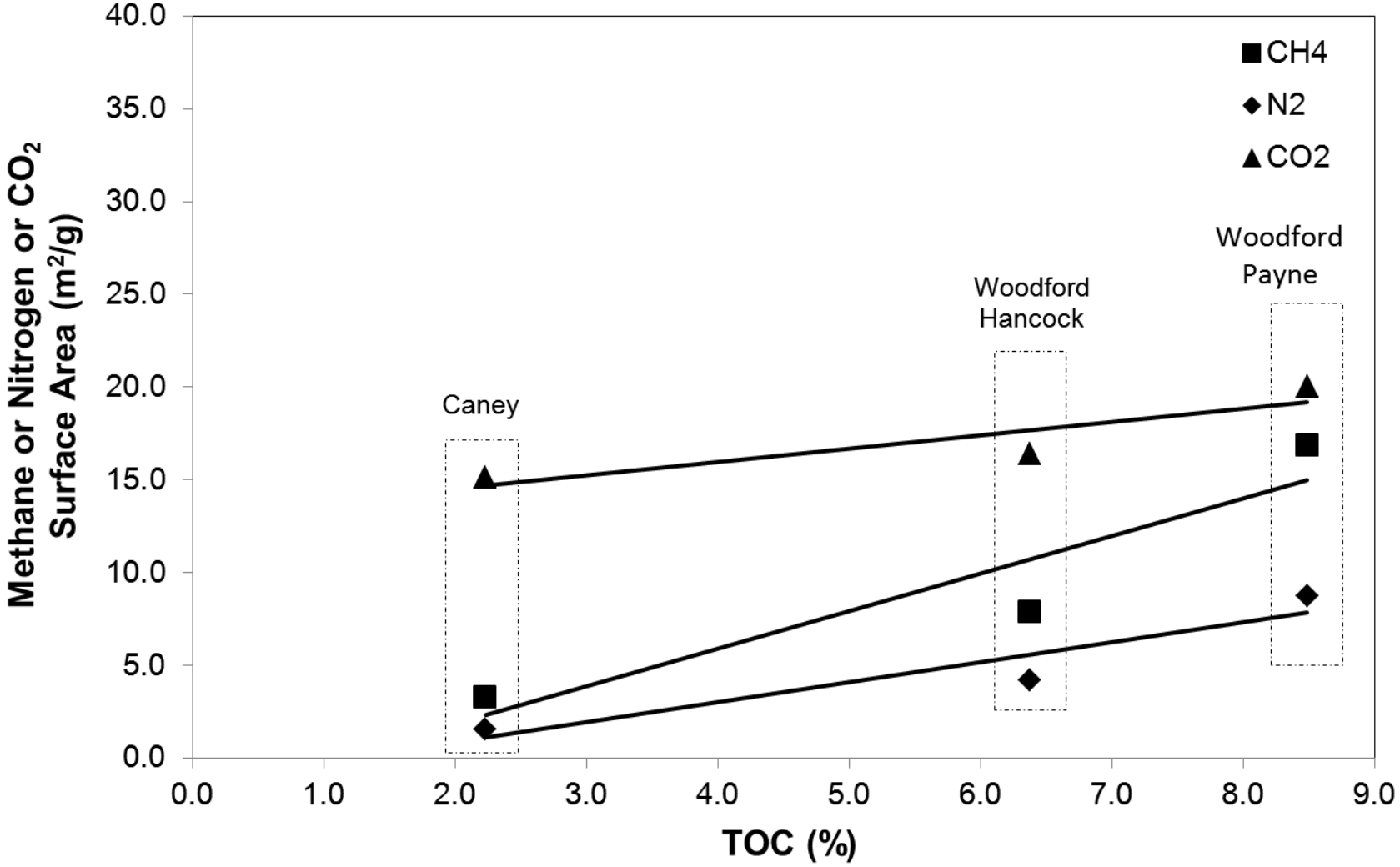

Figure 6(a).—SLD Model Surface Areas vs. TOC Content

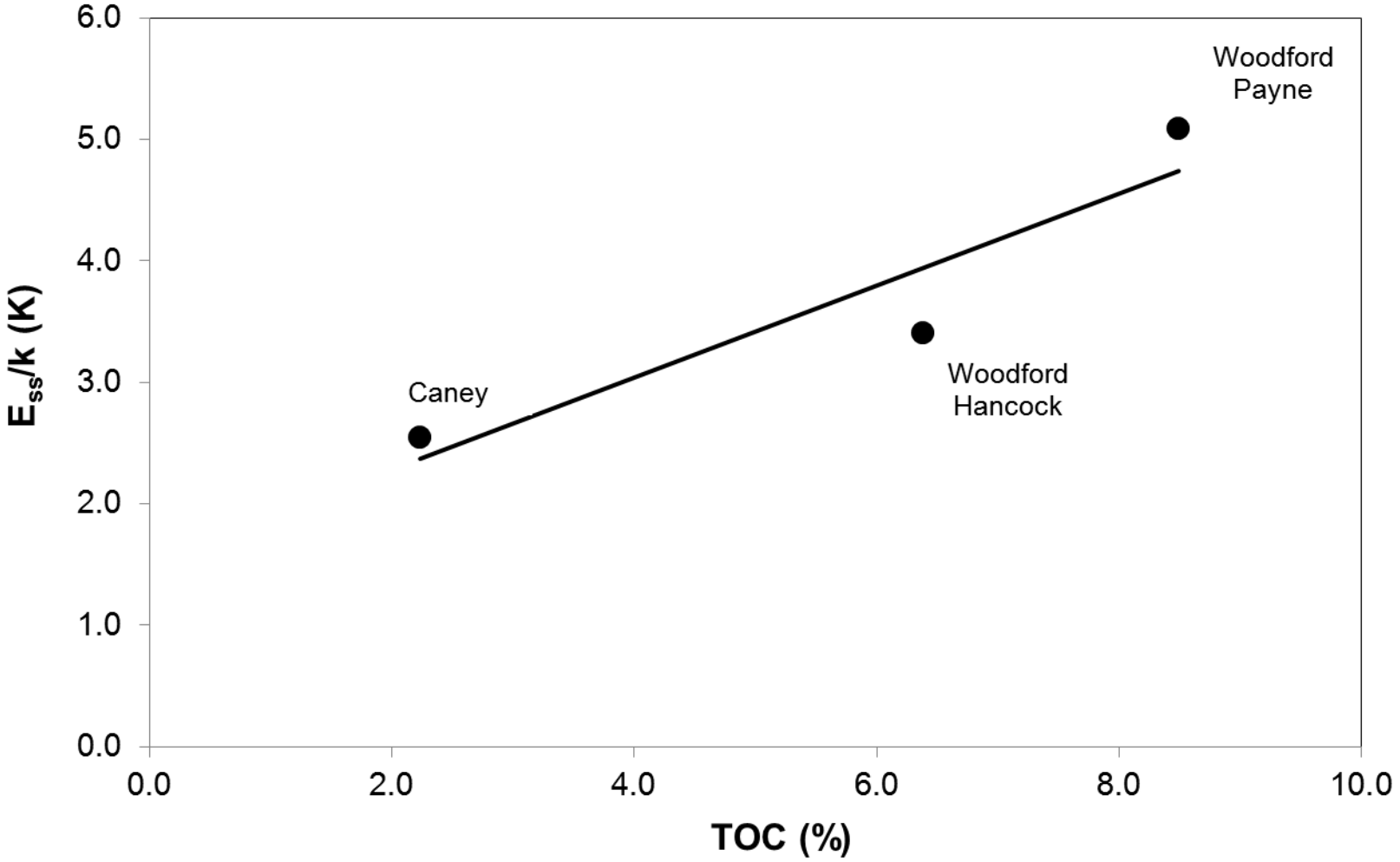

Figure 6(b).—SLD Model Solid-Solid Interaction Energy ($\varepsilon_{ss/k}$) vs. TOC Content

FLUID-ROCK INTERACTIONS

Petrophysics and Tight Rock Characterization for the Application of Improved Stimulation and Production Technology in Shale

FINAL REPORT

Reporting Period: June 27, 2013- June 26, 2016

by

Peter Clark,
Samyukta Koteeswaran
Jack C. Pashin
Jim Puckette

Oklahoma State University

Prepared for the Research Partnership to Secure Energy for America (RPSEA) under Contract 11122-63

Stillwater, Oklahoma
2016

CHARACTERIZATION OF SHALE-FLUID INTERACTIONS THROUGH A SERIES OF IMMERSION TESTS

CONTENTS

FIGURES

TABLES

INTRODUCTION

In order to meet the ever-growing demand for energy, shales have proven to be rich sources of oil and gas. The interaction of shales with fluids used in drilling, completion, and stimulation of shale formations is an important and not well understood aspect of the production optimization process. Shale is a fine-grained sedimentary rock with high clay content (Huang, Azar, & Hale, 1998). Clay content in shale has a great influence on the chemical and mechanical properties of shale. The common clay minerals present in shales are illite, montromillite, smectite, calcite and kaolinite. Each clay mineral when present in abundance significantly changes the shale properties. For instance, illite-rich shales are reactive and smectite causes swelling of shales when in contact with water. Even though shales have common properties each shale behaves uniquely when in contact with injected fluids (Gomez & He, 2012). Hence, formulation of these fluids has to be taken into account. A good example of this is the interaction of polyacrylamides used as friction reducers in the fracturing of shale wells.

Interactivity between shale and fluid are measured by different means. Traditional tests such as the dispersion tests and swelling tests do not fully account for the influence of fluid on the rock structure and fracture development in shale. Some of the commonly used methods use grinding the shale and reconstituting it with water. These tests give completely different results that are often far from reality. Immersion tests give us a visual confirmation of the effect of different types of fluid on the rock structure (Rabe, da Fontoura, & dos Santos Antunes, 2002; Santos, Diek, Da Fontoura, & Roegiers, 1997). Immersion tests are efficient in evaluating the drilling fluid suitable for a particular shale formation. However, the absence of the confining pressure is a major limitation to the method (Santos et al., 1997).

The common additives used in water-based mud (WBM) are friction reducers, acids, gellants, crosslinkers, clay controlling agents and other polymers. High molecular weight polyacrylamides are the most commonly used friction reducer and are thermally stable up to 200 °C (Carman & Cawiezel, 2007; Jia Zhou, Sun, Stevens, Qu, & Bai, 2011). Potassium chloride, sodium chloride and tetramethyl ammonium chloride (TMAC) are some of the common additives that are used to mitigate the harmful effects of clay present in water.

The thermally stable polyacrylamide polymers used as friction reducers are also used as shale inhibitors. High molecular polymers such as polyacrylamides provide better shale inhibition via increasing the membrane efficiency of shale by forming a highly viscous isolation membranes on the shale that prevent water from entering (Mody, Tare, Tan, Drummond, & Wu, 2002). High molecular weight polyacrylamides also provide better friction reduction.

Salts such as NaCl and KCl are widely used in injected fluids for stabilization. Potassium salts are used as clay-swelling inhibitors, the K^+ ions penetrate into the porosity of the shale creating a layer of semi-permeable membrane, which prevents the water from injected fluids from entering the shale (Khodja et al., 2010). Simplified exposure tests were done by (Horsrud, Bostrom, Sonstebo, & Holt, 1998) at simulated downhole conditions, they observed that exposure to KCl caused shrinkage of shale and a permeability increase. The shrinkage of shale is due to the potassium ions replacing the previously adsorbed exchangeable cations on the clay surface leading to the compaction of clay structure (Horsrud et al., 1998; Okoro & Adewale, 2014). The rate of water inflow into the shale formation decreases with salt concentration due to the chemical potential of injected fluid being lower than that of the of the formation and this eventually leads to slower rate of pore pressure increase thereby increasing the effective wellbore wall support (Tan, Richards, & Rahman, 1996). Shale when exposed to salt solutions such as

KCl, NaCl and $CaCl_2$ releases pore fluid and dehydrate due to the transport of water from shale to the contacting fluid (T. Al-Bazali, Zhang, Chenevert, & Sharma, 2008). The ion movement from the shale to the fluid provides a reduction in inter-granular friction that allows the grains to slip over each other as the stress is increased which enhances shale strength (T. Al-Bazali et al., 2008; Tan et al., 1996). However, excessive dehydration can cause a decrease in the formation strength which offsets the wellbore stability improvements (Tan et al., 1996) and also KCl has harmful effect on the friction reduction property of polyacrylamides.

In this work, the interaction of injected fluids with shales was studied as a function of polymer concentration and salt type and concentration. Bentonite, the primary clay component of WBM was used to examine the effects of a competing clay on the polymer-shale interaction.

MATERIALS and METHODS

Experimental Methods

This section is divided into two subsections. In the first , the shale sample is characterized to determine the mineralogy, porosity, total organic content and pressure decay permeability. The section consists of immersion tests and the rheological properties of shale fluid used in order to characterize the shale interactivity with different types of oilfield fluids.

Shale Samples

In order to physically observe the effects of different additives on the shale, immersion tests using different types of fluids were conducted on samples of Chattanooga, Gorgas, Barnett and Woodford shales. Well-preserved core samples were used for the tests. Drying of the samples prior to the test causes a change in water content in the shale. A minimal change in water content drastically changes the reactivity of the shale. Shale samples that are used in the tests are carefully preserved with large surface area that has had minimal exposure to coring fluids.

Shale Characterization

In order to characterize the shale-fluid interaction it is imperative to characterize the shales for mineralogy, total organic content, porosity and permeability to help us understand the shale – fluid interactions. Table 1 shows the various characterization methods used for the study.

Table 1.—Equipment used to characterize shale properties.

Measurement	Equipment	Expected Results
Mineralogy	X- Ray Diffraction	Percentage composition of clay and non clay minerals
TOC	Coulometer	Organic content of shale
Effective Porosity	Porosimeter	Porosity of shale with respect to mobile fluid volume – gas, water or oil
Pressure Decay Permeability	Permeameter	Clay matrix permeability
Surface Characteristics	Scanning Electron Microscopy	Morphology, topography of shale

Shale Mineralogy

XRD is used to determine the clay and non-clay content present in the shale samples quantitatively. XRD is a robust and powerful technique widely used in the characterization of shales. The quantitative analysis of clay, non - clay and expandable clay content is done using XRD. Mineralogy of the shale samples (Table 2) influences the mechanical property of the shale (Kumar, Sondergeld, & Rai, 2012; Nelson, 2009).

Total Organic Content (TOC)

The TOC is a crucial indicator of the development and behavior of shales. Many times TOC is determined in order to measure the kerogen content of the shale, but kerogen has sulphur,

nitrogen, oxygen and hydrogen in addition to carbon. Organic rich shales have higher permeability and also are reactive compared to the less organic shales (Rickman, Mullen, Petre, Grieser, & Kundert, 2008). TOC, effective porosity and pressure-decay permeability are shown in Table 3.

Porosity

Determining the porosity of shale is important to understand the mechanical behavior of shale at different stresses and in understanding shale stability and failure limit (Josh et al., 2012). The permeability of the shale is dependent on the pore sizes, which controls the elasticity and mechanical strength of shales (Khodja et al., 2010). Effective porosity is shown in Table 3.

Pressure Decay Permeability

The pressure decay permeability method is standard for measuring permeability in shale and other nano- to microdarcy rocks. Pressure decay takes a fraction of the time required for steady state methods (Jones, 1997). Pressure decay permeability measurements are shown in Table 3.

Table 2. —Whole rock mineralogy of shale samples from different wells.

Analysis	**Pride Mountain**	**Gorgas**	**Woodford**	**Woodford**
Depth (ft)	9167	2863	10372.1	10382
Clay Content (Wt. %)				
Smectite	0	1		
Ilite/Smectite	5	16	6	3
Ilite+Mica	24	37	33	28
Kaolinite	0	12	Tr	Tr

Chlorite	0	4	1	Tr
Non Clay Mineral Content (Wt. %)				
Quartz	41	21	28	32
K Feldspar	16	3	5	4
Plagiocase	2	2	8	7
Calcite	0	1	Tr	Tr
Ankerite/Fe Dolomite	0	1	2	1
Dolomite	5	0		
Pyrite	5	1	6	4
Fluorapatite	0	0	Tr	0
Barite	1	1	0	0
Siderite	0	1	Tr	Tr
Magnetite	0	0	0	0

Table 3. —TOC, Effective Porosity and Pressure decay permeability

Parameters	Pride Mountain	Gorgas	Woodford (10372.1 ft)	Woodford (10382 ft)
TOC (Wt. %)	3.33	0.80	4.68	3.76
Effective Porosity (% of BV)	2.32	12.30	4.8	4.8
Pressure Decay Permeability (mD)	0.00032	0.00048	0.000362	0.00053

Scanning Electron Microscopy

SEM techniques were used to study the surface properties and morphology of the shale under study. Shale core were core sawed to get 1 – 2 mm shale particles, parallel to the bedding plane. The sample was placed on the stub and the shales being non-conducting materials were sputter coated with conducting layers of gold. The surface of the shale was examined using different magnifications (Figures 1, 2 and 3). In order to determine the elemental composition of shales, the shale samples were coated with layers of carbon and energy dispersive spectroscopy (EDS) analysis of the shale samples are done to determine elemental composition.

Rheology of Oilfield Fluids

Fluid Design

One of the main objectives of this study is to study shale – fluid interaction. The fluids used are commonly used oilfield fluids combined with anionic and cationic polyacrylamide, Wyoming bentonite is used as the clay in this study, KCl, NaCl and TMAC (tetramethyl ammonium chloride). The fluid systems that were used in this study are shown in Table 4.

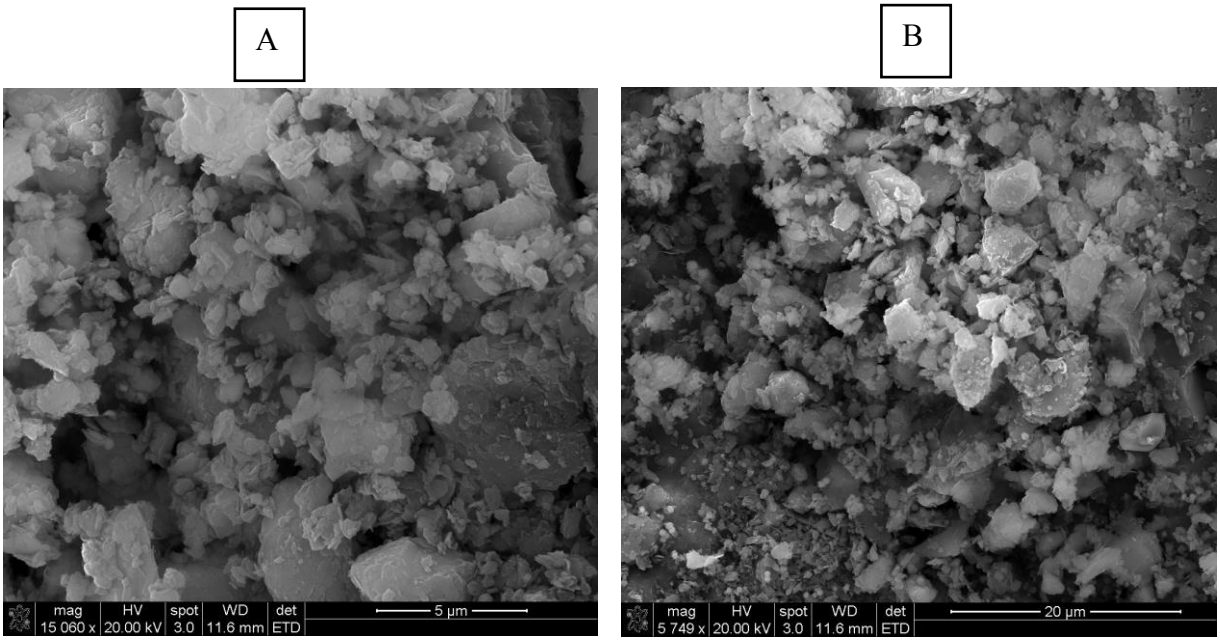

Figure 1.—SEM images of Woodford shale in Rother (10372.1 ft).
(A) Randomly oriented clay platelets (15060 x) (B) Same (5749 x)

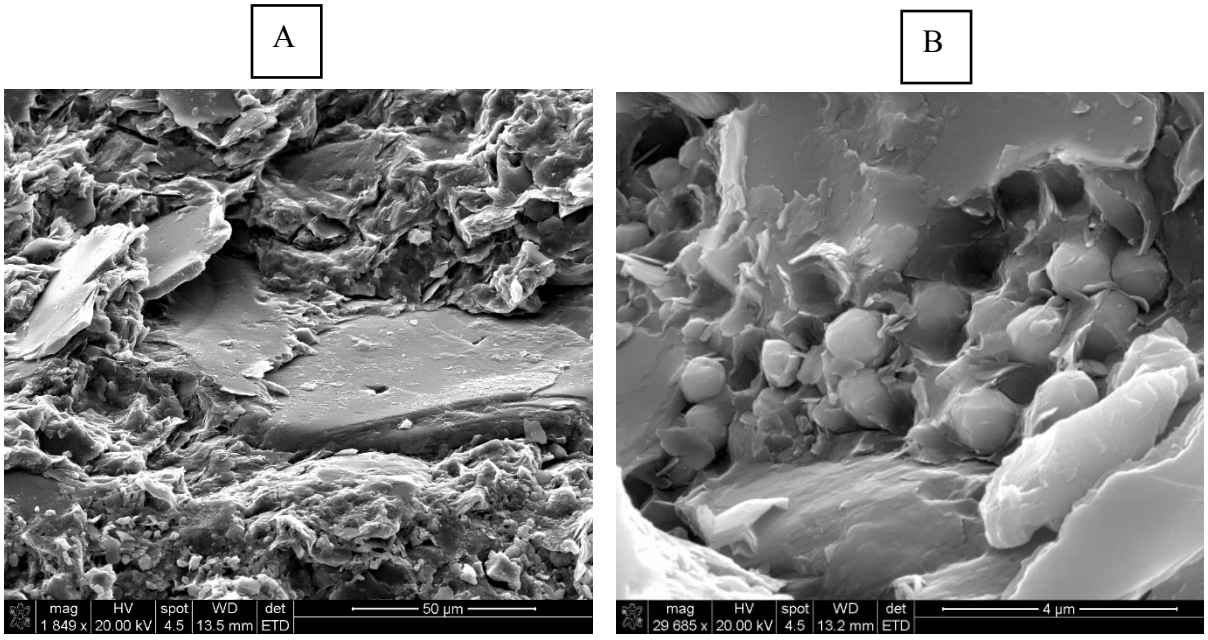

Figure 2.—SEM images of pyrite in the Gorgas #1, Pride Mountain formation (2864.4 ft)
(A) Poorly aligned and folded clay platelets (B) Cluster of spherical to oblate framboids

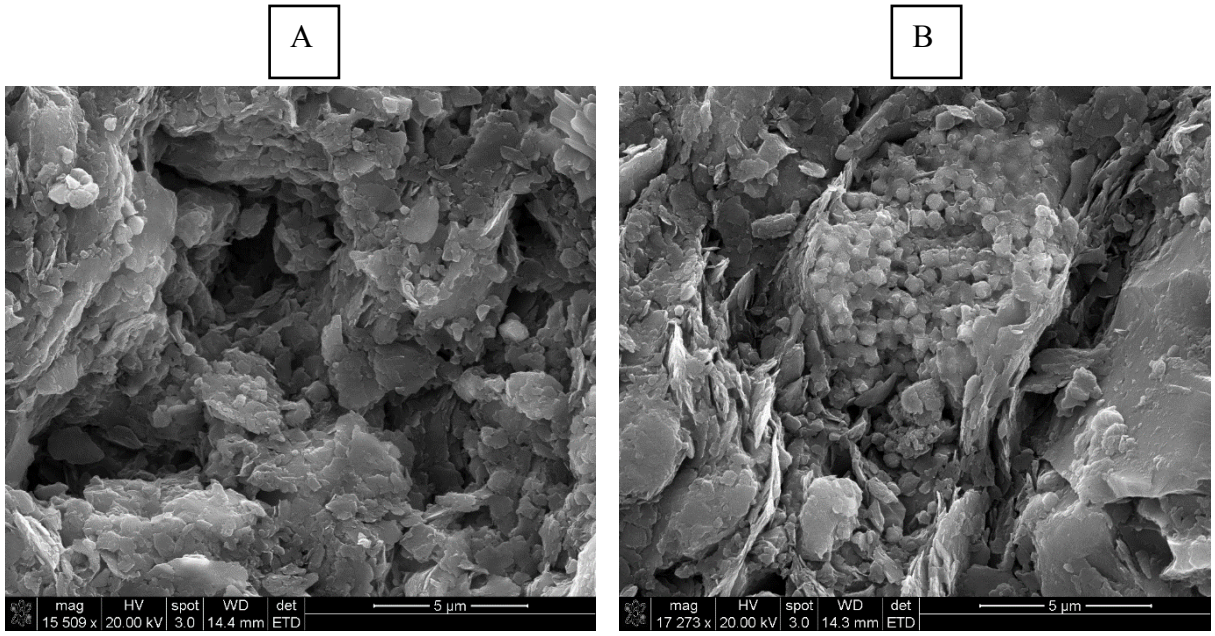

Figure 3.—SEM images of Chattanooga shale in Lamb 1 - 3 #1 (9173.5 ft). (A) Randomly oriented clay platelets (B) Pyrite framboids in matrix of platy illite

Table 4.—Composition of different fluid systems used in the study

S/N	Fluid System	Composition
1	Bentonite	2 lb/bbl bentonite + 0.2 wt.% anionic polyacrylamide 2 lb/bbl bentonite + 0.2 wt.% cationic polyacrylamide
2	KCl – Bentonite	2 lb/bbl bentonite + 0.2 wt.% anionic polyacrylamide + 2 % KCl 2 lb/bbl bentonite + 0.2 wt.% cationic polyacrylamide + 2 % KCl
3	NaCl - Bentonite	2 lb/bbl bentonite + 0.2 wt.% anionic polyacrylamide + 2 % NaCl 2 lb/bbl bentonite + 0.2 wt.% cationic polyacrylamide + 2 % NaCl
4	TMAC - Bentonite	2 lb/bbl bentonite + 0.2 wt.% anionic polyacrylamide + 2 % TMAC 2 lb/bbl bentonite + 0.2 wt.% cationic polyacrylamide + 2 % TMAC

Base Fluid used is DI Water (400 ml)

Equipment

A Discover DHR-3 stress controlled rheometer is used to make rheological measurements of the samples. For the polymer - shale sample vane geometry is used. Vane geometry helps prevent wall slippage at higher shear rates, will help disrupt flow inhomogeneity while shearing

and also is works great for samples that have solids suspended. For polymer solutions the cone and plate geometry is used. Cone and plate is useful for solutions that have low viscosities and that do not have any dispersions with solids suspended greater than 64 μm. Cone and plate geometry (diameter: 60 mm and cone angle 2º) have homogenous shear, shear rate and stress in the geometry gap. All the experiments were done at a temperature of 25 °C ± 0.03 °C. The polymer shale sample is pre sheared at 200 $l \cdot s^{-1}$ before the start of each experiment.

Immersion Tests

Carefully preserved core samples were immersed in different fluid systems of varying compositions at 60°C and were sealed and left for 5 days for inert shales and 2 days for reactive shales. The change in weight of the shale samples before and after the test, linear swelling and the hardness change were measured. SEM images of the samples after exposure to the test fluids were taken to analyze the effectiveness with which the polyacrylamide fluids could form membranes on the shale surface.

RESULTS and DISCUSSION

The change in thickness of shale samples used in study is measured before and after the immersion tests using a Vernier caliper. This gives us a qualitative measurement of the extent of sample expansion/shrinking when in contact with the injected fluids. Additionally the change in weight of the shale sample is also determined. In order to study the isolated effect of salt and polyacrylamides separately immersion tests were done with just salts and polyacrylamides with no additives in it. The Woodford sample was immersed in salt solutions, to study the effect of salt in preventing swelling. Figure 4 shows the percent expansion/shrinkage of Woodford shale immersed in KCl, NaCl, TMAC and DI Water. The shale swells most in DI water. This is

expected and due to the water activity being 1 in DI water, the water is driven towards the shale which causes the swelling. This is reflected in weight gain also where DI water has the maximum weight gain. In absence of any other additives TMAC is most effective in inhibiting swelling of shale. Shrinking of shale causes an increase in the shale strength which increases the wellbore stability.

Figure 5 shows the percent expansion/shrinkage of Woodford shale immersed in anionic polyacrylamide and cationic polyacrylamide in comparison to DI Water. Shale immersed in anionic polyacrylamide shrinks more than the cationic polyacrylamide. When compared with salt solutions, the polyacrylamides as such provide better inhibition to swelling. Polymers have been proven to be effective in bridging the interlayer spacing between the clay platelets and they also form a stable isolation membrane that prevent the water from entering the shale.

To study the effectiveness of salts, TMAC and polyacrylamides as shale inhibitors with bentonite immersion tests were done with the mud system as shown in Table 4. When in contact with the medium, all samples shrunk (Figure 6). The shrinking was more in TMAC, and least with NaCl and cationic polyacrylamide. Samples showed considerable weight gain because of adsorption of the polyacrylamides on the shale surface (Figures 7, 8, 9, 10, 11, 12, and 13). Bentonite has always been associated with shale drilling and is proven to cause swelling and dispersion in shales. But when used with polyacrylamides and salts the swelling can be minimized. The mechanism of shale inhibition investigated in this study is effective adsorption of polyacrylamide and salt on the shale which prevents water from entering the shale. The surface of immersed shale was analyzed using SEM to see the nature of polyacrylamide-salt adsorption.

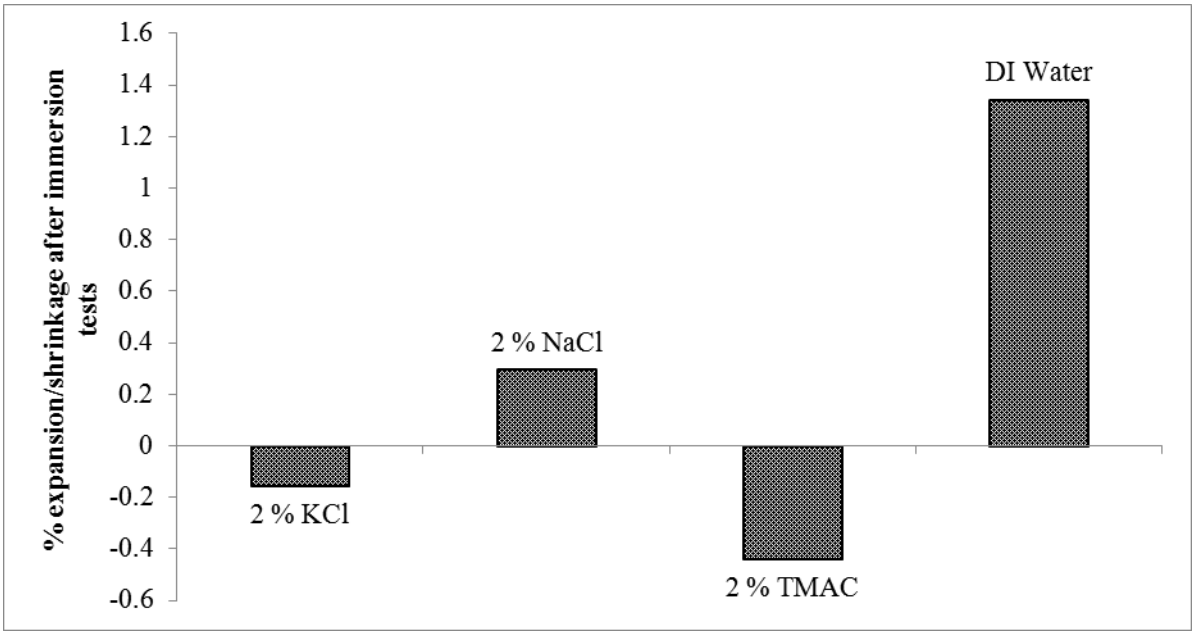

Figure 4.—Percent expansion/shrinkage of Woodford shale after immersion test.

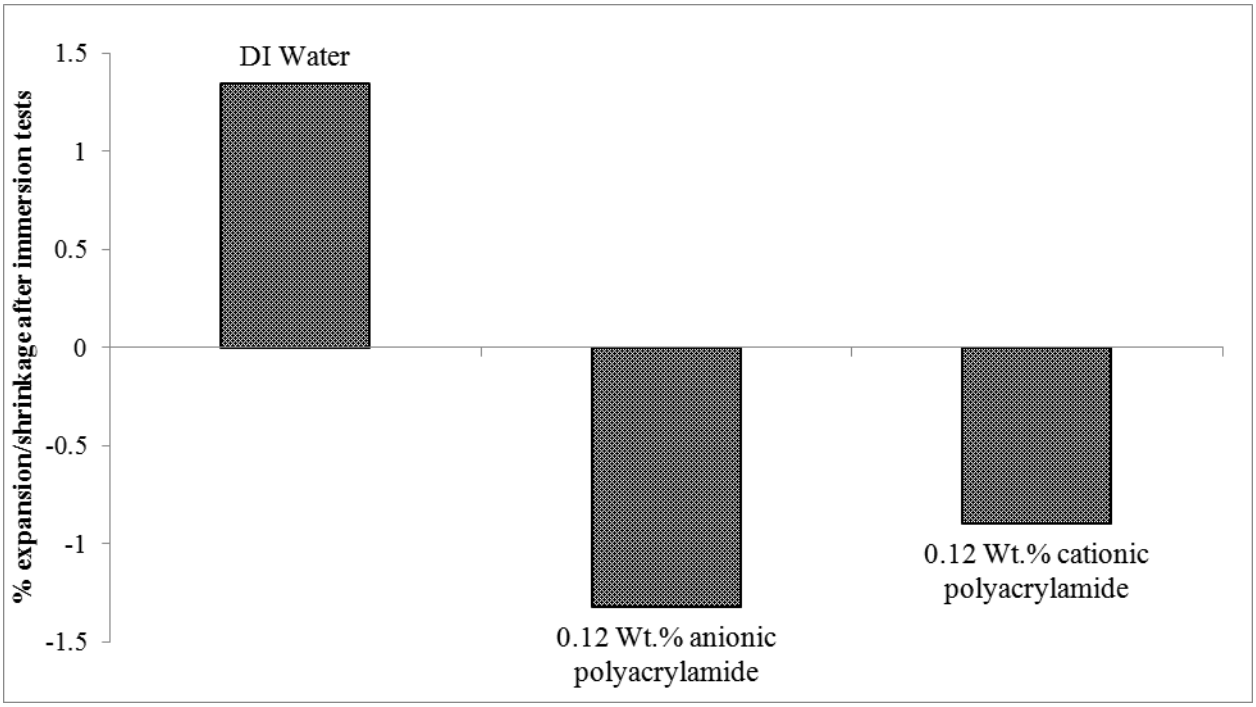

Figure 5.—Percent expansion/shrinkage of Woodford shale after immersion test.

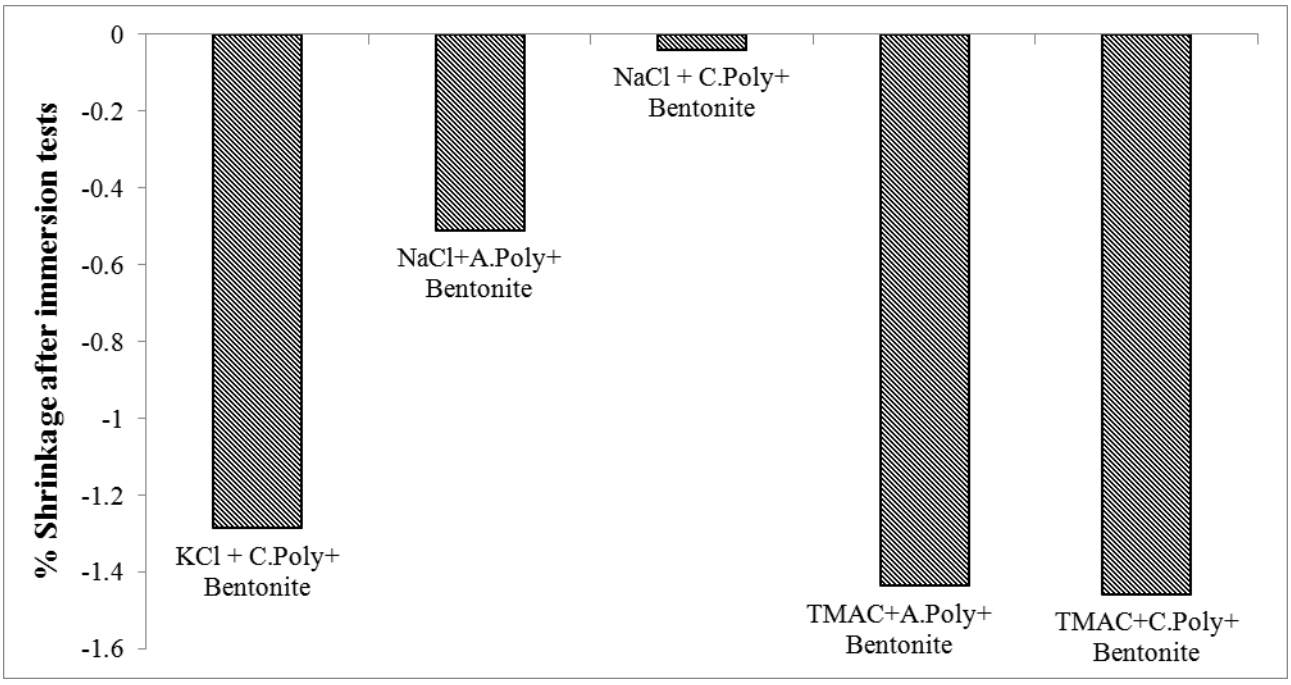

Figure 6.—Percent expansion/shrinkage of Woodford shale after immersion test.

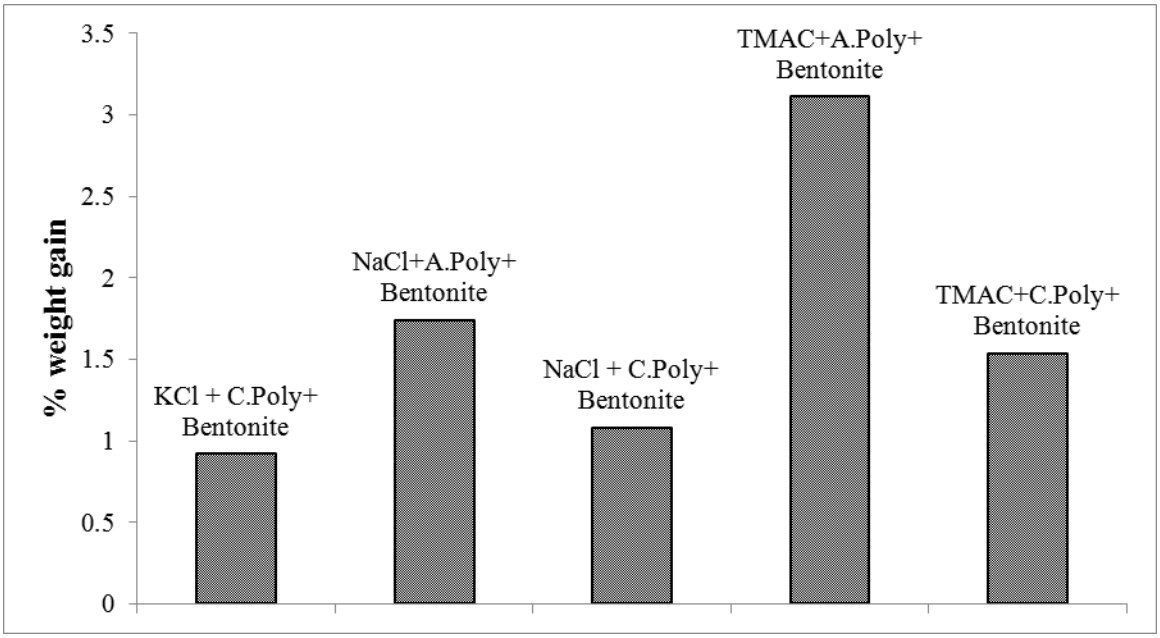

Figure 7.—Percent weight gain of Woodford shale after immersion test.

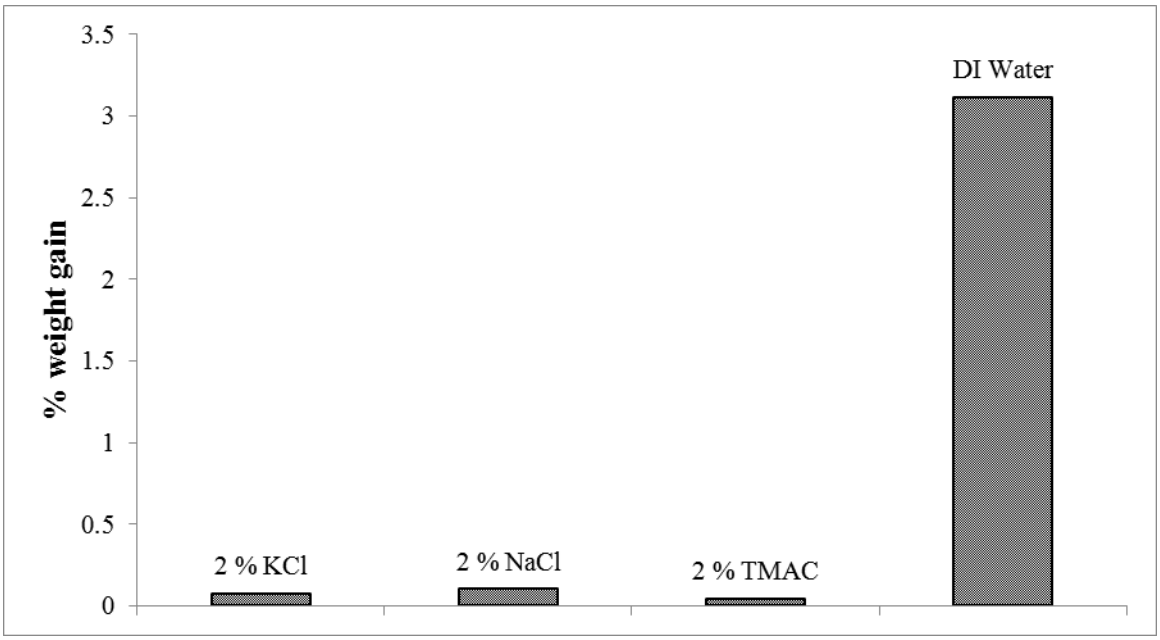

Figure 8.—Percent weight gain of Woodford shale after immersion test.

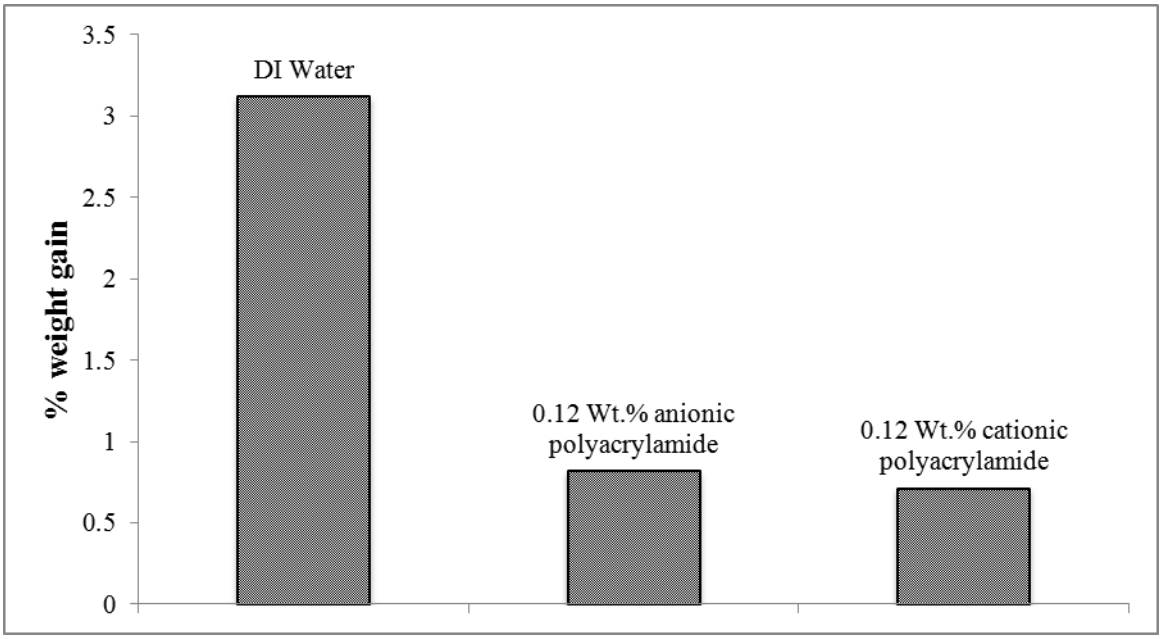

Figure 9.—Percent weight gain of Woodford shale after immersion test.

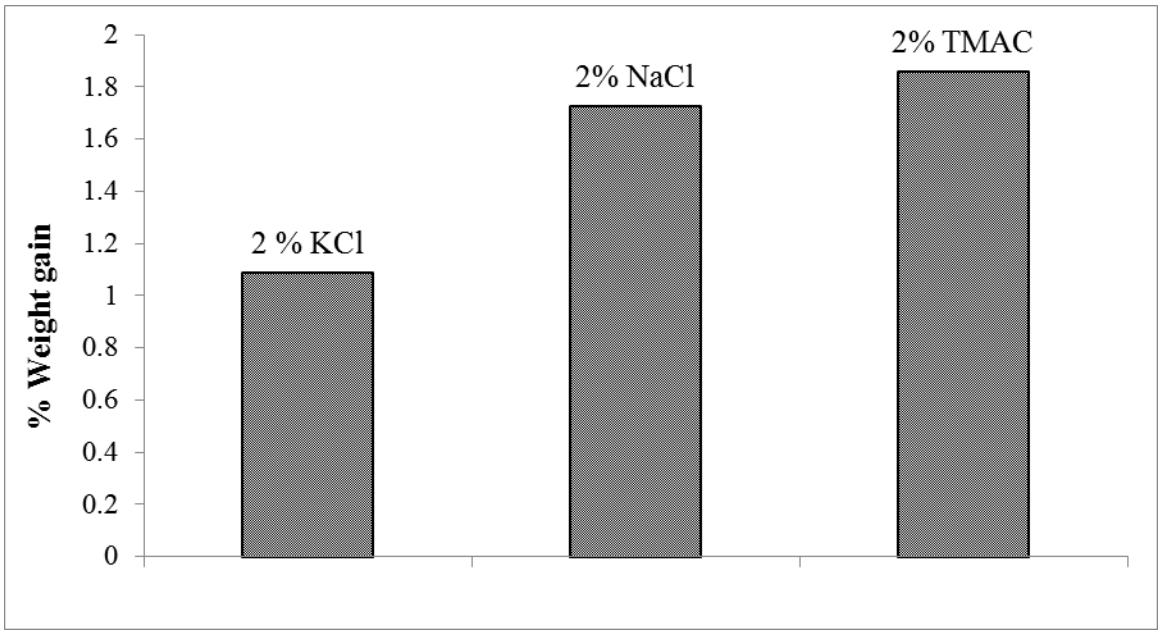

Figure 10.—Percent weight gain of Gorgas shale after immersion test.

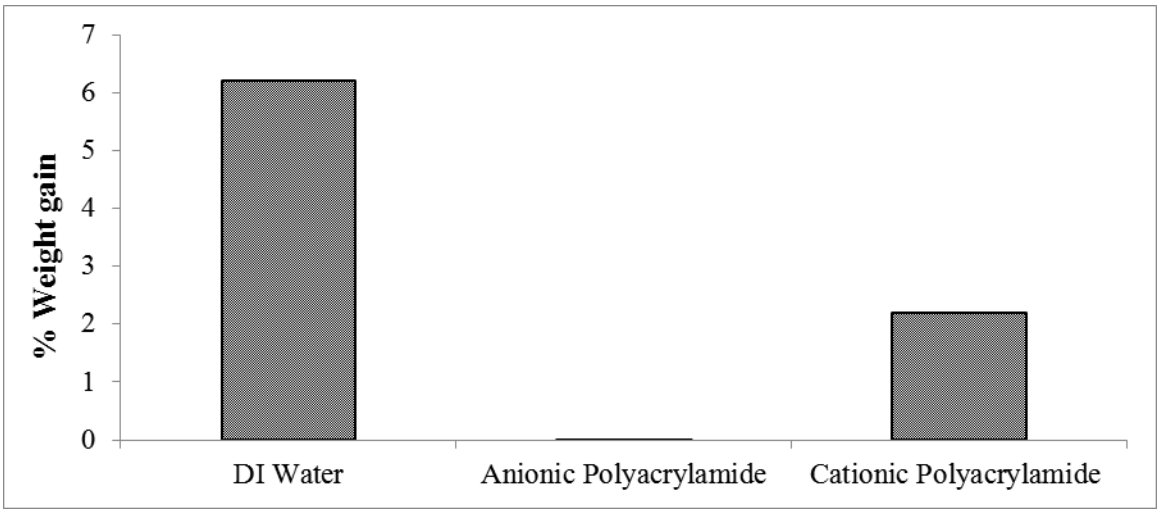

Figure 11.—Percent weight gain of Gorgas shale after immersion test.

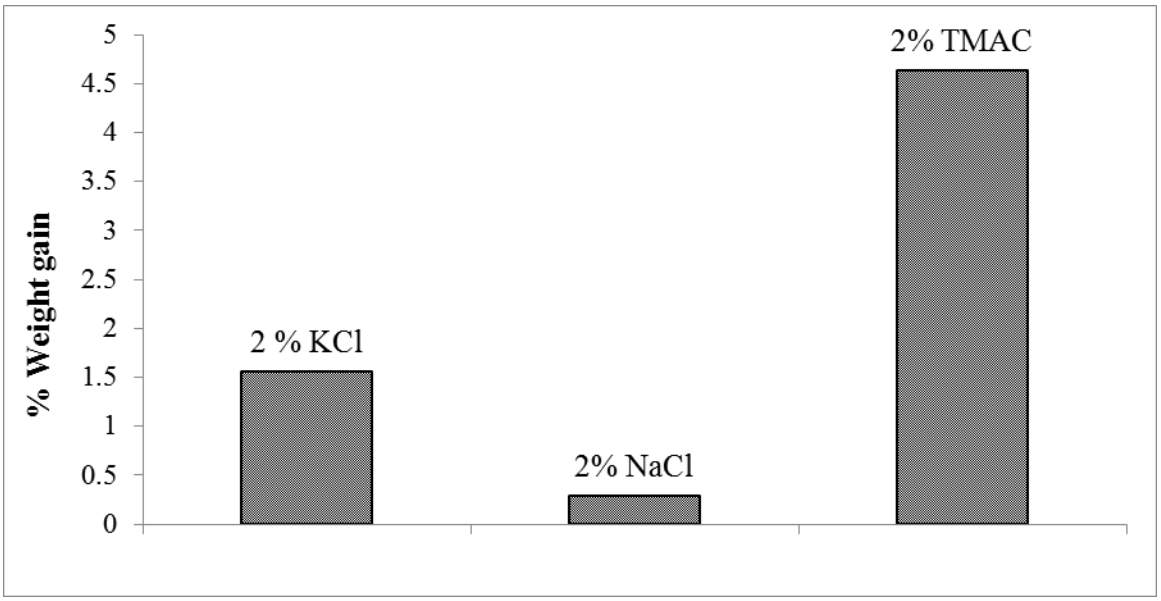

Figure 12.—Percent weight gain of Pride Mountain shale after immersion test.

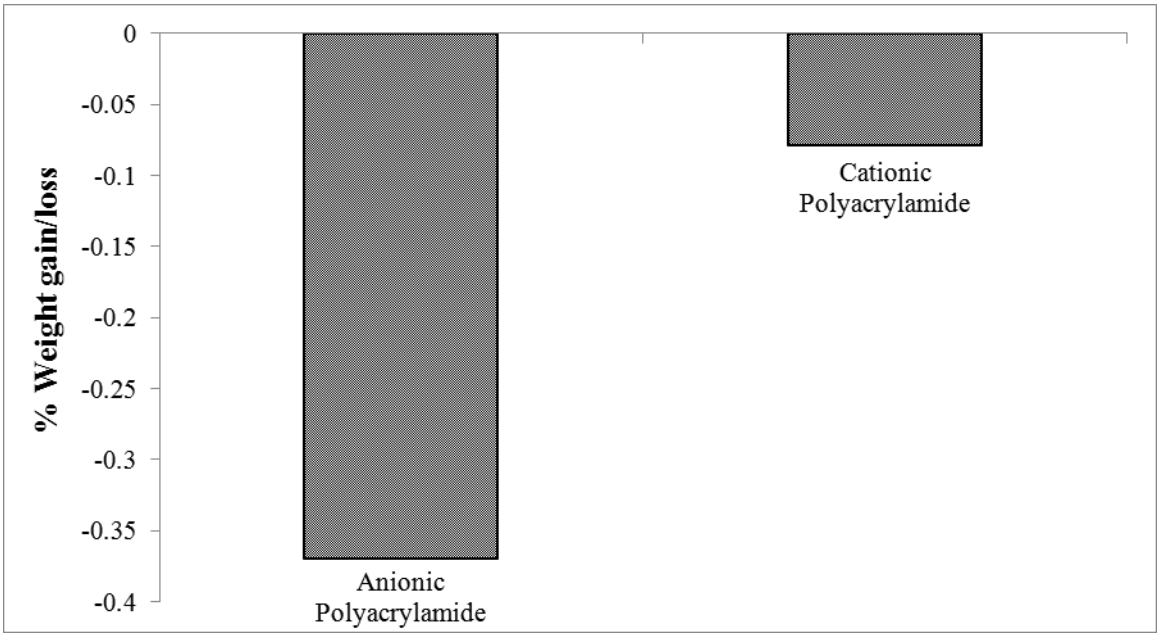

Figure 13.—Percent weight gain/loss of Pride Mountain shale after immersion test.

There was a significant change in the surface morphology of shale immersed in mud system 2, 3 and 4 as observed using SEM as shown in Figures 14,15,16 and 17. Bentonite with NaCl and anionic polyacrylamide forms a uniform membrane over the shale, which prevents the water from entering/leaving the shale, which explains the small percentage of shrinking, caused by immersing this shale. As seen in Figure 15, there is minimal adsorption of polyacrylamide on the Woodford shale surface. TMAC has proven to effectively inhibit polymers from adsorbing onto the shale surfaces from the fracturing fluids (Himes & Simon, 1990). For shale immersed in cationic polyacrylamide with salts, the surface of the shale is accumulated with precipitated salt and polyacrylamide crystals. Especially the KCl – cationic polyacrylamide system provides a better inhibition due to the precipitation of salts on the surface which forms a thicker layer on the shale which prevents the shale from swelling or dispersion.

The qualitative description of Woodford samples is shown in Table 5 after the immersion tests. For most of the tests the Woodford sample remained intact and did not disperse or disintegrate during the test period. This could be attributed to less expandable clay minerals, which promotes swelling and higher quartz content, which imparts mechanical strength. Additionally lesser porosity makes the shale less reactive in nature. The shale was comparatively softer when immersed in TMAC – bentonite mud. There are two possible reasons for this phenomena, TMAC prevents the adsorption of polyacrylamide on the surface of the shale that leads to water and ions entering and leaving the shale. The second possibility is that the potential difference between the fluid surrounding the shale and the pore fluid is higher, causing an osmotic potential difference that leads to shrinking of shale sample. In the previous studies, it has been proved that over shrinking of shales can cause reduction in strength.

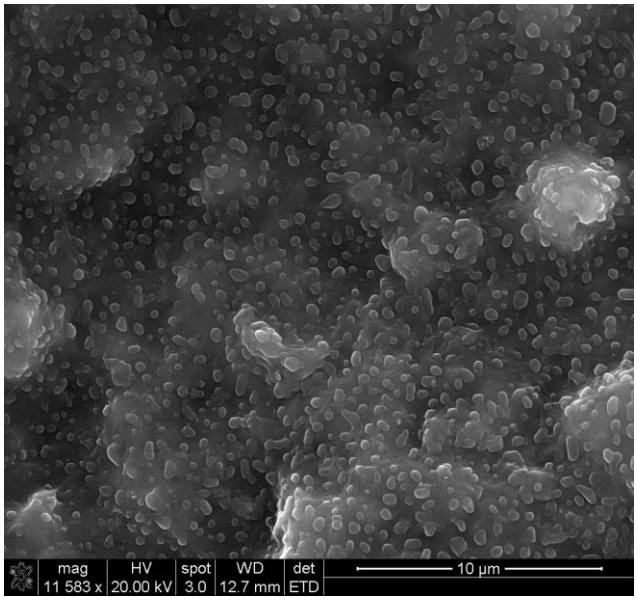

Figure 14.—Shale immersed in Bentonite + NaCl + Anionic Polyacrylamide.

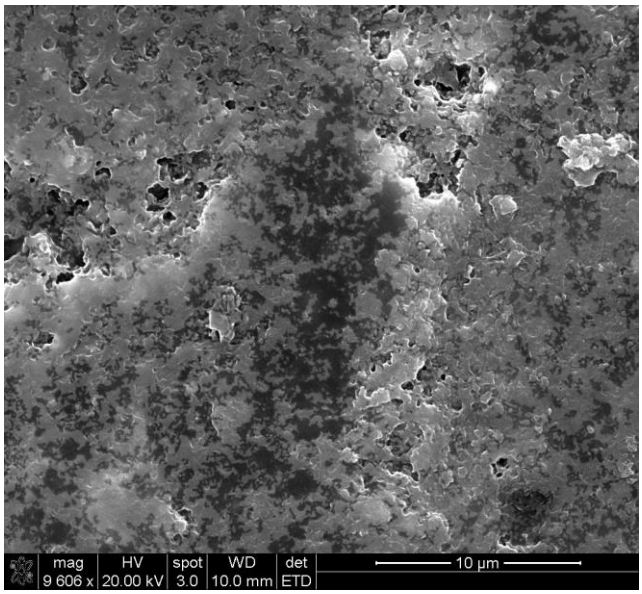

Figure 15.—Shale immersed in Bentonite + TMAC Cationic Polyacrylamide.

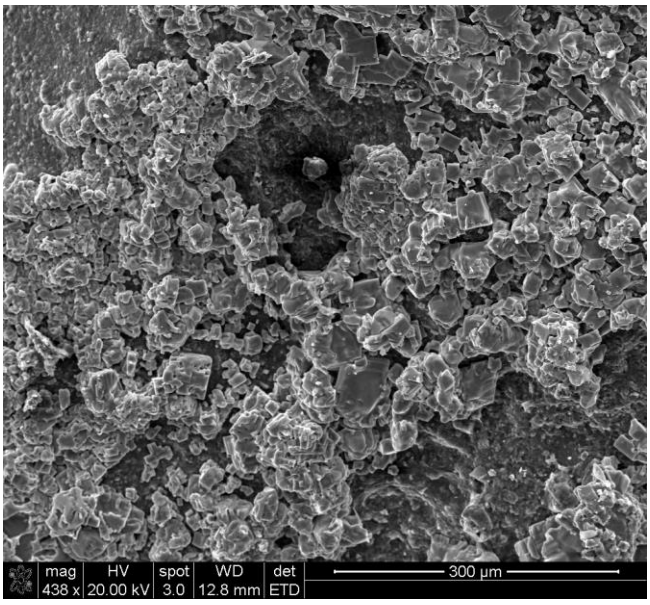

Figure 16.—Shale immersed in Bentonite + KCl + Cationic Polyacrylamide.

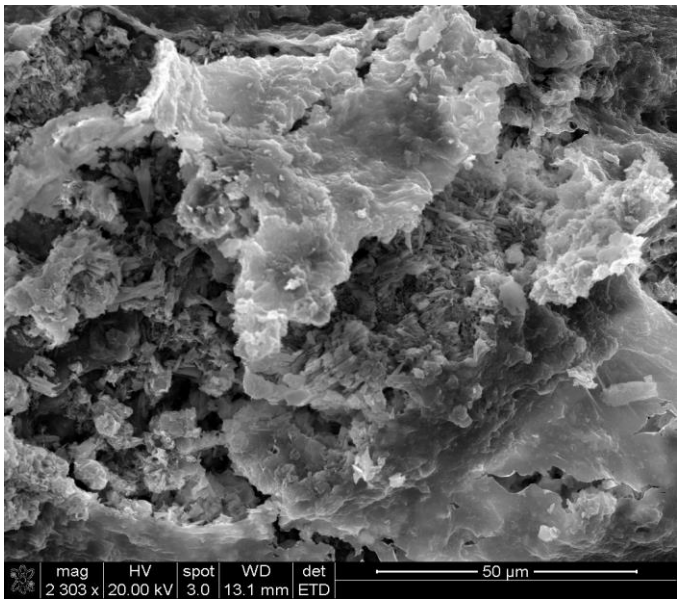

Figure 17.—Shale immersed in Bentonite + NaCl + Cationic Polyacrylamide.

Table 5.—Qualitative description of Woodford shale samples after immersion tests.

Sample	Qualitative description
Anionic Polyacrylamide + Bentonite	Intact, Soft
Cationic Polyacrylamide + Bentonite	Intact, Firm
KCl + Anionic Polyacrylamide + Bentonite	Intact, Soft
KCl + Cationic Polyacrylamide + Bentonite	Intact, Hard
NaCl+Anionic Polyacrylamide + Bentonite	Intact, Hard
NaCl + Cationic Polyacrylamide + Bentonite	Intact, Hard
TMAC + Anionic Polyacrylamide+ Bentonite	Intact, Soft
TMAC + Cationic Polyacrylamide + Bentonite	Intact, Soft
2 % KCl	Intact, Hard
2 % NaCl	Intact, Hard
2 % TMAC	Intact, Hard
DI Water	Intact, Hard
0.12 Wt.% Anionic Polyacrylamide	Intact, Hard
0.12 Wt.% Cationic Polyacrylamide	Intact, Hard

The effect of salts, TMAC and polyacrylamides on the swelling behavior of Woodford Shale samples was studied separately (Figures 4, 5, 6 and 7). As expected, the swelling was most for shale immersed in DI water. The shale immersed in 2% NaCl showed swelling, whereas it shrunk in 2% KCl solution. The hydrated radii of sodium is larger than that of potassium as a result of which a greater amount of water entered Woodford Shale after it was exposed to 2%

NaCl solution (Junhao Zhou, Jung, Pedlow, Chenevert, & Sharma, 2013). Additionally, change in weight of the shale samples was measured after immersion tests. The results were correlated with the linear swelling test results. Maximum weight gain was for shale immersed in DI water followed by 2% NaCl, 2% KCl and 2% TMAC.

The Pride Mountain and Gorgas shales were chosen to study the effect of salt and polyacrylamides on limiting the swelling/dispersion ability of shales. Pride Mountain shale has less expandable clays and higher quartz, which makes it hard shale, on the contrary Gorgas shale is rich in mixed and expandable clays and is soft. The change in weight of both the shales was used as a measure of shale reactivity.

Rheology of Oilfield Fluids

The rheological properties of the fluid under study were measured (Figures 18 and 19). Salts were found to be detrimental to the rheology of the fluids containing anionic polymer. The potassium ions form a strong bond between the smectite layers in the bentonite, thereby leading to clay aggregates and reduction in the fluid viscosity (Guven, Panfil, & Carney, 1988). The addition of potassium salts in bentonite fluids leads to reduction in viscosity, Whereas in cationic fluid system salts improve the rheology of the system, the apparent viscosity is higher in presence of salts in the fluids containing cationic polymers. Addition of salt to the cationic polyacrylamide system leads to polyacrylamide-bentonite aggregates due to the interaction of polyacrylamide with the negative face charge of bentonite.

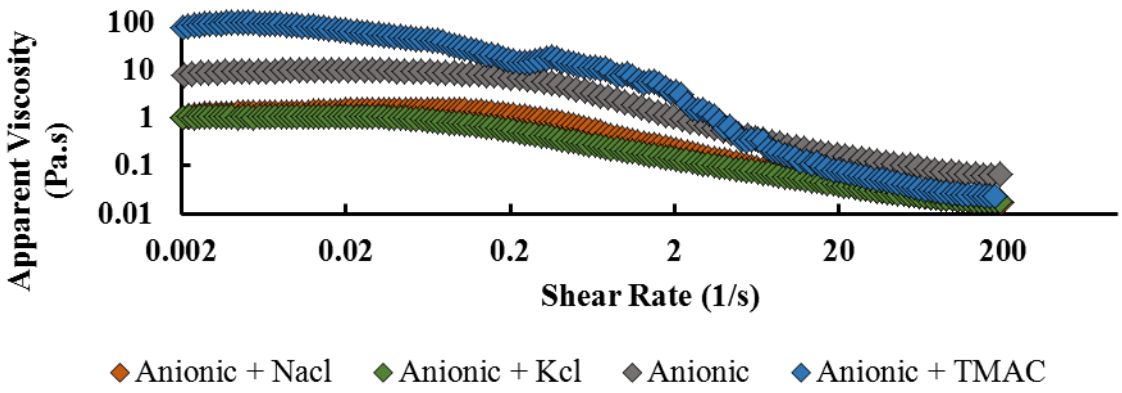

Figure 18.—Change in apparent viscosity of anionic polyacrylamide system with shear rate

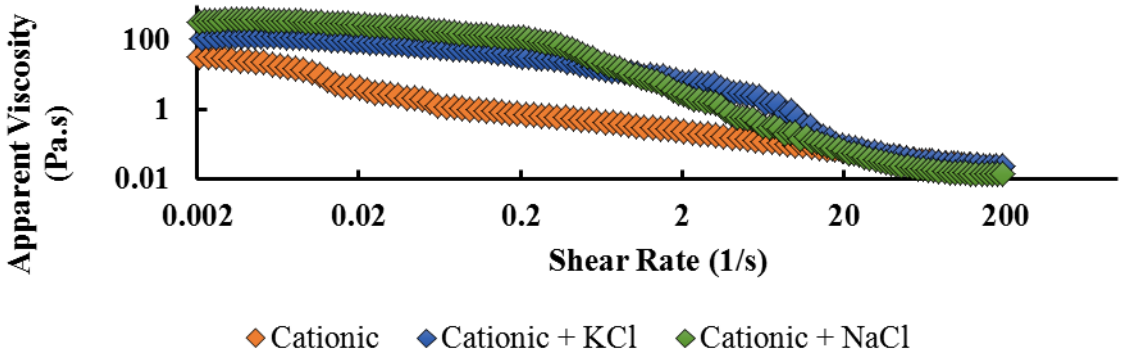

Figure 19.—Change in apparent viscosity of cationic polyacrylamide system with shear rate.

The effect of salt on the rheology of bentonite and polyacrylamides was studied separately (Figure 20). Bentonite forms an important constituent of the drilling fluid, and is used in the production of high density drilling fluids with shear-thinning flow behavior (Goh, Leong, & Lehane, 2011). The zero shear rate viscosity was determined for the bentonite-salt dispersions. Addition of KCl and TMAC leads to the reduction in the viscosity. The potassium and ammonium ions exchange with the more swellable sodium ions in the bentonite and thereby reduce the swelling of the clay, which leads to reduction in the yield stresses and the apparent

viscosity. In contrast, in the presence of NaCl, swelling is increased due to the larger hydration radius of sodium ion.

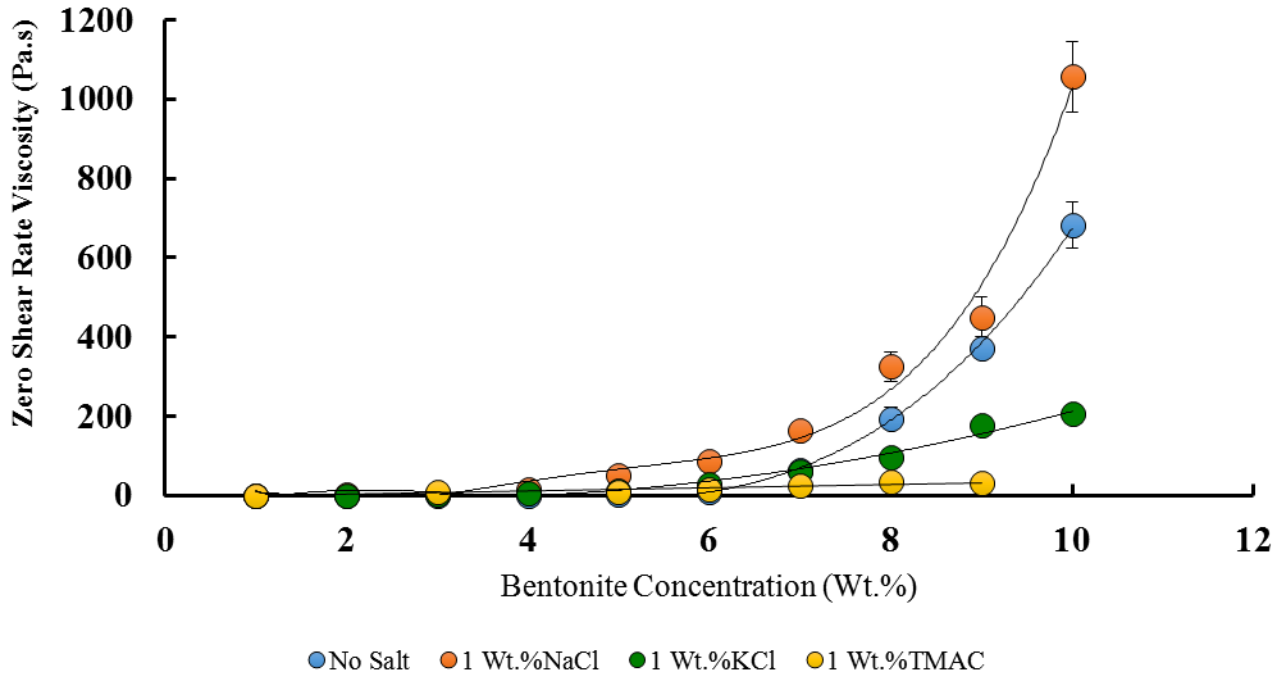

Figure 20.—Change in zero shear rate viscosity of bentonite salt system with shear rate.

Conclusions

In this paper the role of salts, tetramethyl ammonium chloride (TMAC) and polyacrylamides as shale inhibitors is investigated through simple immersion tests and by using rheology as a means of measuring clay-fluid interaction. The following conclusions are drawn from the experimental results

1. Polyacrylamides (anionic and cationic) prevent swelling in all of the three gas-shale samples under study by forming an isolation membrane on the shale and preventing water and ions from entering the shale.

2. High concentrations of TMAC are not recommended. TMAC prevents the adsorption of polyacrylamides and also causes excessive shrinking which can lead to shale losing its mechanical strength at down-hole conditions.
3. NaCl increases swelling in montmorillonite-rich shales. Instead, salts such as KCl and TMAC can be used with shale rich in expandable clays such as sodium montmorillonite.
4. Polyacrylamide with salts and TMAC proved very effective in preventing swelling and dispersion for all three shales.
5. Salts are inimical to the rheology of anionic polyacrylamides. Salts reduce the viscosity of the fluid system and hence can lead to increased fluid losses.
6. The recommendations for suitable salts and polyacrylamides for the three shales under study are given in Tables 6, 7 and 8.

Table 6.—Application of KCl-based fluids for the shales under study.

Shale	**Shale Type**	**Dispersion limiting ability of KCl**	**Swelling limiting ability of KCl**	**Is the use of KCl suggested?**
Woodford	Medium hard, high in illite, with expandable clays, less dispersion shale	Good	Good	Yes
Pride Mountain	Hard, high in quartz, less expandable clays	Good	Fair	Yes
Gorgas	Soft, high expandable, interlayer mixed clays and highly dispersible	Fair	Fair	No

Table 7.—Application of NaCl-based fluids for the shales under study.

Shale	Shale Type	Dispersion limiting ability of NaCl	Swelling limiting ability of NaCl	Is the use of NaCl suggested?
Woodford	Medium hard, illite-rich, with expandable clays, less dispersible shale	Good	Fair	Yes
Pride Mountain	Hard, high in quartz, less expandable clays	Good	Good	Yes
Gorgas	Soft, high expandable content, interlayer mixed clays and highly dispersible	Fair	Fair	Yes

Table 8.—Application of TMAC-based fluids for the shales under study.

Shale	Shale Type	Dispersion limiting ability of TMAC	Swelling limiting ability of TMAC	Is the use of TMAC suggested?
Woodford	Medium hard, high illite content, with expandable clays, less dispersible shale	Fair	Good	Yes
Pride Mountain	Hard, high quartz, less expandable clay content	Good	Fair	No
Gorgas	Soft, high expandable, interlayer mixed clays and highly dispersible shale	Good	Good	Yes

References

Al-Bazali, Talal M., Zhang, Jianguo, Chenevert, Martin E., & Sharma, Mukul Mani. (2006). *Factors controlling the membrane efficiency of shales when interacting with water-based and oil-based muds.* Paper presented at the International Oil & Gas Conference and Exhibition in China.

Al-Bazali, Talal, Zhang, Jianguo, Chenevert, Martin E., & Sharma, Mukul M. (2008). Factors controlling the compressive strength and acoustic properties of shales when interacting with water-based fluids. *International Journal of Rock Mechanics and Mining Sciences, 45*(5), 729-738.

Carman, Paul Scott, & Cawiezel, Kay. (2007). *Successful breaker optimization for polyacrylamide friction reducers used in slickwater fracturing.* Paper presented at the SPE Hydraulic Fracturing Technology Conference.

Ewy, R. T., & Stankovich, R. J. (2002). *Shale-fluid interactions measured under simulated downhole conditions.* Paper presented at the SPE/ISRM Rock Mechanics Conference.

Friedheim, J., Guo, Q., Young, S., & Gomez, S. (2011). *Testing and evaluation techniques for drilling fluids-shale interaction and shale stability.* Paper presented at the 45th US Rock Mechanics/Geomechanics Symposium.

Goh, Raymond, Leong, Yee-Kwong, & Lehane, Barry. (2011). Bentonite slurries—zeta potential, yield stress, adsorbed additive and time-dependent behaviour. *Rheologica acta, 50*(1), 29-38.

Gomez, Sandra L., & He, Wenwu. (2012). *Fighting wellbore instability: customizing drilling fluids based on laboratory studies of shale-fluid interactions.* Paper presented at the IADC/SPE Asia Pacific Drilling Technology Conference and Exhibition.

Guven, N., Panfil, D. J., & Carney, L. L. (1988). *Comparative Rheology of Water-Based Drilling Fluids With Various Clays.* Paper presented at the International Meeting on Petroleum Engineering.

Himes, Ronald E., & Simon, David E. (1990). Fluid additive and method for treatment of subterranean formations: Google Patents.

Horsrud, P., Bostrom, B., Sonstebo, E. F., & Holt, R. M. (1998). *Interaction between shale and water-based drilling fluids: Laboratory exposure tests give new insight into mechanisms and field consequences of KCl contents.* Paper presented at the SPE Annual Technical Conference and Exhibition.

Huang, Hong, Azar, J. J., & Hale, Arthur H. (1998). *Numerical simulation and experimental studies of shale interaction with water-base drilling fluid.* Paper presented at the IADC/SPE Asia Pacific Drilling Technology.

Jones, S.C. 1997. A Technique for Faster Pulse-Decay Permeability Measurements in Tight Rocks. SPE Formation Evaluation, 12 (1): 19.26. Paper SPE 28450.

Josh, M., Esteban, L., Delle Piane, C., Sarout, J., Dewhurst, D. N., & Clennell, M. B. (2012). Laboratory characterisation of shale properties. *Journal of Petroleum Science and Engineering, 88*, 107-124.

Khodja, Mohamed, Canselier, Jean Paul, Bergaya, Faiza, Fourar, Karim, Khodja, Malika, Cohaut, Nathalie, & Benmounah, Abdelbaki. (2010). Shale problems and water-based

drilling fluid optimisation in the Hassi Messaoud Algerian oil field. *Applied Clay Science, 49*(4), 383-393.

Kumar, Vikas, Sondergeld, Carl H., & Rai, Chandra Shekhar. (2012). *Nano to macro mechanical characterization of shale.* Paper presented at the SPE Annual Technical Conference and Exhibition.

Mody, Fersheed K., Tare, Uday A., Tan, Chee P., Drummond, Calum J., & Wu, Bailin. (2002). *Development of novel membrane efficient water-based drilling fluids through fundamental understanding of osmotic membrane generation in shales.* Paper presented at the SPE Annual Technical Conference and Exhibition.

Nelson, Philip H. (2009). Pore-throat sizes in sandstones, tight sandstones, and shales. *AAPG bulletin, 93*(3), 329-340.

Okoro, Emeka Emmanuel, & Adewale, Dosunmu. (2014). EXPERIMENTAL ANALYSIS OF SHALE FOR 3 EVALUATING SHALE DRILLING FLUID 4 INTERACTION IN AGBADA FORMATION 5. *British Journal of Applied Science & Technology, 4*(35), 4878.

Rabe, Claudio, da Fontoura, Sérgio Augusto Barreto, & dos Santos Antunes, Franklin. (2002). Experimental study of interaction shale-fluid through immersion tests. *Revista de Engenharia Térmica, 1*(2).

Rickman, Rick, Mullen, Michael J., Petre, James Erik, Grieser, William Vincent, & Kundert, Donald. (2008). *A practical use of shale petrophysics for stimulation design optimization: All shale plays are not clones of the Barnett Shale.* Paper presented at the SPE Annual Technical Conference and Exhibition.

Santos, H., Diek, A., Da Fontoura, S., & Roegiers, J. C. (1997). Shale Reactivity test: a novel approach to evaluate shale-fluid interaction. *International Journal of Rock Mechanics and Mining Sciences, 34*(3), 268. e261-268. e211.

Tan, Chee P., Richards, Brian G., & Rahman, S. S. (1996). *Managing physico-chemical wellbore instability in shales with the chemical potential mechanism.* Paper presented at the SPE asia pacific Oil and Gas Conference.

Zhou, Jia, Sun, Hong, Stevens, Richard Fowler, Qu, Qi, & Bai, Baojun. (2011). *Bridging the gap between laboratory characterization and field applications of friction reducers.* Paper presented at the SPE Production and Operations Symposium.

Zhou, Junhao, Jung, Chang Min, Pedlow, John W., Chenevert, Martin E., & Sharma, Mukul M. (2013). *A New Standardized Laboratory Protocol to Study the Interaction of Organic-Rich Shales with Drilling and Fracturing Fluids.* Paper presented at the SPE Annual Technical Conference and Exhibition.

FLUID EVALUATION AND

OPTIMIZATION

FRICTION REDUCTION STUDY

CONTENTS

FIGURES

TABLES

INTRODUCTION

In recent years, thanks to the development of hydraulic fracturing technology, oil and gas production from unconventional resources such as shale formations has played an important role in supplying energy in the United State (Larch et al., 2012; Palisch et al., 2010). Reaching economic rates of hydrocarbon production is only possible when micro-fractures are connected and created through effective stimulation treatments such as horizontal fracturing in multiple stages (Barati and Liang, 2014; Loveless et al., 2014; Wu et al., 2013). Creation of openings in the reservoir rock involves pumping fracturing fluids into the wellbore at elevated flow rates and pressures. Viscosity of a fracturing fluid has a remarkable effect on the fracture initiation and the final size of the fracture (Kalgaonkar and Patil, 2012). Based on their viscosities, fracturing fluids can be categorized into two groups. Less viscous fluid or "slickwater", which was widely used during 50's and 60's. The main component of low viscosity fracturing fluids is water and low concentrations of polymer ranging from 0.25 to 10 parts per thousand gallons (Bunger et al., 2013; Palisch et al., 2010). The second type is highly viscous gel-based fluid with viscosity typically on the order of 50-1000 times greater than the viscosity of water (Ames and Bunger, 2015). Guar gum in its linear and cross-linked forms is the oldest water-soluble fracturing fluid (Palisch et al., 2010). By using guar-based fluids, at elevated pressures, a filter cake forms on the faces of the fractures, which is advantageous in preventing the fluid leak-off to the adjacent formation. But, in the last decade, an amazing shift towards using slickwater has occurred. As an example, outside of the Bakken shale, in more than 80 % of fracturing treatments, water and friction reducer are applied as fracturing fluid (Barati and Liang, 2014). Because of the relatively low viscosity of slickwater, cleanup problems and damage associated with using viscous fluids are minimized, which makes slickwater suitable for fracturing low permeability reservoirs (Palisch et al., 2010; Wu et al., 2013). As a result of lower viscosity, slickwater cannot suspend and transport proppants as effectively as gelled fluids. To overcome poor proppant transport, higher pumping rates are applied. High flow rates, in turn, lead to significant energy loss due to friction and turbulence in the tubular pipeline (Kaufman et al., 2008; Palisch et al., 2010). In order to lower the surface pumping pressures and compensate for the energy losses during

pumping, a small amount of high molecular weight polymer is dissolved in the fluid, which acts as a friction reducer (FR). In slickwater treatment, friction reducer is the main component of the fluid. Long chain and flexible polyacrylamide (PAM) based polymers are known to be the best drag reduction polymers (Wu et al., 2013); (Pereira et al., 2013).

When a polymer solution is subjected to turbulent flow regime, the large molecules present in the solution undergo different conformational changes such as flow orientation, stretching, and relaxation. Such conformational changes alter the flow field and dynamics of turbulent structures in the vicinity of pipe wall. In the macroscopic scale, those variations result in large drag reduction. However, mechanical degradation of such polymer solutions has complicated their use (Campolo et al., 2015; Moussa and Tiu, 1994). Several theories have been proposed to explain mechanical degradation of polymer solutions, among which, extreme stretching of polymer chains and scission of the polymer chain have been most accepted (Rodriguez and Winding, 1959). Another study reports that chain scission occurs near the midpoint of the polymer which is caused by the extensional features of the turbulent flow (Merrill and Horn, 1984). In this work, firstly, the effect of PAM concentration on drag reduction (DR) capacity along with shear stability of the solutions is investigated. Then, the possibility of stabilizing flexible PAM polymer molecules with the biodegradable polymer, xanthan gum (XG), is verified.

Materials and Methods

Materials and preparation

Anionic polyacrylamide (PAM) as a linear flexible polymer and XG as a rigid polymer were chosen for this investigation. The molecular weights given for PAM and XG by the vendor are 6-8×10^6 kg.mol^{-1} and 4-5×10^6 kg.mol^{-1}, respectively. To establish a baseline for further studies, deionized water was used throughout. Using an analytical balance polymer powders were weighed with an accuracy of ±1 mg (Mettler Toledo XS603s). For the preparation of the samples, powders were sprinkled into the fluid to prevent particles from clumping on the surface. After mixing the powders, the solutions were stored overnight for complete hydration. The studied concentrations of polymers were C=100, 150, 200, 300, 500, and 1000 weight parts per million (wppm) for PAM. In order to investigate the effect of XG, mixed polymer solutions of 100 wppm PAM+100 wppm XG (total C=200 wppm), 150 wppm PAM+100 wppm XG (total C=250 wppm), and 600 wppm XG solutions were prepared.

Drag reduction and viscosity measurements

A closed loop flow system was used for drag reduction and turbulent flow measurements (Figure 1). The system is comprised of a 60 liter supply tank connected to a progressive cavity pump (SEEPEX BN 10-12) with a conveying capacity of 30 GPM (113.56 l/min), and a seamless stainless steel horizontal pipe test section of L=8 ft. (2.438 m) and inner diameter of 1 inch (2.54cm). The flow rate of the system was measured using a mass flow meter (OPTIMASS 1000, KROHNE) with an accuracy of ±0.15% and a repeatability of ±0.05% as stated by the manufacturer. The pressure drop data along the measuring length of the pipe was gathered using a membrane differential pressure transducer (PX409, OMEGA). In the flow experiments, drag reduction efficiency of the polymer solutions was defined as:

$$DR = \left(\frac{f_w - f_s}{f_w}\right)_{Re=const} \times 100\% \qquad (1)$$

where f is the fanning friction factor, subscripts "w" and "s" stand for water and polymer solution, respectively, and "Re=const." signifies the fact that the comparison between the flows is made at the same Reynolds numbers.

In drag reduction experiments the flow rate was increased stepwise (and kept constant for 1 minute at each flow rate) and then the polymer solutions were sheared in the flow loop at maximum flow of 30 GPM for 2 hours and sampling was performed 8 times at shearing periods of t=0, 15, 30, 45, 60, 80, 100, and 120 min. After the shearing process the flow rate was decreased stepwise in the same manner as it was increased.

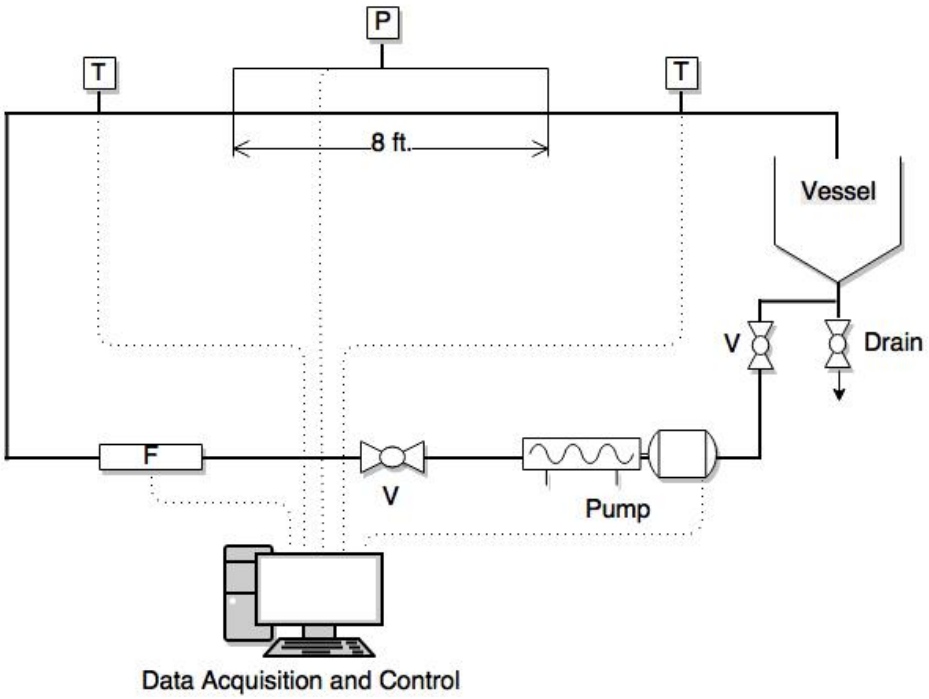

Figure 1. --Schematic illustration of the flow loop. Instrumentation consists of a digital flow meter (F), differential pressure transducer (P), valves (V), and temperature sensors (T).

Viscosity measurement of the samples was carried out in a DHR Hybrid Rheometer. The instrument is equipped with a Peltier system to control sample temperature. In our experiments sample temperature was maintained at 25±0.01 °C. The geometry used in the apparent viscosity measurements was cone and plate. The cone diameter and angle were 60 mm and 2°, respectively. Approximately, 2 ml of the solution was placed between the cone (sliding plate) and the fixed plate and the instrument was set to the strain control mode. In this mode, shear rate ($\dot{\gamma}$) was logarithmically increased from 0.01 to 1000 s^{-1} and shear stress was measured simultaneously and then apparent viscosity was calculated using $\eta_a = \sigma/\dot{\gamma}$ correlation, where σ and η_a are shear stress and apparent viscosity, respectively. The power-law viscosity model, $\eta_a = K(\dot{\gamma})^{n-1}$, was used to fit the viscosity data. In the power-law model, n (behavior index) is a measure of deviation from Newtonian behavior and K (consistency index) is a measure of average viscosity. K and n known as power-law parameters were used in friction factor calculations. The Dodge and Metzner correlation (Govier and Aziz, 2008) was used for calculation of turbulent friction factors of the polymer solutions:

$$\frac{1}{\sqrt{f}} = \frac{4.0}{n^{0.75}} \log\left[Re_{MR} f^{\left(\frac{1-n}{2}\right)}\right] - \frac{0.4}{n^{1.2}} \quad \text{if} \quad Re_{MR} > 2100 \qquad (2)$$

$$f = \frac{16}{Re_{MR}} \quad \text{if} \quad Re_{MR} < 2100 \qquad (3)$$

$$Re_{MR} = \frac{D^n U^{2-n} \rho}{K\left(\frac{1+3n}{4n}\right)^n 8^{n-1}} \qquad (4)$$

where Re_{MR} is the generalized Reynolds number, D is pipe diameter, and ρ stands for density. For water calculations n is equal to 1 and K is equal to the viscosity of water, respectively.

Results and discussion

Polyacrylamide solutions

In order to assess the degree of drag reduction and polymer degradation, several samples were taken at specified intervals. Shear stress and apparent viscosity of the samples were measured in the rheometer and the power-law model parameters were calculated. For Newtonian fluids the value of n is 1 and for shear-thinning fluids such as polymer solutions n is less than 1. As the value of n deviates from 1, the degree of non-Newtonian behavior increases. The power-law parameters calculated for different concentrations of the anionic polyacrylamide are shown in Table 1 and Figure 2a,b. Comparison of power-law parameters of fresh (zero shearing time) PAM solutions shows that by increasing concentrations, values of K increase and n values decrease, indicating increased non-Newtonian behavior. It can also be observed that, as a result of shearing, the values of power-law parameters change for all polymer solutions. Figure 2a shows that, over the shearing time, n values of PAM solutions increase and get close to unity (Newtonian behavior) and K values decrease. The difference in the n values of the solutions before and after the shearing is large (35%-152% increase). The overall Change in n values at the end of the shearing initially is different for each concentration, it increases from 35% for 100 wppm solution and maximizes at 200 wppm (152%) and then with further concentration increase, drops to 69% for 1000 wppm solution. As a result of shear degradation and consequently viscosity reduction, K values decline. Increasing concentration from 100 wppm to

1000 wppm, K values reach a maximum decline of 64% at 200 wppm, but with further concentration increase a 33% decline in K value was observed at 1000 wppm PAM.

Table 2.--Power-law parameters for PAM and XG solutions

Concentration (wppm)	Sample 1 (fresh)		Sample 2 (15min)		Sample 3 (30min)		Sample 4 (45min)		Sample 5 (60min)		Sample 6 (80min)		Sample 7 (100min)		Sample 8 (120min)	
	n	K	n	K	n	K	n	K	n	K	n	K	n	K	n	K
100 ppm PAM	0.62	0.025	0.62	0.027	0.65	0.022	0.70	0.018	0.78	0.013	0.80	0.012	0.81	0.011	0.84	0.010
150 ppm PAM	0.40	0.070	0.48	0.057	0.49	0.055	0.55	0.046	0.58	0.042	0.64	0.033	0.67	0.028	0.68	0.026
200 ppm PAM	0.25	0.110	0.32	0.091	0.40	0.071	0.48	0.061	0.53	0.060	0.58	0.053	0.60	0.046	0.63	0.040
500 ppm PAM	0.25	0.250	0.29	0.243	0.35	0.221	0.4	0.195	0.41	0.201	0.42	0.184	0.45	0.173	0.47	0.151
1000 ppm PAM	0.23	0.617	0.24	0.553	0.29	0.533	0.33	0.497	0.35	0.460	0.36	0.452	0.37	0.431	0.39	0.412
600 ppm XG	0.50	0.100	0.53	0.080	0.55	0.073	0.56	0.070	0.56	0.069	0.56	0.066	0.56	0.066	0.57	0.062
100 ppm PAM + 100 ppm XG	0.50	0.044	0.58	0.034	0.61	0.034	0.62	0.034	0.64	0.032	0.70	0.024	0.72	0.020	0.76	0.017
150 ppm PAM + 100 ppm XG	0.36	0.079	0.45	0.069	0.49	0.067	0.54	0.055	0.60	0.042	0.62	0.038	0.62	0.041	0.65	0.036
50 ppm PAM + 200 ppm XG	0.61	0.034	0.62	0.031	0.64	0.027	0.68	0.023	0.70	0.020	0.71	0.018	0.74	0.016	0.75	0.014

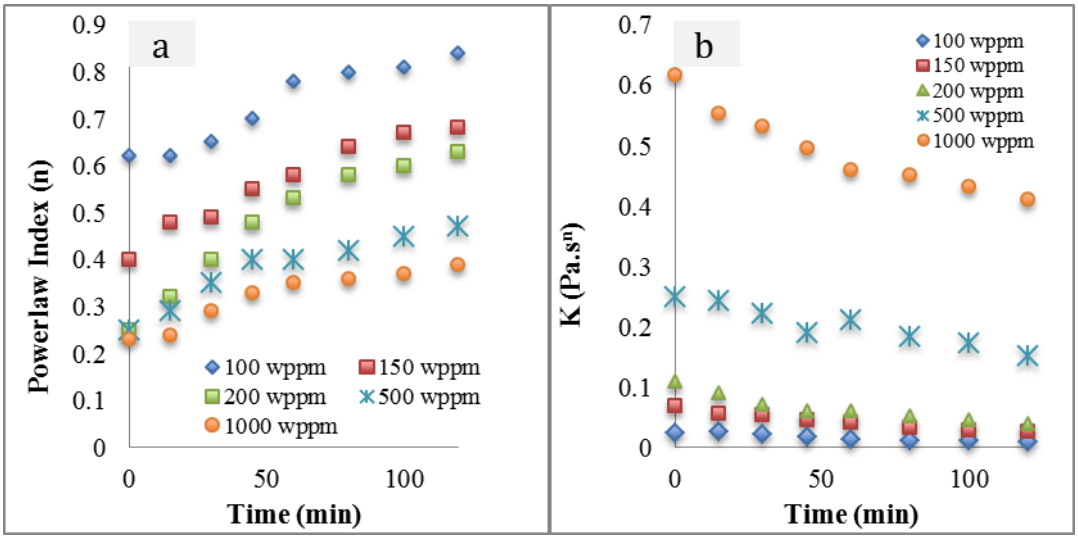

Figure 2.--Power-law model parameters for PAM solutions vs. shearing time

Another indication of shear degradation is shown in Figure 3, where the apparent viscosity of the 200 wppm PAM solution, at shear rates lower than 10 s^{-1}, undergoes drastic reduction as the circulation time increases. The reason that we only see changes at lower shear rates might be related to the scission of the molecules that belong to the high tale of the molecular weight distribution of the polymer (Liberatore et al., 2004). Those molecules contribute to the formation of the zero shear viscosity plateau.

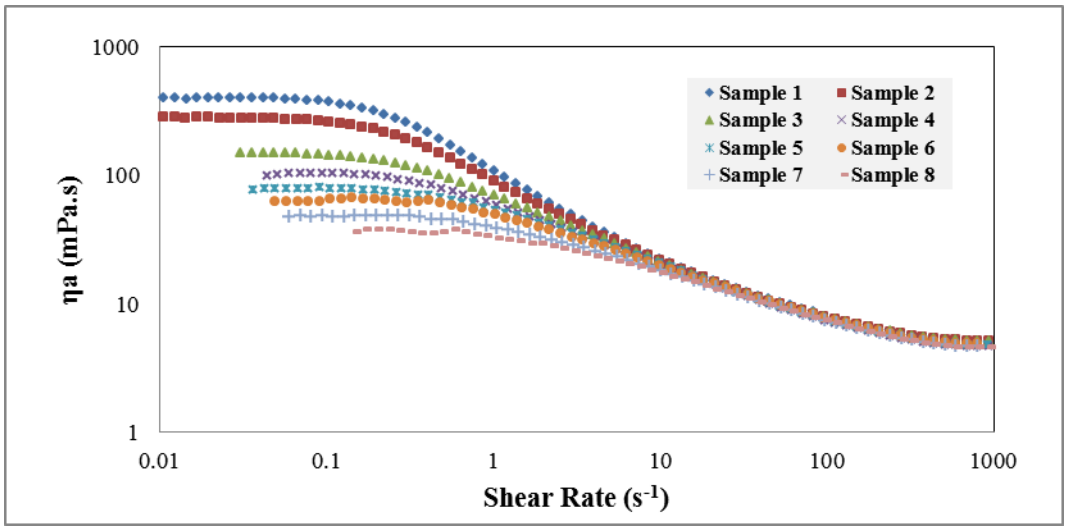

Figure 3.--Apparent viscosity of 200 wppm sheared PAM samples (Sample1 to 8: Fresh, 15, 30, 45, 60, 80, 100, and 120 minutes shearing time)

Prandtl-Karman coordinates is a semi-log graph of $f^{-½}$ versus $Re.f^{½}$, where f and Re are fanning friction factor and Reynolds number, respectively. By plotting the Prandtl-Karman coordinates, the degree of DR of polymer solutions can be compared with respect to the boundaries of drag reduction; the onset of drag reduction as the point of departure from Prandtl-Karman law and maximum drag reduction (MDR) or Virk's asymptote (Virk, 1975; White and Mungal, 2008). Prandtl-Karman plot for different concentrations of PAM is shown in Figure 4. Three flow regimes can be detected:

a) $Re\sqrt{f} < 200$; laminar flow. All polymer solutions obey Poiseuille's law.
b) $200 < Re\sqrt{f} < 350$; laminar to turbulent transition.
c) $Re\sqrt{f} > 350$; turbulent flow.

It is observed that except for the laminar to turbulent transition region, the turbulent friction factor data for the solutions is bounded in the area between the two universal asymptotes and the data points are linear for all concentrations.

Table 3.--Linear fit results of turbulent regime

Concentration	Linear fit equation	R-Squared	Slope Increment (δ)
100 wppm	$1/\sqrt{f} = 6.0\log Re\sqrt{f} - 4.1$	0.99	2.05
150 wppm	$1/\sqrt{f} = 7.1\log Re\sqrt{f} - 4.4$	0.99	3.09
200 wppm	$1/\sqrt{f} = 9.3\log Re\sqrt{f} - 7.3$	0.99	5.28
500 wppm	$1/\sqrt{f} = 9.6\log Re\sqrt{f} - 8.2$	0.99	5.6
1000 wppm	$1/\sqrt{f} = 12.8\log Re\sqrt{f} - 15.9$	0.99	8.81

Results of linear fitting of data points in the turbulent region (table 2) reveal that by increasing the concentration of polymer, the slope of the lines tend to increase. According to the literature the slope increment with respect to the Prandtl-Karman law (δ) is proportional to the square root of polymer concentration ($\delta \propto \sqrt{C}$) with a proportionality constant that is characteristic of the polymer (Virk and Baher, 1970). The slope increment values are reported in table 2. The proportionality constant for the PAM used in this work is calculated to be 0.27±0.05. Figure 4 shows that by increasing PAM concentration, the extent of DR increases and the data points approach Virk's asymptote. Among different concentrations, the extent of DR and slope of data points for 100 wppm PAM solution are closest to the Prandtl-Karman line (the onset of DR). On the other hand, the greatest DR belongs to 1000 wppm solution. For solutions with polymer content greater than 200 wppm, in $200<Re\sqrt{f}<500$ range, the data points are nearly tangent to the MDR line, but by increasing the flow rates (Reynolds number), the data points tend to deviate from MDR. Results indicate that further increase of concentration does not have a large effect on the degree of DR in the experimental conditions of this work.

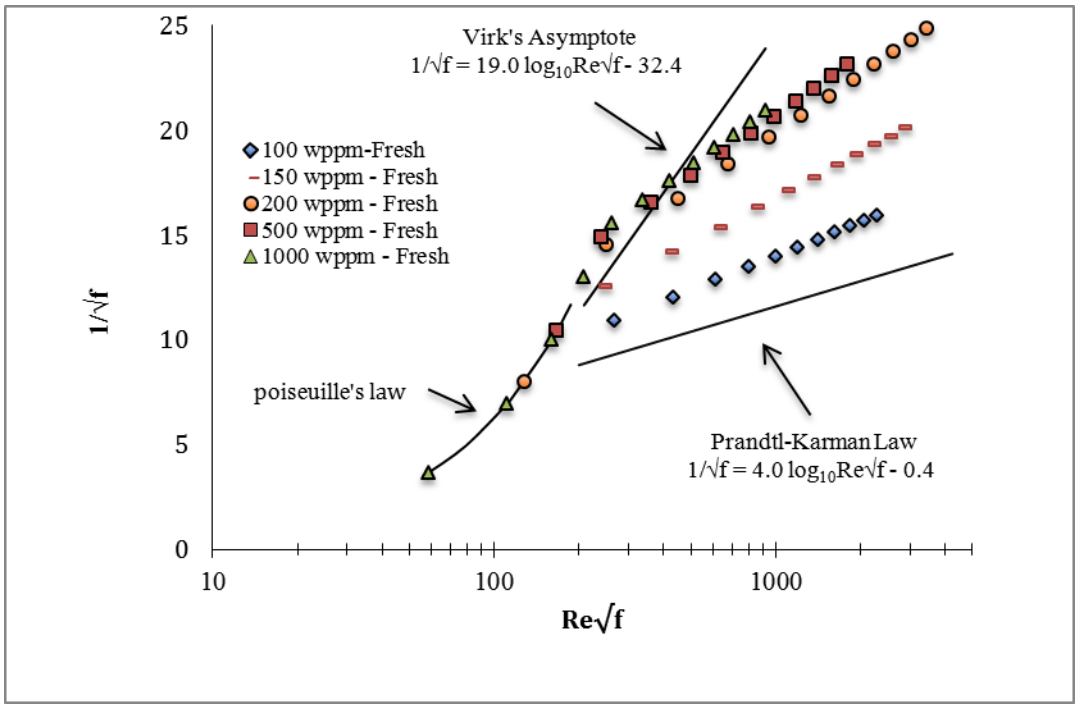

Figure 4.--Prandtl-Karman coordinates for PAM solutions

The effect of polymer concentration and mechanical degradation on Fanning friction factor of PAM solutions is shown in Figures 5a, b, respectively. It can be seen that even at low concentrations of polymer (100 wppm), fanning friction factor values are much lower compared to water. Increasing polymer concentration resulted in further reduction in friction factors and consequently, drag reduction efficiency increased. The lowest values of friction factors at different Reynolds numbers belong to 1000 wppm solution. It is also observed that the difference between turbulent friction factors of 200, 500, and 1000 wppm solutions is very small, which is in agreement with the results shown in Prandtl-Karman coordinates, indicating that at test conditions, further increase in concentration does not change friction factors.

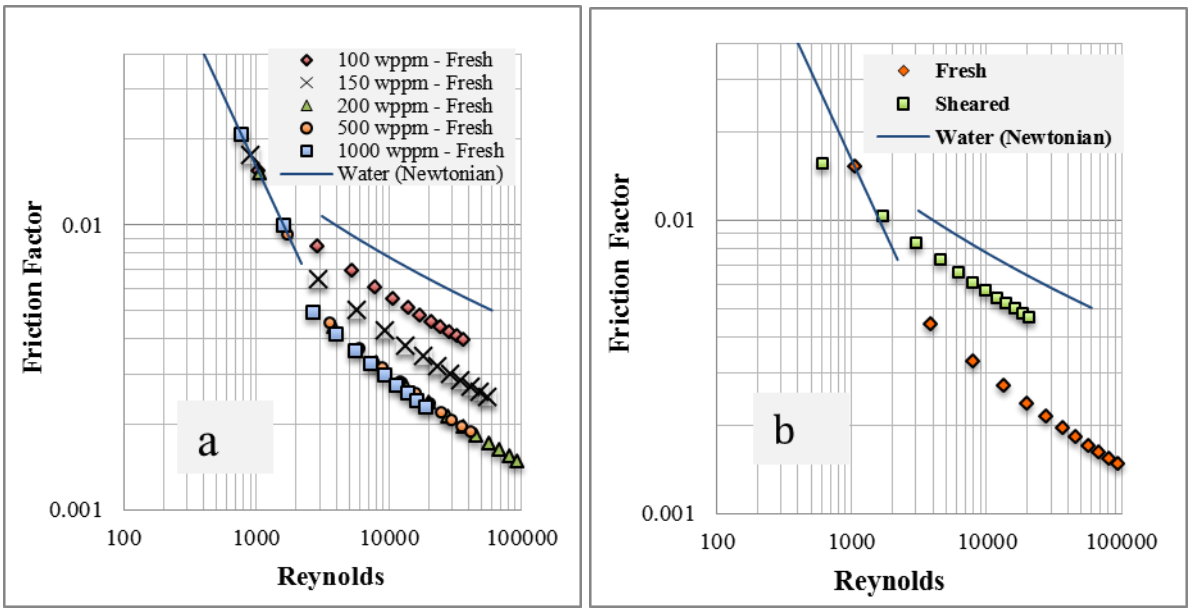

Figure 5.--Friction factor vs. Re: a) Effect of PAM concentration,
b) Effect of shearing on 200 wppm PAM

Shearing has a large impact on reducing the DR ability of polyacrylamide solutions. Comparing the friction factors of 200 wppm PAM solution at different Reynolds (Figure 5b) shows a 30-50% decline after 2 hours of shearing and the values of friction factor shift towards water friction factors. Although flow rate is constant for all experiments, a shift in the data points of the sheared samples towards lower Reynolds numbers is observed. The shift is an indication of alteration in the flow regime, which occurs due to the change in the rheological properties of the solutions as a result of shear degradation. Figure 6 shows the changes in the quantity of DR over shearing time for different concentrations of PAM at constant flow rate. It is observed that the extent of DR before shearing increases from 30% to 67% by increasing polymer concentration from, ranging from 100 wppm to 1000 wppm. Results also indicate that solutions above 200 wppm produce nearly identical DR at the early stages of shearing (< 20 minutes), which corresponds to results shown in Prandtl-Karman coordinates. But beyond 20 minutes, the DR curves tend to diverge, indicating that the degree of shear degradation is different for each polymer concentration. In flexible polymers such as PAM, as the level of shear force reaches a certain level, the molecules stretch and consequently effective viscosity increases, the turbulent buffer layer thickens, and due to dissipation of the energy from turbulent fluctuations drag is reduced (Ptasinski et al., 2003). It is known that drag is also reduced when turbulent flow

interacts with polymer networks. When polymer concentration is high enough (critical overlap concentration, c*), polymer chains are packed closer and begin to interact with each other and form entangled networks (Skelland and Meng, 1996). The decline in the degree of DR was observed in all concentrations of PAM solution. Results show that, although 200 wppm PAM solution had similar initial DR% to 500 and 1000 wppm solutions (figure 6), it had a larger decline in DR (figure 7). The smallest decline in DR belonged to 100 and 1000 wppm solutions and the largest decline was observed for 200 wppm PAM. There are two reasons for the higher DR decline of 200 wppm solution. One is the breakup of the polymer molecules, which occurs in all PAM solutions. The second reason is the breakup of polymer networks. From viscosity measurements critical overlap concentration of the PAM solution is determined to be 200 wppm. At $c < 200$ wppm, there is no polymer network, so there is no decline due to polymer network breakup and at $c > 200$ wppm, the networks are more entangled and upon deformation can recover quickly. Also, it seems that at higher concentrations (>200 wppm) of polymer, the extensional force from the turbulent flow is distributed among larger number of molecules, which results in lower number of chain scissions and higher DR. But at 200 wppm polymer networks just begin to form and are weak. Therefore, at the beginning of the shearing process an increase in DR is observed, but gradually as shear forces act, unstable polymer networks as well as individual polymer molecules breakup, which results in a larger decline in the DR efficiency of 200 wppm PAM solution than other concentrations.

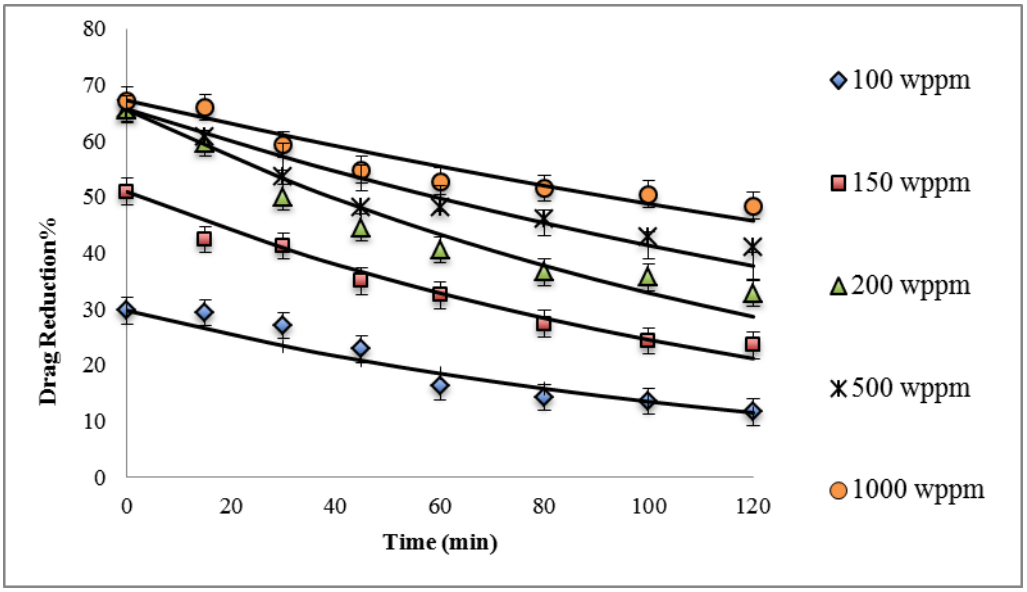

Figure 6.--%Drag reduction for different concentrations of PAM at 30 GPM (113.56 l/min)

Based on the exponential decay model proposed by (Bello et al., 1996), DR follows an exponential decline with time for polyacrylamide and polysaccharide solutions:

$$DR\%(t)/DR\%(0) = e^{(-t/\lambda)} \qquad (5)$$

where DR%(t) and DR%(0) are percent drag reduction at times t and t=0, respectively, and λ is an adjustable parameter. The above model was used to correlate the DR data of PAM solutions. Calculated values for λ are reported in Table 2 and the fitted lines are shown in Figure 6. It can be observed that for the studied concentrations of PAM solution, the exponential decay model describes the degradation behavior very well.

Table 4.--Calculated exponential decay constant, λ for PAM solutions

Concentration (wppm)	**λ (min)**	R-Squared
100	127	0.92
150	137	0.98
200	145	0.92
500	216	0.87
1000	312	0.87

Another observation is that the rate of DR decline is faster in the first 60-80 minutes of the shearing process. This is probably due to the presence of longer chains of polymer in the fresh solutions, which are more susceptible to chain scissions (require less energy to break). After 60 minutes, the gap between DR lines remains nearly constant, which indicates that polymer chains break up at a similar rate in all concentrations. Further investigation of the molecular weight distribution of the samples, similar to the experiments conducted by (Liberatore et al., 2004), is required to fully understand the relationship between drag reduction behavior and molecular weights of the PAM solutions.

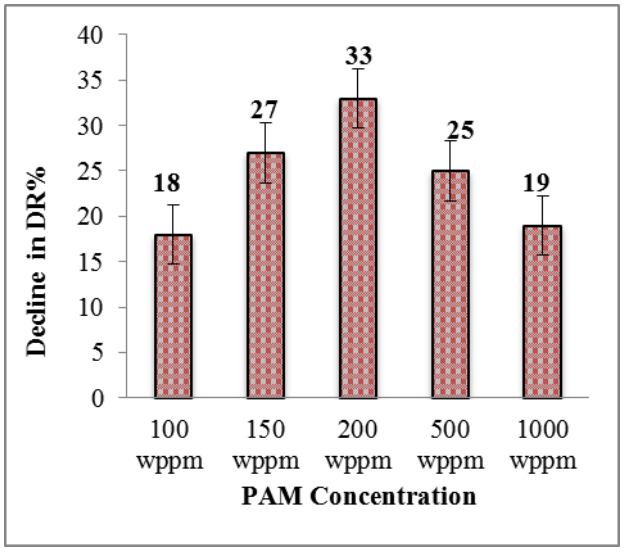

Figure 7.--Effect of shearing on DR decline in PAM solutions

PAM/XG mixed solutions

In order to verify the possibility of stabilizing PAM with XG, different mixed solutions were prepared and sheared in the same manner as the previous section. For comparison, 200 wppm solution, as the minimum concentration used in practical applications, is chosen.
The power-law fitting data of the mixed solutions and a solution containing XG is shown in Table 1. Also, Fanning friction factors of the polymer solutions is graphically presented. Figure 8a compares the friction factors of the mixed solutions with 600 ppm XG and 200 wppm PAM solutions. It is observed that the friction factors of an even high concentrated XG solution (600 wppm) are much lower than that of 200 wppm PAM solution.

Higher flexibility of PAM polymer chains with respect to rigid XG chains results in higher energy adsorption (stretching) due to interactions with dynamic turbulent flow and subsequently, superior drag reduction capability of flexible polymers. Also, it is observed that in the fresh mixed solutions, there is no outstanding synergetic effect between PAM and XG molecules. Even the 150 wppm PAM+100 wppm XG solution, which has a higher total polymer concentration than 200 wppm, showed larger friction factors than 200 wppm PAM. Figure 8b compares the friction factors of the solutions after 120 minutes of shearing.

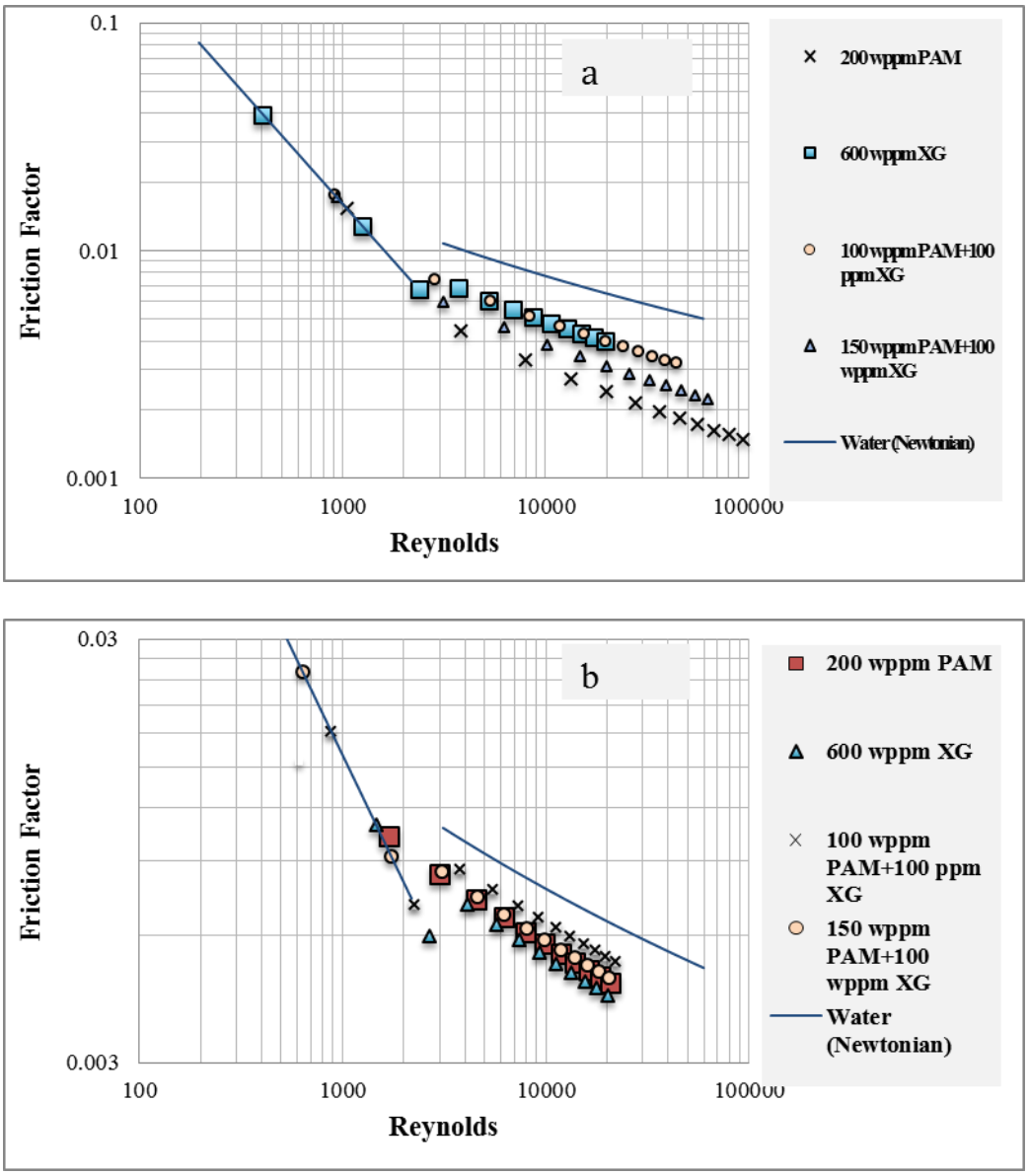

Figure 7.--Fanning friction factor of mixed solutions in a) fresh form and b) after shearing for 120 minutes

Because of high shear stability, XG, as expected, maintains its initial friction factors. But in the mixed PAM/XG solutions, the friction factors increase as a result of shearing. It is interesting to note that, 200 wppm PAM has a larger reduction in its friction factors than mixed solutions. This suggests that addition of XG has been beneficial in controlling the shear degradation of PAM. The decline in the %DR of the samples over shearing time is shown in Figures 9 and 10.

Also, as mentioned earlier, exponential decay model was used to correlate DR with time (Figure 9 and Table 3).

Table 5.--Calculated exponential decay constant, λ for mixed solutions

Concentration (wppm)	**λ (min)**	R-Squared
200 (PAM)	145	0.92
600 (XG)	571	0.94
100 (PAM)+100(XG)	137	0.92
150 (PAM)+100 (XG)	127	0.89

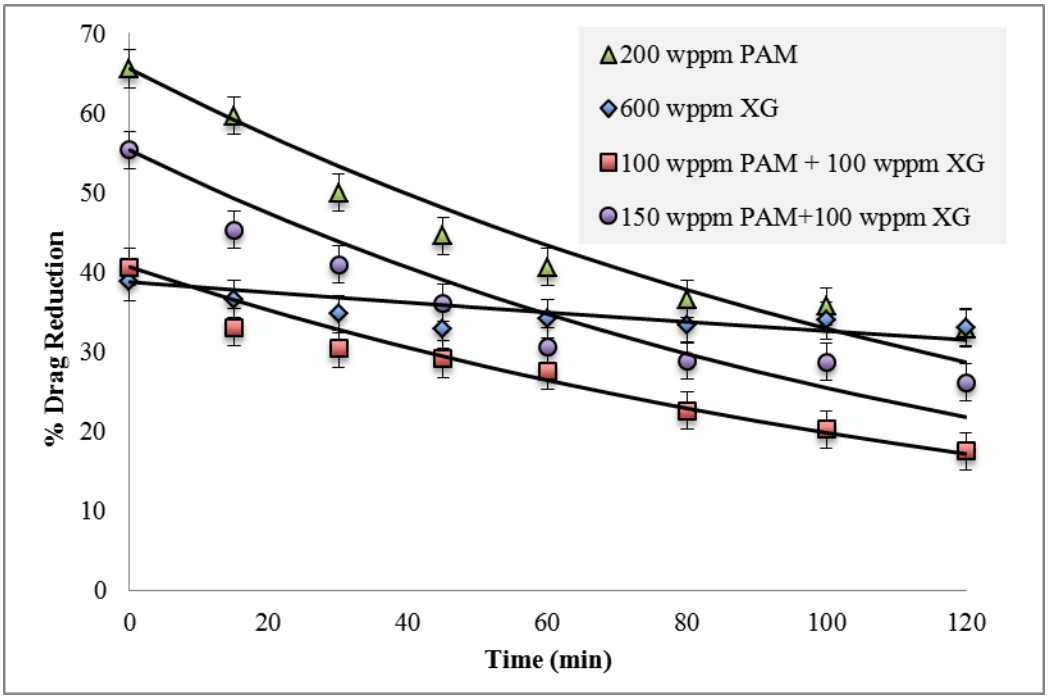

Figure 8.--%Drag reduction for mixed PAM/XG solutions at 30 GPM (113.56 l/min)

Clearly, 600 wppm XG solution has the best shear stability among all solution with only 6% decline in DR. Contrary to XG, 200 wppm PAM has the greatest DR% (65%) and the largest decline in DR efficiency. As expected from friction factor results, it can be inferred that addition of XG reduces the DR capability of mixed solutions (40% and 55%) with respect to 200 wppm

solution. But, XG slightly improves the shear stability of the polymer mixtures. The observed decline in DR efficiency of PAM/XG solutions are 23% and 29%, which are less than the value observed for 200 wppm PAM (33%). Also results suggest that with increasing PAM concentration in mixed solutions, DR decline increases. Since there is only a small amount of chain length degradation in semi-rigid polymers, the extent of DR depends only on the interaction between polymer chains and entanglements, which is directly related to polymer concentration. It should be considered that the concentration of XG was 100 wppm for mixed solutions, which is below its critical concentration of XG (C*≈ 300 ppm). Hence, as suggested by others (Berman, 1978; Wyatt et al., 2011), mixing PAM with higher concentrations of XG would be more beneficial in maintaining high DR efficiency and even better controlling of shear degradation of polyacrylamide solutions, which is the subject of our future work. The exponential decay model describes the DR of the solutions well, although the fittings for mixed solutions are not are good as pure PAM or pure XG solutions.

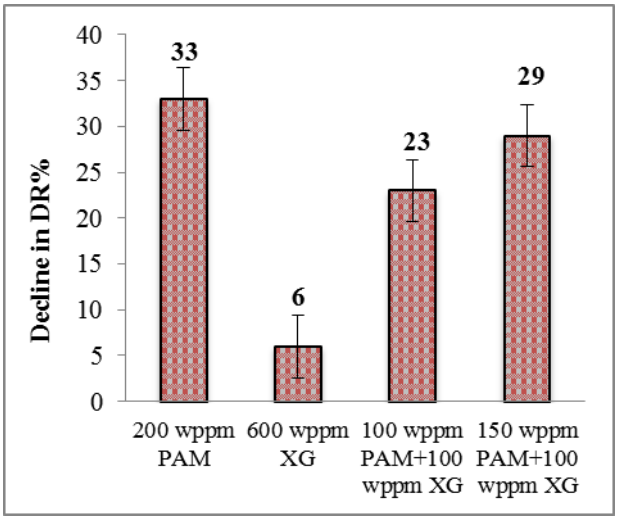

Figure 9.--Effect of shearing on DR decline in PAM/XG mixed solutions

Conclusions

The results from work show that among different concentrations of PAM, 1000 wppm solution has the highest friction reduction efficiency and the lowest decline in DR%. Increasing

the concentration above 200 wppm does not change the DR% of the fresh samples significantly, though at higher concentrations, shear stability is better. PAM solutions lose 20-30% of their DR efficiency in the first 60 minutes of shearing at the tests conditions applied in this work. Mixing flexible PAM molecule with XG molecules did not improve the degree of DR significantly, but slightly improved the DR stability of PAM solutions. Since the friction reduction of rigid polymers depends only on concentration, mixing PAM with higher concentrations of XG might be beneficial in maintaining the DR efficiency of PAM as well as improving its shear stability. Exponential decay model was used to correlate the experimental data. The model describes the DR behavior of polyacrylamide solutions very well.

References

Ames, B.C. and Bunger, A., 2015. Role of Turbulent Flow in Generating Short Hydraulic Fractures With High Net Pressure in Slickwater Treatments. Society of Petroleum Engineers.

Barati, R. and Liang, J.-T., 2014. A review of fracturing fluid systems used for hydraulic fracturing of oil and gas wells. Journal of Applied Polymer Science, 131(16): n/a-n/a.

Bello, J.B., Müller, A.J. and Sáez, A.E., 1996. Effect of intermolecular cross links on drag reduction by polymer solutions. Polymer Bulletin, 36(1): 111-118.

Berman, N.S., 1978. Drag reduction by polymers. Annual Review of Fluid Mechanics, 10(1): 47-64.

Bunger, A.P., McLennan, J. and Jeffrey, R., 2013. Effective and sustainable hydraulic fracturing. InTech, Janeza Trdine, 9: 51000.

Campolo, M., Simeoni, M., Lapasin, R. and Soldati, A., 2015. Turbulent Drag Reduction by Biopolymers in Large Scale Pipes. Journal of Fluids Engineering, 137(4): 041102.

Govier, G.W. and Aziz, K., 2008. The flow of complex mixtures in pipes. Society of Petroleum Engineers New Orleans.

Kalgaonkar, R.A. and Patil, P.R., 2012. Performance Enhancements in Metal-Crosslinked Fracturing Fluids. Society of Petroleum Engineers.

Kaufman, P.B., Penny, G.S. and Paktinat, J., 2008. Critical Evaluation of Additives Used in Shale Slickwater Fracs. Society of Petroleum Engineers.

Larch, K.L., Aminian, K. and Ameri, S., 2012. The Impact of Multistage Fracturing on the Production Performance of the Horizontal Wells in Shale Formations. Society of Petroleum Engineers.

Liberatore, M.W., Baik, S., McHugh, A.J. and Hanratty, T.J., 2004. Turbulent drag reduction of polyacrylamide solutions: effect of degradation on molecular weight distribution. Journal of non-newtonian fluid mechanics, 123(2): 175-183.

Loveless, D., Holtsclaw, J., Weaver, J.D., Ogle, J.W. and Saini, R.K., 2014. Multifunctional Boronic Acid Crosslinker for Fracturing Fluids. International Petroleum Technology Conference.

Merrill, E. and Horn, A., 1984. Scission of macromolecules in dilute solution: Extensional and turbulent flows. Polymer communications, 25(5): 144-146.
Moussa, T. and Tiu, C., 1994. Factors affecting polymer degradation in turbulent pipe flow. Chemical engineering science, 49(10): 1681-1692.
Palisch, T.T., Vincent, M. and Handren, P.J., 2010. Slickwater Fracturing: Food for Thought.
Pereira, A.S., Andrade, R.M. and Soares, E.J., 2013. Drag reduction induced by flexible and rigid molecules in a turbulent flow into a rotating cylindrical double gap device: Comparison between Poly (ethylene oxide), Polyacrylamide, and Xanthan Gum. Journal of Non-Newtonian Fluid Mechanics, 202(0): 72-87.
Ptasinski, P. et al., 2003. Turbulent channel flow near maximum drag reduction: simulations, experiments and mechanisms. Journal of Fluid Mechanics, 490: 251-291.
Rodriguez, F. and Winding, C., 1959. Mechanical Degradation of Dilute Polyisobutylene Solutions. Industrial & Engineering Chemistry, 51(10): 1281-1284.
Skelland, A. and Meng, X., 1996. The critical concentration at which interaction between polymer molecules begins in dilute solutions. Polymer—Plastics Technology and Engineering, 35(6): 935-945.
Virk, P. and Baher, H., 1970. The effect of polymer concentration on drag reduction. Chemical Engineering Science, 25(7): 1183-1189.
Virk, P.S., 1975. Drag reduction fundamentals. AIChE Journal, 21(4): 625-656.
White, C.M. and Mungal, M.G., 2008. Mechanics and prediction of turbulent drag reduction with polymer additives. Annu. Rev. Fluid Mech., 40: 235-256.
Wu, Q. et al., 2013. Experimental Study of Friction Reducer Flows in Microfracture during Slickwater Fracturing. Society of Petroleum Engineers.
Wyatt, N.B., Gunther, C.M. and Liberatore, M.W., 2011. Drag reduction effectiveness of dilute and entangled xanthan in turbulent pipe flow. Journal of Non-Newtonian Fluid Mechanics, 166(1–2): 25-31.

BEST PRACTICES MANUAL

CONTENTS

LIST OF FIGURES

TABLES

BEST PRACTICES MANUAL: PETROPHYSICS AND TIGHT ROCK CHARACTERIZATION

INTRODUCTION

Meaningful shale characterization is based on a foundation of thorough geological and characterization. Reconstructing sedimentologic and tectonic settings during deposition is critical for interpreting the controls on reservoir evolution and predicting the spatial distribution and geomechanical properties of reservoir and seal facies within shales. Geological characterization, including core selection and description, outcrop description, facies modeling, tectonic modeling, sedimentologic interpretation and stratigraphic modeling is inseparable from petrologic characterization. To interpret facies and their stacking pattern for sedimentologic interpretation and stratigraphic modeling, rock composition, authigenesis, rock fabric and pore type and structure must be understood. This study builds in large part on previous shale characterization studies, including Pashin et al. (2011), who developed a work plan for geologic characterization of diverse shale formations. Their comprehensive work plan outlines a work flow for characterization that begins at the outcrop- and wireline-log-scale and works toward determining rock fabric and the controls on fluid storage and mobility at the nano- to microscale.

Once this geological characterization is complete, a robust framework exists that can facilitates the assessment of resources and reserves. The results of integrated outcrop, wireline log, core and thin section studies are combined with geochemical and petrophysical analysis to become the basis for large capital expenditures to develop exploration plays. Rock samples collected from cores, bit cuttings, and in some cases outcrops are crucial for assessing thermal maturity, determining adsorption capacity, and establishing the characteristics of the rock fabric and pore network that are necessary for resource assessment. These same rock samples are

equally important for fluid sensitivity tests that in many cases seem to become important only after failure of a completed well to produce expected volumes of hydrocarbons. The proposed workflow for petrophysics and tight rock characterization (Fig. 1) begins at the megascopic scale and ends at the nanoscopic scale. As this report focuses on petrophysical characterization, fluid-rock interactions, and fluid evaluation and optimization, best practices for geological and petrologic characterization will be summarized without detailed discussion of the methodology and results of the studies that demonstrate these practices. Discussion and results are included with best practices for petrophysical characterization, fluid-rock interactions, and fluid evaluation and optimization. Studies featured in the summary discussions are contained in the body of the Final Report.

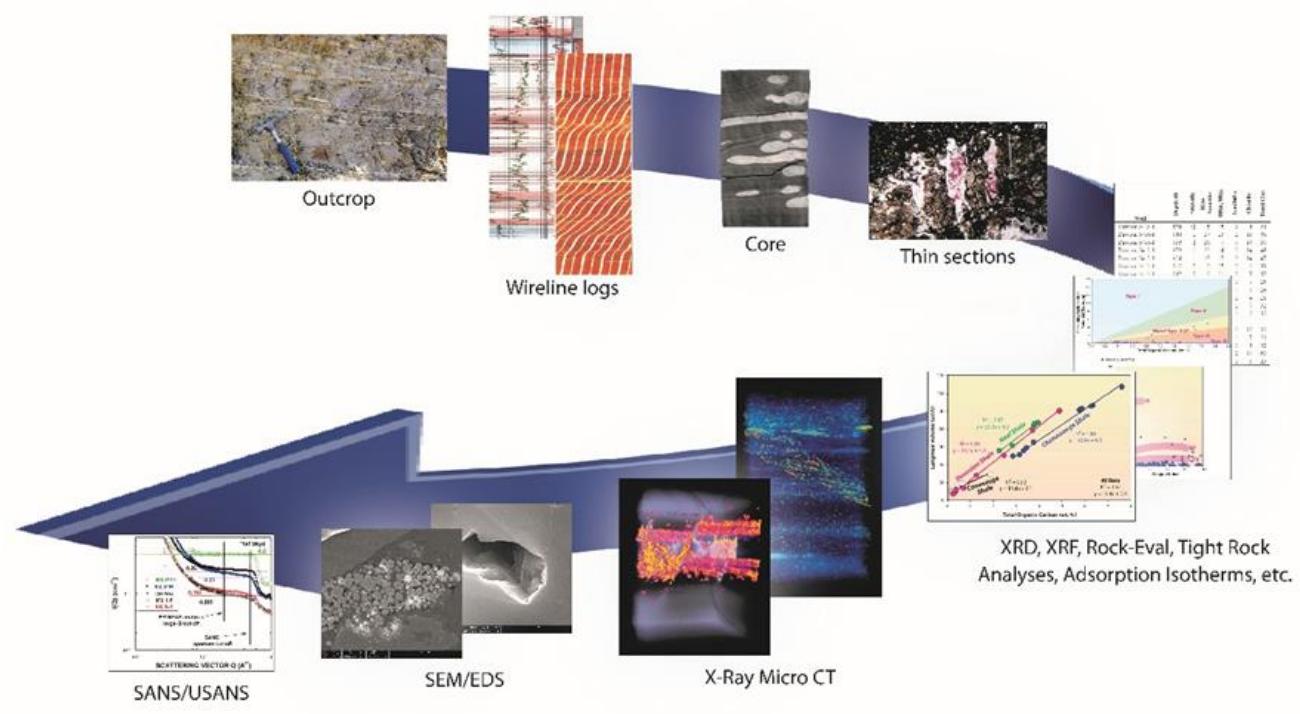

Figure 1.—Integrated workflow for petrophysical and tight rock characterization of shale from the megascopic to nanoscopic scale (after Powers, 2015).

GEOLOGICAL CHARACTERIZATION

SUMMARY

Geological characterization is anchored in rock analysis and includes core description, outcrop description, facies modeling, sedimentologic interpretation and sequence stratigraphic interpretation. Geological characterization is initiated at the megascopic scale, as represented by outcrops, cores, and wireline logs. At mesoscopic to nanoscopic scales, petrologic characterization, including thin section petrography, x-ray tomography, and scanning electron microscopy can contribute immeasurably to geological characterization.

BEST PRACTICES

The best practices for geological characterization center on understanding lateral and vertical stratal relationships and establishing the spatial distribution of source, reservoir and seal lithofacies. Lateral facies distribution, when interpreted concurrently with facies stacking patterns, can be used to reconstruct the depositional history within a sequence stratigraphic framework. To this end, the following best practices are recommended.

1. Detailed description of outcrop and/or core samples noting lithology, color, composition, sedimentary features including physical sedimentary structures and biogenic structures, as well as tectonic features including fractures, faults and zones of brecciation. Macroscopic fossils, cements and resistance to weathering in outcrop or erosion or fracturing during coring are noteworthy.
2. Designate lithofacies based on repeatable patterns in composition, sedimentary features, texture and color.
3. Establish vertical and lateral relationships among lithofacies.

4. Interpret depositional setting (sedimentology) from facies and construct a depositional model.
5. Use vertical stacking patterns, lateral facies transitions, and apparent changes in sedimentary processes as represented by stratigraphic surfaces, to construct a sequence stratigraphic framework.
6. When available, use biostratigraphy/geochronology to add the temporal component to the depositional model and stratigraphic framework, and
7. Survey outcrop and cores with geochemical/geophysical surveys including gamma-ray spectroscopy and hand-held x-ray fluorescence to establish chemostratigraphy.

PETROLOGIC CHARACTERIZATION

SUMMARY

Petrologic characterization occurs at the micro- to nanoscale and as such is an integral component of the overall geological characterization. As shale or mudstone is inherently fine grained, microscopic observation and analysis is critical to understanding rock composition, identifying authigenic minerals and the determining the impact of the diagenetic overprint on the detrital framework. Furthermore, micro- to nanoscale observations are critical to understanding porosity types and distribution and assessing the maturity of organic matter.

BEST PRACTICES

Best practices for petrologic characterization include analyses and techniques that, when used together, allow the observation and imaging of rock features at the meso- to nanoscale and determine mineralogical composition, organic content and maturity, detrital and authigenic components of the rock fabric, and characterize pore types and abundance.

1. Thin section petrography to determine microscale depositional features, detrital grains, biogenic grains and features, and authigenic minerals.
2. Scanning electron microscopy with energy dispersive spectroscopy to provide higher resolution observations of detrital and authigenic components, pore types and abundance, and relationships between rock fabric and porosity evolution and occlusion.
3. Geochemical, x-ray and electron-microscopy based techniques to characterize rock fabric and describe features not readily evident in hand specimen- and micro-scale samples. These include:
    a. Backscatter and secondary electron imaging,
    b. Focused ion beam (FIB) sectioning to allow 3-D mapping of pore systems
    c. Mineral mapping using SEM-EDS,
    d. Micro x-ray computer tomography (Micro CT) imaging,
    e. Discrete fracture network modeling, and
4. Microscale analysis of kerogen to determine type, reflectance, and fluorescence; SEM imaging of kerogen for evidence of relict organic fabric and secondary volatilization; and NMR determination of ratios of organic compounds to kerogen are all recommended practices to evaluate kerogen type, thermal maturity and predict hydrocarbon composition.

Petrologic characterization provides valuable input data such as TOC, thermal maturity, clay mineral composition and microfracture orientation, size and frequency that impact the petrophysical characterization and fluid-rock interactions and fluid evaluation and optimization. As such, these stages of the workflow for petrophysics and tight rock characterization while being distinct, are intertwined and overlap.

PETROPHYSICAL CHARACTERIZATION

PERMEABILITY OF A FRACTURE IN THE PRESENCE AND ABSENCE OF A WETTING PHASE AND THE EFFECT OF CONFINING AND PORE PRESSURES ON MATRIX PERMEABILITY TO GAS

SUMMARY

Three separate experiments were conducted on two shales to determine permeability of a fracture in the presence and absence of a wetting phase and the effect of confining and pore pressure on matrix permeability to gas. Because the confining and pore pressures are among the conditions having the greatest impact on the apparent permeability of gas shales, an investigation of the effect of the pressures was undertaken to examine the sensitivity of the apparent permeability of the Barnett Shale to effective stress and the time dependence of the response of its permeability to change in effective stress.

BEST PRACTICES

1. To be useful for the simulation of production from gas shale reservoirs, measurements of the permeability of shale samples should reproduce the effective stress state in the formation under consideration.
2. Based on our results, the approach of Zeng and Grigg (2006) successfully accounted for intertial effects arising from high velocity gas flow in a fracture and should be used in fractured media. Using their approach, datasets in poor agreement were unified.
3. The method developed by Hildenbrand and coworkers (2002, 2004) for determination of the gas breakthrough pressure of a brine-saturated rock was also applied to a fractured Woodford Shale sample. A function fit to the dependence of effective permeability on

pressure drop suggests that it is useful for the simulation of gas flow in the presence of a wetting phase, but additional work is needed to establish the dependence of irreducible brine saturation and maximum effective permeability on pressure for gas and the rock and wetting phases of interest.

4. The dependence of the permeability of the Barnett Shale on confining and pore pressures was demonstrated by varying the confining pressure at fixed mean pore pressures, using helium. Permeability is presented as a function of the difference between confining pressure and pore pressure, or effective stress. The response of permeability to changes in pressure evidently consists of structural changes of at least two types or in two materials, such as the mineral fabric and the hydrocarbons.

APPARATUS/PROCEDURE

Permeability measurements were made using the Core Lab/TEMCO triaxial core holder in the laboratory at UAB. The set-up of the equipment is shown in Fig. 2. The measurements were made on the as-received samples, without extraction, drying, or other pretreatment. For the second and third experiment the set-up was similar that shown in Fig. 2, but without the flowmeter.

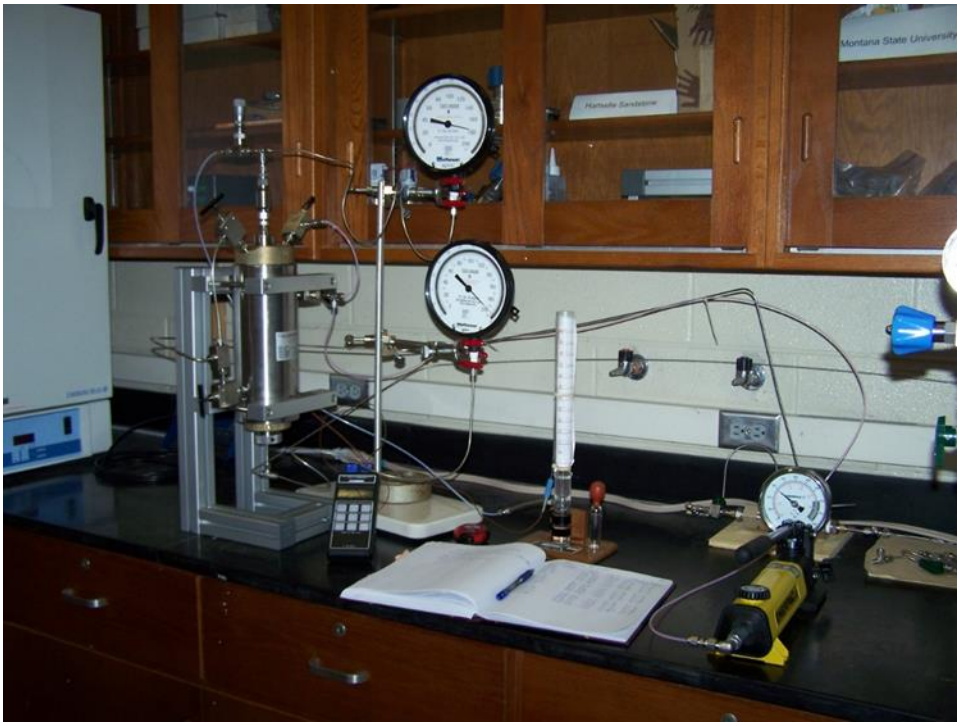

Figure 2.—Triaxial core holder, inlet and outlet pressure gauges, thermocouple readout, flowmeter, and confining pressure pump and gauge in the arrangement for measurement of permeability by steady flow of nitrogen.

RESULTS

The analysis by Zeng and Grigg (2006) based on the Forchheimer equation successfully accounted for inertial effects on the pressure gradient arising from high velocity gas flow through a sample of Woodford shale containing a single fracture. The approach succeeded in unifying four sets of steady flow permeability measurements, whose apparent absolute permeability, obtained by extrapolation of the graphs of apparent permeability versus 1/pressure, were in poor agreement, ranging from 0.97 to 2.53 millidarcy (fig. 3). Zeng and Grigg's method produced an absolute permeability for the four sets of measurements of 3.1 ± 0.2 millidarcy (fig. 4), consistent with correction for inertial effects on the pressure gradient in the fracture. Under the assumption that the permeability of the rock matrix is negligible and the walls of the fracture are

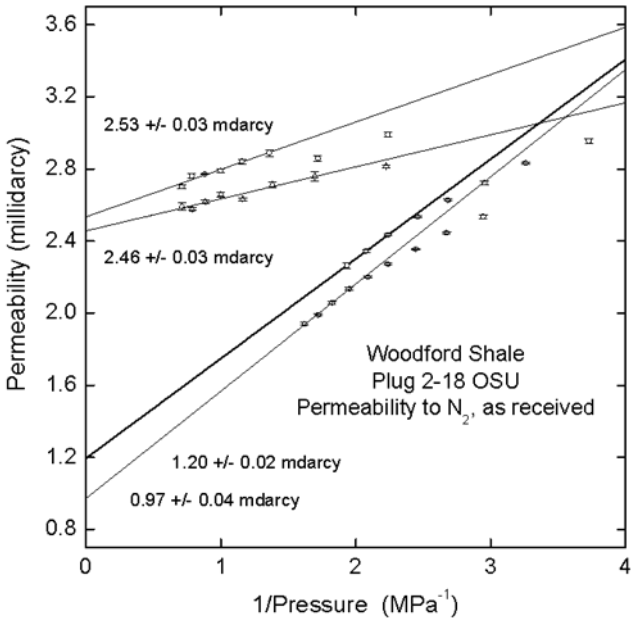

Figure 3.—Apparent permeability of the fractured Woodford Shale plug shown in Figure 1, determined by steady flow of nitrogen. The mean nitrogen pressures in the sample during the two upper sets of measurements were in the range from 0.45 to 1.41 MPa (50 to 189 psig) and during the two lower sets of measurements, in the range from 0.27 to 0.62 MPa (24 to 75 psig).

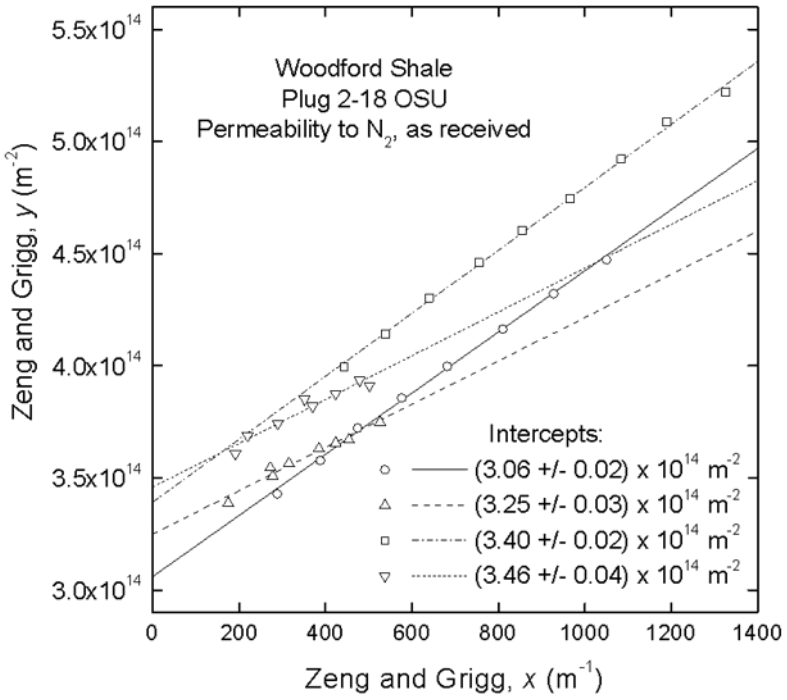

Figure 4.—Plot of the measurements shown in Figure 2 as points redefined using *x* and *y* values from Zeng and Grigg (2006).

smooth parallel plates, the average aperture of the fracture was estimated to be approximately 10 μm.

The method developed by Hildenbrand et al. (2002, 2004) for determination of the gas breakthrough pressure of a brine-saturated rock was also applied to the fractured Woodford Shale sample. The measurement is called, by its authors, the "minimum capillary displacement pressure," because the critical pressure is found by applying a pressure difference greater than the breakthrough pressure to a fully-brine-saturated rock, causing pores and fractures to drain and allowing gas to flow through the sample (fig. 5). As the pressure drop across the sample decreases, it reimbibes the brine, beginning with the smallest open passages through the sample, and comes to equilibrium at the pressure difference equal to the capillary pressure at the smallest aperture in the highest conductivity path through the sample, the same path along which gas flow begins, when the process is reversed (fig. 5).

The dependence of the permeability of a Barnett Shale sample on confining and pore pressures was examined by varying the confining pressure at fixed mean pore pressures, using helium. The permeabilities are presented as functions of the difference between the confining and pore pressures, or effective stress.

The time dependence of permeability was recorded over a period of 10 days, following a decrease in confining pressure from 16.65 MPa (2400 psig) to 5.62 MPa (800 psig) and simultaneous decrease in mean pore pressure from 4.23 MPa (600 psig) to 1.48 MPa (200 psig) (fig 6). An almost instantaneous increase in permeability, by a factor of 1.7, was followed by a slower increase, by another factor of 1.7, over the next 120 hours, after which the permeability remained constant until the end of the observations 50 hours later.

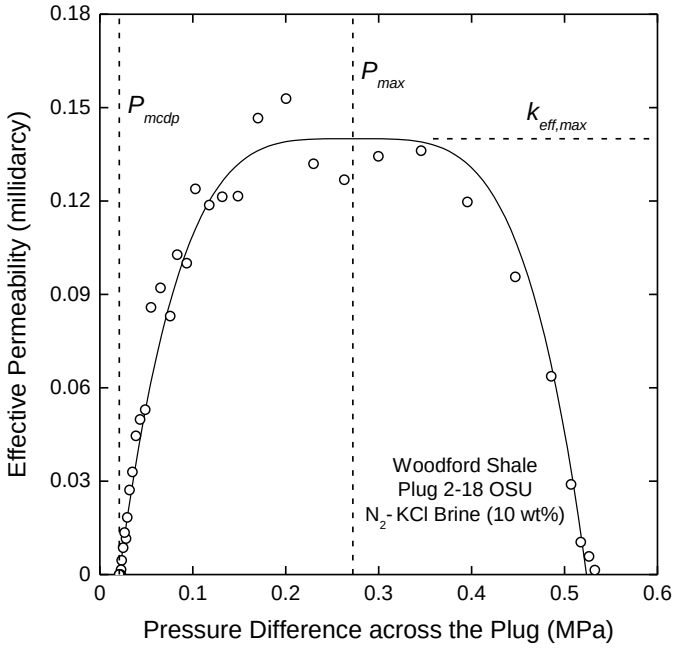

Figure 5.—Dependence of the effective permeability of the brine-saturated Woodford Shale plug on pressure difference following breakthrough. Permeability first increases as brine is displaced and gas saturation increases to a maximum. Permeability decreases as brine reimbides and closes off open channels or pores.

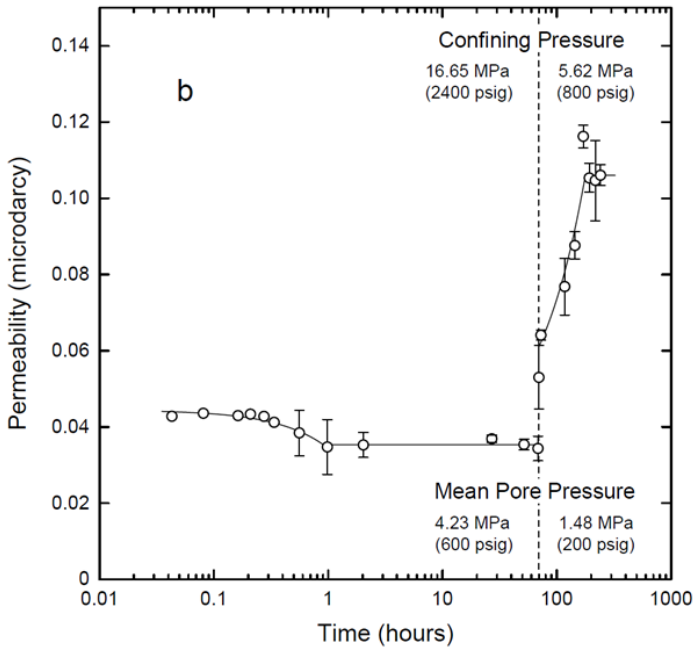

Figure 6.—Response of the permeability of the Barnett Shale sample to helium gas following a decrease in confining pressure from 16.65 MPa (2400 psig) to 5.62 MPa (800 psig) and a simultaneous decrease in mean pore pressure from 4.23 MPa (600 psig) to 1.48 MPa (200 psig).

FULL-IMMERSION PRESSURE PULSE DECAY

SUMMARY

An alternative is proposed to the conventional pressure-pulse decay method for determining the permeability of a cylindrical rock sample. The proposed method has the advantage that permeabilities in both the axial and radial directions in the sample are determined in a single test on a single cylindrical core sample. The method is described as "Full Immersion Pressure-Pulse Decay."

BEST PRACTICE

This newly developed technique, full-immersion pressure-pulse decay, gave promising results in blind tests conducted in cooperation with Weatherford Laboratories. Further refinement of sample dimensions to separate axial and radial lengths should improve results for this innovative method of measuring permeability and porosity.

SCOPE

The industry accepted practices of measuring permeability of cylindrical core plugs using pressure-pulse decay is modified. In this experiment, a research apparatus was designed to measure pressure-pulse decay in both the axial and radial directions on the cylindrical core plug. This new experimental design was tested using several samples in blind tests.

APPARATUS/PROCEDURE

A pressure vessel was designed and fabricated to house a cylindrical core sample and expose the sample to fluid over its entire outer surface, as shown in Fig. 7. The cell and associated valves and tubing were placed in a water bath inside an incubator that maintained the

temperature constant to within ± 0.5 °C. In its present configuration the sample cannot be subjected to axial or radial confining stresses. For each sample, a series of experiments was performed with helium gas at four different initial pressures, ranging from approximately 250 to 1000 psia.

RESULTS

A new method for determination of the permeability of intact cylindrical rock samples has been developed, in which the entire rock surface is exposed to a permeating gas (Fig. 7). The new technique, called "full immersion pressure-pulse decay," has the advantage that permeability can be measured in both axial and radial directions in a sample in a single experiment. For a sample plug cut perpendicular to bedding, this permits the permeabilities parallel and perpendicular to bedding to be determined simultaneously, on the same sample.

The theory was first developed, followed by design of the experiment, then derivation of a procedure for inversion of the data to determine porosity and permeability. A blind test was conducted using samples generously provided by Weatherford Laboratories. Permeability measurements made by the full immersion technique were slightly higher than those measured at Weatherford Laboratories, using their standard methods (Fig. 8). For the sample having the largest deviation between the results from the two laboratories, the axial permeability determined by full immersion was 1.62 times the value determined by Weatherford Laboratories, so agreement between the two methods was considered acceptable. The differences between the results from the two laboratories may be explained by the fact that in the tests at Weatherford the samples were under a confining stress of 500 psi, while in the tests by full immersion pressure-pulse decay the samples were under no confining stress.

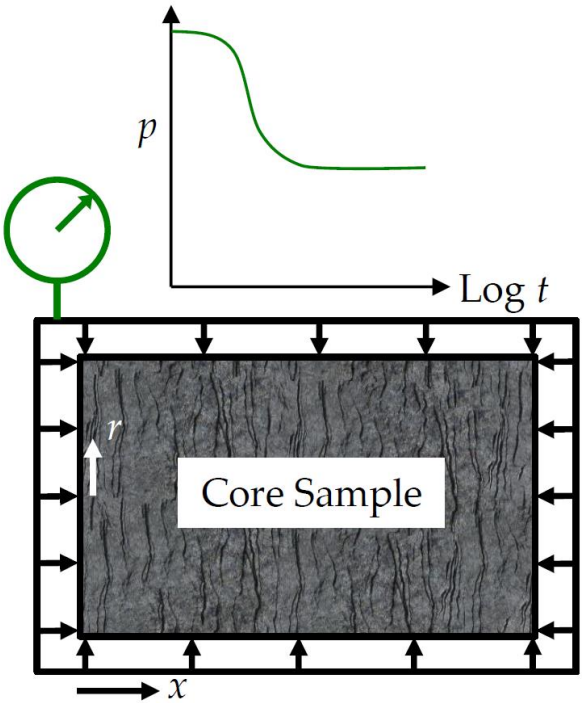

Figure 7.—Pressure-pulse decay with a cylindrical rock sample exposed to fluid over its entire surface.

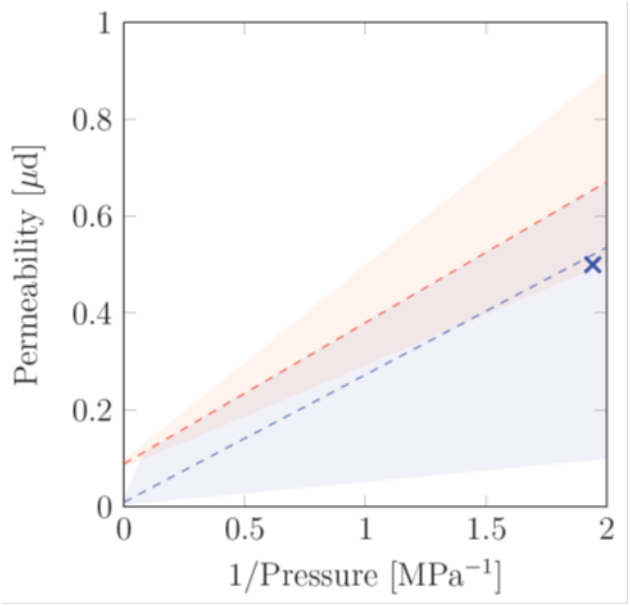

Figure 8.—Klinkenberg plot of apparent permeability to helium, parallel and perpendicular to bedding, for one of the four cylindrical samples provided by Weatherford Laboratories. Red dash: full immersion measurements of radial permeability with uncertainty (pink shading). Blue dash: full immersion measurements of axial permeability with uncertainty (blue shading). Blue x: Weatherford Laboratory measurement of axial permeability to nitrogen at a net confining stress of 500 psi.

GAS ADSORPTION ON SHALE

SUMMARY

Adsorption isotherms were measured for samples of thee shales to determine how mineral composition (ash) and total organic carbon content impact adsorption. The simplified low-density model was used to predict adsorption outcome.

BEST PRACTICES

Based on our experiments, the simplified low-density (SLD) model can be used to describe gas adsorption for shale within experimental uncertainty. Since SLD model parameters surface area and solid-solid interaction appear related to TOC, detailed characterization of shale samples prior to modeling is essential.

SCOPE

Shale reservoirs have gained significance because of their abundant natural gas content and their potential for CO_2 sequestration. Since shale reservoirs generally contain large amounts of adsorbed gas, the modeling of adsorption behavior is essential for obtaining reliable gas-in-place estimates and designing CO_2 sequestration processes in these reservoirs. Two important elements for modeling gas adsorption behavior are (1) adsorption data measured at reservoir operating temperatures and pressures and (2) a reliable model capable of describing accurately the adsorption behavior over wide pressure and temperature ranges.

APPARATUS/PROCEDURE

Fig. 9 presents a schematic of the adsorption measurement apparatus. The apparatus is contained in an air bath maintained at constant temperature. The equilibrium cell contains the shale sample and the cell is under partial vacuum at the start of the experiment. For measurements on moist adsorbent samples, there is a potential for the loss of moisture from the sample when placed under vacuum. To avoid loss of moisture from the sample, the vacuum pressure applied to the sample was limited and maintained above the vapor pressure of water vapor at the temperature used for measuring the isotherms (328.2°K). Further, in order to test for possible loss of moisture and volatile organics, the shale sample was carefully weighed before and after the adsorption isotherm experiments. No appreciable loss of mass was detected from the sample, indicating that there was very little (if any) change in composition of the adsorbent sample.

Samples were pulverized and stored carefully in an inert environment to avoid possible oxidation. Adsorption isotherms were measured on the "as-received" samples without any further drying of the sample. Table 1 presents the compositional analysis of the shale samples in this study. The analysis was conducted by Huffman Laboratories, Colorado. The Woodford Shale from Payne County contains about 8.5% total organic carbon (TOC), 1% moisture and 84% ash content, the Woodford shale from Hancock county contains about 6.4% TOC, 0.8% moisture and 86% ash and the Caney Shale contains about 2% TOC, 1.7% moisture and 92% ash. Although several other types of shale characterization can be obtained, we have focused on characterization that is more *relevant* to describing adsorption on shales. In a previous work (Mohammad et al., 2009) it was shown that adsorption model parameters can be generalized successfully in terms of compositional characterization. We anticipate undertaking similar model-parameter generalization for shales when sufficient data become available.

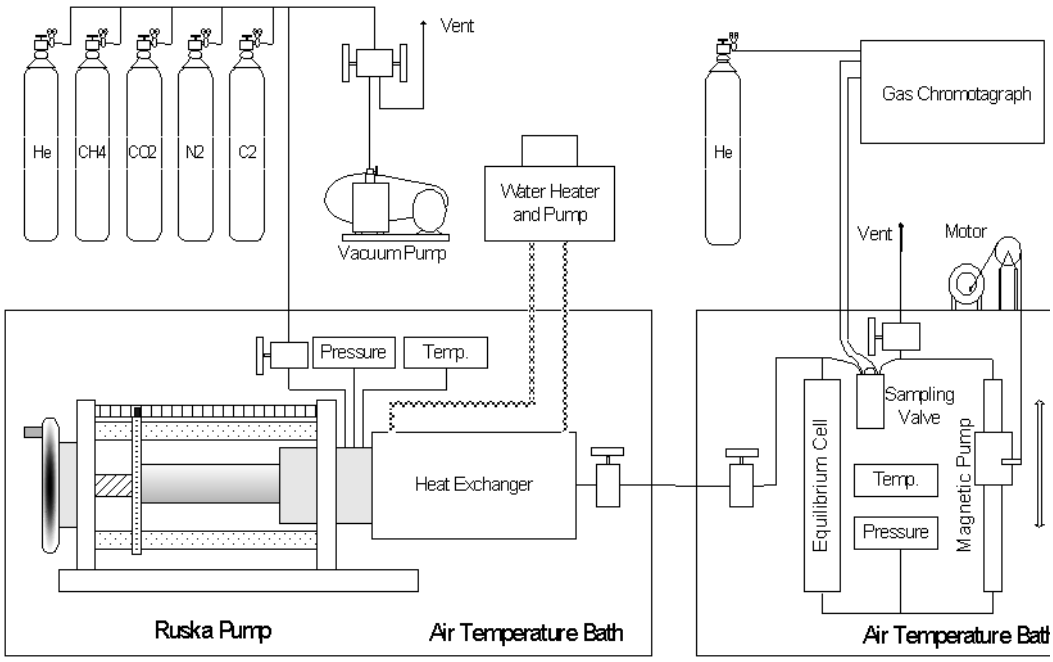

Figure 9.—Experimental Setup for measuring gas adsorption.

RESULTS

In this work, the adsorption of methane, nitrogen and carbon dioxide on three shale samples was measured. Two samples are Woodford Shale from Payne, County, Oklahoma and Hancock County, Texas, respectively. The third sample is the Caney Shale from southern Oklahoma. Pure-gas adsorption was measured at 328.2°K and pressures up to 12.4 MPa. Results indicate that at about 7 MPa, the adsorption ratio of N_2, CH_4, and CO_2 are about 1: 2.9: 6.1 for the Woodford Shale from Payne County (fig.10), 1: 3.0: 12.8 for the Woodford Shale from Hancock County and about 1: 3.5: 30.1 for the Caney Shale. These results show that adsorption capacity of these gases appears to be related to total organic carbon content (TOC) of these shale samples. In addition, the preferential adsorption of CO_2 relative to CH_4 was stronger for samples with higher ash content, indicating that mineral matter is an important contributing factor in the CO_2 adsorption capacity of shale.

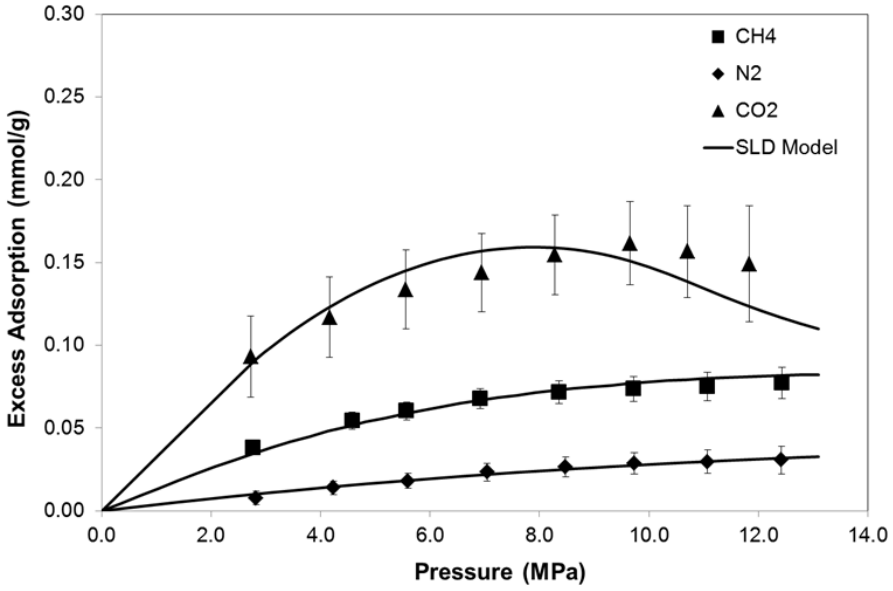

Figure 10.—Adsorption isotherms of CH_4, N_2, and CO_2 on Woodford Shale from Payne County at 328.2°K. Error bars on each point show expected experimental uncertainty. Similar isotherms were measured for the Woodford Shale, Hancock County and the Caney Shale.

The simplified local-density (SLD) model was used to predict the adsorption data obtained in this work. The SLD modeling results indicate that the adsorption data were represented within the experimental uncertainties. Overall, the percentage average absolute deviations for methane, nitrogen and CO_2 adsorption on the three shales were about 7%. In addition, the SLD model surface areas and solid-solid interaction parameters appear related to TOC content. However, additional adsorption data on shale, as well as detailed surface area characterization of such samples, will be necessary for developing a generalized, predictive adsorption model for shale gas systems.

Figure 11 presents the resulting deviations from the SLD model for the Woodford Shale from Payne County. Similar graphs were prepared for the Woodford Shale, Hancock County and Caney Shale.For adsorption on the three samples, about 88% of the data for methane, 74% of the data for nitrogen and 83% of the data for CO_2 were represented within 10% deviation. Overall,

81% of the total data were represented within 10% deviation. Thus, the SLD model was found capable of describing the adsorption data on these shales.

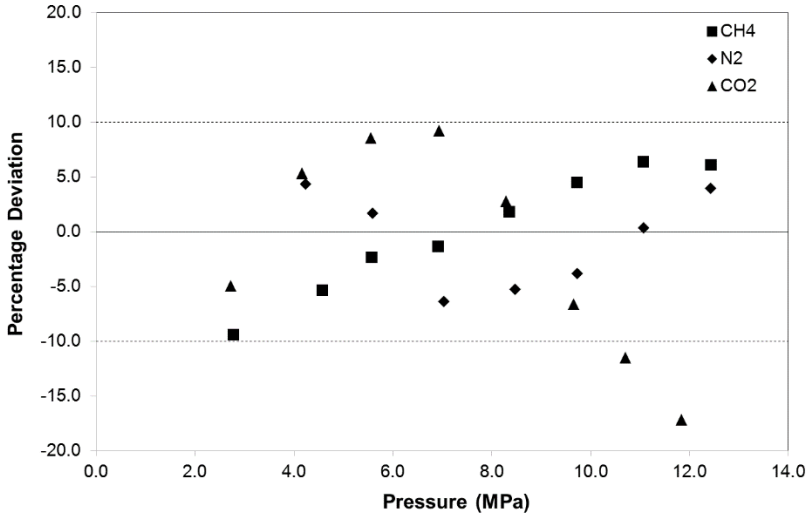

Figure 11.—Percentage deviation of SLD Model representations for methane, nitrogen and carbon dioxide. Adsorption at 328.2 K on Woodford Shale from Payne County

FLUID-ROCK INTERACTIONS:

IMPROVED EVALUATION OF SHALE-FLUID INTERACTION USING IMMERSION TESTS

SUMMARY

In this work, the interaction of injected fluids with shale was studied as a function of polymer concentration and salt type and concentration. Bentonite, the most common clay-mineral in water-based drilling mud (WBDM) was used to examine the effects of a competing clay on the polymer-shale interaction.

BEST PRACTICES

1. Polyacrylamide combined with salts and tetramethyl ammonium chloride (TMAC) is recommended to prevent swelling and dispersion in shale. However, high concentrations of TMAC are not recommended as TMAC inhibits adsorption of polyacrylamides to the shale surface resulting in excessive shrinking of shale at down-hole conditions and loss of shale mechanical strength.
2. Both anionic and cationic polyacrylamides form isolation membranes on shale thereby inhibiting water and solute ions form interacting. However, cationic polyacrylamides do not react detrimentally with salt to cause a reduction in fluid viscosity and increased fluid loss to the shale.

SCOPE

Clay content in shale has a great influence on the chemical and mechanical properties of shale. The common clay minerals present in shales are illite, montromillite, smectite, calcite and kaolinite. Each clay mineral when present in abundance significantly changes shale properties.

Illite-rich shales are reactive and smectite expands when in contact with water, resulting in clay swelling. Shales have common properties, but because of clay mineralogy, shale behaves uniquely when in contact with injected fluids. Interactivity between shale and fluid is measured by different means. Traditional measurements such as those obtained via dispersion tests and swelling tests do not fully account for the influence of fluid on the rock structure and fracture development in shale. Some of the more commonly used methods require grinding the shale and reconstituting it with water. These tests give completely different results that are often far from reality. Immersion tests give us a visual confirmation of the effect of different types of fluid on the rock structure (Rabe, da Fontoura, & dos Santos Antunes, 2002; Santos, Diek, Da Fontoura, & Roegiers, 1997). Immersion tests are efficient in evaluating the drilling fluid suitable for a particular shale formation. However, the absence of confining pressure is a major limitation to the method (Santos et al., 1997).

The common additives used in water-based mud (WBM) are friction reducers, acids, gellants, crosslinkers, clay controlling agents and other polymers. High molecular weight polyacrylamides are the most commonly used friction reducer and are thermally stable up to 200 °C (Carman & Cawiezel, 2007; Jia Zhou, Sun, Stevens, Qu, & Bai, 2011). Potassium chloride, sodium chloride and tetramethyl ammonium chloride (TMAC) are some of the common additives that are used to mitigate the harmful effects of clay present in water.

APPARATUS/PROCEDURE

A Discover DHR-3 stress controlled rheometer was used to make rheological measurements of the samples. For the polymer-shale sample, vane geometry was used. Vane geometry helps prevent wall slippage at higher shear rates, will help disrupt flow inhomogeneity while shearing

and also is works great for samples that have solids suspended. For polymer solutions the cone and plate geometry was used. Cone and plate is useful for solutions that have low viscosities and that do not have dispersions with solids suspended greater than 64 µm. Cone and plate geometry (diameter: 60 mm and cone angle 2º) have homogenous shear, shear rate and stress in the geometry gap. All experiments were conducted at a temperature of 25 °C ± 0.03 °C. Before the start of each experiment, the polymer shale sample was pre sheared at 200 $l \cdot s^{-1}$.

Carefully preserved core samples were immersed in different fluid systems of varying compositions at 60°C and sealed. Inert shale samples were sealed for 5 days; reactive shale samples for 2 days. The change in weight of the shale samples before and after the test, linear swelling and the change in hardness were measured. SEM images of the samples after exposure to the test fluids were taken to analyze the effectiveness with which the polyacrylamide fluids could form membranes on the shale surface. In addition the impact of polyacrylamide on the viscosity of test fluids a series of rheology experiments were conducted on salt and polyacrylamide fluid.

RESULTS

Our results show that the presence of salt increases viscosity of cationic polyacrylamide systems, but reduces the viscosity of anionic polyacrylamide solutions (figs. 12 and 13). The role of salts tetramethyl ammonium chloride (TMAC) and polyacrylamides as shale inhibitors was investigated through simple immersion tests and by using rheology as a means of measuring clay-fluid interaction. The following conclusions are drawn from the experimental results:

1. Polyacrylamides (anionic and cationic) prevent swelling in all of the three gas-shale samples under study by forming an isolation membrane on the shale and preventing water and ions from entering the shale.
2. 2 Polyacrylamide with salts and TMAC proved very effective in preventing swelling and dispersion for all three shales.
3. High concentrations of TMAC are not recommended. TMAC prevents the adsorption of polyacrylamides and also causes excessive shrinking which can lead to shale losing its mechanical strength at down-hole conditions.
4. NaCl increases swelling in montmorillonite-rich shales. Instead, salts such as KCl and TMAC can be used with shale rich in expandable clays such as sodium montmorillonite.
5. Salts can be inimical to the rheology of polyacrylamides. Salts reduce the viscosity of the anionic polyacrylamide fluid system and hence can lead to increased fluid losses. In contrast salts (KCl and NaCl) increased viscosity of the cationic polyacrylamide solution.
6. The recommendations for suitable salts and polyacrylamides for the three shales under study are given in Tables 1, 2 and 3.

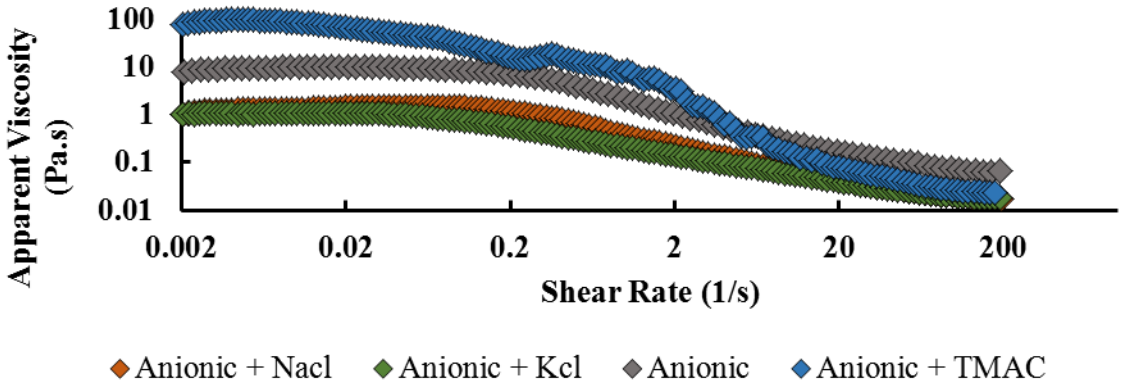

Figure 12.—Change in apparent viscosity of anionic polyacrylamide system with shear rate. Note lower apparent viscosities of anionic polyacrylamide+salt solutions (green and orange) compared to solutions containing only anionic polyacrylamide (gray) and polyacrylamide + TMAC (blue).

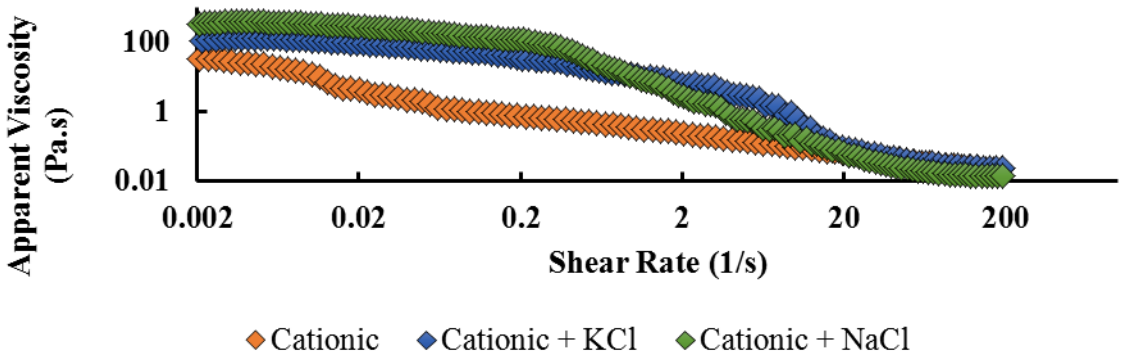

Figure 13.—Change in apparent viscosity of cationic polyacrylamide system with shear rate. Cationic polyacrylamide + salt solutions (blue and green) have higher initial apparent viscosities than a solution containing only cationic polyacrylamide (orange).

Table 1.—Application of KCl-based fluids for the shales under study.

Shale	Shale Type	Dispersion limiting ability of KCl	Swelling limiting ability of KCl	Is the use of KCl suggested ?
Woodford	Medium hard, high in illite, with expandable clays, less dispersion shale	Good	Good	Yes
Pride Mountain	Hard, high in quartz, less expandable clays	Good	Fair	Yes
Gorgas	Soft, high expandable, interlayer mixed clays and highly dispersible	Fair	Fair	No

Table 2.—Application of NaCl-based fluids for the shales under study.

Shale	Shale Type	Dispersion limiting ability of NaCl	Swelling limiting ability of NaCl	Is the use of NaCl suggested?
Woodford	Medium hard, illite-rich, with expandable clays, less dispersible shale	Good	Fair	Yes
Pride Mountain	Hard, high in quartz, less expandable clays	Good	Good	Yes
Gorgas	Soft, high expandable content, interlayer mixed clays and highly dispersible	Fair	Fair	Yes

Table 3.—Application of TMAC-based fluids for the shales under study.

Shale	Shale Type	Dispersion limiting ability of TMAC	Swelling limiting ability of TMAC	Is the use of TMAC suggested?
Woodford	Medium hard, high illite content, with expandable clays, less dispersible shale	Fair	Good	Yes
Pride Mountain	Hard, high quartz, less expandable clay content	Good	Fair	No
Gorgas	Soft, high expandable, interlayer mixed clays and highly dispersible shale	Good	Good	Yes

FLUID EVALUATION AND OPTIMIZATION:

ASSESSING THE EFFECTS OF POLYACRYLAMIDE AND MIXED POLYACRYLAMIDE-XANTHUM GUM ADDITIVES ON DRAG REDUCTION CAPACITY AND SHEAR STABILITY IN LOW-VISCOSITY FRACTURE FLUIDS

SUMMARY

Polyacrylamide (PAM) drag reduction polymers are essential friction reducers in low-viscosity "slickwater" fracture treatments. Because PAM solutions lose 20-30% of their DR efficiency in the first 60 minutes of shearing at experimental conditions, stabilizing these solutions with xanthum gum (XG) is proposed. Mixed polyacrylamide (PAM)-xanthum gum (XG) solutions slightly increased shear stability of low-viscosity fracture fluids, but did not affect the degree of drag reduction (DR). Since the friction reduction of rigid polymers depends only on concentration, mixing PAM with higher concentrations of XG might be beneficial in maintaining the DR efficiency of PAM as well as improving its shear stability.

BEST PRACTICES

Cationic and anionic polyacrylamide (PAM) is an effective friction reducer in "slickwater" fracture treatments. Experiments should continue with mixed PAM and xanthum gum (XG) solutions as additives while increasing the concentration of XG to determine if shear stability and reasonable drag reduction are achieved.

SCOPE

In this work, firstly, the effect of PAM concentration on drag reduction (DR) capacity along with shear stability of the solutions was investigated. Then, the possibility of stabilizing flexible PAM polymer molecules with the biodegradable polymer, xanthan gum (XG), was verified.

As a result of lower viscosity, slickwater fracturing fluids cannot suspend and transport proppants as effectively as gelled fluids. To overcome poor proppant transport, higher pumping

rates are applied. High flow rates, in turn, lead to significant energy loss due to friction and turbulence in the tubular pipeline (Kaufman et al., 2008; Palisch et al., 2010). In slickwater treatments, friction reducer (FR) is a main component of the fluid. Long chain and flexible polyacrylamide (PAM) based polymers are known to be the best drag reduction polymers (Wu et al., 2013); (Pereira et al., 2013). However, mechanical degradation of such polymer solutions has complicated their use (Campolo et al., 2015; Moussa and Tiu, 1994).

The effect of PAM concentration on drag reduction (DR) capacity and shear stability of solutions was investigated. Then, the stabilizing effect of various concentrations of XG on flexible PAM polymer molecules was examined. The concentrations of the polymers involved are shown in Table 4.

Table 4. Concentrations of pure and mixed polymers studied.

Polyacrylamide (PAM) concentrations studied. Values in weight parts per million (wppm)	100, 150, 200, 300 500 and 1000 wppm
Mixed xanthum gum (XG) + PAM solutions studied (wppm)	100 wppm PAM + 100 wppm XG for Total Concentration (TC) = 200 wppm, and 150 wppm PAM + 100 wppm XG for Total Concentration (TC) = 250 wppm
Xanthum gum (XG)solutions (wppm)	600 wppm

APPARATUS/PROCEDURE

A closed loop flow system was used for drag reduction and turbulent flow measurements (fig. 14). The system is comprised of a 60 liter supply tank connected to a progressive cavity pump (SEEPEX BN 10-12) with a conveying capacity of 30 GPM (113.56 l/min), and a seamless stainless steel horizontal pipe test section of L=8 ft. (2.438 m) and inner diameter of 1

inch (2.54cm). The flow rate of the system was measured using a mass flow meter (OPTIMASS 1000, KROHNE) with an accuracy of ±0.15% and a repeatability of ±0.05% as stated by the manufacturer. The pressure drop data along the measuring length of the pipe was gathered using a membrane differential pressure transducer (PX409, OMEGA).

Viscosity measurements were carried out in a DHR Hybrid Rheometer. The instrument is equipped with a Peltier system to control sample temperature. In our experiments, sample temperature was maintained at 25±0.01 °C.

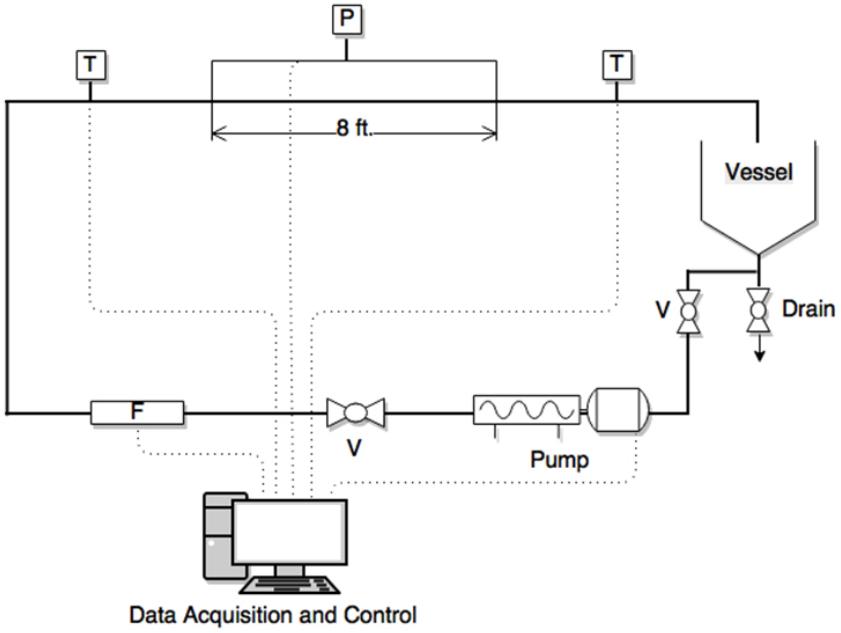

Figure 104. --Schematic illustration of the flow loop. Instrumentation consists of a digital flow meter (F), differential pressure transducer (P), valves (V), and temperature sensors (T).

RESULTS

The results from work show that among different concentrations of PAM, 1000 wppm solution has the highest friction reduction efficiency and the lowest decline in DR% (fig. 15). Increasing the concentration above 200 wppm does not change the DR% of the fresh samples significantly, though at higher concentrations, shear stability is better. PAM solutions lose 20-

30% of their DR efficiency in the first 60 minutes of shearing at the tests conditions applied in this work. Mixing flexible PAM molecule with XG molecules did not improve the degree of DR significantly, but slightly improved the DR stability of PAM solutions (fig. 16). Since the friction reduction of rigid polymers depends only on concentration, mixing PAM with higher concentrations of XG might be beneficial in maintaining the DR efficiency of PAM as well as improving its shear stability. Exponential decay model was used to correlate the experimental data. The model describes the DR behavior of polyacrylamide solutions very well.

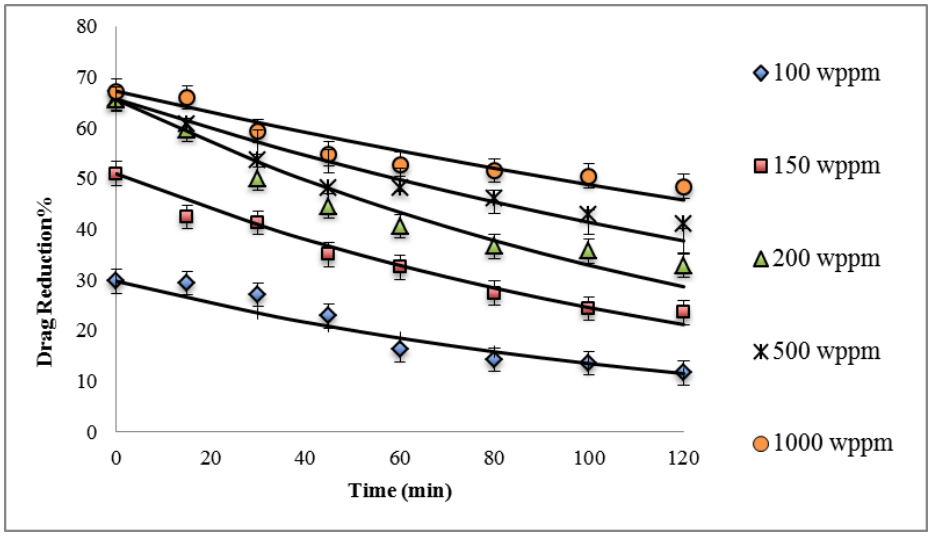

Figure 15.—%Drag reduction for different concentrations of PAM at 30 GPM (113.56 l/min)

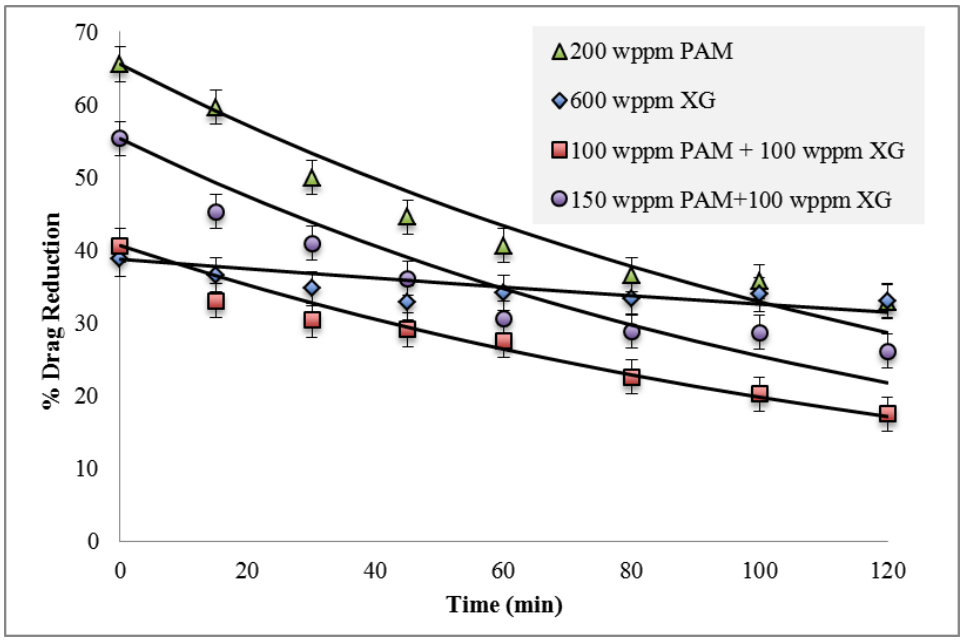

Figure 16.—%Drag reduction for mixed PAM/XG solutions at 30 GPM (113.56 l/min)

REFERENCES CITED

Campolo, M., Simeoni, M., Lapasin, R. and Soldati, A., 2015. Turbulent Drag Reduction by Biopolymers in Large Scale Pipes. Journal of Fluids Engineering, 137(4): 041102.

Carman, P. S., & Cawiezel, K., 2007, Successful breaker optimization for polyacrylamide friction reducers used in slickwater fracturing. Paper presented at the SPE Hydraulic Fracturing Technology Conference.

Hildenbrand, A., Schlömer, S., and Krooss, B. M., 2002, Gas breakthrough experiments on fine-grained sedimentary rocks: Geofluids, v. 2, p. 3-23.

Hildenbrand, A., Schlömer, S., and Krooss, B. M., and Littke, R., 2004, Gas breakthrough experiments on politic rocks: comparative study with N_2, CO_2 and CH_4. Geofluids, v. 4, p. 61-80.

Mohammad, S. A.; Chen, J. S.; Robinson, R. L.; Gasem, K. A. M., 2009, Generalized Simplified Local-Density/Peng−Robinson Model for Adsorption of Pure and Mixed Gases on Coals: Energy & Fuels, v. 23, (12), p. 6259-6271.

Kaufman, P.B., Penny, G.S. and Paktinat, J., 2008. Critical Evaluation of Additives Used in Shale Slickwater Fracs: Society of Petroleum Engineers. SPE 119900-MS, 9 p.

Moussa, T. and Tiu, C., 1994. Factors affecting polymer degradation in turbulent pipe flow: Chemical Engineering Science, v. 49(10), p. 1681-1692.

Palisch, T.T., Vincent, M. and Handren, P.J., 2010. Slickwater Fracturing: Food for Thought: Society of Petroleum Engineers, SPE 115766-PA, 18 p.

Pereira, A.S., Andrade, R.M. and Soares, E.J., 2013. Drag reduction induced by flexible and rigid molecules in a turbulent flow into a rotating cylindrical double gap device: Comparison between Poly (ethylene oxide), polyacrylamide, and xanthan Gum. Journal of Non-Newtonian Fluid Mechanics, v. 202(0), p. 72-87.

Pashin, J.C., Kopaska-Merkel, D.C., Arnold, A.C., and McIntyre, M.R., 2011, Geological foundation for production of natural gas resources from diverse shale formations: Sugarland, Texas, Research Partnership to Secure Energy for America, Final Report, 156 p.

Powers, M.R., 2015, Exploring micro x-ray computed tomography coupled with scanning electron microscopy as tools for Paleozoic shale studies: unpublished M.S. thesis, Oklahoma State University, 108 p.

Rabe, C., da Fontoura, S., Augusto B., & dos Santos Antunes, F., 2002, Experimental study of interaction shale-fluid through immersion tests. Revista de Engenharia Térmica, v.1, no. 2.

Santos, H., Diek, A., da Fontoura, S., and Roegiers, J. C.,1997, Shale reactivity test: a novel approach to evaluate shale-fluid interaction. International Journal of Rock Mechanics and Mining Sciences: v. 34(3), p. 268. e261-268. e211.

Wu, Q., Sun, Y., Zhang, H., Ma, Y., Bai, B., Wei, M. et al., 2013. Experimental Study of Friction Reducer Flows in Microfracture during Slickwater Fracturing: Society of Petroleum Engineers International Symposium on Oilfield Chemistry, SPE 164053-MS, 12 p.

Zeng, Z., and Grigg, R., 2006, A criterion for non-Darcy flow in porous media: Transport in Porous Media, v. 63, p. 57-69.

Zhou, J., Sun, H., Stevens, R. F., Qu, Q.,and Bai, B., 2011, Bridging the gap between laboratory characterization and field applications of friction reducers. Paper presented at the SPE Production and Operations Symposium.